Conference Proceedings

2000 International Conference on

MATHEMATICAL METHODS IN ELECTROMAGNETIC THEORY

MMET 2000

Volume 1

Kharkov. Ukraine

September 12-15,2000

REPORT DOCUMENTATION PAGE

Form Approved OMB No. 0704-0188

1. AGENCY USE ONLY (Leave blank)	2. REPORT DATE	3. REPORT TYPE AND DATES COVERED
ADA 383855	September 2000	Final

4. TITLE AND SUBTITLE

International Conference on Mathematical Methods In Electromagnetic Theory (MMET 2000) Held in Kharkov, Ukraine on September 12-15, 2000. Proceedings, Volume 1.

5. FUNDING NUMBERS

F61775-00-WF084
N68171-00-M-6175

6. AUTHOR(S)

7. PERFORMING ORGANIZATION NAME(S) AND ADDRESS(ES) Source Code: 413809

National Academy of Sciences
Institute of Radiophysics and Electronics
Ulitza Akademika Proskury 12
Kharkov 310085
Ukraine

8. PERFORMING ORGANIZATION REPORT NUMBER

ISBN 0-7803-6347-7

9. SPONSORING/MONITORING AGENCY NAME(S) AND ADDRESS(ES)

European Office of Aerospace Research and Development
PSC 802 Box 14
FPO 09499-0200

10. SPONSORING/MONITORING AGENCY REPORT NUMBER

CSP 00-5084
R&D-8915-EE-02

11. SUPPLEMENTARY NOTES

See also ADA396820 (MMET 2000, Volume. 2). This work relates to Department of the Air Force Grant under Contract No. F61777-00-WF084, issued by the European Office of Aerospace Research and Development. The United States has a royalty-free license throughout the world in all copyrightable material contained herein.

12a. DISTRIBUTION/AVAILABILITY STATEMENT

Approved for Public Release; distribution is unlimited.

12b. DISTRIBUTION CODE

A

12. ABSTRACT (Maximum 200 words)

This is Volume I of the final Conference Proceedings of the 8th International Conference on Mathematical Methods in Electromagnetic Theory (MMET 2000) held in Kharkov, Ukraine on September 12-15, 2000. Topics covered include theoretical and applied aspects of: antenna theory, asymptotic methods, particle beams, complex media, computational techniques, eigenvalue problems, electromagnetic theory, fiber optics, function-theoretic methods, gratings and frequently, inverse problems, lasers, linear accelerator models, nonlinear phenomena, open wavelengths, plasma and waves, radomes, remoting sensing models, waveguide circuits and CAD and more.

13. SUBJECT TERMS

*NUMERICAL METHODS AND PROCEDURES, *ANTENNA ARRAYS, *ELECTROMAGNETISM, SIGNAL PROCESSING, MAXIMUM LIKELIHOOD ESTIMATION, DIELECTRICS, MICROWAVES, ELECTROMAGNETIC WAVE PROPAGATION, ELECTROMAGNETIC SCATTERING, FINITE DIFFERENCE THEORY, INTEGRAL EQUATIONS, TIME DOMAIN, PLANE WAVES, PHASED ARRAYS, WAVE EQUATIONS, UKRAINE, SYMPOSIA
FOREIGN REPORTS, PROCEEDINGS, EOARD, USARDSG-UK

15. NUMBER OF PAGES

16. PRICE CODE

17. SECURITY CLASSIFICATION OF REPORT	18. SECURITY CLASSIFICATION OF THIS PAGE	19. SECURITY CLASSIFICATION OF ABSTRACT	20. LIMITATION OF ABSTRACT
UNCLASSIFIED	UNCLASSIFIED	UNCLASSIFIED	UNCLASSIFIED

Organized and sponsored by

IEEE AP/MTT/AES/ED/GRS/LEO Societies East Ukraine Joint Chapter

in cooperation with

Ukrainian National URSI Committee
Scientific Council of NAS on Radio Physics and Microwave Electronics
Institute of Radio-Physics and Electronics of NAS
Institute of Radio Astronomy of NAS
Kharkov National University

technically co-sponsored by

IEEE AP, MTT and ED Societies
URSI

We wish to thank the following for their contribution to the success of this conference:

IEEE ED, MTT, AP and NPS Societies
IEEE Region 8 Office
URSI
European Office of Aerospace R & D
European Research Office, USARDSG-UK
TICRA

2000 International Conference on Mathematical Methods in Electromagnetic Theory

IEEE Catalog Number: 00EX413
ISBN: 0-7803-6347-7

Library of Congress: 00-01527

This material is based upon work supported by the European Office of Aerospace Research and Development, Air Force Office of Scientific Research, Air Force Research Laboratory, under Contract No. F61775-00-WF084.

MMET*2000 Chairman

Prof. E. I. Veliev, IRE NAS, Kharkov

MMET*2000 Organizing Committee

Prof. V. S. Bakirov, Rector, Kharkov National University

Mrs. N. Y. Bliznyuk, IRE NAS, Kharkov
Conference secretary and Website designer

Prof. V. I. Naidenko, National TU - Kiev Polytechnical Institute
Special representative in Kiev

Prof. A. B. Samokhin, Moscow TU of Radio, Electronics and Automation
Special representative in Moscow

Ms. I. A. Tishchenko, IRE NAS, Kharkov
Proceedings and program editor

Mr. A. D. Ustimenko, IRE NAS, Kharkov

Dr. I. Y. Vorgul, Kharkov National University
Arts and technical assistance

Prof. V. M. Yakovenko, Director, IRE NAS, Kharkov

MMET*2000 Chairman

Prof. E. I. Veliev, IRE NAS, Kharkov

MMET*2000 Technical Program Committee

Co-Chairmen:

Prof. A. I. Nosich, IRE NAS, Kharkov, Ukraine
Dr. W. Ross Stone, IEEE AP-S & URSI, La Jolla, USA

Members:

Prof. T. M. Benson, University of Nottingham, UK
Prof. L. Bertel, Universite de Rennes 1, France
Prof. V. S. Buldyrev, St. Petersburg University, Russia
Prof. N. Engheta, University of Pennsylvania, USA
Prof. F. Gardiol, Ecole Polytechnique, Lausanne, Switzerland
Prof. G. Hanson, University of Wisconsin-Milwaukee, USA
Prof. M. Hashimoto, Osaka Electro-Communication University, Japan
Prof. T. Hinata, Nihon University, Tokyo, Japan
Prof. M. Idemen, Isik University, Istanbul, Turkey
Prof. A. S. Ilinsky, Moscow State University, Russia
Prof. N. A. Khizhnyak, National Center – KIPT, Kharkov, Ukraine
Prof. A. A. Kirilenko, IRE NAS, Kharkov, Ukraine
Prof. K. Kobayashi, Chuo University, Tokyo, Japan
Prof. M. Marciniak, Institute of Telecommunications, Warsaw, Poland
Prof. Z. T. Nazarchuk, PMI NAS, Lviv, Ukraine
Prof. A. G. Nerukh, Kharkov TU of Radio Electronics, Ukraine
Prof. Y. Okuno, Kumamoto University, Japan
Prof. Y. S. Shifrin, Kharkov TU of Radio Electronics, Ukraine
Prof. I. A. Sukhoivanov, Kharkov TU of Radio Electronics, Ukraine
Prof. K. Tanaka, Gifu University, Japan
Prof. O. A. Tretyakov, Kharkov National University, Ukraine
Prof. E. N. Vasiliev, Moscow Power Engn. Institute – TU, Russia
Prof. D. M. Vavriv, IRA NAS, Kharkov, Ukraine
Dr. S. N. Vorobiov, IRA NAS, Kharkov, Ukraine
Prof. T. Yamasaki, Nihon University, Tokyo, Japan
Prof. G. I. Zaginailov, Kharkov National University, Ukraine

CHAIRMEN'S WELCOME

Dear colleagues:

We are very glad to see so many new and familiar faces at MMET*2000, especially of those speakers who have come to MMET for the third and forth time since 1990. This proves that mathematics, computational electromagnetics and physics of microwaves still attract time and efforts of researchers. This also proves that the conference is held at the right place and in the right time. One of the main features of the MMET series of conferences is English as working language. This may be liked or not but it is clear that this single factor has opened many new and exciting opportunities for the scientists of Ukraine and the Former Soviet Union to meet their Western colleagues and communicate in the recognized professional language. Results are seen in the visits, joint projects and publications of Ukrainian scientists and their colleagues from Europe, Japan and USA. Joint papers accepted to the program of MMET are getting common, with some speakers coming from their posts in foreign laboratories. Another feature is accessibility that is guaranteed by convenient location of Kharkov and good transportation network. This city has been for centuries on the crossroads between Ukraine, Russia, Black Sea and the Caucasus and acquired a unique cosmopolitan spirit and broad-mindedness. Still another feature is affordability for low-income participants: registration fee is split into several convenient parts to meet variety of incomes, cheaper accommodations are available. MMET started as a school-seminar for young scientists, and by tradition it keeps a number of absolutely one-of-a-kind opportunities for younger participants. These are reduced registration fee and a moderate travel support, plus a chance of winning an award of the conference that includes a fee waiver for the next meeting. All this would never be possible without very kind and efficient support of a number of international organizations and professional societies.

This year the Technical Program Committee adopted more strict selection criteria. The rate of acceptance of contributed papers was 78% (186 out of 240 submitted). It means that one of every five papers had no chance to be accepted. We hope that their authors will be luckier next time. Local Organizing Committee has shown its best in preparing the proceedings, running the facilities, managing the conference events, and arranging the social program. A new feature was frequently updated Web site of the conference. We are grateful to all the members of LOC and TPC for their contribution to the success of MMET*2000.

Thank you for coming to participate, enjoy the conference, make friends, discuss new joint projects, and plan to attend future MMETs.

Eldar I. Veliev and Alexander I. Nosich

TABLE OF MMET*2000 PAPERS GEOGRAPHY

ENTITY	PAPERS
KHARKOV	80
RUSSIA	48
UKRAINE (non-Kharkov)	20
JAPAN	7
TURKEY	6
POLAND	4
BELARUS	3
ITALY	3
UKRAINE+GERMANY	3
UKRAINE+JAPAN	3
GEORGIA	2
USA	2
UKRAINE+RUSSIA	2
UKRAINE+TURKEY	2
RUSSIA+UK	2
UK	1
The NETHERLANDS	1
TAIWAN	1
BULGARIA+ GERMANY	1
RUSSIA+POLAND	1
UKRAINE+USA	1
UKRAINE+FRANCE	1
UKRAINE+UK	1
UKRAINE+CANADA	1
UKRAINE+ISRAEL	1
UKRAINE+CHINA	1
GEORGIA+USA	1
TOTAL	199

TABLE OF CONTENTS

Volume I

PLENARY SESSIONS

TIME-DOMAIN METHODS

COMPUTATIONAL TECHNIQUES

ANALYTICAL REGULARIZATIONS

SIGNAL PROCESSING

PROPAGATION AND REMOTE SENSING

ANTENNA THEORY

COMPLEX MEDIA, BEAMS AND PLASMAS

Volume II

OPTICAL NETWORKS

SCATTERING AND RADAR CROSS SECTION

GUIDED WAVES

EIGENVALUE PROBLEMS

GRATINGS AND FREQUENCY-SELECTIVE SURFACES

INVERSE AND SYNTHESIS PROBLEMS

IONOSPHERIC ELECTROMAGNETICS

FUNCTION-THEORETIC METHODS

PLENARY SESSIONS

DECOMPOSITION APPROACH TO MULTILAYER CIRCUITS ELECTROMAGNETIC MODELING

Anatoly Kirilenko[1], Protap Pramanick[2], Leonid Rud[1], and Vladimir Tkachenko[1]

[1] Institute of Radiophysics and Electronics of NASU, Ukraine, Kharkov,
fax: 038 0572 441105, e-mail: kirilenko@ire.kharkov.ua
[2] Polar Wave Consulting, Canada

ABSTRACT

A system approach based on transverse resonance technique and well-equipped modeling system is used to calculate eigen-mode spectrum of the multiconductor lines with the piecewise coordinate boundary of cross-section. It serves as the background for calculation of multilayer circuit frequency response by mode-matching and S-matrix techniques.

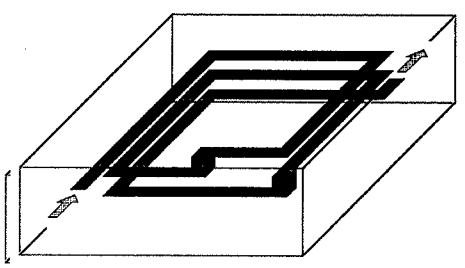

Fig.1

Modeling of multilayer circuits is now a very actual problem in applied electromagnetics [1,2]. It is desirable here to have more flexible algorithms allowing an on-line retuning to some new topology of the cross section within the framework of a unified approach. One of the most popular techniques of computing the eigen modes of the transmission lines of complicated cross- sections is the transverse resonance method that, in fact, reduces to the decomposition of the cross section into fragments with known scattering descriptors (for instance, *S*-matrixes). The availability of modeling systems equipped with tools for electromagnetic "assembling" of scatterers, as well as an advanced library of key elements and archiving, buffering and interpolation tools makes it possible to treat efficiently fairly large classes of problems on the spectrums of eigen modes, at the same time retaining a high effectiveness of solutions. It proves to be close to the effectiveness of the methods being used at computing key elements.

The goal of the given report is to demonstrate a similar unified approach to the calculation of the modes' spectrums of complicated lines and to the analysis of corresponding scattering problems. Here the modeling system *SES-06*, that is based on *C++* classes, is employed both at the stage of building the bases of various lines and at the final stage of calculating the frequency response of the integral circuit. Let us note that the proposed approach to modeling multi-layer circuits allows us also to take into consideration the width of conductors, that was a problem in the algorithm used in the similar situation in [2].

As an example of the object, the calculation of which includes the main features of this technology, let us consider the fragment of the integral circuit as an element of the " inductance " type being put into a rectangular screen. (see Fig. 1). It follows from the very essence of such a scatterer that it naturally splits into a set of regular segments of nonstandard transmission lines that usually have very complicated cross sections (see Fig. 2). The plane junctions couple these lines.

The calculation of the characteristics of the object being treated requires a preliminary analysis of the full spectrum of *TEM*-, *TE*- and *TM*- modes in such lines for their further usage in the projection algorithm of analyzing *S*-matrixes of the plane junctions of such lines. This simplest example already makes it clear that any possible modification of the topology of the above-treated object, for instance, the increase of the number of layers in the integral circuit,

brings a new set of configurations both for the transmission lines themselves and for their junctions. It is clear that the maximum universality can only be achieved on the basis of a well-structured approach which is the transverse resonance method realized on the basis of the corresponding modeling system (in this case the system *SES-06* was used – it is one of the latest versions of *SES-04* described in [3]). As a result, there is a possibility to freely manipulate with the configuration of "assembling" electromagnetic objects.

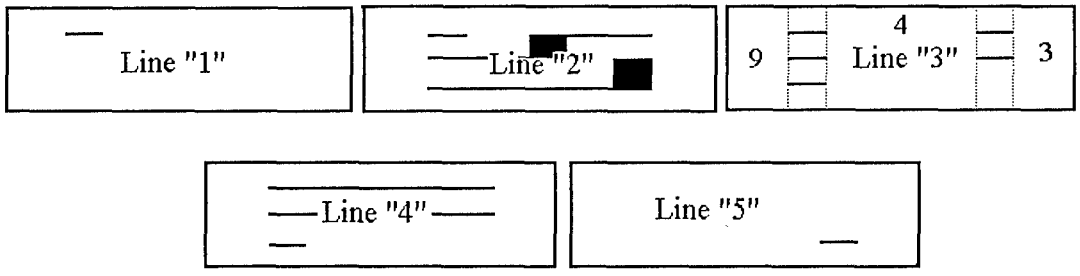

Fig.2

Bases of *TE*-and *TM*- modes.

The calculation of the spectrum of *TE*-and *TM*- modes reduces to the calculation of eigen-frequencies and oscillations of the resonator that is infinite in the longitudinal direction of line under consideration. Matching the fields of partial domains that were formed by the regular segments of the rectangular WG with the help of scattering matrixes of E_z (H_z)-polarized waves on the corresponding steps and bifurcations, we receive two systems of homogeneous equations, nontrivial solutions of which give these desired spectrums for modes of E_z (H_z)-types. However, the well-known idea of transverse resonance requires some comments concerning possible alternatives in the formulation of the dispersion equation. Assuming that the transverse resonance method is known, let us discuss only the three most important solution schemes.

In the simplest **Scheme A,** a homogeneous matrix equation is formulated relevant to the vector $\bar{A}^{(j)}$ of unknown amplitude waves in one of the regular partial domains of the cross section and looks as follows

$$\left(I - S_{left}^{(jj)} E^{(j)} S_{right}^{(jj)} E^{(j)}\right)\bar{A}^{(j)} = 0, \qquad (1)$$

where $S_{left}^{(jj)}$ and $S_{right}^{(jj)}$ are matrixes of reflection correspondingly from the left and the right boundary of a chosen partial domain, $E^{(j)}=diag\left\{\exp\left(i\zeta_n^{(j)}h^{(j)}\right)\right\}$ - is a diagonal transmission matrix dealing with the waves on the segment of a plane WG with the length $h^{(j)}$, $\zeta_n^{(j)} = \sqrt{k^2 - \left(n\pi / a^{(j)}\right)^2}$ -is the constant of propagation in the plane WG of $a^{(j)}$ width.

The advantages of such a scheme in comparison with the others (see below) lie in a smaller amount of time spent on the calculation of the matrix operator determinant in (1), since the calculation of $S_{left}^{(jj)}$ and $S_{right}^{(jj)}$ can by derived by step by step scheme. The disadvantage of Scheme A is the following one: the determinant of the type $\left\|I - S_{left}^{(jj)} E^{(j)} S_{right}^{(jj)} E^{(j)}\right\|$ is characterized by a steep response in the vicinity of the sought-for zeros that, in turn, requires a denser frequency set at the initial localization of roots. The other disadvantage is connected with a possible field localization of one of the oscillations in a domain different from, for instance, a chosen *j*-domain. At the weak electromagnetic coupling of this domain with the

domain of the field localization, a missing zero is here also possible at seeking the roots of the dispersion equation.

Scheme B is used in cases when the cross-section being considered has large-scale domains and one resorts to forming a matrix equation relevant to field vectors in some of them. If we distinguish the domains *9, 4, 0* of *Line 3* (see Fig.2) as dominant, than we pass to a homogeneous system of equations of the type:

$$\begin{pmatrix} I + S^{99}_{(94)}\left(E^{(9)}\right)^2 & 0 & -S^{94}_{(94)}E^{(4)} & 0 \\ S^{49}_{(94)}\left(E^{(9)}\right)^2 & I & -S^{44}_{(94)}E^{(4)} & 0 \\ 0 & -S^{44}_{(40)}E^{(4)} & I & S^{40}_{(94)}\left(E^{(0)2}\right) \\ 0 & -S^{04}_{(40)}E^{(4)} & 0 & I + S^{00}_{(04)}\left(E^{(0)}\right)^2 \end{pmatrix} \begin{pmatrix} \vec{B}^{(9)} \\ \vec{A}^{(4)} \\ \vec{B}^{(4)} \\ \vec{A}^{(0)} \end{pmatrix} = 0, \qquad (2)$$

where $\vec{A}^{(j)}$ and $\vec{B}^{(j)}$ are the amplitudes of forward and back waves in the j domain.

The time for determinant calculation increases in comparison with (1), though the frequency dependence of the latter becomes smoother. Both in Scheme A and especially in Scheme B there are determinant poles on the cutoff frequencies of some domains, that makes the process of searching for the critical frequencies more difficult.

Scheme C does not presuppose preliminary "assembling" of partial elements and is based on the full initial system of equations that describes the couplings between all the vectors of the waves in partial domains with the help of S-matrixes. Since in the general case not all partial domains couple with each other, the matrix operator contains a great number of zero elements. On the one hand, it leads to a more laborious algorithm and to greater time consumption. On the other hand, the determinants being generated by *Scheme C* do not have poles; their frequency dependence is fairly smooth and, on the contrary, decreases calculation time. In the general case, *Scheme C* is also more reliable.

At calculations several dozens of eigen modes of H- and E-types for each transmission line with a complicated cross section are usually taken into consideration. This part of the integral circuit calculation algorithm turns out, for instance, to be more laborious if we lack prior information about the spectrums of these lines. By and large, this procedure consists of two stages: (1) Rough search for the initial approximation for the whole spectrum that in one or another way is based on the analysis of sign variation points in the real and imaginary parts of the complex determinant. In Schemes A and B at the critical frequency, it is typical for one of the two constituents of the complex value determinant really to change its sign, and for the other only to touch the frequency axis. *Scheme B* does not have such problems, since both the real and the imaginary part of the complex determinant change their signs at the corresponding points. (2) The search for the spectrum of the precise values of critical frequencies is based on *Newton* method and on a special algorithm of a gradual building the wave bases being used. At each stage of such an algorithm, a simultaneous refinement of the whole cutoffs' spectrum is carried out.

TEM-MODE BASIS

The transverse resonance method can be also used for determination of the fields of *TEM*-modes, including those multiply degenerate. In fact, we are dealing with the determination of the cross (to the resonator axis) field of the resonator's main oscillation that was formed by $\lambda_0/2$ – section of the corresponding transmission line at the resonance frequency $f_0 = c/2d$, where c -is the light velocity in free space, d -is the resonator length. The conditions of the transverse resonance are formed for the packages of H_{m1} – and E_{m1} – waves that resonate in

the volume built by the sections of the rectangular WG with the dimensions $a^{(j)} \times d$ and lengths $h^{(j)}$. The same approach was repeatedly used in the case of single-conductor transmission lines with internal conductors of various forms (see, for instance, [4]).

If the line being analyzed has N internal conductors, than there is a problem with determination of the package eigen-fields *N*-times degenerated *TEM*-modes. To eliminate degeneration of the eigen frequencies of $\lambda_0/2$ – resonators, an artificial approach was used that consists in the insertion of discontinuities on the end resonator walls. Steps of $\Delta_j/2$ height were inserted to both end walls for rarefaction of the field space spectrum in the resonator.

Let us indicate the critical frequency of H_{01} – wave in the partial domain "*i*" where the steps are inserted as $f_0^{(i)} = c/2(d - \Delta^{(i)})$, and the spectrum of "shifted" eigen frequencies as $f^{(k)}$, $k = 1,2,...N$. It is easy to notice that $f_0 \le f^{(k)} \le f_{0,\max}^{(i)}$, where $f_{0,\max}^{(i)}$ corresponds to the domain with the minimum value $\Delta_{\max}^{(i)}$. Together with it, each new value generates the new frequency of the H_{01} – wave cutoffs, and also an additional "false" determinant zero. All in all, the final problem lies in the determination of the roots of the dispersion equation on the interval $f_0 \le f \le f_{0,\max}^{(i)}$. The choice of equal $\Delta_i = \Delta$ that "brings" determinant false zeros to the boundary of the search domain $f_0 \le f \le f_{0,\max}^{(i)} = c/2(d - \Delta)$ makes the task of determining the spectrum of *TEM*-modes much easier.

At the real choice of dimensions of the "end steps", one should take into account two factors. On the one hand, it is desirable to choose the value Δ as small as possible, in order to, firstly, minimize the difference of the object being viewed from the non-perturbed $\lambda_0/2$-resonator in general, and, secondly, in order to reduce the level of H_{mq} – and E_{mq} – waves with $q = 3,5,...,$ in particular. Let us note that already at $\Delta/d \approx 10^{-2}$ the amplitudes of H_{m3} and E_{m3} waves in the found spectrum of Fourier-expansion of the *TEM*-oscillation turn out to be three or four orders lower than the amplitudes of H_{m1} and E_{m1} waves. Let's point out that the technique of searching for the degenerate *TEM*-modes package used here simultaneously deals away with the well-known orthogonalization problem, since the found field distributions are orthogonal within $10^{-5} \div 10^{-6}$.

To check the adequacy of the data being obtained a series of internal criteria was developed. It is clear that at integrating E_x – or E_y – components along L "from screen to screen" one can estimate the value of field "potentiality" for the found *TEM*-mode. It turned out that already taking account of $10 \div 15$ members in the Fourier field decompositions corresponding conditions are met accurate not worse than to $10^{-6} \div 10^{-7}$.

FIELDS OF EIGEN-MODES

In the approach that was used here the cross section of the p-WG - C_p is presented as a sum of partial subdomains $C_p^{(j)}$, $j = 0,1,...J$, where each of them has two metallized walls and can be given with a set of values $x_p^{(j)}, y_p^{(j)}, a_p^{(j)}, h_p^{(j)}$ that describe the coordinates of the origin, the width and the length of the corresponding WG segment. Practically C_p is given with some matrix of G_p values that contain the numbers of domains and their coordinates. The fields of

eigen modes are described in each of such subdomains by a set of the amplitudes of waves in the corresponding plane WGs (while calculating *TE*- and *TM*-modes) or rectangular WGs (in the case of *TEM*-modes). These amplitudes are nontrivial solutions of homogeneous matrix equations at transverse resonance frequencies and can be found with the aid of a special procedure. The latter is used in case there is lack of any data concerning possible field structure, when the type of the coefficient being extracted can not be given «a priori» and the search for minor with the determinant maximum value is required.

Fig. 3,4 depicts brightness electric fields' distributions for some eigen modes of lines with various complicity (lighter domains correspond to more intensive fields). Fig.3 shows *E*-field

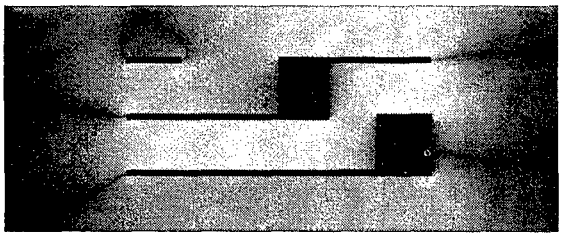

Fig.3 Field of one of TEM-modes(E_x)

Fig.4 Field of one of *TM*-modes (E_z)

distribution for one of *TEM*-modes in the three-conductor *Line2*. In the case of lines with a very complicated geometry, it is difficult to speak about any classification of the modes inside *TE(M)*s. However no doubt it is possible to find some analogy between E_z-component distribution of the sixth *TM*-mode represented in Fig. 4 and the field of TM_{31}-mode of rectangular WG. The field of this mode takes only the right part of WG cross-section.

CALCULATION OF PLANE-PARALLEL JUNCTIONS

To calculate the scattering matrix of the plane junction in two multi-wire lines a traditional projection procedure has been used. (See, for instance, [5]). At calculating the coupling integrals a preliminary analysis of reciprocal crossings of partial subdomains of the enclosing *0*-WG and the *p*-WG being enclosed is required. The thing is that in contrast to the junctions of the WGs with "simple" cross sections (*П*-, *H*-, the rectangular coaxial), where these crossings are obvious, their determination for a pair of WGs with fairly exotic cross sections requires a separate procedure. The implementation of the projection procedure thus starts with the determination of the matrix of the D_{0p} crossings that contain the coordinates crossing area along the matrixes G_0 and G_p that give the configuration of the plane junction.

NUMERICAL REALIZATION

The program realization of the complex of numerical algorithms the basic moments of which are described above was performed on *C++* as the part of the modeling system *SES-06*. The main parameters that determine calculation accuracy were the lengths of projection and descriptor (in the S-matrixes method) bases, as well as, $M^{(j)}$-the number of waves taken into account in expansions for the fields of eigen modes. Below the data are cited those tentatively characterize calculation accuracy and required resources.

As an example, a four-layer integral circuit is considered that is depicted in Fig.1 with the following dimensions: the thickness of one layer is - 3.7 *mil*; the thickness of conductors is - 0.037 *mil*; their width is - 10 *mil*; the gap between the conductors of inductance in the parallel and transverse direction is 35 *mil*; the dimensions of the screen are - 14.8×120 *mil*; the relative

dielectric permittivity of the ceramic surface is- 7.8. In order to range the size of the bases in different lines, the condition of proximity of highest transverse wave numbers in each line to some general value $\widehat{k}$ was used.

At $\widehat{k}=20.5$, for instance, *Line1* basis encloses only one *TEM*-mode, 50 *TE*-modes and 27 *TM*-modes, and basis *Line 4* basis – 3 *TEM*-modes, 60 *TE*-modes and 16 *TM*-modes. Calculation time of the mode bases on *IBM PC* (500 MHz) for each line makes up from one (for *Line1*) to five (for *Line 2*) hours. The calculation of the matrix of coupling integrals for all line junctions requires up to an hour, and the further calculation of the frequency response of the whole "inductance" in 250 points – up to 50 minutes.

The quality of the mode basis being calculated depends on many factors, for instance, already at $M^{(j)}=20\div25$ we get that *TEM*-, *TE*- and *TM*- modes of small numbers (up to $5\div6$) are orthogonal accurate to the values $10^{-4}\div10^{-6}$.

Table1 illustrates the convergence of the calculation results with the increase of the mode numbers in the basis, the length of which in general is determined by the limit wave number value $\widehat{k}$. For a frequency of 1 *GHz* the transmission coefficients of the first *TM*-mode for the junction *Line 1* and *Line 2* are given. Though the mode constitution of lines taking part in calculation is quite complicated, the convergence of the numerical results is apparently quite good.

Table 1

$\widehat{k}$	10.0	15.0	20.5
$S^{21}_{E1,E1}$	0.4547 (i0.043)	0.4416 (i0.021)	0.4423 (i0.020)

The frequency response of "inductance" shown in Fig. 1 was calculated in wide frequency band up to the frequencies, where the input and output rectangular bar lines become multi-mode. A breakdown of response monotony and vivid peaks of the reflection coefficient were noted after 5 GHz and were apparently caused by the resonances of TEM-modes along the full length of the "inductance" conductor or with the resonances within the circuit formed by the inductance itself and intermediate capacities.

CONCLUSION

The idea of the project was not to achieve the limit indexes in speed and accuracy while calculating a complicated WG object with a fixed configuration. It is clear that direct use of projection approaches for solving the corresponding homogeneous problems will provide an advantage in calculation time. Our goal was to develop the tools that allow "in whole" (from algorithm development up to concrete results) a rapid estimation of electromagnetic properties and potential of specified configurations.

REFERENCES

[1] R.Bunger, F.Arndt, Efficient MPIE approach for the analysis of 3D mircostrip structures in layered media, IEEE Trans. on MTT, v. 45, No.8, 1997, 1141-1153.

[2] A.Khalil, A.B.Yakovlev, M.Steer, Efficient method of moments formulation for the modeling of planar conductive layers in a shielded guided wave structure, IEEE Trans. on MTT, v. 47, No.9, 1999, 1730-1736.

[3] A.Kirilenko, V.Tkachenko, System of electromagnetic modeling for microwave-millimeter wave devices, Isv.VUS. "Radioelectronica", v.39, No.9, 1996, 17-28.(in Russian, "Radioelectronics and Communications Systems" in Engl. transl.).

[4] H.Wang, K.L.Wu, J.Litva, A modal analysis of TEM mode in circular-rectangular coaxial WGs, IEEE Trans. on MTT, v. 47, No.3, 1999, 356-359.

[5] A.Kirilenko, D.Kulik, L.Rud', V.Tkachenko, The full-wave model for plane junction of waveguides with piecewise linear coordinate boundaries, Proc. of the 3rd Int.Conf on Ant. Theory and Techn., Sevastopol, Ukr., 1999, p.499-501.

FIBER MODE BEHAVIOUR NEAR THE CUTOFF FREQUENCY: DISPERSION CHARACTERISTICS, MODELLING AND APPLICATIONS

Elena A.Romanova, Ella V.Bekker, Phillip Sewell* and Trevor M. Benson*

Saratov State University,
Astrakhanskaya 83, 410026 Saratov, Russia
E-mail:romanova@optics.sgu.ru

*University of Nottingham,
Nottingham NG7 2RD, U.K.
E-mail:Trevor.Benson@nottingham.ac.uk

ABSTRACT

The spatial transient regime of a fiber mode transformation near the cutoff frequency is analyzed both theoretically and numerically depending on material losses and radial distribution of refractive coefficient of a guiding structure. Kerr-like nonlinearity of a fiber material is shown to be efficiently used to manage the transmittance of the structures near the cutoff frequency of a fiber mode.

INTRODUCTION

When a lossless fiber mode reaches the cutoff, it's longitudinal power flow ceases to decrease radially, and the mode propagates as a plane wave in the fiber cladding. What happens when the characteristic frequency gets lower than the cutoff one? Mathematically, all propagation constants of the mode become complex denoting that transverse power flow appears and radiation leaks out the guiding region. Behavior of a fiber mode near the cutoff frequency (leaky mode) is known to depend on its polarization [1]. The HE_{1n} modes of a step-index fiber have the following kind of behavior: the mode field doesn't tend to zero at $r \to \infty$, the power flow increasing very rapidly as $V \to V_c$. Characteristic equation has the following asymptotic form: $w^2 lnw - 2 = 0$, which differs from the one of the other types of fiber modes. Behavior of the HE_{1n} (LP_{0n}) modes of a weakly guiding fiber was analyzed [2] by numerical solution of the characteristic equation near the cutoff value of the characteristic frequency. The multisheeted Riemann surface of the Macdonald's function has been taken into consideration. Behavior of the dispersion curves was shown to depend on the material losses, the curves corresponding to the lossless fiber being located on the infinite sheet of the Riemann surface. The cutoff value of the characteristic frequency was shown to depend on the magnitude of material losses [3].

Guiding properties of multilayered fibers were analyzed in [4] depending on the radial profile of the refraction coefficient. Full-vectorial mode solver was used to calculate the modal numbers of the fiber modes. These modal numbers were shown to be complex in general and tended to be real as the radiation wavelength decreased.

Other phenomena which can change the guiding properties of a fiber is self-focusing of the propagating radiation resulting from Kerr-like nonlinearity of a fiber material. The

complicated interaction of nonlinear fiber modes is shown [5] to destroy the higher modes even in a regular fiber.

The first part of this paper is a review of some numerical and semi-analytical techniques useful to analyze mode behavior and spatial transient processes of the total field propagation in waveguiding structures including into consideration longitudinal irregularities, losses and Kerr-like nonlineraity of the fiber material, radial dependence of the refraction coefficient. In the second part the results of calculations are shown and some structures are analyzed comparatively by numerical simulations of the guided modes transformation into the leaky ones.

METHODS OF INVESTIGATION

1.Characteristic equation solution near the cutoff frequency

The amplitude of the total time-harmonic scalar field propagating along the z-axis of an irregular linear fiber can be written as a sum of the discrete set of N_g guided waves and the radiation field [6] (in the case of small discontinuities in the weakly-guiding fiber, the backscattering can be neglected):

$$E(r,z) = \sum_{n=1}^{N_g} A_n(z) E_n(r) \exp(i\beta_n z) + E_{rad}(r,z), \tag{1}$$

$$E_{rad}(r,z) = \sum_{j=1}^{\infty} \int_0^{\infty} dw A_j(w,z) E_j(w,r) \exp(i\beta_j(w) z) \tag{2}$$

with A_n and β_n being the amplitudes and the longitudinal wavenumbers of the *n -th* guided mode, A_j and β_j being the amplitudes and the longitudinal wavenumbers of the *j-th* radiation mode. The functions $E_n(r)$ and $E_j(w,r)$ describe radial distributions of the guided and the radiation modal fields, respectively. The integrands $E_j(w,r)$ are meromorphic functions on the multi-sheet Riemann-surface of the complex parameter w, which is treated as the cladding transverse wavenumber of a fiber mode [6]. The poles of the functions $E_j(w,r)$ correspond to the leaky modes and are located in the w -plane depending on the value of the characteristic frequency $V = ka\sqrt{n_{co}^2 - n_{cl}^2}$ determined in the given cross-section of the fiber (here $k = 2\pi/\lambda$ is the free-space wavenumber, a is the radius of the fiber core, n_{co} and n_{cl} are the refraction indices in the core and in the cladding, respectively). Each pole formally is a solution of the characteristic equation of the eigenvalue problem and characterizes the field which increases exponentially in the radial direction.

In the simple case of step-index fiber with infinite cladding the characteristic equation is well known to be of the transcendental form and can be solved numerically by an iteration method of Newton-Raphson. The complex w-plane was shown to be convenient [7] to analyze the solution behavior depending on the characteristic frequency taking into consideration losses of the fiber material.

In order to analyze all-dielectric fibers having a uniform glass core and a multilayered infinite cladding the following semi-analytical technique can be applied. In each layer, $r_{i-1} < r < r_i$, the fields can be decomposed [8] into the sets of Hankel functions such that:

$$E_z(r) = A_i H_n^{(1)}(k_{ti} r) + B_i H_n^{(2)}(k_{ti} r), \tag{3}$$

where

$$A_i = \frac{\left[H_n^{(2)}(k_{ti}r_{i-1})E_z(r_i) - H_n^{(2)}(k_{ti}r_i)E_z(r_i)\right]}{\left[H_n^{(1)}(k_{ti}r_{i-1})H_n^{(2)}(k_{ti}r_i) - H_n^{(1)}(k_{ti}r_i)H_n^{(2)}(k_{ti}r_{i-1})\right]},$$

$$B_i = \frac{\left[-H_n^{(1)}(k_{ti}r_{i-1})E_z(r_i) + H_n^{(1)}(k_{ti}r_i)E_z(r_i)\right]}{\left[H_n^{(1)}(k_{ti}r_{i-1})H_n^{(2)}(k_{ti}r_i) - H_n^{(1)}(k_{ti}r_i)H_n^{(2)}(k_{ti}r_{i-1})\right]}$$

and $H_n^{(i)}(x)$ is the Hankel function of the *n-th* order of the *i-th* kind. $E_z(r_i)$ is the value of E_z at $r = r_i$, and $k_{ti}^2 = n_i^2 k_o^2 - \beta^2$, where β is a longitudinal propagation constant of the field. A similar expansion can be found for H_z. It is noted that in the core ($r < a$) and outer cladding regions ($r > a + (d_1 + d_2)N - d_2$) the expression (1) simplifies to:

$$E_z(r) = \frac{E_z(r_1)}{J_n(k_{t1}r_1)} J_n(k_{t1}r) \quad , E_z(r) = \frac{E_z(r_N)}{H_n^{(2)}(k_{tN}r_N)} H_n^{(2)}(k_{tN}r) \tag{4}$$

From these expressions it is straightforward to derive the tangential field components E_θ and H_θ on each side of the boundaries between the layers in terms of the values of E_z and H_z at the boundaries. Requiring continuity of E_θ and H_θ yields a matrix equation whose determinant will only be zero if β is a modal propagation constant.

2. Numerical simulations of the spatial transient regime of the total field propagation by Beam Propagation Methods.

The most commonly used numerical method to solve the scalar wave equation is the split-step Fourier series method which is in fact an extension of the beam propagation method (BPM) originally developed by Fleck, Morris and Feit [9]. Physically the technique corresponds to replacing the continuous refractive index distribution by an infinitesimally thin lens emerged in a homogeneous reference medium of uniform refractive index.

Conventionally to utilize this method in solution of the wave equation an algorithm is employed which is based on the fast Fourier transformation (FFT) algorithm. The so called beam propagation method (FFT-BPM) proved to be an accurate and efficient tool for solving a variety of propagation problems in waveguide geometries involving one or two transverse Cartesian coordinates. However, in application of this method in cylindrical coordinates one has to cope with the increased storage and reduced efficiency.

An alternate numerical scheme to solve the wave equation is to use a finite difference (FD) approximation [10]. Following the Finite-Difference Beam Propagation Method (FD-BPM) the wave equation is replaced by a finite-difference scheme.

In this work, the finite-difference beam propagation method (FD-BPM) is used, based on the implicit representation of derivatives and recursive procedure known as the sweep-method [11]. Following the weakly-guiding approximation we assume the amplitude of the total electrical field $F(r,z)$ to be slowly varying in axial direction, so that: $E(r,z)=F(r,z)exp(i\beta' z)$, where β' is the real part of the longitudinal wavenumber determined at the input endface of the structure. Propagation of the electrical field in a circularly-symmetric step-index weakly-guiding fiber is characterized by the scalar wave equation for the slowly varying amplitude :

$$\left(2i\frac{\partial}{\partial z} + \frac{\partial^2}{\partial r^2} + \frac{1}{r}\frac{\partial}{\partial r} + \chi\right)F(r,z) = 0 \tag{5}$$

with the normalized radial and longitudinal coordinates $r \to r/a$, $z \to z/z_d$. The diffraction

length $z_d = \beta' a^2$, with a being the core radius determined at the input endface of the fiber. The boundary conditions for the problem are taken to be as follows: $F(\infty,z)=0$, $\partial F(0,z)/\partial r=0$. To avoid nonphysical reflections from the grid boundaries, a complex scaling has proved to be suitable [12].

ANALYSIS OF THE GUIDED MODE TRANSFORMATION INTO THE LEAKY ONE IN DIFFERENT GUIDING STRUCTURES.

1.Down-tapered dielectric fiber.

Numerical techniques described above were used to analyze HE_{1n} mode behavior when it propagates through the cutoff cross-section. The model of a down-tapered fiber with a step-index profile of refraction coefficient and infinite cladding appeared to be suitable for this purpose.

Several dispersion curves representing a path of roots of the characteristic equation are shown in the Fig.1. The value of $V'(z)$ varies along every curve, the value of V'' being fixed. The roots which are located in the *zero-th* sheet are marked by the empty circles, the roots in the first sheet are marked by the filled ones. Assume that some initial value of V' is above the cutoff. When V' decreases (this direction is indicated by arrows), the root moves to the point $w=0$. Behavior of the dispersion curves depends evidently on the losses of the fiber material (the curves 1-3 are obtained with $V''=-0.07$,-0.062, -0.005, correspondingly). The curves can turn several times around the point $w=0$, the number of such turns depending on the losses. In the limit case of nonabsorbing waveguide the number of turns is infinite.

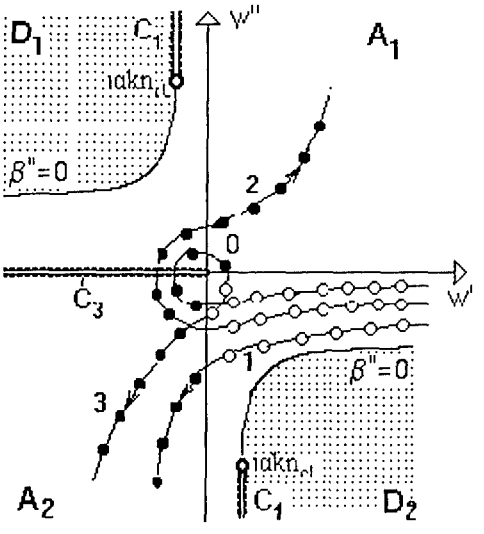

Fig.1.

Propagation of HE_{12} mode along a taper with the length L and the linear longitudinal profile $a(z) = a_1 - \Delta a z / L$ was simulated numerically by FD-BPM. The transverse profile of the field at the input end face of the taper corresponds to the guided HE_{12} mode of a regular step-index fiber with a core radius a_1. The fiber mode is supposed to be excited by a light source with the wavelength λ=1mμ. The corresponding range of the characteristic frequency variation is $3.7<V(z)<4$ containing the cutoff value (for the lossless fiber $V_c \approx 3.83$).

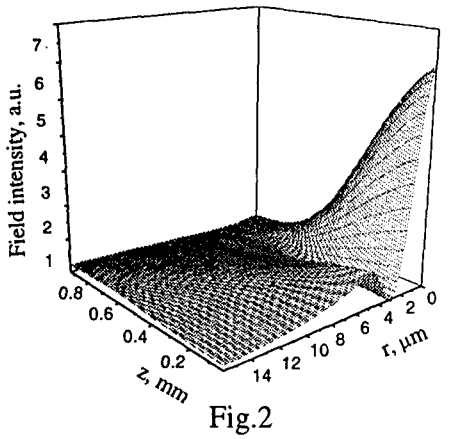

Fig.2

When the fiber radius decreases the wavenumber moves along the dispersion curve and crosses the w''-axis. Accordingly, the guided mode reaches the cutoff cross-section of the taper, passes through it, and forms a spatial wave which goes outsize the fiber core (Fig.2).

However, a part of the radiation which propagates below the cutoff close to the fiber core is of the same transverse distribution as the guided mode was. The total field can be sufficiently described here by the leaky mode field. It propagates over some long distance along the fiber core since the imaginary part of the

longitudinal modal number $\beta'' \approx 10^{-5}$ μm^{-1}. Far from the fiber axis, the radiation field is finite, and goes to zero at infinity.

2. Multilayered all-dielectric fibers.

Multilayered dielectric two-dimensional structures have been used mainly to lower the losses in hollow metallic waveguides [13]. The guiding properties of all-dielectric hollow waveguides were studied recently [4,14].

In this paper we analyze all-dielectric fibers having a uniform glass core and a multilayered infinite cladding as potential bandgap structures. The structure consists of *2N - 1* concentric dielectric layers. The cross-section of the waveguide is presented in Fig.3 together with its refractive index profile. The number of pairs N of adjacent layers with different indices is assumed to be finite and variable.

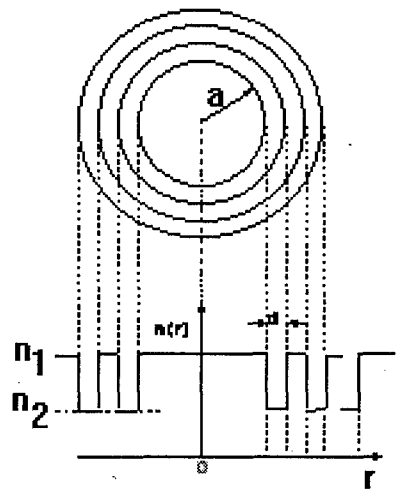

Fig.3

The layered part of the structure is surrounded by an infinite uniform dielectric cladding having the same refractive index as the core. Two different structures were

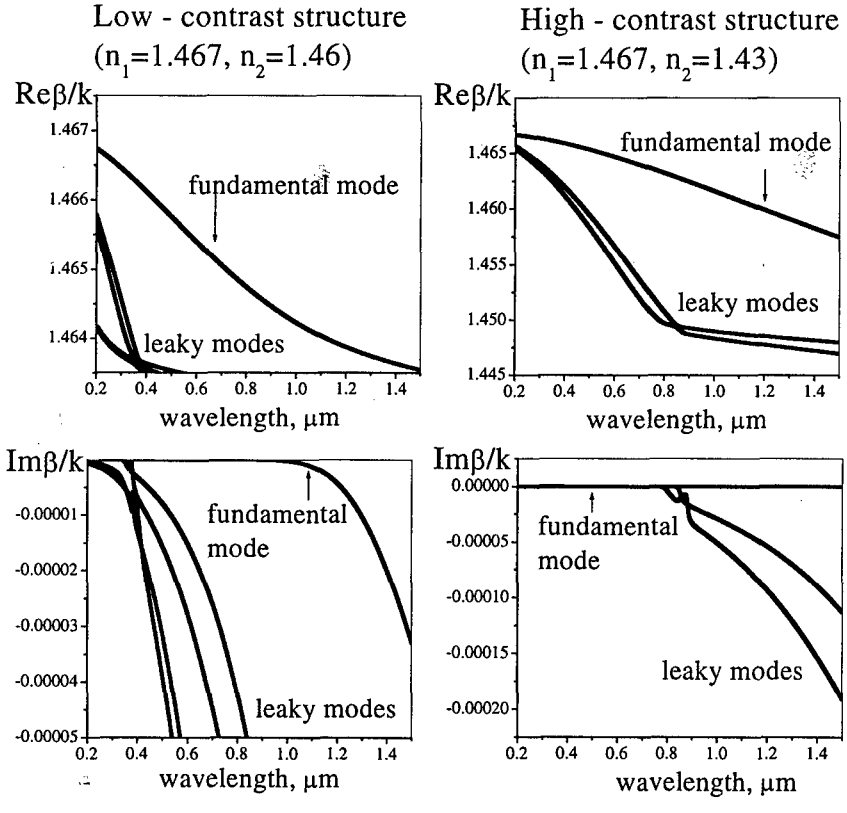

Fig.4

considered using this method. These had low- and high- index contrast in the cladding respectively and $a = 2.5\mu m$, $d_1 = 0.5\mu m$, $d_2 = 0.5\mu m$, $N = 15$. Two types of complex solutions were identified – the modes with $Im\beta/k < 0.1dB\ km^{-1}$ which can be treated as the

as the guided ones and a variety of closely located roots corresponding to leaky waves. The most significant roots are shown in Fig.4. The fundamental mode behaves as the guided one over a wide range of wavelengths depending on the refraction index contrast $(n_1 - n_2)$. The leaky modes transform into the guided ones as the wavelength decreases.

3.Regular fiber with Kerr-like nonlinearity.

When a beam passes through the dielectric medium with a Kerr-like nonlinearity, the refraction coefficients n_{co} and n_{cl} depend on the intensity of the electric field as $n = n_1 + n_2 |F(r,z)|^2$, where n_1 is the linear coefficient and n_2 is the positive nonlinear coefficient. This changes the guiding properties of the structure, resulting in beam self-focusing.

Nonlinear mode propagation was considered based on the model of a double-mode fiber $(V=4.47)$ excited by a linear HE_{12} mode of the regular fiber. When the fiber is linear, the radial distribution of the field doesn't vary along the fiber axis (see Fig.5). In the presence of Kerr-like nonlinearity ($2n_1\eta|F|^2 \sim 0.2$) a small part of the input field transforms into another mode. Two modes interact over some distance. Then just one mode is left to propagate, its radial distribution being of the gaussian-like shape similar to the fundamental mode of a linear fiber.

Linear fiber: Nonlinear fiber:

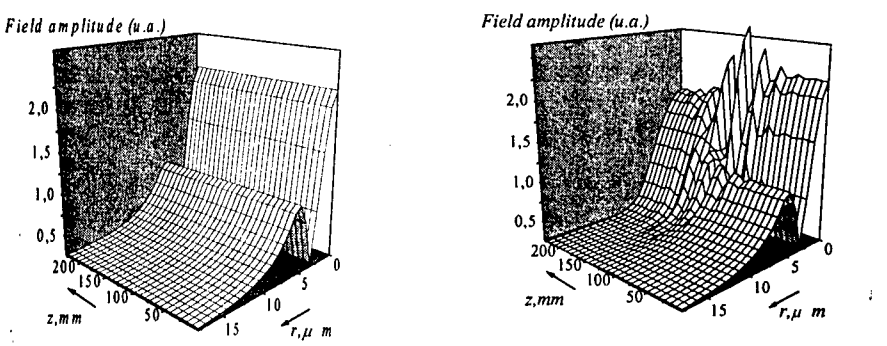

Fig.5

Propagation of the total field through the cutoff cross-section of the linear HE_{12} mode in the down-tapered fiber with a Kerr-like nonlinearity is depicted in Fig.6. The taper was assumed to be excited by a linear HE_{12} mode of the regular fiber with the core radius a_1. The intensity-dependent term was taken to be of the order of $\Delta n = n_{co} - n_{cl}$, the structure dimensions were as follows: $L=3mm$, $a_1 = 5\ \mu m$, $\Delta a = 1\ \mu m$, (a)-lossless fiber, (b) -lossy fiber. It is seen clearly that the radiation field expansion is suppressed by the nonlinear

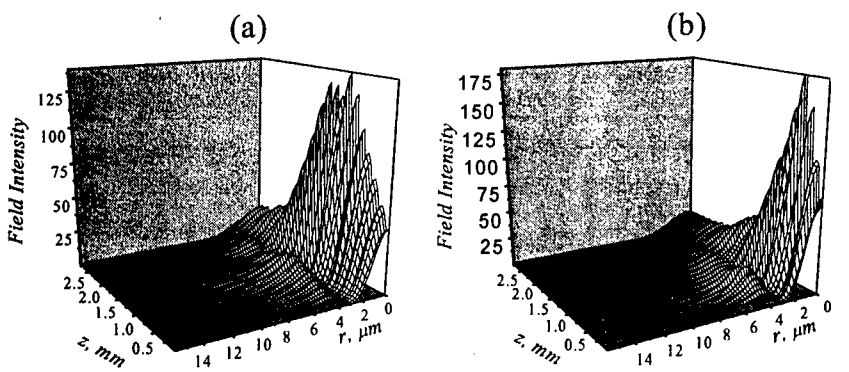

Fig.6

contraction of the beam resulting in the propagation of the HE_{12} mode through the cutoff to depend on the amplitude of the input field. The high intensity beam may experience a transformation from the guided mode into the gaussian-like nonlinear guided mode of the fiber.

CONCLUSIONS

Spatial transient regime of a guided mode transformation into the leaky one is shown to depend on the features of the guiding structure material: losses, Kerr-like nonlinearity, and radial distribution of the refractive coefficient. In the presence of material losses, behavior of a mode near the cutoff cross-section of the lossy fiber becomes more complicated comparing with the lossless one. The length of the transient regime in the lossy fiber is less than the one predicted by the theory of lossless fibers.

Including some layered structure into the fiber cladding one obtains a tool for efficient management of the guiding properties of the fiber. The cutoff value of radiation frequency is proven to depend on the radial distribution of refractive coefficient of the multilayered structure.

Kerr-like nonlinearity of the fiber material causes the nonlinear interaction of the guided modes resulting in transformation of the higher modes into the fundamental one. Transmittance of the nonlinear structures depends on their geometry and can be managed by the appropriate adjustment of their spatial parameters.

The phenomena analyzed above can be efficiently applied for elaboration of novel logical elements, large-core amplifiers, mode-locked fiber lasers.

REFERENCES:

[1] IEICE Trans. Electron., vol. E78-C, No.10, 1323-1329.
[2] Opt.Commun., 116(1995) 358-364.
[3] Microwave Opt.Technol.Lett 25(2000), 27-33.
[4] International Conference on Transparent Optical Networks, 2000, Gdansk, Poland, 57-60.
[5] International Conference on Transparent Optical Networks, 2000, Gdansk, Poland, 69-72.
[6] A.W.Snyder and J.D.Love, Optical Waveguide Theory, Chapman & Hall, London, England, 1983.
[7] Sov.J.Radioteknics Ekectron.14 (1969), 1768-1770.
[8] R.E.Collin, Field Theory of Guided Waves. IEEE Press.1991.
[9] Appl.Phys., V.10, pp.129-160, 1976.
[10] J.of Quantum Electron., V.26, N.8, pp.1335-1339, 1990.
[11] A.N.Tihonov and A.A.Samarskii, Equations of mathematical physics, Nauka, Moscow, Russia, 1972.
[12]Comput.Phys.Commun. 63(1992), 323-330.
[13] J. Lightwave Technol., LT-2, pp.116-126, 1984.
[14] J. Lightwave Technol., LT-17, pp. 2039-2041, 1999.

FRACTIONALIZATION METHODS AND THEIR APPLICATIONS TO RADIATION AND SCATTERING PROBLEMS

Nader Engheta
University of Pennsylvania
Moore School of Electrical Engineering
Philadelphia, Pennsylvania 19104, U.S.A.
Tel: +1 (215) 898-9777, Fax: +1 (215) 573-2068
E-mail: engheta@ee.upenn.edu
Web: http://www.ee.upenn.edu/~engheta/

INTRODUCTION:

Exploring the possible links between the mathematical field of fractional calculus and the electromagnetic theory has been one of the topics of our research interests in recent years. We have studied the possibility of bringing the tools of fractional calculus and electromagnetic theory together, and have explored and developed the topic of *fractional paradigm in electromagnetic theory* (see e.g., [1-10]). Fractional calculus is a branch of mathematics that addresses the mathematical properties of operation of fractional differentiation and fractional integration – operators involving derivatives and integrals to arbitrary *non-integer* orders (see e.g., [11-13]). In our study in recent years, we have applied the tools of fractional calculus in various problems in electromagnetic fields and waves, and have obtained interesting results that highlight certain notable features and promising potential applications of these operators in electromagnetic theory [1-10]. Moreover, since fractional derivatives/integrals are effectively the result of fractionalization of differentiation and integration operators, we have investigated the notion of fractionalization of some other linear operators in electromagnetic theory. Searching for such operator fractionalization has led us to interesting solutions in radiation and scattering problems.

"FRACTIONAL SOLUTIONS" IN RADIATION AND SCATTERING PROBLEMS

Let us consider the time-harmonic Maxwell equations $\nabla \times \boldsymbol{E} = i\omega \boldsymbol{B}$, $\nabla \times \boldsymbol{H} = \boldsymbol{J} - i\omega \boldsymbol{D}$, $\nabla \cdot \boldsymbol{D} = \rho$, and $\nabla \cdot \boldsymbol{B} = 0$ where the time dependence $e^{-i\omega t}$ is assumed, and the electric current density $\boldsymbol{J}$ may be considered either as a primary current source (in radiation problems) or as a secondary, induced current (in scattering problems). The continuity equation is of course satisfied as $\nabla \cdot \boldsymbol{J} = -i\omega\rho$. Now let us choose a linear operator $\underline{\underline{\boldsymbol{L}}}$ from a class of linear operators (or mappings) where the domain and range of any linear operator of this class are similar to each other and have the same dimensions. In other words, the linear operator $\underline{\underline{\boldsymbol{L}}}$ should map an element from the space C^n into generally another element in the space C^n. That is

$$\underline{\underline{\boldsymbol{L}}} : C^n \rightarrow C^n \tag{1}$$

where C^n is an n-dimensional vector space over the field of complex numbers. One can then suggest a "fractional" operator $\underline{\underline{L}}^{\nu}$, where the fractionalization parameter ν can be a noninteger real number (or in some circumstances even complex number), using some techniques one of which is reviewed in [5]. Such a fractional operator $\underline{\underline{L}}^{\nu}$, which also maps the n-dimensional space into the n-dimensional space

$$\underline{\underline{L}}^{\nu} : C^n \to C^n \tag{2}$$

has the semigroup properties, i.e., (1) for $\nu \to 0$, the fractional operator $\underline{\underline{L}}^{\nu}$ approaches the unit operator, $\underline{\underline{L}}^{\nu} \to \underline{\underline{L}}^{o} = \underline{\underline{I}}$; (2) for $\nu \to 1$, the operator $\underline{\underline{L}}^{\nu}$ approaches the original operator $\underline{\underline{L}}$, $\underline{\underline{L}}^{\nu} \to \underline{\underline{L}}^{1} = \underline{\underline{L}}$; and (3) for two parameters ν_1 and ν_2 we will have $\underline{\underline{L}}^{\nu_1} \circ \underline{\underline{L}}^{\nu_2} = \underline{\underline{L}}^{\nu_1+\nu_2}$. If the vector fields $\boldsymbol{E}_o$, $\boldsymbol{H}_o$, $\boldsymbol{B}_o$, and $\boldsymbol{D}_o$ are the solutions to the time-harmonic Maxwell equations with the current density $\boldsymbol{J}_o$, one can pose the following question: If we apply the fractional operator $\underline{\underline{L}}^{\nu}$ on these vector solutions, under which condition(s) will the resulting vector functions, $\underline{\underline{L}}^{\nu}\boldsymbol{E}_o$, $\underline{\underline{L}}^{\nu}\boldsymbol{H}_o$, $\underline{\underline{L}}^{\nu}\boldsymbol{B}_o$, and $\underline{\underline{L}}^{\nu}\boldsymbol{D}_o$ satisfy the Maxwell equations with the new current density $\underline{\underline{L}}^{\nu}\boldsymbol{J}_o$? One can observe that if the fractional operator $\underline{\underline{L}}^{\nu}$ and the curl operator $\nabla\times$ commute, i.e., if

$$\underline{\underline{L}}^{\nu}\nabla\times = \nabla\times\underline{\underline{L}}^{\nu}, \tag{3}$$

one will then have

$$\begin{aligned} \nabla\times\left(\underline{\underline{L}}^{\nu}\boldsymbol{E}_o\right) &= i\omega\left(\underline{\underline{L}}^{\nu}\boldsymbol{B}_o\right) \\ \nabla\times\left(\underline{\underline{L}}^{\nu}\boldsymbol{H}_o\right) &= \underline{\underline{L}}^{\nu}\boldsymbol{J}_o - i\omega\left(\underline{\underline{L}}^{\nu}\boldsymbol{D}_o\right) \end{aligned} \tag{4}$$

which indicates that the new set of vector functions $\underline{\underline{L}}^{\nu}\boldsymbol{E}_o$, $\underline{\underline{L}}^{\nu}\boldsymbol{H}_o$, $\underline{\underline{L}}^{\nu}\boldsymbol{B}_o$, and $\underline{\underline{L}}^{\nu}\boldsymbol{D}_o$ does satisfy the Maxwell equations with the current density $\underline{\underline{L}}^{\nu}\boldsymbol{J}_o$. What this implies is that if we know a set of solutions for an electromagnetic problem with a given current source $\boldsymbol{J}_o$, we will be able to find the set of solutions to the related problem in which the current source is expressed as $\underline{\underline{L}}^{\nu}\boldsymbol{J}_o$ by just applying the fractional operator $\underline{\underline{L}}^{\nu}$ on the solutions of the first problem. This can offer interesting mathematical applications in the treatment of certain electromagnetic problem. As some specific cases, we have considered the operators of fractional integration, fractional integration, and fractional curl to show some of the interesting features of this treatment of certain radiation and scattering problems. [1, 4, 5, 6, 7, 9] In the following section, we present an example of application of the fractional operator in a scattering problem.

FRACTIONAL OPERATION AND PHYSICAL OPTICS APPROXIMATION

Let us consider a flat rectangular patch with certain surface impedance boundary conditions (e.g., a perfectly electric conducting (PEC) rectangular patch). This obstacle is being illuminated by a monochromatic electromagnetic wave. The incident and the scattered fields are denoted by

$\boldsymbol{E}^{inc}(x,y,z)$ and $\boldsymbol{E}^{scat}(x,y,z)$, respectively. Let us now apply the fractional differintegration operator (with respect to a (dimensionless) Cartesian coordinate, say $k_o z$, and with a general fractional order ν on the incident and the scattered fields. That is

$$\boldsymbol{E}^{inc,\nu}(x,y,z) = {}_{-\infty}D^{\nu}_{k_o z}\boldsymbol{E}^{inc}(x,y,z) \tag{5a}$$

$$\boldsymbol{E}^{scat.,\nu}(x,y,z) = {}_{-\infty}D^{\nu}_{k_o z}\boldsymbol{E}^{scat.}(x,y,z) \tag{5b}$$

where ${}_{-\infty}D^{\nu}_{k_o z}$ indicates the operation of fractional differintegration. For the definition of fractional integration, we use the Riemann-Liouville fractional integration [11] which is written as

$${}_aD^{\nu}_z f(z) \equiv \frac{1}{\Gamma(-\nu)}\int_a^z (z-u)^{-\nu-1} f(u)du \qquad \text{for } \mathrm{Re}(\nu)<0 \tag{6}$$

If $\mathrm{Re}(\nu)>0$, one will need to choose an integer m in the expression ${}_aD^{\nu}_z f(z) \equiv \dfrac{d^m}{dz^m}\,{}_aD^{\nu-m}_z f(z)$ such that $\mathrm{Re}(\nu-m)<0$. Then the above definition can be used to evaluate ${}_aD^{\nu-m}_z f(z)$ [11].

We ask the following question: Can the resulting field, $\boldsymbol{E}^{scat.,\nu}(x,y,z)$, be shown to be *approximately* the field that would be scattered from another rectangular patch with the same size and shape but with a different surface impedance boundary condition that would be determined from the knowledge of surface impedance of the original scatterer and the fractional parameter ν? The results of our preliminary theoretical study have shown that, under certain circumstances and approximations (such as physical optics approximation), the answer to the above question is positive for the case of finite-size flat obstacles. In order to express the relationship for the impedance transformation, we first describe below the case of an infinitely extent flat plate.

Let us assume an infinitely extent flat plate with a specified isotropic uniform surface impedance boundary condition, $\underline{\underline{Z}}_{so}$. This requires that the tangential components of the total electric and magnetic fields on the surface of this infinite plate be related as $\boldsymbol{E}_t^{total} = \underline{\underline{Z}}_{so}\boldsymbol{H}_t^{total}$. (See Fig. 1). A Cartesian coordinate system (x,y,z) is used here. For the sake of brevity of discussion here, we consider the transverse electric (TE) case for the incident electromagnetic wave illuminating this plate (i.e. the vector $\boldsymbol{E}^{inc}$ is polarized along the y axis). As shown in Fig. 1, the angle of incidence is chosen to be θ_i (with respect to the unit vector normal to the surface) and the angle of tilt of the plate (with respect to the x-axis) is taken to be θ_o. Obviously the reflected plane wave can be easily written in terms of the reflection coefficient, R_o, which can be explicitly given as a function of the surface impedance $\underline{\underline{Z}}_{so}$. Since we have assumed that the surface impedance is isotropic and uniform, one can write $E_y^{total} = Z_{so}H_t^{total}$, where Z_{so} denotes the surface impedance on this flat boundary, and $\boldsymbol{H}_t^{total}$ indicates the total tangential magnetic field on the surface. Now

we take the fractional differintegral of the total electric field $\boldsymbol{E}^{total} = \boldsymbol{E}^{inc} + \boldsymbol{E}^{ref}$ with respect to variable $k_o z$ and with fractional order ν. We have

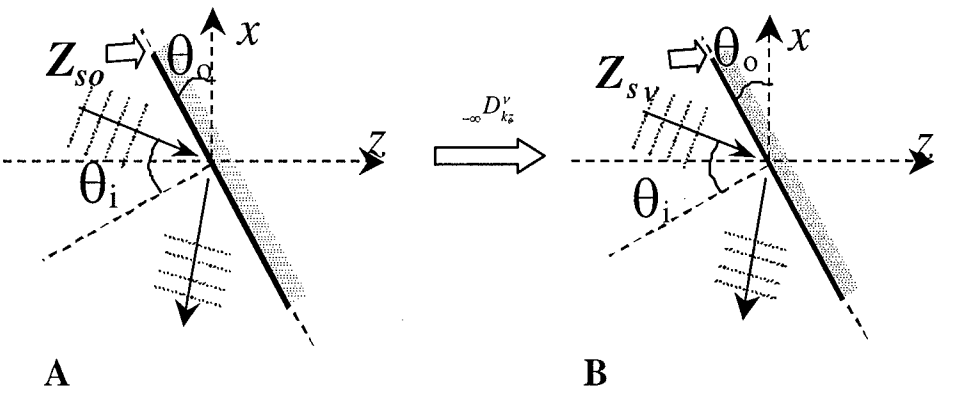

Fig. 1. Panel A depicts the problem of reflection of a TE incident plane wave from an infinitely extent flat boundary with the isotropic uniform surface impedance Z_{so}. (The electric vector is parallel with the y axis.) When the incident and reflected plane waves in such a problem are fractionally differintegrated with order ν with respect to the z variable, the resulting functions can be interpreted as the new incident and new reflected waves in another problem (Panel B) with infinite flat boundary but with a differing surface impedance $Z_{s\nu}$. The relationship between Z_{so}, $Z_{s\nu}$ and other relevant parameters is given in text.

$$E^{total,\nu} = {}_{-\infty}D^{\nu}_{k_o z} E^{total} = {}_{-\infty}D^{\nu}_{k_o z} E^{inc} + {}_{-\infty}D^{\nu}_{k_o z} E^{ref} =$$

$$= E_o \hat{y}\left[\cos^{\nu}(\theta_i - \theta_i) e^{ik_o z\cos(\theta_i-\theta_o)-ik_o x\sin(\theta_i-\theta_o)+i\nu\frac{\pi}{2}} + R_o \cos^{\nu}(\theta_i + \theta_i) e^{-ik_o z\cos(\theta_i+\theta_o)-ik_o x\sin(\theta_i+\theta_o)-i\nu\frac{\pi}{2}}\right] \tag{7}$$

The resulting total field, which can be shown to indeed satisfy the Maxwell equations and thus represent electromagnetic fields, consists of a new incident field, ${}_{-\infty}D^{\nu}_{k_o z}\boldsymbol{E}^{inc}$, that may be regarded as an incident plane wave with the incidence angle θ_i illuminating the plate with the tilt angle θ_o, and the new reflected wave, ${}_{-\infty}D^{\nu}_{k_o z}\boldsymbol{E}^{ref}$, that can be interpreted as the corresponding reflected plane wave. The tilt angle of the plate and the incidence angle remain as θ_o and θ_i, respectively. However, the new reflection coefficient, which relates the new incident plane wave with the new reflected plane wave is different from R_o, and is given as

$$R_\nu = R_o e^{-i\nu\pi}\frac{\cos^{\nu}(\theta_i + \theta_i)}{\cos^{\nu}(\theta_i - \theta_i)} \tag{8}$$

Following a series of mathematical steps, for the TE case we can show that the new plate, which would provide such a reflection coefficient, should have a new surface impedance, denoted as Z_{sv}, that can be explicitly written as

$$Z_{sv} = \frac{\eta_o}{\cos(\theta_i)} \frac{e^{iv\frac{\pi}{2}} + \frac{Z_{so} - \frac{\eta_o}{\cos(\theta_i)}}{Z_{so} + \frac{\eta_o}{\cos(\theta_i)}} \frac{\cos^v(\theta_i + \theta_o)}{\cos^v(\theta_i - \theta_o)} e^{-iv\frac{\pi}{2}}}{e^{iv\frac{\pi}{2}} - \frac{Z_{so} - \frac{\eta_o}{\cos(\theta_i)}}{Z_{so} + \frac{\eta_o}{\cos(\theta_i)}} \frac{\cos^v(\theta_i + \theta_o)}{\cos^v(\theta_i - \theta_o)} e^{-iv\frac{\pi}{2}}} \tag{9}$$

A similar approach can be used to obtain the corresponding expression for the TM case. The above results demonstrate that when the plane wave reflected from an infinite flat plate with the surface impedance Z_{so} is fractionally differintegrated (with the order v) the result can be interpreted as a plane wave that would have been reflected if the infinite plate (with the same tilt angle θ_o and the same angle of incidence θ_i for the incoming plane wave) had had a differing surface impedance Z_{sv} that can be explicitly given in terms of all the quantities involved.

Although the example of reflection of plane wave from an infinite flat boundary with uniform surface impedance is an idealized example and the mathematical connections via fractional calculus for the infinite flat plates is rather formal, our preliminary analysis has shown that for the *finite-size* flat plates the operation of fractional differintegration may be quite useful to link and relate *approximately* the scattered fields for two separate problems with finite-size flat plates of differing surface impedances. To demonstrate this point, let us now return to our example of flat rectangular patch, and consider the problem of electromagnetic wave scattering from a rectangular, flat, thin, perfectly electric conducting (PEC) plate when the incoming plane wave is normally incident on this patch. Using the physical optics (PO) approximation, the scattered field can be easily obtained. Then we apply the fractional differintegration operator (with order v) on the far-zone scattered electric field in the region in front of the illuminated side of the rectangular plate. We then use the impedance transformation given in Eq. (9) to find Z_{sv}, and afterwards using the PO approximation we find the scattered fields from the rectangular plate with the same size and shape but with this new surface impedance Z_{sv}. Our analysis has shown that the result of fractional differintegration of the scattered field from the PEC rectangular plate is approximately similar to the scattered field from the same-size rectangular plate but with the surface impedance Z_{sv}. Figure 2 presents the scattered field in the E-plane and H-plane using the fractional integration (in this figure we used order $v = -0.5$) and using PO approximation from the impedance plate. Good agreement in the magnitude and phase, particularly near the central region, can be easily observed from these plots. This example suggests that instead of re-calculating the scattered field from the impedance plate, one can use the well-known PO results of the scattering from the PEC plate and just apply fractional differintegration on the scattered fields in the far zone in front of the illuminated region, which would provide us with an approximate answer to the far-zone scattering from the impedance plate. So, when we encounter the problem of wave scattering from a finite-size flat plate with a given impedance boundary condition, instead of solving such a problem directly using the PO approximation, one can use the results of PO scattering from PEC version of the same-size same-geometry flat plate, and then apply the fractional differintegration operator on these results. If the variable with respect to which this fractional differintegration is taken is selected appropriately and if the order of the

fractional differintegration is chosen properly using Eq. (9), then the results of such operation would be approximately similar to the results of scattering from the finite-size impedance plate. We have extended the above case to the situation where we can have two adjacent flat panels and the results support the above idea for the application of fractional operators.

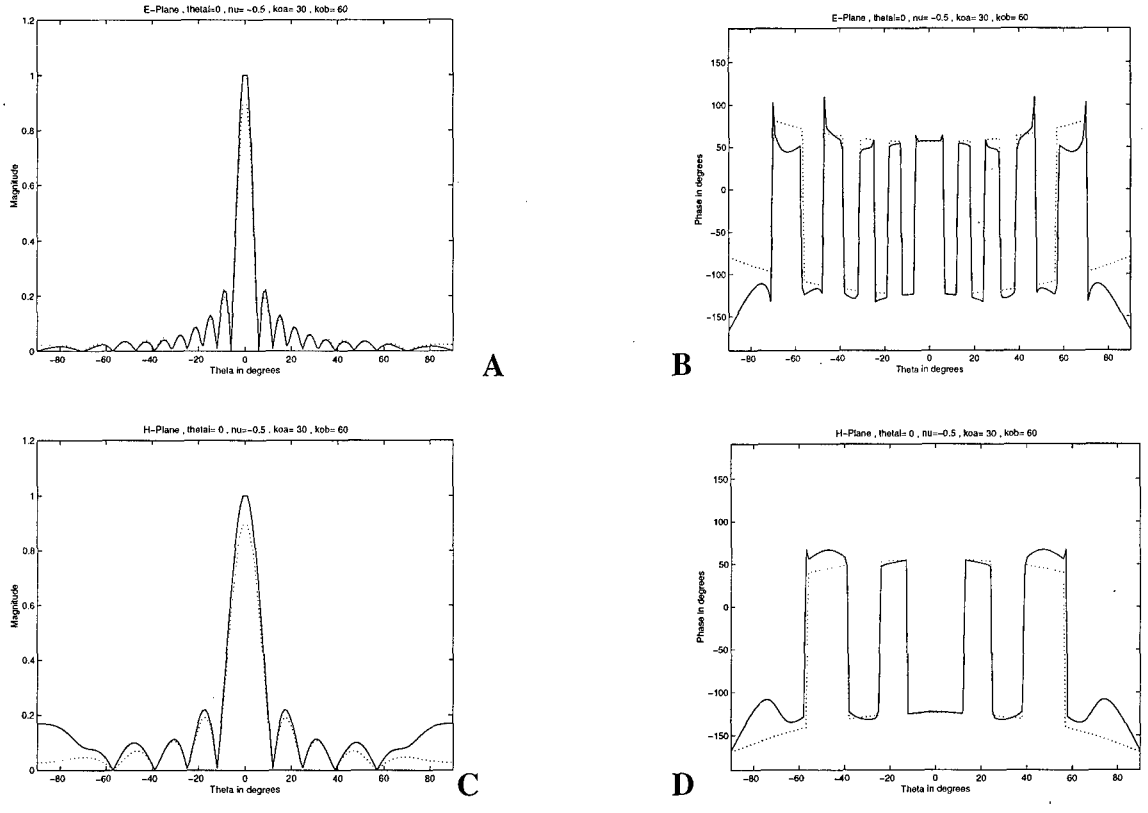

Fig. 2. Scattering of a normally incident EM wave from a rectangular thin plate with dimensions $k_o a = 30$ and $k_o b = 60$. First, using the physical optics (PO) approximation, the far-zone scattered field from such a plate with perfectly electric conductor (PEC) surface impedance was obtained. Then we applied the fractional integration operator (with order $\nu = -0.5$) on such far-zone fields in the region in front of the illuminated side of the rectangular plate. The solid lines show the resulting fields from such fractional integration. We then used the impedance transformation given in Eq. (9) to find $Z_{s\nu}$ for $\nu = -0.5$, $\theta_i = \theta_o = 0°$ and $Z_{so} = 0$; and afterwards using the PO approximation we directly evaluated the scattered fields from the same-size rectangular plate with this new surface impedance $Z_{s\nu}$. The dotted lines depict such fields. Panels A and B show the amplitude and phase for these two calculated fields in the E-plane, whereas Panels C and D show the corresponding quantities in the H-plane. Our preliminary analysis shows that the result of fractional differintegration of the scattered fields using PO approximation from the PEC rectangular plate, (solid line), is approximately similar to the scattered field from the same-size rectangular plate but with the surface impedance $Z_{s\nu}$, (dotted line). Good agreement between the solid line and the dotted line, particularly near the central region, is noticeable.

In this talk, we will present some of the recent results of our research on applications of fractional operators in radiation and scattering problems and discuss their salient features and physical justifications.

REFERENCES:

[1] N. Engheta, "Fractional Paradigm in Electromagnetic Theory" a chapter in *Frontiers in Electromagnetics*, D. H. Werner and R. Mittra (eds.), IEEE Press, New York, chapter 12, pp. 523-552, (2000).

[2] N. Engheta, "On Fractional Paradigm and Intermediate Zones in Electromagnetism: I. Planar Observation," in *Microwave and Optical Technology Letters*, Vol. 22, No. 4, pp. 236-241 (August 20, 1999).

[3] N. Engheta, "On Fractional Paradigm and Intermediate Zones in Electromagnetism: II. Cylindrical and Spherical Observations," in *Microwave and Optical Technology Letters*, Vol. 23, No. 2, pp. 100-103 (October 20, 1999).

[4] N. Engheta, "Phase and Amplitude of the Fractional-Order Intermediate Wave" in *Microwave and Optical Technology Letters*, Vol. 21, No. 5, pp. 338-343 (June 5, 1999).

[5] N. Engheta, "Fractional Curl Operator in Electromagnetics," in *Microwave and Optical Technology Letters*, Vol. 17, No. 2, pp. 86-91 (February 5, 1998).

[6] N. Engheta, "On Fractional Calculus and Fractional Multipoles in Electromagnetism," *IEEE Transactions on Antennas and Propagation*, Vol. 44, No. 4, pp. 554-566 (April 1996).

[7] N. Engheta, "Electrostatic "Fractional" Image Methods for Perfectly Conducting Wedges and Cones," in *IEEE Transactions on Antennas and Propagation.*, Vol. 44, No. 12, pp. 1565-1574 (December 1996).

[8] N. Engheta, "On the Role of Fractional Calculus in Electromagnetic Theory" a feature article in *IEEE Antennas and Propagation Magazine*, Vol. 39, No. 4, pp. 35-46 (August 1997).

[9] N. Engheta, "Use of Fractional Integration to Propose Some "Fractional" Solutions for the Scalar Helmholtz Equation," a chapter in *Progress in Electromagnetics Research (PIER)* Monograph Series *Vol. 12* , Jin A. Kong (ed.), pp. 107-132 (1996).

[10] N. Engheta, "A Note on Fractional Calculus and the Image Method for Dielectric Spheres," *Journal of Electromagnetic Waves and Applications*, Vol. 9, No. 9, pp. 1179-1188 (September 1995).

[11] K. B. Oldham and J. Spanier, *The Fractional Calculus*, Academic Press, New York, (1974).

[12] S. G. Samko, A. A. Kilbas, and O. I. Marichev, *Fractional Integrals and Derivatives, Theory and Applications*, Gordon and Breach Science Publishers, Langhorne, Pennsylvania, 1993. (Originally published in Russian by Nauka i Tekhnika, Minsk, 1987).

[13] K. S. Miller and B. Ross, *An Introduction to the Fractional Calculus and Fractional Differential Equations*, John Wiley & Sons, New York, 1993.

DPT ANALYSIS OF ELECTROMAGNETIC SCATTERING AND RADIATION FROM MULTIANGULAR CYLINDRICAL STRUCTURES INCORPORATING DIELECTRIC

Vitaliy P. Chumachenko

Electronics Engineering Department, Gebze Institute of Technology, 41400 Gebze, Kocaeli, Turkey, on leave from Technical University of Zaporizhzhya, 64 Zhukovsky Str., Zaporizhzhya, 330063 Ukraine

ABSTRACT

Application of the domain product technique for analysis of scattering and radiation from penetrable cylindrical structures with arbitrarily polyhedral boundaries is described. The Mathieu function expansions are used to represent fields in both the interior and exterior regions. The technique allows the fast and accurate evaluation of electrodynamic characteristics for an extensive class of the 2D structures including realistic objects of higher complexity.

INTRODUCTION

Analysis of electromagnetic scattering and radiation from cylindrical structures with polyhedral boundaries plays an important role in electromagnetic theory and practice [1-5]. However, study of those objects quite often meets with difficulties. Geometry is commonly arbitrary that excludes the use of effective analytical methods. Possible application of direct numerical techniques (such as, for example, finite difference and finite element methods) is complicated by overcoming difficulties associated with presence of edges on the scatterer contour and with the mesh truncation in the exterior region.

We present here an alternative approach , named the Domain Product Technique (DPT)[6]. In resonant frequency range, it gives an opportunity to attain an efficient field representation in the form of the Mathieu function series and to reduce the problem to that of determining the set of unknown expansion coefficients. In the past, the DPT was used for analysis of perfectly conducting scatterers [6-10]. Last years, a series of works [11-18] analysing structures incorporating dielectric have been carried out. The report is based on their content.

FIELD REPRESENTATION IN REGION WITH MULTIANGULAR BOUNDARIES

Let us consider a 2D finite or infinite region that is cross-section of a polyhedral cylindrical structure homogeneously filled with a lossless material characterised by $(\varepsilon\varepsilon_0, \mu\mu_0)$. A particular case is shown in Fig. $1(a)$. Axis Oz of the basic co-ordinate system (x, y, z) is directed along the generator of the cylinder. The structure is excited either by E- or H-polarised wave with z-component $u_0(x, y)$ .We shall distinguish between those cases as (E) and respectively (H). The time dependence is $e^{i\omega t}$. The region wave number is $k = (\varepsilon\mu)^{\frac{1}{2}} k_0$, where $k_0 = 2\pi / \lambda$ and λ is the free-space wavelength. Define the longitudinal component of the total field as

$$u = u_0 + u_s \tag{1}$$

where u_s is a scattering contribution due to the presence of the boundaries. The sought-for function u must satisfy the 2D Helmholtz equation, homogeneous Dirichlet or Neumann

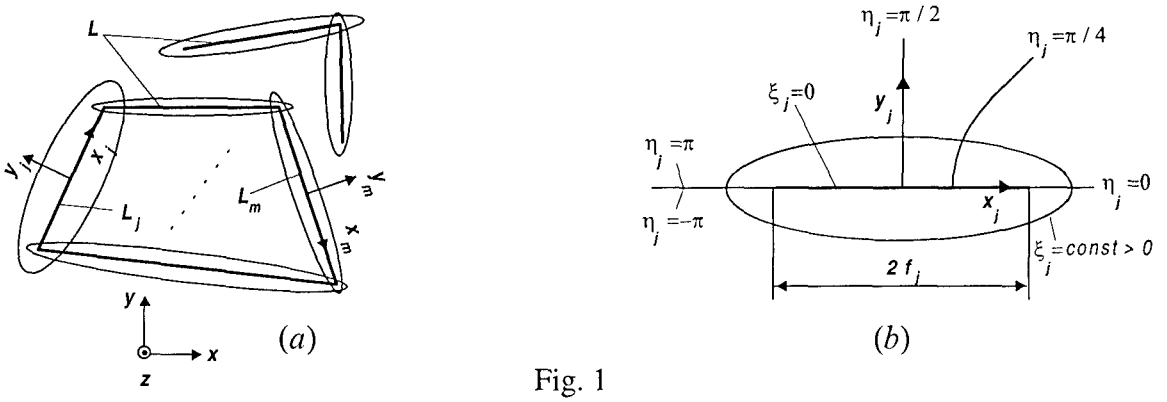

Fig. 1

boundary condition on the conducting part of the boundary and matching condition on the part of the boundary corresponding to interface. In addition, the edge condition and the radiation condition (placed on u_s in the case of an infinite region) must be satisfied.

Multiangular contour of the region is a broken line L consisting of N segments: $L=\bigcup_{j=1}^{N} L_j$. If boundary contour is closed, it divides all the space into two subregions, namely a physical part being domain of the field definition and a non-physical one completing the former to the whole plane. For each the segment we introduce local Cartesian (x_j, y_j) and elliptic (ξ_j, η_j) co-ordinate systems as

$$x_j = f_j \cosh\xi_j \cos\eta_j,\ y_j = f_j \sinh\xi_j \sin\eta_j,\ j=\overline{1,N} \tag{2}$$

The systems are shown in Fig. 1 (a,b). Then, every segment of the boundary may be taken for a degenerate ellipse $\{(\xi_j,\eta_j)\,|\,\xi_j=0;\eta_j\in(-\pi,\pi]\}$ and physical region (it does not matter internal or external one) can be considered as a common part (product) of simple infinite domains $\xi_j>0$ $(j=\overline{1,N})$. Since Helmholtz's equation is a linear one, the quantity u_s can be written in the form of superposition of some other functions being solutions to the equation as

$$u_s=\sum_{j=1}^{N} u_j \tag{3}$$

Suppose region $\xi_j>0$ is the domain of definition of the function u_j and this function satisfies the condition needed at infinity. In elliptic co-ordinates, region $\xi_j>0$ has separable geometry. Assuming L_j is a segment of an open boundary contour and examining boundary conditions, we find that u_j can be expressed as series of angular eigenfunctions in the form

$$u_j=\sum_{n=1}^{\infty} D_n^j\, M_n(\xi_j,q_j)\, ma_n(\eta_j,q_j),\ j=\overline{1,N} \tag{4}$$

Here, $q_j=(kf_j/\lambda)^2$ and $ma_n(\eta_j,q_j)$ stands for the even Mathieu function $ce_{n-1}(\eta_j,q_j)$ in the case of the Dirichlet boundary condition [6]. For the Neumann boundary condition, $ma_n(\eta_j,q_j)$ coincides with the odd Mathieu function $se_n(\eta_j,q_j)$[7]. $M_n(\xi_j,q_j)$ is expressed in terms of relevant radial Mathieu functions as $Me_{n-1}^{(2)}(\xi_j,q_j)/Me_{n-1}^{(2)}(0,q_j)$ or respectively $Ne_n^{(2)}(\xi_j,q_j)/Ne_n^{(2)}(0,q_j)$. Assuming L_j is a part of a closed contour, we ascertain

independently of the type of boundary condition there exists a choice of two possible representations [8,11,15]. Function u_s, possessing physical meaning inside or outside the closed boundary , is continued by (3) and (4) into the whole plane out of L.

For all that in the case of the even function series, expansion coefficients approach zero as $D_n^j = O\left(1/n^{2+\chi}\right)$, $n \to \infty$ provided u_j represents solution of the boundary value problem and transverse components of the field have singularities of the type $O(r^{-\gamma})$ [9]. Here, $\chi = 1 - 2\gamma$ and γ is the greatest of two powers corresponding different end points. The fast enough convergence of series (4) is caused by the fact that both the sought-for function u and its derivatives with respect to ξ_j and η_j have no singularities in this problem. Transverse components of the field, being expressed in terms of $\partial u/\partial \xi_j$ and $\partial u/\partial \eta_j$, involve factor $1/\sqrt{r_1 r_2}$ where r_1 and r_2 are distances between an observation point and the end points of the segment. Since usually $\gamma \le 1/2$, derivatives $\partial u/\partial \xi_j$ and $\partial u/\partial \eta_j$ can be only finite values or infinitesimals of some order when r_1 or r_2 tends to zero. Odd function expansion is, in general, less beneficial in the sense of convergence because, unless u_j vanishes at the ends of the segment, $D_n^j = O(1/n)$ only. The last condition holds provided L_j is cross-section of a separate strip (H) or series relating to both segments adjoining L_j have the even function form [17]. So, we assume further that in the (H) case all parts of the boundary contour are closed or consist of separate strips. Since $M_n(\xi_j, q_j) \sim \exp(-n\xi_j)$ (ξ_j fixed, $n \to \infty$), proper choice of the type of the expansion (4) ensures, with the above restriction, quite efficient representation of the field within the region considered and at its boundary.

PECULIARITIES OF PENETRABLE STRUCTURE MODELING

Fig. 2 shows a penetrable cylinder of a general type. It is composed of regions 1 and 2. Exterior region 2 contains a source. Let $N_c^{(K)}$ and I be sets of the segment's numbers relating to the conducting part of the K-th region boundary and to the interface. $N^{(K)} = N_c^{(K)} \bigcup I$. We define the z-component of the total field in regions 1 and 2 as $u^{(1)} = u_s^{(1)}$ and correspondingly $u^{(2)} = u_s^{(2)} + u_0$. Scattering contribution $u_s^{(K)}$ $(K = 1,2)$ is expressed by formulas similar to (3) and (4) where all the quantities are marked by additional superscript K.

Substitution of the above expansions into boundary conditions on the conducting part of the boundary yields infinite system

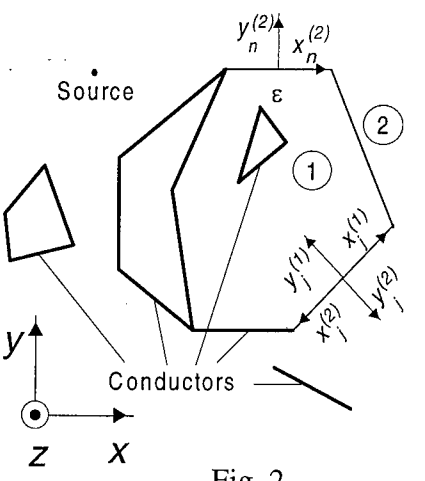

Fig. 2

$$ {}^{K}D_m^j + \sum_{\substack{p \ne j \\ p \in N^{(K)}}} \sum_{n=1}^{\infty} {}^{KK}a_{mn}^{jp}\, {}^{K}D_n^p = {}^{K}c_m^j, \quad m = \overline{1,\infty}, \quad j \in N_c^{(K)}, \quad K = 1,2 \qquad (5) $$

with some known matrix elements [9].

Substitution into matching conditions yields equations completing (5). Here, all matrix elements have the same type as those in (5) except for ${}^{12}a_{mn}^{jj}$ and ${}^{21}a_{mn}^{jj}$ $(j \in I)$ [11,15,17].

The last elements correspond to segments that belong to different regions and are imposed on each other along the interface. Those quantities include as a factor integral

$$I_{m,n} = \frac{2}{\pi}\int_0^{\pi} me_n(\eta_j^{(1)}, q_j^{(2)}) me_m(\eta_j^{(1)}, q_j^{(1)}) d\eta_j^{(1)} \qquad (6)$$

Since $ce_n(\eta,q) \sim \cos n\eta$ and $se_n(\eta,q) \sim \sin n\eta$ as $n \to \infty$, functions $ma_n(\eta_j^{(1)}, q_j^{(2)})$ and $ma_m(\eta_j^{(1)}, q_j^{(1)})$ are asymptotically orthogonal. Based on this property, it is possibly to rewrite ${}^{12}a_{mn}^{jj}$ and ${}^{21}a_{mn}^{jj}$ as ${}^{12}a_{mn}^{jj} = (-1)^n \delta_{mn} + \alpha_{mn}^{j}$ and ${}^{21}a_{mn}^{jj} = (-1)^{n+1}\delta_{mn}/P + \beta_{mn}^{j}$ where $P = \mu$ (E) or $P = \varepsilon$ (H), δ_{mn} is the Kronecker delta, and α_{mn}^{j} and β_{mn}^{j} are some infinitesimal sequences. It can be shown that when $m,n \to \infty$, they approach zero not more slowly than other matrix elements. It means that on replacing ${}^{1}D_m^j$ and ${}^{2}D_m^j$ $(j \in I)$ by new unknowns ${}^{1}\tilde{D}_m^j = {}^{1}D_m^j + (-1)^m {}^{2}D_m^j$ and ${}^{2}\tilde{D}_m^j = {}^{2}D_m^j - (-1)^m {}^{1}D_m^j / P$, we obtain a conventional DPT system. In the case of a purely conducting scatterer, equalities (5) constitute a complete set of equations. It was shown in [9,10] that, dealing with those equations , one could apply truncation procedure provided the frequency of the incident field does not coincide with natural frequencies of the non-physical region. Same is valid and in the case of penetrable structure. It should be noted that natural frequencies of the last region can be easily changed by placing an auxiliary boundary segment inside it (dashed line in Fig. 1(*a*)), adding an appropriate term into (3) and assigning a boundary condition on the segment introduced. Regarding the new segment as a perfectly conducting one, we shift natural frequencies along the real axis [10]. Prescribing auxiliary boundary condition of an impedance type, we make them complex valued.

SAMPLE NUMERICAL RESULTS

In this section, we illustrate the technique described in earlier sections. First for the sake of verification, we consider a triangular dielectric cylinder backed by a conducting strip and excited by a plane wave. The convergence of the algorithm at point A is demonstrated in Fig.3. Here, truncation number M is the order of partial sums in expansions of type (4) after truncation. α is the impinging angle. As seen, quantities $|\partial u^{(1)}/\partial n|$ (E) and $|u^{(1)}|$ (H) , which are proportional to magnitudes of the surface current densities, settle down to their final values for quite low truncation sizes. In a particular case of $\varepsilon = 1$, solutions converge to the known values (dashed lines) obtained by the method of separation of the variables. Corresponding far-field pattern (not given here) level more rapidly with increasing order M . Roughly, truncation number $M_j = [l_j/(0.21\lambda)] + 2$ with $l_j = 2f_j\sqrt{\varepsilon} < 2\lambda$ is recommended for calculation of electrodynamic characteristics in far-zone. It is sufficient to plot quality graphs. This number can be reduced with increasing electrical length of the segment.

Next two examples demonstrate versatility of the technique and its efficiency in dealing with arbitrary geometry. Fig. 4 shows far-field patterns of a flanged parallel-plate waveguide radiator with a plug shaped like a wedge in the case of TEM excitation. Fig. 5 presents radiation patterns obtained for an H-plane horn with dielectric insert that behaves as a lens. Another examples of application of the DPT for analysis of scattering and radiation from different penetrable structures one can find in works [11,14,15,18]. Before closing this section, it should be noted that technique can be also applied to other problems such as eigenmode problem for transmission lines[12,13] or analysis of waveguide discontinuities [16].

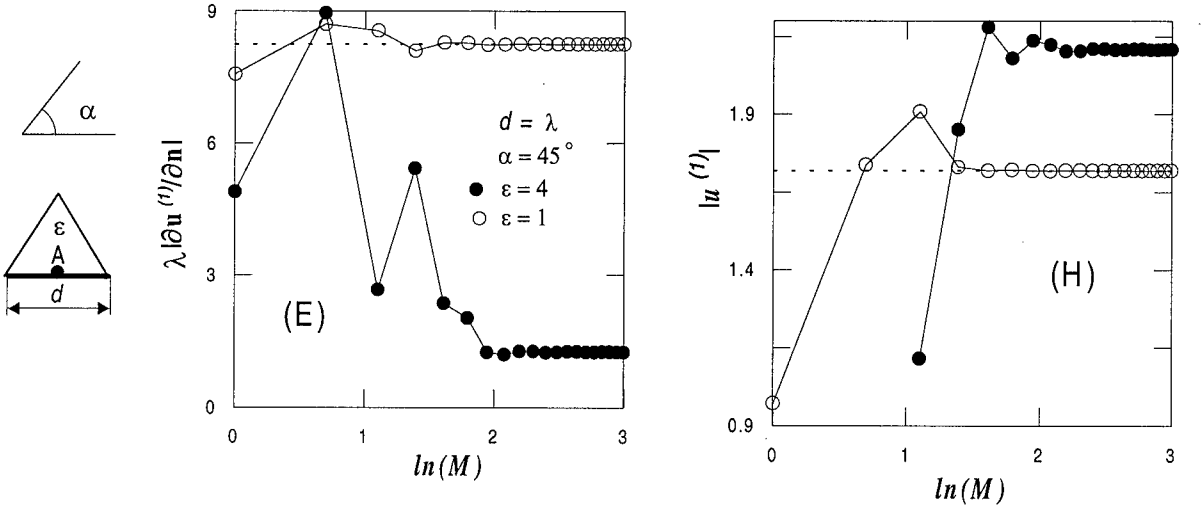

Fig. 3

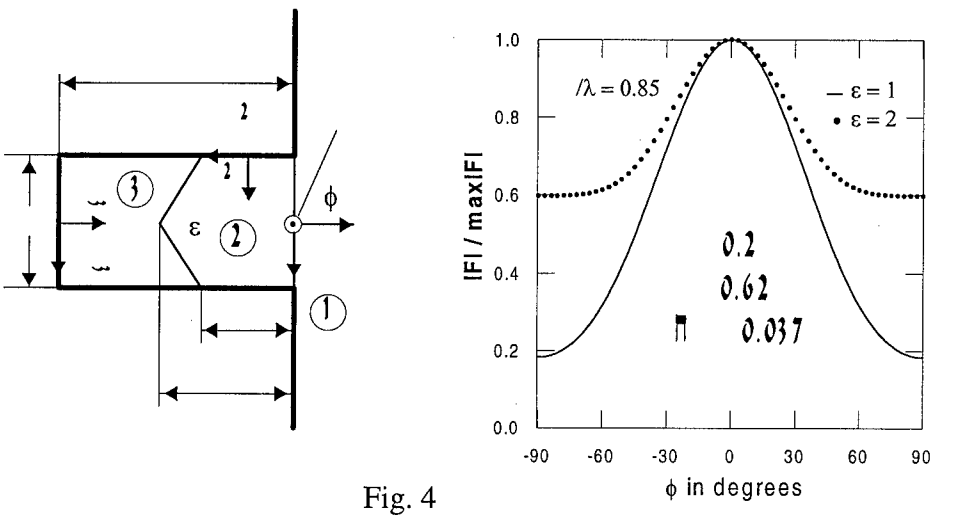

Fig. 4

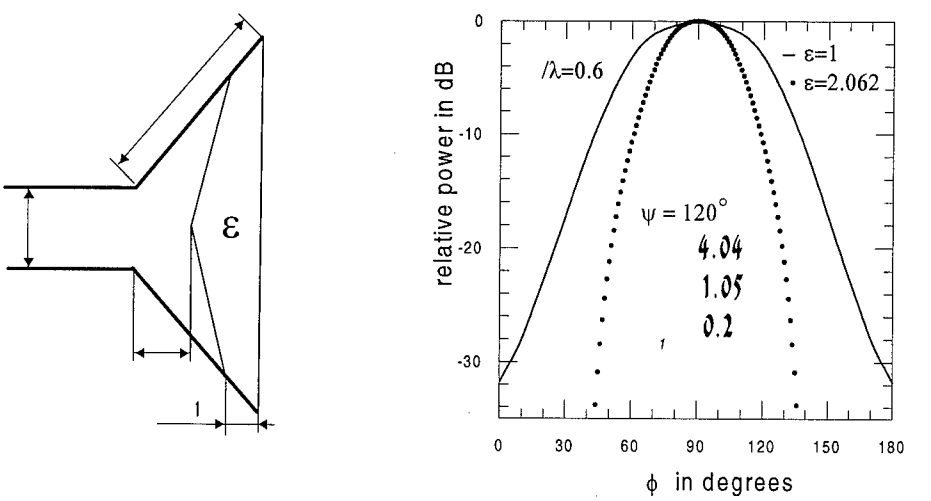

Fig. 5

REFERENCES

[1] V.V. Solodukhov and E.N. Vasil'ev, "Diffraction of a plane electromagnetic wave by a dielectric cylinder of arbitrary cross-section", Soviet Phys.-Tech. Phys., vol.15, pp. 32-36, July 1970.

[2] R. Kastner and R. Mittra, "A spectral-iteration technique for analyzing scattering from arbitrary bodies, part 1: cylindrical scatterers with E-wave incidence", IEEE Trans. Antennas Propagat., vol. AP-31, pp. 499-506, May 1983.

[3] M. Hamid and A. Al-Sulaiman, "New types of dielectric-loaded horn antennas", Int. J. Electron., vol. 55, 729-750, May 1983.

[4] E. Arvas, S.M. Rao and T.K. Sarkar, "E-field solution of TM-scattering from multiple perfectly conducting and lossy dielectric cylinders of arbitrary cross-section", IEE Proceedings, vol. 133, Pt. H, pp. 115-121, Apr. 1986.

[5] S. Eisler and Y. Leviatan, "Analysis of electromagnetic scattering from metallic and penetrable cylinders with edges using a multifilament current model", IEE Proceedings, vol. 136, Pt. H, pp. 431-438, Dec. 1989.

[6] V.P. Chumachenko, "Diffraction of electromagnetic waves by ribbed cylindrical surfaces", Izvestiya VUZ. Radiofizika, vol. 22, pp. 1480-1484, Dec. 1979.

[7] V.P. Chumachenko, "On computation of E-plane waveguide joints having polygon boundary", Radiotekhnika i Elektronika, vol. 33, pp. 19-28, Jan. 1988.

[8] V.P. Chumachenko, "Modified method of calculation of E-plane waveguide junctions having polygonal boundary" Radiotekhnika i Elektronika, vol. 34, pp. 1581-1587, Aug. 1989.

[9] V.P. Chumachenko, "Grounding of the method for solution of two-dimensional problems of electromagnetic wave diffraction by polygonal structures having perfect conductivity", Radiotekhnika i Elektronika, vol. 33, pp. 1600-1609, Aug. 1988.

[10] V.P. Chumachenko "Basing of one method for solving two dimensional problems of electromagnetic waves diffraction by polygonal structures. The uniqueness theorem", Radiotekhnika i Elektronika, vol. 34, pp. 1763-1767, Aug. 1989.

[11] A.M. Kotsur and V.P. Chumachenko, "Solution of the problem of electromagnetic wave diffraction by a multiangular dielectric cylinder using domain product technique", Izvestiya VUZ. Radiofizika, vol. 34, pp. 798-805, July 1991.

[12] V.P.Chumachenko, A.V. Krapyvny, and V.G. Zasovenko, "Solution method of the eigenmode problem for a generalized slot line by the domain product technique", Microwave and optical technology letters, vol. 16, pp. 236-241, Nov. 1997.

[13] V.P. Chumachenko, A.V. Krapyvny and V.G. Zasovenko, "Solution of the eigenmode problem for an open generalized transmission line by domain product technique", IEICE Trans. on Electronics, vol. E80-C, pp. 1476-1481, Nov. 1997.

[14] V.P. Chumachenko, E. Karacuha, and M. Dumanli, "Analysis of TE-scattering from a multiangular groove in a ground plane", Electronics letters, vol. 34, pp. 1425-1427, 1998.

[15] V.P. Chumachenko, E. Karacuha and M. Dumanli, "An analysis of TE-scattering from a multiangular groove in a ground plane", J. Elect. Waves Appl., vol.13, pp. 381-396, Mar. 1999.

[16] V. P. Chumachenko, and V. P. Pyankov, "Numerical analysis of complicated waveguide circuits on the basis of generalized scattering matrices and domain product technique", IEEE Trans. Microwave Theory Tech., vol. 48, pp. 305-308, Feb. 2000.

[17] V.P. Chumachenko, E. Karacuha and M. Dumanli, "TM-scattering from a multiangular groove in a ground plane ", J. Elect. Waves Appl., vol.14, pp. 329-347, Mar. 2000.

[18] V.P. Chumachenko, and A.S. Turk, "Radiation characteristics of wide-angle H-plane sectoral horn loaded with dielectric of multiangular shape", Int. J. Electron. (in press).

Numerical Simulations of Near Field Optics by Boundary and Volume Integral Equation Methods

Kazuo Tanaka, Masahiro Tanaka, Takahiro Yoshida, and Mengyun Yan

Department of Electronics and Computer Engineering of Gifu University,
Yanagido 1-1, Japan 501-1193
E-mail: tanaka@tnk.info.gifu-u.ac.jp

ABSTRACT

The two-dimensional and three-dimensional numerical simulations of scanning near-field optical microscope by integral equation methods, which are performed in our laboratory, have been reported in this paper. The Guided-Mode Extracted Boundary Integral Equations has been applied to the two-dimensional global-model and the conventional volume integral equation with Generalized Minimum Residual Method has been applied to the simplified three-dimensional global-model. The numerical simulations have revealed basic characteristics of near-field optical microscope.

INTRODUCTION

Recently, many researchers of electromagnetic theory have been interested in the technology of Near- Field Optics (NFO) and have proposed various techniques for the analysis of NFO problems [1-4]. Integral equation methods are the most popular method among them, because we can easily treat the NFO global-model and can apply various mathematical techniques in solving the integral equations. First, in this paper, we have applied the boundary-element method (BEM) based on integral equations called Guided-Mode Extracted Integral Equations (GMEIE's) to the simulation of a two-dimensional (2D) scanning near-field optical microscope (SNOM) [5-7]. In this method, the explicit expression of the excited guided-mode in the scanning dielectric-probe can be obtained and it is not necessary to employ any approximations in the formulation of interaction between dielectric-probe and near-fields. Then, we have applied the Moment Method (MoM) based on the conventional volume integral equation (VEI) with Generalized Minimum Residual Method (GMRES) to the three-dimensional (3D) simulation of a simplified model of 3D-SNOM. We can understand the basic physical characteristics of the output image of 2D and 3D SNOM by these numerical simulations.

TWO-DIMENSIONAL SIMULATION

We first explain numerical simulations of 2D SNOM with dielectric-probe. Although the electromagnetic wave propagation in a 2D problem is different in principle from that in 3D one, obvious similarities exist. The geometry of the problem that shows 2D-PSTM considered in this paper and its basic structure are shown in Figs. 1(a), 1(b) and 1(c). In the operation of SNOM, following operation-mode are used experimentally. One is collection-mode (c-mode) and another is illumination-mode (i-mode) as shown in Figs.1(a) and 1(b), respectively.

In the c-mode, the object placed on the semi-infinite dielectric substrate is illuminated by the transmitted evanescent wave which is created by the total reflection of an incident plane wave that comes from inner side of the substrate as shown in Fig. 1(a). The object illuminated by the evanescent wave creates near-fields around the object. This near-field around the object is detected by the probe-tip as shown in Fig. 1(a). After interaction between near-fields around the object and the probe-tip, the transmitted guided-wave is excited in the probe which is a dielectric slab waveguide in this case. If we moved the probe along the x-direction and measure the transmitted power in the probe, we can obtain the scanning image of the object. In the i-mode, the object is illuminated by the near-fields created around the probe-tip by the incident guided-mode that comes from upper direction in the probe as shown in Fig. 1(b). After interaction between near-fields around the probe-tip and the object on the substrate, the reflected guided-mode will transport information concerning the object. Moving the probe along the x-direction, we can also obtain a scanning image of the object placed on the substrate. We can expect

that scanning images obtained by these methods will have higher resolution than that of the conventional optical microscope.

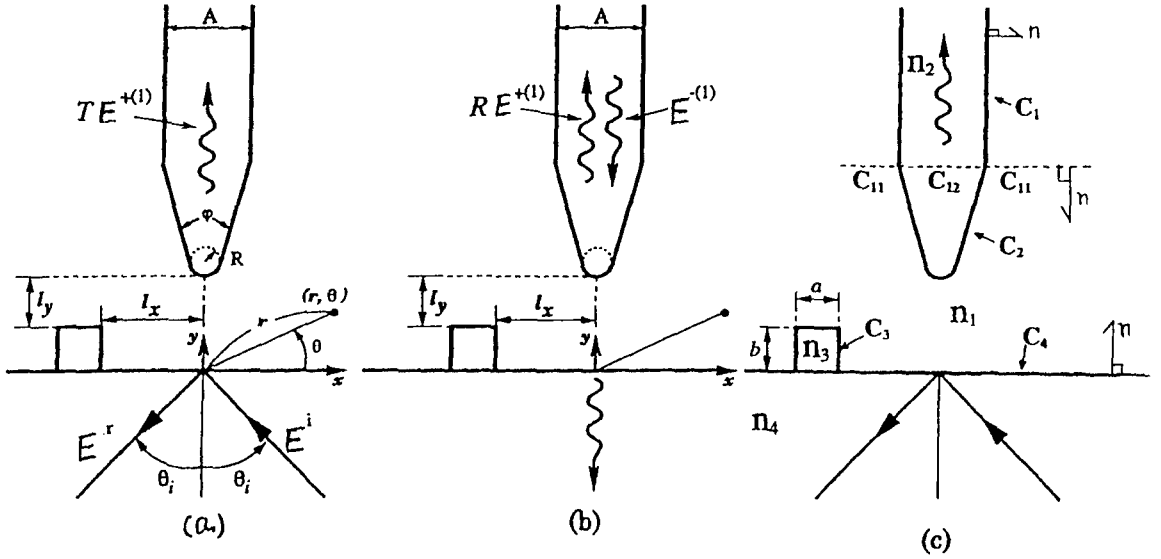

Fig.1 Scanning Near-Field Optical Microscope (SNOM) (a) c-mode (b) i-mode (c) Parameters of 2D-SNOM.

GUIDED-MODE EXTRACTED INTEGRAL EQUATIONS

We consider the case of incident TE-mode (s-polarization). When we treat the problem numerically, we encounter a difficulty that we must treat the infinite-length boundary C_1 where a guided-mode exists as shown in Fig. 1(c). In order to overcome this difficulty on the boundary C_1, we use the following idea: For the case of c-mode, we assume that the z-component of total electric field denoted by $E(x)$ on the boundary C_1 that is the boundary of uniform waveguide is composed of as

$$E(x)=E^c(x) + T\,E^{+(1)}(x) \qquad \text{for } x \text{ on } C_1. \tag{1}$$

Similarly, for the case of i-mode, we assume that the $E(x)$ on the boundary C_1 is composed of as

$$E(x)=E^c(x)+R\,E^{+(1)}(x) + E^{-(1)}(x) \qquad \text{for } x \text{ on } C_1, \tag{2}$$

where $E^{\pm(1)}(x)$ are guided-mode functions which propagate to the upper direction (+) in the probe as shown in Fig. 1(a) and which propagate to the lower direction (-) in the probe as shown in Fig. 1(b). Constants T and R are transmission and reflection coefficients of the guided-mode in the probe as shown in Fig. 1(a) and 1(b), respectively. In Eqs. (1) and (2), we consider that total field in the uniform waveguide region of the probe is composed of the guided-mode and other field denoted by $E^c(x)$. When the probe, which is a dielectric slab waveguide in the 2D-SNOM, satisfies the single-mode condition, we can expected that $E^c(x)$ will vanish at points far away from the probe-tip. We denote the total field on the boundary C_2 that is the boundary of the probe-tip as shown in Fig. 1(c) as

$$E(x) = E^c(x) \qquad \text{for } x \text{ on } C_2 \tag{3}$$

for convenience of notation. For the case of c-mode, we decompose the total field on the boundary C_4 in Fig. 1(c) into field components as

$$E(x) = E^c(x) + E^t(x) \qquad \text{for } x \text{ on the upper side of } C_4, \tag{4}$$
$$E(x) = E^c(x) + E^r(x) + E^i(x) \qquad \text{for } x \text{ on the lower side of } C_4, \tag{5}$$

where $E^i(x)$, $E^r(x)$ and $E^t(x)$ are an incident, reflected and transmitted plane waves, respectively, which make the total reflection by the boundary C_4 as shown in Fig. 1(a). For the case of i-mode, the boundary C_4 can be regarded as finite-length one because of finite-sized field-distribution of the guided-mode. So, we can assume that the total field on the boundary C_4 can be denotes as follows:

$$E(x) = E^c(x) \qquad \text{for } x \text{ on } C_4 \tag{6}$$

for i-mode. The total field on the boundary C_3 of the object on the substrate is denoted by

$$E(x) = E^c(x) \qquad \text{for } x \text{ on } C_3 \tag{7}$$

for both c-mode and i-mode.

It is possible to consider that all fields $E^c(x)$ defined in Eqs. (1)-(7) will be confined in the vicinity of the probe-tip and the object as shown in Fig. 1(c). Substituting expressions Eqs. (1)-(7) into the conventional boundary integral equations and considering that the radiation field does not exist at far points from the probe-tip in the waveguide, we can obtain boundary integral equations for only unknown functions $E^c(x)$ for both c-mode and the i-modes as follows [6,7]:

$$E^c(x)/2=\int_{C_1+C_2+C_3+C_4} [P_1(x|x')\,\partial E^c(x')/\partial n' - E^c(x')\,\partial P_1(x|x')/\partial n']\,dl' + S_1(x), \tag{8}$$

$$E^c(x)/2=\int_{C_1+C_2} [P_2(x|x')\,\partial E^c(x')/\partial n' - E^c(x')\,\partial P_2(x|x')/\partial n']\,dl' + S_2(x), \tag{9}$$

$$E^c(x)/2=\int_{C_3} [G_3(x|x')\,\partial E^c(x)/\partial n' - E^c(x)\,\partial G_3(x|x')/\partial n']\,dl', \tag{10}$$

$$E^c(x)2=\int_{C_4} [G_4(x|x')\,\partial E^c(x)/\partial n' - E^c(x)\,\partial G_4(x|x')/\partial n']\,dl', \tag{11}$$

where impressed terms are given by

$$S_1(x)=y^t(x)\ ,\ S_2(x)=0 \qquad \text{for c-mode,} \tag{12}$$

$$S_i(x)=-U_i^{-(1)}(x) + U_i^{+(1)}(x)\,u_i^{-(1)}(\pi/2)/u_i^{+(1)}(\pi/2)\ (i=1,2) \qquad \text{for i-mode,} \tag{13}$$

respectively. Functions $U_1^{\pm(1)}(x)$ are derived by applying Green's theorem to the uniform waveguide regions surrounded by boundary $C_1 + C_{11}$ as shown in Fig.1(c) and they can be written as

$$U_1^{\pm(1)}(x)=\int_{C_{12}} [G_1(x|x')\,\partial E^{\pm(1)}(x')/\partial n' - E^{\pm(1)}(x')\,\partial G_1(x|x')/\partial n']\,dl'. \tag{14}$$

Kernel functions of Eqs. (8)-(10) are given by

$$P_i(x|x')=G_i(x|x') - g_i(\pi/2|x')U_i^{+(1)}(x)/u_2^{+(1)}(\pi/2)\ (i=1,2), \tag{15}$$

and

$$G_i(x|x')=-j/4H_0^{(2)}(k_0 n_i|x-x'|) \quad (i=1,2,3,4), \tag{16}$$

where k_0=is a wave number in a vacuum and $H_0^{(2)}(x)$ is the 0-th order Hankel function of the second kind.

We have called Eqs. (8) and (9) Guided-Mode Extracted Integral Equations (GMEIE's) so far [5-7]. For fields $E^c(x)$ on boundaries of the object and the substrate, the conventional boundary integral equations are employed as Eqs. (10) and (11). Since all fields denoted by $E^c(x)$ are confined in the

vicinity of object and probe-tip, we can regard the infinite-length boundaries C_1 and C_4 as finite-length boundaries in Eqs. (8)-(11). Introducing boundary conditions in each boundary, the simultaneous boundary integral equations of finite-length boundaries Eqs. (8)-(11) can be solved by the conventional BEM. In our numerical calculations, we used BEM in which the quadratic function as a basic function and the delta-function as a testing function were used [8].

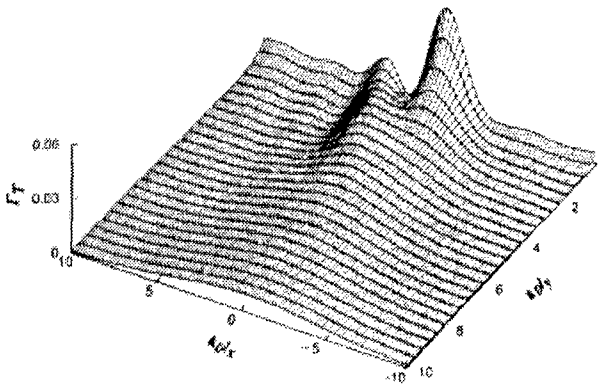

Fig. 2(a) The dependence of Γ_T on the position of the probe-tip (c-mode).

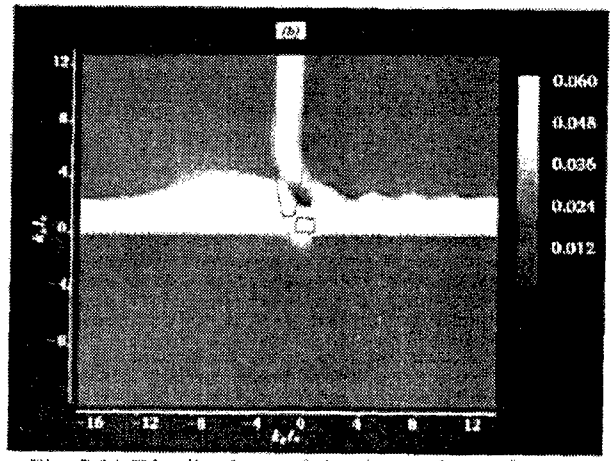

Fig. 2(b) Distributions of absolute values of electric field in the vicinity of object and probe.

When the fields $E^c(x)$ on all the boundaries have been obtained numerically, we can calculate the transmission coefficient T for c-mode and the reflection coefficient R for i-mode by using $E^c(x)$ [5-7]. The dependence of the transmission power Γ_T, which is defined by $|T|^2$, for c-mode on the position of the probe-tip are shown in Fig. 2(a) for $n_1=n_2=n_3=n_4=1.5$, $k_0\times$(width of the probe)$=0.5$, $k_0\times$(tip-radius)$=0.5$, $k_0a= k_0b=1.0$, and $\theta_i=60$ degrees in Fig.1(a). In Figs. 2(a) and 2(b), k_0l_x is a normalized x-direction distance between center axis of the probe and the center of the object and k_0l_y is a normalized y-direction distance between probe-tip and upper surface of the object as shown in Fig. 1(a). The sign of k_0l_x in Fig. 2(a) is positive when the probe exists in the right of the object and negative when the probe exists in the left of the object in Figs. 1(a)-1(c). A square object is located on the substrate surface so that its center exists at $k_0l_x=0$ in Figs. 2(a). Distributions of absolute values of electric field in the vicinity of object and probe-tip are illustrated in Fig. 2(b). The incident and reflected plane waves are extracted from total field in the substrate i.e., $y<0$ in Fig. 2(b), so that small additional fields can be seen in the dielectric substrate.

From these numerical examples, it is found that smaller value of tip-radius (sharp-tip) does not give higher resolution in the case of dielectric-probe without metal coating. We can also find that the following interesting results concerning interaction between probe-tip and evanescent fields around the object of the c-mode. The object and the probe scatter the evanescent field and create standing evanescent fields in the region of positive x region on the substrate. Due to the effects of these standing waves, the most of the energy of the evanescent field enters the dielectric-probe through the side-boundary of the probe, not through the probe-tip.

Figure. 3(a) shows the dependence of reflection power Γ_R for i-mode on the position of probe-tip. The Γ_R is normalized by the incident power in the probe. Distributions of absolute values of electric field in the vicinity of object and probe-tip are also illustrated in Fig. 3(b). It is also found that smaller value of tip-radius (sharp-tip) does not give higher resolution in i-mode. From above-mentioned numerical simulations, it is found that the physical process of interaction between probe-tip and near-field around the object in c-mode is more complicated than that in i-mode.

THREE-DIMENSIONAL SIMULATION

Theoretically, it is possible to extend above-mentioned techniques to the 3D NFO global model as

shown in Figs. 1(a) and 1(b). However, it is difficult to perform numerical calculations in this technique due to the limited ability of our system at present, because the system of linear equations to be solved becomes very large even for small 3D-NFO problems. So, we consider a simplified model of the 3D-SNOM and the geometry of the problem is shown in Fig. 4 [9, 10]. One 3D F-shaped planar dielectric object whose index of refraction is given by n_1 is placed on the rectangular dielectric substrate whose index of refraction is given by n_2 in a vacuum. A dielectric sphere with diameter a, which is a version of the active part of dielectric probe and whose index of refraction is given by n_3, is placed in the vicinity of the object. The dielectric sphere is used as a scanning probe that moves along the plane parallel to the x-y plane above the object as shown in Fig.4. The distance between the sphere center and the upper surface of the object is maintained by a constant value d during the scanning. A plane wave whose wavelength is given by λ is assumed to be incident to this system from the negative x-axis as shown in Fig. 1 and it is scattered by the object, dielectric substrate and the probe-sphere. We can consider that the dependence of the far-field scattered power on the position of the probe-sphere relative to the F-shaped object on the substrate corresponds to an output image of the F-shaped dielectric object of this simplified 3D-NSOM system.

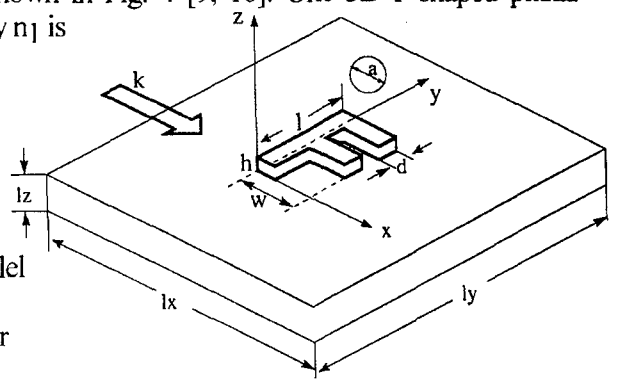

Fig. 4 A simplified 3D-SNOM

It is well known that the one of the simple methods to solve the scattering by the 3D dielectric object is the 3D-VIE method in the computational electromagnetics. The 3D-VIE to be solved for the scattering problem by 3D dielectric objects can be written as [11]

$$-k_0^2 \int_V [n^2(x')-1]\underline{G}(x|x') \cdot \boldsymbol{E}(x')\, dv' + \{[n^2(x) + 2]/3\}\boldsymbol{E}(x) = \boldsymbol{E}^i(x) \qquad (17)$$

where $\underline{G}(x|x')$ is a free space electric dyadic Green's function given by

$$\underline{G}(x|x') = (\underline{I} + 1/k_0^2\, \nabla\nabla) g(x|x'). \qquad (18)$$

and x and x' represent the observation and source points, respectively. In Eq. (18), $\underline{I}$ represents a unit dyadic and $g(x|x')$ is a scalar free space Green's function given by

$$g(x|x') = 1/(4\pi)\exp[(-jk_0|x-x'|)]/|x-x'|. \qquad (19)$$

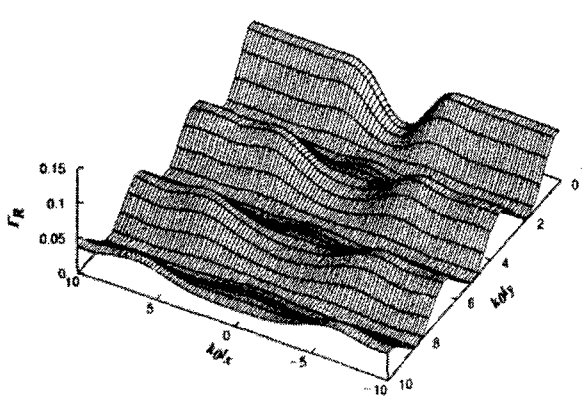

Fig. 3(a) Dependence of P_T on the position of the probe-tip (i-mode).

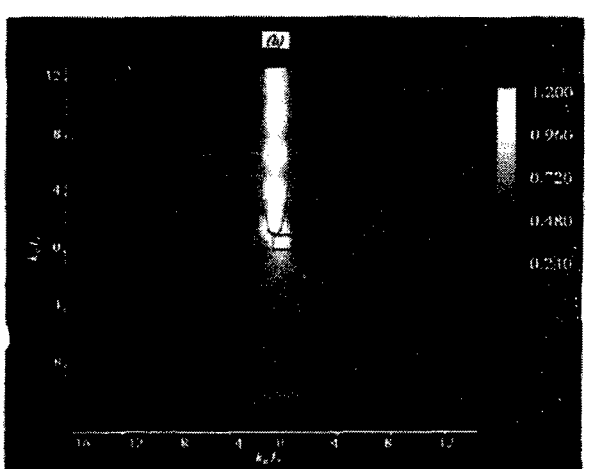

Fig. 3(b) Distributions of absolute values of electric field in the vicinity of object and probe.

In Eq. (17), $\boldsymbol{E}(x)$ is the 3D total electric vectors, $n^2(x)$ represents the distribution of index of refraction of the dielectric objects in a vacuum, $\int dv'$ represents the principal-value of volume integration over the entire space V. We define the incident plane wave whose electric field is parallel to the x-y plane as TE-wave and define that whose electric field is perpendicular to the x-y plane as TM-wave in Fig. 4 [9, 10]. It is assumed that the incident wave $\boldsymbol{E}^i(x)$ has an unit amplitude.

We apply the Moment Method (MoM) to the numerical evaluation of the integral equation (7). We use the pulse function as basis function and use the delta function as testing function in the application of the MoM to Eq. (17) [11]. After discretizing VIE (17), we can obtain a system of linear equations of 3N unknowns, which are values of electric vector at N center points of the cubes that are discretized elements of the object, substrate and probe-sphere. Since the resultant $3N \times 3N$ coefficient-matrix of the system is very large, complex and dense for usual problems in 3D NFO, it is unrealistic to employ Gaussian-elimination (LU decomposition) method in order to solve this large-scale matrix equation. Therefore, we apply an iteration method called Generalized Minimum Residual Method (GMRES) [12, 13] to the inversion of the matrix in order to solve the problem within reasonable computational cost.

The distribution of the absolute value of near-field on the plane above the F-shaped object on the substrate are shown in Fig. 5(a) and 5(b) for incident TE-wave and for incident TM-wave, respectively.

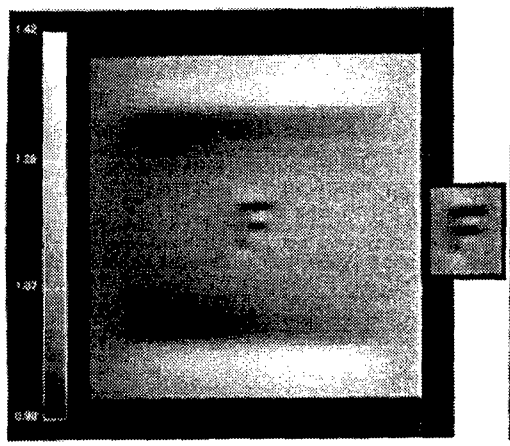

Fig. 5(a) Near-field distribution above the object for incident TE-wave.

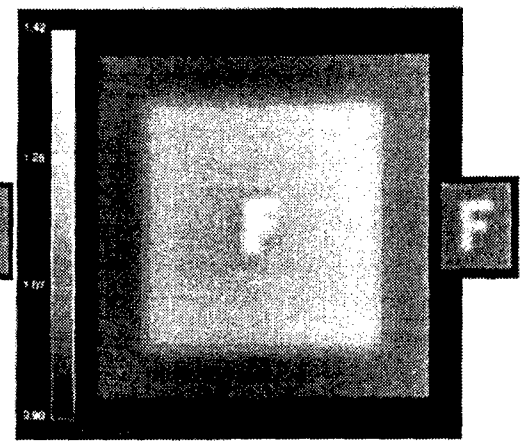

Fig. 5(b) Near-field distribution above the object for incident TM-wave.

The distance between the observing plane and the upper surface of the F-shaped object is d=5 nm. Other parameter used in the numerical calculations is given by λ=632 nm, $n_1 = n_2 = n_3$=1.5, a=10 nm, l=50 nm, w=30 nm, h=7.5 nm, d=10 nm, l_x=230 nm, l_y=250 nm and l_z=20 nm. The size of the F-shaped object is approximately $\lambda/12$. The insets in Fig. 5(a) and 5(b) show the results for the case where there are no dielectric substrate. We can find that the electric field distribution around the F-shaped object is very similar to the electrostatic field distribution. The dependence of the total scattered power on the position of the probe-sphere i.e., output image of this simplified 3D-NSOM, are shown in Fig. 6(a) and 6(b) for incident TE-wave and TM-wave, respectively. Lower figures show the gray scale image of the upper figure in Figs. 6(a) and 6(b). It is found that these output images are very similar to Fig. 5(a) and 5(b). So, ideally, the output images of small object compare to λ represent the electrostatic field distribution around objects in 3D-SNOM as shown in Fig. 4 [14].

CONCLUSION

We have reported the 2D and 3D numerical simulations of NFO microscope and have found many interesting characteristics of the NFO system. Most of basic characteristics of NFO system can be analyzed by the classical electromagnetic theory. A lot of important, interesting and basic NFO problems

have not been solved until now. For example, the relation between the shape of probe-tip and the resolution of 3D-NSOM has not been uncovered clearly.

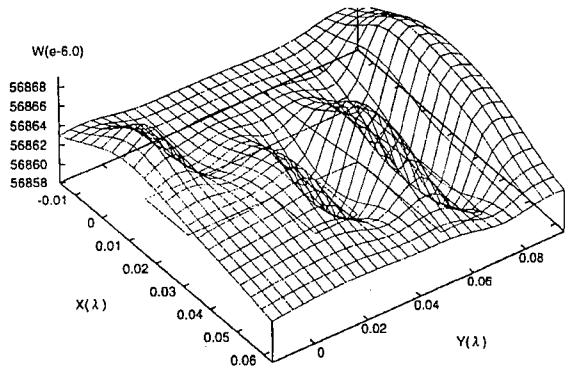

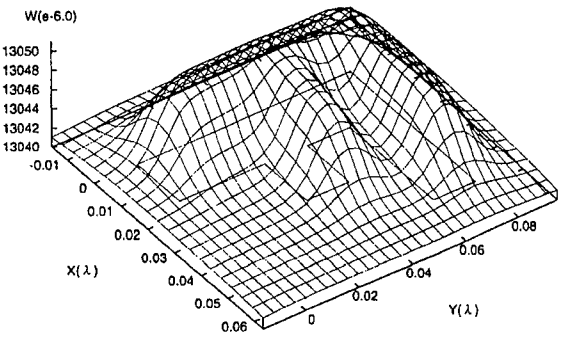

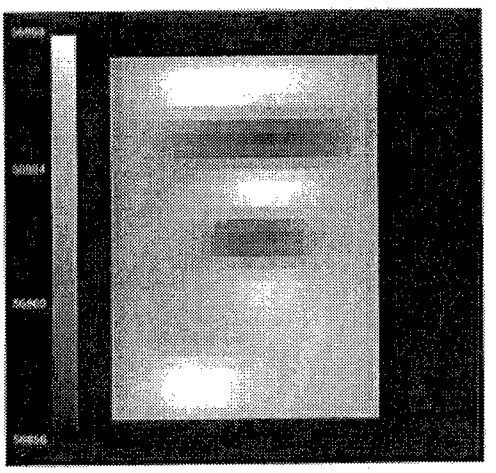

Fig. 6(a) Output image of 3D-NSOM as shown in Fig.4 for incident TE-wave.

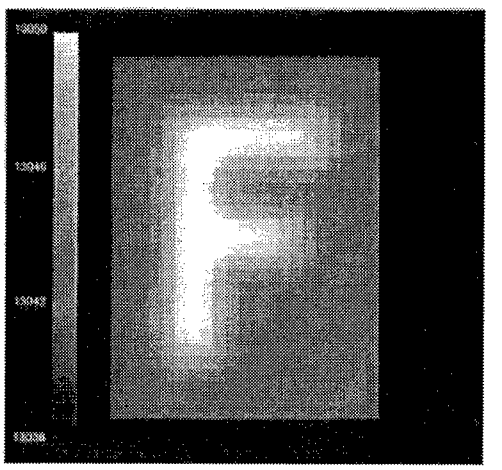

Fig. 6(a) Output image of 3D-NSOM as shown in Fig.4 for incident TM-wave.

REFERENCES

[1] D.W.Pohl and D.Courjon ed., "Near Field Optics", Kluwer Academic (1993).

[2] M. A. Paesler and P. J. Moyer, "Near-Field Optics: Theory, Instrumentation and Applications", John Wiley & Sons, INC. (1996).

[3] J. P. Fillard, "Near Field Optics and Nanoscopy", World Scientific (1996).

[4] M. Ohtsu and H. Hori, "Near-Field Nano-Optics: From Basic Principles to Nano-Fabrication and Nano -Photonics", Kluwer Academic (1999).

[5] M. Tanaka and K. Tanaka, J. Op. Soc. Am. A, **15**, 101(1998).

[6] K. Tanaka, M. Tanaka and T. Omoya, J. Op. Soc. Am. A, **15**, 1918 (1998).

[7] K. Tanaka, M. Tanaka and K. Katayama, Opt. Rev. **6**, 249-256 (1999).

[8] N. Morita, N.Kumagai, and J.R.Mautz. "Integral Equation Methods for Electromagnetics", Artech House (1999).

[9] O. J. F. Martin, C. Giratrd, and A. Dereux, Phys. Rev. Lett., **74**, 529 (1995).

[10] O. J. F. Martin, C. Girard and A. Dereux, J. Opt. Soc. Am. A, **13**, 1801(1996).

[11] J. J. H. Wang, "Generalized Moment Method in Electromagnetics: Formulation and Computer Solution of Integral Equations", John Wiley & Sons, Inc. New York, (1991).

[12] A. B. Samokhin. Journal of Communication Technology and Electronics, **38**(15) 15(1993).

[13] Richard Barrett et. al, "Templates for the Solution of Linear Systems: Building Blocks for Iterative Methods", Society for Industrial and Applied Mathematics, (1994).

[14] K. Tanaka, Mengyun Yan and M. Tanaka, The Second Asia-Pacific Workshop on Near-Field Optics, Program & Abstract, 81(1999).

Applications of Singular and Critical Point Theory to the Analysis and Interpretation of Transform and Time-Domain Guided-Wave Electromagnetics

George W. Hanson and Alexander B. Yakovlev*

Department of Electrical Engineering, University of Wisconsin-Milwaukee
3200 N. Cramer St., Milwaukee, Wisconsin 53211, USA
*Department of Electrical Engineering, The University of Mississippi
University, Mississippi 38677, USA

Abstract

In this paper we summarize some recent progress in applying the theory of critical points to the analysis of guided-wave problems. In particular, we are interested in fold singular points and Morse critical points which occur in spatial/temporal transform space. An important observation is that these points are associated with temporal transform-domain branch-point singularities, which ultimately govern observable modal interactions. Numerical results for a variety of guided-wave structures illustrate the role of critical and singular points in analysis and simulation, and their use in explaining observed modal phenomena.

I. INTRODUCTION

Guided-wave structures are fundamentally important in high-frequency systems, from electronic through optical regimes. Knowledge of the dispersion behavior of the natural modes supported by such structures is crucial for understanding system behavior, and can be utilized for the design of novel guided-wave components. Unfortunately, the dispersion characteristics of all but the simplest waveguiding structures must be determined numerically, which obscures the analytical characteristics of the dispersion function. As such, the mathematical and physical nature of observable modal interaction is not always clear from numerical simulation or experimental results. In this paper we examine modal dispersion behavior, and especially modal interaction, using the concept of critical and singular points. Of principal interest are Morse critical points and fold singular points, and associated branch-point singularities.

The application of Morse critical point theory to the analysis of modal interactions on electromagnetic structures was instigated in [1]– [8]. In [9] this theory was applied to mode leakage on striplines, and in [10], [14] the connection between the theory of Morse critical points and coupled-mode theory was established. Fold points have been found to occur in the cut-off region on waveguiding structures [9], [11], and, along with Morse points, are seen to be related to branch point singularities in the complex-frequency plane [11], [13], [14]. In this paper we discuss these points in a general framework, and show that a wide range of observable modal phenomena are explained in terms of critical and singular point theory.

II. FORMULATION

Consider a two-dimensional waveguiding structure, invariant along the waveguiding (z) axis. Subsequent to a two-dimensional Fourier transform in space and time, $(z,t) \longleftrightarrow (\kappa,\omega)$, source-free Maxwell's equations can be converted to an operator equation for the discrete propagation modes of the structure,

$$A(\kappa, f, \boldsymbol{\xi})X = 0. \tag{1}$$

In (1) A is an operator-function, κ is the spatial Fourier transform variable, representing the modal propagation constant, $f = \omega/2\pi$ where ω is the temporal Fourier transform variable, representing frequency, $\boldsymbol{\xi} \in C^k$ represents a vector of k generally complex-valued parameters associated with the physical structure of the waveguide (dielectric permittivity, dielectric thickness, etc.), and X represents a modal field distribution, typically current density, electric field, or magnetic field, depending on the problem formulation. We consider the analytic continuation of (κ, f) into the complex plane C^2, such that $\boldsymbol{\vartheta} = (\kappa, f, \boldsymbol{\xi})$ forms a vector in the complex space C^{2+k}.

Non-trivial field solutions are obtained from the implicit dispersion equation

$$H(\boldsymbol{\vartheta}) = H(\kappa, f, \boldsymbol{\xi}) = \det(A(\kappa, f, \boldsymbol{\xi})) = 0. \tag{2}$$

Let $\boldsymbol{\vartheta}_0 = (\kappa_0, f_0, \boldsymbol{\xi}_0)$ be the set of solutions of (2), i.e., $H(\boldsymbol{\vartheta}_0) = 0$, and note that we are usually interested in determining the implicit solution $\kappa_0(f_0, \boldsymbol{\xi}_0)$ of (2) for the modal propagation constant as a function of frequency. We assume that the mapping $H : C^{2+k} \rightarrow C$ is continuous, and that all second partial derivatives of H exist and are continuous. Analytical properties of H for $(\kappa, f, \boldsymbol{\xi})$ corresponding to values of physical interest or mathematical significance (e.g., f in the vicinity of the real-frequency axis) govern observable modal characteristics.

The $2 + k$-tuplet $\boldsymbol{\vartheta} = (\kappa, f, \boldsymbol{\xi})$ belongs to one of three possible categories. If

$$\begin{aligned} &\tfrac{\partial H(\boldsymbol{\vartheta})}{\partial \kappa} = H'_{\kappa}(\boldsymbol{\vartheta}) \neq 0, && \tfrac{\partial H(\boldsymbol{\vartheta})}{\partial f} = H'_{f}(\boldsymbol{\vartheta}) \neq 0 \\ &\tfrac{\partial H(\boldsymbol{\vartheta})}{\partial \xi_1} = H'_{\xi_1}(\boldsymbol{\vartheta}) \neq 0, \quad \cdots, && \tfrac{\partial H(\boldsymbol{\vartheta})}{\partial \xi_k} = H'_{\xi_k}(\boldsymbol{\vartheta}) \neq 0 \end{aligned} \tag{3}$$

then $\boldsymbol{\vartheta} = \boldsymbol{\vartheta}_r$ is said to be a *regular point* of the mapping H. If all of the partial derivatives in (3) are zero, we call $\boldsymbol{\vartheta} = \boldsymbol{\vartheta}_c$ a *critical point* of the mapping H. Regular and critical points of H do not necessarily affect solutions of the dispersion equation (2), although most elements of the solution space of (2) will also be regular points of H. Critical points of H which either satisfy (2) (i.e., $\boldsymbol{\vartheta}_0 = \boldsymbol{\vartheta}_c$) or occur in some sense close to solutions of (2) (i.e., $\|\boldsymbol{\vartheta}_c - \boldsymbol{\vartheta}_0\| < \delta$ for some $\delta > 0$) significantly affect modal behavior. From a geometric view, one can consider properties of the surface $(\kappa, f, \boldsymbol{\xi}, H(\kappa, f, \boldsymbol{\xi}))$ in the vicinity of the hyperplane $(\kappa, f, \boldsymbol{\xi}, 0)$.

In addition to the solution set of (2) being comprised of either regular points or critical points of H, obviously it is possible that some, but not all, of the partial derivatives in (3) may be non-zero for points $\boldsymbol{\vartheta}_s$, $H(\boldsymbol{\vartheta}_s) = 0$. We call $\boldsymbol{\vartheta}_s$ a *singular point* of the equation $H = 0$. Every solution of (2) is either a regular point $(\boldsymbol{\vartheta}_0 = \boldsymbol{\vartheta}_r)$ of the mapping H, a critical point $(\boldsymbol{\vartheta}_0 = \boldsymbol{\vartheta}_c)$ of H, or a singular point $(\boldsymbol{\vartheta}_0 = \boldsymbol{\vartheta}_s)$ of the equation $H = 0$.

At a regular point of H which also satisfies (2), or a singular point of (2), the implicit function theorem states that one can obtain from (2) a unique solution for one of the variables in terms of all of the other variables. For example, if $H'_{\kappa}(\kappa, f, \boldsymbol{\xi}) \neq 0$, then (2) admits a unique solution $\kappa(f, \boldsymbol{\xi})$. Furthermore, if H has, for instance, continuous second derivatives, then so does the solution $\kappa(f, \boldsymbol{\xi})$. At regular points of H modal dispersion curves do not exhibit modal interaction (coupling, cutoff, etc.), and so in the following we will concentrate on critical and singular points.

Although sometimes if is useful to work within the general framework discussed above, in what follows we will consider $\boldsymbol{\xi}$ as a fixed vector in C^k, whereas (κ, f) will be variable parameters. In this case we will suppress the dependence on $\boldsymbol{\xi}$ and define regular points (κ, f) of the mapping H by

$$\tfrac{\partial H(\kappa,f)}{\partial \kappa} = H'_{\kappa}(\kappa, f) \neq 0, \qquad \tfrac{\partial H(\kappa,f)}{\partial f} = H'_{f}(\kappa, f) \neq 0. \tag{4}$$

Singular points (κ, f) of the equation $H = 0$ occur when one of the partial derivatives in (4) vanishes, and critical points of H occur when both partial derivatives vanish. In the following sections we consider two types of non-regular points of importance in modal interaction problems, both of which lead to branch-point singularities in the temporal transform plane.

A. Morse Critical Points

Critical points (κ_c, f_c) of H may be broadly classified by study of the Hessian,

$$\Delta(\kappa_c, f_c) = H''_{\kappa\kappa} H''_{ff} - H''_{\kappa f} H''_{f\kappa}$$

where all partial derivatives are evaluated at (κ_c, f_c). For simplicity we assume that $\Delta(\kappa_c, f_c) \in R$, which is found to occur for critical points of interest on lossless waveguiding structures.

If $\Delta(\kappa_c, f_c) = 0$ the critical point is called *degenerate* or *nonisolated.* This type of point occurs, for example, at a trough-like surface (e.g., $H(\kappa, f) = f^2$). These types of points are not of interest here. If $\Delta \neq 0$, then the critical point is *nondegenerate* or *isolated.* For $\Delta(\kappa_c, f_c) > 0$ the solutions of $H(\kappa_c, f_c) = 0$ represent an extremum point (e.g., $H(\kappa, f) = \kappa^2 + f^2$), and are also not of interest here. For $\Delta(\kappa_c, f_c) < 0$ the critical point represents a saddle point, which is found to occur in regions of modal coupling.

In particular, we are interested in Morse critical points (MCP) (κ_m, f_m) of the mapping H, which satisfy the equations

$$H'_\kappa(\kappa, f)|_{(\kappa_m, f_m)} = 0, \quad H'_f(\kappa, f)|_{(\kappa_m, f_m)} = 0, \quad \Delta(\kappa_m, f_m) < 0. \tag{5}$$

In the lossless case for the structures examined here, the MCP (κ_m, f_m) is obtained as a real-valued quantity, as are $H(\kappa_m, f_m)$, and $H''_{\alpha\beta}(\kappa_m, f_m)$ for $\alpha, \beta = \kappa, f$. The Morse lemma shows that H in the vicinity of a MCP can be represented by a quadratic form using a smooth change of variables. The result is the normal form associated with the Morse critical point,

$$(\kappa - \kappa_m)^2 - (f - f_m)^2 = H(\kappa_m, f_m)$$

leading to the dispersion function

$$\kappa(f) = \kappa_m + \sqrt{H(\kappa_m, f_m) + (f - f_m)^2}.$$

More quantitatively useful is the Taylor polynomial of order two (the order of the polynomial justified by the quadratic nature of the normal form),

$$H(\kappa, f) = H(\kappa_m, f_m) + \frac{1}{2} H''_{\kappa\kappa}(\kappa - \kappa_m)^2 + H''_{\kappa f}(\kappa - \kappa_m)(f - f_m) + \frac{1}{2} H''_{ff}(f - f_m)^2 \tag{6}$$

where again all partial derivatives are evaluated at (κ_m, f_m). In the vicinity of the MCP the local dispersion behavior is obtained from (6) as

$$\kappa(f) = \kappa_m - \frac{H''_{\kappa f}}{H''_{\kappa\kappa}}(f - f_m) \pm \frac{1}{H''_{\kappa\kappa}} \sqrt{(H''^2_{\kappa f} - H''_{\kappa\kappa} H''_{ff})(f - f_m)^2 - 2H''_{\kappa\kappa} H(\kappa_m, f_m)}. \tag{7}$$

It is obvious that the square root in (7) defines a two-valued function in the complex frequency plane unless $H(\kappa_m, f_m) = 0$, i.e., if the Morse point is also a solution of (2). This situation arises in the event of a modal degeneracy.

The case $H(\kappa_m, f_m)/H''_{\kappa\kappa} < 0$ is particularly important, relating to co-directional mode coupling [10]. From (7) the branch point pair $(\kappa_{b1,2}, f_{b1,2})$ is obtained as complex-conjugate points centered about the real-valued Morse point (κ_m, f_m),

$$f_{b1,2} = f_m \pm j\sqrt{\frac{-2H''_{\kappa\kappa}H(\kappa_m,f_m)}{H''^2_{\kappa f}-H''_{\kappa\kappa}H''_{ff}}}, \qquad \kappa_{b1,2} = \kappa_m \mp j\frac{H''_{\kappa f}}{H''_{\kappa\kappa}}\sqrt{\frac{-2H''_{\kappa\kappa}H(\kappa_m,f_m)}{H''^2_{\kappa f}-H''_{\kappa\kappa}H''_{ff}}}.$$

For coupling between contradirectional waves, $H(\kappa_m, f_m)/H''_{\kappa\kappa} > 0$, and the branch-point pair is obtained as

$$f_{b1,2} = f_m \pm \sqrt{\frac{2H''_{\kappa\kappa}H(\kappa_m,f_m)}{H''^2_{\kappa f}-H''_{\kappa\kappa}H''_{ff}}}, \qquad \kappa_{b1,2} = \kappa_m \mp \frac{H''_{\kappa f}}{H''_{\kappa\kappa}}\sqrt{\frac{2H''_{\kappa\kappa}H(\kappa_m,f_m)}{H''^2_{\kappa f}-H''_{\kappa\kappa}H''_{ff}}}$$

which relate to complex modes in the modal interaction region [14].

A frequency contour which passes between the branch points results in mode-coupling, i.e., mode transformation (hyperbolic dispersion) behavior, whereas passing above or below the pair $f_{b1,2}$ results in modal interaction but no mode transformation [14]. At a modal degeneracy (of, say, even and odd modes or TM and TE modes, etc.) due to structural symmetry, the branch points $f_{b1,2}$ collapse together at the Morse frequency f_m, such that multivalued behavior of the dispersion function in the complex frequency plane vanishes. Such points are unstable with respect to symmetry-breaking perturbations, having universal unfoldings with co-dimension one.

Morse critical point theory can also be shown to be locally equivalent to the traditional coupled-mode theory [10]. From (7), define uncoupled modes $\tilde{\kappa}$ corresponding to a modal degeneracy $(H(\kappa_m, f_m) = 0)$,

$$\tilde{\kappa}_{\pm}(f) = \kappa_m - \Big(\frac{H''_{\kappa f}}{H''_{\kappa\kappa}} \pm \frac{1}{H''_{\kappa\kappa}}\sqrt{(H''^2_{\kappa f} - H''_{\kappa\kappa}H''_{ff})}\Big)(f - f_m). \tag{8}$$

Then, (7) becomes

$$\kappa(f) = \frac{\tilde{\kappa}_+ + \tilde{\kappa}_-}{2} \pm \sqrt{\Big(\frac{\tilde{\kappa}_+ - \tilde{\kappa}_-}{2}\Big)^2 - 2\frac{H}{H''_{\kappa\kappa}}}. \tag{9}$$

Compared with the classical coupled-mode result

$$\kappa(f) = \frac{\tilde{\kappa}_+ + \tilde{\kappa}_-}{2} \pm \sqrt{\Big(\frac{\tilde{\kappa}_+ - \tilde{\kappa}_-}{2}\Big)^2 \pm K^2} \tag{10}$$

where K is the coupling factor, we obtain $K = \sqrt{\pm 2\frac{H}{H''_{\kappa\kappa}}}$.

B. Fold Singular Points

Fold singular points (also known as turning or limit points) (κ_f, f_f) of the equation $H = 0$ satisfy

$$\begin{aligned} &H(\kappa_f, f_f) = H'_\kappa(\kappa, f)|_{(\kappa_f,f_f)} = 0 \\ &\zeta = H''_{\kappa\kappa}(\kappa, f)|_{(\kappa_f,f_f)}\, H'_f(\kappa, f)\Big|_{(\kappa_f,f_f)} \neq 0. \end{aligned} \tag{11}$$

The associated normal form is

$$\begin{aligned} &(\kappa - \kappa_f)^2 + (f - f_f) \qquad \zeta > 0 \\ &(\kappa - \kappa_f)^2 - (f - f_f) \qquad \zeta < 0 \end{aligned}$$

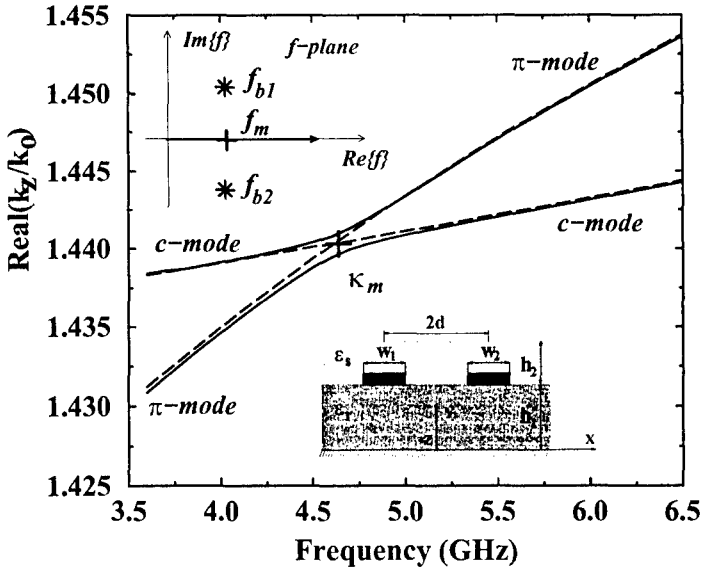

Fig. 1. Dispersion behavior for dominant modes of symmetrical and nonsymmetrical conductor-backed coplanar strip line with infinite superstrate. Degeneracy occurs for the symmetric structure (dashed line, $w_1/h_1 = w_2/h_1 = 0.25$), and is broken by the perturbation of symmetry due to unequal strip widths (solid line, $w_1/h_1 = 0.25$, $w_2/h_1 = 0.27$), $d/h_1 = 0.25$, $h_1 = 1cm$, $h_2 = 0.1h_1$, $\epsilon_r = 2.25$, $\epsilon_s/\epsilon_r = 1.15$. Insert shows the path of frequency variation.

leading to the dispersion function

$$\begin{aligned} \kappa(f) &= \kappa_f \pm j\sqrt{f - f_f} \qquad \zeta > 0 \\ \kappa(f) &= \kappa_f \pm \sqrt{f - f_f} \qquad \zeta < 0. \end{aligned} \tag{12}$$

The square root in (12) clearly implicates frequency-plane branch points, although a more general proof of this using the Weierstrass preparation theorem is provided in [11]. It is found that fold singular points occur in the vicinity of cutoff on a variety of guided-wave structures [9], [11], and are persistent with respect to small structural perturbations, having co-dimension zero. Complex singular points satisfying (11) have been also identified in the analysis of eigenmode coupling in open waveguide resonators [4] and cylindrical strip and slot lines [5], [8].

III. NUMERICAL RESULTS AND DISCUSSION

It is shown above that Morse critical points and fold singular points lead to frequency-plane branch points. If those branch points lie near to a region of interest on the real-frequency axis, then as frequency is varied near to these points modal behavior will be significantly affected. As an example, a coplanar coupled microstrip transmission lines with a dielectric superstrate will be considered.

Fig. 1 shows the dispersion behavior for frequency variation through the point f_m on the real-frequency axis, between the branch points $f_{b1,2}$. Mode coupling occurs, resulting in the transformation c-mode $\longleftrightarrow$ π-mode. In Fig. 2 frequency is varied along a contour through the branch point f_{b1}, and in Fig. 3 frequency is varied along a contour above the

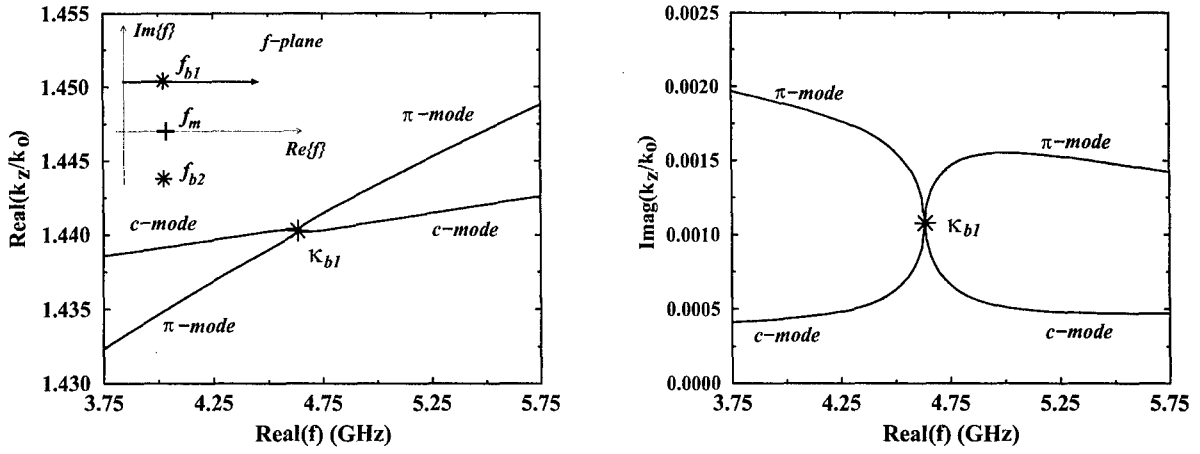

Fig. 2. Propagation constant characteristics for dominant modes in nonsymmetrical conductor-backed coplanar strip line versus complex frequency with $Im\{f\} = 0.2083$ GHz. A bifurcation of characteristic curves occurs at the κ_{b1} point when the path of frequency variation crosses the branch point f_{b1} in the complex f-plane.

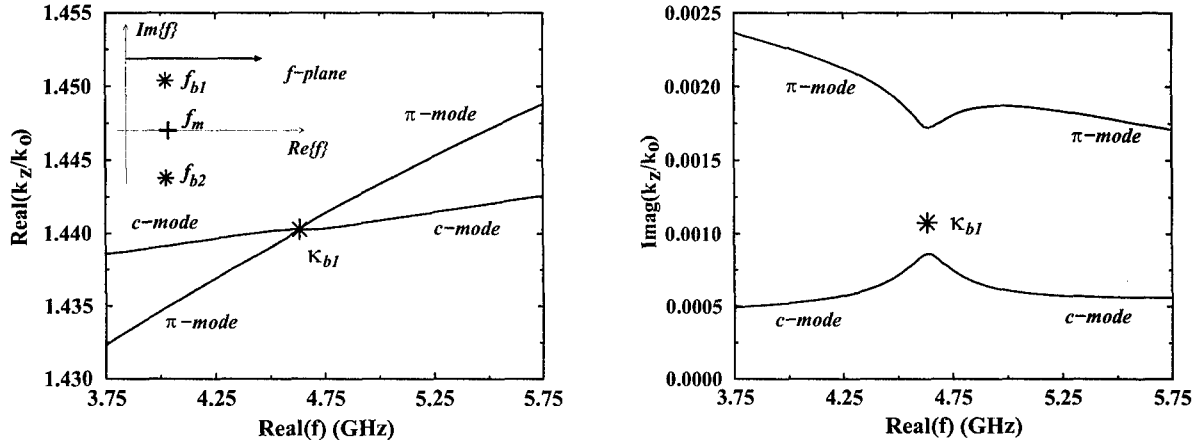

Fig. 3. Propagation constant characteristics for dominant modes in nonsymmetrical conductor-backed coplanar strips versus complex frequency with $Im\{f\} = 0.25$ GHz. No mode transformation occurs when the frequency variation path is deformed above the branch point f_{b1} in the complex f-plane.

branch point pair. Whenever the frequency contour passes outside of the region between the branch point pair, mode interaction but not mode transformation occurs. For lossless structures this phenomena does not occur for the real-valued frequencies of interest, since the real-frequency axis lies between the branch point pair ($f_{b1,2}$). However, as loss is introduced the Morse point (κ_m, f_m) and the associated branch point pair migrates into the complex plane, as shown in Fig. 4. When the branch point pair move sufficiently far from the real-frequency axis, the unusual modal behavior depicted in Fig. 3 can occur. Further numerical results will be shown in the presentation, including the effect of branch-point singularities on the transient analysis of waveguiding structures.

REFERENCES

[1] P.N. Melezhik, A.Y. Poyedinchuk, Y.A. Tuchin, and V.P. Shestopalov, "Properties of spectral characteristics of the open two-mirror resonator," *Dokl. Akad. nauk URSR*, Ser. A, n. 8, pp. 51-54, 1987.

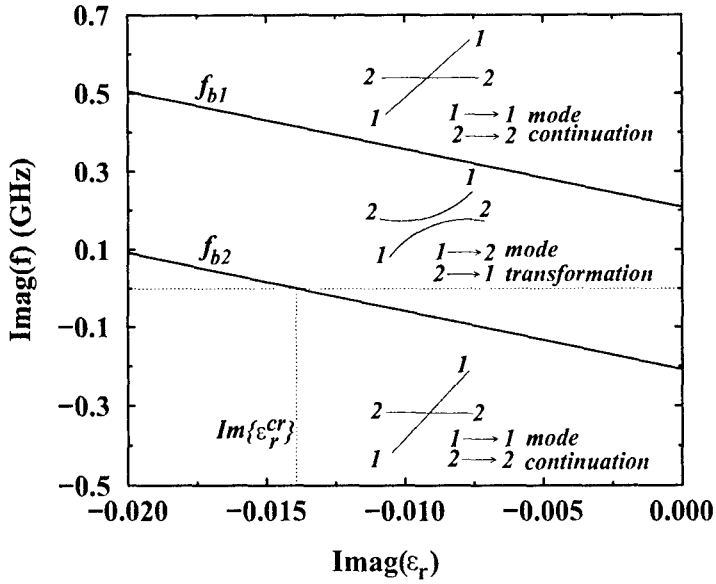

Fig. 4. Evolution of complex frequency-plane branch points parameterized by dielectric loss in non-symmetrical conductor-backed coplanar strip line (see inset in Fig. 1): $d/h_1 = 0.25$, $w_1/h_1 = 0.25$, $w_2/h_1 = 0.27$, $h_1 = 1cm$, $h_2 = 0.1h_1$, $\epsilon_s/Re\{\epsilon_r\} = 1.15$.

[2] P.N. Melezhik, A.Y. Poyedinchuk, Y.A. Tuchin, and V.P. Shestopalov, "Analytical nature of the vibrational mode-coupling phenomenon," *Dokl. Akad. Nauk SSSR*, v. 300, n. 6, pp. 1356-1359, 1988.

[3] V.P. Shestopalov, "Morse critical points of dispersion equations," *Dokl. Akad. Nauk SSSR*, v. 314, n. 6, pp. 1396-1401, 1990.

[4] I. E. Pochanina and N.P. Yashina, "Coupling and degeneracy of eigen modes in open waveguide resonators," *Int. Seminar on Mathematical Methods in Electromagnetic Theory*, Alushta, Ukraine, pp. 346-350, 1991.

[5] A. Svezhentsev, "Coupling effects for complex waves in multilayer cylindrical strip and slot lines," *Int. Symp. Antennas Propagat.*, Sapporo, Japan, pp. 1285-1288, 1992.

[6] V.P. Shestopalov, "Morse critical points of dispersion equations of open resonators," *Electromagnetics*, v. 13, pp. 239-253, 1993.

[7] I. E. Pochanina and N.P. Yashina, "Electromagnetic properties of open waveguide resonators," *Electromagnetics*, v. 13, pp. 289-300, 1993.

[8] A. Svezhentsev, "Special points of dispersion equations of metal-dielectric cylindrical waveguides," *Dokl. Akad. nauk URSR*, n. 4, pp. 82-87, 1994.

[9] A.B. Yakovlev and G.W. Hanson, "On the nature of critical points in leakage regimes of a conductor-backed coplanar strip line," *IEEE Trans. Microwave Theory Tech.*, v. 45, pp. 87-94, Jan. 1997.

[10] A.B. Yakovlev and G.W. Hanson, "Analysis of mode coupling on guided-wave structures using Morse critical points," *IEEE Trans. Microwave Theory Tech.*, v. 46, pp. 966-974, July 1998.

[11] G.W. Hanson and A.B. Yakovlev, "An analysis of leaky-wave dispersion phenomena in the vicinity of cutoff using complex frequency plane singularities," *Radio Science*, v. 33, no. 4, pp. 803-820, July-Aug. 1998.

[12] G.W. Hanson, "An analysis of mode coupling on waveguiding structures from the theory of universal unfoldings," *USNC/URSI Nat. Radio Sci. Meeting*, Atlanta, GA p. 161, June, 1998.

[13] G.W. Hanson and A.B. Yakovlev, "Investigation of mode interaction on planar dielectric waveguides with loss and gain," *Radio Science*, v. 34, n. 6, pp. 1349-1359, Nov.-Dec., 1999.

[14] A.B. Yakovlev and G.W. Hanson, "Mode-transformation and mode continuation regimes on waveguiding structures," *IEEE Trans. Microwave Theory Tech.*, v. 48, pp. 67-75, Jan. 2000.

[15] M. Golubitsky and D.G. Schaeffer, *Singularities and Groups in Bifurcation Theory*, v. 1, Berlin: Springer-Verlag, 1985.

DIFFRACTION TOMOGRAPHY METHOD DEVELOPMENT IN WIDE FREQUENCY RANGE

A. Vertiy* (1), (2), S. Gavrilov (1), (2), I. Voynovskiy(1), S. Aksoy(1,3), A.O.Salman(1)

(1) TUBITAK – MRC, Turkish-Ukrainian Joint Research Laboratory, TURKEY;
(2) IRE, National Academy of Sciences of Ukraine, UKRAINE; (3) Gebze Institute of Technology
Mailing address: Marmara Research Center, P.O. Box 21, 41470 Gebze – Kocaeli, Turkey
Telephone: +90 262 641 23 00/4794 (A. Vertiy), 4767 (S. Gavrilov, I.Voynovskiy)
Fax: +90 262 643 04 67
E-mail: alex @ mam.gov.tr, sergiy@mam.gov.tr, igorv@mam.gov.tr
salman@mam.gov.tr,saksoy@penta.gyte.edu.tr

ABSTRACT

The described systems combine possibilities as well of tomograph operating "on passage" as tomograph operating in regime of undersurface measurements.

It is shown that if incident wave is arranged at Brewster angle, surface reflection is decreased and the imaging by microwave tomography method or the stepped frequency radar method of buried weakly scattered objects like mine etc. is better than at non Brewster angle.

The new reduction method of the surface contribution in an image of subsurface objects is offered and considered. The essence of the method consists in using leaky waves of a transmission line of electromagnetic energy, when the line is located close to a surface, for illumination of subsurface objects.

The suggesting version of tomography is orientated towards applications in industry, medicine, detection and identification of abandoned objects and other fields.

INTRODUCTION

Development of millimeter wave and microwave tomography for nondestructive testing and subsurface investigations is suggested. It may be manufactured as well in waveguide modification as in quasioptical one. Using both of these approaches will allow us to create microwave or millimeter wave tomograph providing the image reconstruction of the object under investigation.

The modeling and experimental results of the image reconstruction of the buried objects are given and studied with the using of the angle spectrum of scattered field and the microwave tomography method. In the inverse problem, a complex function of space coordinates representing the normalized polarization currents, have been reconstructed. A modulus of the complex function is the image of the object under investigation. The reconstruction algorithm is based on Fourier inverse formulas.

The tomography setups contain electrodynamical systems operating in frequency range 2.5-4.5 GHz, 4-12 GHz and 100 GHz. A vectorial network analyzer measures real and imaginary parts of the scattered field and allows to sample the data about scattered field at 512 frequency points. Scanner can move two dielectric antennas (transmitter antenna and receiver antenna) in the plane and rotate the object studied.

One of the most important problems for imaging of buried objects by microwave tomography method is the reflection from surface. Experiments show that the level of surface reflection is very high. Because of this reflection from surface, it is very hard to get images from weakly scattered objects like mine etc. if they are buried close to surface. This paper shows that if

incident wave is arranged at Brewster angle, surface reflection is decreased and the imaging by microwave tomography method of buried weakly scattered objects like mine etc. are better than at non Brewster angle.

The new reduction method of the surface contribution in an image of subsurface objects is offered and considered. The essence of a method consists in using leaky waves of a transmission line of electromagnetic energy, when the line is located close to a surface, for illumination of subsurface objects.

RECONSTRUCTION OF MICROWAVE CROSS-SECTION IMAGES OF IMMERSED DIELECTRIC BODIES BY FIRST ORDER DIFFRACTION TOMOGRAPHY

The basic equation of the diffraction tomography [1] may be obtained as a result of solution of a scattering inverse problem of a plane electromagnetic wave by the object under investigation. So, the scattered field in the first-order Born approximation $U_S^{(1)}(\vec{r})$ may be written in integral form:

$$U_S^{(1)}(\vec{r}) = \int G(\vec{r} - \vec{r}')Q(\vec{r}')U_I(\vec{r}')d\vec{r}' \qquad (1)$$

where $G(\vec{r} - \vec{r}')$ is Green function; $Q(\vec{r}')$ is the object function; $U_I(\vec{r}')$ is the incident field; $\vec{r}, \vec{r}'$ are coordinates. In inverse scattering problem, function $Q(\vec{r}')$ should be find at known scattered field $U_S^{(1)}(\vec{r})$. Solution of such problem using the integral equation (1) allows to obtain the main equation of diffraction tomography. Results of the image reconstruction of dielectric cylinders immersed in sand are obtained by the main equation of diffraction tomography and described in this section. Functional scheme of experiment is shown in Fig.1.

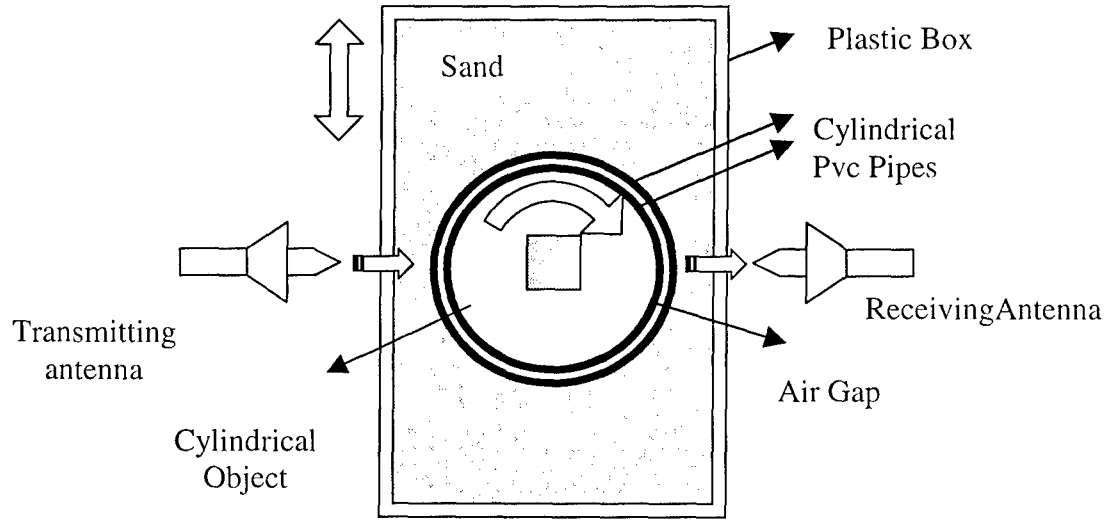

Fig.1. Functional scheme of experiment with dielectric objects immersed in sand.

In the test the data are collected on distance 0.3 meter with space step $\Delta x \cong 0.005$m. The rotation angle step is $\Delta\phi \cong 19°$, the number of slices is 19. After obtaining amplitude and phase distributions of scattered field, the image processing is carried out by using the image reconstruction program. Only the data at 7.5 GHz (λ=4cm) are used for image reconstruction. In the experiment some dielectric materials of different shapes: like paper, marble, wood, PVC (plastic) and also two kinds of landmine were used. In Fig.2 one can see cross-sectional images of two ceramic rods (a)) and antipersonnel mine of M14 type (b)), which were obtained with using experimental data. In the figures, there are real cross-sections of objects as well.

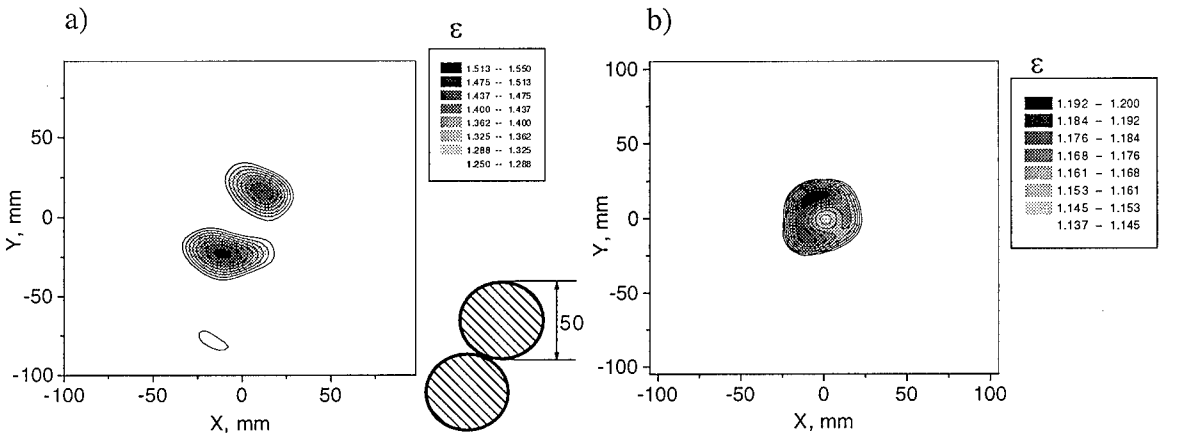

Fig.2. Images of two ceramic rods (a)) and antipersonnel mine of M14 type (b)).

SUBSURFACE TOMOGRAPHIC ALGORITHM

In this part we will briefly consider our approach [2] to the image processing in subsurface diffraction tomography. The scattered field $\psi(x, y_1)$ at line $y = y_1$ (1-D case, Fig.3) can be represented in the form of Fourier integral

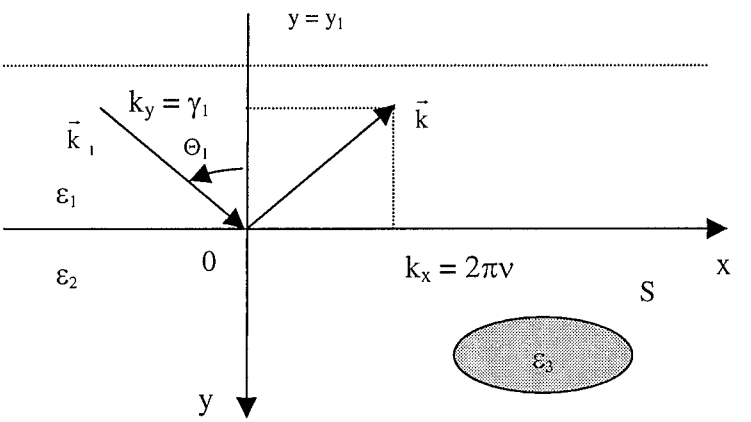

Fig.3. The region under consideration in plane x, y and projections of wave vector on axes of the coordinates.

$$\psi(x, y_1) = \int_{-\infty}^{\infty} \hat{\psi}(\nu, y_1) \exp(2\pi i x \nu) d\nu \qquad (2)$$

where $\hat{\psi}(\nu, y_1)$ the Fourier image of $\psi(x, y_1)$ and it is defined as

$$\hat{\psi}(\nu, y_1) = \varphi(\nu)\exp\left[-iy_1\sqrt{k^2-(2\pi\nu)^2}\right] = \varphi(\nu)\exp(-i\gamma_1 y_1); \quad (3)$$

$\gamma_1 = \sqrt{k^2-(2\pi\nu)^2}$; $k = (\omega/c)$ is wave number of plane wave in free space; ω is cyclic frequency; c is velocity of light. Function $\varphi(\nu)$ can be written as

$$\varphi(\nu) = c_1(\nu)c_2(\nu) \quad (4)$$

where $$c_1(\nu) = \frac{ik_2^2 T}{\gamma_1+\gamma_2} \quad ; \quad (5)$$

T is Fresnel transmittance of the boundary between two media with dielectric permittivities $\varepsilon_1 = \varepsilon_0$ (air) and $\varepsilon_2 = \varepsilon_{r2}\varepsilon_0$ (ε_{r2} is relative dielectric permittivity); $\gamma_j^2 = k_j^2 - (2\pi\nu)^2$; $k_j = \omega^2\varepsilon_j\mu_0 + i\omega\mu_0\sigma_j$, $j = 1,2$; ε_2, σ_2 are electrodynamical parameters characterizing medium where cylindrical dielectric objects under investigation are embedded, ε_2 is dielectric permittivity; σ_2 is conductivity. Function $c_2(\nu)$ may be written in the integral form

$$c_2(\nu) = \iint_S K(x', y')\exp\left[-2\pi i(\alpha x' + \beta y')dx', dy'\right] \quad (6)$$

where $\alpha = \alpha(\nu, \omega, \theta_1)$; $\beta = \beta(\nu, \omega, \theta_1, \varepsilon_{r2}, \sigma_2)$ are functions [3]; symbol S denotes that integration is over the cross section S of object under investigation; function $K(x', y')$ represents normalized the polarization current which is sought for; θ_1 is an angle of incidence; symbol S denotes that integration is over the cross section S of object under investigation; function $K(x', y')$ represents normalized the polarization current which is sought for. Thus desired function $K(x', y')$ is found by means of inverse Fourier transformation and by function $\hat{\psi}(\nu(\alpha, \beta), y_1)$.

In numerical experiment, a reconstruction of imaging function $\tilde{K}(x, y) \sim |K(x, y)|$ at normal angle of incident $\theta_1 \cong 0$ was carried out in the frequency band $\Delta f = 4.0 \div 3.52$ GHz at 17 frequencies (the currents were summarized) with step of $\Delta f = 0.03$ GHz. Relative dielectric permittivities and conductivities of the mediums are equal: $\varepsilon_{r1} = 1$; $\varepsilon_{r2} = 5$; $\sigma_2 = 0.0$; $\varepsilon_{r3} = 4$ (object). Relative magnetic permeabilities of the media were taken as 1. The electric field amplitude of incident plane wave is equal $1\,V/m$ and an incidence $\theta_1 \cong 0$. Scattered field $\psi(x, y_1)$ has been calculated using formula (1) in the bounded limits of integration by $\nu = -30 \div 30m^{-1}$ at values of $x = -4\lambda_0 \div 4\lambda_0$ ($\lambda_0 = 0.1m$) with constant step $\Delta x = 0.002m$. These values of ν are used also in the inverse problem. Images were reconstructed in the field $4\lambda_0 \times 4\lambda_0$ at values of $x = -2\lambda_0 \div 2\lambda_0$ and at values of $y \cong 0 \div 4\lambda_0$.

Fig.4 shows the reconstructed images of studied dielectric cylinder (black contour) by method described above. Data about scattered field was calculated at $y_1 = -0.01\lambda_0$. In the picture 4.a) one can see the subsurface object at using in calculation of scattered fields of the region $0.0 < |\nu| < 11.0m^{-1}$, corresponding only to the propagating waves in the spectrum of field. We can conclude that in this case the position of the image corresponds to the position

of object. But the cross-section shapes are different. In h-direction (into depth) the size of the image bigger than in x-direction. The structure of the image cross-section is smooth. The best results can be obtained if in the image reconstruction the full range (including evanescent waves of the field spectrum at all frequencies from 3.52 GHz to 4.0 GHz) of $0.0 < |\nu| < 30.0m^{-1}$ is used. In the picture 4 b) one can see the object image in this case.

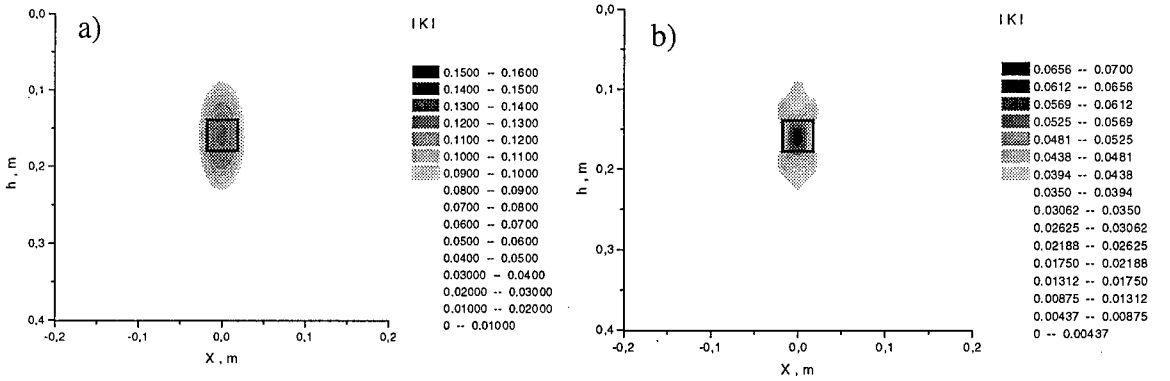

Fig.4. Reconstructed images with using only of the nonevanescent part (a)) of the plane waves spectrum of scattered field and full spectrum (b)).

Fig.5 shows the reconstructed images of two marble rods, which are placed in the sand. Experimental data about back-scattered field were measured on the line above surface of sand. It was used into the image processing only the nonevanescent part of the plane waves spectrum of scattered field. In picture 5 a) one can see rods located "in depth", and picture 5 b) illustrates the case when rods are distributed "in cross direction".

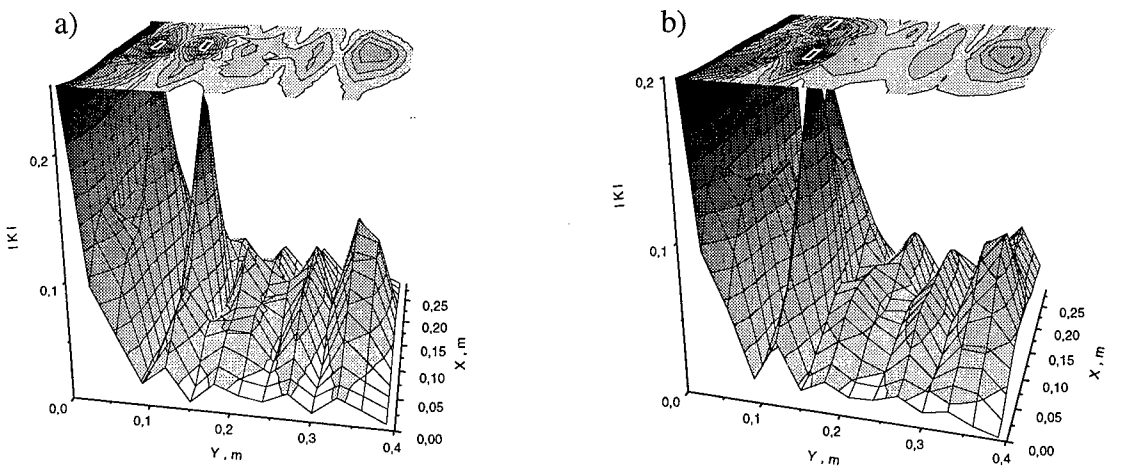

Fig.5. Reconstructed images with using only of nonevanescent part of the plane waves spectrum of the back-scattered field measured by experimental setup.

IMAGING OF BURIED OBJECTS BY MICROWAVE TOMOGRAPHY METHOD IN CONDITIONS OF LOW REFLECTION ON SURFACE MEDIUM

Reflection coefficient between two medium with relative dielectric constans $\varepsilon_0 = 1$; ε_r for the case of parallel polarization are introduced according to the following equation,

$$\eta = \frac{(\varepsilon_r - \sin^2 \alpha_1)^{1/2} - \varepsilon_r \cos\alpha_1}{(\varepsilon_r - \sin^2 \alpha_1)^{1/2} + \varepsilon_r \cos\alpha} \quad . \tag{7}$$

An important feature of η is that it vanishes for an angle of incidence $\alpha_1 = \alpha_b$, called *Brewster Angle,* where from reflection coefficient equation, can be found as follow,

$$\alpha_b = \arcsin\left(\left(\frac{\varepsilon_r}{\varepsilon_r + 1}\right)^{1/2}\right) \quad . \tag{8}$$

At this particular angle of incidence, all the incidence power is transmitted into the dielectric medium.

In our case, objects such that different kinds of mines, metals etc. are buried in sand and general viewing of this subsurface experimental setup are given in Fig.6.

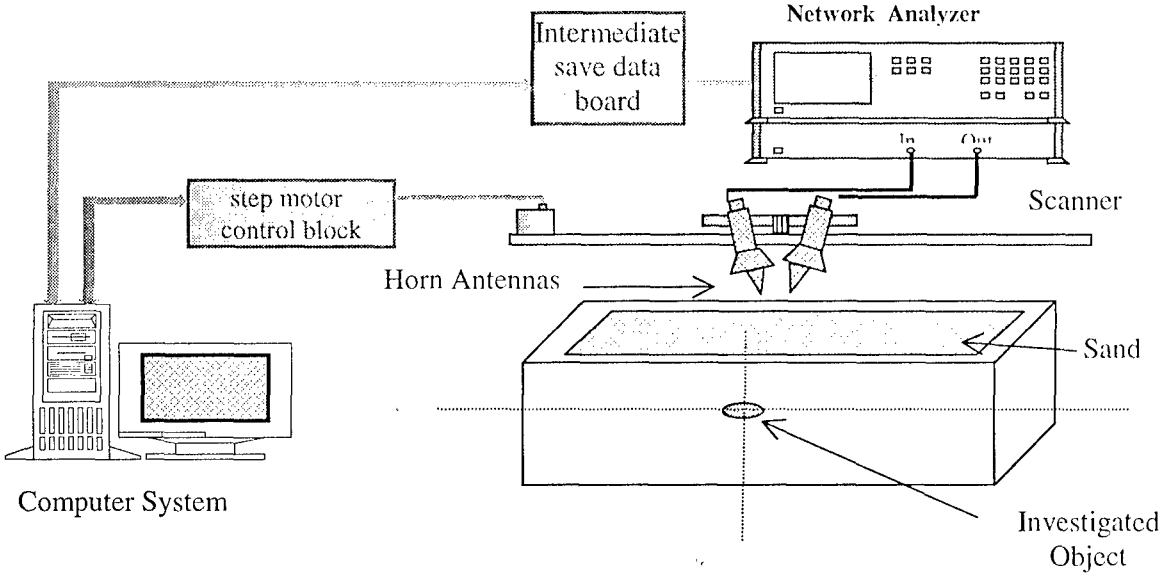

Fig.6. Experimental setup for the investigations of buried objects.

According to figure 6, receiving and transmitting antennas are moved by scanner to get scattered field data for diffraction tomography processing. In our case, transmitting antenna is arranged at Brewster angle [4], which is obtained 50 degree experimentally for soil. Brewster angle of soil is calculated experimentally and drawn graphics in figure 7. Two experimental results are given in Fig.8 and Fig.9. Fig. 8 shows the tomography image of buried mine at 60 degree which is not Brewster angle for sand. Fig.9 shows the image of buried mine at 50 degree which is Brewster angle for sand.

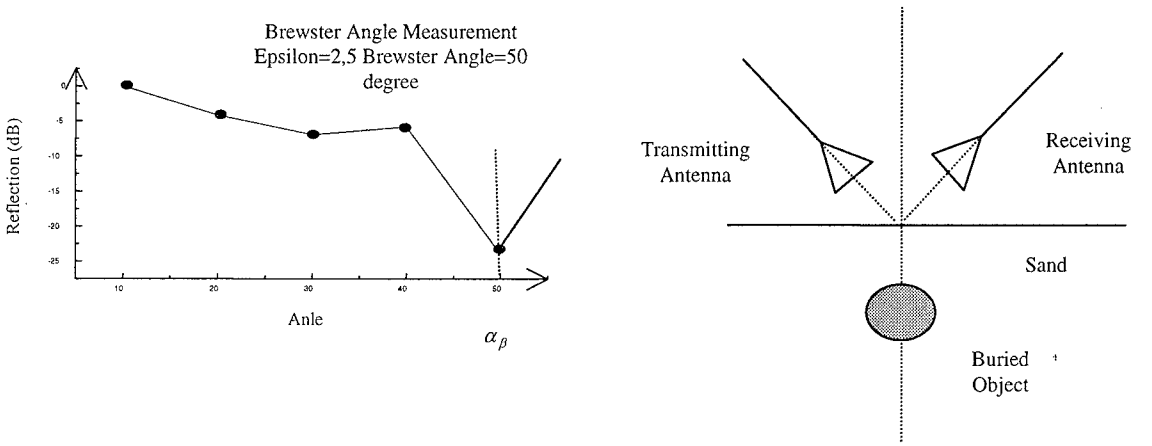

Fig.7. Brewster angle calculation for soil (measured)

If one compares these results, it is clear that at Brewster angle, reflection from surface is decreased and reflection from object is increased according to non-Brewster angle.

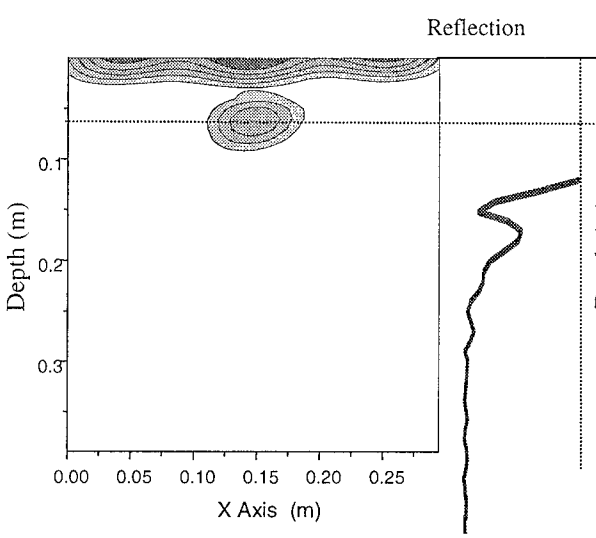

Fig.8. The image of buried mine at 60 degree (non Brewster angle)

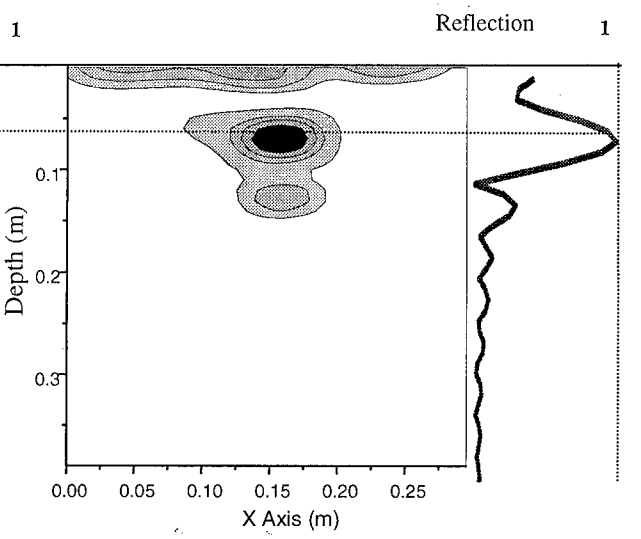

Fig.9. The image of buried mine at 50 degree (Brewster angle)

REFERENCE

1. F.Natterer.The Mathematics of Computerized Tomography.- M.: Mir, 1990.-288P, (in Russian).

2. Vertiy A.A., Gavrilov S.P.,"Microwave imaging of cylindirical inhomogenities by using a plane wave spectrum of diffracted field", Second International Conference the detection of abandoned land mines, Conference publication No:458,pp.91-95,IEE 1998,Edinburg,UK

3. Chommeloux *A*, L. Pichot, Ch. Bolomey, J. – Ch., 1986, Electromagnetic modelling for microwave imaging of cylindrical buried inhomogeneties, *IEEE Trans. Microwave Theory Tech.*, Vol. MTT – 34, No. 10, pp. 1064 – 1076.

4. Phlip M. Reppert, F.Dale Morgan, M. Nafi Toksoz, "GPR Velocity Determination Using Brewster Angles", 8th International Conference on GPR,pp.485-490,1998, Kansas,USA

ANTENNA SUB SYSTEM FOR METEOSAT SECOND GENERATION SATELLITES: MODELING TOOLS AND NEEDS

*Kees van 't Klooster
**Massimo Di Fausto, I. Florio,
***Alessandro Rosa, (****) Bernard Robert

*ESA/ESTEC, POBox299, 2200 AG Noordwijk, The Netherlands, kvtkloos@estec.esa.nl
**Alenia Spazio, Spa. Via Saccomuro 24, 00131 Roma, Italy, fax +39-06-4151-2389,
***Space Engineering, Via Berio 91, 00131 Roma, Italy, fax +39-06-2280739,
****Alcatel Space Industries, 100 B., 06156 Cannes la Bocca, France, fax +33-49292-3470

ABSTRACT

The Meteosat Second Generation (**MSG**) program concerns the launch and operation of three new satellites in the coming years. **MSG** continues meteorological services, which are currently provided by the very successful first generation of satellites (Meteosat Operational Program - **MOP**), operated by Eumetsat. **MSG** expands on services offered by **MOP** by providing more frequently data in more observation bands, with higher resolution. A telecommunication system on-board the **MSG** satellite transmits measured data to the primary ground station and receives and re-transmits pre-processed images and meteorological data as received from the latter station. Meteorological data are collected from data collection platforms. The **MSG** satellite carries a Search and Rescue transponder. The antenna sub-system has been specifically designed for the telecommunication functions and permits appropriate data throughput with the satellite spinning at a rate of 100 revolutions per minute.

The antenna sub-system for **MSG** is described, after a short general description.

BACKGROUND

The first pre-operational Meteosat satellite was launched in 1977. Meteosat Operational Program was started in 1983 after a 'pre-operational' period with an agreement to launch three operational satellites. A prototype pre-operational satellite called P2, was prepared and launched with an ARIANE 4 launcher in 1988. The last **MOP**-satellite was launched in 1997, it continues service today (Meteosat Transitional Program or **MTP**). **ESA** carried out operations of Meteosat satellites ([1] data collection, pre-processing and redistribution of meteorological information), until the new European organisation **Eumetsat** took over these tasks in 1995. Eumetsat operates the MOP satellites and MTP [2] today. Services continue untill 2001 after which

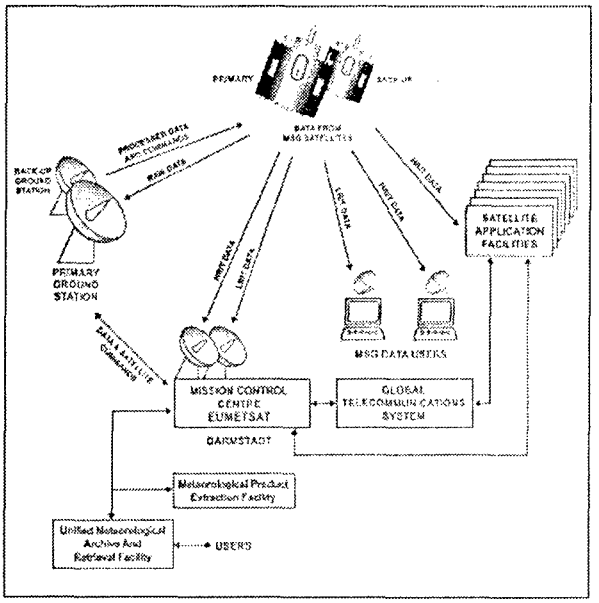

Figure 1: *MSG Mission Scenario with RF links for the raw radiometer data to the primary ground station (with back-up) and the up- and downlinks for the processed data to primary and secondary users*

MSG satellites shall take over. ESA and Eumetsat are preparing this **MSG** program, with ESA responsible for procurement of the satellites.
First some descriptive information is given for both MOP and MSG satellites. It is followed by the main subject of this paper: a description of the MSG antenna-system. Modelling, optimisations and associated tools are outlined, with decisions made. Realised performances of this specific antenna sub-system, functioning on a spinning satellite, are shown.

MOP AND MSG SATELLITES

A **MOP**–type satellite orbits the Earth at an altitude of 35.800 km, in geostationary orbit, thus leading to a satellite position above the equator on a fixed meridian (for Meteosat the Greenwich meridian). It is a spin-stabilised spacecraft, rotating at a speed of 100 revolutions per minute (100 RPM). It has its spin-axis perpendicular to the orbital plane. The primary payload for MOP is a high resolution three channel radiometer instrument, which images the Earth in less than half an hour in three spectral bands (λ = 0.5–0.9 μm, 10.5–12.5 μm and 5.7-7.1 μm). One image line is taken each revolution of the satellite over the Earth disc over the angular range from +10° to –10° (as seen from the geostationary orbit). An image composed out of 2500 scan-lines results after 2500 revolutions, thus in 25 minutes.
The stored image line data are re-sampled and transmitted down to the Earth during remainder part of the 360° arc outside this ±10° interval. The data are processed at a dedicated location (at Eumetsat in Darmstadt), where also other meteorological products are derived. Processed images with additional data are sent up again towards the satellite, which redistributes data to users within the coverage zone. Much more info is found in [1] and [2]. Meteosat (MOP and MTP) are also received in Ukraine [3]. The satellite collects also meteorological data from remote (automatic) platforms within its coverage zone and relays this information to the central ground station (this is the so-called DCP mission). A very broad basis of experiences has been created with the satellite, with its operations, with data processing and data utilisation, after more than 25 year. It provided a very good starting point for a configuration of a new satellite, the Meteosat Second Generation satellite.

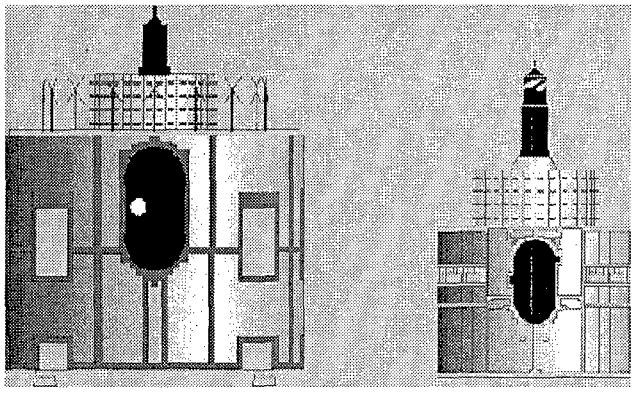

Figure 2: *MSG satellite (left) and MOP satellite at a similar scale*

MSG satellite will also be a spin-stabilised spacecraft, operating from a geo-stationary location, with a number of enhanced capabilities. The radiometer generates images at double the speed (15 min) and operates in 12 spectral bands with better resolution (1 km for the visible channel, 3 km for other spectral channels). This permits to extract three-dimensional data about the atmospheric composition.
The reader is invited to estimate the pointing and localisation correctness (1 km from 35800 km). The larger amount of data from MSG is also transmitted to a new primary ground station of Eumetsat (in Usingen in Germany), from where processed data are transmitted up to the satellite again for re-distribution to primary and secondary users within the coverage [2]. Fig.1 shows the link schema. MSG provides the data collection mission (DCP) with a larger number of channels than available on the MOP satellite. A Search and Rescue transponder is carried. It makes use of the UHF and L-band antenna for respectively reception (up) of emergency messages and transmission (down).MSG is a much larger

spacecraft than MOP, due to the enhanced capabilities with the much larger radiometer, the need for a longer lifetime and the associated supporting equipment. Fig. 2 shows the MOP spacecraft and the MSG spacecraft (left) with relative dimensions. Fig.2 indicates also already a very important constraint for the antenna farm, located on top of the spacecraft. The height permitted for the antenna farm of MSG is relatively small, much less than the height available on top of the MOP satellite body. This is very important; it has led to many calculations to optimise the antennas for MSG in the presence of the satellite body as indicated below. Conversion of the transfer orbit to the geostationary orbit is also different: MOP used a solid fuel apogee boost motor to change from the transfer orbit to the geostationary orbit with one motor firing. MSG will use a set of two apogee boost motors, which use bi-propellant fuel. Three motor firings are planned to convert the transfer orbit to geostationary orbit (fig.3).

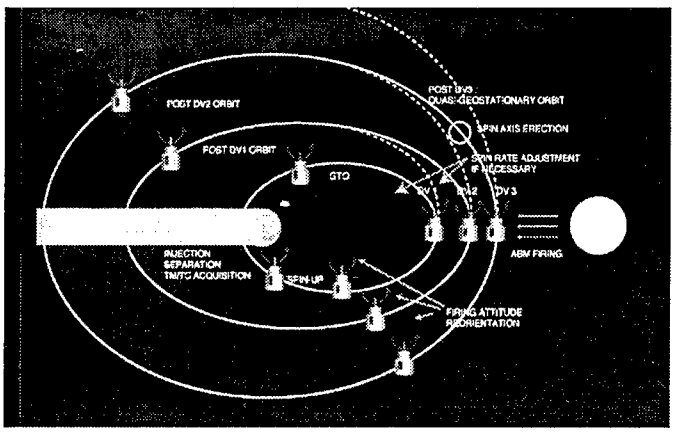

Figure 3: *From a high elliptic trasnfer orbit to a geostationary orbit. MSG will use three motor firings*

ANTENNAS USED IN THE TELECOMMUNICATION SYSTEM

The MSG telecommunication system performs a number of tasks, using dedicated antennas:

- Reception of telecommands and transmission of house keeping data. Two (redundant) S-band transponder are connected to a dedicated telemetry and telecommand antenna, (TT&C antenna), the antenna is not redundant.
- Transmission of measured radiometry data, coming from the data handling subsystem to a primary groundstation. The electronically despun antenna (EDA) is used for this task in L-band.
- Reception of pre-processed images with associated data, using a toroidal pattern S-band antenna.
- Transmission to users, using the L-band EDA antenna for low resolution and high-resolution data.
- Receiving data from Data Collection Platforms (DCP) by means of an Electronically Switched Circular array antenna (UHF-EDA, operating at 402 MHz).
- Transmission of the DCP data, using the L-band EDA antenna.

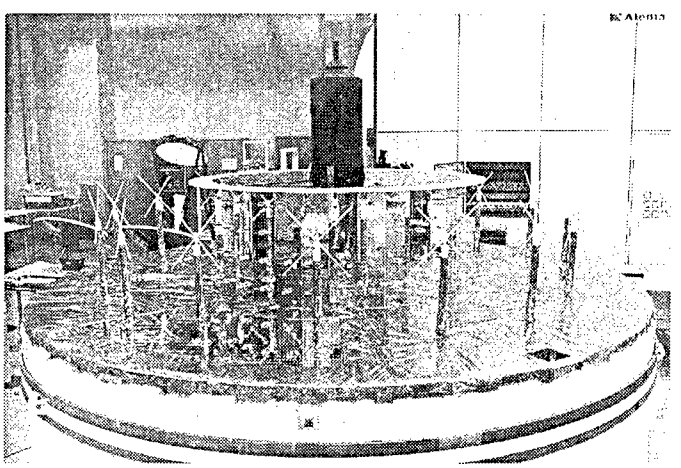

Figure 4: *MSG Antenna Farm, Engineering Model, (courtesy Alenia Spazio)*

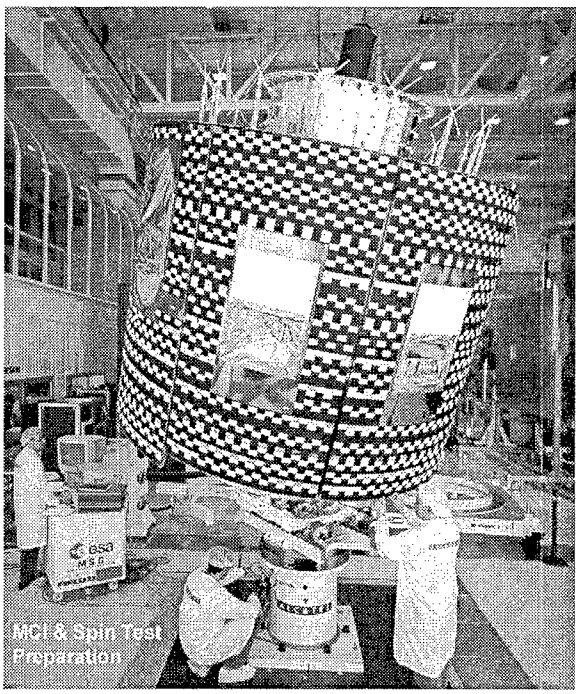

Figure 5: *MSG Satellite with Antenna Farm on top (Qualification Model, courtesy Alcatel)*

Figure 6: *TT&C antenna for MSG, wiregrid model for design calculations at ESTEC (right)*

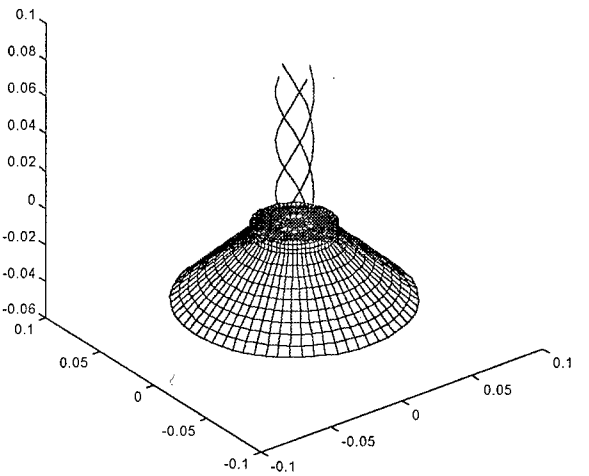

- Receiving emergency messages (Search and Rescue). The UHF – EDA is used at 406 MHz.
- Transmission of S&R messages, using the L-band EDA antenna near 1544 MHz.

Alenia Spazio is responsible for design, manufacture and test of the MSG antenna sub-system.

The Engineering Model antenna sub-system was completed early 1999 and the first Flight Model antenna sub-system has been tested last summer on a dedicated antenna test range at Alenia.

Fig.4 shows the flight model with the different antennas from top to bottom:

-1- TT&C antenna on top,

-2- S/L-band toroidal pattern antennas inside a black cylindrical radome,

-3- L-band Electronically Despun Antenna, using 32 columns, 4 dipole radiators in each column.

-4- UHF Electronically Despun Array (16 crossed dipole radiators), in front of the L-Band EDA.

See also other references for more details on design and analyses references [5] (MOP), [6,7] (MSG).

Fig.5 shows the qualification (thermal/mechanical) model of the MSG satellite with the antenna platform on top, just before the spin test in Alcatel in Cannes.

TT&C ANTENNA

A low-gain wide-coverage antenna, mounted on top is used for the link for telemetry and telecommanding (TT&C) of the satellite. During launch and early orbit phase (LEOP, fig.3) a more wide coverage is needed than when MSG is in the operational phase (on-station). MOP type satellites use such type of antenna of a much older design (quadri-filar helix). Relative pattern information for such antenna was derived from tests during the LEOP phase [4] and compared with predictions and tests before launch. However, the MOP TT&C could not be used directly. A MOP satellite is much smaller than a MSG satellite (fig.2). A detailed design and optimisation had to be carried out with the much larger MSG geometry taken into

account. The antenna uses four spiral conductors printed on a cylinder and fed in phase quadrature. The antenna has a mass below 200 gram and operates in S-band (2000 MHz band for telecommand and 2200 MHz band for telemetry).

The coverage from the spinning MSG satellite is within an angular volume from $\theta=0°$ (satellite spin-axis, North) to $\theta=120°$ for all azimuth angles in right hand circular polarisation. Optimisation of the antenna was done in a sequence of steps, initially at antenna level alone, followed by taking into account the effect of the complete satellite body. This resulted into an optimum antenna geometry. For the antenna alone, the associated electrical field integral equation has been solved using Method of Moments (MoM). Various parameter settings have been explored to optimise gain and axial ratio for a maximum coverage. Fig.6 shows a wire grid model, used in such type of calculations. Software like NEC or comparable tools are readily available for such analyses.

The presence of the satellite body and the part of the antenna farm below the TT&C antenna must be taken into account, which is possible with GTD analyses. The use of MoM is not advisable, as the number of segments required in the model to represent the antenna with also the satellite-body (very big in terms of wavelength). It would lead to too big sizes for the matrix to be inverted. The main scattering elements are a few wavelengths away, permitting to use geometrical theory of diffraction. The MoM pattern of the antenna alone was used as input to the calculations. The effects due to the nearly rotationally symmetric spacecraft structure are predominantly affecting the visibility region for larger theta angles, as is visible from test results shown below. For $\theta=120°$ the pattern level drops fast. The axial ratio is clearly influenced by the satellite body. This is observed in the predictions. Fig. 7 shows radiation patterns for antenna (measured with a mock-up for the satellite). The antenna has been designed, manufactured and tested by SAAB Ericsson (who also produced the TT&C antenna for MOP). Extensive supportive calculations have been carried out in the design phase by Estec and by Space Engineering.

TOROIDAL PATTERN ANTENNAS IN S- AND L-BAND

Two toroidal pattern antennas (TPA) are used, operating in S-band (2101–2107 MHz) and L-band (1684- 1690 MHz) respectively. These antennas are narrow band resonant slotted waveguides antennas and provide a toroidal pattern in the plane perpendicular to the spin-axis. Each slotted waveguide has three slots on each broad-wall side of its (reduced height) waveguide. The antennas are mounted side-by-side inside a black painted radome. Such S/L TPA is also used for MOP.

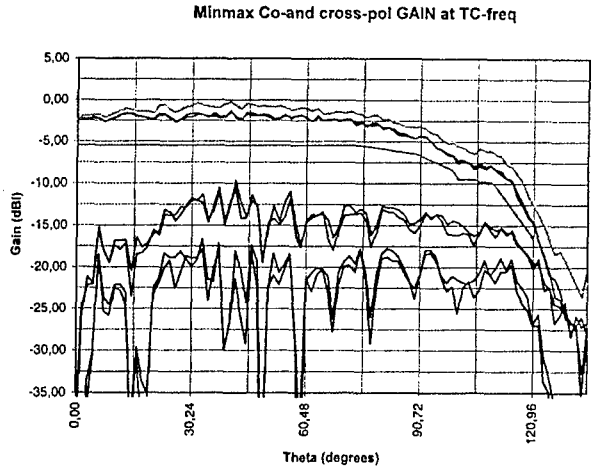

Figure 7: *TT&C antenna for MSG. Min and max level for co-polar pattern with spec (upper two curves) and cross-polar pattern (any azimuth) evaluated using a S/C mock-up (courtesy SaabEricsson)*

Geometric constraints for MSG led to a need for a position more near to the upper platform (compared to the previous relative location on MOP). Such a lower position combined with the larger diameter of the satellite (fig.2) has clear effect, as is observed in the radiation pattern. Analyses and tests showed that the TPA could be used to cover Europe as required (the S-

band uplink will be from a dedicated groundstation in Usingen – Germany). The use of narrow bandwidth resonant slots implies a low coupling between respective S and L-band Rx- and Tx channels. It is an interesting feature of the configuration with the antennas side-by-side, that a remarkably good (toroidal) antenna pattern is provided in the azimuth plane, even in the azimuth direction, where there is the neigh-bouring L-band antenna. The far-field phase behaves cosine-like, as expected due to the offset of the wave-guide axis from the spin-axis. The L-band toroidal pattern antenna is the back-up transmit antenna for a highly unlikely situation of a failure of the L-band Electronically Despun Antenna.

L-BAND EDA ANTENNA

The L-band Electronically Despun Antenna (EDA) is a transmission-only antenna, used to send data to the primary groundstation and to re-transmit processed images to the users. Also DCP messages and Search and Rescue messages are transmitted with this antenna. A toroidal pattern antenna can not achieve the necessary gain and with the limited volume available for the antenna, one or another despun antenna is a natural choice. Mechanical despun antennas are used in several telecommunication (spinning) satellites and have been used for meteorological satellites. A mechanical despun antenna has a disadvantage, that it may give potential disturbances due to micro-vibrations, which can lead to a degraded image quality. This is the case in particular for MSG with its resolution and localisation requirements from an orbit of 35800 km altitude.

The advantage of an electronically despun antenna (EDA) was already recognised for the first Meteosat satellite[5]. The EDA has demonstrated itself as a very robust and elegant antenna. It has been selected also for the **MSG** antenna subsystem. Fig 4 shows the EDA cylindrical array, just below the black radome for the toroidal antennas. The circular array of crossed UHF dipoles is located around the EDA. Fig 8 shows the L-band EDA antenna with TPA and TTC antenna on top.

The EDA antenna consists of a cylindrical array with 32 columns with four dipole elements in each column. The radiating columns are connected to pin-diode switches, which regulate the actual number of 4 or 5 active radiating columns out of the 32 columns.

Fig.9 gives a schema [5] for the feed network. The incoming transmit-signal is split in 4 equi-phase and equi-amplitude signals by means of a four-way power divider (4WPDV). Each of the four branches is connected to a variable power divider (VPD). Each VPD has two outputs, each connected to pin-diode switches (single-pole, 4-through – SP4T). The SP4T's route the power to the radiating columns, as selected to form a radiating set of 4 or 5 out of 32 columns on the Earth facing side. The 4WPDV consists of 3 Wilkinson-type 2-way power dividers. The VPD uses a power division scheme in which an input hybrid divides the power into two channels. In one of the channels a phase-shift φ between 0° to -90° is provided, synchronously with a phaseshift φ between 0° to +90° phase-shift in the other

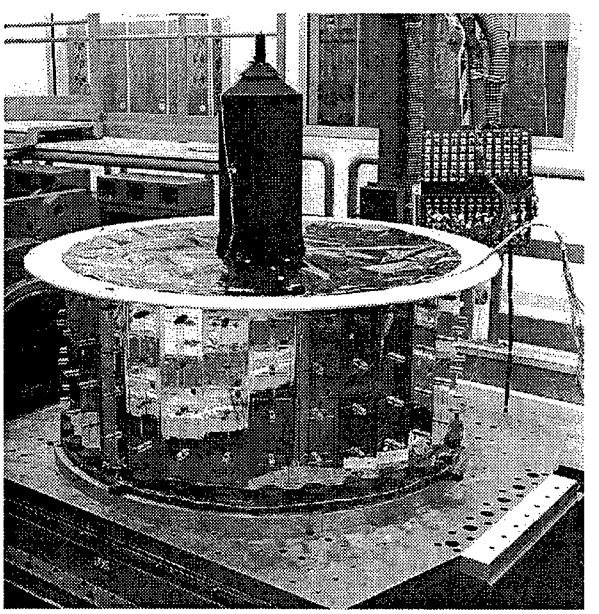

Figure 8: *L-Band EDA with S/L TPA and TTC antenna on top, before environmental testing (courtesy Alenia)*

branch. Then the two channels are combined again using a 3-dB hybrid circuit. The two output ports of the latter hybrid provide a power level as a function of this phase shift φ:

$$P_{out\text{-}1} = ½ (\cos \varphi + \sin \varphi)^2$$

$$P_{out\text{-}2} = ½ (\cos \varphi - \sin \varphi)^2$$

Seven pre-selected phase settings for φ lead to seven distinct power division steps, between 1 and 0, respectively 0 and 1 in complement for the two VPD-output power levels. With this scheme, the incoming power is routed to four adjacent columns (step '1'). One out of the four VPD's switches gradually (in 7 steps) the power from the first column to the fifth column, after which a next VPD switches over from column 2 to column 6, after this the next VPD takes over, etc. In this way a set of 4 (step '1' and step '7') or 5 adjacent radiating columns (step '2' through step '6') out of the 32 available is provided, by an appropriate VPD and SP4T control. A logical circuitry, which is synchronised with the spinrate, provides the actual control signals for VPD and SP4T. Earth-sensors are used to provide the correct angular reference to this logical circuitry. In this way the active set of radiating columns can be kept automatically pointed towards the Earth, while the satellite is spinning. The antenna operates between 1670 and 1695 MHz and provides a link also for the Search and Rescue downlink (1544.5 MHz). The switching scheme for the VPD is designed to have a minimum amplitude and phase ripple. The resulting pattern is very characteristic for the EDA and is in fact its 'fingerprint'. An example of one out of the seven switching states is the EDA beam for a VPD step 4 setting (the lowest gain is obtained for step '4') is given in fig.10. There are 32 of VPD '4' beams realised in one revolution.

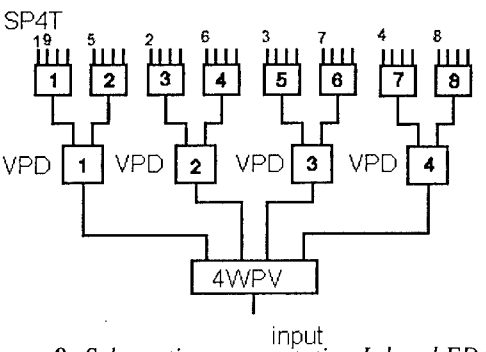

Figure 9: *Schematic representation L-band EDA beam-forming network [5]*

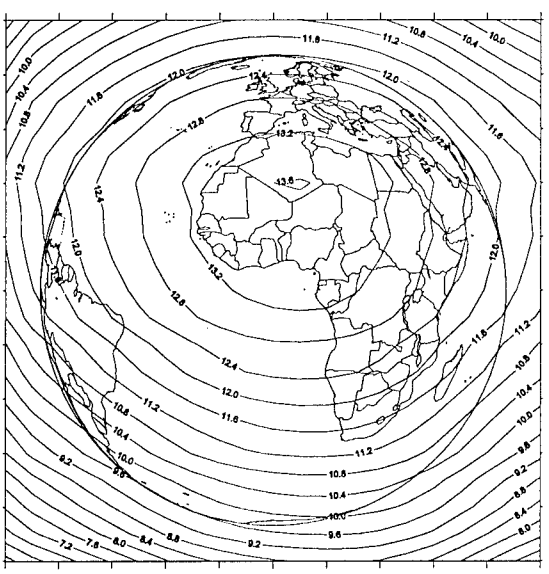

Figure 10: *Typical L-band EDA antenna pattern for a fixed beam for VPD setting in step '4', derived from tests on the EM model on Alenia's far-field test range. Courtesy Alenia/Space Engineering*

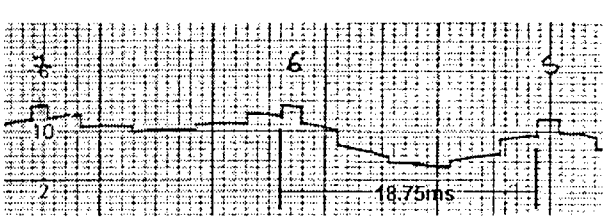

Figure 11: *Typical L-band EDA dynamic antenna pattern fragment, taken on the Alenia far-field test range (2 dB/div vertical, 10 %div horizontal)*

The larger diameter of the MSG platform (compared to MOP) causes obviously an impact on the EDA antenna pattern. This was carefully analysed and precautions were taken. The large platform leads to a slight more northward pointing of the EDA beam. Installation of a UHF electronically despun

array in front of the L-band EDA causes obviously an impact. This was thoroughly analysed and checked by testing. A characteristic fragment of a dynamic diagram over a small azimuth interval (22.5°) is shown in Fig.11. The switching sequencing (7 steps during 11.25°) is noticed.

THE UHF-BAND ELECTRONICALLY DESPUN ANTENNA

The data collection task (DCP) in the UHF band (402.1 MHz) could be handled for MOP with an antenna with –0.5 dBi gain over the coverage. For MSG, with the increased number of DCP channels, a higher gain has been desirable. Furthermore, the installed Search & Rescue transponder uses this antenna for its receiver at 406 MHz and requires higher gain. Moreover, with the geometry constraints for the satellite, the height available to accommodate the antenna farm has been reduced compared to MOP. It led after many analyses of performances to the choice of an electronically switched antenna. Some antenna elements are needed to provide some gain and then smooth switching at this frequency (λ=75 cm) requires a relative large diameter. With the available L-band EDA antenna drum, with a diameter of 1.30 meter, the UHF antenna has been designed with 16 elements, at a distance of about ¾λ in front of the L-band EDA. The L-band EDA drum is used as reflecting surface. There are 4 out of 16 dipoles actively used for a beam. The other elements are switched to a load. Every 22.5°, the next UHF dipole is actively connected to this group of four, while one dipole at the other side of the group of 4 is switched off. In this way an active set of 4 dipoles is switched around, thus providing an antenna with a contra-rotating switched beam. The beamforming circuitry for this receive-only antenna is more simple than for the L-band EDA. One 4-way power divider connects to four 4-way switches, which switch in the active elements. The control of the latter switches is also synchronised with the spin-rate. The antenna elements are crossed dipoles, installed on a mast above the satellite platform. Fig. 4 shows the dipoles. More directive elements could have been used, but at a cost of mass and also increased blockage of the L-band EDA performances. Alenia Spazio, as responsible for the antenna design, has been supported by Space Engineering for analysis and optimisation work. Several extensive calculations have also been carried out at ESA-Estec. At this frequency the satellite is only a few wavelength in size and the configuration is rotationally symmetric. This permits to handle the analysis work by using Method of Moment approaches, in which rotational symmetry is exploited. It is observed, that the current

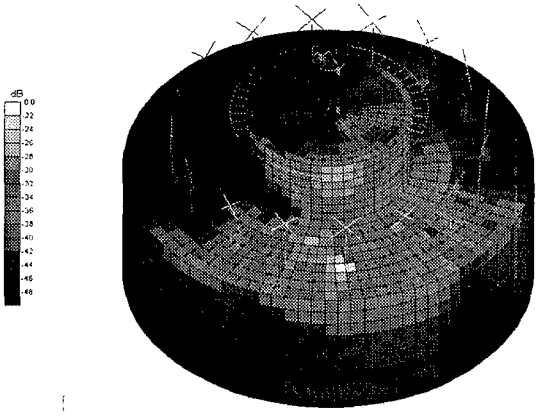

Figure 12: *UHF antenna element in presence of the structure and 15 terminated elements (Courtesy: Space Engineering)*

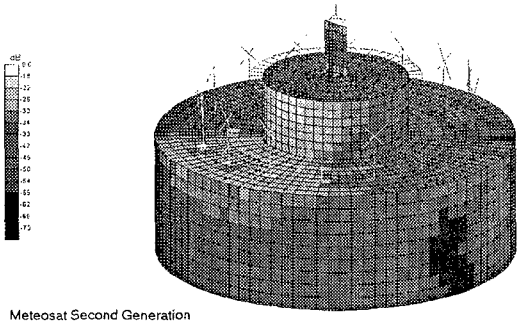

Figure 13: *Four UHF antenna elements in the presence of the structure and the other 12 terminated elements (Courtesy Space Engineering)*

distributions on the antenna elements as well as on the scattering satellite structure contribute to the pattern (the whole satellite acts as antenna). The current representation on the structure elements of the model can be derived and an example of such a result is shown in fig. 12, where one dipole as active element is located in the 16-element UHF array. The current distribution (and – note - its asymmetry) is clearly observed. Fig.13 shows the relative current distribution for the full array. Interesting perceptions are made: the bottom locations of the UHF dipoles are important. One notes also the secondary excitation of dipoles not actively used in the array of 4 elements, but switched in the line to a load (in the 4way switch).

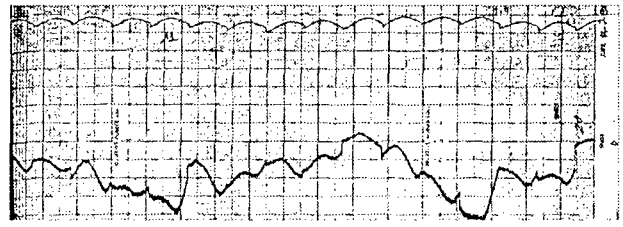

Figure 14: *UHF dynamical pattern over 360°(2 dB/div vertical, 10°/div horizontal). The periodicity related to the switching every 22.5° is observed, co and cross polarisation levels are shown, measured for 5° elevation South (406 MHz) (Courtesy Alenia Spazio)*

It has been proved useful to add a scattering structure on top of the L-band EDA (fig.4). This structure has been designed, such, that it is scattering at UHF, but nearly transparent in L-band. The latter structure is noticed in the models in fig.12 and 13 and the relative current level indicates, that it is functional for the UHF radiation pattern (it has led to a gain improvement of about 0.3 dB). The blockage effect of the UHF antenna for the L-band EDA has been analysed and led to the geometry as used. Indeed, there is an impact of about 0.2 a 0.3 dB, but this has to be allowed for. Fig.14 shows dynamical pattern for a UHF EDA antenna measured on Alenia's test range over 360° in azimuth at a frequency of 406 MHz.

CONCLUDING REMARKS

The specific antenna sub-system for the spinning Meteosat Second Generation satellite was discussed. An initial description of the satellite tasks was given. Differences between the MOP and the MSG antenna systems were highlighted. Modeling aspects and decisions, based on modeling, for antenna configuration selections were indicated, like for instance the location of the UHF array in front of the L-band array. The available analysis tools provided a possibility to take such design decisions.

The impact of scattering by the spacecraft has been an important issue for all antennas. The resulting configuration as designed, built and tested by Alenia Spazio is very interesting both in theoretical and actual realised sense. Currently, the first Flight Model Antenna sub-system has been fully tested at Alenia Spazio and it has also been checked out, after installation on the complete satellite.

REFERENCES

[1] http://www.esa.int/, also under remote sensing, /msg

[2] http://www.eumetsat.de/

[3] http://www.cri.chernigov.ua/, http://www.nas.gov.ua/d/d5/nas_d5i10.html/

[4] 'Antennas for Scientific and Remote Sensing Satellites', C.G.M.van 't Klooster, N.E.Jensen, Invited paper JINA Antenna Conference, Nice,1990.

[5] 'Meteosat Antenna System' Nicolai, Alenia Spazio, Alenia Revista, 1976.

[6] 'The Antenna Subsystem for the New Earth Weather Observation Satellites Meteosat Second Generation.' P.Carati, M.Di Fausto, V.Santachiara, A.Rosa,P.Russo, JINA Antenna Conference Nice, Nov. 1998.

[7] 'EMC Aspects in Meteosat Second Generation Antenna Subsystem', G. Di Benardo, P.Russo, L.Di Cecca, V.Santachiara, G.A.J. van Dooren, C.G.M. van 't Klooster, Partnership for Peace Symposium on EMC, San Miniato, 1996, Italy.

The Concept of Confluence and the Edge Conditions for a Wedge Bounded by Material Sheets

Mithat IDEMEN

ISIK university, Büyükdere Cad.,80670 Maslak, Istanbul,Turkey.
E-mail: idemen @ ISIKUN.edu.tr

Abstract. The *edge conditions* which dictate the asymptotic behaviour of the electromagnetic field near the edges play a crucial role in solving boundary-value problems involving boundaries having edges. In analytical studies they permit one to determine some unknown functions while in numerical investigations they enable one to improve the convergence of some processes by introducing beforehand the edge singularities into the field functions. This work is devoted to the analysis of wedge configurations bounded by *material sheets* having different constitutive parameters. From mathematical point of view, the problem can be reduced to 9 *canonical* types. These canonical types are investigated in full detail by introducing the *confluence concept* which permits one to reveal also the *logarithmic singularities*, if any.

1.Introduction

From both experimental and theoretical works it is known that some components of the electromagnetic field exhibit singularities of certain types near edges. Many investigations concerning structures involving edges require the knowledge of the types and orders of these singularities beforehand because their knowledge in analytical investigations (based, for example, on the Wiener-Hopf or Riemann- Hilbert techniques) permits one to determine some auxiliary functions while in numerical works it enables one to improve the convergence of some procedures if the singularities are incorporated into the field expressions explicitly. The aim of the present paper is to investigate the edge conditions for a wedge with boundaries formed by arbitrary *material sheets* in its most general form by a rather simple but rigorous approach.

The history of the edge conditions for the electromagnetic field goes back to a work by Bouwkamp in 1946. In this work connected with a perfectly conducting half-plane located in an infinite homogeneous space, he showed that it is possible to find many solutions satisfying both the Maxwell equations and the boundary conditions. They differ from each other by their singularities near the edge, which are, in general, not physically acceptable. If one knows the physically acceptable singularity, then one can find the unique, physically meaningful solution. The problem was then considered by many researchers. For example

-in 1949 Meixner [1] postulated the expansions in the form of power series of $r^{1/2}$, namely:

$$\Pi(r,\phi) = A(\phi) + B(\phi)r + C(\phi)r^{3/2} + \ldots,$$

where (r,ϕ,z) stand for the circular cylindrical coordinates such that $r = 0$ corresponds to the edge.

-in 1972 Meixner [2] proposed a modification of his first expansion, namely:

$$E_r(r,\phi) = a_0(\phi)r^{t-1} + a_1(\phi)r^t + a_2(\phi)r^{t+1} + \ldots.$$

(similar expressions for the other components).Here t stands for a number which will be determined through both the Maxwell equations and the boundary conditions.

-in 1976 Hurd[3] proposed to use the results to be derived from the solution of the *static field* problems connected with the same geometrical and physical conditions.

-in 1985 Van Bladel [4] used the same concept.

-in 1964 Jones [5] postulated an expansion which depends on the concept of *separable solutions*, namely:

$$\Pi = \sum\sum a_{m\nu}\, Y_\nu\{(k^2 - m^2)^{1/2} r\} e^{imz} \begin{matrix}\sin \nu\phi \\ \cos \nu\phi\end{matrix},$$

where Y_ν stands for the usual Neumann function which is singular when $r \to 0$.

-in 1988 Braver and his colleagues [6] proposed to write

$$\Psi(r,\phi) = r^\tau \sum_{m=0}^{\infty} \sum_{n=0}^{m} C_{mn}(\phi) r^m \ln^n r, \qquad \tau \geq 0.$$

The Ansatzes of Meixner were criticized by several investigators because i) they had no sound basis and, consequently, although the first terms they yield are correct, their higher order terms are invalid (nonexisting), and ii) they do not involve logarithmic singularities and, consequently, their results are sometimes wrong.

As to the *static field approachs*, they start from the Laplace equation and consider merely an electric (or a magnetic) field not coupled to a magnetic (or an electric) field whereas many boundary conditions which are actually in extensive use involve electric and magnetic fields simultaneously.

The critiques directed to Meixner can also be repeated for Braver. For example, according to the well-known theory of the ordinary linear differential equations, near a regular-singular point the solution of an equation of the second order may involve only lnr but not $(\ln r)^n$ with $n \geq 2$. Secondly, from the recurrence relations to be satisfied by C_{mn}, it is not easy to find the maximum power of the logarithms. Furthermore, it is rather hard to elaborate the postulated expressions to derive results concerning rather complicated boundary conditions and geometrical configurations.

Finally, to conclude this short historical introduction we want also to draw the attention to some methods depending on integral equations used by Maue [1949] and Jones [1950].Though they are much more general as compared to the above-mentioned ones and allows directly for curved edges as well as those which change direction discontinuously, in a situation similar to the present investigation which concerns the most general boundary conditions they seem to result in too complicated equations.

Now, by considering the diversity of the boundary conditions which frequently appear in the open literature as well as those which seem to have important practical applications in near future, we will try to formulate the problem in its most general form. To this end we will consider a wedge with faces formed by arbitrary material sheets and apply the above-mentioned method of *separable solutions* combined with the concept of *confluence*, which will both produce the logarithmic singularity, if any , and clarify the reason behind this type of singularity. A time dependence exp(-iωt) is assumed and omitted throughout the paper.

2.Formulation of the Problem

For the sake of mathematical simplicity, we will define a coordinate system Oxyz such that the wedge is symmetrical with respect to the plane y = 0 and the edge is coincident with the z-axis. We will also assume that the given point is the origin and the field does not depend on the z-coordinate (see Fig.-1). The faces S

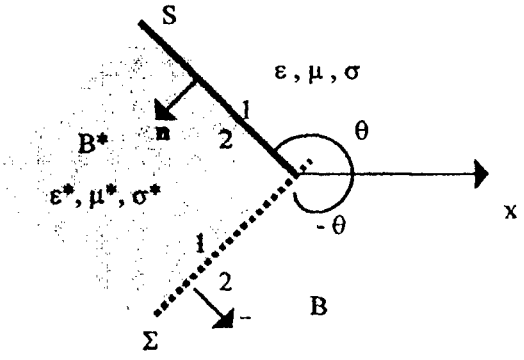

Figure-1

and Σ of the wedge are supposed to be *material* half-planes which may, in general, be *penetrable*. Hence, one has to consider both regions B and B* separated by the wedge. Then the limiting field values on the boundary S, observed from sides 1 and 2, are interrelated by two boundary conditions which can be written in the following forms(see [7,8]):

$$(1)\quad a_1\mathbf{n}\times\mathbf{H}+a_2\mathbf{n}\times\mathbf{H}^*+a_3\mathbf{E}_t+a_4\mathbf{E}_t^*+a_5\mathbf{n}\times\mathrm{grad}H_n+a_6\mathbf{n}\times\mathrm{grad}H^*_n+a_7\mathrm{grad}E_n+a_8\mathrm{grad}E^*_n=0$$

$$(2)\quad b_1\mathbf{n}\times\mathbf{H}+b_2\mathbf{n}\times\mathbf{H}^*+\ \ldots\ldots\ +b_8\mathrm{grad}E^*_n=0.$$

In these equations **n** stands for the unit normal on S directed from side 1 to side 2 while the subindices n and t refer to the normal and tangential components, respectively. As to the superindex (*), it refers to the values observed inside the region B. The coefficients a_i and b_i are known complex constants which can be determined through the constitutive parameters of the material of the sheet modelled by S [8].If the material of the sheet is isotropic in tangential directions (it may be anisotropic when both the tangent and the normal directions are considered together), then (1,2) can model the sheet S rather accurately [7,8].Similar relations are also written for the face Σ. In what follows, the coefficients related to Σ will be denoted by α_i and β_i, namely:

(3) $\alpha_1 \mathbf{n}\times\mathbf{H}^*+\alpha_2 \mathbf{n}\times\mathbf{H}+\alpha_3 E^*_t+\alpha_4 E_t+\alpha_5 \mathbf{n}\times \mathrm{grad} H^*_n+\alpha_6 \mathbf{n}\times \mathrm{grad} H_n+\alpha_7 \mathrm{grad} E^*_n+\alpha_8 \mathrm{grad} E_n =0$

(4) $\beta_1 \mathbf{n}\times\mathbf{H}^*+\beta_2 \mathbf{n}\times\mathbf{H}+ \quad \ldots\ldots\ldots \quad +\beta_8 \mathrm{grad} E_n =0.$

If all the coefficients with even indices in (1) and odd indices in (2) are zero (or (1) and (2) can be reduced to such a system), then S constitutes an impenetrable boundary. The same is true for (3),(4) and Σ also. When both S and Σ are impenetrable, the boundary S+Σ becomes a shield and separates the regions B and B* completely from each other. In such a case the regions B and B* have to be considered separately. In what follows we will first consider the case where the boundary S+Σ is penetrable. The results concerning the impenetrable wedge will then be derived from those concerning the penetrable one by straightforward simplifications.

3.The Wedge With Penetrable Boundary

In this case all the cartesian components of the electromagnetic field satisfy the same reduced wave equation near the edge, namely:

(5) $\Delta u(r,\phi) + k^2 u(r,\phi) = 0, \quad r\in[0,r_0),\ (r,\phi)\in B$

(6) $\Delta u(r,\phi) + k^{*2} u(r,\phi) = 0, \quad r\in[0,r_0),\ (r,\phi)\in B^*,$

where r and ϕ are the usual cylindrical polar coordinates while k and k^* stand for the wave numbers of the regions B and B*, respectively. As to r_0, it is a certain positive number determined by the sources.

As is well known, every particular solution to equ. (5), which satisfies certain boundary conditions, consists, in general, of discrete or continuous combinations of its *separable solutions*. These latter are of the form $u = R_\nu(r)\Phi_\nu(\phi)$ with

(7) $$R_\nu(r) = \begin{cases} J_\nu(kr) \text{ when } \nu \notin \{0,\pm1,\pm2,\ldots\} \\ J_n(kr) + A_n Y_n(kr) \text{ when } \nu = n \in \{0,1,2,\ldots\} \end{cases}$$

and

(8) $$\Phi_\nu(\phi) = \begin{cases} B_\nu \cos\nu\phi + C_\nu \sin\nu\phi \quad \text{when } \nu \neq 0 \\ B_0 + C_0\phi \quad \text{when } \nu = 0 \end{cases}$$

Here ν stands for the separation parameter while J_ν and Y_n denote the usual Bessel and Neumann functions. The set of ν which has to be taken into account to construct a particular solution $u(r,\phi)$ is the *spectrum* of u. The spectrum as well as the constants A_n, B_ν and C_ν appearing in (7) and (8) can be determined by considering also the sources as well as the boundary and radiation conditions, which is beyond our present aim. Our aim consists of revealing the asymptotic behaviours of the field components when $r \to 0$. In order to this end we have to consider the following expresssions of J_ν and Y_n, which are valid near r = 0:

(9) $J_\nu(kr) = \alpha r^\nu + \beta r^{\nu+2} + \ldots., (\nu \neq -1,-2, \ldots)$

(10) $Y_n(kr) = \alpha_1 r^{-n} + \beta_1 r^{-n+2} + \ldots + [\gamma_1 r^n + \gamma_2 r^{n+2} + \ldots] \ln r.$

Here α, α_1 etc are certain numbers. From (9) and (10) one concludes at first glance that when $r\to 0$ the field can become singular having infinitely large values as a negative power of r or logarithm of r. To reveal the asymptotic behaviours (and admissible singularities) of the field components for $r \to 0$, we will (and must!) take into account the fact that i)the field components satisfy the Maxwell equations , ii) the energy stored near the edge is finite, and iii) the boundary conditions on S +Σ are satisfied.In what follows we will study the contributions of these restrictions separately. In order to reduce useless mathematical complications, we will consider the E- and H-cases separately. In E-case the electric field is parallel to the edge while in H-case the magnetic field is parallel to it.

3.1.The H-case

In this case, all the non-zero components of the electromagnetic field near the edge in B can be written in terms of a scalar potential u satisfying (5), namely:

(11) $$H_z = k^2 u, \qquad E_r = (i\omega\mu)/r\partial u/\partial\phi, \qquad E_\phi = -i\omega\mu\partial u/\partial r.$$

By replacing k and μ in (11) by k^* and μ^*, respectively, one gets the expressions valid in B^*. By considering these expressions with the restrictions (i-iii) mentioned above we get the following results.

A.Contribution of the energy restriction

As is well known, the densities of the stored electric and magnetic energies are proportional to $|\mathbf{E}|^2$and $|\mathbf{H}|^2$, respectively. In order for the total electromagnetic energy stored in a finite volume including the edge to be finite, one has to have

(12) $$(r)^{1/2} H_z(r,.),\ (r)^{1/2}E_r(r,.),\ (r)^{1/2}E_\phi(r,.) \in L^2[0, r_0].$$

On the other hand, (7,8) and (9,10) yield

(13) $$R_\nu(r) \sim \begin{cases} \text{constant}.r^\nu & \text{when } \nu \neq n \\ \text{constant}.r^n + \text{constant}.A_n r^{-n} & \text{when } \nu = n \geq 1 \\ 1 + \text{constant}.A_0 \ln r & \text{when } \nu = n = 0 \end{cases}$$

By using (13) and (8) in (12) one gets easily

(14) $$\Re\nu > 0 \text{ when } \nu \neq n, \qquad A_n = 0 \text{ when } n = 0,1,\ldots \text{and} \qquad C_0 = 0.$$

Here $\Re\nu$ stands for the real part of ν.From these we conclude that the separable solutions can not individually involve logarithmic singularities. Such a singularity in the field may come from certain kind of *confluence* which generates *nonseparable* solutions (see Sec.G below).

B.Contribution of the Maxwell equations

Because of (14), the above-mentioned potential function u consists of a combination of certain functions u_ν whose *dominant* asymptotic expressions are as follows:

(15) $$u_\nu \sim \begin{cases} B_0 \text{ when } \nu = 0 \\ \left[B_\nu \cos\nu\phi + C_\nu \sin\nu\phi\right] r^\nu \text{ when } \Re\nu > 0. \end{cases}$$

The parameter ν appearing above is the number which both belongs to the spectrum and has the *smallest* real part. All the numbers ν which will appear below will designate this *minimal* ν. We suppose first that

(16) $$\nu \neq 1,2,\ldots.$$

The case where $\nu = n \in \{1,2,\ldots\}$will then be treated as to be a limiting case $\nu \to n$ as certain parameters approach some critical values (see the remark in Sec.E below). By using (15) and (16) in (11) we get

(17a) $$E_r \sim r^{\nu-1}[P\cos\nu\phi + Q\sin\nu\phi]$$

(17b) $$E_\phi \sim r^{\nu-1}[Q\cos\nu\phi - P\sin\nu\phi]$$

(17c) $$H_z \sim k^2 B_0 + ik^2/(\nu\omega\mu)\, r^\nu[Q\cos\nu\phi - P\sin\nu\phi],$$

where P, Q and B_0 are certain constants to be determined through the boundary conditions.

The expressions related to the region B^*, for which $\phi \in (\theta, 2\pi-\theta)$, are quite similar, namely:

(18a) $E_r \sim r^{\nu-1}[P^* \cos\nu\phi + Q^* \sin\nu\phi]$

(18b) $E_\phi \sim r^{\nu-1}[Q^* \cos\nu\phi - P^* \sin\nu\phi]$

(18c) $H_z \sim k^{*2}B^*_0 + ik^{*2}/(\nu\omega\mu^*)\, r^\nu[Q^* \cos\nu\phi - P^* \sin\nu\phi]$.

C.Contribution of the boundary conditions

If we consider (16), (17a-c) and (18a-c) in (1), then the coefficients of the powers $r^{\nu-2}$, $r^{\nu-1}$ and r^ν permit us to write

(19) $f(a_7,a_8) = 0, \quad g(a_3,a_4) + g_1(a_7,a_8) = 0, \quad f(a'_1,a'_2) + f_1(a_3,a_4,a_7,a_8) = 0,$

where we put

$$a'_1 = ik^2 a_1/(\omega\mu\nu), \qquad a'_2 = ik^{*2}a_2/(\omega\mu^*\nu),$$

$$f(a,a') = a[P \sin\nu\theta - Q \cos\nu\theta] + a'[P^* \sin\nu\theta - Q^* \cos\nu\theta]$$

and

$$g(a,a') = a[P \cos\nu\theta + Q \sin\nu\theta] + a'[P^* \cos\nu\theta + Q^* \sin\nu\theta].$$

As to the functions $f_1(a_3,a_4,a_7,a_8)$ and $g_1(a_7,a_8)$, they exist only when the points $\nu+1$ and $\nu+2$ belong to the spectrum, and are homogeneous linear functions of their arguments as well as of the additional unknown coefficients connected with the spectral points $\nu+1$ and $\nu+2$. In what follows we will not need the explicit expressions of f_1 and g_1.

The result to be obtained from (19) can be summarized as below:

$$\begin{aligned}\text{Cond.(1) on } S \Rightarrow \text{ if } |a_7|+|a_8| \neq 0 &\Rightarrow f(a_7,a_8) = 0\\ \text{if } |a_7|+|a_8| = 0 &\Rightarrow \text{when } |a_3|+|a_4| \neq 0 \Rightarrow g(a_3,a_4) = 0\\ &\quad\ \text{when } |a_3|+|a_4| = 0 \Rightarrow f(a'_1,a'_2) = 0.\end{aligned}$$

The discussion made for (1) can also be repeated for (2). The result is quite the same except that the constants a_i are now replaced by b_i.

Consider finally the conditions written on Σ. They give the similar results

$$\begin{aligned}\text{Cond.(3) on } \Sigma \Rightarrow \text{ if } |\alpha_7|+|\alpha_8| \neq 0 &\Rightarrow \psi(\alpha_8,\alpha_7) = 0\\ \text{if } |\alpha_7|+|\alpha_8| = 0 &\Rightarrow \text{when } |\alpha_3|+|\alpha_4|\neq 0 \Rightarrow \chi(\alpha_4,\alpha_3)=0\\ &\quad\ \text{when } |\alpha_3|+|\alpha_4| = 0 \Rightarrow \psi(\alpha'_2,\alpha'_1)=0.\end{aligned}$$

Here we put

$$\alpha'_1 = ik^{*2}\alpha_1/(\omega\mu^*\nu), \qquad \alpha'_2 = ik^2\alpha_2/(\omega\mu\nu),$$

$$\psi(\alpha,\alpha') = -\alpha[P \sin\nu\theta + Q\cos\nu\theta] + \alpha'[P^*\sin\nu(2\pi-\theta) - Q^*\cos\nu(2\pi-\theta)]$$

and

$$\chi(\alpha,\alpha') = \alpha[P\cos\nu\theta - Q\sin\nu\theta] + \alpha'[P^*\cos\nu(2\pi-\theta) + Q^*\sin\nu(2\pi-\theta)].$$

Notice that the same results are also valid when α_i are replaced by β_i.

D.An example

In order to clarify the above discussion let us reconsider a generalization of a configuration studied earlier by both Lang and Braver. In this example S is perfectly conducting while Σ consists of a resistive half-plane. One supposes also that the spaces B and B* have the same constitutive parameters.Then, the boundary condition tables are

$$S \Rightarrow \begin{bmatrix} 0 & 0 & 1 & 0 & 0 & 0 & 0 & 0 \\ 0 & 0 & 0 & 1 & 0 & 0 & 0 & 0 \end{bmatrix}, \qquad \Sigma \Rightarrow \begin{bmatrix} 0 & 0 & 1 & -1 & 0 & 0 & 0 & 0 \\ 1 & -1 & 1/R & 0 & 0 & 0 & 0 & 0 \end{bmatrix},$$

which yield

$$P\cos\nu\theta + Q\sin\nu\theta=0\ , \qquad P^*\cos\nu\theta + Q^*\sin\nu\theta=0$$

$$-P\cos\nu\theta + Q\sin\nu\theta+P^*\cos\nu(2\pi-\theta) +Q^*\sin\nu(2\pi-\theta)=0\ , \qquad P^*\cos\nu(2\pi-\theta) +Q^*\sin\nu(2\pi-\theta)=0.$$

The compatibility of these homogeneous equations requires $\Delta(\nu) = -\sin2\nu\theta\ \sin2\nu(\pi-\theta) = 0$ and gives

$$\nu = \min\{\pi/2\theta,\pi/2(\pi-\theta)\}$$

whenever $\theta \neq \pi/2$ (the case of $\theta = \pi/2$ will be discussed at the end of Sec.G below).

E.Determination of ν and canonical types

The four equations such as $f = 0$, $g = 0$ etc, derived in subsection C above constitute a system of linear and homogeneous algebraic equations in terms of the constants P, Q, P* and Q*. Since at least one of these latter is different from zero, the determinant formed of the coefficients appearing in these equations, say $\Delta(\nu)$, is zero. It is the equation $\Delta(\nu)=0$ that will permit us to determine the minimal exponent ν. Since the left hand-sides of the equations are always f or g and ψ or χ and the numerical values of the constants a_i ,b_i,α_i and β_i taking place in these equations are not mathematically important, the cases which have to be considered in full detail are only the following nine *canonical* types:

$$(ff\psi\psi)\ (ff\psi\chi)\ (ff\chi\chi)\ (fg\psi\psi)\ (fg\psi\chi)\ (fg\chi\chi)\ (gg\psi\psi)\ (gg\psi\chi)\ (gg\chi\chi)$$

The determinants corresponding to all these canonical cases except the fifth one can be computed very easily.The results are recapitulated in TABLE-I . From this table it is evidently seen that in four cases (i.e.the types $(ff\psi\psi)$, $(gg\chi\chi)$, $(ff\chi\chi)$ and $(gg\psi\psi)$) the value of ν is determined only via the geometry of the wedge, i.e. via the angle θ, while in the other cases the constitutive parameters of the boundary of the wedge as well as those of the regions B and B* affect also the value of ν.To find the numerical value of ν in these rather complicated cases except the case $(fg\psi\chi)$ one has to solve a trigonometric equation of the form

$$\sin2\nu(\pi - \theta)\cos2\nu\theta = A\sin2\nu\theta\cos2\nu(\pi -\theta),$$

which can be solved, in general, through numerical methods. As to the most complicated case $(fg\psi\chi)$, the resulting equation is as follows:

$$(20) \qquad \Delta(\nu) = \begin{vmatrix} a\sin\nu\theta & -a\cos\nu\theta & a'\sin\nu\theta & -a'\cos\nu\theta \\ b\cos\nu\theta & b\sin\nu\theta & b'\cos\nu\theta & b'\sin\nu\theta \\ \alpha'\sin\nu\theta & \alpha'\cos\nu\theta & -\alpha\sin\nu(2\pi - \theta) & \alpha\cos\nu(2\pi - \theta) \\ \beta'\cos\nu\theta & -\beta'\sin\nu\theta & \beta\cos\nu(2\pi - \theta) & \beta\sin\nu(2\pi - \theta) \end{vmatrix} = 0\ .$$

Notice that the constants appearing in (20) are the parameters which take place in the expressions of the equations (f g ψ χ) successively, namely: $f(a, a') = g(b, b') = \psi(\alpha',\alpha) = \chi(\beta',\beta)=0$.

F.Determination of the constants B_0 and B^*_0

From (17c) it is obvious that when $B_0\neq0$, the dominant behaviour of E_z is not like $O(r^\nu)$ but rather $O(1)$. Therefore one has always to check whether B_0 and B^*_0 are zero or not. The first relations involving these constants can be obtained by considering the terms of order $O(r^0)$ in the boundary conditions mentioned in Subsec.-C above. Now we don't want to consider this point further.

G.Confluence of the zeros of Δ(ν). Logarithmic singularities

The minimal exponent ν which satisfies certain equation $\Delta(\nu)=0$, where $\Delta(\nu)$ denotes an entire function of ν, is obviously a function of the parameters such as θ, a_i, α_i, ε', ε'* etc. Let τ denote any one of these parameters. If we write now the above-mentioned entire function $\Delta(\nu)$ more explicitly as $\Delta(\nu,\tau)$ and consider all the roots of the equation $\Delta(\nu,\tau) = 0$, which are in general of infinite number, then we obtain a relation similar to what is shown in Fig.-2.The minimal exponent ν is, in general, such that the point (τ,ν) is an

ordinary point of the curve which represents all branches of the function $\nu = \nu(\tau)$. In this case $\nu = \nu(\tau)$

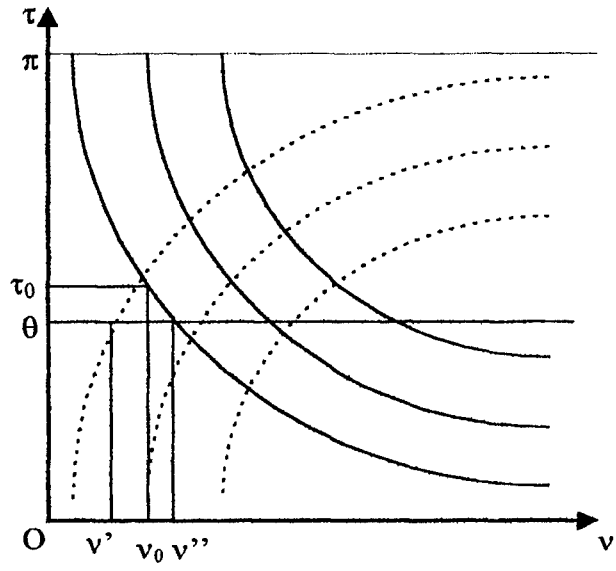

Figure-2

generates the solutions (17a-c) and (18a-c). When τ tends, however, to a certain critical value, say τ_0, the point (τ_0,ν_0) may become a branch point of the curve mentioned above, such that at this point $\nu' \to \nu'' \to \nu_0$ when $\tau \to \tau_0$. Here $\nu'$and ν'' stand for the first two solutions of the equation$\Delta(\nu,\tau)= 0$, i.e. $\Delta(\nu',\tau)=0$ and $\Delta(\nu'',\tau)= 0$. Now it is an easy matter to show that for the couple (τ_0 ,ν_0) one has $[\partial/\partial\nu\, \Delta(\nu,\tau_0)]_{\nu=\nu 0} = 0$, which implies that ν_0 is a *double* root of the equation $\Delta(\nu,\tau_0) = 0$.

Now return to the field expressions given by (17a-c) and suppose that $\tau = \tau_0$. Since this critical case can be thought as to be the limiting case when $\tau \to \tau_0$, we have to consider both exponents $\nu' \to \nu_0$ and $\nu'' \to \nu_0$ together and write

(21) $$E_r \sim \lim_{\tau \to \tau o}\{r^{\nu'-1}\,[P'\cos\nu'\phi + Q'\sin\nu'\phi] + r^{\nu''-1}[P''\cos\nu''\phi + Q''\sin\nu''\phi]\}.$$

Here P',Q',P'' and Q'' denote certain constants which can also depend on the parameter τ, or, inversely, on ν' and ν''. If these coefficients individually tend to certain finite limits, then (21) reduces to (17a). But this is not the only possibility which produces a finite limit. Indeed, if P', Q', P'' and Q'' tend individually to infinity such that

$$P'(\nu') \to (P_0/2)/(\nu' - \nu_0) + P_1 \to P_0/(\nu' - \nu'') + P_1$$

$$P''(\nu'') \to (P_0/2)/(\nu'' - \nu_0) + P_2 \to P_0/(\nu'' - \nu') + P_2$$

$$Q'(\nu') \to (Q_0/2)/(\nu' - \nu_0) + Q_1 \to Q_0/(\nu' - \nu'') + Q_1$$

$$Q''(\nu'') \to (Q_0/2)/(\nu'' - \nu_0) + Q_2 \to Q_0/(\nu'' - \nu') + Q_2,$$

where P_0 ,Q_0 ,P_1, Q_1, P_2 and Q_2 are certain constants, then (21) will also produce a finite limit , namely:

(22) $$E_r \sim r^{\nu o-1}\,[P\cos\nu_0\phi + Q\sin\nu_0\phi] + r^{\nu o-1}[Q_0\,\phi\cos\nu_0\phi - P_0\,\phi\sin\nu_0\phi] + r^{\nu o-1}\ln r\,[P_0\cos\nu_0\phi + Q_0\sin\nu_0\phi].$$

The first term in (22) is quite similar to that in (17a). Therefore, by substituting ν_0 again by ν we can claim that when the minimal exponent ν is a double root of the equation $\Delta(\nu) = 0$, the expressions (17a-c) are replaced by the following *confluent* expressions:

$$E_r \sim r^{\nu-1}[P\cos\nu\phi + Q\sin\nu\phi] + r^{\nu-1}[-P_0\,\phi\sin\nu\phi + Q_0\,\phi\cos\nu\phi] + r^{\nu-1}\ln r\,[P_0\cos\nu\phi + Q_0\sin\nu\phi]$$

$$E_\phi \sim r^{\nu-1}[Q\cos\nu\phi - P\sin\nu\phi] - r^{\nu-1}[Q_0\,\phi\sin\nu\phi + P_0\,\phi\cos\nu\phi] + r^{\nu-1}\ln r[Q_0\cos\nu\phi - P_0\sin\nu\phi]$$

$$H_z \sim k^2B_0 + ik^2/(\nu\omega\mu)r^\nu[Q\cos\nu\phi - P\sin\nu\phi] - ik^2/(\nu\omega\mu)r^\nu[Q_0\,\phi\sin\nu\phi + P_0\,\phi\cos\nu\phi] + ik^2/(\nu\omega\mu)r^\nu\ln r[Q_0\cos\nu\phi - P_0\sin\nu\phi].$$

Notice that these expressions involve also such terms as $r^{\nu-1}[\ln r \cos\nu\phi - \phi\sin\nu\phi]$ and $r^{\nu-1}[\ln r \sin\nu\phi + \phi\cos\nu\phi]$, which are not in separated form (Cf. 7,8).

The relations valid in the region B* (i.e. for $\phi\in(\theta, 2\pi - \theta)$), which corresponds to (18a-c), are obtained from the above expressions through the substitution

$$k\rightarrow k^*,\ B_0 \rightarrow B^*_0,\ \mu\rightarrow \mu^*,\ P\rightarrow P^*,\ Q\rightarrow Q^*,\ P_0\rightarrow P^*_0,\ Q_0\rightarrow Q^*_0.$$

An Example

As an example reconsider the case studied in Sec.-D above. The first two roots of the equation $\Delta(\nu) = 0$ are $\nu' = \pi/2\theta$ and $\nu'' = \pi/2(\pi-\theta)$.They obviously depend on the angle θ and when $\theta\rightarrow\pi/2$, $\nu'\rightarrow\nu''\rightarrow 1$.That means that in the case of a two-part plane with the above-mentioned physical properties there is a coalescence of the roots, which gives rise to logarithmic singularities. Beyond this critical case, the minimal exponent is always simple and results algebraic singularities. It is worthwhile to remark that this configuration was also considered by Lang and Braver et al. Lang has considered the cases of $\theta = 3\pi/4$ (or $\theta = \pi/4$) and $\theta = \pi/2$ while Braver et al. have considered only the case $\theta=\pi/2$. Our results are quite identical to those obtained by Braver et al. for $\theta = \pi/2$ with a different approach except for H_z. According to our results $H_z=o(1)$ while Braver et al.have given $H_z=O(1)$.As to the results given by Lang for $\theta = 3\pi/4$ and $\theta = \pi/2$, they all are quite different from our results.

3.2.The E-case

Consider now the case when the electric field is parallel to the edge. In this case the non-zero components of the electromagnetic field can be obtained from (11) by making the substitutions $-\mu \rightarrow \varepsilon'$, $H_z \rightarrow E_z$, $E_r \rightarrow H_r$ and $E_\phi \rightarrow H_\phi$.But we don't dwell on this topic.

TABLE-I

Minimal exponent ν for the canonical types of a penetrable wedge

Type	Typical equations	ν	validity conditions
(ffψψ)	$f(a,a') = f(b,b') = 0$ $\Psi(\alpha',\alpha) = \Psi(\beta',\beta) = 0$	$\min\{\pi/(2\theta),\pi/(2(\pi-\theta))\}$ $(1/2<\nu<1)$ $\nu = 1$ (double⇒log singularity).	$ab'-a'b \neq 0,\quad \theta \neq \pi/2$ $\alpha\beta'-\alpha'\beta \neq 0$ $\theta \rightarrow \pi/2$
(ggχχ)	$g(a,a') = g(b,b') = 0$ $\chi(\alpha',\alpha) = \chi(\beta',\beta) = 0$	$\min\{\pi/(2\theta),\ \pi/(2(\pi-\theta))\}$ $(1/2<\nu<1)$ $\nu = 1$ (double⇒log singularity).	$ab'-a'b \neq 0,\ \theta \neq \pi/2$ $\alpha\beta'-\alpha'\beta \neq 0$ $\theta \rightarrow \pi/2$
(ffχχ)	$f(a,a') = f(b,b') = 0$ $\chi(\alpha',\alpha) = \chi(\beta',\beta) = 0$	$\min\{\pi/(4\theta),\pi/(4(\pi-\theta))\}$ $(1/4<\nu<1/2)$	$ab'-a'b \neq 0$ $\alpha\beta'-\alpha'\beta \neq 0$
(ggψψ)	$g(a,a') = g(b,b') = 0$ $\psi(\alpha',\alpha) = \psi(\beta',\beta) = 0$	$\min\{\pi/(4\theta),\pi/(4(\pi-\theta))\}$ $(1/4<\nu<1/2)$	$ab'-a'b \neq 0$ $\alpha\beta'-\alpha'\beta \neq 0$
(ffψχ)	$f(a,a') = f(b,b') = 0$ $\psi(\alpha',\alpha) = \chi(\beta',\beta) = 0$	$tg2\nu(\pi-\theta) = Atg2\nu\theta$ $A = -\alpha'\beta/(\alpha\beta')$	$ab'-a'b \neq 0$
(fgψψ)	$f(a,a') = g(b,b') = 0$ $\psi(\alpha',\alpha)=\psi(\beta',\beta)=0$	$tg2\nu(\pi-\theta) = Atg2\nu\theta$ $A = -ab'/(a'b)$	$\alpha\beta' - \alpha'\beta \neq 0$
(fgχχ)	$f(a,a') = g(b,b') = 0$ $\chi(\alpha',\alpha) = \chi(\beta',\beta) = 0$	$tg2\nu(\pi-\theta) = Atg2\nu\theta$ $A = -a'b/(ab')$	$\alpha\beta' - \alpha'\beta \neq 0$
(ggψχ)	$g(a,a') = g(b,b') = 0$ $\psi(\alpha',\alpha) = \chi(\beta',\beta) = 0$	$tg2\nu(\pi-\theta) = Atg2\nu\theta$ $A = -\alpha\beta'/(\alpha'\beta)$	$ab'-a'b \neq 0$
(fgψχ)	$f(a,a') = g(b,b') = 0$ $\psi(\alpha',\alpha) = \chi(\beta',\beta) = 0$	equa.(3.14)	

4.The Wedge With Impenetrable Boundary

If the boundaries of the wedge are impenetrable material sheets, then the electromagnetic fields inside B and B* can exhibit different asymptotic behaviours when $r \to 0$. That means that the expressions in (17a-c) and (18a-c) are written with different exponents ν and ν^* inside B and B*, respectively. Since the expressions valid for B* can be obtained from those for B by making $k \to k^*$, in what follows we will consider only the region B.

Without loss of generality we can assume that

$$a_2 = a_4 = a_6 = a_8 = 0, \qquad b_i = 0 \qquad (i = 1,\ldots,8)$$

$$\alpha_1 = \alpha_3 = \alpha_5 = \alpha_7 = 0, \qquad \beta_i = 0 \qquad (i = 1,\ldots 8).$$

In such a case the canonical types consist only of $(f\psi)$, $(f\chi)$, $(g\psi)$ and $(g\chi)$. The value of the minimal exponent ν corresponding to these cases are shown in TABLE-II. It is interesting to observe that the value of ν is always determined only by the geometry of the wedge (i.e. by the angle θ).

TABLE-II

Minimal exponent ν for the canonical types of an impenetrable wedge

Type	ν	validity conditions
$(f\psi)$, $(g\chi)$	$\pi / (2\theta)$	$\theta > \pi / 2$
$(f\chi)$, $(g\psi)$	$\pi / (4\theta)$	$\theta > \pi / 4$

For detail see the forthcoming paper [9].

Acknowledgement.

This work was supported by Turkish Academy of Sciences (TÜBA).

References

[1] J.Meixner,Die Kantenbedingung in der Theorie der Beugung Elektromagnetischer Wellen an vollkommen leitenden ebenen Schirmen, Ann.der Phys.,6,s:2-9,1949

[2] J.Meixner,The behavior of electromagnetic fields at edges, IEEE Trans. on Antennas and Propagat.,vol.AP-20,pp:442-446,1972

[3]R.A.Hurd,The edge condition in electromagnetics,IEEE Trans.on Antennas and Propagat.,pp:70-73,1976

[4]J.V.Bladel,Field singularities at metal-dielectric wedge,IEEE Trnas.on Antennas and Propagat.,vol.AP-33,pp:450-455,1985

[5]D.S.Jones,The Theory of Electromagnetism,p.567, Pergamon Press, London,1964

[6]I.M.Braver, P.S.Fridberg, K.L.Garb and I.M.Yakover,The behavior of the electromagnetic field near the edge of resistive half-plane, IEEE Trans.on Antennas and Propagat.,vol.AP-36,pp:1760-1768,1988

[7]M.Idemen, Universal boundary conditions and Cauchy data for the electromagnetic field,in:Essays on the formal aspects of electromagnetic theory,pp:657-698,A:Lakhtakia (Ed.),World Sci.,N.J.,1993

[8]M.Idemen,Universal boundary relations of the electromagnetic field, J.Phys..Soc. Japan,vol.59,pp:71-80,1990

[9]M.Idemen, Confluent edge conditions for the electromagnetic wave at the edge of a wedge bounded by material sheets, Wave Motion, vol.32, pp:37-75,2000

GROWTH CHARACTERISTICS OF A CHERENKOV LASER FILLED WITH INHOMOGENEOUS AND COLLISIONAL PLASMA

T. Shiozawa and T. Thumvongskul
Department of Communication Engineering, Osaka University,
Yamada-oka 2-1, Suita-shi, Osaka, 565-0871, Japan
E-mail: shiozawa@comm.eng.osaka-u.ac.jp

ABSTRACT – With the aid of the multilayer approximation method, growth characteristics of a two-dimensional Cherenkov laser filled with transversely inhomogeneous and collisional background plasma at millimeter wavelengths are investigated. The accuracy of numerical results is confirmed by comparison with the available analytical solution. We show that the injection of a dense plasma into the background of a Cherenkov laser improves the beam-wave coupling and growth characteristics. Degradation due to electron-ion collisions in background plasma can be kept at an acceptable level by appropriate choices of the plasma and beam parameters. From numerical results, we can identify the main parameter of the inhomogeneous background plasma which affects growth characteristics of a plasma-filled Cherenkov laser.

1 INTRODUCTION

The Cherenkov free-electron laser (CFEL) is a coherent high-power and tunable source, possessing a promising future in various applications at short millimeter and sub-millimeter wavelengths, such as space-communications, high-resolution radars, remote sensing, and so forth [1]. In a typical vacuum Cherenkov device, however, the electromagnetic (EM) field which interacts with a relativistic electron beam concentrates around the dielectric surface of a waveguide and decays exponentially in the transverse direction, leading to a weak beam-wave interaction. This becomes more significant at higher frequencies, since the field decays more rapidly from the dielectric surface. In such a situation, an attempt to inject an electron beam into the region of high field intensity near the dielectric surface can cause more difficulties regarding dielectric breakdown and the control of beam transport. Further, increasing the beam thickness in a weak field would not help enhance the beam-wave interaction, but result in essentially low efficiency devices [2].

With the recent development of plasma technologies, it has been reported that the injection of a dense plasma into the background of the CFEL provides a more effective beam-wave coupling, leading to a device with greatly enhanced performances covering those drawbacks for the vacuum device stated above [3],[4]. The background plasma also plays an important role in neutralizing the space-charge force in the electron beam, and facilitating the beam transport. Since the plasma lightens the repulsive force which causes the beam to broaden, increasing the space-charge limited current of the electron beam [5], it is easier to achieve a higher output power with a higher beam current.

In this work, on the basis of the multilayer approximation method [6], we investigate the growth characteristics of a CFEL filled with a transversely inhomogeneous and collisional background plasma at millimeter wavelengths. The accuracy of numerical results is confirmed by comparison with the analytical results available for a cold plasma with

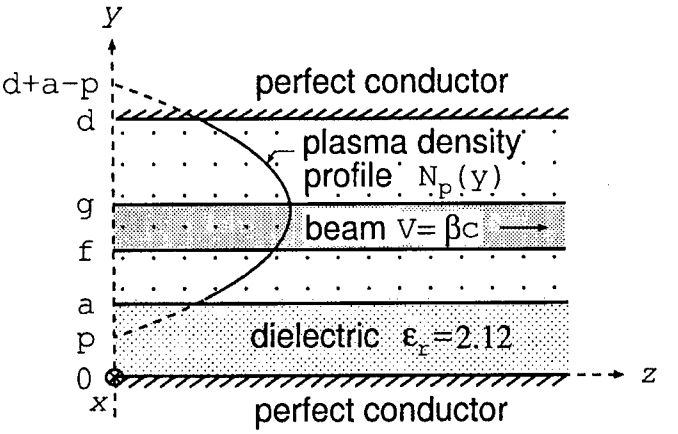

Fig. 1. Geometry of the problem.

a parabolic density profile [7],[8]. We show that the injection of a dense plasma into the background of a CFEL improves the beam-wave coupling and growth characteristics. Degradation due to the effect of electron-ion collisions [4] in the background plasma which cannot be ignored at millimeter wavelengths is briefly mentioned. We also discuss how the plasma inhomogeneity affects the growth characteristics of a CFEL, and compare with the results obtained from the simplified analysis where the plasma is assumed to be homogeneous. From the above discussion, we can identify the main parameter of the inhomogeneous background plasma which affects the growth characteristics of the CFEL.

2 MULTILAYER APPROXIMATION METHOD AND DISPERSION RELATION IN THE ABSENCE OF ELECTRON BEAM

A two dimensional (2-D) parallel-plate model of a CFEL filled with a dense background plasma with a parabolic density profile illustrated in Fig. 1 is considered. For simplicity, we assume that both the background plasma and the electron beam are restricted to move only along the z direction by a sufficiently large axial magnetic field. On the basis of the multilayer approximation method [6], a plasma slab with a transverse density profile described by

$$N_p = -\frac{N_{p,peak}}{\left(\frac{a+d}{2}-p\right)^2}\left(y-\frac{a+d}{2}\right)^2 + N_{p,peak}$$

is approximated by n homogeneous layers with different densities as shown in Fig. 2. From Maxwell's equations, the relativistic equation of motion, and the continuity equation, we can find the field expressions for the TM waves in each region specified in Fig. 1, as well as in each plasma layer [4],[9]. By imposing proper boundary conditions at each interface on the field components, we obtain the dispersion relation which describes the coupling between the negative-energy space-charge wave propagated along the relativistic electron beam and the slow EM wave propagated along the dielectric waveguide filled with plasma. Then, from the dispersion relation, we can numerically determine the values of

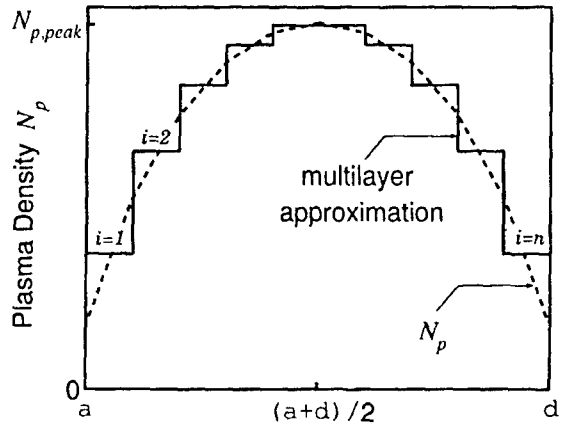

Fig. 2. Multilayer approximation method.

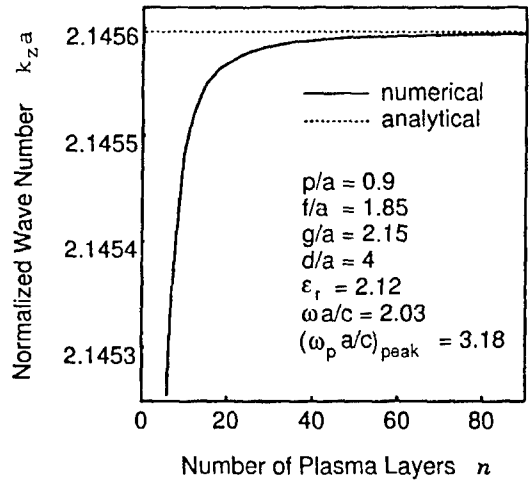

Fig. 3. Normalized wave number $k_z a$ for the lowest-order TM mode versus the number of plasma layers n.

propagation constant k_z and spatial growth rate α for the coupled space-charge and EM waves at a certain frequency.

As seen from Fig. 3, the accuracy of the numerical results for the case of inhomogeneous plasma in the absence of the electron beam can be confirmed by comparison with the exact solution obtained from the analytical approach for a parabolic profile of plasma density [7],[8]. When $n \geq 20$, the values of $k_z a$ obtained from the approximation method have relative errors less than 0.001%, and they gradually converge to the exact values as n increases. Hence, with a sufficiently large n, the multilayer approximation method gives a stable solution, and is expected to be applicable to the plasma with an arbitrary density profile without significant computational errors.

The dispersion curves in the absence of the electron beam calculated from the multilayer approximation method are shown in Fig. 4. We see that, due to the presence of the background plasma, the modified dispersion curves are up-shifted to higher frequencies,

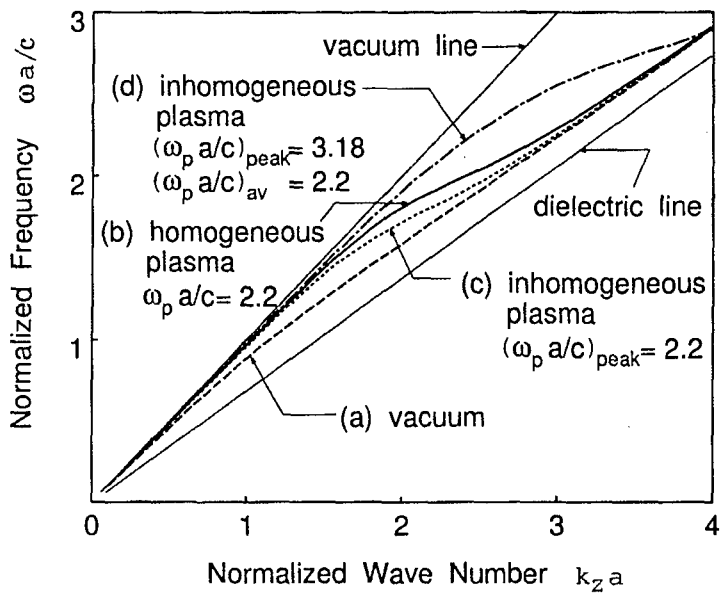

Fig. 4. Dispersion relation for the lowest-order TM mode in the absence of electron beam.

depending on the value of plasma frequency ω_p or number density N_p. Since in general the operating point of the coupled system can be approximately obtained at the intersection of the dispersion curve for the unloaded waveguide and the beam line approximated by $\omega = k_z V_0$. Then, it is obvious from the dispersion diagram that the system with background plasma can operate at higher frequencies when the beam with an appropriate value of drift velocity is injected, or can be driven by a higher beam current at the same operating frequency, leading to a higher output power.

Besides the modification of EM wave branches, the background plasma also results in an appearance of some additional plasma modes near the dielectric asymptotic line (not shown in Fig. 4), when the background plasma owns a rather large density [3]. A relativistic electron beam with a certain value of beam velocity can couple with both the modified up-shifted EM mode and the plasma modes. The synchronous frequency for the fundamental plasma wave (which is expected to have the largest spatial growth rate among the plasma modes) is well lower than those for the modified EM waves. This may introduce undesired lower frequency components which consume a fraction of energy in the coupling process. However, the maximum growth rate for the plasma waves for the values of the parameters used in our calculation is found to be much lower than those for the modified EM waves.

3 GROWTH CHARACTERISTICS IN THE PLASMA-FILLED DEVICE

For the coupling between the modified EM and space-charge waves which is of our interest, we see from Fig. 5 that the spatial growth rate is greatly enhanced by the injection of background plasma. This is because, at a distance apart from the dielectric surface, the EM field in the plasma device is yet strong enough to interact effectively with the

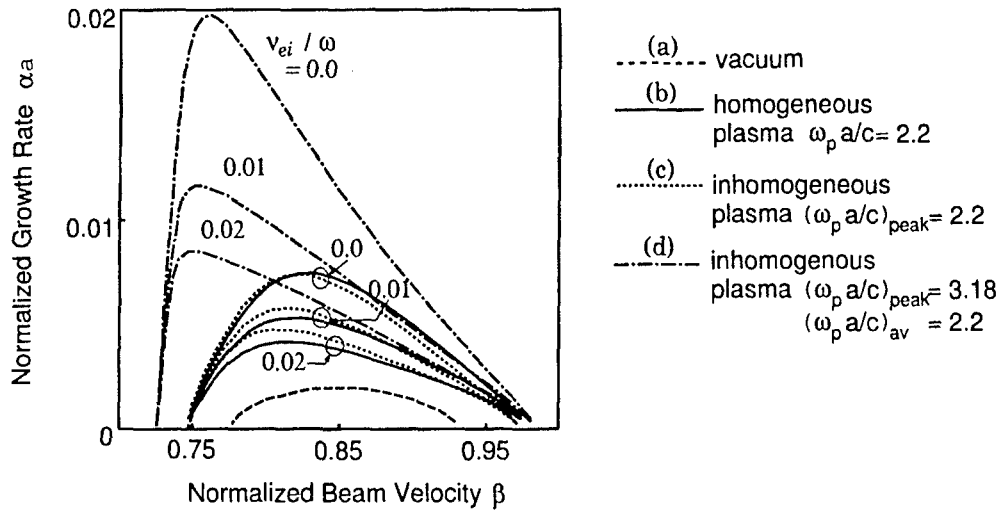

Fig. 5. Spatial growth rate versus beam velocity for various plasma-filled waveguides. ((a)~(d) are the same as those in Fig. 4.)

beam. This also suggests us possibilities (*i*) to inject the beam at a distance far enough from the dielectric surface in order to improve the heat transfer condition and relax the requirements on the beam transport [3], and (*ii*) to use the beam with larger thickness in order to gain a more effective coupling and higher output power. Furthermore, due to a larger growth rate, the plasma device is expected to reach saturation earlier than the device without background plasma, leading to a more compact device. (See, for example, the transient growth and saturation characteristics for vacuum and plasma devices in [4].)

3.1 EFFECT OF ELECTRON-ION COLLISIONS

As for an operation at millimeter wavelengths, a stationary plasma with a peak density about 2~3 orders larger than that at microwave frequencies is required. Because of such a high density of the background plasma, we could not possibly ignore the effect of electron-ion collisions in the plasma. We take into account this effect in terms of the collision frequency ν_{ei}. For our model at millimeter wavelengths, the ratio ν_{ei}/ω is of the order of 10^{-2} [4]. The introduction of small ν_{ei} into the dispersion relation does not affect much the values of propagation constant k_z. But, as seen from Fig. 5, it brings damping to the EM waves, resulting in degradation of spatial growth rates. However, with suitable values of parameters, we can yet expect that the spatial growth rate in the plasma device is enhanced beyond that for the vacuum one.

3.2 EFFECT OF PLASMA INHOMOGENEITY

As seen from the above results, the plasma device provides enhanced spatial growth rates beyond that for the vacuum one, due to a strong EM field interacting with the electron beam. Especially, in the case of inhomogeneous plasma, the EM field component can have a large magnitude and a nearly flat transverse distribution over the cross section

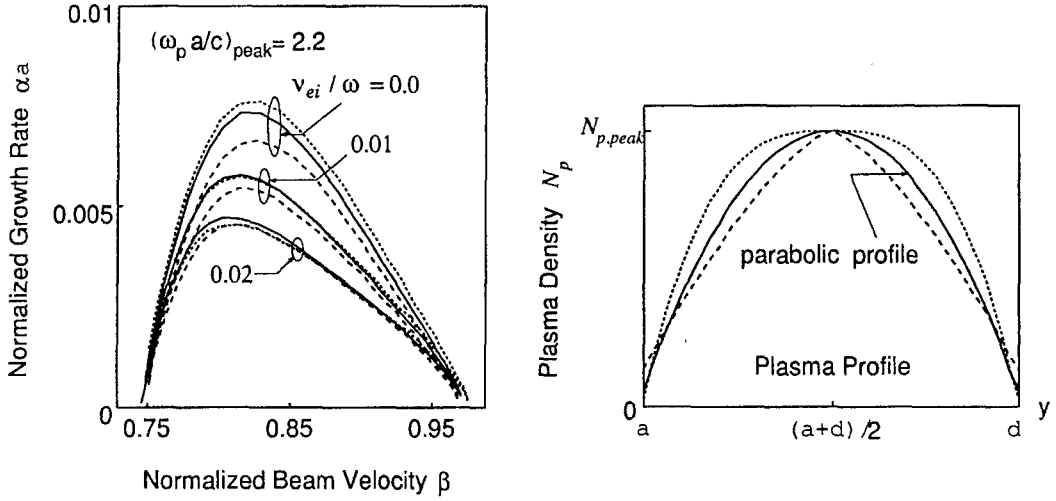

Fig. 6. Spatial growth rate versus normalized beam velocity β for various plasma profiles. The parabolic profile is used in previous calculations (see Figs. 3~5).

of the beam. In this case, we can have a more enhanced growth rate and a more stable interaction. From Fig. 5, in the case (c) where the inhomogeneous plasma has a peak value of plasma frequency equal to that for the homogeneous case (b), the spatial growth rate slightly deviates from that of (b). However, in the case (d) where the peak value of plasma density is increased and the average value of plasma frequency equals that for the case (b), the spatial growth rate is greatly raised. Even in the absence of the electron beam, the dispersion characteristics for the cases (b) and (c) are quite similar (see Fig. 4). We can therefore judge that the main parameter of the background plasma which affects the value of the spatial growth rate is not the average plasma density, but the peak plasma density. This issue is confirmed by the investigation of growth characteristics for various plasma profiles with the same peak density. Results in Fig. 6 indicate that differences in plasma profile do not affect much the growth characteristics of the plasma-filled CFEL, provided that the peak values of plasma density are the same. Consequently, for simplified analysis, we can properly treat the inhomogeneous background plasma as the homogeneous one with a plasma density equal to the peak value.

4 CONCLUDING REMARKS

Growth characteristics of the 2-D Cherenkov free-electron laser (CFEL) filled with inhomogeneous and collisional background plasma at millimeter wavelengths were investigated with the aid of the multilayer approximation method. The accuracy of the numerical results was confirmed by comparison with the available analytical solution. We found that the CFEL with background plasma can provide a more effective beam-wave coupling and enhanced spatial growth rates, suggesting a possibility of a more compact device.

In this paper, we also discussed the effect of electron-ion collisions and plasma inhomogeneity in the background plasma. The presence of electron-ion collisions resulted in a significant decrease in the spatial growth rate for the coupled waves. However, by

proper choices of the plasma and beam parameters, the value of the spatial growth rate was found to remain well over that for the vacuum device. On the other hand, only a little difference was found between the waveguides filled with homogeneous plasma and inhomogeneous one with the same peak plasma density as that of the former. From these results, we can conclude that the main parameter of the background plasma which affects the value of the spatial growth rate is the peak plasma density.

For simplicity, a sufficiently large static axial magnetic field was assumed to be applied to our model to restrict the movement of the background plasma and the electron beam only to the longitudinal direction. In fact, an important role of the background plasma in neutralizing the space-charge force in the electron beam can help relax the requirements on beam focusing and alignment. Therefore, the device can be down-sized by making use of smaller solenoids for generating a guiding magnetic field [3].

ACKNOWLEDGMENT

The authors would like to thank Prof. G. I. Zaginaylov, Kharkov State University, Ukraine, and Dr. A. Hirata, Osaka University, Japan, for their valuable comments on this work.

REFERENCES

[1] A. V. Gaponov-Grekhov, and V. L. Granatstein, Eds., *Applications of High-Power Microwave* (Norwood, MA: Artech House, 1994).

[2] T. Ueda, and T. Shiozawa, *Appl. Phys. Lett.*, vol. 67(26), p. 3838, 1995.

[3] G. S. Nusinovich, Y. Carmel, T. M. Antonsen, D. M. Goebel, and J. Santoru, *IEEE Trans. Plasma Sci.*, vol. 26(3), p. 628, 1998.

[4] T. Thumvongskul, A. Hirata, G. Zaginaylov and T. Shiozawa, *J. Appl. Phys.*, vol. 87(4), p. 1626, 2000.

[5] B. N. Brejzman, and D. D. Rutov, *Nucl. Fusion*, vol. 14, p. 879, 1974.

[6] S. Pasquiers, *J. Appl. Phys.*, vol. 67(12), p. 7246, 1990.

[7] G. I. Zaginaylov, *Tech. Phys.*, vol. 40(6), p. 542, 1995.

[8] T. Thumvongskul, and T. Shiozawa, Abstracts, P1.33, *IEEE International Vacuum Electronics Conference 2000.*

[9] T. Shiozawa, and T. Nakashima, *J. Appl. Phys*, vol. 55, p. 637, 1984.

MILLIMETER-WAVE RADAR FOR ENVIRONMENTAL STUDIES: IMAGE PROCESSING AND INTERPRETATION

D. M. Vavriv
Institute of Radio Astronomy
4, Chervonopraporna St., 310002 Kharkov,Ukraine
vavriv@rian.kharkov.ua

Importance of mm-wave radar as a highly efficient instrument for the environmental studies has been generally recognised. Present-day requirements imposed on such instruments call for the development of radar systems capable for long-term unattainable operation, which allows for conducting real-time measurements of various atmospheric and earth surface characteristics.

In this presentation, a review is given two such devices recently developed at the Institute of Radio Astronomy NASU that include a side-looking airborne radar remote sensing system and cloud radar systems. These systems are designed to perform measurements at frequencies of 36 GHz and 95 GHz. The setup of these instruments, novel technical solutions, and signal processing technique are discussed. Results obtained during measurement campaigns with such instruments are summarized. The side-looking radar system is capable for investigation of the radar scattering properties of various surfaces at millimeter wavelengths. At the first stage of exploitation, the system was used for the study of millimeter-wave backscatter characteristics of water surfaces in the presence of oil spills.

This study aims at development of efficient instruments and methods for oil-spill detection and quantification. The developed 36 and 95 GHz cloud radar systems provide real-time measurements of profiles of radar backscatter, Doppler spectrum and Doppler moments. Each radar includes a reliable system of permanent calibration, with a possibility of remote control and opportunity of a network access to the radar data. The calibration system introduced enables one to perform a permanent accurate measurement of reflectivity in terms of dBZ through a measurement of the transmitted power, and radar sensitivity including antenna gain.

The developed software package having client-server architecture supports both remote and local control of radar operation, data acquisition and processing. The radar images can be viewed in a local Ethernet in real time. The Internet access allows viewing the current images and previously stored radar data. The cloud radar systems have demonstrated a high capability for the study of structure and dynamics of various types of clouds, airflow, and precipitation. Results of these measurements are also discussed in this presentation and compared to those obtained by other instruments.

ELECTROMAGNETIC SCATTERING BY COMPLEX-SHAPE OBJECTS PARTIALLY COATED WITH ABSORBING MATERIALS

Oleg I. Sukharevsky, Vitaliy A. Vasilets, Stanislav A. Gorelyshev, and Alexander Z. Sazonov*,

Kharkov Military University, Kharkov, Ukraine
E-mail: sukharevsky@dinos.kharkov.com

*Scientific and Research Institute of Radiotechnical Measurements, Kharkov, Ukraine

ABSTRACT

The calculation method is presented for scattering of plane electromagnetic wave by a perfectly conducting electrically large object wholly or partly covered with an absorbing coating. The object admits surface breaks with toroidal absorbing coating. This method is based on the calculation of contributions to scattering field by smooth surface parts (physical optics approximation) and local break scattering parts (proposed asymptotical method). The Radar Cross Section (RCS) results are demonstrated for "Space Shuttle" and B-2 bomber.

INTRODUCTION

In a number of problem of applied electrodynamics and radar [1,2], it is necessary to get a prior information about scattering characteristics of complex shape objects wholly or partly covered by radioabsorbing materials (RAM). Such problems, in particular, are to detect aircrafts made by "Stealth" technology.

1. SCATTERING BY SMOOTH OBJECTS WITH RADIOABSORBING COATING

We consider a plane monochromatic wave with polarization unit vector $\vec{p}^{\,0}$ and propagation direction $\vec{R}^0$

$$\begin{aligned} \vec{E}^0(x) &= \vec{p}^{\,0} \exp\left(-jk_0\left(\vec{R}^0 \cdot \vec{x}\right)\right) \\ \vec{H}^0(x) &= \sqrt{\frac{\varepsilon_0}{\mu_0}}\left(\vec{p}^{\,0} \times \vec{R}^0\right)\exp\left(-jk_0\left(\vec{R}^0 \cdot \vec{x}\right)\right) \end{aligned} \qquad (1)$$

incident to a smooth electrically large object with surface S. Here ε_0, μ_0 are dielectrical and magnetic permeabilities of free space respectively, k_0 is a wave number for free space, $\vec{x}$ is vector to considered space point. Then, through Lorenz lemma [3], the object field scattered in direction $\vec{r}^{\,0}$ is

$$\vec{p}\cdot\vec{E}^{p}\left(R\,\vec{r}^{\,0}\right)=-jk_0\sqrt{\frac{\mu_0}{\varepsilon_0}}\frac{\exp\left(jk_0R\right)}{4\pi R}\left(\vec{p}\cdot\vec{I}\left(\vec{r}^{\,0}\right)\right), \tag{2}$$

$$\vec{I}\left(\vec{r}^{\,0}\right)=\int_S\left[\vec{H}_\perp-\sqrt{\frac{\varepsilon_0}{\mu_0}}\left(\vec{E}_\perp\times\vec{r}^{\,0}\right)\right]\exp\left(-jk_0\left(\vec{r}^{\,0}\cdot\vec{x}\right)\right)ds \tag{3}$$

where $\vec{E}_\perp=\vec{n}\times\vec{E}$, $\vec{H}_\perp=\vec{n}\times\vec{H}$, $\left(\vec{E},\vec{H}\right)$ is a full field, $\vec{n}$ is a external normal unit vector to surface S.

Let perfectly conducting scattering object (or its part) be coated by a thin RAM layer with a constant depth.

Taking into account the electrically large sizes of object, the values $\vec{H}_\perp(x),\vec{E}_\perp(x)$ in (3) can be replaced approximatively by values $\hat{\vec{H}}_\perp(x),\hat{\vec{E}}_\perp(x)$ on the surface of plane equidistant layer (from absorber material) on metal backing substituted in point $x\in S$ and tangent to S.

Thus it is necessary to solve the model problem of (1) plane wave scattering from a plane equidistant absorber layer on a metal backing.

The solution of the problem for arbitrary polarization of an incident wave and arbitrary incident angle (in particular, near normal incidence) has been obtained in this paper. We write the expression for scattering field outside the layer

$$\begin{pmatrix}\hat{\vec{E}}(x)\\ \hat{\vec{H}}(x)\end{pmatrix}=\begin{pmatrix}\vec{p}^{\,0}\\ \left(\vec{p}^{\,0}\times\vec{R}^{0}\right)\sqrt{\frac{\varepsilon_0}{\mu_0}}\end{pmatrix}\exp\left(-ik_0\left(\vec{R}^{0}\cdot\vec{x}\right)\right)+\begin{pmatrix}\vec{p}^{\,1}\\ \left(\vec{p}^{\,1}\times\vec{R}^{1}\right)\sqrt{\frac{\varepsilon_0}{\mu_0}}\end{pmatrix}\exp\left(-ik_0\left(\vec{R}^{1}\cdot\vec{x}\right)\right), \tag{4}$$

where $\vec{R}^{1}=\vec{R}^{0}-2\vec{n}\cdot\left(\vec{R}^{0}\cdot\vec{n}\right)$, $\left(\vec{R}^{0}_T\cdot\vec{x}\right)=\left(\vec{R}^{0}\cdot\vec{x}\right)_{x_2=0}$, $\vec{p}^{\,1}=\vec{p}^{\,1}_T-\vec{n}\dfrac{\left(\vec{p}^{\,1}_T\cdot\vec{R}^{0}\right)}{\cos\theta}$,

$$\vec{p}^{\,1}_T=\frac{jc\cos\theta+1}{jc\cos\theta-1}\vec{p}^{\,0}_T-\frac{2jc}{jc\cos\theta-1}\left[\vec{R}^{0}_T\frac{\left(\vec{R}^{0}_T\cdot\vec{p}^{\,0}\right)}{jc-\cos\theta}+\vec{R}^{0}_\perp\frac{\left(\vec{R}^{0}_\perp\cdot\vec{p}^{\,0}\right)}{\varepsilon_1'\mu_1'\left(jc-\dfrac{\cos^2\theta_1}{\cos\theta}\right)}\right].$$

If we substitute the found expressions for $\hat{\vec{E}}$, $\hat{\vec{H}}$ to (2) and replace the surface S by its illuminated part S', we obtain an approximate expression for scattering field:

$$\vec{p}\cdot\vec{E}^{p}\left(R\,\vec{r}^{\,0}\right)\approx-jk_0\frac{\exp\left(jk_0R\right)}{4\pi R}\int_{S'}f\left(\vec{r}\right)\exp\left(jk_0\Omega\left(\vec{r}\right)\right)dS, \tag{5}$$

where $f\left(\vec{r}\right)=\vec{h}\left(\vec{r}\right)\cdot\vec{p}+\vec{e}\left(\vec{r}\right)\cdot\left(\vec{p}\times\vec{r}^{\,0}\right)$, $\Omega\left(\vec{r}\right)=-\left(\vec{r}^{\,0}+\vec{R}^{0}\right)\cdot\vec{r}$, $\vec{e}\left(\vec{r}\right)=\vec{n}\times\left(\vec{p}^{\,0}+\vec{p}^{\,1}\right)$,

$\vec{h}\left(\vec{r}\right)=\vec{n}\times\left[\left(\vec{p}^{\,0}\times\vec{R}^{0}\right)+\left(\vec{p}^{\,1}\times\vec{R}^{1}\right)\right]$, $\vec{r}$ is vector of integration point.

Integral in (5) requires using a special cubature formulae, because its integrand function is quick-oscillating. The cubature formulae have been obtained for similar integrals in [4]. These formulae are based on linear approximations of functions $f\left(\vec{r}\right)$ and $\Omega\left(\vec{r}\right)$.

The concept of formula [4] structure is following. Let the set of points $M_i(i=1,2,...,n)$ be given on surface S. Points are located on S densely and unregularly. The values of $f(\vec{x})$ and $\Omega(\vec{x})$ are known in these points. S is covered by triangular system with vertices in points M_i and integral (2) is a sum of integrals for each triangle. Inside each triangle functions $f(\vec{x})$ and $\Omega(\vec{x})$ are interpolated by linear functions (through values in three vertices). After transformation to baricentric system of coordinates, obtained integrals are calculated analytically.

Note that the object RCS is quick-oscillating function of frequency in considered high-frequency band. The RCS average has to be carried in some frequency band for obtaining stable values. In addition, in spite of certain advantages of cubature formula, if illumination wave length is reduced, then necessary quantity of integration surface separations is increased. For electrically large objects (for example, aircraft) it is difficult to realize the sufficiently dense separation of surface. In this case it is necessary to use RCS averaged in certain frequency band. Calculations for simple objects (sphere, ellipsoid) show, that, by determining the quantity of surface separation, it is possible to choose the frequency band width (with prescribed mean value) such that RCS obtained by average in this band is close to the corresponding averaged value for real surface.

2. SCATTERING BY OBJECTS WITH THE COATED SURFACE BREAKS

If breaks of object with perfectly conducting piecewise smooth $\hat{S}$ surface are covered by toroidal absorbing coating, then the integration surface in (3) formula is

$$S=S_1+S_0, \tag{6}$$

where S_0 is surface, cross-section of which by Π plane is a part of circle with the P center and $\rho_0 \geq \rho$ radius. Here ρ is radius of circle in the section of coating by Π plane, which is orthogonal to the rib in each of its P points, $\rho, \rho_0 \langle\langle \lambda$; λ is probing signal wave length. Surface $S_1 \subset \hat{S}$, and all points of this surface in Π plane cross-section are spaced from M point by a distance, that is more than ρ_0 . Thus in (3) $\vec{I}(\vec{r}^{\,0})$ is a sum of integrals by S_1, S_0 :

$$\vec{I}(\vec{r}^{\,0})=\vec{I}_{S_1}(\vec{r}^{\,0})+\vec{I}_{S_0}(\vec{r}^{\,0}). \tag{7}$$

$\vec{I}_{S_0}(\vec{r}^{\,0})$ integral assumes the representation

$$\vec{I}_{S_0}(\vec{r}_0)=\int_L \exp\left[jk_0(\vec{R}^0-\vec{r}^{\,0})\,\vec{x}(l)\right]\vec{M}(l,\vec{r}^{\,0})dl, \tag{8}$$

where $$\vec{M}(l,\vec{r}^{\,0})=\int_{S'} \exp\left[-jk_0(\vec{r}^{\,0}\vec{\xi})\right]\vec{G}(\vec{\xi})\,dq,$$

$\vec{R}^0$ is an illumination unit vector, $\vec{x}(l)$ is a radius-vector of P point with l coordinate on L break line, S_0' is a curve (circle part) on S_0 surface placed in Π

plane, which is orthogonal to L, $\vec{G}(\vec{\xi})$ is $\vec{\xi}$ vector-function containing the tangential components of $(\vec{E},\vec{H})$ field at absorbing torus surface in indicated cross-section, $dq=\rho_0 d\varphi$ is S_0' element.

Estimating (8) integral by stationary phase method, we can obtain, that for the break line as convex smooth curve, at least, two stationary phase points must be existed (with the exception of some special case; e. g. for body of revolution with breaks - it is a case of axial probing and monostatic receiving). In this "special" case we can calculate $\vec{I}_{S_0}(\vec{r}^{\,0})$ by numerical integration. This is a simple task, if $\rho_0/\lambda << 1$. In other cases the stationary phase method for (8) yields

$$\vec{I}_{S_0}(\vec{r}^{\,0}) \sim \sum_{(l_0)} \exp\left[jk_0(\vec{R}^0-\vec{r}^{\,0})\vec{x}(l_0)+j\beta\frac{\pi}{4}\right]\cdot\vec{M}(l_0,\vec{r}^{\,0})\sqrt{\frac{2\pi}{k_0\chi(l_0)\left|(\vec{R}^0-\vec{r}^{\,0})\vec{\nu}(l_0)\right|}}, \qquad (9)$$

where $\chi(l_0)$, $\vec{\nu}(l_0)$ are a curvature and a main normal unit vector of L line in P_0 point with l_0 arc coordinate, $\beta=\mathrm{sgn}\left[(\vec{R}^0-\vec{r}^{\,0})\vec{\nu}(l_0)\right]$, and (l_0) symbol, under the sum shows that summation must be carried out by all "visible" stationary phase points (from illumination and reception directions) [5].

Taking into consideration the electrically large sizes of scatterer and small curvatures of its surface smooth parts, $(\vec{E},\vec{H})$ field tangential components on S_0' line approximated by corresponding values on surface of absorbing circle cylinder covered the rib of tangent perfectly conducting wedge $(\rho=\rho_0)$ in P_0 point. Consequently, the main problem of (9) formula is the problem of oblique plane electromagnetic wave incident on ideal conducting wedge with radioabsorbing cylinder on rib.

The main difficulty of the problem is associated with the three-dimension character of its solution. The solution cannot be represented as a union of two independent two-dimensional problems, so in the problem of oblique plane wave incident on ideally conducting wedge and in the problem about normal (to rib) incidence of plane wave on the considered structure. Nevertheless, we have shown, that the problem can be reduced to a system of two two-dimensional problems, solutions of which are associated with the boundary conditions (by means of same matrix-differential operator).

If $E_3=u(x_1,x_2)\exp(jk_0x_3\vec{R}_3^0)$, $H_3=v(x_1,x_2)\exp(jk_0x_3\vec{R}_3^0)$, $\vec{w}=\begin{pmatrix}u\\ v\end{pmatrix}$, then $\vec{w}$ vector is represented by Fourier-Bessel series with (2õ2) matrix coefficients. For example, outside absorbing cylinder

$$\vec{w}=\sum_{m=0}^{\infty}\left[B_m J_{\nu_m}(\chi_0 r)+C_m H_{\nu_m}^{(1)}(\chi_0 r)\right]\vec{f}_m(\varphi), \qquad (10)$$

where $J_{\nu_m}(z)$ is the Bessel function, $H_{\nu_m}^{(1)}(z)$ is the Hunkel function,

$$\vec{f}_m(\varphi)=\begin{pmatrix}\sin(\nu_m\varphi)\\ \cos(\nu_m\varphi)\end{pmatrix},\quad \chi_0=k_0\sqrt{1-(R_3^0)^2},\quad \nu_m=m/\tau(l),$$

$\pi\tau(l)$ is the wedge opening $(0 \le \varphi \le \pi\tau(l))$. B_m, C_m are matrix coefficients determined from conjunction conditions for u,v functions and their derivatives on absorbing cylinder boundary.

Series of (10) type converge well for r small values ($r \le \rho_0$) [6].

The integral $\vec{I}_{S_0}(\vec{r}^{\,0})$ is estimated by the method, which is described above for smooth parts of surface.

Using the results for monochromatic object illumination, the scattered field calculation methods can be developed for pulse (transient) illumination.

In particular, the main term of transient asymptotics for edge contribution of scattering field has been obtained in bistatic case by replacing of the real surface by wedge surface near the break line. For example, if probing pulse signal is $\Omega(t)$ $(\Omega(t) \equiv 0$ at $t \in (0, \delta_0), \delta_0 << 1)$, and its spectrum is centered near $k = k_0$, then the response of scattering edge local parts is

$$\vec{H}_{S_0}(t) \sim \sum_{(l_0)} \vec{A}(l_0) 1(t - t(l_0)) \int_0^{\min\{\delta_0, t - t(l_0)\}} \frac{\Omega(s)}{\sqrt{t - t(l_0) - s}} ds \,, \qquad (11)$$

where $t(l_0) = (\vec{R}^0 - \vec{r}^{\,0})\vec{x}(l_0) + C$, C is constant, depending from configuration of transmitter, receiver and object. $\vec{A}(l_0)$ is vector coefficient corresponding to scattering edge local center with l_0 arc coordinate. This coordinate depends on material and parameters coating, directions and polarizations of illumination and reception fields.

3. RCS CALCULATION RESULTS FOR COMPLEX OBJECTS ("SPACE SHUTTLE" AND B-2 BOMBER)

We use the described method to calculate the averaged scattering characteristics (RCS) for "Space Shuttle" (Fig.1) and B-2 bomber (Fig.3). "Space Shuttle" (Fig.1) is covered by isolating materials for prevention of its combustion when entering the air. The most vulnerable parts (for example, bow and leading edges of fin and wings) are covered with a carbon-carbonic composite material (CCM) (relative permeabilities are approximately $\varepsilon' = 4 + 3{,}5 \cdot 10^5 i$, $\mu' = 1$). The bottom surface of Shuttle is covered with black plates from high-temperature isolation (HTI) made from quartz fibre (parameters are approximately $\varepsilon' = 4{,}5 + 3{,}5i$, $\mu' = 1$).

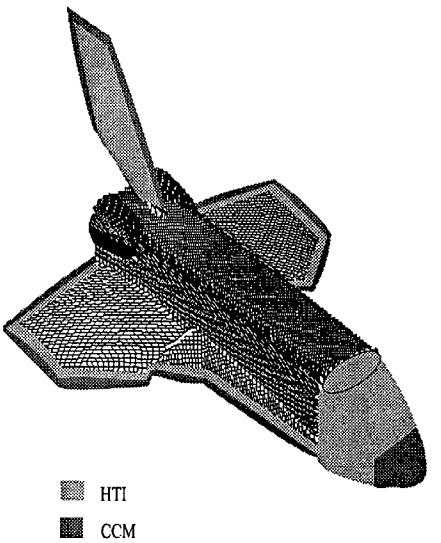

Fig.1. Approximated surface of "Space Shuttle".

Fig.2 illustrates the dependences of "Space Shuttle" RCS averaged in the band from 2.25 to 3.75 GHz for different illumination and reception angles. The solid line corresponds to the perfectly conducting model. The dash line corresponds to the model with the coating described above.

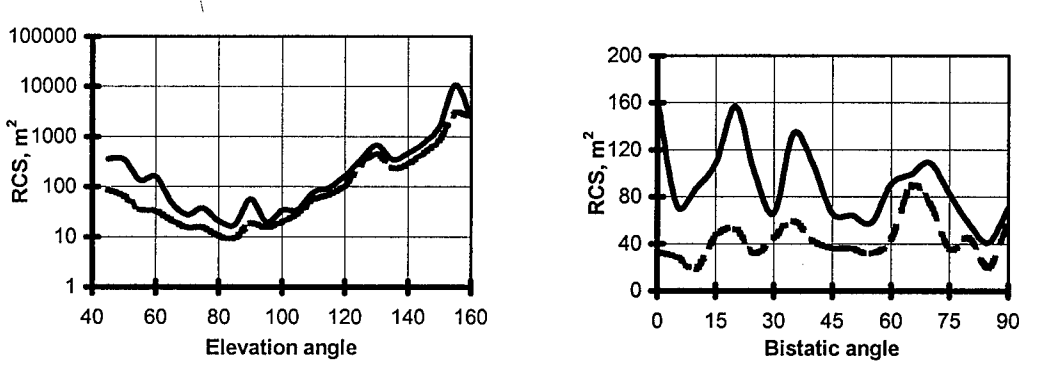

à) b)

Fig.2. Dependences of "Space Shuttle" averaged RCS on elevation and bistatic angles for perfectly conducting model (solid line) and model with isolating materials.

Dependence of RSC on elevation angle is illustrated in Fig.2.a. Elevation angle 90° corresponds to the frontal sounding, angles less than 90° correspond to sounding from lower half-sphere and angles more then 90° are from upper half-sphere. At elevation angles 45°-60° the RCS of the covered object is reduced in 4...5 times as the main contribution to RCS in these angles is made by the object bottom surface covered by HTI. At elevation angles 65°-110° the main contribution to RCS is carried in bow and leading edges of wings covered by CCM with large conductivity. So at these angles the RCS reducing by coating is small. At the

sounding from upper half-sphere (elevation angles are 120°-145°), RCS is reduced in 1.5...2 times by the coating. To the end, at the sounding angles 145°-160° the RCS is reduced in 3...4 times because the main contribution to RCS is made by a bow covered by HTI. At the same elevation angles, the RCS absolute values are more increased (values by order 10^5 ì^2).

RCS dependences of bistatic angle are presented in Fig.2.b. Analyzing Fig.2, one can made the following conclusions:

1. Heat-insulating coatings of "Space Shuttle" can significantly reduce RCS (in 3...4 times) at certain sounding angles in SHF band.

2. If object surface parts with IHT dominate over the RCS, then influence of heat-insulating coating on the RCS is most considerable.

The research of B-2 model averaged RCS (Fig.3) is partly theoretical because we do not know the real parameters of radioabsorbing coating. We use 5 cm material layer with constant permeabilities $\varepsilon' = \mu' = 1+10i$ as a coating. These parameters correspond to some types of real ferromagnetic coating [3]. Some typical results have been shown in Fig.4. The middle lines in Fig.4.a,b correspond to partial covering of bomber surface (dark color in Fig.3). There are RCS values averaged in band 2.25...3.75 GHz in Fig.4.a,b. The analysis of Fig.4 allows us to make the following conclusions:

1.The partial covering of B-2 model reduce the aircraft RCS by the same value as for wholly covered model for the certain sounding angles (in particular, for frontal sounding).

2.The RCS dependencies on bistatic angle in Fig.4.b show that if the bistatic angle is 70°...80° the RCS is more increased for all three models. It is a basic conception used in "Stealth" technology: the object surface geometry provides the electromagnetic scattering in side direction irrespective of coating type.

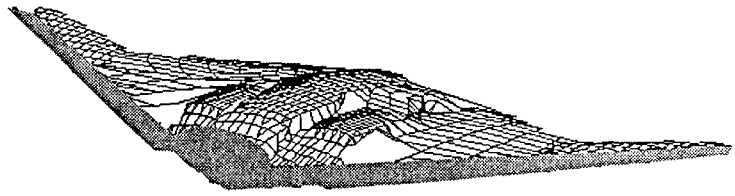

Fig.3. Approximated surface of B-2 bomber.

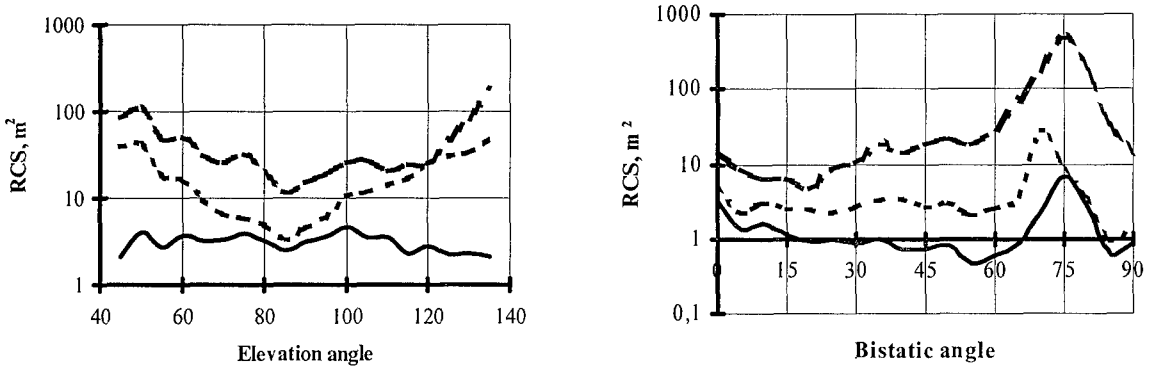

à) b)

Fig.4. Dependences of B-2 averaged RCS on elevation and bistatic angles for perfectly conducting model (solid line), model partly coated by RAM and model wholly coated by RAM.

REFERENCES

[1] Sukharevsky O.I., Vasilets V.A., Sazonov A.Z., Tkachuk K.I. // Radiophysics and radioastronomy, 2000, v.5, ¹1, pp. 47-54 (in Russian).

[2] Masalov S.A., Ryzhak A.V., Sukharevsky O.I., Shkil V.M. Physical foundations of Stealth band technologies. - S.Peterburg. Mozhaiskiy VIKU, 1999 , 163p. (in Russian).

[3] Vainshtein L.A. Electromagnetic waves. - Moscow, Radio i svyaz, 1988 , 440p. (in Russian).

[4] Zamyatin V.I., Bahvalov B.N., Sukharevskiy O.I. // Radiotechnics and electronics, 1978, v.23, ¹6, pp. 1289-1293 (in Russian).

[5] Sukharevsky O.I., Dobrodnyak À.F. // Izvestiya vuzov USSR. Radiophysics, 1989, v.32., ¹ 12, pp.1518-1524 (in Russian).

[6] Sukharevsky Î.I., Dobrodnyak À.F. // Izvestiya vuzov USSR. Radiophysics, 1988, v.31, ¹ 9, pp. 1074-1081 (in Russian).

PHOTONIC CRYSTAL THEORY, MODELLING AND TECHNOLOGY

Marian Marciniak

National Institute of Telecommunications
Department of Transmission and Fibre Technology
Szachowa 1, 04-894 Warsaw, Poland
E-mail: marian.marciniak@ieee.org

ABSTRACT

The all-optical network should take the advantage of photonic devices of various kind that above all should provide the means for all-optical signal processing. Photonic band-gap structures (PBG, photonic crystals) are expected to be very helpful for achievement of several functions that an all-optical network asks for. In the paper the state-of-art and potential future applications of PBG structures in optical telecommunication systems are reviewed. In wavelength-division-multiplexed systems the wavelength sensitivity of PBGs and their filtering properties resulting from it are of particular interest. Possible locations of PBG-based devices within the advanced all-optical network architecture are indicated and their functional parameters are discussed.

INTRODUCTION

Photonic band-gap (PBG) structures, also known as photonic crystals, are one of the crucial technology factors leading to the achievement of several functions that an all-optical network asks for. PBG-based devices have numerous potential functional locations within the advanced all-optical network architecture. In the paper the state-of-art and also the possibility of potential future applications of PBG structures in optical telecommunication systems are reviewed, and their impact on the development of all-optical transport networks is discussed.

Although it is commonly accepted that optical fiber-based telecommunication systems are actually in an advanced and mature stage, qualitatively new concepts are still developed in laboratories and commercially applied as well. One should mention wavelength-division-multiplexed (WDM) systems, and a concept of so-called "opticalization" of the network, a notion that stands for an observed actually trend to eliminate electronic components from optical transmission links and evolution towards transparent optical networks.

Transparent optical networks

The optically transparent terabit network is an ultimate goal that should lead to a much more efficient exploitation of enormous transmission bandwidth that is offered by the fiber and the light itself [1]. This way the future information society needs for reliable means of transmission and the foreseen necessity of general and easy access to multimedia and hypermedia services should be satisfied. Actually the process of migration of today's fiber-based transmission networks to future all-optical transport networks (OTN) is in an advanced stage [2].

The optical transparency of the network offers various economic advantages in both cases of backbone and access networks. Cost-effective wavelength cross-connects and add/drop multiplexers and high-capacity, ultra-long-reach, all-optical transmission over conventional fibers are shown to make the economics of transparent optical networking quite compelling

[3]. Nevertheless, the idea of transparent networks is the subject of a variety of constraints arising from physical effects as well as operations and business issues [4]. At the present stage of the transparent network evolution it is essential to elucidate the direction networks are likely to take.

The introduction of Erbium-Doped Fibre Amplifiers (EDFA) which have replaced electronic regenerators in fibre based transmission links in early 90s resulted in optical transparency of the links. This was in contrary with electronic regenerator based links. In those a combination of electronic logic circuit along with electro-optical and opto-electrical conversions of the digital signal transmitted has been used in order to cope with signal distortion. In optical links the distortion results from physical limitations of the transmission of light signals through fibres, namely from fibre attenuation, dispersion, and nonlinear distortion.

Optical transparent transmission offers almost infinite optical bandwidth. This is especially attractive in view of future information society needs for exchange of enormous information streams, resulting from a general use of multimedia and hypermedia services.

Transparency is very attractive also from user point of view: he/she sends his/her own data streams and the transparent network transmits them regardless of their format, bitrate etc. A functional model of a transparent passive network consists of an optical telecommunication cloud through which clients send and receive their messages of various kinds.

Recent years have shown a rapid growth of demand for capacity of telecommunication networks. It has inspired many laboratories to explore new techniques of more efficient utilisation of the huge bandwidth offered by optical fibre links. WDM technology is one of the most promising and cost effective ways to increase optical link total throughput.

In a WDM system many information channels are transmitted through one fibre using different optical wavelengths modulated by independent data streams. This method is analogous to Frequency Division Multiplexing (FDM) which is widely exploited in other communication systems, especially in radio broadcasting. Using WDM we can easily increase the capacity of already existing fibre links that is particularly significant in the areas where placing new cables is impossible or too expensive. WDM is a technique compatible with the idea of all-optical networks, where one can create transparent optical paths connecting successive network nodes by switching optical channels organised at the different light wavelengths. One can also envision the application of WDM in broadcast networks and/or in subscriber loop [5].

These and other advantages of WDM have prompted the beginning of standardisation work [6]. Nevertheless the task is not yet completed and further research and estimations are required [7].

Non-Linear Limitations

In spite of its merits the WDM technique is not free from limitations. The most characteristic and essential problem for multichannel optical systems, beside attenuation and dispersion, is interchannel crosstalk [8]. In WDM systems the interchannel crosstalk is caused by non-linear interplay between many different spectral components of the aggregate optical signal. The non-linear optical phenomena involved are self-phase modulation (SPM), cross-phase modulation (XPM), four-wave mixing (FWM), stimulated Raman scattering (SRS), and stimulated Brillouin scattering (SBS). One can distinguish crosstalk caused by non-linear interactions between the light in different channels or between the light and the fibre material. In spite of the intrinsically small values of the nonlinearity coefficients in fused silica, the nonlinear effects in silica glass fibres can be observed even at low power levels because of

very large interaction distances. This is possible because of important characteristics of single-mode fibres, a very small optical beam spot size, and extremely low attenuation [9].

EMERGING TECHNOLOGIES

The transparent photonic transport network insures the scalability, i.e. possibility of future upgrades. Emerging technologies as distributed Raman amplification technique enables to construct large-scale transport networks. As an example, recent experiments with 10 Gbit/s x 16-channel recirculating loop demonstrated that the network scale can be expanded over 2 times [10]. In the commercial systems scale the European all optical transparent network based on the 16x 2.5 Gbit/s WDM transmission with the use of fiber gratings and dispersion management technique is actually investigated [11].

A commercial deployment of broadband D-WDM systems with hundreds of transmission channels is foreseen in the near future. Also systems with channel number approaching or surpassing thousand of very closely spaced (50 GHz, 25 GHz or even less) channels are investigated in mature laboratory experiments. They require sophisticated narrow-band light sources with extreme wavelength stability, as well as a variety of photonic devices for all-optical signal processing. Therefore research challenges for system components based on new concepts arise. In that research, (quasi) periodic photonic structures in one-, two- and three-dimensions, along with nonlinear optics applications are among the most promising technologies.

Optically transparent technology is actually advancing very fast. Almost unlimited capacity is available, however, the future technology has to meet new demands especially in the field of optical signal digital processing, including full 3R regeneration. Moreover, a concept of the 4R regeneration where the fourth "R" means the regeneration of the optical signal spectrum has been introduced recently [12].

Reduced cost of bandwidth enabled by the optical amplifier and wavelength-division-multiplexing (WDM) technologies have resulted in a dramatic reduction of cost of transmission bandwidth. Moreover, WDM offers the orthogonality between wavelength and time, so they can be processed independently and simultaneously [13]. However, significant research challenges still remain to realise the huge potential offered by optical networking.

Attractiveness of photonic crystals in all-optical networks

Photonics is a key enabling technology in telecommunications. In the last decade, the technology to fabricate structures on an optical to sub-optical wavelength scale has matured, and opened for a new generation of photonic devices, which once inserted in the telecom fabric is expected to increase systems performance significantly. An international co-operation in the field of wavelength-scale photonics for telecommunications is undergoing and there are several international projects exploiting advanced photonics in telecommunication applications [14].

Photonic crystals are periodic structures that influence the behavior of photons in similar way as atomic lattice of natural solid state crystals influences the behavior of electrons. In particular, photonic crystals forbid the propagation of photons within a certain range of energies, which is called photonic bandgap [15]. Those unique optical properties of photonic crystals have great potential to stimulate development of truly-VLSI-type photonic circuits [16]. PBGs are directly scalable in frequency by a scaling of the periodicity, making the PBG concept generic.

Photonic crystals have a unique possibility of inhibiting spontaneous emission in active electro-optic devices. If the propagation is inhibited in any direction, then a complete and absolute photonic band-gap occurs. For some applications like vertical cavity surface emitting semiconductor lasers (VCSEL) complete and absolute band-gap is necessary. This can be achieved in photonic crystals with higher-order of symmetry [17].

1-D PBGs

The most common realization of one-dimensional photonic crystal is the optical waveguide Bragg-grating. It appears in two variants: planar waveguide Bragg grating, and Fiber Bragg-Grating.

Planar waveguide Bragg gratings are increasingly used in manufacturing of efficient narrow-band laser sources for telecommunications. Semiconductor waveguide lasers in DBR (Distributed Bragg-Reflector) and DFB (Distributed Feed-Back) technologies are increasingly exploited in commercial systems and field trials. In those cases wavelength-selective Bragg reflection helps to obtain single-longitudinal mode light sources that are mostly suitable for high-speed data modulation.

A special case of 1-D grating is circular Bragg grating. In that case the refractive index changes in radial co-ordinate direction. The technology is used for VCSEL fabrication taking advantage of the possibility to suppress lateral spontaneous emission.

An addition to that also quasi-periodic or self-similar 1-D dielectric structures are exploited widely for the purpose of assuring the quasi-phase matching condition in experiments involving interaction of optical beams that differ in the wavelength. The triadic Cantor and the Fibonacci sequence are typical examples. The structures are obtained by alternating two dielectric layers of different refractive indices such that the highest refractive index layers belong to some fractal set. This way an efficient second-harmonic generation is possible [18].

Fiber Gratings

The Fiber Bragg-Grating (FBG) is a short piece of fiber in which permanent refractive-index changes in the core are "written" by exposing to a diffraction pattern of an ultraviolet light beam. Fiber gratings are an emerging broad class of structures that will enhance the performance of future generations of communication systems [19]. Specially designed chirped Moiré gratings can be used for either transmission as passband filters for WDM either reflection to decompose short broadband pulses for encoding/decoding operations [20]. Also, electro-optically tunable fiber Bragg gratings have been demonstrated recently [21]. Tunable FBGs have strong potential applications in all-fiber amplitude modulators and high-speed tunable filters.

2-D PBGs

Two-dimensional photonic crystals exhibit periodicity of electromagnetic properties (e.g. of the index of refraction) in two perpendicular directions. One way to achieve this is by assembling dielectric fibers. The technology exploiting that phenomenon is known as photonic crystal fibers.

Photonic Crystal Fibers

By a proper introduction of defects into the photonic crystal fiber structure a single-mode guiding of light in a photonic crystal fiber can be obtained regardless of the optical wavelength [22]. In addition, the dispersion curve of such fiber is very flat, and can be very accurately determined with the use of analytic and numerical modeling techniques as the finite element method. E.g. the unimodal broad band behavior of photonic crystal fibers was

analyzed, and the chromatic dispersion was reliably predicted at any wavelength versus the geometric parameters [23].

3-D PBGs

The fabrication of three-dimensional photonic crystals for infrared wavelengths that are used in optical telecommunications is at the beginning stage and serious technological difficulty results from the fact that lattice constants of the order of micrometer are involved. Recently a complete photonic band gap centered at 1.55μm has been obtained with macroporous silicon [24]. Also scheme of automatic fabricating 2-D and 3-D photonic crystals with an autocloning method has been proposed recently [25].

Modelling of PBG structures

For photonic-crystal based optical waveguide structures standard numerical techniques as finite-difference and finite-element methods are usually applied for investigating the modal and dispersion characteristics of the waveguide. An overview of different theoretical models for analysis of photonic crystal fibers can be found in [26].

An efficient method of modeling the evolution of spatial beams and wide-band temporal pulses in 2-D photonic crystals has been reported recently [27]. In that work a time-domain beam propagation method (BPM) based on the finite-element scheme is applied for the analysis of reflections of both TE and TM polarized pulses in waveguiding structures containing arbitrarily shaped discontinuities. Perfectly matched layer boundary conditions were introduced in that analysis in order to avoid non-physical reflections from the computational window edges. The method was proved to be applicable to various photonic crystal circuit components.

Actual and prospective PBG applications in optical telecommunications

The all-optical network should take an advantage of photonic devices of various kind that also should provide the means for all-optical signal processing. Photonic band-gap structures are expected to be a crucial technology factor leading to an achievement of several functions that an all-optical network asks for. To this purpose many proposals have been elaborated and an intense research is currently underway.

Dispersion Compensation

Chromatic dispersion is an inherent feature of an optical link that severely limits the transmission distance of high bit-rate data streams. Although dispersion-compensating fibers (DCF) are commonly used in order to cope with dispersion, they have a substantial drawback as they introduce additional power losses. Another way to combat dispersion effects is to use chirped fiber Bragg gratings as dispersion compensators. The transmission performance of a system with chirped Bragg gratings has been shown to be significantly superior to that of an equivalent DCF module [28].

As a recent example, dispersion equalizers for the arbitrary dispersion characteristics of optical fiber links in the form of cascading chirped fiber Bragg gratings and optical circulators were proposed [29]. Also it has been shown that the dispersion slope can be efficiently controlled to match that of current transmission fibers by chirping the sampling function of a sampled fiber grating [30]. Dispersion compensating gratings of 3-nm bandwidth and 700 ps/nm total dispersion were fabricated [31]. A broadband dispersion-compensating grating module can be efficiently used for compensation of both dispersion and dispersion slope in high bit-rate WDM transmission systems [32].

Also technology possibility to manufacture tunable fiber Bragg gratings enables dynamic post dispersion compensation instead of classical fixed post compensation. That issue has been applied successfully in a multi-span 40 Gbit/s NRZ transmission system [33].

All-Optical Switching

All-optical switching is a key factor for the realization of future photonic transport network. It can be achieved by exploiting optical nonlinearities in the free-space, an optical waveguide or photonic crystal structure. Recently a first observation of an all-optical switching operation based on the bistable characteristic of a GaInAsP nonlinear directional coupler loaded with Bragg reflector at telecommunication wavelength 1.55 μm has been reported [34]. Also nonlinear pulse switching using long-period fiber gratings has been demonstrated very recently [35].

CONCLUSIONS

Photonic crystals have fascinating properties that actually are far from being well understood. They have a potential to revolutionise fiber telecommunications and optical signal processing in new millennium in a similar way as semiconductor technology has changed electronics over last half-century. The future transparent all-optical network, all-optical signal processing, optoelectronics, and optical computing are the domains to be mostly influenced.

ACKNOWLEDGMENT

The author expresses his thanks to Dr. Irena Yu. Vorgul and Prof. Alexander G. Nerukh from Kharkov, Ukraine, as well as to Prof. Igor S. Nefedov, Dr. Elena Romanova and Mrs. Ella Becker from Saratov, Russia, for their valuable co-operation and fruitful discussions.

REFERENCES

1 Marciniak, M., "Transparency of optical networks: How to manage it? ", *1st International Conference on Transparent Optical Networks* ICTON'99, Kielce, Poland, June 9-11, 1999.

2 ITU Recommendation G.709 "Network node interface for the Optical Transport Network (OTN)", planned for February 2001.

3 Saleh, A., "Economic advantages of optical transparency in backbone and access networks", ECOC'99.

4 Tkach, R.W., "How transparent should an optical network be?" ECOC'99.

5 Namihira Y., Electron. Lett. 30, 262-264 (1994).

6 Agrawal, G.P., Nonlinear fiber optics, Academic Press, San Diego, 1997.

7 Marcuse, D., Chraplyvy, A.R., and Tkach, R.W., IEEE J. Lightwave Technology 12, 885-890 (1994).

8 Sabella, R., and Lugli, P., High Speed Optical Communications, Kluwer Academic Publishers, Dordrecht/Boston/London, 1999, pp. 239-245.

9 Kowalewski, M., Marciniak, M., and Sedlin, A., "Nonlinear interactions in wavelength-multiplexed optical fibre telecommunication systems", *Journal of Optics A: Pure and Applied Optics* (2000).

10 Watanabe, T., et al., "Scale expansion of transparent photonic transport network based on distributed Raman amplification", ECOC'99.

11 Joindot, M., et al, "Study of an European all optical transport transparent network", ECOC'99.

12 Thylén, L., "Some aspects of photonics and electronics in communications and interconnects", *1st International Conference on Transparent Optical Networks* ICTON'99, Kielce, Poland, June 9-11, 1999.

13 Alferness, R. C., "Research challenges in optical networking", ECOC'98, 20-24 September 1998, Madrid, Spain.

14 COST Action 268 "Wavelength scale photonic components for telecommunications", Memorandum of Understanding, 1998.

15 Joannopoulos, J. D., Meade, R. D., and Winn, J. N., "Photonic Crystals", Princeton University Press, Princeton USA, 1995.

16 Krauss, T.F., and De La Rue, R. M., "The potential of photonic microstructures in optoelectronics", ECOC'97.

17 Zoorob, M.E., et al., "Complete photonic bandgaps in twelve-fold symmetric photonic quasicrystals', ECOC'99.

18 Sibilia, C., and Bertolotti, M., "Nonlinear optical propagation in periodical and quasiperiodical layered structures", *Proceedings of the 2nd International Conference on Transparent Optical Networks* ICTON 2000, Gdansk, Poland, June 9-11, 2000.

19 Strasser, T. A., "Fibre gratings in novel device structures", ECOC'99.

20 Chen, L. R., and Smith, P. W. E., "Specially designed chirped Moiré gratings for optical communications", ECOC'99.

21 Srinivasan, B., and Jain, R.K., "First demonstration of thermally-poled electro-optically tuneable fibre Bragg gratings", ECOC'99.

22 Monro, T. M., Broderick, N. G., and Richardson, D. J., "Exploring the optical properties of holey fibres", International Summer School of Quantum Electronics, 29th Course on "Nanoscale Linear and Non-Linear Optics", Erice-Sicily, Italy, 2-14 July, 2000

23 Bréchet, F., et al., "Accurate computation of the chromatic dispersion in unimodal photonic crystal fibres", ECOC'99.

24 Rowson, S., Chelnokov, A, and Lourtioz, J.M., "Macroporous silicon : photonic crystal substrates at 1.55 μm", ECOC'99.

25 Kawashima, T., Sato, T., Miura, K., Ohtera, Y., Ishino, N., and Kawakami, S., "Autocloning Technology: Fabrication Method for Photonic Crystals based on Sputtering Process", International Summer School of Quantum Electronics, 29th Course on "Nanoscale Linear and Non-Linear Optics", Erice-Sicily, Italy, 2-14 July, 2000.

26 Bjarklev, A., Broeng, J., and Barkou, S.E., "Modelling of photonic crystal fibres", ECOC'99.

27 Koshiba, M., Tsuji, Y., and Hikari, M., IEEE J. of Lightwave Technology 18, 102-109 (2000).

28 Rourke, H., Pugh, B., Kanellopoulos, S., Baker, V., Napier, B., Greene, P., Goodchild, D. , Fells, J., Epworth, and Collar, R., A., "Fabrication and system performance of dispersion compensating gratings", ECOC'99.

29 Komukai, T., Inui, T., and Nakazawa, M., IEEE J. Quantum Electronics 36, 409417 (2000).

30 Loh, W. H., et al., "Dispersion slope compensator based on an interleaved chirped sampled fibre Bragg grating", ECOC'99.

31 Fujii, K., Terao, Y., Kotani, K., Nishiki, A., Ozeki, Y., Nomoto, T., Rastokin, V., Tan, R., Kung, P., Beaulieu, C., and Lefebvre, P., "Broadband chirped fibre Bragg grating for dispersion compensator", ECOC'99.

32 Gnauck, A.H., Wiesenfeld, J.M., Garrett, L.D., Eiselt, M., Forghieri, F., Arcangeli, L., Agogliati, B., Gusmeroli, V., and Scarano, D., "16 x 20 Gbit/s - 400 km WDM transmission over NZDSF using a slope-compensating fibre-grating module", ECOC'99.

33 Nielsen, T.N., et al, Fibre Bragg grating tuneable dispersion compensator for dynamic post dispersion optimisation at 40 Gbit/s, ECOC'99.

34 Nakatsuhara, K., et al., "All-optical switching in a nonlinear directional coupler loaded with Bragg reflector", ECOC'99.

35 Perlin, V. E., and Winful, H. G., IEEE J. Lightwave Technology 18, 329-333 (2000).

TIME DOMAIN METHODS

TRANSIENTS OF AN AXIAL SYMMETRIC ELECTROMAGNETIC SOURCE IN A FLAT WAVEGUIDE WITH A TIME VARYING PLASMA

N. Sakhnenko, A. Nerukh, and F. Fedotov

Kharkov Technical University of Radioelectronics, 14 Lenin Ave., Kharkov, 61166, Ukraine
E-mail: nks@au.ru

ABSTRACT

A flat waveguide filled by a homogeneous cold time-varying plasma is considered. A problem of an excitation and propagation of an axial symmetric electromagnetic waves in such a waveguide is solved. To obtain a solution, the resolvent operator in a polar coordinate system is constructed that allows to write an exact and explicit expression for the electromagnetic field.

INTRODUCTION

When a plasma time changing begins at zero moment then an electromagnetic field in a waveguide is described by the equation according to [1]

$$\vec{E}(t,\vec{r}) = \vec{E}_0(t,\vec{r}) - \frac{4\pi}{c^2}\int_0^{\infty} dt' \iint_{\infty} dx'dy' \int_0^{b} dz' \hat{G}(t-t',\vec{r}-\vec{r}') \frac{\partial^2}{\partial t'^2}(\hat{V}_e(t')\vec{E}(t',\vec{r}')) \qquad (1)$$

where $\vec{r} = (x, y, z)$, $\vec{E}_0$ is the initial field, $\vec{E}$ is the transformed field, $\hat{G}$ is a tensor Green's function, $\hat{V}_e = \frac{1}{4\pi}(\omega_e^2 \int_0^t dt'(t-t') - (\varepsilon - 1))$ is a medium operator written down for the case of a plasma density changing from zero moment of time, ε is a permittivity of a medium that has filled a waveguide until zero moment of time, c is the light velocity in vacuum. In (1) x and y are longitudinal coordinates and z is a lateral coordinate directed across the waveguide. The distance between the planes of the waveguide is equal to b.

THE GREEN'S FUNCTION IN THE CYLINDRICAL COORDINATES

For the considered problem it is convenient to use the polar coordinates. The equation (1) in polar coordinates is written down as

$$\vec{E} = \vec{E}_0 + \hat{K}\vec{E}, \quad \hat{K} = \frac{1}{\varepsilon}\hat{\Phi}^{-1}\int_0^{\infty} dt' \int_0^{\infty} \rho' d\rho' \int_0^{2\pi} d\varphi \int_0^{b} dz' \hat{G} \cdot \hat{V}_e \hat{\Phi} \qquad (2)$$

$\hat{K}$ is a kernel of integral equation, the matrix $\hat{\Phi} = \begin{pmatrix} \cos\varphi & \sin\varphi & 0 \\ -\sin\varphi & \cos\varphi & 0 \\ 0 & 0 & 1 \end{pmatrix}$ takes into account the transformation of vector components. The Green's function must satisfy boundary conditions on the waveguide boundaries so it can be presented as a Fourier expansion of eigenfunctions of a flat waveguide. It can be presented also as a series to axial angle. The coefficients of this expansion written down in the form of the Hankel transform with respect to the polar radius

$$\frac{\partial^2}{\partial t^2}\hat{G} = -\frac{v^2}{4\pi}(graddiv - \frac{1}{v^2}\frac{\partial^2}{\partial t^2}\hat{I})\sum_{k,n} g_{kn}(\tau,\rho,\rho')e^{ik(\varphi-\varphi')}\hat{\psi}_n(z)\hat{\psi}_n(z'),$$

where

$$g_{kn}(\tau,\rho,\rho') = \frac{4v}{b}\int_0^\infty sJ_k(s\rho)J_k(s\rho')\Theta(v\tau)\frac{\sin v\tau\sqrt{s^2+\lambda_n^2}}{\sqrt{s^2+\lambda_n^2}}ds$$

$\hat{\psi}_n = \begin{pmatrix} \sin\lambda_n z & 0 & 0 \\ 0 & \sin\lambda_n z & 0 \\ 0 & 0 & \cos\lambda_n z \end{pmatrix}$ is the matrix of eigenfunctions of a flat waveguide,

$\lambda_n = \frac{n\pi}{b}$, $n = 0,1,2...$, $\tau = t - t'$, $\Theta(.)$ – here is the unit Heaviside function.

THE INITIAL FIELD OF LINEAR SOURCE

By virtue of the obtained Green's function, the initial field created by the source in general case is presented as

$$\vec{E}_0 = -\frac{4\pi}{c^2}\hat{\Phi}^{-1}\int_{-\infty}^{t} dt'\int_0^\rho \rho' d\rho'\int_0^{2\pi} d\varphi'\int_0^b dz'\hat{G}\cdot\hat{\Phi}\frac{\partial}{\partial t'}\vec{j}$$

Now find the linear source arranged on axes Z, which has a random time dependence.

$$\vec{j} = \vec{e}_z\frac{\delta(\rho)}{\rho}j(t)$$

We will restrict ourselves to the simplest case ($\varepsilon = 1, v = c$). In that case

$$\vec{E}_0 = \frac{2\pi b}{c^2}\int_{-\infty}^{t} dt'\frac{j'(t')\Theta(c(t-t')-\rho)}{\sqrt{c^2(t-t')^2-\rho^2}}\vec{e}_z \qquad (4)$$

Radiation of such source generates a lowest wave mode with the number $n = 0$.

THE TRANSFORMED FIELD

To obtain the transformed field, it is necessary to construct the solution of integral equation (1). The Volterra integral equation of the second kind and its solution can be derived by the resolvent method

$$\vec{E} = \vec{E}_0 + \hat{R}\vec{E}_0 \qquad (4)$$

The resolvent must obey the operator equation

$$\hat{R} - \hat{K}\hat{R} = \hat{K} \qquad (5)$$

where the K is the kernel of (2). The equation for the resolvent is conveniently made in the impulse notation (the Fourier-Hankel- Laplace notation). That allows obtaining an exact and explicit expression for the resolvent of the integral equation.

$$\hat{R} = \omega_e^2\cdot\int_0^t dt'\int_0^\infty \rho' d\rho'\int_0^{2\pi}\frac{d\varphi'}{2\pi}\int_0^b\frac{2dz'}{b}\sum_{k,n}\int_0^\infty \xi d\xi\hat{\Phi}^{-1}\times[graddiv\frac{1}{\lambda_n^2+\xi^2}(\frac{\sin\omega_e\tau}{\omega_e} - \frac{\sin\omega_{we}\tau}{\omega_{we}}) -$$

$$-\frac{\sin\omega_{we}\tau}{\omega_{we}}]\times J_k(\xi\rho)J_k(\xi\rho')e^{ik(\varphi-\varphi')}\hat{\psi}_n(z)\hat{\psi}_n(z')\hat{\Phi}\Theta(\tau)$$

where $$\omega_{we} = \sqrt{c^2(\lambda_n^2+\xi^2)+\omega_e^2} \qquad (6)$$

The transformation of an electromagnetic radiation of an axial source in the plate waveguide filled by the flash created plasma is carried out from (4) by using the obtained resolvent.

$$\vec{E} = \vec{e}_z \frac{2\pi b}{c^2} \int_0^\infty ds \frac{J_0(s\rho)}{\omega_{we}} [\int_0^t dt' cs \sin \omega_{we}(t-t') j'(t') -$$

$$- \frac{\omega_e^2}{2} \int_{-\infty}^0 dt' (\frac{\sin(\omega_{we}t + cst')}{\omega_{we} + cs} - \frac{\sin(\omega_{we}t - cst')}{\omega_{we} - cs}) j'(t')]$$

It is also a lowest wave mode with the number $n = 0$.

EXCITATION OF A WAVEGUIDE BY STEP CURRENT

Consider the excitation of a waveguide by the step current $j(t) = \Theta(t - t_0)$. The incident field in the empty waveguide from (3) is

$$\vec{E}_0 = \frac{2\pi b}{c^2} \frac{\Theta(c(t-t_0) - \rho)}{\sqrt{c^2(t-t_0)^2 - \rho^2}} \Theta(t - t_0) \vec{e}_z$$

The field occupies the region between the source and the wave front. That differs from the case of a flat front, when the field has δ – singularity [2].

After forming the plasma, the field is determined by the moment of switching on the source.

$$\vec{E} = -\vec{e}_z \frac{\pi b \omega_e^2}{c^2} \Theta(t) \int_0^\infty ds \frac{J_0(s\rho)}{\omega_{we}} \left[\frac{\sin(\omega_{we}t + cst_0)}{\omega_{we} + cs} - \frac{\sin(\omega_{we}t - cst_0)}{\omega_{we} - cs} \right] \quad \text{for } t_0 < 0$$

$$\vec{E} = \vec{e}_z \frac{2\pi b}{c^2} \frac{\cos(\frac{\omega_e}{c}\sqrt{c^2(t-t_0)^2 - \rho^2})}{\sqrt{c^2(t-t_0)^2 - \rho^2}} \Theta(c(t-t_0) - \rho)\Theta(t - t_0) \quad \text{for } t_0 > 0$$

The presence of the plasma yields the oscillatory character of the wave.

CONCLUSION

The Green's function for Maxwell's equations in a flat waveguide where a homogeneous cold time-varying plasma is formed at the zero moment of time is derived. By virtue of the obtained Green's function the four-dimensional integral equation for an electromagnetic field is presented. An equation resolvent for the case of axial symmetric problems is obtained that allows to present the exact and explicit expressions for an axial symmetric distribution of an electromagnetic field.

REFERENCES

[1] G.Nerukh, and N.A. Khizhnyak, Modern problem of Transient Macrockopic Electrodynamics (in Russian), Test-radio Publ., Kharkov, Ukraine, 1991

[2] V.V. Borisov. The transient fields in waveguides (in Russian), Leningrad State university, Russia, 1991

[3] L. Felsen, and N. Markuviz. Radiation and propagation of waves. New Jersey, USA, 1973.

CONCERNING TRANSITION RADIATION BY A RELATIVISTIC ELECTRON IN A THIN METALLIC PLATE

S.N. Dobrovol'sky [1], and N.F. Shul'ga[2]

National Science Center «Kharkov Institute of Physics and Technology»,
61108 Kharkov, Ukraine

E-mail: [1] dobrovolsky@kipt.kharkov.ua, [2] shulga@kipt.kharkov.ua

ABSTRACT

In the present paper, the influence of transverse target's size on the transition radiation spectrum of relativistic electron moving through the thin metallic plate is considered. It has been shown that significant spectrum distortion can occur in the millimeter range of waves in comparison to the case of an infinite metallic plate. This effect takes place for "forward" and "backward" radiation in both cases, i.e. for normal incidence of electron on the target as well as for oblique incidence.

INTRODUCTION

A series of experiments (see, e.g. [1]) was recently performed in order to study the coherent effects in the transition radiation emitted by bunching relativistic electrons in a thin metallic targets. The measurements were performed on electron beams with energy in the range of 100MeV. The coherent transition radiation emitted by short bunches of electron beams was studied in the millimeter and submillimeter range of waves. The experimental results were analyzed using formulas from the theory of transition radiation for target with an infinite transverse size.

THEORY

This work is devoted to the theory of transition radiation for transverse-bounded thin ideally conducted targets. It is a "backward" transition radiation of relativistic electron moving inclined through a thin metallic plate being considered in this work for millimeter wave range. The theory that assumes the influence of the target transverse size on the transition radiation spectrum in the case of normal electron incidence on the target, was proposed in [2-3]. It was shown that not only longitudinal ($L \approx 2\gamma^2\lambda$), but also transversal distances ($\rho_{eff} \approx \gamma\lambda$, where γ is a Lorentz-factor of electron and λ is a radiated wave length) that are responsible for transition radiation can be macroscopic values in this case. A consideration of finite macroscopic transversal target sizes can lead to a significant distortion of the transition radiation spectrum in comparison to the case of infinite target. The spectral-angular density of radiation, emitted in both «forward», and «backward» directions by relativistic electron that penetrate the center of metallic disk is given by the equation [2,3]

$$\frac{dE}{d\omega d\Omega} = \frac{dE_{\infty}}{d\omega d\Omega}\left| F(\gamma \sin \vartheta, \frac{\omega}{\omega_{\perp}}) \right|^2 , \tag{1}$$

where $\frac{dE_{\infty}}{d\omega d\Omega}$ is the spectral-angular density of transition radiation of electron on the target having the infinite transverse size, $d\Omega = \sin\vartheta d\vartheta d\varphi$ (ϑ and φ are polar and azimuthal radiation angles) and F is the function to assign influencing of the target transverse sizes on the transition radiation.

$$F(y,x) = \frac{1}{y}\left(y^2+1\right)\int_0^x u du K_1(u) J_1(yu) . \tag{2}$$

Here $x = \omega/\omega_{\perp}$, $\omega_{\perp} = \frac{c\gamma}{a}$, a is the radius of a disk, $y = \gamma \sin\vartheta$ and $K_1(x), J_1(x)$ - McDonald's and Bessel's functions, respectively. The equations (1) and (2) show, for $y \approx 1$, that density of transition radiation does not practically depend on the transverse target size in the frequency range $\omega \geq \omega_{\perp}$ (in this case $F \to 1$). If $\omega << \omega_{\perp}$, then the consideration of limited transverse target sizes leads to a significant decrease of transition radiation intensity in comparison to the case of an infinite transverse target radius ($F << 1$ in this case for $y \approx 1$). Thus, under the experimental conditions [1] ($\lambda \approx 0.1$ and $\gamma \approx 200$), the value of the radiation intensity suppression effect can reach several orders. The displacement of the main angular maximum and the appearance of new oscillating maximum (in the spectral-angular distribution of radiation intensity) should be observed as well.

We shall focus our attention on the fact that, for relativistic electrons, an influence of the transverse size on the radiation spectrum takes place also for oblique electron incidence on the target. The equation for the electron "forward" and "backward" transition radiation spectrum in the case when electron is moving through a metallic disk is

$$\frac{d^3E}{d\omega d\Omega} = \frac{e^2}{\pi^2 c}\beta^2 \cos^2\phi \frac{\left((\beta\sin\phi - \sin\vartheta\cos\varphi)^2 \cdot A^2 + \beta^2 \sin^2\phi \cos^2\vartheta \sin^2\varphi \cdot B^2\right)}{\left((1-\beta\sin\phi\sin\vartheta\cos\varphi)^2 - \beta^2\cos^2\vartheta\cos^2\varphi\right)^2} \tag{3}$$

were ϕ is an angle between electron velocity $\mathbf{v}$ and the normal vector to the target surface (normal vector coincides with OZ axis), $\beta = vc^{-1}$ and

$$A = \frac{\int_{-\pi}^{\pi} d\alpha \int_0^u t dt K(t,\phi,\alpha)\cos\alpha \exp\left[-it\gamma\cos\alpha(\sin\vartheta - \beta\sin\vartheta)\right]}{\int_{-\pi}^{\pi} d\alpha \int_0^{\infty} t dt K(t,\phi,\alpha)\cos\alpha \exp\left[-it\gamma\cos\alpha(\sin\vartheta - \beta\sin\vartheta)\right]}, \tag{4}$$

$$B = \frac{\int_{-\pi}^{\pi} d\alpha \int_{0}^{u} tdtK(t,\phi,\alpha)\sin\alpha\exp[-it\gamma\sin\alpha\sin\vartheta\sin\varphi]}{\int_{-\pi}^{\pi} d\alpha \int_{0}^{x} tdtK(t,\phi,\alpha)\sin\alpha\exp[-it\gamma\sin\alpha\sin\vartheta\sin\varphi]},$$

where $u = \frac{\omega a}{v_z\gamma}$, $K(t,\phi,\alpha) = \frac{K_1\left(t\sqrt{1-\sin^2\phi\cos^2\alpha}\right)}{\sqrt{1-\sin^2\phi\cos^2\alpha}}$.

DISCUSSION

Values $A(x,\vartheta,\varphi,\gamma,\phi)$ and $B(x,\vartheta,\varphi,\gamma,\phi)$ in (3) are functions that define the influence of the target transversal size on the transition radiation in the case of oblique electron incidence. These functions are sufficiently complex even for the case of metallic disk but the main tendency that determines influence of transversal geometry of target in the case of normal incidence remains the same for oblique incidence. For $\omega \geq \omega_\perp$ (now $\omega_\perp = \frac{v_z\gamma}{a}$), i. e. for the case when transverse size ρ_{eff} is less then the target radius a, we have $A(x,\vartheta,\varphi,\gamma,\phi) \to 1$, $B(x,\vartheta,\varphi,\gamma,\phi) \to 1$, and spectral-angular density of radiation coincides with the well known result for infinite metallic plate [4]. Within the frequency range $\omega \leq \omega_\perp$ we have $A(x,\vartheta,\varphi,\gamma,\phi) << 1$ and $B(x,\vartheta,\varphi,\gamma,\phi) << 1$, and consideration of the transversal target size results in a significant decrease of the transition radiation intensity in the infrared and far-infrared range of waves in comparison to the case of an infinite plate.

REFERENCES

[1] Y. Shibata et al. // Phys Rev. E 49, 1994, P. 785-789.

[2] N. F. Shul'ga, and S. N. Dobrovol'sky // Phys. Lett. A259, 1999, P. 291-294.

[3] N. F. Shul'ga, and S. N. Dobrovol'sky // JETP, 2000, V.117, P.668-672. (in Russian)

[4] M.L.Ter-Mikaelian High-Energy Electromagnetic Processes in Condensed Media (Wiley-Interscience, New-York, 1972).

DIPOLE CURRENTS AND INTERSTELLAR PROPAGATION OF ELECTROMAGNETIC SIGNALS

Henning F. Harmuth,
Formerly of The Catholic University of America, Washington DC,
and Konstantin A. Lukin,
Institute of Radiophysics and Electronics, NASU, Kharkiv, Ukraine
E-mail: lukin@ire.kharkov.ua; Phone: +38 0572 448349

Most of the information we have obtained about the universe beyond the planet Earth came from electromagnetic (EM) waves, and most of the information obtained from EM waves came from steady state waves. Whenever received EM waves are decomposed into sinusoidal waves with various frequencies one thinks and acts in terms of steady state waves theory. For instance, the Doppler shift frequency – implied every time the term *red-shift is used* –is a steady state concept even though the Doppler effect is not. A power spectrum density (Fourier frequency spectrum) of received waves is a steady state concept as well. However, in reality there are many electromagnetic events and phenomena which can not be described using a steady state concept, and one have to apply a different approach for their proper description and understanding. For example, a sunrise and sunset being considered as a single events provide us with non steady state events since we can determine their beginning and ending times. In this way, we are coming to the necessity of use of a different concept in describing EM waves, namely to the concept of EM signals. *Electromagnetic signal is an electromagnetic wave that is zero before a certain finite time and has finite energy* [1, 2]. In terms of mathematics a signal can be represented by a function of a real variable with the usual topology of the real numbers and denoted time, the function being zero below a certain finite value of the variable and quadratically integrable. Pulsars provide us with electromagnetic signals since we can observe the increase of the electric and magnetic filed strength from zero or the decrease to zero.

In the paper, we present results of our investigations on propagation of EM signals through interstellar medium that is supposed to be formed by neutral atomic hydrogen gas with rather low density. We describe the model under consideration and obtaining of the partial differential equation for one of the EM field components, as well as formulation of initial-boundary value problem for that equation and the method for its solution in time domain. EM signals propagation over Billions light years distance through such medium is studied for various combinations of its parameters.

Step-like changing of the EM signal field requires solving of the problem in time domain and application of a non-conventional description of the above medium. Propagation of EM waves is governed by Maxwell equations. However, those equations should be modified according to the media properties where EM waves propagate. In the case under consideration, EM signals have to propagate through the medium consisting of atomic hydrogen gas with a very low density. Since the atoms are neutral and signals are supposed to be rather weak they cannot carry an electric monopole current, but only dipole currents. Electric field strength will pull the positive proton and the negative electron slightly apart and produce an electric dipole. A dipole current flows while this pulling apart is in progress and also when the electric field strength drops to zero and the hydrogen atom returns to its original, non-polarized state. Similarly, the hydrogen atom

has a magnetic momentum like a little bar magnet. A magnetic field strength will rotate the atoms to make them line up with the field strength. A magnetic dipole current flows while this rotation is in progress and also when the magnetic field strength drops to zero and the magnetic dipoles return to their original random orientation. So, we have to take into account the reaction of the medium onto the action of the EM field of the propagating signal. Conventional approaches to solution of that problem suppose that both intrinsic characteristic time of the media and its relaxation time are much smaller the characteristic time of the EM field variation. Besides, they also suppose performing of space averaging of the EM fields introducing into consideration both electric and magnetic flux densities. Since in our case we have both very low density of the neutral atomic hydrogen and very fast variation of the EM signal fields those methods are not applicable anymore. In order to solve the problem we modify Maxwell equations for "empty space" using both electric and magnetic dipole current densities rather then electric and magnetic flux densities [3]. This implies description of the medium in the frame of *microscopic* approach using representation of a hydrogen atom as a combination of electric and magnetic dipoles. Those dipoles produce *electric and magnetic dipole currents* under the EM field action that is to be calculated in a self-consistent way.

Self-consistent system containing both modified Maxwell equations and equations for the dipole current densities evolution under the EM field action can be written in the following form [3]:

where

$$-rot\vec{E} = \mu\frac{\partial\vec{H}}{\partial t} + g_m; \quad rot\vec{H} = \varepsilon\frac{\partial\vec{E}}{\partial t} + g_e; \quad \varepsilon\, div\vec{E} = \mu\, div\vec{H} = 0; \tag{1}$$

$$\vec{g}_e + \tau'\frac{\partial\vec{g}_e}{\partial t} + \frac{\tau''}{\tau^2}\int\vec{g}_e\,dt = \sigma_p\vec{E}; \quad \vec{g}_m + \tau'\frac{\partial\vec{g}_m}{\partial t} + \frac{\tau'}{\tau^2}\int\vec{g}_m\,dt = 2s_p\vec{H}; \tag{2}$$

$$\sigma_p = \frac{N_0 e^2\tau'}{m}; \quad s_p = \frac{N_0 q_m{}^2\tau'}{m}; \quad q_m = \frac{\mu\, m_{m0}}{2R};$$

$\vec{E}$ *and* $\vec{H}$; $\vec{g}_e$ *and* $\vec{g}_m$; σ_p *and* s_p; ε *and* μ; e *and* m; m_{m0} *and* q_m are electric and magnetic fields; dipole electric and magnetic current densities; electric and magnetic dipole current conductances; permittivity and permeability of the vacuum; charge and mass of electron; magnetic dipole moment and fictitious magnet charge, respectively; τ' and τ are the relaxation time and period of eigen-frequency of the dipoles-oscillator used as the model of atomic hydrogen.

Let consider a planar, transverse electromagnetic (TEM) wave propagating in the direction y. A TEM planar wave requires

$$E_y = H_y = 0; \quad E_x = E_z \cong E; \quad H_x = -H_z \cong H;$$

With this simplification, the above system of partial integro-differential equations are reduced to the sixth order linear PDE for either electric E or magnetic H field component [3]. In order to investigate propagation of EM signal through the above medium one have to solve initial-boundary-value problem for that equation with the following boundary $(y=0)$ and initial $(t = 0)$ conditions:

$$E(y,0)=\frac{\partial^n E(y,0)}{\partial t^n}=\int\frac{\partial^2 E}{\partial y^2}\,dt=\iint\frac{\partial^2 E}{\partial y^2}dt\,dt'=0;\qquad n=1,2,3; \tag{3}$$

$E(\infty,t)\ = finite$

$E(0,t)=E_0\,S(t)\,(1-e^{-t/\tau_s})=\begin{cases}0: & t<0\\ E_0\,(1-e^{-t/\tau_s}): & t\geq 0\end{cases}$; The above problem is solved [3]

by the variables separation method. The solution has the following form:
where k is the separation constant; $\gamma(k)$ are six roots of characteristic equation for PDE derived from Eq.(1)-(2); $A(k)$ are six constants to be determined by six initial conditions (3). The

$$E(y,t)=E_0\left[w(y,t)+e^{-\left(y/L+t/\tau_s\right)}\right];\quad w(y,t)=\int_0^\infty\left(\sum_{i=1}^{6}A_i(k)\,e^{\gamma_i(k)\,t/\tau_{mp}}\right)\sin(2\pi ky)\,dk \tag{4}$$

expressions for $L(\tau,\tau')$, $\gamma(k)$ and $A(k)$ have an explicit, but rather complicated
form and can be found in the monograph [3]. Here we only note that because of the higher symmetry of the modified Maxwell equations (1) we were able to find analytical solutions for the sixth order characteristic equation. This enabled us of both performing of the Eq.(4) integrand analysis as function of k and developing of efficient algorithms for numerical evaluation of the electric and magnetic fields of propagating signals. In particular, the solution (4) has rather different form depending on the ratio p of the dipoles relaxation time τ' to its eigen-oscillation period τ'. We found that for $p<1/2$ only two terms $A(k)$ are oscillating ones in the integrand in Eq.(4) while for $p>1/2$ all of them have an oscillating form. However, this gives a qualitative difference for EM signal precursor only while the main lobe of the signal is p independent when it is propagating through interstellar medium.
Solutions of that equation for various combinations of the interstellar medium parameters and initial signal-like E-field distributions are presented in the monograph [3]. Behavior of both signal main lobe and its precursor for various EM signals, such as exponential step function, sinusoidal and rectangular pulses when they are propagating over Billions light years distance are studied in [3].
It is worth to stress that in our model, we did not use any representation of the EM fields based upon steady state concepts, such as Fourier transform, but obtained the solutions in time domain directly. In particular, this gave us possibility of studying of details in EM field transients while signal-like waves are propagating in a medium that permits no monopole (conductivity) currents but only electric and magnetic dipole currents.

REFERENCES:

[1] Henning F. Harmuth, Propagation of Nonsinusoidal Electromagnetic Waves. Academic Press, N.-Y., 1986.
[2] Henning F. Harmuth, R.N. Boules, and M.G.M Hussein. Electromagnetic Signals (Reflection, Focusing, Distortion, and Their Applications), Kluwer Academic/Plenum Publishers, N.-Y., 1999.
[3] Henning F. Harmuth and Konstantin A. Lukin. Interstellar Propagation of Electromagnetic Signals. Kluwer Academic/Plenum Publishers, N.-Y., 2000.

NUMERICAL–ANALYTICAL SPATIAL–TEMPORAL CHARACTERISTICS OF A TEM–HORN

G. V. Ermakov
Kharkov Military University, P. O. 9063, Kharkov 61204, Ukraine
Tel.: 380 (572) 404141 (285), E–mail sima@skynet.kharkov.com

ABSTRACT

The principles of calculation of the ultrawide-band signals radiators are considered. The electromagnetic analysis of a TEM - horn is carried out. The distortions of a pulse are considered at the radiation and the peak pattern of the radiator are parsed.

One of the major problems at the construction of the videopulse radars is to develop an efficient antenna systems which will satisfy the requirement of a directed radiation alongside with the requirement of the minimal distortion of a pulse at radiating and receiving.

To achieve a high gain it is necessary to use radiating structures of the surface type with large electrical sizes that allow forming a directed radiation of the UWB signals, as well as to provide a rather smooth transition from output resistance of the generator to a wave resistance of the free space, thus achieving a gain which is significantly larger than that of the elementary radiators.

In the present paper, the numerical-analytical solution of the task on excitation of a TEM–horn with the exponential vertical and cross-sectional profiles is offered, the distortions of the shape of the radiated signal are calculated and the peak pattern of the radiator are determined.

To solve the task of the TEM–horn excitation we shall consider a system consisting of the two limited ideal conductive surfaces $S = S_1 \bigcup S_2$ with the exponential profiles located in the free space. Consider the position of the sources is constant in the space, and the electromagnetic field is excited by the electrical dipoles with the moment directed along the vertical axis.

To define the electromagnetic field outside of the surface S it is necessary to solve a set of equations of the Maxwell satisfying to the boundary conditions on the surface S, to the zero initial conditions and conditions of the radiation on the infinity.

If suppose a field $\vec{E}_0(Q,t)$, $\vec{H}_0(Q,t)$, which excited by the electrical dipoles, as Fourier integrals, the solution of the given task outside of the surface S can be expressed through tangential components of the electrical and magnetic vectors on the surface S [1]:

$$\begin{aligned}\vec{H}(M,\omega) = \frac{1}{4\pi}\int_D \left[\vec{J}_0(Q,\omega), grad_Q \frac{\exp\left(-ik(\omega)R_{MQ}\right)}{R_{MQ}}\right] dv_Q + \\ + \frac{1}{4\pi}\oint_S \left\{\left[grad_P \frac{\exp\left(-ik(\omega)R_{MP}\right)}{R_{MP}}, \left[\vec{n}_P, \vec{H}(P,\omega)\right]\right] + \right. \\ \left. + i\omega\varepsilon\left[\vec{n}_P, \vec{E}(P,\omega)\right]\frac{\exp\left(-ik(\omega)R_{MP}\right)}{R_{MP}} - \left(\vec{n}_P, \vec{H}(P,\omega)\right) grad_P \frac{\exp\left(-ik(\omega)R_{MP}\right)}{R_{MP}}\right\} dS,\end{aligned} \tag{1}$$

where $\vec{J}_0(Q,w)$ is the surfaces density of a source current, $k(\omega)=\omega\sqrt{\varepsilon\mu}$ is the wave number, $_{MP}$, R_{MQ} is a distance between points M and P, M and Q accordingly, $\vec{n}_P$ is external to area S a normal in a point P.

In a case of an ideal conductive surface the tangential components of the electrical field on the surface become zero. If we enter for a surface current, that is induced on a surface of an ideal conductive body, the denotation

$$\vec{J}(P,\omega)=\left[\vec{n}_P,\vec{\mathrm{H}}(P,\omega)\right] \qquad (2)$$

and direct on the normal the point M to the point P_0 of the surface S, then, using properties of a potential of a double layer, we shall receive an equation of the Fredholm integral equations of the second kind for the area density of the current on an ideal conductive surface S

$$\vec{J}(P_0,\omega)+\frac{1}{2\pi}\oint_{S_1+S_2}\left(\frac{1}{R_{PP_0}^2}+\frac{jk(\omega)}{R_{PP_0}}\right)\left[\vec{J}(P,\omega),\vec{r}_{PP_0}\right]\exp\left(-ik(\omega)R_{PP_0}\right)dS_P=2\left[\vec{n}_{P_0},\vec{H}_0(P,\omega)\right], \quad (3)$$

where R_{PP_0} is a distance between the points P and P_0, and $\vec{r}_{PP_0}$ is the unit vector in the direction from point P to point P_0.

For the implementation of the numerical algorithm at the definition of the surfaces density of the current the surface S is divided into N cells. Within the limits of each cell, as usual in similar cases, we consider the current density J as a constant (in the n cell $\vec{J}$ has components J_n^x, J_n^y, J_n^z in the rectangular coordinate system). The sizes of the cells are $0{,}1\lambda$ (λ – wavelength). For the registration of the edge effects the Meixner condition is used [1].

Having conducted a discretization (3) similarly to [2], we shall reduce it to a system of the linear algebra equations with the unknown components of area density of the current. At the coincidence of the integration points the kernel has a feature, to eliminate which, it is cut by a circle of radius $\varepsilon=10^{-6}\lambda$. The presence of these features allows generating a system of the linear algebraic equations with a dominant main diagonal. Taking into account the distribution of the currents on the surface of the horn, the field in the far-field region can be retrieved according to expression (2).

To estimate the practical applicability of the technique mentioned above, a number of calculations was carried out. At the realization of the numerical calculations the function of [3] type was used as a model of the a magnetic field of sources

$$H_0(t)=\mathrm{B}_0\left(\frac{t}{T}\right)^n\left[M^{n+1}\exp\left(-\frac{Mt}{T}\right)-\exp\left(-\frac{t}{T}\right)\right]\chi(t). \qquad (4)$$

where B_0 is the normalized coefficient, and $\chi(t)$ is the Heaviside step function.

Model (4) satisfies the statement of the task and requirement sign-variability of the radiated electromagnetic field. Non-dimensional values $M>1$, $n>0$, T (there is a dimension of the time) characterize the shape and duration of a signal, and determine a spectral content. In Fig.1, the shape radiated of the UWB signal with characteristics is represented: $M=5$, $n=2$, $T=0{,}8$ at geometrical parameters of the antenna $y=0{,}005\exp(2{,}9z)$; $x=0{,}2\exp(0{,}46z)$; $\alpha=15^0$.

At all the values of the parameters n, M, T (used during the present researches) the radiated signal represents the sequence of 3 signals which differs in the amplitude. Each of the partial pulses

qualitatively keeps up the shape of the initial one. The presence of postpulse oscillations represents the rereflection of the initial pulse from a source of load. The distortions of the radiated signal shape are explained by a dispersion of the reflection coefficient. For an integral estimation of the radiated signals distortions the temporary moments, described in [3], can be used.

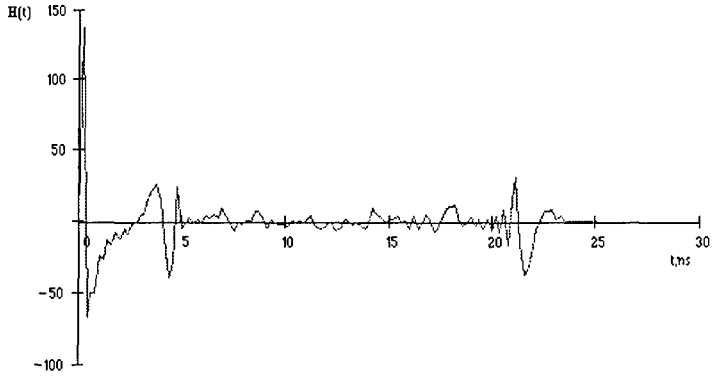

Fig. 1. The shape of the radiated pulse.

In Fig. 2, and 3, the peak pattern (relation of the amplitude from the direction of the radiation) in the planes *E* and *H*, respectively, are shown. The width of the pattern on a peak amplitude on the level *0,5* in the *E*-plane is about 60^0, and in the *H*-plane – 150^0. The found difference of spatial distributions of amplitudes are connected to the distinction of the electrical sizes of the antenna in these planes. The longitudinal size of the antenna exceeds the spatial duration of the pulse and that provides the radiation of energy mainly in a longitudinal direction of the TEM–horn, thus narrowing the pattern in E-plane.

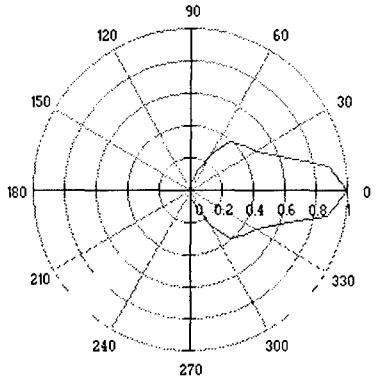

Fig. 2 The peak pattern in E–plane

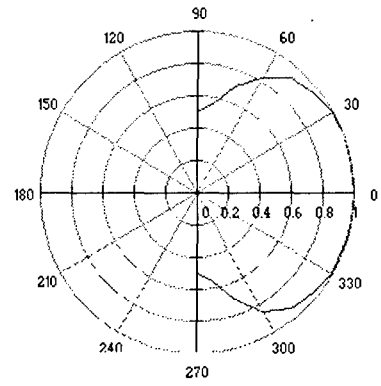

Fig.3. The peak pattern in H–plane

REFERENCES

[1] A.S. Ilyinsky, V.V. Kravtsov, and A.G. Sveshnikov. Mathematical Models for Electromagnetics. M.: Vysshaya shkola, 1991.

[2] R. Mittra Computer Techniques For Electromagnetics. M.: Mir, 1977.

[3] A.M. Stadnik., G.V. Ermakov //Radiotechniques and electronics. 1995. V.40. №7. P. 1009.

MODEL PROBLEMS OF THE TIME-DOMAIN ELECTROMAGNETIC THEORY

Lyudmyla Velychko and Andrey Perov

Institute of Radiophysics and Electronics, Department of Mathematical Physics,
12 Acad. Proskura st., Kharkov, 61085, Ukraine; sirenko@ire.kharkov.ua

ABSTRACT

Some model direct problems of pulse sensing are considered. The suggested numerical algorithms based on the Finite-Difference Time-Domain (FDTD) schemes utilize the exact conditions on virtual boundaries for truncating the computational domain. The numerical results obtained confirm the efficiency of the proposed approach. All programs are completed with a vivid interface.

We present the algorithms and programs for solving model open-region plane problems in a time domain with a predictable accuracy. The algorithms are based on finite-difference schemes with the original exact conditions on virtual boundaries of the computational domain [1,2]. On this approach we, realizing the versatility inherent in finite-difference methods, increase their efficiency without adding the model distortions into the simulated physical processes.

The proposed algorithms are adaptable for a wide range of geometries of scattering objects, namely, arbitrary shaped plane gratings and waveguides with compact inhomogeneities; locally-inhomogeneous objects in a free space near an irregular boundary between two different media; cylindrical open resonators with perfectly conducting mirrors and arbitrary inclusions; and various plane radiating structures. There is no restrictions on the type and characteristics of sources and waves of excitation (concentrated sources, pulses of various shape and duration, etc.), hence the results in time domain are convertable if required into a frequency domain. Thus, it is a relatively simple matter to solve a lot of classical problems in the framework of the approaches developed.

All algorithms were tested by the computational experiments as exemplified in Fig. 1. Here the errors caused by the presence of virtual boundary in FDTD algorithm are shown for two simple perfectly conducting structures (Fig. 1,a,b). Fig.1,c–f present the local errors $D(n,m,l)$ calculated at grid points (n,m,l) on the imaginary boundary $\rho = 0.5$, $0 < \theta < \pi$ ($t = 0.6$ in Fig. 1,c,d and $t = 0.9$ in Fig. 1,e,f). The dashed lines correspond to the classical absorbing boundary conditions of the first approximation order [3], the full lines refer to the errors resulting from the incorporation of the exact conditions on a virtual boundary into FDTD scheme. Fig.1,g,h display the averaged error $D(l) = N^{-1}\sum D(n,m,l)$ on the lth time step within the limits of the whole grid (N is the number of grid nodes).

The programs are completed with the vivid interface; their operation can be demonstrated in the course of the presentation.

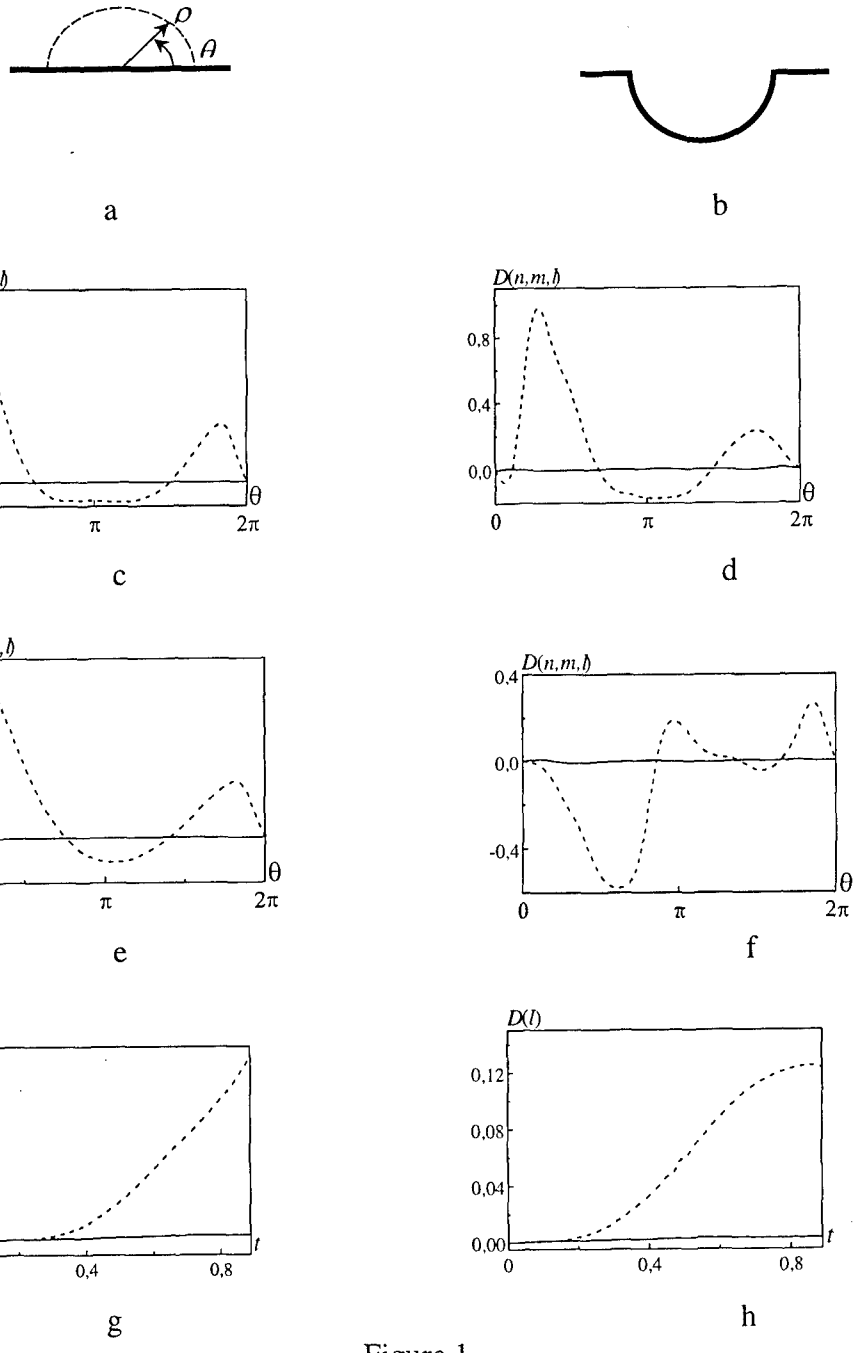

Figure 1.

REFERENCES

[1] A. O. Perov, Y. K. Sirenko, and N. P. Yashina, Explicit conditions for virtual boundaries in initial boundary value problems in the theory of wave scattering, JEWA. 13, No.10: 1343 (1999).

[2] L. G. Velychko, A. O. Perov, Y. K. Sirenko, and E. Yaldiz, Model problems of pulse sensing, Proc. EUROEM 2000, Edinburgh, Scotland (2000).

[3] B. B. Engquist and A. Majda, Absorbing boundary conditions for the numerical simulation of waves, Mathematics of Computation. 31, No.39: 629 (1977).

COMPARATIVE ANALYSIS OF APPROXIMATE AND EXACT SOLUTIONS OF TRANSIENT WAVE RADIATION PROBLEMS

Alexander N. Dumin, Victor A. Katrich, Sergey N. Pivnenko, and Oleg A. Tretyakov

Kharkov National University, Svobody Sq.4., Kharkov, 61077, Ukraine,
e-mail: Alexander.N.Dumin@univer.kharkov.ua

ABSTRACT

The problem of transient wave radiation from open end of coaxial waveguide is solved by means of Modal Basis Method in time domain. The analytical expressions of fields radiated into free space and reflected inside the waveguide are obtained for step-wise time dependence of amplitude of exciting TEM-wave. The solution for exciting TEM-wave with arbitrary time dependence of amplitude is obtained by calculation of Duhamel's integral. The exact solution of the problem is compared with the same one obtained in Kirchhoff approximation. The spatial and time dependencies of the field radiated from the coaxial aperture are obtained experimentally to examine theoretical results. The comparative analysis of the theoretical and experimental results is made.

INTRODUCTION

The essence of Modal Basis Method is the expansion of the transversal electromagnetic field components in the cross section plane. So the three-dimensional electromagnetic problem is converted into one-dimensional problem for the system of evolutionary equations. In the case of a radiation problem we can obtain two independent evolutionary equations of Klein-Gordon type describing propagation TE- and TM-waves in free space [1]. Using the separation of variables method one can get a general solution of these equations without employing Fourier transform.

The purpose of this work is the theoretical and experimental investigation of the transient wave diffraction on the open end of a coaxial waveguide and comparing the result with the same one obtained by Kirchhoff approximation.

THE STATEMENT OF THE PROBLEM

Let TEM-wave with step-wise time dependence propagates in the semi-infinite coaxial waveguide with inner radius b and outer radius a. Reaching the open end of the waveguide in $z = 0$ the wave will be partially reflected, radiated and converted into the other modes of the coaxial waveguide (see Figure 1).

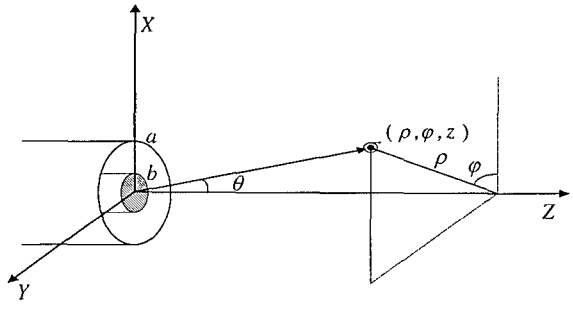

Fig.1. Problem geometry.

We represent the transient electromagnetic field in the waveguide as an infinite sum of modes [2]. The field in free space is presented in terms of the Modal Basis as well [1]. Using mode matching method and the general solution of Klein-Gordon equation [3] one can obtain analytical expressions for the radiated field and the field of reflected TEM-wave in the coaxial waveguide.

THE ANALYTICAL SOLUTION OF THE PROBLEM

It will readily be seen that the radiated field is the TM-wave with axial symmetry. According to [1], the field in free space can be written in the following form:

$$\vec{H}(\rho,\varphi,z,t)=\int_0^\infty d\xi\left[\vec{z}_0\times\nabla\phi^s(\rho,\varphi;\xi)\right]\varepsilon_0\frac{\partial}{\partial t}B(z,t;\xi);\qquad \vec{E}(\rho,\varphi,z,t)=-\int_0^\infty d\xi\nabla\phi^s(\rho,\varphi;\xi)\frac{\partial}{\partial z}B(z,t;\xi);$$

$E_z(\rho,\varphi,z,t)=-\int_0^\infty \xi^2 d\xi\phi^s(\rho,\varphi;\xi)B(z,t;\xi)$, where $\phi^s(\rho,\varphi;\xi)=J_0(\xi\rho)/\sqrt{\xi}$, $J_m(\cdot)$ – Bessel function of the first kind, $B(z,t;\xi)$ is the evolutionary coefficient, which has the form

$$B=-D\frac{\left[J_0(\xi a)-J_0(\xi b)\right]}{\xi^{3/2}}\left\{\left(\frac{ct-z}{ct+z}\right)^{1/2}J_1\left(\xi\sqrt{c^2t^2-z^2}\right)+2\sum_{m=1}^{\infty}\left(\frac{ct-z}{ct+z}\right)^{m+1/2}J_{2m+1}\left(\xi\sqrt{c^2t^2-z^2}\right)\right\},$$

in the case of our diffraction problem, where $D=c\mu_0\sqrt{2(a^2-b^2)/\ln(a/b)}$. The same radiation problem was solved in Kirchhoff approximation [4]. In this case the evolutionary coefficient is of the form

$$B(z,t;\xi)=-D\frac{\left[J_0(\xi a)-J_0(\xi b)\right]}{\xi^{3/2}}\left\{\sum_{m=0}^{\infty}\left(\frac{ct-z}{ct+z}\right)^{m+1/2}J_{2m+1}\left(\xi\sqrt{c^2t^2-z^2}\right)\right\}.$$

With the use of these expressions we can calculate numerically the amplitudes of all components of radiated field for an arbitrary time dependence of exciting TEM-wave by means of Duhamel's integral.

EXPERIMENTAL RESEARCH

The block schematic of the experimental setup is depicted in Figure 2. Generator of short pulses (GSP) forms a sequence of triangular pulses with the amplitude controlled in the range from 1 to 6 kV on the load 50 Ohm, with duration 1.2 ns and with the frequency of repetition up to 30 kHz. GSP feeds the coaxial cable with wave impedance 50 Ohm loaded to the coaxial cone antenna with the length 10 cm and the following aperture sizes: outer diameter- 67 mm, inner diameter- 2 mm.

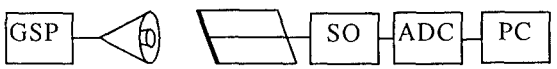

Fig. 2. Block schematic of the setup.

Radiated videopulse signal is received by special sensor – dipole-slotline probe. Stroboscopic oscilloscope (SO) C7-13 with the working range from 0 to 10 GHz is exploited in setup to observe and scale the pulses under study. Scanning signal of SO is digitized by ADC and transferred into computer for the processing.

The theoretical and experimental time dependencies of the transversal and longitudinal components of the electrical field are depicted in Figure 3. It is easy to see that at the angle $\theta=45^\circ$ ($z=6$ cm, $\rho=6$ cm) the exact solution is in the better agreement with experiment than the approximate one. The dependencies of the amplitudes of the electrical field components on ρ are illustrated in Figure 4. The differences between theoretical and experimental curves can be explained by the influence of the finite sizes of the dipole-slotline probe.

CONCLUSIONS

The transient TEM-wave diffraction problem is solved by Modal Basis Method for the first time. The exact solution and the approximate one obtained by Kirchhoff approximation are checked by performing the experiment in time domain. It is shown that theory is in good agreement with the experiment.

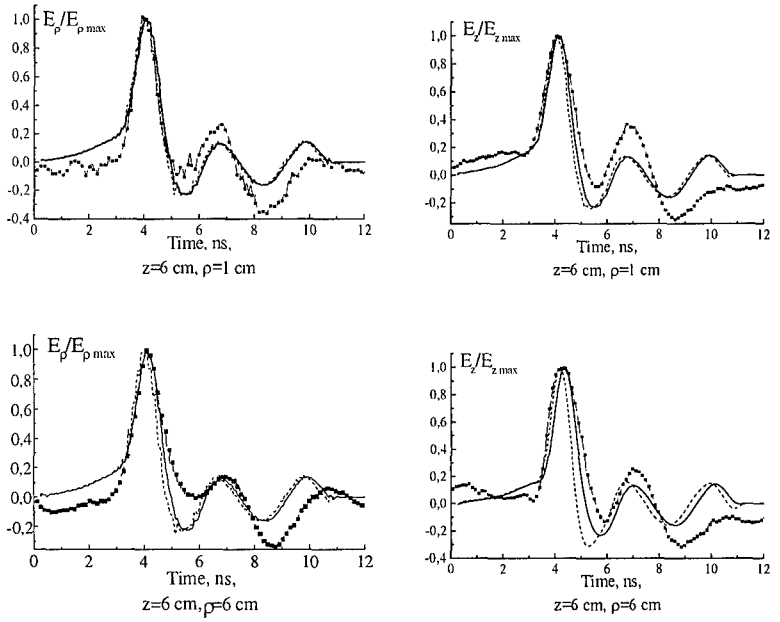

Fig.4. Theoretical (exact and approximate) and experimental time dependencies of the amplitudes of the electrical field components
(—— – exact solution, ····· – approximate solution, —•— – experiment).

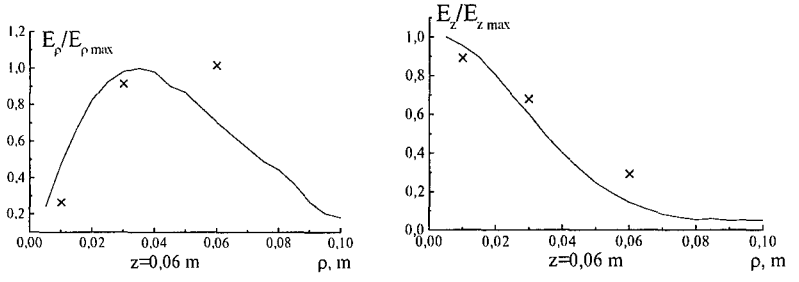

Fig.5. Theoretical — and experimental × dependencies of the amplitudes of the electrical field components on ρ.

REFERENCES

[1] A.N. Dumin, O.A. Tretyakov, "Radiation of Arbitrary Signals by Plane Disk", Conf. Proc. MMET'96, Lviv, Ukraine, pp. 248-251.

[2] O.A. Tretyakov. Essentials of Non-stationary and Nonlinear Electromagnetic Field Theory. Analytical and Numerical Methods in Electromagnetic Wave Theory. Edited by M. Hashimoto, M. Idemen, and O.A. Tretyakov, Tokio, Science House Co., Ltd, 1993, 572 p.

[3] S. Nikitskiy, O. Tretyakov, K. Yemelyanov, "An Arbitrary Signal Propagation in Waveguides", Conf. Proc. MMET'96, Lviv, Ukraine, pp.260-263.

[4] A.N. Dumin, O.A. Tretyakov, "Arbitrary Signal Radiation of Coaxial Waveguide Aperture", Conf. Proc. MMET'98, Kharkov, Ukraine, pp. 330-332.

ANALYSIS OF PLANAR STRUCTURES WITH ARBITRARY DISTRIBUTION OF PERMITTIVITY IN THE TIME-DOMAIN MODE

Konstantin N. Klimov, Boris V. Sestroretsky* and Sergey V. Soldatov**

Moscow State Institute of Electronics and Mathematics
Bolshoy Trechsvytitelsky lane 3/12, Moscow 109028, Russia, ph. (095) -916-88-17
E-mail: const@glasnet.ru

* Lavochkin Association
Leningradskay st. 24, Chimki-2 Moscow Area 141400, Russia, ph. (095) -575-50-69
E-mail: const@glasnet.ru

**Russian Research Center "Kurchatov Institute"
Nuclear Fusion Institute, Kurchatov sq. 1 ,Moscow 123182, Russia, ph. (095)-196-16-11
E-mail: vershkov@nfi.kiae.ru

ABSTRACT

The algorithm of the electromagnetic analysis in time-domain mode of planar structures with arbitrary distribution of permittivity ($\varepsilon > \varepsilon_0$, $\varepsilon < \varepsilon_0$, $\varepsilon = 0$, $\varepsilon < 0$) is stated. A 2-parametric algorithm and expressions for $R\tau$-elements of the equivalent circuit of volume of space are presented. The given expressions also allow to form a thin (1 layer of a grid) absorbing wall for a flat wave and eigen wave rectangular waveguide H_{m0}. The accuracy of the method is appreciated. The technique is implemented in the Rt-H Planar Analyzer program. The obtained characteristics of the program are described which allows to analyze the area 150x90 of wavelengths ($5.4 \cdot 10^6$ of nodes of a grid) on the computer Pentium-II (128 Mb, 433MHz) for 7.5 hours.

INTRODUCTION

Solving of such problems as research of biological objects and plasma requires analyzing the scattering of electromagnetic waves in structures, whose geometry allows to reduce the problem to a planar one. The geometrical size of area of the analysis makes about $100\lambda \times 100\lambda$ (λ-wavelength in free space). Inside the area, there is an arbitrary distribution of permittivity ε, and ε can be either $> \varepsilon_0$ or $< \varepsilon_0$, including the investigated area with the sites $\varepsilon = 0$ and $\varepsilon < 0$. The geometry contains the following types of boundary conditions: metal, magnetic wall, absorber. Usually system is excited by using a system of waveguide horns. In this paper, we shall consider the approach allowing to solve the task of wave scattering in the given area for H polarization.

CONSIDERATION

We used an impedance analogue of electromagnetic space [1] - [3]. To analyse the system we shall decompose it to elementary cells having the sizes Δx, Δy, Δz, and find equivalent circuits with lumped parameters (Fig. 1a) or with distributed parameters (Fig. 1b,c) to the

obtained elementary cells [2]. The set of the equivalent circuits describing elementary volumes, represents an equivalent circuit (Fig. 1d) analysed system - its impedance model.
Then, we locate an arbitrary node in the constructed $R\tau$-grid. The given node is connected to four next nodes by pieces of long lines with wave admittance Y_1, Y_2, Y_3, Y_4. The delay time of signal distribution in lines is $\tau_0 = \Delta\sqrt{\varepsilon_0\mu_0}/\sqrt{2}$. For free space, $Y_1 = Y_2 = Y_3 = Y_4 = Y_0 = \sqrt{\varepsilon_0/\mu_0}\cdot\Delta/\Delta z/\sqrt{2}$ [4]. Admittance Y describes the generalized losses in the node. At the presence of a non-uniform dielectric filling with $\varepsilon > \varepsilon_0$, superfluous value of capacity in the node is simulated by an open stub (Fig. 1b). For modeling a filling with $\varepsilon < \varepsilon_0$, including $\varepsilon = 0$ and $\varepsilon < 0$, a short stub was used (Fig. 1c), that was equivalent to the inductance, which reduces the capacity of an element of space. A stub, that was used for modeling the dielectric filling has a wave admittance Y_5 and length appropriate to the delay time $\tau_0/2$.

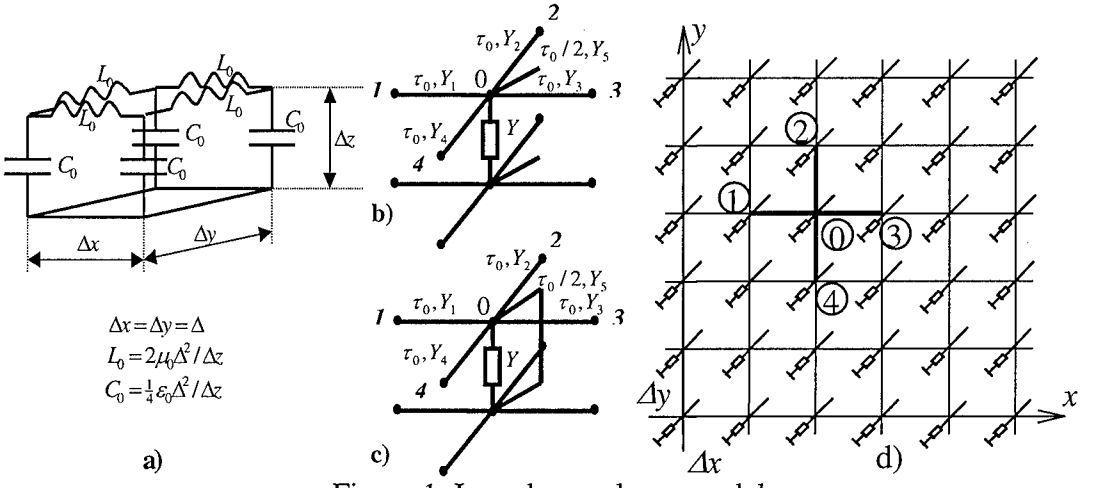

Figure 1. Impedance planar model

For the given circuit, similarly [2], we obtain expression that allows to organize iterative procedure of calculation of value of a voltage in each node U^τ in current a time step τ, if the values of voltage in two previous time steps $\tau-1$ and $\tau-2$ are known.

$$U^\tau = \frac{2(Y_1U_1^{\tau-1} + Y_2U_2^{\tau-1} + Y_3U_3^{\tau-1} + Y_4U_4^{\tau-1} \pm Y_5U_5^{\tau-1} + YU^{\tau-2})}{Y_1 + Y_2 + Y_3 + Y_4 + Y_5 + Y} - U^{\tau-2} \qquad (1)$$

The expression (1) allows to analyze domains with $\varepsilon > \varepsilon_0$ (sign '+' for Y_5) and with $\varepsilon < \varepsilon_0$, including $\varepsilon \le 0$ (sign '-' for Y_5).
For excitation and matching of system waveguides or flat waves we derived expressions determining the phase speeds of the eigen waves in the given planar $R\tau$-grid and corresponding wave admittance [4]. For the eigen waves of the rectangular waveguide H_{m0}, the phase difference of one node is $\alpha_m = 2\pi(\Delta/\lambda_m)$, where λ_m is the wavelength in grid, and is defined by the expression

$$\alpha_m = \arccos\left(2\cos\omega\tau_0 - \cos\pi m/N\right) \qquad (2)$$

where N is the number of node in cross section waveguide.

For a flat wave extending in infinity grid structure, $m = 0$, and, hence, the phase difference on one spatial interval will be equaled, as it follows from the previous equations.

$$\alpha = \arccos(2\cos\omega\tau_0 - 1) \tag{3}$$

The value determining the characteristic admittance Y_{0k} of grids for waves H_{m0} and a flat wave was obtained [4].

$$Y_{0k} / Y_0 = \sin\alpha_m / \sin\omega\tau_0 \tag{4}$$

The expression (4) is similar to the optics Snellius law and represents a condition of the matching of eigen waves at the left and to the right of border. Since Y_0 is the admittance of line of grid and α_m is the phases difference for the eigen waves to the left of border $i = 0$, Y_{0k} is the admittance of line and $\omega\tau_0$ is the phases difference for one time step in a line to the right of border $i = 0$. The received expressions (2) - (4) allow to calculate the excitation and matching of elements of a matrix of scattering [4].

The expression (2) allows to estimate a phase error and shows the difference between the wavelength of a flat wave of a grid λ' and the exact value wavelength λ at a different step of a grid Δ.

$$\lambda' / \lambda = \arccos(2 \cdot \cos(\omega\tau_0) - 1) / (\sqrt{2} \cdot \omega\tau_0) \tag{5}$$

where $\omega\tau_0 = \pi\Delta / (\sqrt{2}\lambda)$.

CONCLUSION

In the present paper, the theory of the electromagnetic analysis in time-domain mode is considered on the basis of the planar device $R\tau$ of grid structures with arbitrary dielectric filling. The suggested algorithm allows to analyze domains with $\varepsilon > \varepsilon_0$ and $\varepsilon < \varepsilon_0$, including $\varepsilon = 0$ and $\varepsilon < 0$.

REFERENCES

[1] B.V. Sestroretsky. RLC and Rτ analogues of ED space. Proceeding of MIREA "CAD of microwave devices and systems", MIREA, 1977, pp. 127-158.

[2] B.V. Sestroretsky, E.S. Kuharkin. "Dialogue optimization of devices topology in electrodynamic CAD". Moscow, MPEI, 1987.

[3] B.V. Sestroretsky. Balance RLC and Rτ-circuits of elementary volume. Problems of radio electronics, ser. "General problems of radio electronics", 1983, vol.5, pp56-85.

[4] B.V. Sestroretsky, A.S. Petrov, A.S. Ivanov, K.N. Klimov, S.A. Korolev, S.V. Fastovich. The analysis of electromagnetic processes on a basis *RLC* and $R\tau$ of grids. Moscow, MSIEM, 2000.

FLUCTUATION CHANNELING AND TIME DELAY OF A PULSE SIGNAL IN A RANDOMLY STRATIFIED MEDIUM

V. D. Freilikher
Department of Physics, Bar-Ilan University, Ramat-Gan, 52900 Israel
E-mail: freiliv@mail.biu.ac.il

Y. V. Tarasov
Institute of Radiophysics and Electronics, National Academy of Sciences of Ukraine,
12 Acad. Proskura St., Kharkov 61085, Ukraine
E-mail: yutarasov@ire.kharkov.ua

The method of resonance expansion of one-dimensional fields is extended to the case of point-source-radiated narrow-band signals propagating in randomly layered low-dissipative media. Pulse ducting within a fluctuation waveguide and unification of the intensity spectrum far away from the source are predicted. It is an interference (Anderson) localization of multiply scattered constituent plane harmonics that causes the appearance of the low-decaying pulse tail in a 1D disordered system. The same phenomenon is responsible for the strong time delay of the pulse as long as the receiver is slightly shifted transverse to the strata vs the source position.

One-dimensional (1D) random systems hold a particular place in a theory of wave and particle propagation in randomly inhomogeneous media. In such systems the effect of Anderson localization is exclusively pronounced. All eigenstates are localized in infinite 1D random systems, whatever strength of disorder, and the transmittance of a finite 1D system falls exponentially when the system length exceeds the so called localization length.

In the wave theory, it is exactly fluctuational channeling of the finite-source radiation in a medium with one-dimensional fluctuations of the refractive index (i.e. in a randomly stratified medium [1]) that serves as a manifestation of Anderson localization. In Ref. [2], it was shown, using the method of resonance expansion of fields, that monochromatic radiation of a point source should be "locked" in the finite thickness parallel to the strata, even though nonuniformity is rather weak. Formation of such a "waveguide" (called the fluctuation waveguide) without a regular refraction in the medium is caused by the interference of plane harmonics comprising the bulk signal on their multiple backscattering at medium inhomogeneities.

Interferential localization is known to appear in the case of elastic scattering only. As regards the classical waves, it was previously predicted for monochromatic point-source signals [2]. In this paper, the problem is solved with regard to the propagation of *non-stationary* narrow-band signals. In this case correlation of harmonics of different genuine frequencies is of decisive importance and should be properly taken into account. We start from the wave equation for the electromagnetic field $G(\mathbf{R},\mathbf{R}_0\,|\,t)$ (scalar for simplicity) radiated by a point source located at a point $\mathbf{R}_0$ of 3D medium which is stratified along z-axis,

$$\left[\Delta-\frac{1}{c^2}\frac{\partial}{\partial t}\left(\varepsilon(z)\frac{\partial}{\partial t}+4\pi\sigma\right)\right]G(\mathbf{R},\mathbf{R}_0\,|\,t)=4\pi\delta(\mathbf{R}-\mathbf{R}_0)A(t)\mathrm{e}^{-i\omega_0 t}. \qquad (1)$$

Here Δ is Laplacian, $\varepsilon(z)=\varepsilon_0+\delta\varepsilon(z)$ is the random dielectric permeability with the mean value ε_0, σ is the conductivity of the medium, $A(t)$ is the envelope of a wave packet (pulse signal) with the carrier frequency ω_0. The problem of finding the "bulk" average intensity

$< I >=< |G|^2 >$ in a randomly layered medium can be easily reduced to calculating the binary correlation function of *one-dimensional* stochastic fields $\Gamma(z, z_0 \mid q^2, \omega)$ obeying equation (1) being Fourier-transformed over in-plane coordinates and time, but corresponding to different values of the "transverse energy" q^2 and the genuine frequency ω. The key point of the calculation technique is application of so-called resonance expansion of the field Γ, which is valid for the case of weak scattering (WS) when all extinction lengths are large compared to the carrier wavelength and the correlation radius r_c of medium inhomogeneities,

$$\Gamma(z, z_0 \mid q^2, \omega) = \Gamma_1(z, z_0)e^{iq(z-z_0)} + \Gamma_2(z, z_0)e^{-iq(z-z_0)} + \Gamma_3(z, z_0)e^{iq(z+z_0)} + \Gamma_4(z, z_0)e^{-iq(z+z_0)}. \qquad (2)$$

The WS conditions imply that the "amplitude" functions $\Gamma_i(z, z_0)$ in Eq. (2) are smooth as compared to the corresponding "fast" exponentials. By this is meant that at weak inhomogeneity of the medium not all spatial harmonics of permeability $\delta\varepsilon(z)$ are of decisive importance for wave scattering but only *resonant* harmonics whose momenta are close to zero (they are responsible for the forward scattering) and $\pm 2q$ (backward scattering).

By averaging of the exact equation for $\Gamma(z, z_0 \mid q^2, \omega)$ over a mesoscopic space interval, for the matrix of smooth amplitudes in Eq. 2 a set of coupled stochastic first-order differential equations follows. It can be solved in a functional form for arbitrary random $\delta\varepsilon(z)$, the appropriate calculation procedure is described in detail in Ref. [3]. The main advantage of the method is that it enables the field $\Gamma(z, z_0 \mid q^2, \omega)$, which is a solution of a boundary-value problem, to be expressed in terms of a set of solutions of some auxiliary Cauchy problems with initial conditions given at either of two ends of the interval $-\infty < z < \infty$. This makes it possible to accurately perform statistical averaging over the random $\delta\varepsilon(z)$ to arbitrary order of the scattering theory, thus allowing for the interference of multiply scattered waves, which results in Anderson localization in 1D systems.

Using the developed technique, in the present work it is shown that regardless of the radiated pulse spectral content the space-time dependence of the average intensity in the wave zone of the fluctuation waveguide is described by the universal function

$$\left\langle I(\mathbf{R}, \mathbf{R}_0 \mid t) \right\rangle \propto \frac{1}{t^2}\left[1 - \left(\frac{\rho}{ct}\right)^2\right]^{-3/2} \int_0^\infty d\mu\, W(\mu)\nu^2(\mu) \exp\left\{-\frac{\nu(\mu) \mid z - z_0 \mid}{L_m[1 - (\rho/ct)^2]}\right\}, \qquad (3)$$

where ρ is the in-plane distance between the source and the receiver, $L_m \approx c^2 / \omega_0^2 r_c$ is the *localization length* of the field harmonics which is most "energetic" in z-direction. In Eq. (3), the functions $W(\mu)$ and $\nu(\mu)$ are

$$W(\mu) = \frac{\pi^2}{2} \frac{\mu \sinh(\pi\mu/2)}{\cosh^3(\pi\mu/2)}, \qquad \nu(\mu) = \frac{1+\mu^2}{4}.$$

From Eq. (3), it can be readily seen that pulse radiation of the point source, similar to monochromatic radiation, is ducted parallel to the medium strata within the layer of $\sim L_m$ thick, i.e. within the fluctuation waveguide which is generated due to the Anderson localization of *all* plane harmonics of the pulse signal. Unification of the pulse spectral content in the wave zone is due to narrowity of band and high selectivity of a 1D random system as regards the constituent spatial harmonics. In Fig. 1, the pulse sweep at a given point (ρ, z) is shown for different values of the parameter $\varsigma = | z - z_0 | / L_m$ that characterizes the receiver displacement

from the symmetry plane of the fluctuation waveguide. Considerable temporal extent of the received pulse is due to the fact that at a given moment t the local intensity of the field is determined by those plane harmonics that have reached a given point z after being multiply re-scattered by irregularities of the medium. In a randomly stratified medium these are proven to be the harmonics whose "transverse" energies (i.e. squared wave number z-components) are close to $q_s^2 = (\omega_0 / c)^2 [1 - (\rho / ct)^2]$. The time dependence of "effective" harmonics that make up a signal at a given space point accounts for such an interesting phenomenon as the Wigner-Smith time delay of the signal. In Fig. 2, the moment t_m (in units ρ / c) of the pulse burst arrival at the reception point is shown for the case of $\rho >> L_m$. This delay of the pulse relative to its *expected* arrival cannot be attributed to lengthening of the signal run in the waveguide. In the present work, the delay is interpreted as being caused by multiple re-scattering (entanglement) of the signal in a disordered medium [4,5].

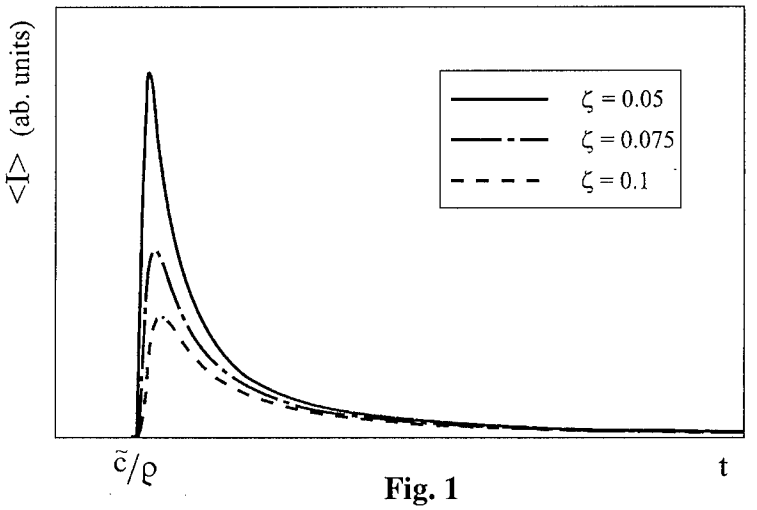

Fig. 1

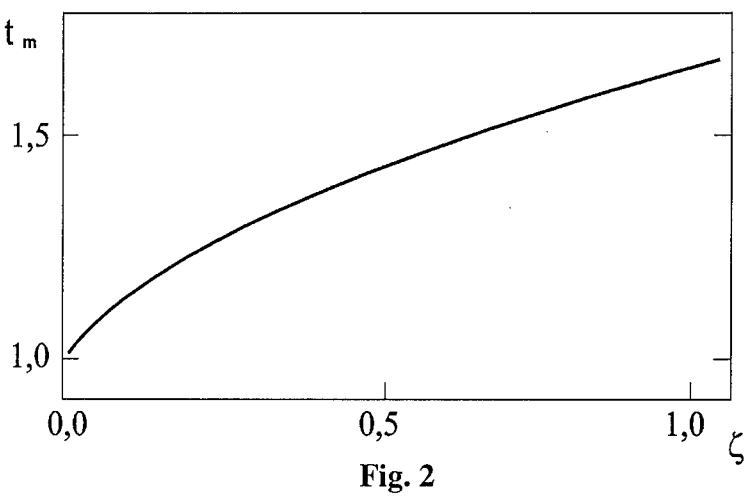

Fig. 2

It should be noted that the solution to the point-source problem in a layered medium, unlike the case of purely one-dimensional source (the infinite radiative plane), enables one to make reliable conclusions about localization effects in *individual realizations* of the refractive index despite the fact that intensity, as well as a delay time, is known to be not a self-averaging quantity. It is exactly the integration over the point-source spatial harmonics that serves as an additional averaging factor in the problem. It is natural to expect the additional averaging to "wash out" large fluctuations of the intensity, which are typical for individual plane harmonics propagating in a medium disordered in one dimension.

References:

[1] Freilikher V D and Gredeskul S A 1990 J. Opt. Soc. Am. A **5** 868–874
[2] Freilikher V D and Tarasov Yu V 1991 IEEE Trans. on AP **39** 197–203
[3] Kaner E A and Tarasov Yu V 1988 Phys. Rep. **165** 189–274
[4] Wigner E P 1955 Phys. Rev. **98** 145–147
[5] Smith F T 1960 Phys. Rev. **118** 349–356

ADIABATIC INVARIANTS FOR ELECTROMAGNETIC WAVES GUIDED BY TIME-VARYING PLASMA STRUCTURES

Michael I. Bakunov*, Vladimir B. Gildenburg**, Nina A. Zharova** and Sergey N. Zhukov*

*Department of Radiophysics, University of Nizhny Novgorod,
Nizhny Novgorod 603600, Russia
E-mail: bakunov@rf.unn.runnet.ru

**Institute of Applied Physics, Russian Academy of Sciences,
Nizhny Novgorod 603600, Russia
E-mail: gil@appl.sci-nnov.ru

ABSTRACT

Propagation of an electromagnetic wave along a planar waveguiding structure containing gaseous/solid-state plasma slabs with time-varying free carrier density is considered in the case when the time-scale of density variations is much greater than the wave period. Both ionization and deionization (recombination, attachment) processes are included. General relations describing frequency shifting and energy losses of a guided wave are derived for arbitrary open/closed waveguiding structure. Adiabatic invariants, i.e. combinations of wave energy and frequency conserving in the course of temporal variations of the waveguiding medium, are found. Detailed analyses are given for surface waves guided by the boundary of a time-varying plasma half-space and a plasma slab.

INTRODUCTION

Frequency upshifting of electromagnetic radiation via rapid plasma creation has drawn considerable attention in recent years due to its potential applications to the generation of tunable microwave radiation over a broad frequency range. However, frequency shifting of bulk radiation was examined only. Recently, frequency upshifting of surface electromagnetic waves guided by the boundary of a plasma half-space [1] and a plasma slab [2] via instantaneous growth of the plasma density in time was considered. In the present paper we extend this work and present results of the theoretical study of the propagation of an electromagnetic wave along an arbitrary open/closed waveguiding structure that contains gaseous/solid-state plasma slabs with time-varying free carrier density in the case when the time scale of the density variation is much greater than the wave period (adiabatic approximation).

FORMULATION OF THE PROBLEM AND GENERAL RELATIONS

We consider a planar waveguiding structure layered in y-direction. The structure contains one or several gaseous/solid-state plasma slabs with time-varying plasma density N(y,t). In general, the structure may also contain dielectric slabs and can be placed both in free-space and on a perfectly conducting (metal) substrate (open waveguide) or between two parallel metal planes (closed waveguide). We assume that at time $t = 0$ the electromagnetic field in the structure is a traveling eigenmode with longitudinal wave number h_0 and transverse dependence which is determined by the structure. In the absence of processes of ionization and de-

ionization ($\partial N/\partial t = 0$) and collision losses (electron collision frequency $\nu = 0$) the wave is monochromatic with eigenfrequency ω_0. If parameters of nonmonochromaticity are small, i.e.

$$\nu << \omega, \qquad \frac{1}{N_c}\left|\frac{\partial N(y,t)}{\partial t}\right| << \omega, \tag{1}$$

where $N_c = m\omega^2/4\pi e^2$, the guided wave mode at $t > 0$ can be written in the quasi-monochromatic form with electric and magnetic fields $\vec{E}$, $\vec{B}$ given by the real parts of complex fields $\hat{\vec{E}}$, $\hat{\vec{B}}$

$$\begin{Bmatrix}\hat{\vec{E}}\\ \hat{\vec{B}}\end{Bmatrix} = \begin{Bmatrix}\vec{E}(y,t)\\ \vec{B}(y,t)\end{Bmatrix}\exp\left[i\varphi(t) - ih_0 x\right] \tag{2}$$

with slow time-varying real frequency $\omega(t) = d\varphi/dt$ and complex amplitudes $\vec{E}$, $\vec{B}$. The longitudinal wave number h_0 is fixed due to the spatial homogeneity of the waveguide in the x-direction. The amplitude and frequency of the mode (2) can change significantly after a considerable length of time (much longer than ω^{-1}). Under condition (1) transformation of this mode into other guided modes and outgoing radiation (for open waveguides) is negligible. Time evolution of the mode can be found within the adiabatic approximation suggested in [3]. According to this approach the solution procedure is separated into two stages.

The first stage of the procedure implies the solution of an eigenvalue problem on the basis of the stationary wave equation for monochromatic field

$$\vec{\nabla}\times\vec{\nabla}\times\hat{\vec{E}} - (\omega/c)^2\varepsilon\hat{\vec{E}} = 0, \tag{3}$$

with real permittivity $\varepsilon(y,t)$, and usual boundary conditions at the dielectric interfaces and metal surfaces; for open waveguiding structure, we also use the condition of vanishing fields at the infinity ($|y| \to \infty$). The permittivity of the ionized layers is taken in the form $\varepsilon = \varepsilon_b(1-\omega_p^2/\omega^2)$ where $\omega_p = \sqrt{4\pi e^2 N/m\varepsilon_b}$ is the plasma frequency and ε_b is the background dielectric constant of the solid-state plasma ($\varepsilon_b = 1$ for gaseous plasma). By solving Eq. (3) for each time moment, we obtain the eigenfunction $\vec{E}(y,t)$ and the dispersion equation

$$D(\omega, h_0) = 0, \tag{4}$$

that determines the real eigenfrequency $\omega(t)$. Undefined time-dependent normalization factor in the $\vec{E}(y,t)$ should be found by solving the equation for the energy of the wave.

The complex amplitudes $\vec{E}(y,t)$ and $\vec{B}(y,t)$ and frequency $\omega(t)$ defined from the above formulated eigenvalue problem satisfy the following general integral relations:

$$\int_\Omega \varepsilon\left|\vec{E}\right|^2 dy = \int_\Omega \left|\vec{B}\right|^2 dy\ , \tag{5}$$

$$\frac{d\omega^2}{dt}\int_\Omega \varepsilon_b\left|\vec{E}\right|^2 dy = \int_\Omega \frac{\partial\omega_p^2}{\partial t}\varepsilon_b\left|\vec{E}\right|^2 dy\,. \tag{6}$$

Here Ω is the region of the y-axis where electromagnetic fields exist (i.e., region between metal walls in a closed waveguide or the (semi-)infinite interval in an open structure).

As the second stage of the solution procedure, we derive the energy evolution equation which is valid for arbitrary waveguiding structure filled with a time-varying plasma. Our analysis is based on the Poynting's theorem in the following form,

$$\frac{\partial}{\partial t}\frac{\varepsilon_b\vec{E}^2 + \vec{B}^2}{8\pi} + \frac{c}{4\pi}\vec{\nabla}\cdot(\vec{E}\times\vec{B}) = -\left(\vec{J}\cdot\vec{E}\right) \tag{7}$$

and the equation for the current density $\vec{J}$ of free electrons in a time-varying plasma [4,5]

$$\frac{\partial \vec{J}}{\partial t} = \frac{e^2 N}{m}\vec{E} - (\nu + \mu_d)\vec{J} \tag{8}$$

where μ_d is the rate of deionization ($\mu_d << \omega$). We will use the constitutive relation (8) for the investigation of two practically interesting situations: when the plasma density grows in time due to ionization ($\mu_d = 0$) and in the opposite case of plasma decay ($\mu_d = -\partial(\ln N)/\partial t$). In general, Eq. (8) is valid even when processes of ionization and deionization go simultaneously but only if μ_d is independent on time [6]. The later condition is realized when attachment prevails over recombination, otherwise Eq. (8) can be used as an approximation. By substituting $\vec{E}$ from Eq. (8) into the right-hand side of Eq. (7), averaging the latter on the wave period $2\pi/\omega$ and integrating it over y, we derive the desired equation

$$\frac{dW}{dt} = -Q, \tag{9}$$

$$W = \int_\Omega \frac{\varepsilon_b |\vec{E}|^2}{8\pi} dy, \qquad Q = \frac{1}{16\pi\omega^2}\int_\Omega \varepsilon_b |\vec{E}|^2 \left[\frac{\partial \omega_p^2}{\partial t} + 2(\nu + \mu_d)\omega_p^2\right] dy. \tag{10}$$

The expression in square brackets in Eq. (10) can be rewritten as $\gamma \partial \omega_p^2 / \partial t$ with $\gamma = 1 + 2(\nu + \mu_d)/\mu$, $\mu = \partial \ln N / \partial t$. If γ is independent on y, Eq. (9) can be reduced to

$$\frac{dW}{dt} = -\gamma \frac{W}{\omega}\frac{d\omega}{dt}. \tag{11}$$

If γ is independent on time we can integrate Eq. (11) and obtain the relation between the energy of the wave and its frequency (adiabatic invariant):

$$W\omega^\gamma = \text{const}. \tag{12}$$

The assumption of constant γ is satisfied in the most important in-practice situations. The first situation is when ionization dominates ($\mu > 0$, $\mu >> \nu$, $\mu >> \mu_d$) and $\gamma = 1$. Then Eq. (12) reduces to

$$W\omega = \text{const} \tag{13}$$

which is valid for an arbitrary dependence of $\mu(t)$. The second situation is when the plasma decays exponentially: $N(t) = N_0 \exp(-\mu_d t)$, $\mu_d = \text{const}$, $\mu = -\mu_d$. This situation occurs when attachment prevails over recombination. In this case $\gamma = -(1 + 2\nu/\mu_d)$ and Eq. (12) reduces to

$$W / \omega^{(1+2\nu/\mu_d)} = \text{const}. \tag{14}$$

Moreover, if elastic collisions are negligible ($\nu << \mu_d$) we arrive at a simpler formula

$$W/\omega = \text{const} \tag{15}$$

which is valid for an arbitrary dependence of $\mu_d(t)$.

The invariants (13)-(15) are valid not only for planar waveguides but for waveguides of arbitrary cross-section as well.

This work was supported by the Russian Foundation of Basic Research, Grant 00-02-17490.

REFERENCES

[1] M. I. Bakunov and S. N. Zhukov, Plasma Phys. Rep. **22**, 649 (1996).
[2] M. I. Bakunov, A. V. Maslov, and S. N. Zhukov, J. Opt. Soc. Am. **B 16**, 1942 (1999).
[3] B. Gildenburg, A. G. Litvak and N. A. Zharova, Phys. Rev. Lett. **78**, 2968 (1997).
[4] P. Kuo, A. Ren and G. Schmidt, Phys. Rev. E **49**, 3310 (1994).
[5] V. B. Gildenburg, A. V. Kim, V. A. Krupnov, V. E. Semenov, A. M. Sergeev and N. A. Zharova, IEEE Trans. Plasma Sci. **21**, (1993).
[6] N. S. Stepanov, Sov.Radiophys. and Quantum Electron. **19**, 683 (1976).

Time-Domain System Identification Modeling for Microwave Structures

V. Chtchekatourov, L. Vietzorreck, W. Fisch, P. Russer
Institut fuer Hochfrequenztechnik, Technische Universitaet Muenchen
Arcisstrasse 21, D-80333 Muenchen, e-mail: chtcheka@hft.ei.tum.de

Abstract — *Some system identification (SI) and spectral analysis (SA) methods for computing the* **S***-parameters and the admittance Foster-represented matrix (AFM) to generate the lumped element equivalent circuits for linear reciprocal distributed microwave circuits are analyzed. The methods, based on the parameter models, use measured or simulated data obtained by the Transmission Line Matrix method (TLM). Applying the time-domain SI and SA modeling allows us to find poles and residues system locations which satisfy AFM restrictions of the equivalent circuits technical feasibility. Furthermore the real-time modeling can avoid long calculation time of TLM. The behavior of a microelectromechanical (MEMS) capacitive switch, for which the calculation time usually is extremely long, was investigated by using these methods. The advantage of the applied approaches are made obvious in a dramatic reduction of computation time.*

1 INTRODUCTION

The model-based parameter estimation methods to compute the S-parameters and to generate the lumped element equivalent circuits for linear reciprocal distributed microwave circuits were developed and investigated recently [1, 2]. In our paper we present some extended approaches to calculate directly the S-parameter from the truncated time-domain TLM-calculated signals. Furthermore we can create the equivalent models of microwave structures by finding the AFM [3]:

$$\mathbf{Y}(p) = \mathbf{A}^{(0)} + \sum_{n=1}^{N} \left\{ \frac{A_0^{(n)}}{p - \alpha_n} + \frac{A_0^{(n)^*}}{p - \alpha_n^*} \right\} \mathbf{A}^{(n)} + \mathbf{A}^{(\infty)} p \tag{1}$$

where $\mathbf{A}^{(n)}$ are real, symmetric and positive semi-definite matrices, $A_0^{(n)}$ - complex constants and α_n denote stable poles with $\Re\{\alpha_n\} < 0$, N is the system order. The advantages and disadvantages of parameter estimation methods used to generate the model from the field theoretical analysis data, simulated with TLM, are shown. The 3-D full wave time-domain TLM simulation can yield to high computation efforts for some real multi-port structures. So if input-output sequences are longtime, then parameters of the equivalent model (1) and their updates can be built in real time of TLM simulation. The validation of the created model and estimation of the model errors in real-time allow to generate a "stop signal" for the full-wave analysis procedure and so decrease the total time of TLM calculation. A coplanar capacitive MEMS shunt switch [4], which can be used for antenna and phased array applications for communication system, automotive radar and other applications, is analyzed with TLM and model-based parameter estimation approaches. The purely TLM analysis of the MEMS in different switching states is time consuming because of the longtime oscillating behavior of the signal in time domain. The use of the above mentioned methods reduces the needed calculation time and therefore makes the numerical analysis much more efficient and suitable for optimization procedures. A very good consistency of simulated data, obtained by TLM and by using parameter estimation techniques, as well as measurement results are shown for different switching states.

2 HIGH RESOLUTION SA AND SI METHODS FOR AFM CONSTRUCTION

SI approaches, which analyze an excitation pulse and corresponding system responses simultaneously, or SA methods for separate analyze can be used to find the AFM parameters. Table 1 describes some possibilities for the AFM construction. The ARMA, AR, MA, non-parametrical (e.g. matrix-shifting) and Prony approaches seem to be the most obvious way to find the parameters α_n and $\mathbf{A}^{(n)}$ [5]. According to the singularity expansion method by Baum [1] one can express the electromagnetic response of physical structures in an expansion of complex resonances. Furthermore the transient part of the response can be separated from the driven one by considering the late-time term of system output signals. That allows us to construct

AFM by applying SA methods for truncated signals as it is shown in Fig.1. If the input signal band width is not sufficiently high to overlap the natural spectrum of the system or if the investigated system has fast decaying components, the transient time-separation will be impossible and SI methods should be applied.

Table 1

Input conditions	α_n determination	A(n) determination
No input information; assumed input is a white noise	**1.** ARMA, AR, MA - based parametrical and non- parametrical methods for system output; ARMA-MA-AR transformation	Integral residue estimation
No input information; Assumed input is a $\delta(t)$	**2.** Prony method for the system output	Prony residue estimation
Modeled wide-band input	**3a.** ARMA, AR, MA, Prony methods for system input and output for the purpose of signal prolongation; Laplace transformation and direct poles extraction of prolongated signals	Residue extraction from the Laplace transformation
	3b. ARMA, AR, MA, Prony methods for system input and output Model relations; ARMA-MA-AR transformation	Integral residue estimation
	3c. Finding impulse responses via deconvolution; Prony method for the impulse responses	Prony residue estimation
	3d. Prony methods for the system truncated output; Input modeling; Available transformation	Prony residue estimation and transformations
	3e. SI methods	Integral residue estimation

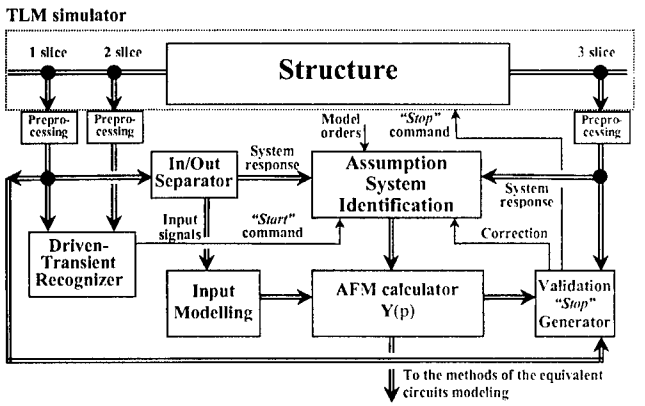

Figure 1: Applying high resolution spectra analysis methods for the real-time AFM construction.

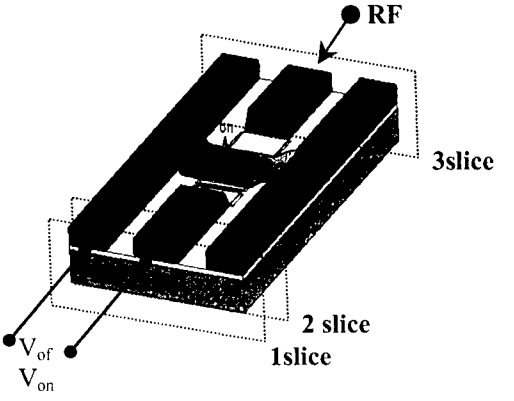

Figure 2: Micromechanical capacitive switch.

3 MEMS STUDY WITH TLM AND TIME-DOMAIN MODELLING

The capacitive switch [4] under study (Fig. 2.) consists of a thin metallic membrane connected to the ground of a CPW-line which - when actuated by a DC voltage - forms a virtual short with the center conductor of the CPW. The TLM model of the structure exhibits $268 \times 88 \times 90$ nodes. A time discretization interval of $2.058^{-15}s$ was chosen for the TLM simulation. For signal processing of the TLM simulation results the sampling interval has been increased by up to two orders of magnitude. The data were preprocessed by trend removal and SVD-based noise suppressing methods when it was necessary. The truncated signals were determined by comparison system responses at different slices. From the big set of the SA and SI methods OE common-denominator method (SI), parametrical least square AR-based (LS-AR) method, parametrical least square (LS-Prony) and non-parametrical matrix-shifting Prony (Pencil-of-Function, PoF-Prony) methods were chosen [5, 6]. Two different criteria - a threshold of the validation error and unchanging of the found AFM parameters can be used to estimate the quality of the created model and to generate a "stop signal" for the TLM simulator. All found poles should be inside of the unit circle on z-domain to avoid instability, otherwise the frequency factorization is used [5]. The validation errors for different sample numbers, used for the AFM calculation, and for different number of AFM parameters are depicted in Fig. 3. The 10000-samples validation window was used to check the created model. The validation errors for all the methods do not change significantly if the number of poles exceeds some value, which so can be calculated and optimized. PoF-Prony approach gave us the smallest order threshold which e.g. is less than 20 for 20000 used samples. For LS-AR, LS-Prony methods it is about 30 and for SI approach it

is more. The sample threshold for Prony approaches is less than for methods with usual residue position estimation. Found with LS-Prony, LS-AR and SI poles position more regular distribute around the unit circuit in z-domain and for small model order they do not overlap the most significant signal components, which in our case are low frequency. Matrix-shifting based PoF-Prony method puts poles in order and in the case yields to less calculation efforts to find the correct low frequency pole set. It is especially important when it is known that the physical device can produce natural frequencies up to some frequency limit. Also equivalent circuits modeling needs the pole positions of AFM placed in the low frequency range of interest. For big model order the positions of most significant signal components found with the methods overlap each other. So the system order can be chosen more than is in fact and only the poles which place in the space of interest are used for the estimation of suitable residue. Note, that SI method describes also the transient part of the system response and so need more filter order and samples in our case. Applying low order sequential SI algorithm or matrix-shifting SI technique can be suggested, if the input signal band width is not sufficiently high or if the system components decay so fast that transient part separation is not possible [7]. Otherwise the matrix-shifting Prony methods for truncated signals are proposed for the AFM construction. The "stop signal" generation and the reduction of the total calculation TLM time for AFM construction strongly depends on the investigated structures. E.g. by applying the PoF-Prony method for the used MEMS structures the total time was reduced by about factor 10.

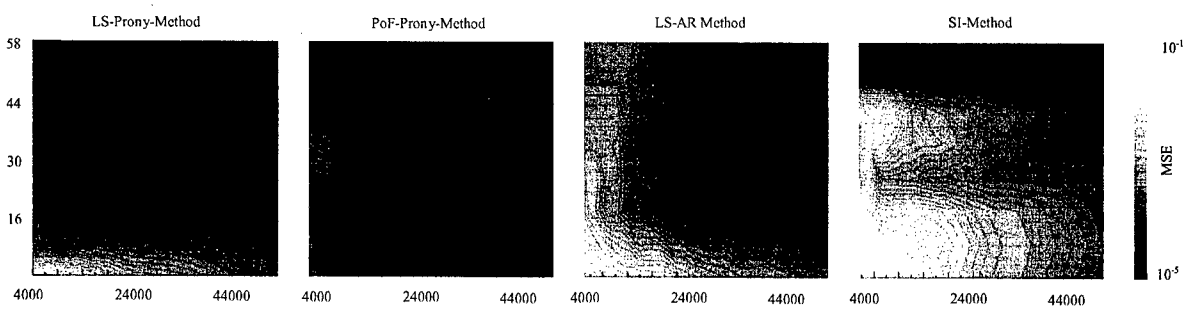

Figure 3: The relative mean-square validation error as a function of poles number(vertical) and used for AFM construction TLM samples (horizontal)

4 CONCLUSION

Some SI and SA methods for computing the **S**–parameters and the admittance Foster-represented matrix (AFM) were investigated. The methods based on the OE-SI, AR, Prony models were combined with the TLM full-wave analysis. Found system poles and residues can satisfy AFM restrictions of the equivalent circuits technical feasibility. The MEMS capacitive switch was investigated by using these methods. PoF-Prony approach gave us the smallest order threshold, which e.g. is less than 20 for 20000 used samples. Applying the PoF-Prony method the total time was reduced by about factor 10. A decreasing memory and computation time of TLM analysis allows us to simulate more complex structures.

References

[1] E. K. Miller and T. K. Sarkar, "An Introduction to the use of Model-Based Parameter Estimation in Electromagnetics", in Review of Radio Science, 196-99, ed. by R. Stone, Oxford University Press, August 1999, pp. 139-174.

[2] Ch. Eswarappa, W. J. R. Hoefer, "Autoregressive (AR) and Autoregressive Moving Average (ARMA) Spectral Estimation Techniques for faster TLM Analysis of Microwave Structures", IEEE Trans. on Microwave Theory and Techniques, Vol. 42, No. 12, pp. 2407 ff., Dec. 1994.

[3] T. Mangold and P. Russer, "Full-Wave Modelling and Automatic Equivalent-Circuit Generation of Millimeter-Wave Planar and Multilayer Structures", IEEE Trans. on Microwave Theory and Techniques, 47, (6), pp. 851-858, June 1999.

[4] K.M.Strohm, C.N. Rheinfelder, A. Schurr, and J.-F Luy, "SIMWIC Capacitive RF Switches", in European Microwave Conference, Muenchen, Germany, Oct.1999, pp.411-414.

[5] S. Lawrence Marple Jr., "Digital Spectral Analysis", Prentice Hall, Inc., Englewood Cliffs, NJ, 1987.

[6] V. K. Jain and T. Sarkar, "Multivariable System Identification by Pencil-of-Function Method", IEEE Trans. on Instrumentation and Measurement, Vol. IM-34, No.4., Dec.1985.

[7] L. Ljung, "System Identification. Theory for the User", Prentice Hall PTR,Upper Saddle River, NJ, 1999.

MODELING OF TIME DISTORTION OF RECTANGULAR PULSE PROPAGATING IN THE SCATTERING LOSSY MEDIA

A.A. Galuza, A.S. Mazmanishvili

Kharkov State Polytechnical University, 21 Frunze st., Kharkov, 61002, Ukraine
E-mail: mazmani@kpi.kharkov.ua

ABSTRACT

The paper considers a model of EM pulse propagation in a random homogeneous lossy medium. Explicit expression for the Green's function of is problem was obtained and a algorithm for calculating the shape of the output pulse is developed. A number of numerical experiments for various values of parameters of the medium and the input pulse are presented. The results enable us to make conclusions concerning the extent of pulse edges distortion.

A study of a lossy scattering medium properties can be based on the analysis of evolution of EM pulses propagating in them (Fig. 1). In this paper, we consider such an important characteristic of a scattered pulse as its edge time distortion. In the case of linear scattering media it is convenient to characterize the problem of propagation of a monochromatic EM pulse $I_{out}(t)$ in terms of the Green's function

$$I_{out}(t) = \int G(t-t')I_{in}(t')dt', \tag{1}$$

where $I_{in}(t)$ is the initial (input) pulse. The Green's function $G(t)$ and coherence function $\Gamma(\eta)$ are connected with the Laplace transformation

$$G(t) = \frac{1}{2\pi i}\int \Gamma(\eta)\exp(\eta t)\,d\eta \tag{2}$$

There is a well-known problem consisting in determination of the time shape of an EM pulse incident at the entrance ($z=0$) of a plane-parallel medium and received at the distance $z=L$ by an on-axis ($\mathbf{r}=0$) receiver. It was considered by Ishimaru [1] neglecting attenuation of radiation. To take this effect into account we constructed [2] the following equation

$$\left(\frac{\partial}{\partial z}+\frac{\nu}{2}\frac{\partial}{\partial \mathbf{r}}\mathbf{r}+a_\eta\frac{\partial^2}{\partial \mathbf{r}^2}+b\mathbf{r}^2\right)\Gamma(z,\mathbf{r};\eta)=0, \qquad \Gamma(0,\mathbf{r};\eta)=1. \tag{3}$$

Here $a_\eta = \eta/2ck^2$ and $b=\rho\sigma_p k^2/4\alpha_p$, where k is wavenumber of EM radiation; c is the light velocity; ρ is the scatterers concentration; σ_p is the single scatterer scattering cross section; is the angular scattering parameter. In is known [3] that solution to a parabolic differential equation with quadratic potential can be represented in terms of conditional path integral taken over all possible paths $\{\mathbf{r}(z)\}$ starting at the plane $z=0$ and finishing at point $\{z=L,\mathbf{r}_L=0\}$. This integral is as follows:

$$\Gamma(z,\mathbf{r};\eta)=\int d^2\mathbf{r}_0\left\langle z=0,\mathbf{r}_0\left|\exp\left(-\int_0^L|\mathbf{r}(z)|^2\,dz\right)\right|z=L,\mathbf{0}\right\rangle. \qquad (4)$$

In our case, the correlator $K_\eta(z,z')$ of the random process $\mathbf{r}(z)$ is given by equation

$$K_\eta(z,z')=g\eta\exp(-\nu|z-z'|), \quad , \quad 0\le z\le L. \qquad (5)$$

Thus, pulse propagation in random media, under certain conditions [1], can be considered a diffusion process. Correlator (5) corresponds to the Ornstain-Uhlenbeck stochastic process. This process is a solution to Langevin equation $d\mathbf{r}(z)=\nu\mathbf{r}(z)dz+\mathbf{u}(z)dz$ with attenuation ν and "white noise" $\mathbf{u}(z)$ as generating process [3]. Within random paths model output pulses can be represented as a superposition of sub-pulses arriving at the detector along different trajectories. On having taken integral (4), one obtains that

$$\Gamma(z,\mathbf{r}_L;\eta)=\frac{4\nu\xi}{(\xi+\nu)^2\exp(\xi L)-(\xi-\nu)^2\exp(-\xi L)}, \qquad \xi=\sqrt{\nu^2+2\eta\nu g}\,. \qquad (6)$$

So, (1) and (6) bring an expression for the output pulse $I_{out}(t)$

$$I_{out}(t)=\frac{1}{2\pi i}\int dt'\,I_{in}(t')\int d\eta\frac{4\nu\xi\exp(\eta t-\eta t')}{(\xi+\nu)^2\exp(\xi L)-(\xi-\nu)^2\exp(-\xi L)}. \qquad (7).$$

In (7), internal integral (with integration variable η) is taken along the Bromvich contour and the limits of the external integral (with integration variable t') correspond to the length of the input pulse $I_{in}(t)$. Expression (7) is a general solution to the problem. By changing in (7) the length τ of the rectangular pulse $I_{in}(t)$, medium parameters and distance it is not difficult to get (by numerical integration) the sets of pulses $I_{out}(t)$. It is possible to show that in case of $I_{in}(t)=\delta(t)$, the time shape of $I_{out}(t)$ has the following features: a) $I_{out}(0)\equiv 0$; b) $I_{out}(t)$ exponentially decreases as $t\to\infty$; and c) has one maximum and two inflection points. Fig. 2 shows output pulses for $\nu=10^{-6}\,m^{-1}$ and various L. One can see that two processes influence the shape of a pulse, namely, a general energy decrease and the edges distortion. Fig. 3 shows output pulses for various lengths τ of the input pulse ($\nu=10^{-3}\,m^{-1}$, $L=3\,km$). Fig. 4 ($L=1\,km$) and Fig. 5 ($L=3\,km$) illustrate pulse shape dependence on the attenuation coefficient ν. Fig. 4 shows that in case the pulse is distorted slightly, ν does not effect edges of the pulse and forces only its energy attenuation. But if the edges are distorted significantly (Fig. 5), then attenuation increase leads to an "improvement" of the pulse shape (Figures 5a and 5b differ only with their scales; every curve at (b) is normalized by its maximum). All the plots were calculated for $\rho=10^8\,m^{-3}$ and $\tau=100\,ns$ (except of Fig. 3). Thus, evolution of time pulses $I_{out}(t)$ propagating in the homogeneous scattering media has been studied. The plots of the output pulses are given for various sets of medium parameters and parameters of the input pulse. Analysis of time distortion of the pulses is made. Results obtained in this work can be used to solve direct (e.g., limiting resolution, pulse fronts distortion) and inverse problems (e.g., signal identification, determination of the medium parameters).

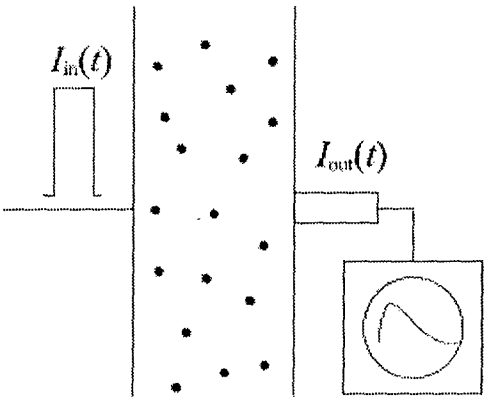

Figure 1

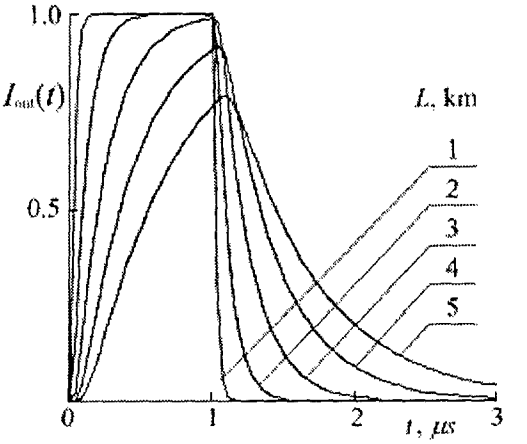

Figure 2

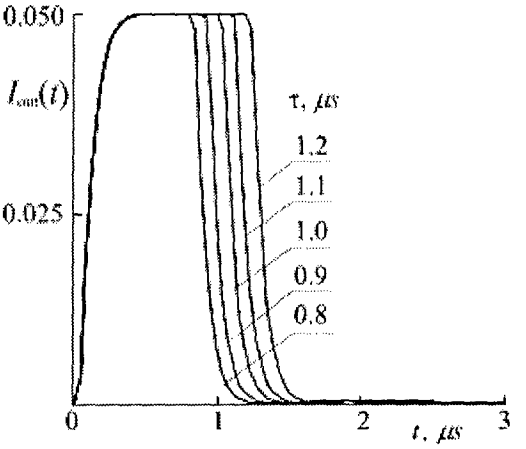

Figure 3

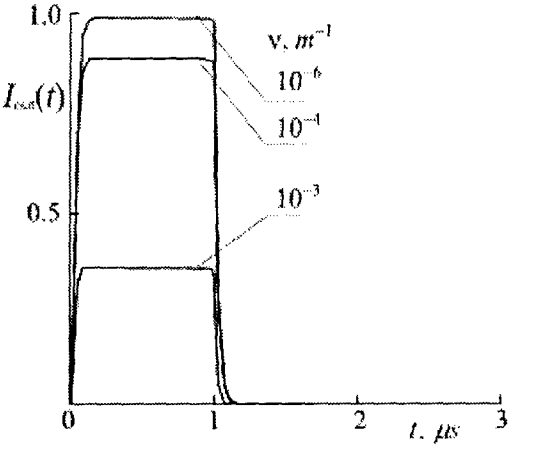

Figure 4

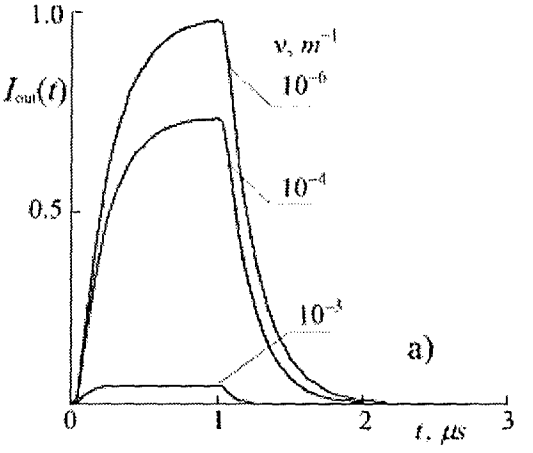

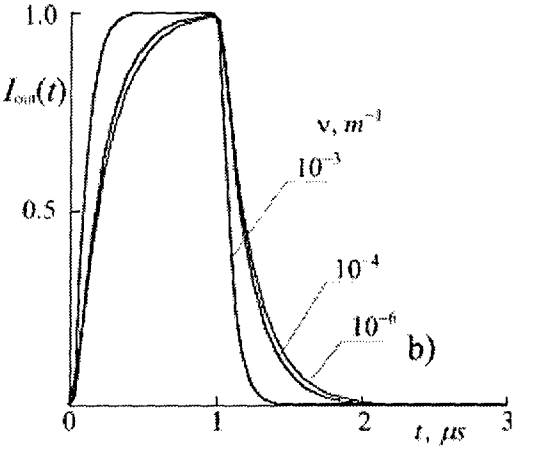

Figure 5

References

1. Ishimaru A. *Proc. IEEE*, 1977, vol. 65, 1030-1061.

2. Galuza A., Mazmanishvili A. *Proc. Int. Conf. Mathematical Methods in Electromagmetic Theory,* Kharkov, Ukraine, 1998, p.429.

3. Rytov S., Kravcov Yu., Tatarskij V. *Introduction to Statistical Radiophysics.* Part II. *Random Fields,* Nauka, Moscow, 1978 (in Russian).

ATMOSPHERIC DISTORTIONS OF ULTRA-WIDEBAND PULSES: METHOD OF TEMPORAL MOMENTS

A.M. Stadnik, and G.V. Ermakov

Kharkov Military University, P.O. Box 9063, Kharkov 61204, Ukraine
E-mail: Alex_Stadnik@yahoo.com

Results of numerical simulation of ultra-wideband electromagnetic pulses distortions in the Earth atmosphere using the concept of temporal moments are presented. The relative broadening, the skewness, and the kurtosis of the ultra-wideband pulses as functions of a distance from source to the point of observation are computed under standard atmospheric conditions. Generalization of the form of ultra-wideband pulse radiated by the source used earlier in [1] is also proposed, thereby allowing more wide and flexible variation of its initial shape.

INTRODUCTION

Ultra-wideband (UWB) electromagnetic pulses used for communication and ranging purposes can be modified by propagation effects arising from dispersion and absorption. However, so far there seems to be no studies published in the literature discussing their waveforms distortions due to propagation effects in natural media. To describe these effects quantitatively it was proposed to use the concept of temporal moments [1], the first few of which have clear physical meaning. At present, available exact solutions [2] are limited to some special cases, whereas numerical estimates of atmospheric distortions of UWB pulses, based on the first and the second moments only [1], are not at all sufficient.

The aim of this paper is to investigate numerically the combined effects of dispersion and absorption on the higher temporal moments of plane pulsed wave propagating through the homogeneous earth's atmosphere. These quantities give more detailed information on the pulse shape: the third moment is related to the skewness or asymmetry of the pulse and the forth – to its kurtosis or concentration.

ASSUMPTIONS AND FORMULATIONS

Consider a plane pulsed wave propagating in the positive z-axis direction in the homogenous isotropic medium. The evolution of the pulse waveform quantitatively can be estimated using the temporal moments, defined by the equation

$$\overline{t^k(z)} = \int_{-\infty}^{\infty} dt\, t^k E^2(z,t) \Big/ \int_{-\infty}^{\infty} dt\, E^2(z,t), \quad k = 1,2,\ldots, \tag{1}$$

where $E(z, t)$ is one of the real-valued components of the pulse field.

The travel time required by the pulse to propagate from the source at $z = 0$ to the point of interest at z (mean arrival time) may be found as $\tau_a(z) = \overline{t(z)} - \overline{t(0)}$. The mean square pulse width (effective duration) is related to the second moment by $\delta t(z) = \sqrt{\overline{t^2(z)} - \overline{t(z)}^2}$ and gives a measure of pulse broadening. In this paper the asymmetry $\gamma_3(z) = \mu_3(z)/\mu_2^{3/2}(z)$ and the kurtosis $\delta t(0)$, defined via $\mu_k(z) = \overline{\left(t(z) - \overline{t(z)}\right)^k}$, are also computed.

The initial shape $E(t) = E(z = 0, t)$ of the ultra-wideband pulse is proposed as follows:

$$E(t) = E_0 (t/T)^n \left\{ M^{n+1} \exp[-(Mt/T)^m] - \exp[-(t/T)^m] \right\} H(t), \qquad (2)$$

where $H(t)$ is the Heaviside unit step function, which must be included in order to establish the time origin and ensure the fulfillment of the causality principle.

The model (2) satisfies the condition $\int_{-\infty}^{\infty} dt E(t) = 0$, corresponds to the intuitive idea on the initial form of the irradiated UWB signal, and allows us to advance the analytical calculations. In particular, initial values of the moments (1) for the waveform (2) are given by

$$\overline{t^k(0)} = \left(\frac{T}{2^{1/m}\sqrt{M}} \right)^k \frac{\Gamma\left(\frac{2n+k+1}{m}\right)}{\Gamma\left(\frac{2n+1}{m}\right)} \frac{\cosh\left(\frac{k-1}{2}\ln M\right) - \sin^{\frac{2n+k+1}{m}}\left(2\arctan\sqrt{M^m}\right)}{\cosh\left(\frac{1}{2}\ln M\right) - \sin^{\frac{2n+1}{m}}\left(2\arctan\sqrt{M^m}\right)}. \qquad (3)$$

For convenience of interpretation it is assumed that the field $E(t)$ is normalized so, that $\int_{-\infty}^{\infty} dt\, E^2(t) = 1$. This implies the choice of E_0 in the following form:

$$E_0 = \left\{ \Gamma\left(\frac{2n+1}{m}\right) \frac{TM^{1/2}}{n2^{\frac{2n-m+1}{m}}} \left[\frac{M^{1/2} + M^{-1/2}}{2} - \left(\frac{M^{m/2} + M^{-m/2}}{2} \right)^{-\frac{2n+1}{m}} \right] \right\}^{-1/2}. \qquad (4)$$

Naturally, in the special case $m = 1$ formulas (2)-(4) are reduced to those obtained by authors earlier in [1]. Additional degree of freedom, related to the parameter m, enables to vary the pulse initial form more widely and flexibly.

NUMERICAL RESULTS

The computation of the UWB pulse shape requires a knowledge of the complex index of refraction $n_c(\omega)$ in the large frequency range (VHF through UHF and even into the SHF ranges for picosecond pulses), so one of the most complete models of $n_c(\omega)$ developed by H.J. Liebe [3] was used. In Figs. 1-3 relative broadening $\delta t(z)/\delta t(0)$, coefficients $\gamma_3(z)$ and $\gamma_4(z)$ calculated using FFT under standard atmospheric conditions (air pressure was taken as $p = 1013{,}25$ mbar, temperature T = 298°K, and relative humidity RH = 25%) are presented as functions of a distance z from the source for different initial waveforms.

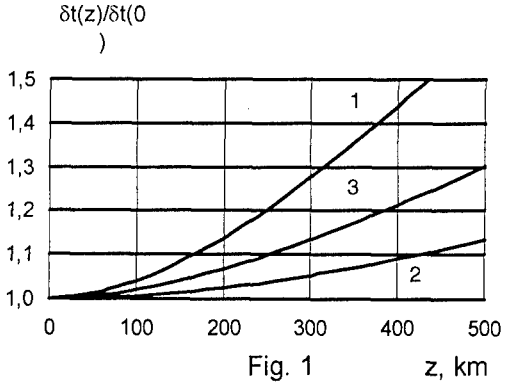

Fig. 1

In all figures for pulses with δt(0) = 0.1 ns (solid lines) the following parameters of the model (2) were chosen:
1 - $M = 2$, $n = 5$, $m = 1{,}2$, $T = 0{,}025$ ns;
2 - $M = 2$, $n = 5$, $m = 1{,}4$, $T = 0{,}087$ ns;
3 - $M = 3$, $n = 4$, $m = 1{,}4$, $T = 0{,}071$ ns.
For pulses with δt(0) = 1 ns (dotted lines) the following parameters were chosen:
1 - $M = 2$, $n = 5$, $m = 1{,}2$, $T = 0{,}25$ ns;
2 - $M = 2$, $n = 5$, $m = 1{,}4$, $T = 0{,}87$ ns;
3 - $M = 3$, $n = 4$, $m = 1{,}4$, $T = 0{,}71$ ns.

For ultra-wideband pulses of duration up to 0.1 ns under standard atmospheric conditions the main propagation effect is attenuation of higher frequency components mainly. In time domain this results in pulse broadening, whereas

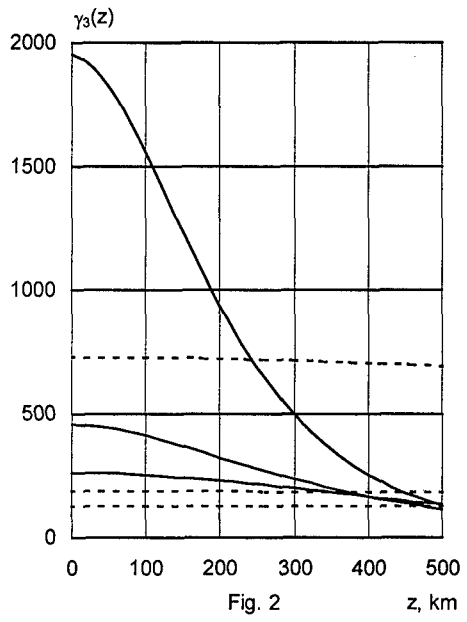

Fig. 2

distortions due to dispersion at distances up to 500 km may be neglected.

As can be seen from Figs. 2 and3 effective duration is inadequate to characterize the degree and character of the ultra-wideband pulse distortions. So, pulses with the same initial effective duration $\delta t(0)$ may have quite different values of $\gamma_3(z)$ and $\gamma_4(z)$. One can also see that while values of $\gamma_3(z)$ and $\gamma_4(z)$ for UWB pulses with $\delta t(0) = 0.1$ ns vary rather severally (by one or two orders), those for pulses with $\delta t(0) = 1$ ns at distances up to 500 km are practically unchanged.

Given prior information about the duration of the input UWB pulses, the last observation can be used to gain qualitative knowledge of initial pulse shape by examining the behavior of the integral characteristics $\gamma_3(z)$ and $\gamma_4(z)$ along a distance.

Computations like the above-mentioned ones may estimate the upper limits of the distances from the source and the low limits of the duration of those pulses, for which such considerations with some degree of error still can be made.

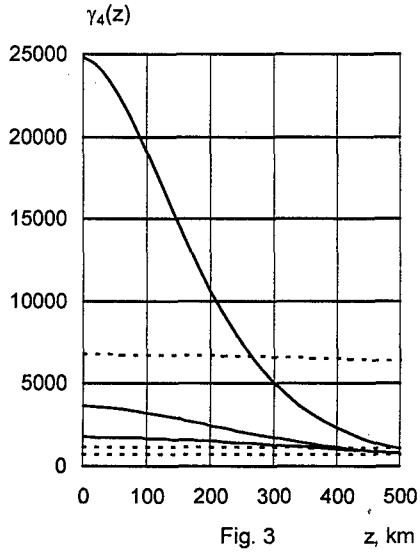

Fig. 3

CONCLUSION

Temporal moments of the orders greater than the second are necessary in order to describe quantitatively the outcome of the UWB pulses in a more complete way. Behavior of the output pulse waveform can be qualitatively predicted, based on the knowledge of the spectrum and initial duration of the UWB pulse under study.

REFERENCES

[1] A.M. Stadnik, G.V. Ermakov, "Ultra-wideband electromagnetic pulses distortions in the Earth's atmosphere", *Radiotekhnika i Elektronika*, vol. 40, no. 7, pp. 1009-1016, 1995 (*in Russian*).

[2] A.B. Shvartsburg, "Transient waveforms and nonperiodic waves in dispersive media (exactly solvable models)", *Physics-Uspekhi*, vol. 41, no. 1, pp. 77-94, 1998.

[3] H.J. Liebe, "An updated model for millimeter wave propagation in moist air", *Radio Sci.*, vol. 20, no. 6, pp. 1069-1089, Nov. 1985.

TIME-DOMAIN FRESNEL'S FORMULAS FOR A PLANE INTERFACE BETWEEN MEDIA

Nerukh A.G.

Kharkov Technical University of Radioelectronics,
14 Lenin Ave., Kharkov, 61166, Ukraine
Tel.: +380 572 40 93 72, E-mail: nerukh@ddan.kharkov.ua

ABSTRACT

The time-domain operators are obtained that allow to describe a transformation of an arbitrary initial field by a flat interface between two media in the 3-D case. The medium in one of the two halfspaces changes its permittivity and acquires a conductivity. The description includes a case when a boundary is created at some moment of time. Transmitted and reflected signals are determined by integral operators that take into account the field polarisation characteristics. Weight factors in kernels of these operators are just analogues of Fresnel formulae. The obtained resolvent consists of two parts the first of which is a mere generalisation of a resolvent for an unbounded medium and the second occurs through availability of an interface between media.

THE INTEGRAL OPERATORS FOR SCATTERED FIELD

The transmitted field in the nonstationary half-space ($x \geq 0$) where the medium changes its permittivity at zero moment from ε into ε_1 is equal to $\boldsymbol{E} = \boldsymbol{E}_0 + \boldsymbol{E}_1 + \boldsymbol{E}_2$. Here, $\boldsymbol{E}_0$ is the initial (source) field, $\boldsymbol{E}_1$ is the field corresponding to unbounded case

$$\boldsymbol{E}_1 = \theta(x)\frac{1-n^2}{4\pi v_1^{\,2}}\left[v_1^{\,2}\hat{Q} - \frac{\partial^2}{\partial t^2}\hat{I}\right]\overline{W}_0, \tag{1}$$

and determined by the medium parameters and the initial field,

$$\overline{W}_0 = \int_0^\infty dt' \int_0^\infty dx' \theta(t - t' - |x - x'|/v_1) \int_\infty^\infty dr' \int_0^\infty dk k J_0(kR_\perp) J_0\left(k\sqrt{v_1^{\,2}\tau^2 - |x-x'|^2}\right) \boldsymbol{E}_0(t', \boldsymbol{r}') \tag{2}$$

where $\theta(t)$ is the Heaviside unit function, $J_0(z)$ is the Bessel function, $\hat{Q}$ is the differential matrix, $\hat{I}$ is the unit matrix, $n = v_1 / v = \sqrt{\varepsilon} / \sqrt{\varepsilon_1}$.

The direct influence of the boundary on the electromagnetic field is described by the third term that is determined by differential matrices $\hat{Q}_\perp, \hat{T}, \hat{I}_\perp$ and contains three functions – magnetic, electric and mixed – the analogues of the Fresnel coefficients.

$$\boldsymbol{E}_2 = \theta(x)\frac{1-n^2}{4\pi v_1}\left[v_1^{\,2}\hat{Q}_\perp \overline{W}_m - 2v v_1 \hat{T}\overline{W}_{em} + \frac{\partial^2}{\partial t^2}\hat{I}_\perp \overline{W}_e\right]. \tag{3}$$

are. Each term in (3) consists of four functions which dependence on time and longitudinal-spatial variables is determined by the functions $L_a^{(j)}(\tau, x, x', k)$:

$$\overline{W}_a = \int_0^\infty dt' \int_0^\infty dx' \theta(t - t' - \frac{x + x'}{v_1}) \int_\infty^\infty dr' \int_0^\infty dk k J_0(kR_\perp) \sum_{j=0}^{3} N_a^{(j)} L_a^{(j)}(\tau, x, x', k) \boldsymbol{E}_0(t', \boldsymbol{r}'), \tag{4}$$

The reflected field in the half-space $x < 0$ is

$$\boldsymbol{E}_r = \boldsymbol{E}_0 + \theta(-x)\frac{n^2-1}{4\pi v_1 n}\left[-vv_1\hat{\mathrm{S}}_\perp \overline{\boldsymbol{U}}_m + \frac{\partial^2}{\partial t^2}\hat{\mathrm{I}}_\perp \overline{\boldsymbol{U}}_e\right] \tag{5}$$

where $\overline{\boldsymbol{U}}_a = \int_0^\infty dt' \int_0^\infty dx' \theta(t - t' - \frac{|x|}{v} - \frac{x'}{v_1}) \int_\infty dr' \int_0^\infty dk k J_0(kR_\perp) \sum_{j=0}^{3} \overline{N}_a^{(j)} M_a^{(j)}(\tau, x, x', k) \boldsymbol{E}_0(t', \boldsymbol{r}')$, (6)

$\hat{S}_\perp$ is the differential matrix and $M_a^{(j)}(\tau, x, x', k)$ are analogues of $L_a^{(j)}(\tau, x, x', k)$.

The constant coefficients $N_a^{(j)}$ in (4) and (6) are determined by a jump of the permittivity only but their dependence on the jump magnitude is very different.

REFLECTION AND TRANSMISSION OF A PLANE WAVE ONTO FLAT BOUNDARY THAT HAS COME INTO BEING

It is known [*Fante R L 1971*] that transformation of a plane wave $\boldsymbol{E}_0(\boldsymbol{x}) = \boldsymbol{E}_0 \exp[i(\omega t - \boldsymbol{sr})]$, where $s = \omega/v$, yields monochromatic waves only when a wave impinges normally on a newly created flat boundary of a medium whose permittivity changes in time.An oblique incidence of the wave on a flat boundary of a medium changes the picture of the phenomena significantly, because this process is followed by a transient, Figure 1. There are two regions. In the region $x > v_1 t$ the changing medium yields two splitting waves with new frequencies $\omega_1 = \omega v_1 / v$

$$\boldsymbol{E}_1^{(+)} + \boldsymbol{E}_1^{(-)} = \frac{v_1}{2v}\left(\frac{v_1 + v}{v} e^{i\omega_1 t} + \frac{v_1 - v}{v} e^{-i\omega_1 t}\right)\boldsymbol{E}_0 e^{i\omega t - i\boldsymbol{sr}}. \tag{7}$$

These waves have the same form as the transformed field in the unbounded medium [*Morgenthaler F R 1958*]. In the region $0 < x < v_1 t$ remains the inverse wave with the frequency ω_1 only. There are also the ordinary refracted wave $\boldsymbol{E}_{refract}$ with the frequency ω of the incident wave and a transient field in this region.

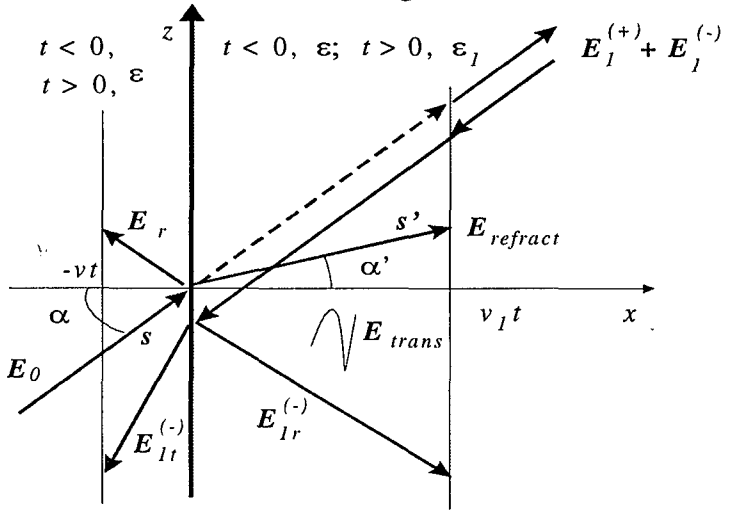

Figure 1. Transient in the electromagnetic field after the permittivity jump in the half-space.

The transient has a complex form and in the case of an oblique incidence the process is described exactly by obtained spatial-time Fresnel's formulas. The time behaviour of the

function $\overline{W_0}$ that determines the component E_1 of the transmitted field is shown in Fig. 2 and 3.

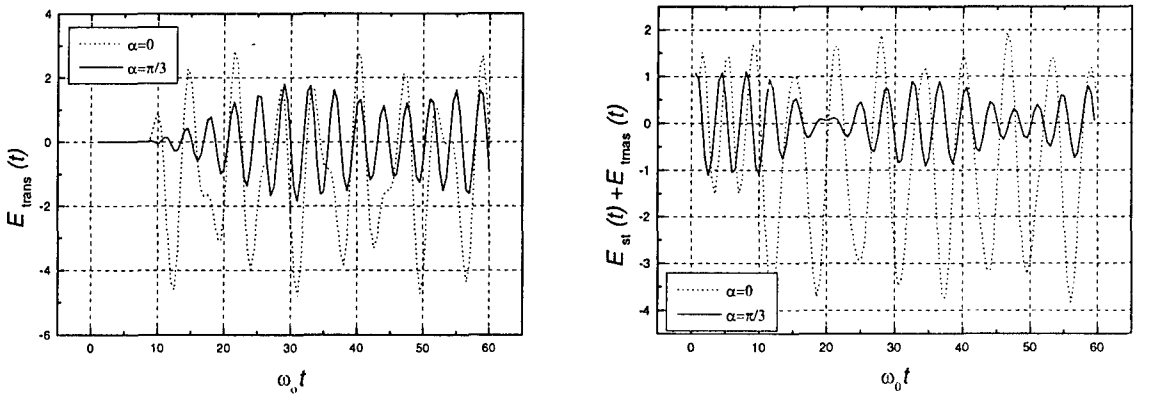

a) *b)*

Figure 2. The time behavior of the first part of transmitted field for the case of $n=1.7$ *and* $\omega_0 x/v=15$, $\omega_0 t_{front}=8.8$; *a) the transient part of the field, b) the total field*

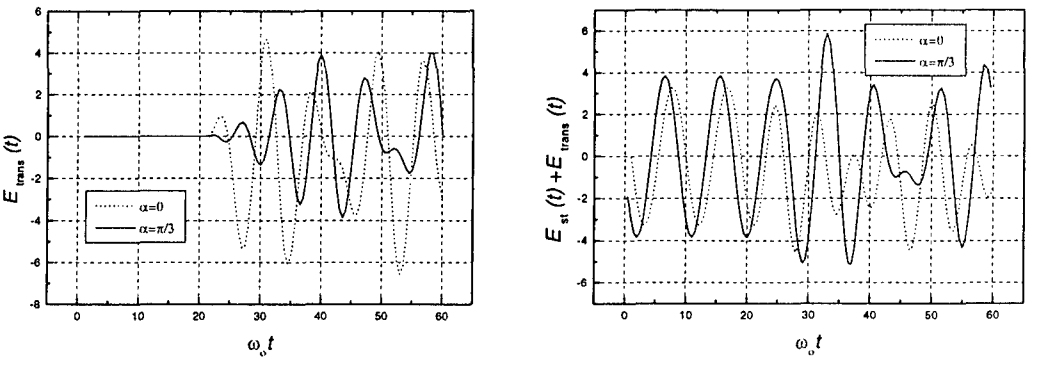

a) *b)*

Figure 3. The same as in the figure 2 for the case of $n=0.7$ *and* $\omega_0 x/v=15$, $\omega_0 t_{front}=21.4$

Steady-state monochromatic waves that are identical to the case of the normal impingement of the initial wave are separated from this transient field asymptotically with $t\to\infty$. Exact expression for the steady-state waves in the nonstationary half space $x\geq 0$ for an arbitrary polarised initial wave is given in the form

$$\boldsymbol{E}_{1r}^{(-)}+\boldsymbol{E}_{refract}=\frac{v_1(v_1-v)}{2v^2}\boldsymbol{E}_0 e^{-i(\omega_1 t+\boldsymbol{sr})}+\frac{s_1'+s_1}{2s_1'}\boldsymbol{E}_0 e^{i(\omega t-\boldsymbol{s'r})}. \qquad (8)$$

It follows that the asymptotic complete suppression of the direct wave with frequency ω_1 occurs in the case of an initial wave impingement on a medium boundary with an arbitrary angle.

ONE CLASS OF WAVEGUIDE RESONATORS: ALGORITHMS BASED ON SEMI-INVERSION TECHNIQUE IN TIME AND FREQUENCY DOMAIN

N.P.Yashina

Institute of Radiophysics and Electronics, NAS of the Ukraine
Ul. Proskury 12, Kharkov 61085, Ukraine
Tel. +380-(572)-14-10-66, e-mail: nataliya@lincom.kharkov.ua

Among huge body of various approaches, widely used nowadays in greatly computerized electromagnetic theory the very special place belongs to rigorous technique [1]. As well known the rigorous approaches are rather complicated in their implementations both mathematical and numerical. These methods have quite bounded range of geometrical configurations and structures that may be considered. But, having great intellectual content, they provide the investigator as an award for great efforts with decent advantages: they give incomparable chance to investigate complicated resonant electromagnetic phenomena with any required in advance accuracy, practically without limits for parameters; and even to come over to the new subtle properties and features or very peculiar displaying of the known ones for the well known structures.

The approach, based on extraction and analytical inversion of the singular part of boundary value problem (BVP) operator in frequency (FD) and time domain (TD) is applied to the one class of resonant structures in waveguides (coaxial type plane discontinuities bifurcation's, shunts, slots, irises, steps, disks etc.). Thus the initial BVP [2] and BVP [3] are reduced to the matrix equation of the second kind or to Volterra integral equation of the second kind (with straightforward scheme of time marching). All steps of technique are mathematically proved. The convergence of numerical algorithms is proved also and estimated analytically.

Special attention is paid to computer implementation of algorithms developed and various tests of them.

Thus the convergence of numerical solutions is thoroughly investigated and analytical estimates are illustrated by numerical results. Special study of the condition numbers of matrix equations the problems are reduced to has been carried out (FD): the limited, practically constant (after certain number of equation in truncated system) and rather small condition number (10-15) confirms the stability of the algorithm developed.

Boundary conditions (both in FD and TD) and additional relations derived from reciprocity principle, various symmetry properties of the resonant structures, edge conditions and energy conservation low have been verified for wide range of parameters. The high accuracy of their fulfillment illustrates numerically not only the validity of the algorithms, but their equivalence to the original BVP or initial BVP under consideration.

Fast convergence of the results, flexibility and accuracy of algorithms make them an efficient and powerful tool for investigation of complicated resonant phenomena in TD and FD that can be simulated by this class of waveguide resonators.

1. V.P.Shestopalov, Y.A.Tuchkin, A.Y.Poyedinchuck, and Y.K.Sirenko [1997], New Methods for Solving Direct and Inverse Problems in Diffraction Theory. Analytical Regularization of Boundary Value Problems in Electrodynamics, Kharkov, Osnova (in Russian). 385 p.
2. Y.K.Sirenko, V.P.Shestopalov, and N.P.Yashina [1997]. "New Methods in the Dynamic Linear Theory of Open Waveguide Resonators", Comp. Math. and Math. Physics, 37, No 7. pp.845-853.
3. N.P.Yashina. [1999]."Accurate Analysis of Coaxial Waveguide Slot Bridge". Electronic and Optical Technology Letters. 1999.Vol. 20. No.5. March 5, pp. 345-349.

TRANSVERSE-MAGNETIC ELECTROMAGNETIC WAVES IN A WAVEGUIDE WITH SPACE-TIME MULTIPERIODICALLY MODULATED FILLING

E.A.Gevorkyan

Moscow State University of Economics, Statistics and Informatics
Contact address: Nezhinskaya str., 7, 119501, Moscow, Russia
Tel: (095)4427133, (095)4427066. Fax: (095)4427066.
E – mail: ***vblagodatskikh@rector.mesi.ru***

ABSTRACT

Propagation of electromagnetic TM waves in a waveguide filled with space-time multiperiodically modulated nonmagnetic dielectric filling is discussed. The analytic expressions for the TM filled are obtained on the assumption of a small modulation indexes of the filling. The frequency of the «strong interaction» between the signal wave and the modulation wave is found.

Propagation of transverse–electric electromagnetic (TE) waves in a waveguide with multiperiodically nonuniform and nonstationary dielectric filling was discussed in [1]. Here we consider the analogous problem for transverse–magnetic electromagnetic (TM) waves.

We shall consider an ideal regular waveguide whose generatrix lies along the axis OZ. We assume that the permeability of the waveguide filling is $\mu=1$ and the permitivity is modulated multiperiodically in space and time with help of pump wave in the following way:

$$\varepsilon = \varepsilon_0[1+m_1\cos k_1(z-ut)+m_2\cos k_2(z-ut)]. \tag{1}$$

In (1), m_1 and m_2 are the modulation indices, k_1, k_2 and u are, consequently, the wave numbers and the velocity of the pump waves, ε_0 is the permitivity of the filling in the absence of modulation.

The electromagnetic TM field in this case will be described with help of the longitudinal component of the electric vector $\tilde{E}_z(x, y, z)=\varepsilon E_z(x, y, z)$. From Maxwell`s equations we can derive the following wave equation for $\tilde{E}_z$

$$\Delta_\perp \tilde{E}_z + \varepsilon \frac{\partial}{\partial z}\left(\frac{1}{\varepsilon}\frac{\partial \tilde{E}_z}{\partial z}\right) - \frac{\varepsilon}{c^2}\frac{\partial^2 \tilde{E}_z}{\partial t^2} = 0, \tag{2}$$

where $$\Delta_\perp = \frac{\partial^2}{\partial x^2} + \frac{\partial^2}{\partial y^2}.$$

Equation (2) with variables $\xi = z - ut$, $\eta = \frac{z}{u} - \frac{1}{u}\int_0^{z-ut} \frac{d\xi}{1-\beta^2\frac{\varepsilon(\xi)}{\varepsilon_0}}$,

where $\beta^2 = u^2\varepsilon_0/c^2$, c is the velocity of the light, transforms to

$$\Delta_\perp \tilde{E}_z + \varepsilon \frac{\partial}{\partial \xi}\left[\frac{1}{\varepsilon}\left(1-\beta^2\frac{\varepsilon}{\varepsilon_0}\right)\frac{\partial \tilde{E}_z}{\partial \xi}\right] - \frac{\varepsilon}{\left(1-\beta^2\frac{\varepsilon}{\varepsilon_0}\right)c^2}\frac{\partial^2 \tilde{E}_z}{\partial \eta^2} = 0. \tag{3}$$

If we solve the equation (3) in the form $\tilde{E}_z = \sum_{n=0}^{\infty} e^{i\gamma n} \tilde{E}_{nz}(\xi)\psi_n(x,y)$, where $\psi_n(x,y)$ are the eingenfunctions of the first boundary value problem for the transverse cross section of the waveguide , for $\tilde{E}_z$ we derive the following equation

$$\frac{d}{d\xi}\left[\frac{1}{\varepsilon}\left(1-\beta^2\frac{\varepsilon}{\varepsilon_0}\right)\frac{d\tilde{E}_{nz}}{d\xi}\right]+\frac{\chi^2{}_n}{\varepsilon\left(1-\beta^2\frac{\varepsilon}{\varepsilon_0}\right)}\tilde{E}_{nz}=0, \tag{4}$$

where $\chi_n{}^2 = \frac{\gamma^2}{c^2}\varepsilon - \lambda_n{}^2\left(1-\beta^2\frac{\varepsilon}{\varepsilon_0}\right)$.

Note that the functions $\psi_n(x,y)$ satisfy to the following equation

$$\Delta_\perp\psi_n(x,y)+\lambda_n\psi_n(x,y)=0, \psi_n(x,y)|_\Sigma = 0,$$

where λ_n are the eigenvalues of the first boundary value problem, and Σ is the boundary.
Let us introduce a new variable into the equation (4) and we obtain

$$s=\frac{(mk_1+mk_2)b}{2\varepsilon_0}\int_0^\xi \frac{\varepsilon d\xi}{1-(\beta^2\varepsilon)/\varepsilon_0}, \tag{5}$$

where m,p=1,2,3,..., b=1-β^2, assuming that m_1«1, m_2«1 and $l_1=(m_1\beta^2/b)$ «1, $l_2=(m_2\beta^2/b)$«1, $l_1 \sim l_2$. Simple algebra then transforms the equation (4) into the Mathiew – Hill equation, which to a first approximation with respect to m_1, m_2 and l_1, l_2 has a form

$$\frac{d^2\tilde{E}_{nz}(s)}{ds^2}+\sum_{k=-1}^{1}\theta_k{}^n e^{2iks}\tilde{E}_{nz}(s), \tag{6}$$

where

$$\theta_0{}^n = \frac{4}{(mk_1+pk_2)^2b^2}\left(\frac{\gamma^2}{c^2}\varepsilon_0-\lambda_n{}^2b\right), \tag{7}$$

$$\theta_{-1}{}^n=\theta_1{}^n=\frac{2}{\pi(mk_1+pk_2)^2b}\left(\frac{\gamma^2}{u^2}-\frac{2-\beta^2}{\beta^2}\lambda_n{}^2\right)\left(\frac{\alpha\sin 2\pi\alpha}{1-\alpha^2}l_1+\frac{\beta\sin 2\pi\beta}{1-\beta^2}l_2\right), \tag{8}$$

$$\alpha=\frac{k_1}{mk_1+pk_2},\ \beta=\frac{k_2}{mk_1+pk_2}.$$

The equation (6) is solved by using the method developed in [1-4]. Then $\tilde{E}_{nz}(s)$ can be represented as

$$\tilde{E}_{nz}(s)=e^{i\mu_n s}\sum_{k=-1}^{1}c_k{}^n e^{2iks}, \tag{9}$$

where the value of μ_n satisfy to the following dispersion equation

$$\mu_n{}^2=\theta_0{}^n+\frac{(\theta_1{}^n)^2}{(\mu_n-2)^2-\theta_0{}^2}+\frac{(\theta_1{}^n)^2}{(\mu_n+2)^2-\theta_0{}^n}. \tag{10}$$

Substituting (9) into equation (6) and taking into account, that $\mu_n{}^2 \approx \theta_0{}^n$ in the region of "weak" (non-resonant) interaction between the signal wave and the modulation wave, we obtain a solution of equation (6) by the variables t and z in the form

$$E_z = \frac{1}{\varepsilon_0}\sum_{n=0}^{\infty}\psi_n e^{i(p_0{}^n z-\omega_0{}^n t)} c_0{}^n \sum_{k=-1}^{1}\left\{k\left[\left(\frac{\Delta^n{}_{k_1}}{2}-k\frac{m_1}{2}\right)e^{ikk_1(z-ut)}+\left(\frac{\Delta_{k_2}}{2}-k\frac{m_2}{2}\right)e^{ikk_2(z-ut)}\right]+\frac{c_k{}^n}{c_0{}^n}e^{ik(mk_1+pk_2)(z-ut)}\right\}^{|k|}, \quad (11)$$

where

$$c_{\pm 1}{}^n = \frac{\theta_1{}^n c_0{}^n}{(\mu_n \pm 2)^2 - \theta_0{}^n}, \quad (12)$$

$$p_0{}^n = \frac{\gamma}{u}-\frac{\gamma}{ub}+\frac{mk_1+pk_2}{2}\mu_n, \quad \omega_0{}^n = \frac{(mk_1+pk_2)u}{2}\mu_n - \frac{\gamma}{b}, \quad (13)$$

$$\Delta_{k_1}{}^n = \left[\frac{(\mu_n+2k)(mk_1+pk_2)}{2k_1}-\frac{\gamma}{ubk_1}\right]l_1, \quad \Delta_{k_2}{}^n = \left[\frac{(\mu_n+2k)(mk_1+pk_2)}{2k_2}-\frac{\gamma}{ubk_2}\right]l_2. \quad (14)$$

and $c_0{}^n$ is found from condition of normalization.

As known (see [2]), the dispersion equation (10) has a complex solution, when $\theta_0{}^n \approx 1$. In this case, at a certain frequency, the "strong" interaction between the signal wave and the modulation wave of the filling takes place and $|c_{-1}{}^n| \sim c_0{}^n$, $|c_1{}^n| \sim l_1 l_2$, i.e. the amplitude of the mines first harmonic is of the same order as the amplitude of the zero harmonic. The expression for the frequency of strong interaction $\omega_{0,s}$ can be obtained from the condition $\theta_0{}^n \approx 1$, taking into account (7), and (13).

Then we obtain

$$\omega_{0,s} = \frac{u(mk_1+pk_2)}{2\beta}(\eta_n+\beta), \eta_n = \sqrt{1+\frac{4\lambda_n{}^2}{(mk_1+pk_2)^2 b}}. \quad (15)$$

For a stationary nonhomogeneous multiperiodically modulation ($u \to 0$) the formulas (11) and (15) transform to

$$E_z = \frac{1}{\varepsilon_0}\sum_{n=0}^{\infty}\psi_n(x,y)e^{i(\bar{p}_0{}^n z-\bar{\omega}_0{}^n t)}\sum_{k=-1}^{1}\bar{c}_k{}^n e^{ik(mk_1+pk_2)z}, \quad (16)$$

$$\omega_{0,s} = \frac{c(mk_1+pk_2)}{2\sqrt{\varepsilon_0}}\sqrt{1+\frac{4\lambda^2{}_n}{(mk_1+pk_2)^2}}, \quad (17)$$

where the values of $\bar{c}^n{}_{\pm 1}, \bar{p}^n{}_0, and \bar{\omega}^n{}_0$ can be found by the limit from (12), and (13) when u $\to 0$.

In conclusion note, that the transverse components of the TM field in this case are given by

$$\vec{H}_\tau = -\frac{1}{c}\sum_{n=0}^{\infty}\lambda_n{}^{-2}\frac{\partial[\tilde{E}_n(z,t)]}{\partial t}[\vec{z}_0\nabla\psi_n(x,y)], \quad \vec{E}_\tau = \frac{1}{\varepsilon}\sum_{n=0}^{\infty}\lambda_n{}^{-2}\frac{\partial[\tilde{E}_n(z,t)]}{\partial z}\nabla\psi_n(x,y), \quad (18)$$

where $\vec{z}_0$ is a unit vector along the z axis.

REFERENCES

[1] E.A.Gevorkyan, Electromagnetic waves in a waveguide with a space-time multiperiodic dielectric filling, Proc. of Inter. Conference of MMET, Kharkov. June 2-5, 1998, p.853.

[2] K.A.Barsukov, E.A. Gevorkyan, On the theory of propagation of electromagnetic waves in a waveguide filled with nonstationary and nonhomogeneous dielectric material, Radiotekhnika i electronica. 1983,v. 28, p. 237.

[3] E.A. Gevorkyan. On the theory of propagation of electromagnetic waves in a waveguide with a multiperiodically modulated filling. Physica A, 1997, v. 241, p. 236.

[4] E.A. Gevorkyan. Electromagnetic waves in a waveguide with a periodically modulated filling. Proc. of Inter. Symp. on Elektr. Theory ,Thessaloniki, May 25-28, 1997, p. 236.

FAMILY OF 12-, 6- AND 3-PARAMETRICAL ALGORITHMS FOR ELECTRODYNAMIC ANALYSIS OF 3D STREAM Rτ-NET

Boris V. Sestroretsky, Sergey A. Ivanov, Valery M. Seredov and Konstantin N. Klimov*

Lavochkin Association
Leningradskay st. 24, Khimki-2 Moscow Region 141400, Russia, ph. (095) -575-50-69
E-mail: tamic@mail.ru

* Moscow State Institute of Electronics and Mathematics
Bolshoy Trechsvyatitelsky lane 3/12, Moscow 109028, Russia, ph. (095) -916-88-17
E-mail: const@glasnet.ru

ABSTRACT

Efficient computing algorithms based on division of an electromagnetic process in the stream Rτ grids in two independent processes are analyzed. Ii is shown that on the basis of the 12-parametric algorithm one can generate 2 variants of 6-parametric algorithms: with usage of a half of nodes or a half of ports. New more efficient 3-parametrical algorithm is found on the basis of combination of ideas of the mentioned algorithms, where a half of ports and a half of nodes are used.

INTRODUCTION

In 1983, the stream Rτ operator was suggested for engineering 3D analysis of electromagnetic processes in the time-domain mode ([1], see Fig. 1.a). Later in the Western works it has been investigated under the name of 12-port symmetrical condensed node (SCN), see [2], [3]. Here, it is supposed that the whole space is divided into elementary volumes Δ^3 ($\Delta << \lambda$), like shown in Fig. 1.a, each having 12 inputs (circles on the sides of Δ^3) with two orthogonal inputs on each side.

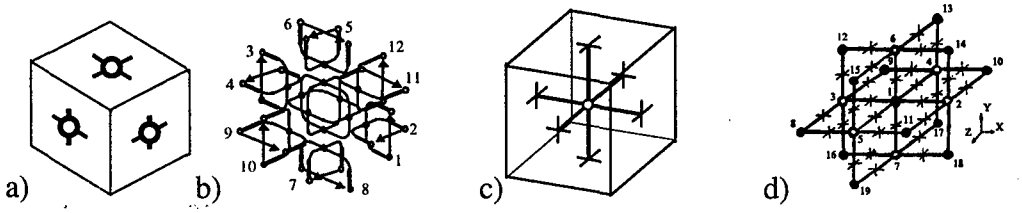

Fig. 1. Explanation of the "chess" algorithm for the Rτ operator.

For this operator, it was suggested an equivalent 12-port circuit shown in Fig. 1.b containing transmission-line sections $\Delta/2$ with wave impedance $W_0 = 120\pi$ and the time of delay of a signal $\frac{\tau}{2} = \frac{\Delta}{4}\sqrt{\mu_0\varepsilon_0}$, joined at the center of Δ^3 through ideally symmetrical transformers, whose internal windings cross at 6 points. The arrows with indices $i = 1 \div 12$ focused on the coordinates x, y, z, denote voltage variations Π_i and so-called scattered Rτ-pulses O_i at external inputs of the circuit in Fig. 1.b. The circuit in Fig. 1.b. is convenient for representing, connecting pairs of sections for each side of Δ^3 by thick lines coming to the central transformer (Fig. 1.c.). The orientation of waves Π_i and O_i in the circuits in Fig. 1.b. and Fig. 1.c. is identical. According to the circuit in Fig. 1.b. ([1]), if the pulses Π_i come to 12 inputs of the circuit at the moment of time $t = n\tau$, then the scattered pulses O_i are formed at the moment of time $t = (n+1)\tau$.

$$O_1 = \frac{\Pi_6 - \Pi_8 + \Pi_{10} + \Pi_{12}}{2} \quad O_2 = \frac{\Pi_5 + \Pi_7 + \Pi_9 - \Pi_{11}}{2} \quad O_3 = \frac{-\Pi_6 + \Pi_8 + \Pi_{10} + \Pi_{12}}{2} \quad O_4 = \frac{\Pi_5 + \Pi_7 - \Pi_9 + \Pi_{11}}{2}$$
$$O_5 = \frac{\Pi_{10} - \Pi_{12} + \Pi_2 + \Pi_4}{2} \quad O_6 = \frac{\Pi_9 + \Pi_{11} + \Pi_1 - \Pi_3}{2} \quad O_7 = \frac{-\Pi_{10} + \Pi_{12} + \Pi_2 + \Pi_4}{2} \quad O_8 = \frac{\Pi_9 + \Pi_{11} - \Pi_1 + \Pi_3}{2} \qquad (1)$$
$$O_9 = \frac{\Pi_2 - \Pi_4 + \Pi_6 + \Pi_8}{2} \quad O_{10} = \frac{\Pi_1 + \Pi_3 + \Pi_5 - \Pi_7}{2} \quad O_{11} = \frac{-\Pi_2 + \Pi_4 + \Pi_6 + \Pi_8}{2} \quad O_{12} = \frac{\Pi_1 + \Pi_3 - \Pi_5 + \Pi_7}{2}$$

From (1), the organization of the 12-parametric algorithm of the electromagnetic analysis follows on the basis of grids from the Rτ operators in Fig. 1.b. For each interval of time τ, in all elements Δ^3 $N_p = 12$ numbers Π_i are stored. For the interval τ, computer on the basis of (1) makes calculation of 12 scattered pulses O_i, which become incident for 6 next elementary volumes in the subsequent time interval. The total number of arithmetic operations on each step for one operator is $N_o = 30$. The basic idea of new algorithms allowing to reduce N_p (memory) and N_o (number of arithmetic operations), consists in the following: original electromagnetic process taking place in the infinite Rτ grid is split in two energetically independent sub-processes. These two sub-processes can be considered independently, although they are correlate with each other in accordance with the set of equations (1). The correlation of sub-processes actually means a redundancy of their simultaneous use, i.e. in electromagnetic analysis only one of sub-processes can be kept without a loss of accuracy of calculations.

ALGORITHM "HALF OF NODES"

The first variant of a 6-parametrical algorithm [4] is designed as follows: the nodes in infinite grid (Fig. 1.c) are painted in the chess order (Fig. 1.d). In Fig. 1.d, a grid with 19 nodes of transformers, from which 13 are "black" and 6 are "white" is presented. For the central black node with the number 1 all set of lines of the circuit in Fig. 1.c are marked. For the nodes 2÷7 marked with white circles, five lines are shown. For peripheral black nodes 8÷19 two lines are shown. By analogy with Fig. 1.c, thin lines show orientation of electric fields of two polarizations. All the lines between central nodes in Fig. 1.d have geometrical length Δ with time delay τ. Remarkable feature of the circuit in Fig. 1.d is that 12 pulses outgoing from the black node 1 at the moment $t = n\tau$ come, at the moment $t = (n+1)\tau$, to white nodes 2÷7 and, without reflections but with twice reduced magnitudes, go from them in the directions of peripheral nodes 8÷19, coming to them at the moment $t = (n+2)\tau$. In the circuit in Fig. 1.d, signals are stored only at black nodes (up to 12 pulses at one black node) that enables one to reduce the required memory twice. It is necessary to store only 6 numbers in average on a node in the infinite grid. The calculations on the grid can be carried out in two steps. Suppose that at the moment $t = n\tau$ the pulses-causes incoming at black nodes are known. At the same moment the scattering on the black nodes takes place. The scattering requires 30 operations at a black node, i.e. in average 15 operations at a node for time τ. At the moment $t = (n+1)\tau$, the pulses-effects outgoing from black nodes are interpreted as the pulses-causes incoming at white nodes. After that the same scattering on white nodes requiring 30 operations on a node, i.e. in average 15 operations on a node in time τ is carried out. After the scattering at the moment $t = (n+2)\tau$ the pulses incoming at black nodes become known and the calculations are iterated in the above-stated order. Thus, for two steps the full duration 2τ requires in average 15+15=30 operations at one node. Finally we obtain that given variant of calculations needs in average 15 operations at a node in the time τ. The introduction of boundary conditions should be carried out in specific way for the algorithm with the pulse storing only

at black nodes (Fig. 1.d) unlike it is done for other algorithms. Fig. 2 illustrates forming of various boundary conditions for new 6-parametric algorithm. In Fig. 2.a, a simplified view of the circuits in Fig. 1.b and Fig. 1.c is shown, where central node consisting of transformers intersecting at 6 points A, B, C, D, E, F is marked. The indexing of 12 lines is identical to Fig. 1.c. Consider the cases of the cube in Fig. 2.a with a black or white node is located in the plane of magnetic or electric walls. For example, suppose that white node 2 (Fig. 1.d) is located in the plane of electric wall (metal). Assume that the system of transformers can be divided in certain symmetrical parts. In Fig. 2.b, the case of division of the node in two parts by a metal wall is shown. In this case the lines 1, 3, 6, 8 become shortcut, and the intrinsic impedance for lines 2, 4, 5, 7 decreases twice because of division of them in center by the wall that is normal to electric field. It is easy to find the scattering matrix of the circuit in Fig. 2.b by using the matrix in Fig. 1.b.

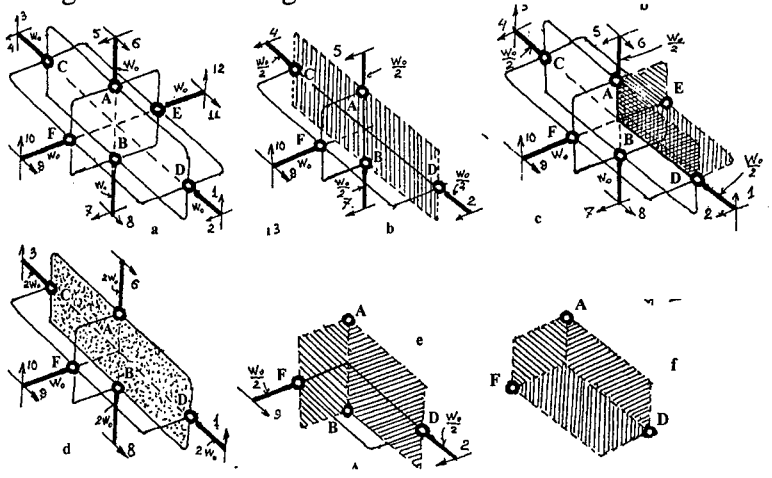

Fig. 2. Boundary conditions.

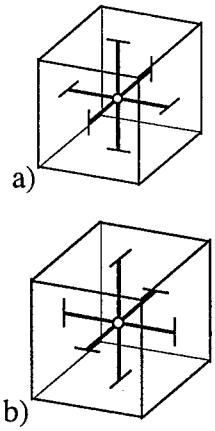

Fig. 3. Groups of ports.

The circuit appears not reflecting at the inputs 8 and 10, only the magnitudes of transmitted waves in lines 2, 4, 5, 7 vary. The total 6-parametric algorithm with step 2τ is developed. Thus the node in Fig. 2.b can be both white and black. The circuit in Fig. 2.c illustrates the case when the node is located at the edge of three metal surfaces forming a protuberant wedge. In this case all the lines are maintained in the circuit. Thus the lines 1,2,5,6,11,12 have intrinsic impedance $W_0/2$. In Fig. 2.d, the case is shown where a node is located on the magnetic wall. In this circuit, only the lines 1, 3, 6, 8 with the intrinsic impedance $2W_0$ are maintained. In Fig. 2.e, the circuit of a concave wedge consisting of two metal surfaces is considered. At the wedge, the lines 9 and 2 with intrinsic impedance $W_0/2$ are maintained only. In Fig. 2.f, the circuit for a concave wedge consisting of three metal surfaces is shown. The transmission lines are absent in such a node. The calculations on the boundaries of the type shown in Fig. 2 slightly complicate the algorithm in boundary areas, not breaking considered 6-parametric algorithm.

ALGORITHM "HALF OF PORTS"

The second variant of 6-parametrical algorithm turns out to be a generalized "chess" method at the inputs of elementary volume. Accordingly, the sub-processes are defined not on two arrays of nodes, but on two arrays of inputs.

Divide 12 pairs of pulses Π_i in the circuit in Fig. 1.b in two groups of 6 pulses according to Fig. 3.a and 3.b. For each side of Δ^3, waves Π_i split in two orthogonal groups. The summary

excitations in Fig. 3.a and 3.b, obviously, are equivalent to excitation in Fig. 1.c. For a mode in Fig. 3.a from (1) we obtain:

$$O_1 = \frac{\Pi_6-\Pi_8+\Pi_{10}+\Pi_{12}}{2} \quad O_2 = 0 \quad O_3 = \frac{-\Pi_6+\Pi_8+\Pi_{10}+\Pi_{12}}{2} \quad O_4 = 0 \quad O_5 = \frac{\Pi_{10}-\Pi_{12}+\Pi_2+\Pi_4}{2} \quad O_6 = 0$$
$$O_7 = \frac{-\Pi_{10}+\Pi_{12}+\Pi_2+\Pi_4}{2} \quad O_8 = 0 \quad O_9 = \frac{\Pi_2-\Pi_4+\Pi_6+\Pi_8}{2} \quad O_{10} = 0 \quad O_{11} = \frac{-\Pi_2+\Pi_4+\Pi_6+\Pi_8}{2} \quad O_{12} = 0 \qquad (2)$$

For a mode in Fig. 3. b from (1) we obtain:

$$O_1 = 0 \quad O_2 = \frac{\Pi_5+\Pi_7+\Pi_9-\Pi_{11}}{2} \quad O_3 = 0 \quad O_4 = \frac{\Pi_5+\Pi_7-\Pi_9+\Pi_{11}}{2} \quad O_5 = 0 \quad O_6 = \frac{\Pi_9+\Pi_{11}+\Pi_1-\Pi_3}{2}$$
$$O_7 = 0 \quad O_8 = \frac{\Pi_9+\Pi_{11}-\Pi_1+\Pi_3}{2} \quad O_9 = 0 \quad O_{10} = \frac{\Pi_1+\Pi_3+\Pi_5-\Pi_7}{2} \quad O_{11} = 0 \quad O_{12} = \frac{\Pi_1+\Pi_3-\Pi_5+\Pi_7}{2} \qquad (3)$$

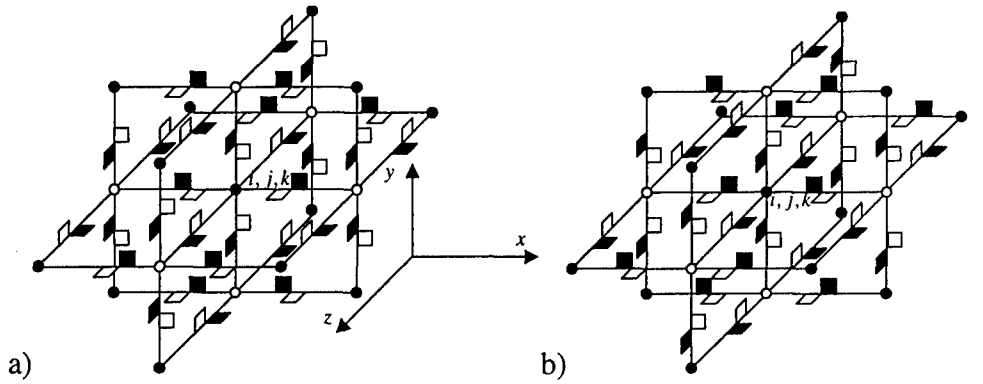

Fig. 4. Groups of pulses.

By analogy with Fig. 1.d on the site Rτ of the grid of 19 nodes (see Fig. 4.a and b) we place two orthogonal arrays of pulses Π_i of 6 on each element of volume Δ^3. For the subsystem of pulses in Fig. 4.a, to the central "black" node i, j, k (node 1 in Fig. 1.d) the pulses come according to the variant of excitation shown in Fig. 3.a. To the neighboring to 6 "white" nodes 2-6 (Fig. 1.d and Fig. 4), the pulses come according to the variant of excitation shown in Fig. 3.b. Pulses in Fig. 4 are marked with rectangles, in whose plane it is located, normally to the lines, a vector of voltage Π_i. To show the direction of propagation, the pulses are shifted respectively to the middle of the dual lines connecting the next nodes of the grid, in the direction of the node to which they propagate. The rectangles of "white" color correspond to the mode of excitation of Fig. 3.a, and rectangles of "black" color to the mode of excitation of Fig. 3.b. In Fig 4, the arrangement of pulses is fixed at the moment of time $t = n\tau$. At this moment of time a half of nodes, in the chess order, begin to be excited by "white" pulses, and the second half by "black" ones. At the next time step $t = (n+1)\tau$, incident to the node i, j, k "white" pulses leave for the next nodes as "black" ones. Thus in the next volumes after the time step the mode in Fig. 3.b will be excited again, i.e. in the grid of Fig. 4.a, the mode shown in Fig. 3.a and 3.b will alternate repeatedly after each step. In Fig. 4.b, the second set of pulses Π_i is presented. To "black" nodes, the pulses come according to (3) (Fig. 3.b), and to "white" nodes they come according to (2) (Fig. 3.a). Two modes of excitation represented in Fig. 4 illustrate an opportunity of division of general excitation (1) Fig. 1.c, in two independent processes, each enabling one to solve the analysis problem. For the mode in Fig. 4.a (as well as for the mode shown in Fig. 4.b), at each node it is necessary to store only 6 numbers (amplitudes of pulses Π_i) and to run 15 arithmetic operations for determining the amplitudes of the scattered pulses O_i, according to (2) for "black" nodes and according to (3) for "white" ones. Thus, all the basic integral characteristics of the analyzed stationary electromagnetic process can be found: error of dispersion of propagation of plane waves in

the Rτ grid are kept [5], structure of fields and phase velocities of all the waves in regular waveguides, parameters of matrices of dispersion of the waveguide devices, etc. If a device is excited from a rectangular waveguide with the wave H_{10}, this wave can be characterized not only by complete system of the Rτ pulses according to (1), and also by a system with a half of pulses.

ALGORITHM "HALF OF PORTS + HALF OF NODES "

Suppose that in the structure of excitation in Fig. 4 the storing of pulses Π_i is done not at all the nodes of the grid but only at a half of nodes. For example, "black" pulses pass through "white" nodes at once up to the next "black" nodes, like for the algorithm "half of nodes". Then the total numbers N_p (memory) and N_o (number of arithmetic operations) in recalculation at one node for one time step decrease twice and turn to be $N_p = 3$ and $N_o = 7.5$. Thus the account of boundary conditions is carried out according to Fig. 2, i.e., metal and magnetic walls should pass through nodes of a grid.

CONCLUSION

It has been found that electromagnetic analysis on the basis of the Rτ grids formed from the stream Rτ operators in vacuum can be carried out without loss of accuracy by using only a half of inputs for each operator, and also with using the "chess" order of operations of storing of amplitudes of pulses. As a result, an average volume of memory and number of arithmetic operations at one node for single time step of calculations become equal to 3 and 7.5, respectively.

REFERENCES

[1] B.V. Sestroretsky. Balance RLC and Rτ-circuits of elementary volume. Problems of radio electronics, ser. "General problems of radio electronics", 1983, vol.5, pp56-85.
[2] W.Y.R. Hoefer. The Transmission Line Matrix Method – Theory and Application. IEEE Trans. Vol. MTT-33,Oct. 1985, pp882-893.
[3] P.B. Johns. Symmetrical condensed node for the TLM method. IEEE Trans. Vol. MTT-35,April 1987, pp370-377.
[4] B.V. Sestroretsky., S.A. Ivanov. A new 6-parametrical 3D algorithm for 12-port symmetrical condensed node. TLM-99, III International Workshop on TLM, Modeling Theory and Applications, October 27-29, 1999, Nice, France, pp. 197-200.
[5] S.A. Ivanov, B.V. Sestroretsky. Dispersion on Plane Waves in 3D Stream Type Grids. MMET-98, VII International Conference on Mathematical Methods in Electromagnetic Theory, June 2-5, 1998, Kharkov, Ukraine, vol.2, pp. 600-602.

AN ELECTROMAGNETIC SIGNAL PROPAGATION IN A TRANSIENT MAGNETIZED PLASMA WITH A TIME-VARYING EXTERNAL MAGNETIC FIELD

Alexander G. Nerukh and Konstantin M. Yemelyanov *

Kharkov Technical University of Radio Electronics,
14 Lenin Ave., Kharkov 61166, Ukraine, E-mail: nerukh@ddan.kharkov.ua

*Kharkov National University
4 Svobody Sq., Kharkov 61077, Ukraine, E-mail: k.yemelyanov@univer.kharkov.ua

ABSTRACT

In this paper, the problem of an electromagnetic wave transformation in unbounded plasma is considered when an external magnetic field changes in time abruptly and the time jumps occur at different moments. A general expression for the transformation of the electromagnetic wave after n jumps in the external magnetic field is obtained.

INTRODUCTION

Consider an electromagnetic field in plasma when the external magnetic field and the plasma density vary in time starting from the zero moment. We consider the external magnetic field being constant between jumps. The problem is formulated as the Volterra integral equation of the second kind and its solution is found by the resolvent method. With the aid of the resolvent the expression for the intensity of the electromagnetic field after the n-th jump in the external magnetic field can be written as:

$$\boldsymbol{E}^{(n)}(t,\boldsymbol{r}) = \boldsymbol{F}^{(n)}(t,\boldsymbol{r}) + \int_0^t dt' \int_\infty d\boldsymbol{r}' \left\langle \boldsymbol{x} \middle| R^{(n)} \middle| \boldsymbol{x}' \right\rangle \boldsymbol{F}^{(n)}(t',\boldsymbol{r}'). \tag{1}$$

The free term of this equation is equal to:

$$\boldsymbol{F}^{(n)}(t,\boldsymbol{r}) = \boldsymbol{F}^{(0)}(t,\boldsymbol{r}) + \sum_{k=1}^{n-1} \int_{t_k}^{t_{k+1}} dt' \int_\infty d\boldsymbol{r}' \left\langle \boldsymbol{x} \middle| \hat{\Gamma} \middle| \boldsymbol{x}' \right\rangle \boldsymbol{P}_r^{(k)}(t',\boldsymbol{r}') + \int_{t_n}^{t} dt' \int_\infty d\boldsymbol{r}' \left\langle \boldsymbol{x} \middle| \hat{\Gamma} \middle| \boldsymbol{x}' \right\rangle \boldsymbol{P}_r^{(n)}(t',\boldsymbol{r}'), \tag{2}$$

where $\left\langle \boldsymbol{x} \middle| \hat{\Gamma} \middle| \boldsymbol{x}' \right\rangle = \left(\nabla\nabla - \frac{1}{c^2}\frac{\partial^2}{\partial t^2} \right) \frac{\delta\left(t - t' - |\boldsymbol{r} - \boldsymbol{r}'|/c\right)}{|\boldsymbol{r} - \boldsymbol{r}'|}$, c is the velocity of light, $\delta(t)$ is a Dirac delta function, and $\boldsymbol{x} = (t,\boldsymbol{r})$ denotes the time-spatial four-vector.

The first term in (2) takes into account only the prehistory of the electromagnetic field interaction with the plasma until the beginning of the change in the magnetic field, the other terms describe after-effects caused by the external magnetic field jumps.

The polarization vector $\boldsymbol{P}^{(n)}$ is determined by the following relations:

$$\boldsymbol{P}^{(n)}(t) = \boldsymbol{P}_r^{(n)}(t) + \frac{\omega_e^2}{4\pi} \int_{t_n}^{t} \hat{\alpha}^{(n)}(t - t') \boldsymbol{E}^{(n)}(t') dt', \tag{3}$$

$$\boldsymbol{P}_r^{(n)}(t) = \boldsymbol{P}^{(n-1)}(t_{n-1}) + \hat{\alpha}^{(n)}(t - t_{n-1}) \frac{d\boldsymbol{P}^{(n-1)}(t_{n-1})}{dt}, \quad \boldsymbol{P}_r^{(0)} = 0,$$

where $\omega_e^2 = 4\pi e^2 n/m$ is the plasma frequency, $\hat{\alpha}$ is the susceptibility tensor, t_n is the moment of the n-th jump in the external magnetic field.

The expression for the resolvent operator of the problem $R^{(n)}$ is presented in [1]. It should be noted that the expression for the resolvent for the sequence of jumps is the same as the resolvent for a single jump in the external magnetic field if the Larmor frequency Ω is changed from step to step.

TRANSFORMATION OF A PLANE WAVE

Consider the initial field as a plane wave: $\boldsymbol{E}_0(t,\boldsymbol{r}) = \boldsymbol{E}_0 \exp[i(\omega t - \boldsymbol{sr})]$, where $s^2 = (\omega^2 - \omega_e^2)/c^2$. Suppose that it exists till the switching on of the external magnetic field. Let us consider that the transformations of the wave are made for a single jump in the magnetic field. For this case a general expression which determines the transformed electromagnetic field for an arbitrary orientation of the external magnetic field is obtained [1]. This expression is a bulky one so we do not write it here. It is interesting to investigate two special cases of the mutual orientation of the magnetic field $\boldsymbol{B}_0$ and the wave vector $\boldsymbol{s}$.

1. The external magnetic field $\boldsymbol{B}_0$ is orientated along the propagation direction of the primary wave, i.e. $\boldsymbol{b} \parallel \boldsymbol{s} = \{0,0,s\}$, $\boldsymbol{E}_0 = \{E_0,0,0\}$. In this case, the electromagnetic field is defined by the following expression:

$$\boldsymbol{E}^{(1)}(t,\boldsymbol{r}) = \int_{-i\infty}^{i\infty} \frac{dp}{2\pi i} \frac{e^{pt-isr}}{\omega H(p)} \left\{\omega(p+i\omega)Q^{(1)}(p) - i\omega_e^2\Omega^2(p^2+c^2s^2),\ -i\omega_e^2\Omega\, p^2(p+i\omega),\ 0\right\}, \quad (4)$$

where $H(p) = p^2(p^2+\omega^2)^2 + \Omega^2(p^2+c^2s^2)^2$, $Q^{(1)}(p) = p^4 + (\omega^2+\Omega^2)p^2 + \Omega^2c^2s^2$.

The analysis of (4) enables to conclude that the transformed electric field consists of three pairs of waves with the frequencies p_k, which are the roots of the polynomial $H(p)$ (see Fig. 1). Waves in each pair remain transversal, preserve the wave vector $\boldsymbol{s}$, and propagate in the opposite directions.

2. The external magnetic field is switched on normally to the wave vector, i.e. $\boldsymbol{b} \perp \boldsymbol{s} = \{s,0,0\}$, $\boldsymbol{E}_0 = \{0, E_2, E_3\}$. Then, the transformed electric field will be determined by the expression

$$\boldsymbol{E}^{(1)}(t,\boldsymbol{r}) = \boldsymbol{E}_{\parallel}^{(1)} \exp[i(\omega t - \boldsymbol{sr})] + \sum_{m=0}^{1}\sum_{k=1}^{2} \boldsymbol{E}_{\perp mk}^{(1)} \frac{\exp((-1)^m i\omega_k t - i\boldsymbol{sr})}{\omega Q^{(2)}((-1)^m i\omega_k)}, \quad (5)$$

where $\boldsymbol{E}_{\parallel}^{(1)} = \{0,\ 0,\ E_3\}$ is directed along the magnetic field and is the same as the primary wave,

$$\boldsymbol{E}_{\perp mk}^{(1)} = \left\{-\Omega\omega_e^2((-1)^m\omega_k + \omega),\ i\omega((-1)^m\omega_k + \omega)(-\omega_k^2 + \omega_e^2 + \Omega^2) - i\Omega^2\omega_e^2,\ 0\right\}E_2,$$

$$Q^{(2)}(p) = \omega_k^4 - \omega_k^2(\omega^2 + \omega_e^2 + \Omega^2) + \omega^2\omega_e^2 + \Omega^2c^2s^2.$$

The new frequencies are defined as:

$$\omega_k^2 = \frac{1}{2}\left(\omega^2 + \omega_e^2 + \Omega^2 + (-1)^{k-1}\sqrt{(\omega^2 - \omega_e^2 - \Omega^2)^2 + 4\omega_e^2\Omega^2}\right), \quad (6)$$

and presented in Fig. 2.

In this case, the component of the primary electric vector parallel to $\boldsymbol{b}$ is not changed. The component normal to $\boldsymbol{b}$ forms two pairs of waves with the frequencies $\pm\omega_k$. These waves have both longitudinal and transversal components and correspond to the fast and the slow extraordinary waves, respectively.

TRANSFORMATION OF THE PLASMA OSCILLATIONS

Substituting $\omega = \omega_e$ in (4) yields the transformation of plasma oscillations when the external magnetic field is switched on at the zero moment and its vector $\boldsymbol{b}$ is normal to the electric field in the plasma oscillations. The latter transforms into two elliptically polarized oscillations:

$$\boldsymbol{E}^{(1)}(t) = \sum_{k=1}^{2} \frac{E_0}{2(\omega_e^2 - \omega_k^2) + \Omega^2} \left\{ (\omega_e^2 - \omega_k^2 + \Omega^2)\cos\omega_k t,\ \frac{\omega_e^2 \Omega}{\omega_k}\sin\omega_k t,\ 0 \right\} \tag{9}$$

where $\omega_k^2 = \frac{1}{2}\left(2\omega_e^2 + \Omega^2 + (-1)^{k-1}\Omega\sqrt{4\omega_e^2 + \Omega^2}\right)$.

In the case of a weak magnetic field: $\Omega << \omega_e$, the both types of oscillations are almost circularly polarized and have the frequencies $\omega_k{}^2 \approx \omega_e{}^2 \pm \omega_k \Omega$, which are slightly different from each other. In the case of a strong magnetic field: $\Omega >> \omega_e$, the oscillation with the frequency $\omega_1 \approx \Omega$ will be a circularly polarized cyclotron oscillation with a small amplitude: The other oscillation will have the frequency $\omega_2{}^2 \approx \omega_e{}^4 / \Omega_1{}^2$ and almost linear polarization. When the external magnetic field is parallel to the electric field of the plasma oscillations, i.e. $\boldsymbol{b} \parallel \boldsymbol{E}_0 = \{E_0, 0, 0\}$, the latter are not changed as it follows from (5), (6).

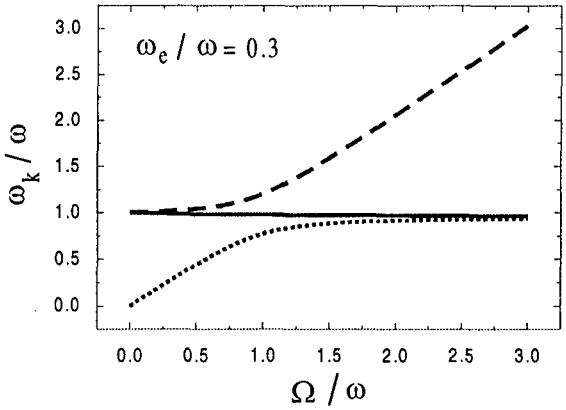

Figure 1. New frequencies in the case when the external magnetic field is orientated along the propagation direction of the primary wave ($\boldsymbol{b} \parallel \boldsymbol{s}$).

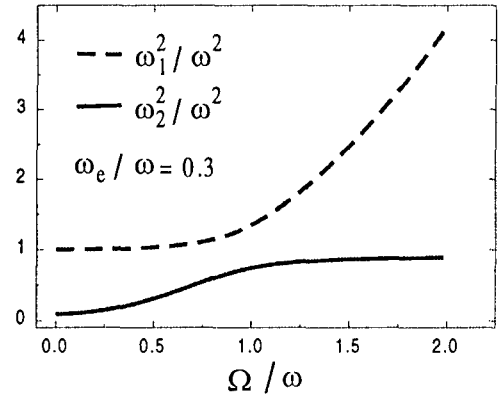

Figure 2. New frequencies in the case when the external magnetic field is normal to the direction of the primary wave $\boldsymbol{b} \perp \boldsymbol{s}$.

CONCLUSION

In this paper, a solution to the problem of electromagnetic wave propagation in a plasma with a time-varying magnetic field has been obtained. The method which is used allows to consider the simultaneous changes in the external magnetic field as well as in the plasma density. The transformation of the primary plane wave and plasma oscillations with respect to arbitrary orientated external magnetic field has been considered.

REFERENCES

[1] A.G. Nerukh, K.M. Yemelyanov, Journal of Applied Electromagnetism, Vol. 2, No 3, pp. 51–64, 1999.

COMPUTATIONAL TECHNIQUES

NUMERICAL ANALYSIS OF SCATTERING IN 2-D SPACE BY WAVE EQUATION-BASED FDTD METHOD

Koichi Ichige†, Yutaka Uchimura and Hiroyuki Arai

Division of Electrical and Computer Engineering,
Yokohama National University, Yokohama, Japan
†E-mail: koichi@dnj.ynu.ac.jp

ABSTRACT

This paper presents the novel concept of the condensed node FDTD method. The previous approach by the same authors can update only E_z of 2-D TM mode, and cannot update H_x and H_y. This paper studies to update such components. Moreover, the proposed algorithm is evaluated in comparison with Yee's FDTD method.

INTRODUCTION

It is well-known that Yee's Finite-Difference Time-Domain (FDTD) method [1] is obtained by applying the mid-point method to Maxwell's equations. Since Maxwell's equations are first-order simultaneous differential equations, the application of the mid-point method causes a half cell length and a half time-step distances between electric and magnetic filed components. The distances do not matter by Yee's spatial arrangement of field components, and this considerable arrangement causes the widespread use of his algorithm. However, it would be more adequate if any approximation does not derive such distances. Actually it is natural to evaluate all the components at the same discrete points.

To solve such problem, some efficient FDTD algorithms have been already proposed based on the finite-difference approximation of wave equation by mid-point method [2]. Those algorithms enable to update only the electric component E_z independently without calculating magnetic components H_x and H_y in the case of 2-D TM mode. However, they cannot analyze the spaces including magnetic objects like magnetic walls, since the algorithms are given as the finite-difference equation of only E_z, excluding H_x and H_y.

The present authors have proposed an algorithm which enables to update the electric component E_z when the analyzed field includes magnetic walls [3]. The remaining problem is to update the magnetic components H_x and H_y when electric and magnetic walls are placed. This paper tries to update such magnetic components. The proposed algorithm is mainly based on the Huang's wave equation approach, and partially based on the finite-difference approximation of Maxwell's equation by the trapezoid method. The proposed method can establish the condensed node 2-D FDTD method while the computation time is almost as much as Yee's FDTD method. The following sections describes the case of 2-D TM mode, however, they can be easily applied to 2-D TE mode case.

PROPOSED APPROACH

The way to update the magnetic component H_x is as follows. The proposed algorithm is mainly based on the finite-difference approximation of wave equation by the mid-point method:

$$H_x^{n+1}(i,j) = 2H_x^n(i,j) - H_x^{n-1}(i,j) + \left(\frac{c\Delta t}{\Delta x}\right)^2 \{H_x^n(i+1,j) - 2H_x^n(i,j) + H_x^n(i-1,j)\} + \left(\frac{c\Delta t}{\Delta y}\right)^2 \{H_x^n(i,j+1) - 2H_x^n(i,j) + H_x^n(i,j-1)\}, \quad (1)$$

where $E_z^n(i,j)$ denotes the component E_z at the point $(i\Delta x, j\Delta y)$ when $t = n\Delta t$. The parameter c denotes the speed of light in a vacuum. Note that (1) can be applied only when H_x can be regarded to be continuous at the five points $(i\Delta x, j\Delta y)$, $((i\pm 1)\Delta x, j\Delta y)$ and $(i\Delta x, (j\pm 1)\Delta y)$. In the case H_x is discontinuous at any of those points, the following equations are applied instead of (1).

$$\begin{aligned} H_x^{n+1}(i,j) &= -H_x^{n+1}(i,j+1) + H_x^n(i,j+1) + H_x^n(i,j) \\ &\quad -\frac{\Delta t}{\mu\Delta y}\{E_z^{n+1}(i,j+1) - E_z^{n+1}(i,j) + E_z^n(i,j+1) - E_z^n(i,j)\}, \qquad (2) \\ H_x^{n+1}(i,j) &= -H_x^{n+1}(i,j-1) + H_x^n(i,j) + H_x^n(i,j-1) \\ &\quad -\frac{\Delta t}{\mu\Delta y}\{E_z^{n+1}(i,j) - E_z^{n+1}(i,j-1) + E_z^n(i,j) - E_z^n(i,j-1)\}, \qquad (3) \end{aligned}$$

where μ denotes the permeability. The equations (2) and (3) is derived by the finite-difference approximation of Maxwell's equation by trapezoid method.

For example, suppose the electric wall of length L is placed along the x-axis in a 2-D free space, as the electric wall B of Fig. 1. The condition of this wall is given as

$$E_z(i,j) = 0, \quad i = I, I+1, \ldots, I+L, \ j = J. \qquad (4)$$

In this case, the behavior of H_x becomes discontinuous around the wall. Here we assume the two magnetic values $H_x(i,J_+)$ and $H_x(i,J_-)$ at the point $(i\Delta x, J\Delta y)$ for $i = I, I+1, \ldots, I+L$, where $H_x(I,J_\pm) = \lim_{j\to J\pm 0} H_x(I,j)$. Then the components H_x around the wall are undated by the following procedure.

1. $H_x(i,J_+)$ and $H_x(i,J_-)$, $i = I, I+1, \ldots, I+L$ are updated by (2) and (3) respectively, while $H_x(I+1,J)$ and $H_x(I-1,J)$ should be updated by (1) in advance.
2. $H_x(I-1,J)$ is updated by (1), however, $H_x(I,J)$ is replaced by the average $\{H_x(I,J_+) + H_x(I,J_-)\}/2$. $H_x(I+L+1,J)$ can be updated similarly.

The components around the other walls are updated similarly, however the space does not permit to describe them in detail. Overall, (1) is generally applied, and (2) and (3) are partially applied due to the discontinuity of H_x. Also, the component H_y can be updated in a same manner.

SIMULATION

The proposed algorithm is evaluated in comparison with Yee's FDTD method by analyzing a simple field of free space with electric and magnetic walls. The field is drawn as Fig. 1. Electric and magnetic walls are placed to surround the feed point, 25mm away from the boundary. Specifications of the simulation is shown in Table 1.

Figure 2 shows the behavior of the magnetic component H_x in dB. Note that the values below -100dB are replaced by -100dB for the illustration. Figure 2 shows that the proposed method works almost the same with Yee's FDTD method, except the right side of the magnetic wall B. This is because FDTD method deal the magnetic walls one cell longer than the original (Space does not permit to prove this fact).

CONCLUDING REMARKS

This paper presented the novel concept of the condensed node FDTD method, mainly based on the finite-difference approximation of wave equation (1) and partially based on the trapezoid approximation (2) and (3). The proposed realize more accurate analysis than Yee's FDTD method. Although only the 2-D TM mode case is described, the 2-D TE mode case can be easily analyzed by replacing E_z, H_x and H_y by H_z, E_x and E_y, respectively.

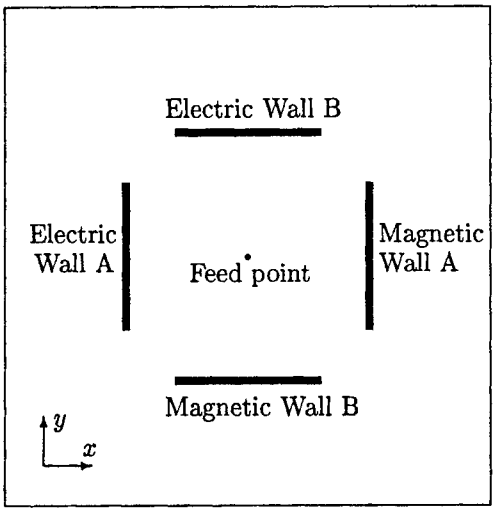

Figure 1: The analyzed field

Table 1: Specifications of the simulation

Field size	100mm × 100mm
Feed point	Center of the field
Length of each wall	30mm
Cell size $\Delta x, \Delta y$	1mm
Time step Δt	$\Delta x/c\sqrt{2}$
Boundary condition	Mur's 2nd-order
Incident voltage	Gaussian pulse, $E_z^n = e^{-\alpha(n-\beta)^2}$, $\beta = 32, \alpha = 4\beta^{-2}$

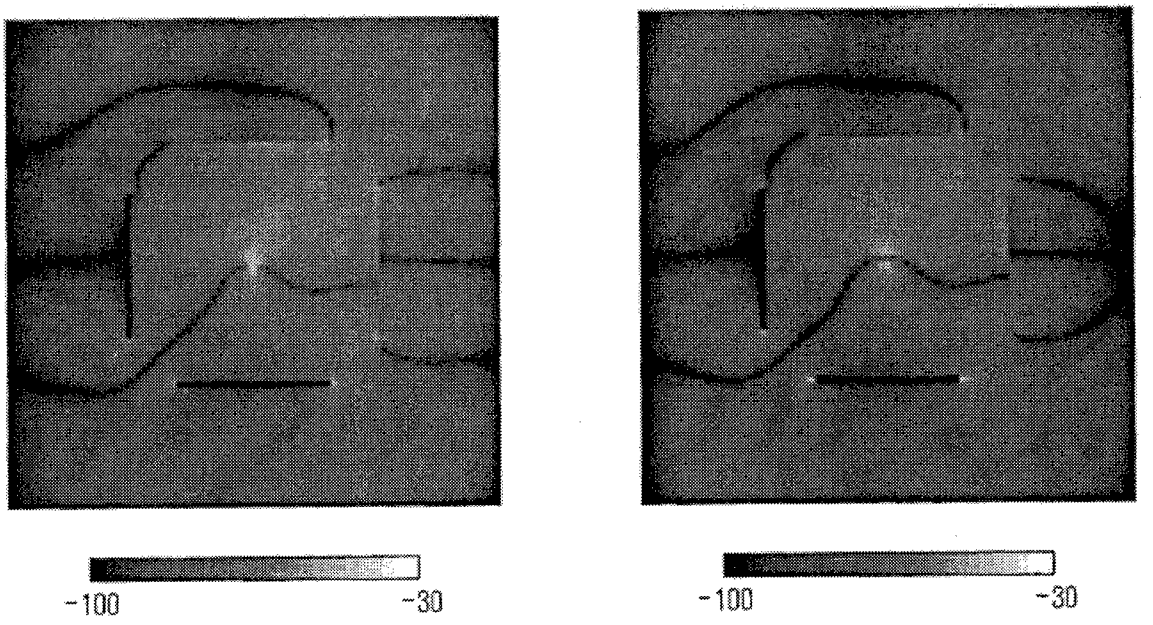

(a) Yee's FDTD method (b) Proposed method

Figure 2: Behavior of $20\log_{10}|H_x|$ in the case $t = 100\Delta t$ ($t = 100.5\Delta t$ in the FDTD method).

REFERENCE

[1] K. S. Yee: "Numerical Solution of Initial Boundary Value Problems Involving Maxwell's Equations in Isotropic Media," *IEEE Trans. Antennas and Propagation*, vol. 14, no. 4, pp. 302–307, Apr. 1966.

[2] W. P. Huang, S. T. Chu and S. K. Chaudhuri: "A Semivectorial Finite-Difference Time-Domain Method," *IEEE Photonics Technology Letters*, vol. 3, no. 9, Sep. 1991.

[3] K. Ichige and H. Arai, "An Efficient Algorithm of 2-D FDTD Method Based on Finite-Difference Approximation of Wave Equation," *Proc. Int'l Sympo. on Antennas and Propagation*, 1F4-3, Fukuoka, Japan, Aug. 2000.

INVESTIGATION AND OPTIMIZATION OF A WAVEGUIDE SLOT ANTENNA ARRAY BY FINITE-DIFFERENCE TIME-DOMAIN METHOD

S. Martynyuk
Dept. of Radio-Engineering of National Technical University of Ukraine (Kiev).

INTRODUCTION

Classical planar waveguide slot antenna arrays are well-known and widely used in frequency range from 4 to 14 GHz. Among advantages of this type of antennas are low level of cross-polarisation (-35 dB or better is achievable), high levels of radiated power, low losses and simplicity. The main problem is that due to the resonant nature of the slots and their serial fed in waveguide the frequency band of this arrays are usually limited by several percents. Often different tuning posts, E-plane shorted stubs and metal plates are applied to obtain improvement of characteristics in frequency range. Method of moments (MoM) was used before to analyse such arrays. But MoM can be hardly implemented in the cases, when more complicated waveguide structures together with radiating slots are to be studied. In this paper finite difference time domain method (FDTD) method was used. Due to it's high flexibility it gives the opportunity to investigate different complex structures accurately and at a high speed. Coupling between slots through the free space and waveguide and the coupling between slots and waveguide's discontinuities are taken into account.

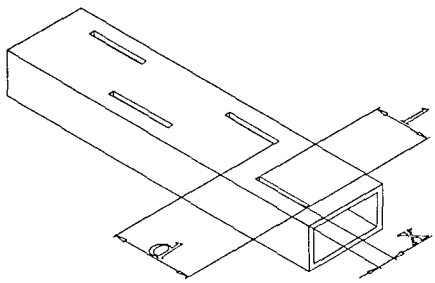

Fig. 1.

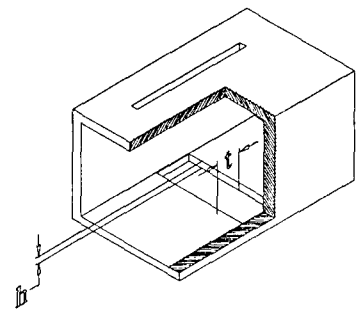

Fig. 2.

GEOMETRY DESCRIPTION

Section of rectangular waveguide with narrow longitudinal radiated slots in broad wall are investigated in this paper (fig 1). The length of slots l is usually near to the half of wavelength in free space at the desired frequency. Slots are assumed to be with 180 degree phase shift and placed at the distance d equal to the half of wavelength in waveguide to radiate in phase in the far zone.

FDTD APPLICATION

FDTD method was firstly proposed in [1] and its backgrounds are not discussed here. When one analyse radiated slots in waveguide, the computational domain is obviously subdivided into two parts. The first is free space above waveguide. Here it is limited by perfectly match layer (PML) [2]. The second domain is the space inside the rectangular waveguide. Here impedance boundary conditions (IBC) [3] were used at the input and output planes of waveguide to excite and terminate propagating modes in waveguide. If the discontinuity in waveguide is situated far from the IBC only mode TE10 in rectangular waveguide can be taken into account to obtain accurate results of S-parameters in waveguide. The value of impedance of IBC is chosen equal to the characteristic impedance in waveguide

at the frequency, where the radiation pattern is calculated. This way avoid the reflections from the ports in waveguide that can lead to the distorted values of radiated pattern. At the other frequencies we are interested only in the S-parameters of waveguide sections and radiating P-parameter (1), that indicates the radiated part of input power.

$$P = 1 - |S11|^2 - |S21|^2 \qquad (1)$$

For the calculation of radiation pattern standard near-to-far zone transformation in frequency domain is used for the plain close to the outer metal plane of waveguide.

NUMERICAL REZULTS

At first the properties of a single longitudinal slot at the wide wall of rectangular waveguide (cross-sections dimensions 23x11 mm) were investigated. Fig. 3. shows the family of characteristics of P-parameters for the slot with the length $l = 14{,}7mm$, width $1mm$ and a different displacements x ,that vary from 11 to 6.8 mm with a step 0.7 mm (the higher curve corresponds to the lower value of displacement x). In Fig. 4 one can see the similar family for the slot of length $l = 12mm$, width $1mm$ and the various displacements x ranged from 8 to 2,4 with step 1,4 mm. In this case two propagating modes were taken into account (TE10, TE20). As it seen from figures at the resonant frequencies the radiated efficiency P increase. The slots with smaller length in waveguide of fixed cross-sectional dimensions and displacement x at the resonant frequencies have smaller values of parameter P. The characteristic of reflection (S11) for each slot also has maximum, which appears at the frequency close to the resonant frequency of P-parameter. This fact is very important for the slot antenna arrays, in which the slots placed at distance equal to the half of wavelength in waveguide, because the reflections from all slots added producing high level of VSWR.

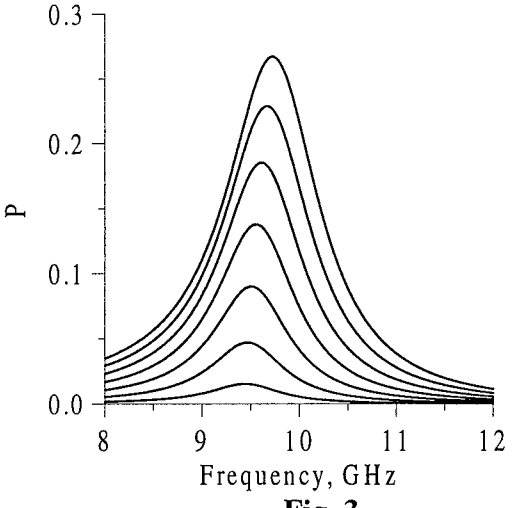

Fig. 3.

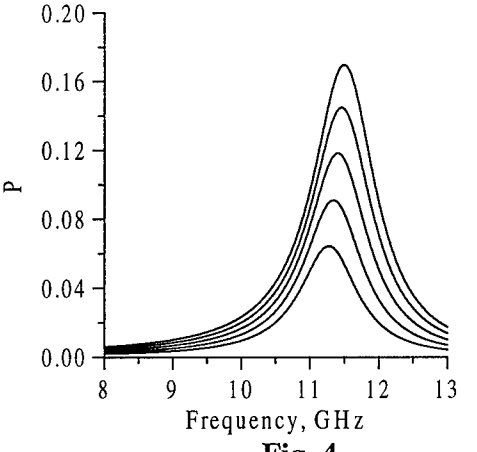

Fig. 4.

As an example four slot antenna array was calculated. It consists of equal transverse slots of length 14,4 mm with width 1mm and displacement $x = 7.6mm$. Distance between slots was 22,4 mm ($\lambda / 2$ for the waveguide with cross-sectional dimensions 23x11 mm at the frequency 9,42 GHz). The radiation pattern at the frequency 9,42 GHz both in H- and E-planes are given in Fig. 5. S and P parameters are presented in Fig. 6. The value of S11 at the 9,42 GHz exceed 0.26 even for the relatively short array.

To decrease the S11 the waveguide slot section with E-plane shorted stub is analysed (Fig. 2). The shorted E-plane stub is used to compensate reflections from a single radiating slot (l=13,4 mm, x=4,9 mm, width=1mm) in waveguide (23x5 mm). The E-plane stub's width

is 2mm and it's depth is 4mm. Values of S11 for the single slot structure with stub and without it is shown in Fig 7. It should be noted that the normalised radiation pattern for the single slots in examined cases was almost the same as demonstrated in Fig. 8.

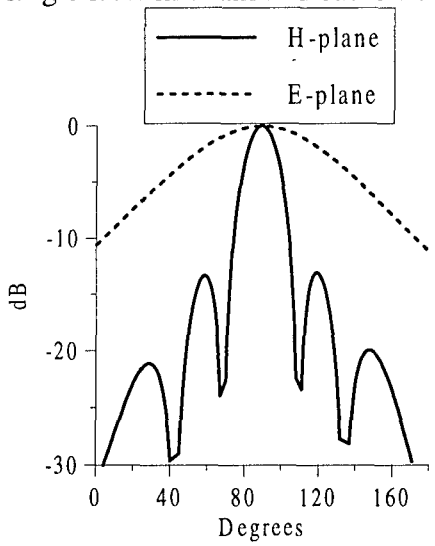

Fig. 5

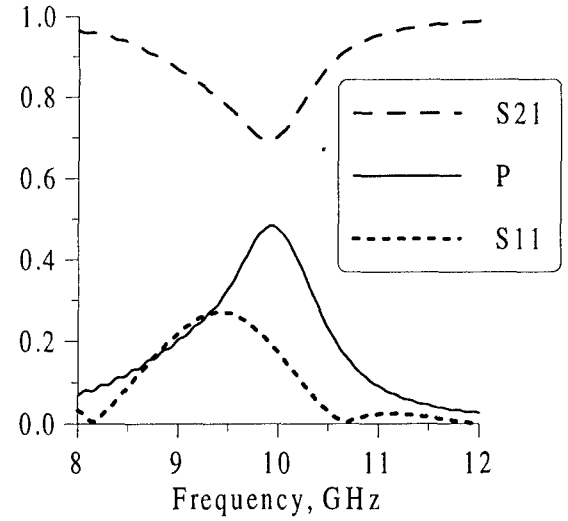

Fig. 6.

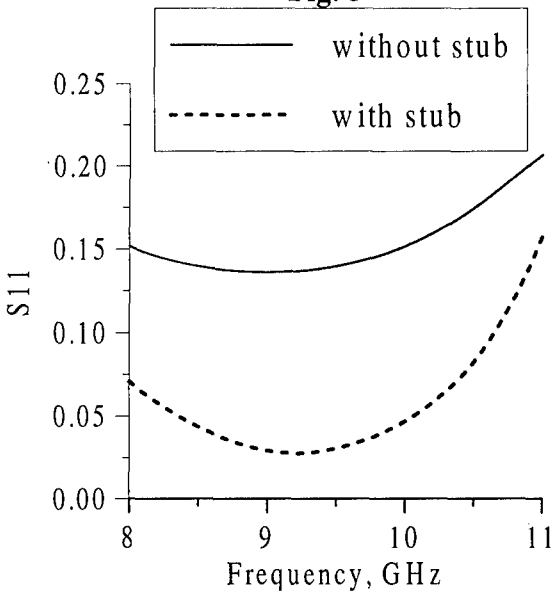

Fig. 7.

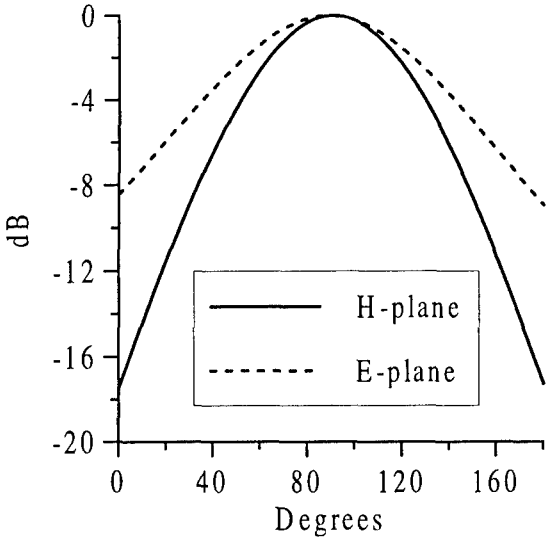

Fig. 8.

REFERENCES

[1]. K.S. Yee. Numerical Solution of Initial Boundary Value Problems Involving Maxwell's Equations // IEEE Trans. on AP, Vol. AP-14, pp. 302-307, May 1966.

[2]. J.P. Berenger, Perfectly Matched Layer For The Absorption of electromagnetic waves // J. Comput. Phys., vol 114, pp. 185-300, Aug. 1994.

[3]. T. Shibata, T. Itoh. Generalized-Scattreing-Matrix-Modelling of Waveguide Circuits Using FDTD Simulations.// IEEE Trans. on MTT, vol.46, No. 11,pp. 1742-1751, November 1988.

QUASI-MINIMAL RESIDUAL METHOD IN ELECTROMAGNETIC SCATTERING

Alexander B. Samokhin, Yuri U. Kapustin

Moscow Institute of Radiotechnics, Electronics and Automatics, Russia
E-mail: alex@samohin.dnttm.rssi.ru

INTRODUCTION

We consider a wide range of electromagnetic (EM) scattering problems on finite inhomogeneous bodies characterized by general $\hat{\varepsilon}(x)$ and $\hat{\mu}(x)$. A system of singular integral equations over the domain of inhomogeneity is used to formulate the problem. An iterative quasi-minimal residual procedure is applied to solve the operator equation.

STATEMENT OF THE PROBLEM

Let arbitrary tensor functions $\hat{\varepsilon}(x)$ and $\hat{\mu}(x)$ equal $\varepsilon_0\hat{I}$ and $\mu_0\hat{I}$ outside finite domain $Q \subset E_3$. According [1], the problem of EM scattering by Q can be described by the following system of singular integral equations:

$$\begin{aligned}
&\mathbf{E}(x) = \mathbf{E}^{(0)}(x) - \tfrac{1}{3}\left(\tfrac{\hat{\varepsilon}(x)}{\varepsilon_0} - \hat{I}\right)\mathbf{E}(x) + k_0^2 \int_Q \left(\tfrac{\hat{\varepsilon}(y)}{\varepsilon_0} - \hat{I}\right)\mathbf{E}(y)G(r)dy + \\
&+ V.p.\int_Q \left\langle \left(\tfrac{\hat{\varepsilon}(y)}{\varepsilon_0} - \hat{I}\right)\mathbf{E}(y), \nabla_x \right\rangle \nabla_x G(r)dy + i\omega\mu_0 \int_Q \left[\left(\tfrac{\hat{\mu}(y)}{\mu_0} - \hat{I}\right)\mathbf{H}(y), \nabla_x\right] G(r)dy \\
&\mathbf{H}(x) = \mathbf{H}^{(0)}(x) - \tfrac{1}{3}\left(\tfrac{\hat{\mu}(x)}{\mu_0} - \hat{I}\right)\mathbf{H}(x) + k_0^2 \int_Q \left(\tfrac{\hat{\mu}(y)}{\mu_0} - \hat{I}\right)\mathbf{H}(y)G(r)dy + \\
&+ V.p.\int_Q \left\langle \left(\tfrac{\hat{\mu}(y)}{\mu_0} - \hat{I}\right)\mathbf{H}(y), \nabla_x \right\rangle \nabla_x G(r)dy - i\omega\varepsilon_0 \int_Q \left[\left(\tfrac{\hat{\varepsilon}(y)}{\varepsilon_0} - \hat{I}\right)\mathbf{E}(y), \nabla_x\right] G(r)dy
\end{aligned} \tag{1}$$

where $G(r) = \exp(-ikr)/4\pi r$.

ITERATIVE METHOD

Consider a general system in Hilbert space H with continuous linear operator:

$$\hat{A}u = f \tag{2}$$

where $\hat{A}$ can be, for example, the result of discretization of (1) or operator (1) itself. If $\hat{A}$ satisfies coercitivity condition, then solution of (2) exists, is unique and can be found with the multistep minimal discrepancies method (MMD) [2]:

$$
\begin{aligned}
&u_n^{(0)} = u_n, \quad v_1 = h_n^{(0)} = \hat{A}u_n^{(0)} - f, \\
&h_n^{(l)} = h_n^{(l-1)} - \tau_l w_l, \quad u_n^{(l)} = u_n^{(l-1)} - \tau_l v_l, \quad l = \overline{1,m}, \\
&w_1 = \hat{A}v_1, \quad w_l = \hat{A}h_n^{(l-1)} - \sum_{k=1}^{l-1} \alpha_{lk} w_k, \quad v_l = h_n^{(l-1)} - \sum_{k=1}^{l-1} \alpha_{lk} v_k, \quad l = \overline{2,m}, \\
&\tau_l = \left\langle h_n^{(l-1)}, \hat{A}h_n^{(l-1)} \right\rangle \Big/ \|w_l\|^2, \quad \alpha_{lk} = \left\langle \hat{A}h_n^{(l-1)}, w_k \right\rangle \Big/ \|w_k\|^2 \\
&u_{n+1} = u_n^{(m)}
\end{aligned}
\tag{3}
$$

Effective application of (3) in scattering problems, characterized by electrically dense media or large domain volume, may require large values for m. For instance, let f is a sum of k eigenfunctions of $\hat{A}$ corresponding to different eigenvalues and $u_0 = f$. Then, from the fact that the span of $\hat{A}h_0, \ldots, \hat{A}^k h_0$ coincides with a space based on eigenfunctions, it is obvious that $m = k$ gives exact solution within k iterations. For $m < k$, the number of iterations may greatly exceed k. Algorithm (3) with non-fixed m is often referred to as *complete GMRES*, whose practical application is essentially determined by available memory and CPU resources, since for each iteration number L calculation of the iteration requires storage and processing of L vectors v_l.

An iterative method described below is based on the idea of biorthogonalization [4]. Variation iterative methods, such as MMD, can be represented as follows:

$$u_k = u_0 - \sum_{l=1}^{k} \tau_l^{(k)} \hat{A}^{l-1} h_0 , \tag{4}$$

where $u_k \to u$ and $\tau_l^{(k)} \to \tau_l$ as $k \to \infty$. Parameters $\tau_l^{(k)}$ differ for various iterative methods, but have the same limits.

Let introduce the following sequence

$$\hat{A}v_1 = \hat{A}h_0, \quad \hat{A}v_l = \hat{A}^l h_0 + b_{l-1}^{(l)} \hat{A}^{l-1} h_0 + \ldots + b_1^{(l)} \hat{A}h_0, \quad l = \overline{2,N}, \tag{5}$$

where $b_i^{(l)}$ are complex parameters. Since subspace based on $\left\{\hat{A}v_l\right\}_{l=1}^{N}$ does not depend on $b_i^{(l)}$, we can write $h_0 = \sum_{l=1}^{N} \tau_l \hat{A}^l h_0 = \sum_{l=1}^{N} \gamma_l \hat{A}v_l$ and define the sequence $u_k = u_0 - \sum_{l=1}^{k} \gamma_l v_l = u_{k-1} - \gamma_k v_k$.

Let $q_1 \in H$ is an arbitrary vector and $p_1 = \hat{A}v_1 \equiv \hat{A}h_0$. According [3], [4] we define

$$
\begin{aligned}
&p_2 = \hat{A}p_1 - \alpha_1 p_1, \quad q_2 = \hat{A}^* q_1 - \overline{\alpha}_1 q_1 \\
&p_{l+1} = \hat{A}p_l - \alpha_l p_l - \beta_l p_{l-1} \\
&q_{l+1} = \hat{A}^* q_l - \overline{\alpha}_l q_l - \overline{\beta}_l q_{l-1} \\
&\alpha_l = \left\langle \hat{A}p_l, q_l \right\rangle \Big/ \left\langle p_l, q_l \right\rangle, \quad l = 1,2,\ldots \\
&\beta_l = \left\langle p_l, q_l \right\rangle \Big/ \left\langle p_{l-1}, q_{l-1} \right\rangle, \quad l = 2,\ldots
\end{aligned}
\tag{6}
$$

so that vectors $p_l = \hat{A}v_l$ and q_n satisfy biorthogonal condition $\left\langle p_l, q_n \right\rangle = \left\langle p_l, q_l \right\rangle \delta_{ln}$. Therefore, parameters γ_l and vectors v_l can be calculated as follows:

$$\gamma_l = \langle h_0, q_l \rangle / \langle p_l, q_l \rangle$$
$$v_1 = h_0, \quad v_2 = Av_1 - \alpha_1 v_1 \tag{7}$$
$$v_{l+1} = Av_l - \alpha_l v_l - \beta_l v_{l-1}$$

Iterative procedure (6)-(7) has the two features very important for applications. (1) If the number of terms k in expansion of f is finite (which is the case for finite algebraic systems), then iteration $k = N$ will give exact solution; (2) increase of N does not require more memory. Unlike MMD, the described method does not assure that discrepancies steadily decrease to zero. Nevertheless, for a wide range of problems, the number of iterations (6)-(7) is essentially smaller than in MMD in the case of $m < N$. For this reason, iterative method (6)-(7) is known as quasi-minimal residual method (QMR). With respect to scattering problems, the number of iterations in MMD and QMR are determined solely by operator $\hat{A}$. Hence, neither discretization method, nor collocation density or the number of basis functions has an essential impact.

For QMR method it is possible, however, that for some r vectors p_r and q_r become orthogonal while the entire iterative procedure is not completed. It is possible to show [4] that such situations are rather rare and can be excluded by appropriate choice of vectors p_0, q_0.

Operator (1) of scattering problems is not self-conjugate, but satisfies condition

$$\hat{A}^* = \overline{\hat{A}}. \tag{8}$$

Assuming $q_1 = \overline{p}_1 \equiv \overline{Ah_0}$ we have $q_l = \overline{p}_l$, and QMR procedure can be simplified:

$$h_0 = \hat{A}u_0 - f, \quad p_1 = \hat{A}h_0, \quad v_1 = h_0,$$
$$p_2 = \hat{A}p_1 - \alpha_1 p_1, \quad v_2 = \hat{A}v_1 - \alpha_1 v_1$$
$$p_{l+1} = \hat{A}p_l - \alpha_l p_l - \beta_l p_{l-1}$$
$$v_{l+1} = \hat{A}v_l - \alpha_l v_l - \beta_l v_{l-1} \tag{9}$$
$$\alpha_l = \langle \hat{A}p_l, \overline{p}_l \rangle / \langle p_l, \overline{p}_l \rangle, \quad \beta_l = \langle p_l, \overline{p}_l \rangle / \langle p_{l-1}, \overline{p}_{l-1} \rangle$$
$$\gamma_l = \langle h_0, \overline{p}_l \rangle / \langle p_l, \overline{p}_l \rangle, \quad u_l = u_{l-1} - \gamma_l v_l, \quad l = 1,2,\ldots$$

REFERENCES

[1] A.B. Samokhin, Y.U. Kapustin, "Mathematical Modeling of Electromagnetic Scattering Problems", Proceedings of MMET'1998, pp. 618-620.

[2] A.B. Samokhin, "An iterative method for the solution of integral equations applied to a scattering problem on a three-dimensional transparent body", Differential Equations, vol. 30, no. 12, 1994.

[3] M. H. Gutknecht, "Lanczos-type Solvers for Nonsymmetric Linear Systems of Equations", Technical Report of CSCS/SCSC, 1997.

[4] D. K. Faddeev, V. N. Faddeeva, "Computational Methods of Linear Algebra", W. H. Freeman, 1963.

COMPARISON OF SYMBOLIC COMPUTATION TECHNIQUES FOR PROBLEMS IN ELECTROMAGNETICS

Bahattin Türetken[1] and S.Eren San[2]

[1]TÜBİTAK-UEKAE PO.Box:21 41470,
Gebze, Kocaeli, TURKEY bahattin@mam.gov.tr

[2]TÜBİTAK-UME PO.Box:21 41470,
Gebze, Kocaeli, TURKEY eren@ume.tubitak.gov.tr

ABSTRACT
Symbolic computation techniques (SCT) are applied for the evaluation of problems in Electromagnetic(EM) by making use of Mathematica and Macsyma packages[1,2]. The results are compared in terms of the obtained numerical and analytical information.

INTRODUCTION
Actually in some problems it is better to use symbolic techniques rather than numerical evaluations. In some cases solutions of this kind are very useful for the interpretation of results. These symbolic computations are applicable for lots of mathematical manipulations particularly differentiation, integration, solutions of linear equations, expansion functions in series, solutions of differential equations, curve analysis, tensor algebra and topological approaches[3].
In this study we have concentrated on the solution possibilities of some EM problems. It is very important to obtain exact solutions for design applications of Radio Frequency (RF). Especially it is required to solve the problem exactly for some antenna designs and in such cases trustability of the used program packages is very important. That is why comparison of alternative SCT with different program packages is analysed in different problems.

INTERESTED PROBLEMS
In order to examine the results of these packages two well-known problems of electromagnetic were studied. One of the problems is a short wire problem (flux density **B** due to a short current carrying wire) and the other one is an antenna analysis.

Short Wire Problem
A short copper wire of length L and a cross sectional area a is concerned and current **I** exists in positive **z** direction. Current I is assumed to be uniform throughout the wire and it is time independent. If we deal with the situation at a large distance from the wire (r >>L) (see Fig.1) we make use of vector potential **A** in order to calculate the magnetic flux density **B** everywhere [4,5].
The vector potential **A** at a distance r from wire for the current ***I*** in the z direction and uniform is given by A=(0,0,c/r) where $c = \frac{\mu_0 IL}{4\pi}$.
A = the vector potential at the distance r from wire, Wb/m, **I** = the current in the wire,A, **L** = the length of the wire, m, **r** = the distance from the wire, m,
μ_0=the permeability of air=400pi ,nH/m

The vector potential is in the positive **z** direction and is inversely proportional to the distance r from the wire. We obtain the flux density B by taking the curl of **A**

$$B = \nabla x A . \tag{1}$$

Magnetic flux density of a short copper wire is studied and symbolically visualised in the following figures by Macysma & Mathematica.

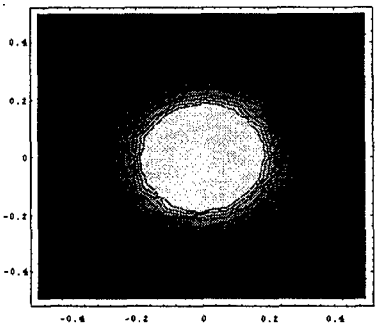

a)

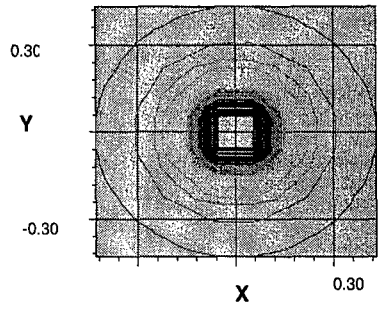

b)

Fig. 1. Magnetic flux density (**B**) of the short copper wire
a) By Mathematica
b) By Macsyma

Antenna Analysis

The behaviour of antennas is primarily governed by Maxwell's equations [6,7]. One can obtain the electromagnetic fields at any point outside the source region for known ***A*** at the time harmonic variations.

$$B = \nabla x A , \; H = B/\mu , \; E = q \nabla x H \tag{2a,b,c}$$

We consider a conductor of the length ***L*** and cross section area a carrying a current ***I*** in **z** direction of angular frequency ***w*** . Such a current element is known as a Hertz dipole. The vector potential at an arbitrary point P is given by in Cartesian coordinates
A=(0,0,exp (-jkr)/r) or in spherical coordinates

$$A = (p\frac{\exp(-jkr)}{r}\cos\theta, 0, -p\frac{\exp(-jkr)}{r}\sin\theta), \tag{3}$$

where $p = \frac{\mu_0 IL}{4\pi}$, $q = \frac{1}{jw\varepsilon\mu}$

Electromagnetic fields of the Hertz dipole is studied and symbolically visualised in the following figures by Macysma (Fig. 2b) & Mathematica (Fig. 2a).

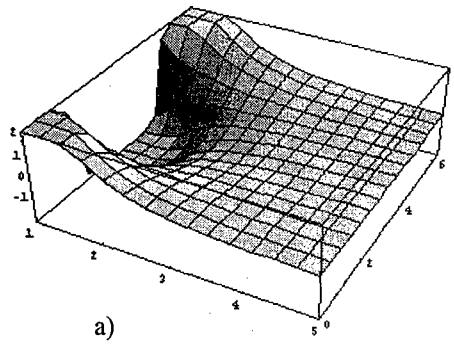

a)

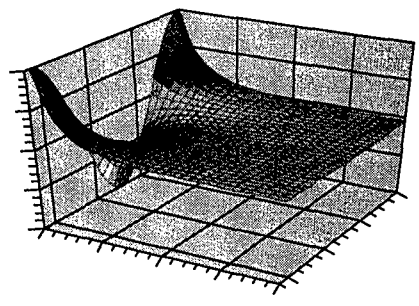

b)

Fig. 2. Electromagnetic fields of Hertz dipole (**r** component)

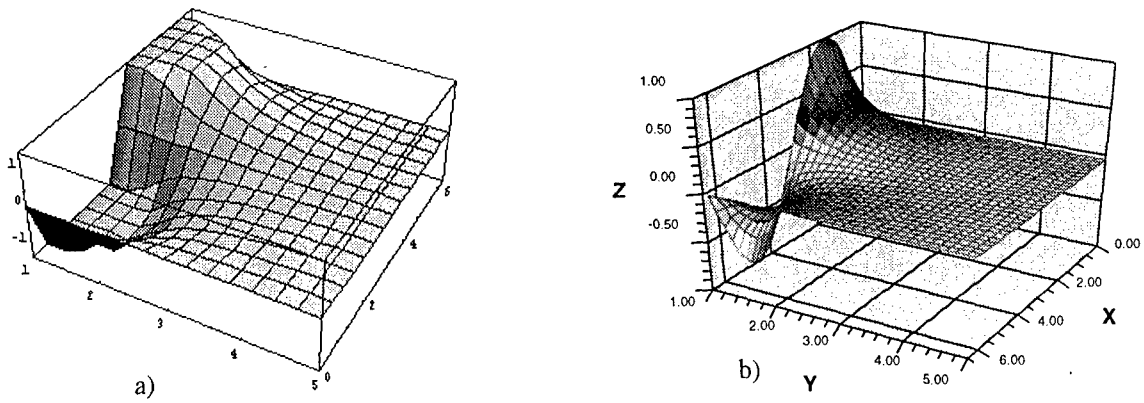

Fig. 3. Electromagnetic fields of Hertz dipole (θ component)
a) By Mathematica
b) By Macsyma

CONCLUSION

In fact these problems have been studied so that the trustability and compatibility of symbolic computation should be presented in a commentary manner, SCT could also be applied for much more complicated problems in different coordinate systems
If we analyse the obtained figures by two different packages we can easily notice the fact that the forms of the graphs are very similar. There exist some discrepancies that are supposed to be caused by different numerical procedures followed in the structures of these two packages.

REFERENCES

[1] MACSYMA Reference Manual Version 16, 1998, Symbolic Inc.
[2] MATHEMATICA Reference Guide Version 2 1992, Addison Wesley Pub.Co.
[3] ARI N., TURETKEN B., "*Symbolic Comtutaions Techniques for Electromagnetics*" Second International Symposium on Mathematical & Computational Applications 1999, Baku, Azerbaycan
[4] N. ARI, "*Application of computer code MACSYMA for electromagnetics, Proceedings of the IASTED International SymposiumExpert Systems Theory & Applications*", Zurich, Switzerland
1989,pp 77-80
[5] KRAUS J. D. *Electromagnetics*, McGraw-Hill Book Company, New York, 1984 pp. 190-192
[6] KRAUS J. D. *Antennas*, 2. Edition, McGraw-Hill Book Company, New York,1988
[7] LEE KAI FONG, *Principles of Antenna Theory*, John Wiley & Sons, 1984, pp. 12-30

THE TECHNIQUE FOR CALCULATION OF THE ELECTROMAGNETIC PROPERTIES OF COMPOSITE MATERIALS AND NONUNIFORM MEDIA

S. V. Maly

Belarus State University, Department of Radiophysics
1 Kurchatova str., Minsk, 220064, Belarus
maly@rfe.bsu.unibel.by

ABSTRACT

The basic stages of the technique of calculation of effective electromagnetic parameters of composite materials and nonuniform media are presented. The technique is based on the method of minimum autonomous blocks. The example of usage of this technique for calculation of effective parameters of a composite containing segments of conductive fibrils is given.

BASIC STEPS OF THE TECHNIQUE

Generally, a method of calculation of effective electromagnetic properties of composite materials and nonuniform media includes: a choice of the key electromagnetic problem; solution of the key problem taking account of the interior structure of composite; finding of the effective electromagnetic parameters through the solution of inverse problem. As a key problem we shall consider the interaction of a plain linearly polarized electromagnetic wave with a flat stratum of a composite. The interior structure of a composite can be periodic or statistically homogeneous. If the sizes of structural inhomogeneities of composite are small in comparison with the wavelength λ, then the electromagnetic properties of the flat stratum of a composite illuminated by the electromagnetic wave can be characterized with the aid of the scattering matrix S. For calculation of this matrix, the use of the technique outlined in [1] is possible. This technique is based on the method of minimum autonomous blocks (MAB) [2] and the theory of periodic structures [3]. The basic stages of this technique are given in Fig. 1.

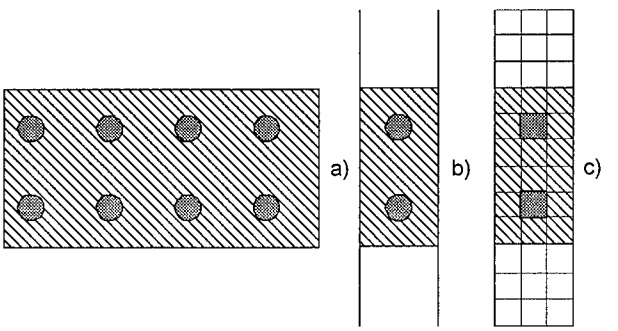

Figure 1

In Fig. 1a, a fragment of a flat stratum of a composite relevant to the initial key electromagnetic problem is shown. Transition to an electromagnetic equivalent problem is carried out. The virtual waveguide shown in Fig. 1b corresponds to a single period of composite. On its walls the requirements of periodicity are imposed. In view of the smallness

of the cross section of the virtual waveguide, in the spectrum of scattered on the wavequide inhomogeneity electromagnetic field, it is possible to take into account only the zeroth Floquet harmonic. The area of the virtual waveguide containing spatial inhomogeneity is divided into system of rectangular blocks, as shown in Fig. 1c. According to the MAB method, each of these blocks is considered as an independent block, whose electromagnetic properties are characterized by the scattering matrix. The scattering matrices of separate blocks are used in calculation of a multichannel scattering matrix within the framework of the procedure of integration of the neighboring blocks. The relations for the elements of the scattering matrices and a relevant recomposition procedure were explicitly presented in [2]. The required scattering matrix of a flat stratum of a composite is obtained by the relevant averaging of elements of a multichannel scattering matrix.

For calculation of the effective electromagnetic parameters of a composite ($\varepsilon_{eff}, \mu_{eff}$) it is possible to use the relations of [4,5]:

$$\varepsilon_{eff} = \sqrt{\frac{C_2}{C_1}}, \quad \mu_{eff} = \sqrt{C_1 C_2}; \; C_1 = \left(\frac{1+\rho}{1-\rho}\right)^2, \quad C_2 = -\left(\frac{\lambda}{2\pi d}\ln\frac{1}{\tau}\right)^2, \tag{1}$$

$$\rho = x \pm \sqrt{x^2 - 1}, \; |\rho| \le 1; \tag{2}$$

$$\tau = (V_1 - \rho)/(1 - V_1\rho); \tag{3}$$

$$x = \frac{1 - V_1 V_2}{V_1 - V_2}, \quad V_1 = S_{21} + S_{11}; \quad V_2 = S_{21} - S_{11}. \tag{4}$$

where S_{11}, S_{21} are the elements of the scattering matrix S of a flat stratum of a composite.

NUMERICAL RESULTS

As an example of usage of designed technique, we shall consider the results of calculation of an effective permittivity of the composite material, whose fragment and the notations of design factors are shown in Fig. 2.

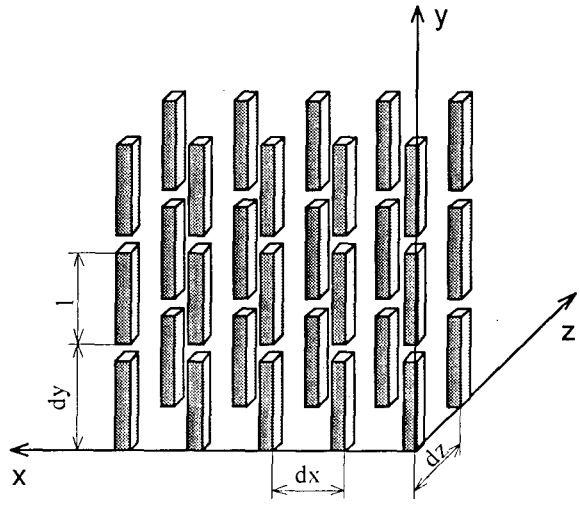

Figure 2

The composite is formed from short perfectly conducting wires having square section with the side length δ. Other parameters are as follows: $d_x = 7\delta, d_y = 9\delta, d_z = 11\delta$. The effective

electromagnetic parameters of composite are calculated for the case of a plain electromagnetic wave propagating along the z-axis, and electric field $\vec{E} \parallel \vec{y}$. The calculations were performed in the assumption that $d_{x,y,z} \square \lambda$. In Fig. 3, the dependences of the effective permittivity of the composite on value of separation between end faces of wires $\Delta = (d_y - l)$ are presented for different values of permittivity of material filling this gap.

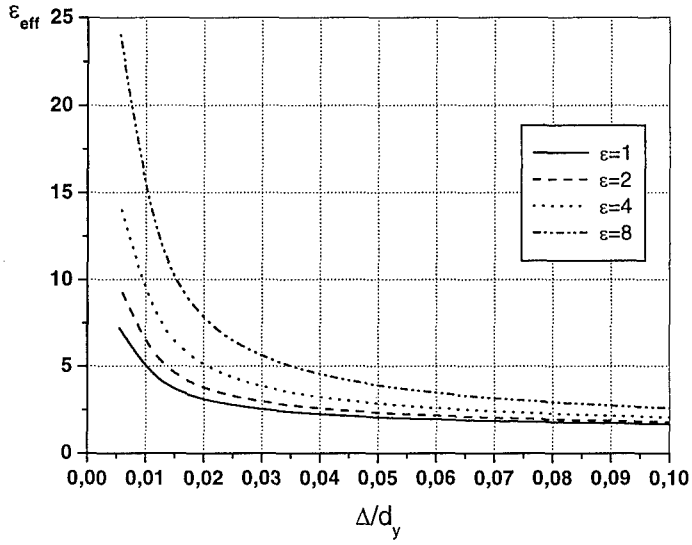

Figure 3

A strong dependence of ε_{eff} on Δ can be used in development of artificial dielectric materials with controllable properties.

CONCLUSION

The offered technique ensures an opportunity to calculate the effective electromagnetic parameters of materials and media with a composite interior structure and does not put restrictions on the density of particles and their shape. The usage of the technique will enable one to develop and examine composite materials with new electromagnetic properties.

REFERENCES

[1] S.V.Maly. The Numerical Technique for Analysis of the Electromagnetic Scattering by Complicated Periodic Structures. *Proc. Int. Conf. Mathematical Methods in Electromagnetic Theory*, 1996, Lviv, Ukraine, pp. 490-493.

[2] V.V.Nikolsky and T.I.Nikolskaya. *Decomposition Approach to Electrodynamic Problems*, Nauka, Moscow, 1983 (in Russian)..

[3] N.Amitay, V.Galindo, and C.P.Wu, *Theory and analysis of phased array antennas*, New York, 1972.

[4] A.M.Nicolson and G.F.Ross, *IEEE Trans.*, IM-19, 377, 1970.

[5] M.S.Freeman, R.N.Nottenburg and J.B.Dubow, *J.Phys. E: Sci. Instrum.*, 12, 899, 1979

NUMERICAL MODELS IN THE PROBLEMS OF THE SCATTERED FIELDS INTERACTION

Amur B. Hashimov

The South Ural State University, Chelyabinsk, Russia
E-mail: xab@kipr.susu.ac.ru

ABSTRACT

The numerical method is suggested for analysis of electromagnetic interaction by scattering fields of perfect conducting obstacles. It is based on the using of cell collocation technique. Parameters of the numerical models are defined by minimizing of the regularization functional. The estimations of accuracy for the different obstacles are obtained.

The electromagnetic interaction of the antenna systems and the scattering obstacles can be determined by integral equations method. These equations are used for determination of the scattering fields by appropriate numerical model. When an incident electromagnetic field of the antenna system $\vec{\mathbf{E}}^i, \vec{\mathbf{H}}^i$ is scattered by a perfect conducting obstacles with surface S, the scattered fields can be determined by integration when the surface current density $\vec{\mathbf{j}}_s$ induced on surface S is known. This surface current density can be determined from the incident field by solving either the magnetic field integral equation or electric field equation, which are consequences of the boundary condition at the perfect conducting surface:

$$\vec{\mathbf{j}}_s = 2\vec{\mathbf{n}} \times \vec{\mathbf{H}}^i + \frac{1}{2\pi}\vec{\mathbf{n}} \times \int_S \vec{\mathbf{j}}_s \times grad' G(\vec{\mathbf{r}}, \vec{\mathbf{r}}')ds';$$

$$\vec{\mathbf{n}} \times \vec{\mathbf{E}}^i = -\frac{i}{4\pi\omega\varepsilon_a}\vec{\mathbf{n}} \times \int_S \left(-\omega^2 \varepsilon_a \mu_a \vec{\mathbf{j}}_s + Div\vec{\mathbf{j}}_s \cdot grad' G(\vec{\mathbf{r}}, \vec{\mathbf{r}}')\right)ds',$$

where $G(\vec{\mathbf{r}}, \vec{\mathbf{r}}') = exp(-ik|\vec{\mathbf{r}} - \vec{\mathbf{r}}'|)/|\vec{\mathbf{r}} - \vec{\mathbf{r}}'|$; $\vec{\mathbf{r}}, \vec{\mathbf{r}}'$ – radius-vectors of the observation and source points respectively; Div denotes the surface operator; $\vec{\mathbf{n}}$ is the unit normal vector in an outward direction from S.

These equations can be arranged in the form

$$Lu = f,$$

where L is an integral operator; u is an any scalar component of the $\vec{\mathbf{j}}_s$; f is the known incident function.

Let us consider the method for calculating the unknown functions u by using the cell collocation technique. Assume that the integral equations solving results can be transformed into a numerical model of the appropriate scattering problem. The cell collocation technique as a part of the method of weighted residuals allows approximating u in terms of a finite series of basis functions $\{\varphi_n\}$ as

$$u = \sum_{n=1}^{N} a_n \varphi_n,$$

where a_n is an arbitrary constants to be determined. For any numerical model the residual function can be determined as

$$\varepsilon = \sum_{n=1}^{N} a_n \cdot L\varphi_n - f \neq 0.$$

Then we follow the traditional procedure of the weighted residuals method [1] by using the auxiliary weight function w, which is defined as a finite series of basis function $\{\psi_m\}$:

$$w = \sum_{n=1}^{M} b_m \psi_m,$$

where M is a number of basis elements. The functional in form inner product of the residual function and auxiliary weight function is defined as (ε, w) and determined the weak form of the operator equation

$$(\varepsilon, w) = \int_S \left\{ \sum_{n=1}^{N} a_n L\varphi_n - f \right\} \sum_{m=1}^{M} b_m \psi_m ds = \sum_{m=1}^{M} b_m (\varepsilon, \psi_m).$$

and equality $(\varepsilon, w) = 0$ must be fulfilled. We obtain the system of linear equations with a_n to be found

$$\int_S \left\{ \sum_{n=1}^{N} a_n L\varphi_n - f \right\} \psi_m ds = \sum_{n=1}^{N} a_n (L\varphi_n, \psi_m) - (f, \psi_m); \quad m = 1, \ldots, M.$$

The matrix form of this system may be represented in the following way

$$\hat{\mathbf{A}} \cdot \mathbf{a} = \mathbf{F};$$

$$A_{nm} = (L\varphi_n, \psi_m); \quad \mathbf{a} = \left[a_1 a_2 \ldots a_N \right]^t; \quad F_m = (f, \psi_m).$$

The appropriate choice of the pair $\{\varphi_n\}, \{\psi_m\}$ determines successive solution of the problem. The often used pairs of functions are given in [2]. The cell collocation technique basis as $\{\varphi_n\}$ employs as a rule the series of δ-functions and a pulse basis as $\{\psi_m\}$ [1]. We propose a successive modification of the cell collocation method for calculation of the surface current density $\bar{\mathbf{j}}_s$. We shall use pulse basis of several shape both $\{\varphi_n\}, \{\psi_m\}$:

$$\varphi_n(s') = \begin{cases} 1; & s' \in [s'_n - \Delta'/2, s'_n + \Delta'/2]; \\ 0; & s' \notin [s'_n - \Delta'/2, s'_n + \Delta'/2]. \end{cases}; \quad \psi_m(s) = \begin{cases} 1/\Delta; & s \in [s_n - \Delta/2, s_n + \Delta/2]; \\ 0; & s \notin [s_n - \Delta/2, s_n + \Delta/2]. \end{cases}. \tag{1}$$

$$\varphi_n(s') = \begin{cases} 2[s' - (s_n - \Delta'/2)]/\Delta'; & s' \in [s'_n - \Delta'/2, s'_n + \Delta'/2]; \\ 2(s_n - \Delta'/2)/\Delta'; & s' \notin [s'_n - \Delta'/2, s'_n + \Delta'/2]. \end{cases}; \tag{2}$$

$$\psi_m(s) = \begin{cases} 2\left[s - \left(s_m - \Delta/2\right)\right]/\Delta; & s \in \left[s_m - \Delta/2,\, s_m + \Delta/2\right]; \\ 2\left(s_m - \Delta/2\right)/\Delta; & s \notin \left[s_m - \Delta/2,\, s_m + \Delta/2\right]. \end{cases},$$

where (1), (2) is rectangular and triangle two-dimensional basis respectively, Δ', Δ – pulse basis parameters, s', s denotes coordinates of the source and observation points respectively in the inner products. For these simple basis it is possible to calculate coefficients of linear system by using simple three-point Simpson's integration formula. It is important to note that the Green's function derivatives in weak form of the operator equation are absent. The surface derivatives can be moved outside the inner integral of weak form and apply to pulse basis. Thus, dominant diagonal elements of linear system provides stability of the numerical computations. Obviously, optimal choice of the basis parameters is defined by properties of surface S and prescribed accuracy. Often it is necessary to expand basis series in case of unstable numerical integration results for sharp irregularities of S. In other cases substituting the truncated series of the finite basis function into the integrands and integration will occur with Δ', Δ which have no instabilities. Successive way for determining Δ', Δ is followed from the known variational approach. According to [3], consider the functional

$$M\left[\vec{\mathbf{j}}_s\right] = \left\|\vec{\mathbf{j}}_s\right\|^2.$$

The choice of optimal basis parameters is reduced to minimize prescribed functional under condition $\left\|\vec{\mathbf{j}}_s\right\| = const$. The resulting matrix of the linear system is still valid and optimal basis parameters satisfy main problem conditions, i.e. a stable computation, appropriate accuracy must be fulfilled. This method was applied to the test problem of scattered field computation by perfect conducting two-dimensional cylinder solved previously by the finite-element method. The comparison of the numerical solutions with the exact one shows that the method described here is more efficient. Numerical results for other cases will be presented.

REFERENCES

[1] C.A.Brebbia, J.C.F.Telles, L.C.Wrobel, Boundary Elements Techniques, Springer-Verlag, Berlin and New York, 1984.

[2] A.J.Poggio and E.K.Miller, "Integral equation of three-dimensional scattering problems", Computer Techniques for Electromagnetics, (Ed. R.Mittra), Pergamon Press, Oxford and New York, 1973.

[3] M.I.Andriychuk, N.N.Voitovich, P.A.Savenko, V.P.Tkachuk. Synthesis of antenna according to amplitude radiation pattern. Numerical method and algorithms. Naukova Dumka Publ. Kyiv, 1993. (In Russian).

CALCULATION OF SINGULAR INTEGRALS IN SCALAR DIFFRACTION PROBLEMS

Oleg I. Ovsyannikov, and Yuriy V. Kasyanyuk

Karpenko Physico–Mechanical Institute
of the National Academy of Sciences of Ukraine, Lviv, Ukraine
E-mail: oleg@ipm.lviv.ua, yurka@ipm.lviv.ua

ABSTRACT

The axissymmetric scalar diffraction problem is presented. The singular and hypersingular integrals with normal derivative of double layer potential are considered. The methods of singular and hypersingular integrals calculation are proposed.

STATEMENT OF THE PROBLEM

Suppose the scatterer is symmetric to the axis Oz and infinitely thin with finite disclosed surface S. Generatrix of scatterer is a smooth contour L in the plane xOy. Let us assume that the considered body is illuminated by Oz symmetric wave in the form $\mathbf{H}^*(t,\tau)=\mathbf{H}^*(t)\exp(-\omega\tau), t\in R^3$ (τ is time, ω is circular frequency). We have to find the solution of three–dimentional Helmholtz equation, that satisfies the conditions: of Neumann on the surface S; of Meixner type near the scatterer ribs; of Sommerfeld which excludes waves propagating from infinity (except the exciting one).

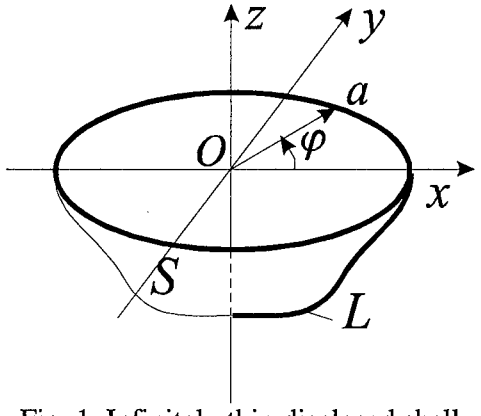

Fig. 1. Infinitely thin disclosed shell with curvilinear profile

Let us find a solution as a double layer potential [1]:

$$H^s(T)=\int_S \frac{\partial}{\partial n}\left(\frac{\exp(i\chi r(T,t))}{r(T,t)}\right)f(t)dS\,. \tag{1}$$

Satisfying the Neumann condition on the surface S and taking into account the axis symmetry of the problem, the ribs' conditions and applying parametric equations of surface S: $x=l(\tau)\cos(\varphi)$, $y=l(\tau)\sin(\varphi)$, $z=z(\tau)$, $-1\le\tau\le 1$, $-\pi\le\varphi\le\pi$ (φ is polar angle in the plane xOy) we obtain:

$$\int_{-1}^{1}\tilde f(\tau)\sqrt{1-\tau}\int_{-\pi}^{\pi}\frac{\exp[i\chi r(\tau,\tau_0,\varphi)]}{(r(\tau,\tau_0,\varphi))^2}\left\{\frac{1}{r(\tau,\tau_0,\varphi)}-i\chi\right\}\mathrm{Re}\left(\frac{\bar t-\bar t_0}{t-t_0}t'_0\right)d\varphi d\tau+$$

$$+\frac{1}{2}\int_{-1}^{1}\tilde f(\tau)\sqrt{1-\tau}\int_{-\pi}^{\pi}\left[\frac{\exp[i\chi r(\tau,\tau_0,\varphi)]}{r(\tau,\tau_0,\varphi)}\times\right.$$

$$\left.\times\left\{\frac{1}{(r(\tau,\tau_0,\varphi))^2}-\frac{i\chi}{r(\tau,\tau_0,\varphi)}-\chi^2\right\}\mathrm{Re}\left(\frac{\bar t-\bar t_0}{t-t_0}\frac{t't'_0}{|t'||t'_0|}-\frac{t'\bar t'_0}{|t'||t'_0|}\right)\right]d\varphi d\tau=-|t'_0|\frac{\partial\tilde H(\tau_0)}{\partial n_0}, \tag{2}$$

where $f(\tau)l(\tau)\big|_{\varphi_0=\pi}\equiv\tilde f(\tau)\sqrt{1-\tau}$.

We can rewrite (2) in the following form:

$$\int_{-1}^{1}\sqrt{1-\tau}\,\tilde f(\tau)g(\tau,\tau_0)\int_{-\pi}^{\pi}\left\{\frac{\exp(i\chi r(\tau,\tau_0,\varphi))}{(r(\tau,\tau_0,\varphi))^3}-\frac{i\chi\exp(i\chi r(\tau,\tau_0,\varphi))}{(r(\tau,\tau_0,\varphi))^2}\right\}d\varphi d\tau+$$

$$+\frac{1}{2}\int_{-1}^{1}\sqrt{1-\tau}\,\tilde{f}(\tau)g1(\tau,\tau_0)\int_{-\pi}^{\pi}\frac{\exp(i\chi r(\tau,\tau_0,\varphi))}{(r(\tau,\tau_0,\varphi))^3}d\varphi d\tau -$$

$$-\frac{1}{2}\int_{-1}^{1}\tilde{f}(\tau)g1(\tau,\tau_0)\sqrt{1-\tau}\int_{-\pi}^{\pi}\frac{i\chi\exp(i\chi r(\tau,\tau_0,\varphi))}{(r(\tau,\tau_0,\varphi))^2}d\varphi d\tau -$$

$$-\frac{1}{2}\int_{-1}^{1}\tilde{f}(\tau)g1(\tau,\tau_0)\sqrt{1-\tau}\int_{-\pi}^{\pi}\frac{\chi^2\exp(i\chi r(\tau,\tau_0,\varphi))}{r(\tau,\tau_0,\varphi)}d\varphi d\tau = -|t_0'|\frac{\partial\tilde{H}(\tau_0)}{\partial n_0},\ t_0\in S, \quad (3)$$

where $g(\tau,\tau_0)=\mathrm{Re}\left(\frac{\bar{t}-\bar{t}_0}{t-t_0}t't_0'\right)$, $g1(\tau,\tau_0)=\mathrm{Re}\left(\frac{\bar{t}-\bar{t}_0}{t-t_0}t't_0'-t'\overline{t_0'}\right)$, $g(\tau_0,\tau_0)=|t_0'|^2$, $g1(\tau_0,\tau_0)=0$.

It is clear that integrals in (3) have logarithmic singularity and hypersingularity as $\frac{1}{(\tau-\tau_0)^2}$ type at $\tau\to\tau_0$.

We shall consider the regularization method of these integrals [2].

Let us make the following steps:

$$I_3^*(\tau_0)=\int_{-1}^{1}\tilde{f}(\tau)g(\tau,\tau_0)\sqrt{1-\tau}\int_{-\pi}^{\pi}\left\{\frac{\exp[i\chi r(\tau,\tau_0,\varphi)]}{(r(\tau,\tau_0,\varphi))^3}\right\}d\varphi d\tau = \quad (4)$$

$$=\int_{-1}^{1}\tilde{f}(\tau)g(\tau,\tau_0)\sqrt{1-\tau}\int_{-\pi}^{\pi}\frac{\exp[i\chi r(\tau,\tau_0,\varphi)]-1-i\chi r(\tau,\tau_0,\varphi)-\frac{(i\chi r(\tau,\tau_0,\varphi))^2}{2}}{(r(\tau,\tau_0,\varphi))^3}d\varphi d\tau + \quad (5)$$

$$+I_{33}(\tau_0)+I_{32}(\tau_0)-I_{31}(\tau_0),$$

where

$$I_{33}(\tau_0)=\int_{-1}^{1}\tilde{f}(\tau)g(\tau,\tau_0)\sqrt{1-\tau}\int_{-\pi}^{\pi}\frac{1}{(r(\tau,\tau_0,\varphi))^3}d\varphi d\tau, \quad (6)$$

$$I_{32}(\tau_0)=i\chi\int_{-1}^{1}\tilde{f}(\tau)g(\tau,\tau_0)\sqrt{1-\tau}\int_{-\pi}^{\pi}\frac{1}{(r(\tau,\tau_0,\varphi))^2}d\varphi d\tau, \quad (7)$$

$$I_{31}(\tau_0)=\frac{\chi^2}{2}\int_{-1}^{1}\tilde{f}(\tau)g(\tau,\tau_0)\sqrt{1-\tau}\int_{-\pi}^{\pi}\frac{1}{r(\tau,\tau_0,\varphi)}d\varphi d\tau. \quad (8)$$

Making the similar steps with integrals (6-8) we obtain singular and hypersingular integrals:

$$I_{330}(\tau_0)=\int_{-1}^{1}\sqrt{1-\tau}\,g(\tau,\tau_0)\int_{-\pi}^{\pi}\frac{1}{(r(\tau,\tau_0,\varphi))^3}d\varphi d\tau, \quad (9)$$

$$I_{33\tau}(\tau_0)=\int_{-1}^{1}\sqrt{1-\tau}\,g(\tau,\tau_0)(\tau-\tau_0)\int_{-\pi}^{\pi}\frac{1}{(r(\tau,\tau_0,\varphi))^3}d\varphi d\tau, \quad (10)$$

$$I_{33\tau\tau}(\tau_0)=\int_{-1}^{1}\sqrt{1-\tau}\,g(\tau,\tau_0)(\tau-\tau_0)^2\int_{-\pi}^{\pi}\frac{1}{(r(\tau,\tau_0,\varphi))^3}d\varphi d\tau, \quad (11)$$

$$I_{320}(\tau_0)=\int_{-1}^{1}\sqrt{1-\tau}\,g(\tau,\tau_0)\int_{-\pi}^{\pi}\frac{1}{(r(\tau,\tau_0,\varphi))^2}d\varphi d\tau, \quad (12)$$

$$I_{310}(\tau_0)=\int_{-1}^{1}\sqrt{1-\tau}\,g(\tau,\tau_0)\int_{-\pi}^{\pi}\frac{1}{(r(\tau,\tau_0,\varphi))}d\varphi d\tau, \quad (13)$$

$$I_{32\tau}(\tau_0)=\int_{-1}^{1}\sqrt{1-\tau}\,g(\tau,\tau_0)(\tau-\tau_0)\int_{-\pi}^{\pi}\frac{1}{(r(\tau,\tau_0,\varphi))^2}d\varphi d\tau. \quad (14)$$

Using proposed approach we can calculate all integrals. It is possible to calculate effectively the integrals in arbitrary points of their definitions:

$$M(\tau)\approx\frac{\pi}{n}\sum_{k=0}^{n-1}S_k^n(\tau)M(\tau_\kappa), \tag{15}$$

where $S_k^n(\tau)=\frac{1}{\pi}\left(1+2\sum_{m=1}^{n-1}\cos(m\varphi_k)\cos(m\arccos(\tau))\right),\varphi_k=\frac{(2k-1)}{2n}\pi$.

We have tested the presented approach for singular integral (13) when complex coordinate t of contour L describes parabola $t=a/2\left(1+\tau+\varepsilon(1+\tau)^2/2\right)$; χa=1, ε=1:

points	Integral (13)	Interpolation polinomial for (13)
-0.9	11.7864	11.7864
-0.8	9.88613	9.88613
-0.7	8.87401	8.87401
-0.6	8.24451	8.24451
-0.5	7.82819	7.82819
-0.4	7.54292	7.54292
-0.3	7.34070	7.34070
-0.2	7.19013	7.19013
-0.1	7.06929	7.06929
0	6.96214	6.96220

points	Integral (13)	Interpolation polinomial for (13)
0.1	6.85673	6.85673
0.2	6.74371	6.74371
0.3	6.61591	6.61591
0.4	6.46763	6.46763
0.5	6.29430	6.29430
0.6	6.09220	6.09220
0.7	5.85830	5.85830
0.8	5.59005	5.59005
0.9	5.28532	5.28532

As seen, it is enough to calculate the integrals in node points.

After regularization of the left part of (3) we obtain the sum of regular and singular parts. Note that hypersingular integrals diverge in normal sense, but they converge in the sense of Hadamard's finite part [3]. All regular integrals are smooth on the integral interval. Therefore we can use quadrature formula for these integrals [4]:

$$\int_{-1}^{1}\sqrt{1-\tau}f(\tau)d\tau\approx\frac{\pi}{n}\sum_{k=1}^{n}f(\varphi_k)\tilde{\eta}_k^n, \tag{16}$$

where $\tilde{\eta}_k^n=\frac{1}{\pi}\left(\frac{4}{3}\sqrt{2}+2\sum_{m=1}^{n-1}\cos(m\tau_k)J_m\right)$, $J_m=\int_0^\pi\cos(m\tau)(1-\cos(\tau))\sqrt{1+\cos(\tau)}d\tau$,

$$\varphi_k=\cos\left(\frac{2k-1}{2n}\pi\right),\tau_k=\frac{2k-1}{2n}\pi,\ k=1..n,$$

and $$\int_{-1}^{1}j(\tau)d\tau\approx\sum_{k=1}^{n}j(\tau_k)\eta_k^n,\ \eta_k^n=\frac{1}{n}\left(2-2\sum_{m=2,4,\ldots}^{n-1}\cos(m\varphi_k)\frac{(-1)^m+1}{(m+1)(m-1)}\right). \tag{17}$$

Thus, using the proposed approach we can calculate the singular and hypersingular integrals and then obtain the system of linear algebraic equations using quadrature formulae (16-17).

REFERENCES

[1] Colton D., Kress R. Integral Equation Methods in Scattering Theory. – New York: John Wiley & Sons, 1983, – 311 p.

[2] Ovsyannikov O. I. The Numerical Method of Scalar Scattering Problem Solution// Proc. VI Intern. Conference MMET'96. P. 121-124.

[3] Nazarchuk Z. T. Singular Integral Equations in Diffraction Theory. – Lviv: Karpenko Physico–Mechanical Institute, 1994, – 210 p.

[4] Panasyuk V. V., Savruk M. P., Nazarchuk Z. T. Method of Singular Integral Equations in Two–dimensional Diffraction Problems, – Kiev: Naukova Dumka, 1984, – 344 p. (In Russian)

DIFFR — A UNIVERSAL SIMULATION ENVIRONMENT FOR TWO-DIMENSIONAL DIFFRACTION PROBLEMS

M.Gilman, A.Mikheev
Institute of Problem in Mechanics, Russian Academy of Sciences,
and S.Sadov
Keldysh Institute of Applied Mathematics, Russian Academy of Sciences

ABSTRACT

A universal environment for computer simulation of two-dimensional time-harmonic diffraction problems has been created. The purpose is to provide a convenient and reliable tool for testing and benchmarking of diffraction solvers with an up-to-date interface and a number of well-tested and calibrated solvers that cover a wide domain in the space of the problem parameters. Interface conventions will allow users to add their own solvers to the product's front-end. The software may be used for direct field calculation in presence of a particular scatterer and for tests of new numerical methods that deal with diffraction problems.

PURPOSE OF *DIFFR* AND *DIFFR*-LIKE SYSTEMS

Numerical solution of diffraction problems is of crucial importance in design of elements of wireless and optical communication lines, various nondestructive testing techniques, acoustics, etc.

While a huge literature on numerical methods for diffraction problems is available (see, e.g., our recent survey [2]), every group working in this area encounters a necessity to create its own software, which is often "reinventing a wheel". Having a software like *DIFFR* can sometimes eliminate this necessity, especially for those interested primarily in running simulations rather than in numerical methods for their own sake. When a custom software is really needed, *DIFFR*-like systems would largely reduce debugging time and help to understand applicability limits of custom algorithms. Another possible application of such software is testing solvers of inverse scattering problems.

ANNOTATION OF THE *DIFFR* SOFTWARE

DIFFR is designed as an umbrella for various solvers of diffraction problems and as a testing/validation tool. It deals with a well defined, restricted, still a wide class of diffraction problems that occur in electromagnetics and acoustics. Roughly speaking, its scope embraces most standard problems described by a two-dimensional scalar or vector Helmholtz equation (including time-harmonic Maxwell equations) with appropriate boundary and radiation conditions.

DIFFR software consists of two parts: (1) a shell — user interface for 2D diffraction solvers with modern graphical look and feel and scripting facilities for automated serial computations; (2) a set of diffraction solvers that covers a big part of the parameter space for common 2D diffraction problems. The supplied solvers are thoroughly tested; their areas of applicability and numerical behavior is described.

Hence *DIFFR* may be directly used for solving many standard problems. User-supplied solvers can be added, too. *DIFFR* provides convenient and reliable tools for testing and benchmarking of Diffraction solvers, both embedded and external.

DIFFR is designed to be cross-platform portable at the code level. Currently, compilation of the code is carried out for Windows-9* and Linux operating systems on Intel-based computers.

CLASS OF DIFFRACTION PROBLEMS

Time dependence: harmonic. This excludes transition processes.

Space dimensionality: 2. The reasons that essentially 3-dimensional problems are set aside are as follows:

- Many real diffraction problems can be treated as two-dimensional if the scatterer is a long cylinder of an arbitrary cross-section.
- Most important 2D scattering configurations can be easily classified, while 3D problems are much more individual.
- A number of recent state-of the-art algorithms for two-dimensional problems combine high precision and excellent performance, thus making available instant on-click two-dimensional simulations.
- For educational and research purposes, 2D simulations are often sufficient.
- Some 3-dimensional features are preserved in a 2D-model, such as polarization and direction of incidence (arbitrary, i.e. not necessarily orthogonal to the cylinder's grooves).

Frequency range: resonant, i.e. a typical size of the inhomogeneity is comparable to the wavelength.

Boundary conditions/polarization: all types of physical boundary conditions and/or polarization.

Direction of incidence: arbitrary. In particular, in case of an EM wave incident on a cylindrical surface and the Pointing vector not in the cross-section plane, two polarizations do not separate, and instead of a scalar Helmholtz equation one gets a vector Helmholtz equation.

Geometry of the scatterer: either a bounded obstacle or an infinite periodic diffraction grating. The boundary can be smooth or piecewise linear. In periodic case, the scatterer can be a continuous surface or a discontinous periodic grid. Smooth boundary is described by a finite number of Fourier coefficients (in Cartesian or polar coordinates, depending on problem type).

Properties of media:

From mathematical point of view, properties of the wave-carrying media determine a number of regions where the Helmholtz equations are solved, and (together with polarization) a type of boundary conditions. Currently, the number of media is limited to 2. The following problem types are possible:

- reflection from a perfectly conducting boundary;
- reflection from an imperfectly conducting boundary (Leontovich's boundary condition);
- transmission (refraction) through an interface between two dielectric or lossy materials.

Results of simulations

DIFFR-conforming solvers can provide amplitudes of diffracted waves in a far zone: in a given or all possible directions (radiation pattern), or the whole scattering matrix; surface current; near-zone field where available.

Far-zone results are considered to be more important and are in general more reliable. Classical energy criterion is used for validation of results in case of a conservative problem (if the whole scattering matrix is available, the energy criterion is the unitarity check). Another simple criterion that is employed can be called a "back flux" criterion. It consists in calculation of an "incident" field from a "diffracted" field in the problem with reversed radiation condition. This criterion is applicable even to problem with losses.
Solvers may provide some data from their process of resolution, such as resolution time or condition number of the linear system obtained as a discretization of an integral equation.

Solvers

DIFFR provides fast asymptotic solvers: for small slope profiles (Voronovich's Small Slope Approximation), for high frequencies (Kirhhoff with corrections; GTD); simple Rayleigh solver for shallow analytical profiles; and solvers based on boundary integral equations, implementing different discretization schemes, from a robust collocation method with piecewise constant elements to high precision quallocation schemes (due to R.Kress and others).
Smooth and piecewise linear boundaries require quite different numerical methods, so the solvers are accordingly divided into the two categories.
Besides the problem's physical parameters, each solver possesses such internal parameters as a number of mesh points, etc. They can be set up via the graphical user interface or a script.
Although *DIFFR* is not as intelligent as to suggest a solver most appropriate for a given problem, the supplied solvers are provided with a description that should help in this respect.
DIFFR uses a standardized gateway between the shell and solvers, which allows the users to add their own solvers.

MORE ABOUT *DIFFR*

Predecessor of *DIFFR* Version 2, which is currently being developed, *DIFFR*-1, had been released in 1993 and described in [1].
A reflection of research activity that lead to the creation of *DIFFR*-1, as well as results of numerical experiments regarding areas of validity of various asymptotic methods for diffraction problems, can be found in [3].
The authors have set up a website where an up-to-date information regarding the *DIFFR* project can be found at URL: http://www.DIFFR.com.

REFERENCES

[1] M.A.Gilman, A.G.Mikheev. *DIFFR:* a graphical software simulating diffraction by rough surfaces. User's Manual. Moscow: Institute for Problems in Mechanics, 1993.
[2] M.A.Gilman, S.Yu.Sadov, A.S.Shamaev, S.I.Shamaev. On some problems of computer simulation of scattering of electromagnetic waves by rough surfaces associated with remote sensing of sea surface. Radiotechnics and Electronics, special issue no.2, 2000 (translated from Russian) (in print).
[3] Methods, algorithms and facilities of aerospace computer radar tomography of Earth surface regions (S.V. Nesterov, S.I. Shamaev, A.S. Shamaev, eds.) Moscow, Nauchnyj Mir, 1997. (in Russian)

ANALITICAL REGULARIZATION

DIFFRACTION OF A PLANE WAVE BY A THIN MATERIAL STRIP: SOLUTION BY THE ANALYTICAL-NUMERICAL APPROACH

Eldar I. Veliev[1], Shoichi Koshikawa[2], and Kazuya Kobayashi[3]

[1] Institute of Radiophysics and Electronics, National Academy of Sciences, Ulitsa Proskury, 12, Kharkov 310085, Ukraine
E-mail: veliev@dut.kharkov.ua
[2] Antenna Giken Co., Ltd., 4-72 Miyagayato, Omiya 330-0011, Japan
E-mail: skoshi@mail.raidway.ne.jp
[3] Department of Electrical, Electronic, and Communication Engineering, Chuo University
1-13-27 Kasuga, Bunkyo-ku, Tokyo 112-8551, Japan
E-mail: kazuya@kazuya.elect.chuo-u.ac.jp

ABSTRACT

The plane wave diffraction by a thin material strip is analyzed for both E and H polarizations using a new analytical-numerical approach together with approximate boundary conditions. The problem is reduced to the solution of infinite systems of linear algebraic equations. The final results are valid provided that the thickness of the strip is small compared with the wavelength. The scattered field is evaluated asymptotically and a far field expression is derived. Illustrative numerical examples on the radar cross section are presented and the far field scattering characteristics are discussed. Some comparisons with the other existing method are also given.

INTRODUCTION

Analysis of the scattering by imperfectly conducting and absorbing strips is an important subject in electromagnetic theory, and it is relevant to many engineering applications such as antenna and radar cross section (RCS) studies. A resistive sheet can be regarded as a suitable model of thin material layers and there have been investigations on the scattering by resistive strips based on some analytical methods [1,2]. It is also known that a thin material layer with arbitrary permittivity and permeability can be modeled more accurately by a pair of modified resistive and conductive sheets each satisfying given boundary conditions [3-5].

In a previous paper [6], we have analyzed the plane wave diffraction by a thin dielectric strip using a new analytical-numerical approach [7] based on the orthogonal polynomial expansion in conjunction with the Fourier transform, where an efficient solution has been obtained for the strip thickness small compared with the wavelength. In this paper, we shall consider a thin strip consisting of a homogeneous material with arbitrary permittivity and permeability as a generalization to our previous geometry in [6], and analyze the plane wave diffraction for both E and H polarizations. Applying the approximate boundary conditions to an integral representation of the scattered field, the problem is formulated as two integral equations satisfied by the unknown current density functions. Expanding the current density functions in terms of the orthogonal polynomials, our problem is reduced to the solution of two infinite systems of linear algebraic equations (SLAE) satisfied by the unknown expansion coefficients. These coefficients are determined numerically with high accuracy via appropriate truncation of the SLAE. The scattered field is evaluated asymptotically and a far field expression is derived.

We shall present illustrative numerical examples on the RCS and discuss the far field scattering characteristics in detail. Some comparisons with Volakis [4] are also given to validate the present method. In the following, the analysis procedure is presented only for the E-polarized

case, but numerical results are given for both polarizations. The time factor is assumed to be $e^{-i\omega t}$ and suppressed throughout this paper.

SOLUTION BASED ON THE ANALYTICAL-NUMERICAL APPROACH

Let us consider the diffraction of an E-polarized plane wave by a thin material strip as shown in Fig.1, where the relative permittivity and permeability of the strip are denoted by ε_r and μ_r, respectively. Let the total field be $E_z(x,y) = E_z^i(x,y) + E_z^s(x,y)$, where $E_z^i(x,y)$ $[= e^{-ik(x\alpha_0 + y\sqrt{1-\alpha_0^2})}]$ is the incident field with $\alpha_0 = \cos\theta_0$ for $0 < \theta < \pi/2$ and $k(=\omega\sqrt{\varepsilon_0\mu_0})$ being the free-space wavenumber, and $E_z^s(x,y)$ is the unknown scattered field. The material strip is replaced by a strip of zero thickness satisfying the boundary condition corresponding to modified resistive and conductive sheets [5] under the condition that the strip thickness is small compared with the wavelength. Then the total field satisfies the boundary condition on the strip as given by

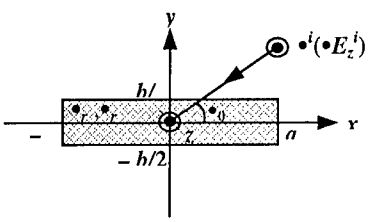

Fig.1. Geometry of the problem.

$$H_x(x,+0) + H_x(x,-0) + 2R_m[E_z(x,+0) - E_z(x,-0)] = 0 \quad , \tag{1a}$$

$$\left[\frac{1}{2R_e} + \frac{1}{2\tilde{R}_m}\left(1 + \frac{1}{k^2}\frac{\partial^2}{\partial y^2}\right)\right][E_z(x,+0) + E_z(x,-0)] = H_x(x,+0) - H_x(x,-0), \tag{1 b}$$

where $R_e = iZ/[kb(\varepsilon_r - 1)]$, $R_m = iY/[kb(\mu_r - 1)]$, and $\tilde{R}_m = iZ\mu_r/[kb(\mu_r - 1)]$ with $Z(=1/Y)$ being the intrinsic impedance of free space. Using Green's formula, we can express the scattered field as

$$E_z^s(x,y) = \frac{kZ}{4}\int_{-a}^{a}\left[J_z(x') - \frac{iY}{k}J_x^*(x')\frac{\partial}{\partial y}\right]H_0^{(1)}\left[k\sqrt{(x-x')^2 + y^2}\right]dx' \tag{2}$$

with $H_0^{(1)}(\square)$ being the Hankel function of the first kind, where $J_z(x)[\equiv H_x(x,+0) - H_x(x,-0)]$ and $J_x^*(x)$ $[\equiv E_z(x,+0) - E_z(x,-0)]$ are the unknown electric and magnetic current density functions, respectively. Taking into account the boundary condition as given by (1a,b), we obtain from (2) that

$$2ZR_m J_x^*(x) = 2\sqrt{1-\alpha_0^2}\,e^{-ikx\alpha_0} + \lim_{y\to 0}\frac{1}{2k}\frac{\partial^2}{\partial y^2}\int_{-a}^{a} J_x^*(x')H_0^{(1)}\left[k\sqrt{(x-x')^2 + y^2}\right]dx', \tag{3a}$$

$$J_z(x) = -\left(\frac{1}{R_e} + \frac{\alpha_0^2}{\tilde{R}_m}\right)e^{-ikx\alpha_0} - \lim_{y\to 0}\frac{kZ}{2}\left[\frac{1}{2R_e} + \frac{1}{2\tilde{R}_m}\left(1 + \frac{1}{k^2}\frac{\partial^2}{\partial y^2}\right)\right]\int_{-a}^{a} J_z(x')H_0^{(1)}\left[k\sqrt{(x-x')^2 + y^2}\right]dx'. \tag{3b}$$

Equations (3a,b) are the integral equations to this diffraction problem. Taking the finite Fourier transform of (3a,b) over the interval $|x| < a$ and using the integral representation of the Hankel function, we are led to

$$2ZR_m F_x(\beta) = 4\sqrt{1-\alpha_0^2}\,\frac{\sin\kappa(\beta+\alpha_0)}{\kappa(\beta+\alpha_0)} - \frac{1}{\pi}\int_{-\infty}^{\infty} F_x(\alpha)\sqrt{1-\alpha^2}\,\frac{\sin\kappa(\alpha-\beta)}{\alpha-\beta}d\alpha, \tag{4a}$$

$$F_z(\beta) = -2\left(\frac{1}{R_e} + \frac{\alpha_0^2}{\tilde{R}_m}\right)\frac{\sin\kappa(\beta+\alpha_0)}{\kappa(\beta+\alpha_0)} - \frac{Z}{2\pi}\left(\frac{1}{R_e} + \frac{1}{\tilde{R}_m}\right)\int_{-\infty}^{\infty}\frac{F_z(\alpha)}{\sqrt{1-\alpha^2}}\frac{\sin\kappa(\alpha-\beta)}{\alpha-\beta}d\alpha$$
$$+\frac{Z}{2\pi\tilde{R}_m}\int_{-\infty}^{\infty}F_z(\alpha)\sqrt{1-\alpha^2}\,\frac{\sin\kappa(\alpha-\beta)}{\alpha-\beta}d\alpha \qquad (4b)$$

with $\kappa = ka$, where

$$F_x(\alpha) = \int_{-1}^{1} J_x^*(ax')e^{-i\kappa\alpha x'}dx', \quad F_z(\alpha) = \int_{-1}^{1} J_z(ax')e^{-i\kappa\alpha x'}dx'. \qquad (5)$$

It can be shown that the unknown functions $J_x^*(x)$ and $J_z(x)$ are expanded in the form

$$J_x^*(x) = \sqrt{1-\left(\frac{x}{a}\right)^2}\sum_{n=0}^{\infty}J_n^x U_n\left(\frac{x}{a}\right), \quad J_z(x) = \frac{1}{a\sqrt{1-(x/a)^2}}\left[J_0^z + 2\sum_{n=1}^{\infty}\frac{J_n^z}{n}T_n\left(\frac{x}{a}\right)\right], \qquad (6)$$

where $T_n(\square)$ and $U_n(\square)$ denote the Chebyshev polynomial of the first and second kinds, respectively. In (6), $J_n^{x,z}$ for $n = 0,1,2,\cdots$ are unknown coefficients to be determined. Substituting (6) into (4a,b) and applying some properties of the Weber–Schafheitlin discontinuous integrals, we derive the two infinite systems of linear algebraic equations (SLAE) as in

$$\sum_{n=0}^{\infty}(A_{mn} + 2ZR_m B_{mn})J_n^x = \gamma_m^x, \qquad \sum_{n=0}^{\infty}(-C_{mn} - D_{mn} + E_{mn})X_n^z = \gamma_m \qquad (7)$$

for $m = 0,1,2,\cdots$, where $X_0^z = J_0^z$, $X_n^z = 2(-i)^n J_n^z / n$ for $n = 1,2,3,\cdots$. In (7), A_{mn}, B_{mn}, C_{mn}, D_{mn}, E_{mn}, γ_m^x, and γ_m are known coefficients. The unknowns $J_n^{x,z}$ are determined with high accuracy by solving (7) numerically via truncation.

NUMERICAL RESULTS AND DISCUSSION

We shall now present illustrative numerical examples of the RCS for both E and H polarizations to discuss the far field scattering characteristics of the strip in detail. Figure 2 shows the monostatic RCS as a function of incidence angle, where the strip width is $2a = 2\lambda$, 3λ, and

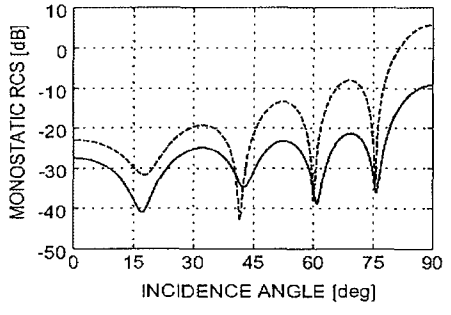

(a) $2a = 2\lambda$.

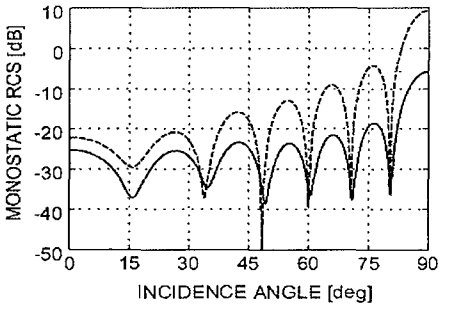

(b) $2a = 3\lambda$.

Fig. 2. Monostatic RCS versus incidence angle for $b = 0.05\lambda$, $\varepsilon_r = 2.5 + i1.25$, $\mu_r = 1.6 + i0.8$. •• :E polarization; - - - -

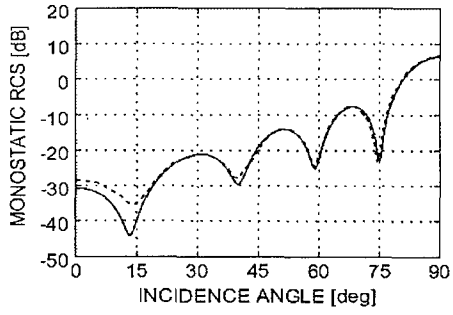

Fig. 3. Monostatic RCS versus incidence angle for H polarization, $2a = 2\lambda$, $b = 0.05\lambda$, $\varepsilon_r = 4.0$, $\mu_r = 1.0$ and its comparison with Volakis [4]. •• : this paper; - - - - : Vo-

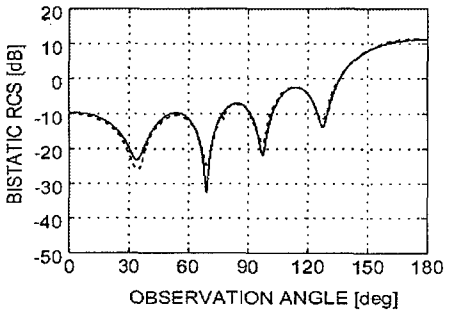

Fig. 4. Bistatic RCS versus observation angle for H polarization, $\theta_0 = 1°$, $2a = 2\lambda$, $b = 0.05\lambda$, $\varepsilon_r = 1.5 + i0.1$, $\mu_r = 1.0$ and its comparison with Volakis [4]. •• : this paper; - - - - :

the strip thickness is $b = 0.05\lambda$.

As an example of existing lossy materials, we have chosen the ferrite with $\varepsilon_r = 2.5 + i1.25$ and $\mu_r = 1.6 + i0.8$ in numerical computation. It is obvious that the peaks at 90° in the figure correspond to the specular reflection from the upper surface of the strip. We also notice that the RCS shows sharp oscillation with an increase of the strip width as can be expected. It is interesting to note that the RCS level for the *E* polarization is lower than that for the *H* polarization over the whole range of the incidence angle.

This problem has previously been analyzed by Volakis [4] for the *H*-polarized case based on the plane wave spectrum method together with the extended spectral ray method. In the formulation, Volakis employed the same approximate boundary conditions as in this paper. Figures 3 and 4 show comparisons with the results obtained by Volakis, where the monostatic RCS as a function of incidence angle and the bistatic RCS as a function of observation angle are illustrated. It is seen from the figure that our results agree reasonably well with Volakis's results.

ACKNOWLEDGMENT

This work was supported in part by the Institute of Science and Engineering, Chuo University.

REFERENCES

[1] Senior, T. B. A., "Backscattering from resistive strips," *IEEE Trans. Antennas Propagat.* Vol. AP-27, pp. 808–813, 1979.

[2] Herman, M. I., and J. L. Volakis, "High frequency scattering by a resistive strip and extension to conductive and impedance strips," *Radio Sci.*, Vol. 22, pp. 335–349, 1987.

[3] Senior, T. B. A., and J. L. Volakis, "Sheet simulation of a thin dielectric layer," *Radio Sci.*, Vol. 22, pp. 1261–1272, 1987.

[4] Volakis, J. L., "High frequency scattering by a thin material half-plane and strip," *Radio Sci.*, Vol. 23, pp. 450–462, 1988.

[5] Senior, T. B. A., and J. L. Volakis, *Approximate Boundary Conditions in Electromagnetics*, IEE, London, 1995.

[6] Veliev, E. I., K. Kobayashi, T. Toda, and S. Koshikawa, "Analytical-numerical approach for the solution of the diffraction by a thin dielectric strip," *Proc. 1997 IEICE General Conference*, No. C-1-40, 1997.

[7] Veliev, E. I., and V. V. Veremey, "Numerical-analytical approach for the solution to the wave scattering by polygonal cylinders and flat strip structures," in *Analytical and Numerical Methods in Electromagnetic Wave Theory*, Chap. 10, M. Hashimoto, M. Idemen, and O. A. Tretyakov, Eds., Science House, Tokyo, 1993.

PLANE WAVE SCATTERING BY SLOTS ON A GROUND PLANE IN THE CASE OF OBLIQUE INCIDENCE AND ARBITRARY POLARIZATION

O.V.Alpatova

Taganrog State University of Radioengineering, Nekrasovsky, 44, GSP - 17A, Taganrog, 347928, Russia, Phone (863- 44) 6-17-33, e-mail: airpu@tsure.ru

ABSTRACT

Plane wave scattering by single or double slots is investigated in the case of oblique incidence and arbitrary polarization. To this end, systems of singular integral — integro-differential equations of the first kind are constructed and discretized by a Krilov - Bogolubov method. Several tests and extensive comparisons with available results were made in order to validate the numerical results. Surface magnetic current densities, angular radiation pattern, equivalent surface impedance and the radar cross sections were calculated for different geometrical parameters of the structure and space parameters.

THEORY

Dielectric loads are often used as convenient means for modifying the scattering properties of the basic slot scatterer. In particular radar cross-section reduction can be achieved by selection of physical parameters dielectric constants, slot dimensions and angle of incidence.

The problem is formulated in the following statement. The unlimited space is divided by the indefinitely thin perfect conducting screen into two areas V_1 and V_2 (Fig. 1). The area V_1 with parameters $\tilde{\varepsilon}_{a1}, \mu_{a1}$ contains stimulating sources, located in volume V_j. Area V_2 with parameters $\tilde{\varepsilon}_{a2}, \mu_{a2}$ is without stimulating sources. The area V_1 borrows the whole top half-space and is limited by a surface S_1, the area V_2 — by a surface S_2. The areas are connected by two parallel

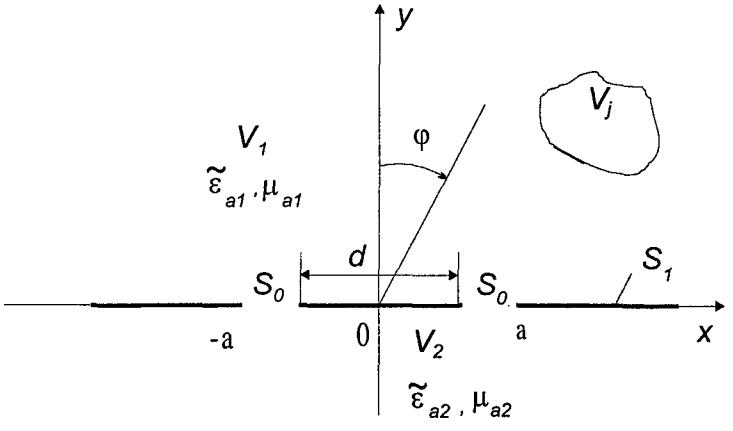

Fig. 1 Geometry of the problem

cracks of width S_0 each, divided by strip conductor of width d. From the upper half-space drops plane electromagnetic waves $(\mathbf{E}^{exc}, \mathbf{H}^{exc})$ under a angle φ, counted from perpendicular to a surface of a screen. We consider the characteristic of exciting sources and design parameters to be independent from coordinate z. It is necessary to define scattering field.

The solution of the problem is carried out by a method of the integral equations. Using the relation of Lorenz lemma in the integral form, boundary conditions, conditions of radiation in the case of H(TE)-polarization results to integral equation

$$\int_{S_0} J_z^{\mathrm{M}}(x')\left(\frac{\omega\varepsilon_{a1}}{2}\mathrm{H}_0^{(2)}(k_1|x-x'|)+\frac{\omega\varepsilon_{a2}}{2}\mathrm{H}_0^{(2)}(k_2|x-x'|)\right)dx' = H_z^{\mathrm{exc}}(x_0,y_0)$$

where J_z^{M} is the equivalent surface magnetic current, $k_1=\omega\sqrt{\varepsilon_{a1}\mu_{a1}}$, $\mathrm{H}_0^{(2)}(k_2|x-x'|)$ is the Hankel function of the second kind and order 0.

Set $y'=0, x'\in[-a,a]$ and apply the boundary condition $\left[\mathbf{n}_1,\mathbf{H}_1^{scat}(x',0)\right]+\left[\mathbf{n}_1,\mathbf{H}^{exc}(x',0)\right]=\left[-\mathbf{n}_1,\mathbf{H}_2^{scat}(x',0)\right]$ where $\mathbf{n}_1=-\mathbf{i}_y$. Then, after some transformations [1], we end up with the integrodifferential equation in the case of E(TM)-polarization:

$$\frac{\partial}{\partial x}\left(-\frac{1}{2\omega\mu_{a1}}\int_{-a}^{a}J_x^M(x')\frac{\partial H_0^{(2)}(k_1R)}{\partial x'}dx'\right)+\frac{\omega\varepsilon_{a1}}{2}\left(\int_{-a}^{a}J_x^M(x')H_0^{(2)}(k_1R)dx'\right)+$$

$$+\frac{\partial}{\partial x}\left(-\frac{1}{2\omega\mu_{a2}}\int_{-a}^{a}J_x^M(x')\frac{\partial H_0^{(2)}(k_2R)}{\partial x'}dx'\right)+\frac{\omega\varepsilon_{a2}}{2}\left(\int_{-a}^{a}J_x^M(x')H_0^{(2)}(k_2R)dx'\right)=H_x^{exc}(x_0,y_0)$$

where $J_x^M(x)$ is the equivalent surface magnetic current, $R=\sqrt{(x-x')^2+(y-y')^2}$.

In the solution procedure $J_x^M(x)$ and $J_z^M(x)$ are approximated by a linear combination of known linearly independent basis functions. In this paper using pulse functions $J_z^M(x)$ or $J_x^M(x)$ is represented in $[-a,a]$ by a plecewise – constant approximation as

$$J_{x,z}^M(x)=\sum_{n=1}^{N}C_nP_n(x)$$

where C_n are unknown constants and the pulse functions $P_n(x)$ are defined as

$$P_n(x)=\begin{cases}1, x\in(x_n-\Lambda/2, & x_n+\Lambda/2)\\ 0, otherwise\end{cases}$$

NUMERICAL RESULTS AND DISCUSSION

To validate algorithms internal as well external tests [2] have been carried out. Following results were obtained: 1) surface magnetic current densities for the single slot and for the double slots; 2) angular radiation pattern; 3) radar cross sections and 4) equivalent surface impedance. Fig. 2 shows the equivalent surface magnetic currents across a slot. Fig. 3 shows formation of field pattern i the case of H-polarization/E-polarization. These numerical results may be easily used for error valuing of the field pattern for $|k|R \approx \lambda$.

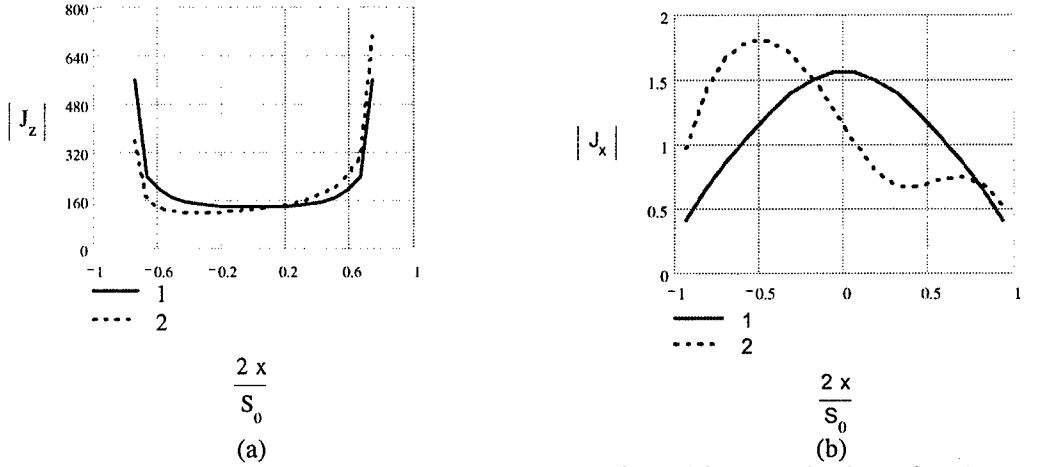

Fig. 2. Surface magnetic current distribution for $S_0 = 0.4\lambda$ and for several values of φ (structure of Fig. 1, $d = 0$, $\varepsilon_{a1} = \varepsilon_{a2} = \varepsilon_0$, $\mu_{a1} = \mu_{a2} = \mu_0$). 1— $\varphi = 0^0$, 2— $\varphi = 30^0$

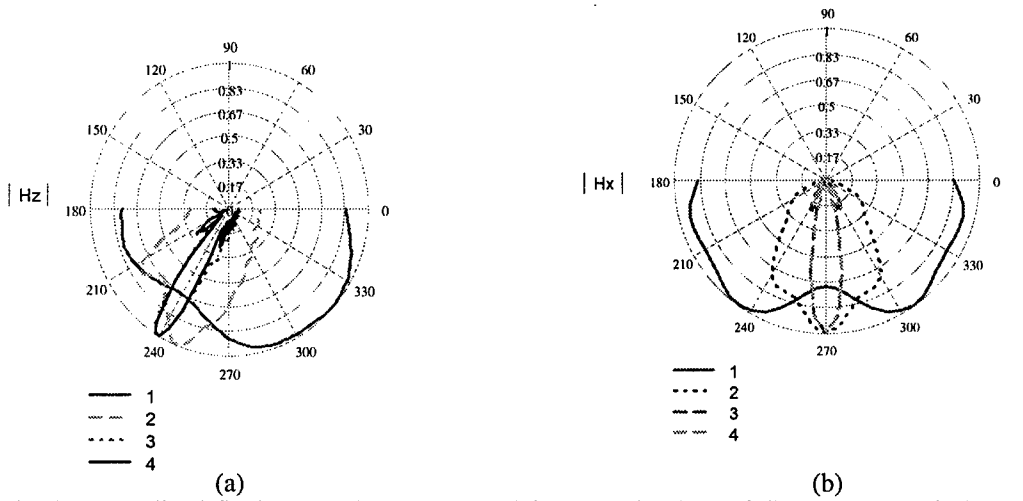

Fig. 3. Normalized field pattern in area V_2 and for several values of R (structure of Fig. 1 $d = 0$, $S_0 = 3\lambda$ $\varepsilon_{a1} = \varepsilon_0$, $\mu_{a1} = \mu_{a2} = \mu_0$) in case H-polarization (a) ($\varphi = 60^0$ $\varepsilon_{a2} = (2.68 - 10.2 \cdot 10^{-4} i)\varepsilon_0$) and E-polarization (b) ($\varphi = 0^0$ $\varepsilon_{a2} = \varepsilon_0$). 1— $R = 0.5\lambda$, 2— $R = 2\lambda$, 3— $R = 7\lambda$, 4— $R = 100\lambda$.

REFERENCES

1. Zaharov, Yu. V. Pimenov, Numerical analysis of waves diffraction, Moscow: RiS. 1982. p. 183 [in Russian].

2. H. Honl, A. Maue, K. Westpfahl, Diffraction theory, Moscow: Mir. 1964. p.428 [in Russian].

THE ELECTROMAGNETIC WAVE DIFFRACTION BY A PARTIALLY SCREENED ANISOTROPIC DIELECTRIC CYLINDER

A.V.Brovenko, P.N. Melezhik, and A.Y. Poyedinchuk

Usikov's Institute of Radiophysics and Electronics, the National Academy of Sciences of Ukraine
12 Akademika Proskury Str., 61085, Kharkov, Ukraine
E-mail: brove@ire,kharkov.ua; chuk@ire.kharkov.ua

A solution method is suggested to the difraction problem of a homogeneous plane H-polarized wave on a partially screened dielectric anisotropic (hyrotropic) cylinder. In the method, the original boundary value problem in terms of the Maxwell's equation is equivalently reduced to the system of dual series equations whose singular part is converted using the direct solution of the corresponding Riemann-Hilbert boundary value problem with the specially developed analytical regularization procedure. The result is the second-kind system of linear algebraic equations with Hilbert - Schmidt operators in the l_2 -space to be effectively solved with the reduction method.

The plane electromagnetic wave diffraction is considered as applied to a partially screened circular dielectric cylinder with the related permittivity tensor as following

$$\hat{\varepsilon} = \begin{Vmatrix} \varepsilon_1 & i\varepsilon_2 & 0 \\ -i\varepsilon_2 & \varepsilon_1 & 0 \\ 0 & 0 & \varepsilon_3 \end{Vmatrix}.$$

The screening is realized with an infinitely thin and perfectly conducting unclosed circular cylinder with the generator parallel to the geometrical axis of the anisotropic cylinder taken for the oZ axis of a Cartesian coordinate system $Oxyz$.The open system extends infinitely in the oz direction, and the excitation electromagnetic field has no z- dependence, suggesting the two - dimensional diffraction problem consideration.

1.In mathematical terms, the problem is as follows. Let S be a section through the uncloused screen in the XoY plane, with the completion ΔS of the circle, $\hat{S} = S \cup \Delta S$. The partially screened dielectric anisotropic cylinder is illuminated with an H- polarized wave $V_0(x,y) = \exp\left(-\left(ikr\cos(\varphi - \alpha)\right)\right)$ which is incident normal to the cylinder axis. Here (r,φ) are polar coordinates originating at the anisotropic cylinder axis, a is the screen radius, $k = \dfrac{2\pi}{\hat{\lambda}}$, and $\hat{\lambda}$ is the excitation wavelength. The electrodynamical system is buried in vacuum. The problem reduces to finding the diffracted field described by two functions $V_1(x,y)$ and $V_2(x,y)$ which are the solution of the boundary value problem

$$\begin{aligned} &\varepsilon_1 \Delta V_2(p) + k^2\left(\varepsilon_1^2 - \varepsilon_2^2\right)V_2(p) = 0, r < a, \\ &\Delta V_1(p) + k^2 V_1(p) = 0, r > a; \end{aligned} \tag{1}$$

$$\begin{aligned} &\lim_{0<h\to 0} \frac{\partial\left(V_0(p+h\vec{n}) + V_1(p+h\vec{n})\right)}{\partial\vec{n}}\Big|_{p\in S} = \\ &= \lim_{0<h\to 0}\left(\frac{\partial V_2(p-h\vec{n})}{\partial\vec{n}} - i\tau\frac{\partial V_2(p-h\vec{n})}{\partial\vec{\nu}}\right)\Big|_{p\in S} = 0; \end{aligned} \tag{2}$$

$$\lim_{0<h\to 0}\left(\left(\varepsilon_1^2-\varepsilon_2^2\right)V_2\left(p-h\vec{n}\right)-V_0\left(p+h\vec{n}\right)-V_1\left(p+h\vec{n}\right)\right)\Big|_{p\in\hat{S}}=0,$$

$$\lim_{0<h\to 0}\left(\varepsilon_1\left(\nabla V_2\left(p-h\vec{n}\right),\vec{n}\right)-i\varepsilon_2\left(\nabla V_2\left(p-h\vec{n}\right),\vec{\nu}\right)-\left(\nabla V_1\left(p+h\vec{n}\right),\vec{n}\right)-\right.$$

$$\left.-\left(\nabla V_0\left(p+h\vec{n}\right),\vec{n}\right)\right)\Big|_{p\in\hat{S}}=0. \qquad (3)$$

The boundary conditions are that the tangential component of the total electric field vanishes at the screen
(condition (2)) and the tangential components of the electric and magnetic fields are continuous across the boundary of the dielectric anisotropic cylinder (condition (3)).

In addition, for $V_m(x,y), m = 1,2$, the Meixner condition holds in any compact in R^2, and $V_1(x,y)$ must fit the Sommerfeld radiation condition at infinity. The time dependence is $\exp(-i\omega t)$; $\vec{n}$ and $\vec{\nu}$ are, respectively, the unit vectors of an outer normal and a tangent taken at an arbitrary point of the screen. Functions $V_1(x,y)$ and $V_2(x,y)$ are related to the H_z - component of the scattered magnetic field as

$$H_z=\begin{cases}\left(\varepsilon_1^2-\varepsilon_2^2\right)V_2(x,y), r<a;\\ V_1(x,y), r>a.\end{cases}$$

The rest electromagnetic field components are obtained from the Maxwell's equations using $V_1(x,y)$ and $V_2(x,y)$.

2. In terms of the Fourier series expansion of $V_m(x,y), m=1,2$ in function system $\left\{e^{im\varphi}\right\}_{m=-\infty}^{+\infty}$ and with Sommerfeld radiation condition imposed, original boundary value problem (1) - (3) reduces to the system of dual series equations

$$\sum_{n=1}^{+\infty} n x_n e^{in\hat{\varphi}}-\frac{(1-\tau)(1+\lambda+\tau)}{(1+\tau)(1+\lambda-\tau)}\sum_{n=-1}^{-\infty} n x_n e^{in\hat{\varphi}}=g\left(e^{i\hat{\varphi}}\right);|\hat{\varphi}|<\hat{\theta},$$

$$\sum_{n=-\infty}^{+\infty} x_n e^{in\hat{\varphi}}=0;\hat{\theta}<|\hat{\varphi}|\le\pi. \qquad (4)$$

Here $\left\{x_n\right\}_{n=-\infty}^{+\infty}$ are the unknown coefficients corresponding to function $V_m(x,y), m=1,2$, $\hat{\varphi}=\pi+\varphi$, $\hat{\theta}=\pi-\theta$, where θ describes the considered system geometry, $\lambda=\dfrac{\varepsilon_1^2-\varepsilon_2^2}{\varepsilon_1}$, *and* $\tau=\dfrac{\varepsilon_2}{\varepsilon_1}$.

For reasons of space, a quite cumbersome expression of function $g(\zeta)$ is not presented. We only notice that it depends on the excitation field and coefficients x_n.

System (4) differs from typical systems of this kind by $\dfrac{(1-\tau)(1+\lambda+\tau)}{(1+\tau)(1+\lambda-\tau)}\neq 1$. On the other hand, if we use, say, the orthogonality of functions $e^{im\varphi}, m=0,\pm1,\pm2,\ldots$ on interval $[-\pi,\pi]$, (4) is easily reduced to the infinite system of linear algebraic equations for coefficients x_n. This change however

is not good in view of the Meixner condition indicating that $x_n = O\left(|n|^{-\frac{3}{2}}\right)$. This will cause a poor convergence of the Fourier series in (4) and consequently a clow decrease of the matrix coefficients of the corresponding infinite system of linear algebraic equations. In addition, the condition numbers of the corresponding truncated systems of equations rapidly decrease with the truncation order. Therefore a direct computer calculation of (4) is not possible.

We suggest an alternative approach to the solution of system (4). It rests on the analytical regularization of system (4) and yield a closed - form regularizer on basis of the Riemann - Hilbert boundary value conjugation problem. This approach is presented in [1] and involves two stages.

At the first stage, functions $X^+(z) = \sum_{n=1}^{+\infty} n x_n z^n$, $X^-(z) = -\sum_{n=1}^{+\infty} n x_{-n} z^{-n}$ -

which are analytic, respectively, in the interior and exterior of circle $|z| < 1$ make it possible to reduce system (4) to the boundary value conjugation (Riemann - Hilbert) problem of the form

$$X^+(\zeta) - X^-(\zeta) = 0, \zeta \in \gamma_1; \tag{5}$$

$$X^+(\zeta) + \frac{(1-\tau)(1+\lambda+\tau)}{(1+\tau)(1+\lambda-\tau)} X^-(\zeta) = g(\zeta), \zeta \in \gamma_2, \tag{6}$$

where $e^{im\varphi}, m = 0, \pm 1, \pm 2, \ldots$

Here γ_1 is the arc of circle $|z| = 1$ which connects points $\exp(-i\hat{\theta})$ and $\exp(i\hat{\theta})$ and passes through point $z = -1$, arc γ_2 is the γ_1 extension to complete circle $|z| = 1$.

At the second stage, Riemann - Hilbert problem (6) is solved with the following application of Sokhotsky - Plemel formulae [2]. A change to the Fourier coefficients yields the solution of (4) in the operator form

$$\hat{x} = B\hat{x} + \hat{w} \ . \tag{7}$$

Here $B = A \times U$, where $A = \left\| A_{nm} \right\|_{n,m=-\infty}^{+\infty}$ is given in [1], and $U = \left\| U_m \delta_m^n \right\|_{n,m=-\infty}^{+\infty}$, where

$$U_m = \begin{cases} (1 + \varepsilon_1 - \varepsilon_2) f_0(ka); m = 0, \\ \zeta_m |m| \delta_m; m \neq 0. \end{cases}$$

Here δ_m^n is the kroneccker delta, and $\zeta_m = \begin{cases} 1; m > 0 \\ \dfrac{1 + \varepsilon_1 + \varepsilon_2}{1 + \varepsilon_1 - \varepsilon_2}; m < 0, \end{cases}$ where δ_m is the smallness parameter, with $\delta_m = O\left(\frac{1}{m^2}\right)$ as $m \to \pm\infty$.

Matrix $B = \left\| B_{nm} \right\|_{n,m=-\infty}^{+\infty}$ gives the Hilbert - Schmidt operator in l_2 and $\hat{w} = (w_n)_{n=-\infty}^{+\infty} \in l_2$. On this basis and in accordance with the Fredholm alternative and the uniqueness theorem it follows that a solution of system (7) exists and it is unique. It can be obtained on computer with the reduction method. A knowledge of x_n readily gives $V_m(x, y)$, $m = 1,2$.

REFERENCES

[1] A. V. Brovenko and A. Ye. Poyedinchuk. A regularization Method for a class of dual Series Equation in Diffraction Theory MSMW' 98 Symposium proceedings p. 320 - 322.

[2] N.I. Mushelishvily. Singular Integral Equations. M.,1962.-599 p. (in Russian).

REGULARIZATION BY THE INTEGRAL IDENTITIES METHOD FOR INTEGRAL AND SERIES EQUATIONS IN DIFFRACTION PROBLEMS

Pleshchinskii N.B., and Tumakov D.N.

Kazan State University
P.O.Box 234 Kazan, 420503, Russia
E-mail: pnb@ksu.ru

A method of integral identities for the regularization of some problems of the diffraction theory of the electromagnetic waves is proposed. Two auxiliary overdetermined Cauchy problems for the Helmholtz equation for a half-plane and for a half-strip are considered. It is shown that the Fourier transforms of the boundary functions must satisfy some condition. The special integral identities can be obtained from this condition. In the periodical case the integral identities have a summatorial identities form.
Two particular problems are studied: the plane electromagnetic wave diffraction on a periodic metallic grating and the problem of diffraction on a step in the plane waveguide with metallic walls. It is shown that these problems are equivalent to infinite systems of linear algebraic equations (ISLAE) of the second kind.

INTEGRAL AND SUMMATORIAL IDENTITIES

Consider the Cauchy problem for the Helmholtz equation in the half-plane

$$\frac{\partial^2 u}{\partial x^2}+\frac{\partial^2 u}{\partial z^2}+k^2 u(x,z)=0, \quad z>0. \tag{1}$$

We will seek the solutions of equation (1) in the Sobolev space $H_s(R_2^+)$, $s>3/2$ of distributions of slow growth at infinity. Denote

$$\gamma(\xi)=\{|\,\xi\,|\geq k : +i\sqrt{\xi^2-k^2}; \quad |\,\xi\,|\leq k : -\sqrt{k^2-\xi^2}\}.$$

It is proved in [1] (see [2], too) that

Lemma 1 . *The solution $u(x,z)$ of the equation (1) belongs to the class of solutions outgoing from the straight line $z=0$ into a half-plane $z>0$ and satisfies the boundary conditions*

$$u(x,0)=u_0(x), \quad \frac{\partial u}{\partial z}(x,0)=u_1(x), \quad -\infty<x<+\infty$$

if and only if when Fourier transforms of the boundary functions satisfy the equality

$$u_1(\xi)-i\gamma(\xi)u_0(\xi)=0. \tag{2}$$

From (2) it follows that the following integral identities are valid

$$u_1(x)=\int_{-\infty}^{+\infty} u_0(\tau)\left(\frac{1}{2\pi}\int_{-\infty}^{+\infty} i\gamma(\xi)e^{i\xi(\tau-x)}d\xi\right)d\tau, \tag{3}$$

$$u_0(x)=\int_{-\infty}^{+\infty} u_1(\tau)\left(-\frac{1}{2\pi}\int_{-\infty}^{+\infty}\frac{i}{\gamma(\xi)}e^{i\xi(\tau-x)}d\xi\right)d\tau. \tag{4}$$

Suppose that the distribution $u(x,z)$ is l-periodical by the variable x. Denote $\Lambda=2\pi/l$ and $\gamma_n=\gamma(\Lambda n)$, $n=0,\pm1,...$ We obtain two summatorial identities from (3) and (4)

Lemma 2.

$$\int_0^l \left(\sum_{n=-\infty}^{+\infty} a_n \gamma_n e^{i\Lambda n\tau} \right) \frac{1}{l} \sum_{m=-\infty}^{+\infty} \gamma_m e^{i\Lambda m(y-\tau)}\, d\tau = \sum_{n=-\infty}^{+\infty} a_n e^{i\Lambda n y}, \quad y \in (0,l), \tag{5}$$

$$\int_0^l \left(\sum_{n=-\infty}^{+\infty} a_n e^{i\Lambda n\tau} \right) \frac{1}{l} \sum_{m=-\infty}^{+\infty} \frac{1}{\gamma_m} e^{i\Lambda m(y-\tau)}\, d\tau = \sum_{n=-\infty}^{+\infty} a_n \gamma_n e^{i\Lambda n y}, \quad y \in (0,l). \tag{6}$$

Now we consider two Cauchy problems for the equation (1) in the half-strip $x > 0$, $0 < z < h$ [2]. Denote $\Gamma = \pi / h$, $\phi_n(z) = \sin n\Gamma z$ or $\phi_n(z) = \cos n\Gamma z$, $n = (0),1,\ldots$ and

$$\delta_n = \{k^2 - n^2\Gamma^2 \geq 0 : \sqrt{k^2 - n^2\Gamma^2};\ \ k^2 - n^2\Gamma^2 \leq 0 : -i\sqrt{n^2\Gamma^2 - k^2}\}.$$

Lemma 3. *The solution $u(x,z)$ of the equation (1) belongs to the class of solutions outgoing from the straight line $x > 0$ to the right and satisfies the boundary conditions*

$$u(0,z) = u_0(z), \quad \frac{\partial u}{\partial x}(0,z) = u_1(z), \quad 0 < z < h,$$

$$u(x,0) = 0, \ \ u(x,h) = 0, \ \ x > 0 \quad or \quad \frac{\partial u}{\partial z}(x,0) = 0, \ \ \frac{\partial u}{\partial z}(x,h) = 0, \ \ x > 0$$

if and only if when Fourier coefficients of the boundary functions satisfy the equalities

$$u_{1n} + i\delta_n u_{0n} = 0, \quad n = (0),1,\ldots \tag{7}$$

From equalities (7) it follows that

Lemma 4.

$$\int_0^h \left(\sum_{n=(0)1}^{\infty} a_n \gamma_n \phi_n(t) \right) \frac{2}{h} \sum_{m=(0)1}^{\infty} \frac{1}{\gamma_m} \phi_m(t)\phi_m(z)\, dt = \sum_{n=(0)1}^{\infty} a_n \phi_n(z), \quad z \in (0,h), \tag{8}$$

$$\int_0^h \left(\sum_{n=(0)1}^{\infty} a_n \phi_n(t) \right) \frac{2}{h} \sum_{m=(0)1}^{\infty} \gamma_m \phi_m(t)\phi_m(z)\, dt = \sum_{n=(0)1}^{\infty} a_n \gamma_n \phi_n(z), \quad z \in (0,h). \tag{9}$$

TWO DIFFRACTION PROBLEMS

Suppose that a plane TE-polarisated wave falls on the l-periodical ideally conducting infinitely thin metallic grating [3]. We will search the potential functions of electromagnetic fields in the forms

$$u^+(y,z) = \sum_{n=-\infty}^{+\infty} a_n e^{i\gamma_n z} e^{i\Lambda n y}, \ \ z > 0, \quad u^-(y,z) = \sum_{n=-\infty}^{+\infty} b_n e^{-i\gamma_n z} e^{i\Lambda n y}, \ \ z < 0.$$

We denote by M the part of the interval $(0, l)$ corresponded to the metallic bands and by N the rest part of the interval. It is easy to show that the diffraction problem is equivalent to the summatorial equation

$$\sum_{n=-\infty}^{+\infty} a_n e^{i\Lambda n y} = -1, \quad y \in M, \tag{10}$$

$$\sum_{n=-\infty}^{+\infty} a_n \gamma_n e^{i\Lambda n y} = 0, \quad y \in N. \tag{11}$$

Denote

$$I_k = \int_M e^{i\Lambda k\tau} d\tau, \quad J_k = \int_N e^{i\Lambda k\tau} d\tau, \quad k = 0,\pm 1,...$$

From the identity (5) and the equation (11) it follows that

$$\sum_{n=-\infty}^{+\infty} a_n e^{i\Lambda ny} = \frac{1}{l} \sum_{n=-\infty}^{+\infty} a_n \gamma_n \sum_{m=-\infty}^{+\infty} \frac{1}{\gamma_m} I_{n-m} e^{i\Lambda my}, \quad y \in N. \tag{12}$$

Theorem 1 . *The diffraction problem on the metallic periodical grating is equivalent to the ISLAE of the second kind*

$$\sum_{n=-\infty}^{+\infty} a_n e^{i\Lambda ny} = \frac{1}{l} \sum_{n=-\infty}^{+\infty} a_n \gamma_n \sum_{m=-\infty}^{+\infty} \frac{1}{\gamma_m} I_{n-m} e^{i\Lambda my}, \quad k = 0,\pm 1,... \tag{13}$$

We consider the diffraction problem on the step in the planar waveguide with metallic walls [3]. Let the plane $x=0$ separates two waveguides $x<0$, $\alpha<z<\beta$ and $x>0$, $a<z<b$, here $a \le \alpha < \beta \le b$. We denote $N=(\alpha,\beta)$, $M=(a,\alpha)\cup(\beta,b)$, $h^+=b-a$, $h^-=\beta-\alpha$, $\Gamma^{\pm}=\pi/h^{\pm}$, $\phi_n^-(z)=\sin\Gamma^- n(z-\alpha)$, $\phi_n^+(z)=\sin\Gamma^+ n(z-a)$, $n=(0),1,...$ and $\delta_n^{\pm}=\sqrt{(k^{\pm})^2-(\Gamma^{\pm}n)^2}$, $n=(0),1,...$ Let an eigen wave with the potential function

$$u^0(x,z) = A^0 e^{-i\delta_{n^0}^- x} \phi_{n^0}^-(z), \quad x<0$$

falls from the left waveguide on the junction of the waveguides. The diffracted field is presented in the form

$$u^+(x,z) = \sum_{n=(0)1}^{\infty} A_n e^{-i\delta_n^+ x} \phi_n^+(z), \quad x>0, \quad u^-(x,z) = \sum_{n=(0)1}^{\infty} B_n e^{+i\delta_n^- x} \phi_n^-(z), \quad x<0.$$

We obtain from the conjucation conditions at the media interface and from the identity (8)

Theorem 2 . *The diffraction problem on the step in the planar waveguide is equivalent to the ISLAE of the second kind*

$$\frac{h^+}{2} A_k + \frac{2}{h^-} \sum_{n=(0)1}^{\infty} A_n \delta_n^+ \sum_{m=(0)1}^{\infty} \frac{1}{\delta_m^-} I_{nm} I_{km} = 2A^0 I_{kn^0}, \quad k = (0),1,... \tag{14}$$

where

$$I_{nm} = \int_N \phi_n^+(t) \phi_m^-(t) dt, \quad n,m = (0),1,...$$

It is proved that the ISLAE (13) and (14) can be numerical solved by reduction method.

REFERENCES

[1] I.E.Pleshchinskaya, N.B.Pleshchinskii, The Cauchy problem and potentials for elliptic partial differential equations and some of their applications, Advances in Equations and Inequalities (A.E.I) (ed. J.M.Rassias), Athens, Greece, 1999.

[2] N.B.Pleshchinskii, D.N.Tumakov, Method of fractional fields for the scalar coordinate diffraction problems of the electromagnetic waves in the classes of distributions, Kazan Mathematical Society, Preprint 2000-1, Kazan, 2000 (in Russian).

[3] V.P.Shestopalov, A.A.Kirilenko, S.A.Masalov, Convolution Type Matrix Equations in Diffraction Theory, Kiev: Naukova Dumka, 1984 (in Russian).

ELECTROMAGNETIC WAVE DIFFRACTION BY INFINITELY THIN PERFECTLY CONDUCTING CIRCULAR RING

Y.A.Tuchkin [1,2], F.Dikmen[2], S.I.Tarapov [1,2]

[1] *Institute of Radiophysics and Electronics, NAS of the Ukraine, 12 Ac. Proscura St., Kharkov 310085, Ukraine*

[2] *Gebze Institute of Technology, PK. 141, 41400 Gebze-Kocaeli, Turkey.*

Abstract

A new strong mathematically rigorous and numerically effective method for solving a boundary value problem of electromagnetic wave diffraction by an infinitely thin perfectly conductive circular ring screen is proposed.

The method is based on the combination of the Orthogonal Polynomials Approach and he ideas of the Analytical Regularization Methods. As a result of the suggested regularization procedure, the initial boundary value problem is equivalently reduced to the infinite system of the linear algebraic equations of the second kind in the space of square summable sequences.

This equation can be solved numerically by means of truncation method with, in principle, any desired accuracy.

The perspective of the method also includes the solution to the problem of electromagnetic wave diffraction by a few infinitely thin circular ring screens.

Pilot experiments show good perspective of such ring reflector for development of individual antenna tag for rescue radar systems.

MODELING OF A SLOT-EXCITED SPHERICAL-CIRCULAR MICROSTRIP ANTENNA

Valery V. Radchenko [1,2], Alexander I. Nosich [1,2], Jean-Pier Daniel [2], Sergey S. Vinogradov [3]

[1] Institute of Radiophysics and Electronics, National Academy of Sciences
Kharkov 310085, Ukraine
[2] Laboratoire Antennes et Reseaux, Universite de Rennes 1, Rennes, 35042, France
[3] Department of Mathematical Sciences, University of Dundee
Dundee, DD1 4HN, Scotland, UK

INTRODUCTION

Conformal printed antennas are frequently used in mobile and wireless communications and radar due to their low profile and light weight. In this paper, the problem of modeling of a spherical-disk conformal printed antenna is considered assuming an excitation by a slot. The slot is modeled by a tangential magnetic dipole (TMD) located at the surface of the metal sphere covered with dielectric. Previously, similar problems have been analyzed by the method-of-moments [1,2]. However, accuracy of these numerical approximations suffer if narrow resonances are present [3]. We propose an exact mathematical method based on the analytical inversion of the free-space static problem for a spherical disk [4,5]. This method is remarkable for the stable and fast numerical solutions. Our study is a further development of [6], where we analyzed a similar conformal microstrip antenna excited by a probe simulated with an electric dipole.

PROBLEM FORMULATION

Consider a zero-thickness perfectly conducting spherical disk of the curvature radius c and angular width $2\theta_0$ located on a dielectric substrate of the thickness h and dielectric constant ε (see Fig. 1) and backed by a metal sphere of the radius a. The disk is symmetrically excited by a TMD located at the surface of the metal sphere. The time dependence is assumed to be $e^{-i\omega t}$.

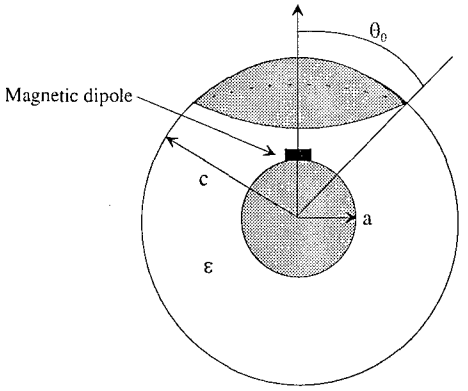

Fig.1 Geometry of the problem.

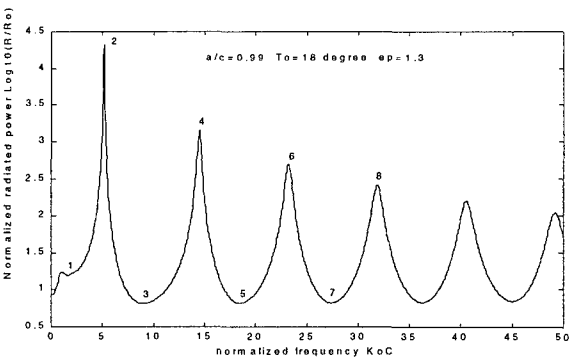

Fig.2 Frequency scan of the radiated power.

METHOD OF SOLUTION

Denote the substrate as the region « (1) » and the outer space as the region « (2) ». To comply with the solution uniqueness, the total field components must satisfy the following requirements: (A) time-harmonic Maxwell's equations with the wavenumber k_0 or $k = k_0\sqrt{\varepsilon}$, (B) the set of the boundary and continuity conditions on the complete spherical surfaces $r = a$ and $r = c$, (C) the set of dual conditions on the complementary segments of the spherical surface $r = c$:

$$E_\theta^{(1,2)}\big|_{r=c} = 0, \quad E_\varphi^{(1,2)}\big|_{r=c} = 0 \quad \theta \in (0, \theta_0), \tag{1}$$

$$H_\theta^{(1)}\big|_{r=c} = H_\theta^{(2)}\big|_{r=c}, \quad H_\varphi^{(1)}\big|_{r=c} = H_\varphi^{(2)}\big|_{r=c} \quad \theta \in (\theta_0, \pi), \tag{2}$$

(D) the Silver-Muller radiation condition at $r \to \infty$ that can be written as an asymptotic request to the field to behave as an outgoing electromagnetic spherical wave, (E) the power boundedness condition in any finite space domain enclosing the disk rim. Fulfillment of these conditions provides uniqueness of the solution. The method of solution includes the following steps: 1) reducing of the boundary-value problem to the dual series equations in terms of a global set of the associated Legendre functions; 2) separation of the static part of the problem of a free-space disk, 3) static part inversion based on the Abel integral equation technique. To obtain the unknown fields we use the expressions for electric and magnetic Debye potentials in the form of spherical harmonic series expansions. The problem is finally reduced to determination of the expansion coefficients $z_n^{(e)}, z_n^{(m)}$ from the following matrix equation (see [4,5] for details):

$$\begin{cases} z_m^{(e)} - \sum_{n=1}^{\infty} z_n^{(e)} \varepsilon_n R_{nm}(\theta_0) + 2k_0 c(1+\sqrt{\varepsilon}) A\, R_{0m}(\theta_0) - B\, R_{0m}(\theta_0) = \sum_{n=1}^{\infty} \alpha_n^{(e)} \left[\delta_n^m - R_{nm}(\theta_0)\right], \\ -\sum_{n=1}^{\infty} z_n^{(e)} \varepsilon_n R_{n0}(\theta_0) + 2k_0 c(1+\sqrt{\varepsilon}) R_{00}(\theta_0) A + (1 - R_{00}(\theta_0)) B = -\sum_{n=1}^{\infty} \alpha_n^{(e)} R_{n0}(\theta_0) \quad m = 0 \\ z_m^{(m)} - \sum_{n=1}^{\infty} z_n^{(m)} \mu_n Q_{nm}(\theta_0) - \dfrac{1}{k_0 c} A\, Q_{0m}(\theta_0) + B\, Q_{0m}(\theta_0) = \sum_{n=1}^{\infty} \alpha_n^{(m)} \left[\delta_n^m - Q_{nm}(\theta_0)\right], \\ 0 = -2k_0 c(1+\sqrt{\varepsilon}) A\, R_{00}(\theta_0) - B\, (1 - R_{00}(\theta_0)) + \sum_{n=1}^{\infty} z_n^{(e)} \varepsilon_n R_{n0}(\theta_0) - \sum_{n=1}^{\infty} \alpha_n^{(e)} R_{n0}(\theta_0) \quad m = 0 \end{cases} \tag{3}$$

Here, δ_n^m is Kronecker's delta, A, B are some auxiliary constants, $\varepsilon_n, \mu_n, \alpha_n^{(e)}, \alpha_n^{(m)}$ are the functions of $kc, a/c, \varepsilon_n$ and μ_n, and

$$R_{nm}(\theta_0), Q_{nm}(\theta_0) = \frac{1}{\pi}\left[\frac{\sin(n-m)\theta_0}{n-m} \mp \frac{\sin(n+m+1)\theta_0}{n+m+1}\right] \tag{4}$$

The matrix equation (3) has favorable features. Its exact solution can be approximated as accurately as desired by solving progressively larger truncated counterparts.

RADIATION CHARACTERISTICS

On solving (3), one can easily find the far-field patterns, total radiated power, directivity and surface current density. The normalized radiated power as a function of the normalized frequency is shown in Fig. 2. The far-field radiation patterns computed at the frequencies marked by numbers in Fig.2 are presented in Fig.3. One can see the appearance of new sidelobes when antenna is excited at higher-order modes of the disk.

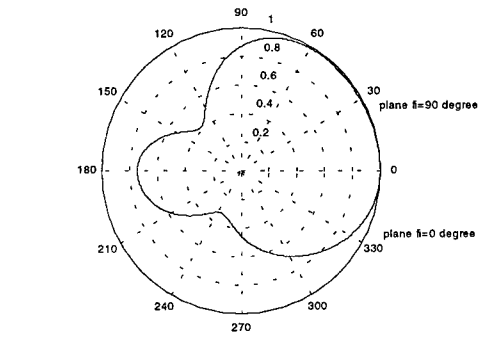

1

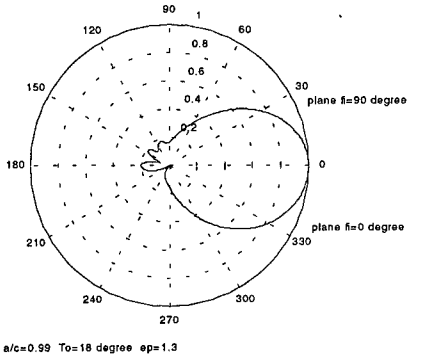

2

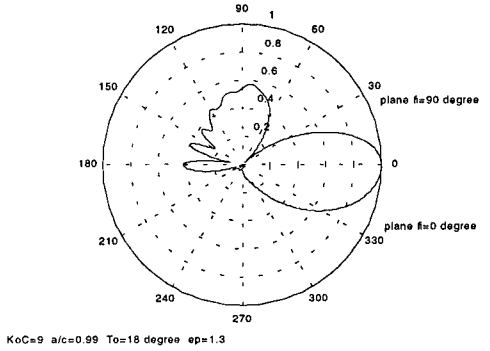

3

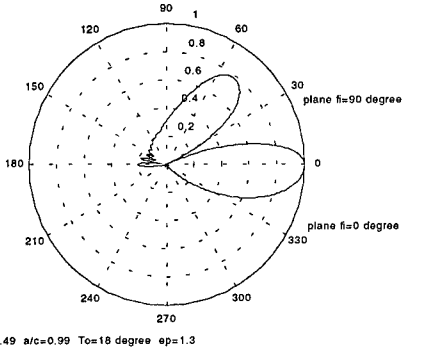

4

Fig.3

CONCLUSIONS

The presented approach enables one to analyze the basic antenna characteristics in full-wave manner. Due to analytical inversion of the singular part of the problem, the resulting algorithm is very efficient. Numerical study hence delivers a reliable information on the antenna performance both in and off resonances. Such a study confirms intuitive considerations that a patch can enhance the radiation conductance of a slot.

References

1. B. Ke, A.A. Kishk, Analysis of spherical circular microstrip antennas, *Proc. IEE, Pt. H,* vol. 138, pp. 542-548, 1991.

2. K.-L. Wong, S.-F. Hsiao, H.-T. Chen, Resonance and radiation of a superstate-loaded spherical-circular microstrip patch antenna, *IEEE Tr.Ant. Propagat.,* vol. AP-41, no 5, pp. 686-690, 1993.

3. G.L. Hower, R.G. Olsen, J.D. Earls, J.B. Schneider, Inaccuracies in numerical calculation of scattering near natural frequencies of penetrable objects, *IEEE Trans. Antennas Propagat.,* vol. AP-41, no 7, pp. 982-986, 1993.

4. S.S. Vinogradov, A soft spherical cap in the field of a plane sound wave, *USSR J. Comput. Maths Math. Physics (Engl. Transl.),* vol. 18, no 5, pp. 244-249, 1978.

5. S.S. Vinogradov, Y.A. Tuchkin, V.P. Shestopalov, Summatory equations with kernels in the form of Jacobi polynomials, *Soviet Physics Doklady (Engl. Tr.),* vol. 25, no 7, pp. 531-532, 1980.

6. V.V. Radchenko, A.I. Nosich, J.-P. Daniel, S.S. Vinogradov, A conformal spherical-circular microstrip antenna: axisymmetric excitation by an electric dipole, *Microwave Optical Technol. Lett.*, vol. 26, no 3, pp. 176-182, 2000.

ACCURATE NUMERICAL SOLUTION OF A DIFFRACTION PROBLEM FOR A NON-EQUIDISTANT AXISYMMETRIC STRUCTURE CONSISTING OF CIRCULAR DISKS

Alexander N. Khizhnyak [1]

[1] Kharkov Branch of Scientific and Industrial Concern "Nauka"
Krasnoznamennaya str, 4, Kharkov, 310002, Ukraine
E-mail alex@khizh.kharkov.ua

Wave diffraction problem associated with an electric dipole radiation in the presence of a finite non-equidistant array of circular perfectly conducting identical disks is considered in this paper. An axial dipole placed on the axis of rotational symmetry. The aim of the work is to obtain mathematically and numerically exact solution of the appropriate boundary problem. By using the moment method combined with a partial inversion of the problem operator, the problem reduces to numerical solving of infinite matrix equation set of the 2-nd kind. The Fredholm nature of obtained equations ensures the existence of the unique solution.

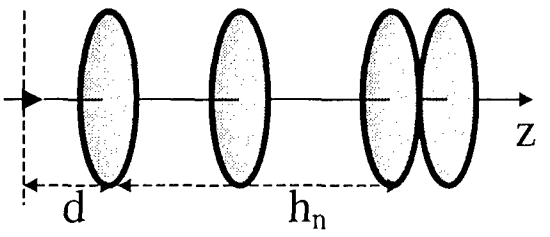

Fig.1.Scattering structure

The scheme to obtain the solution is as follows. The unknown scattered fields are written using Hankel integral transform which is convenient accounting the problem symmetry. From the boundary conditions, one can obtain the set of dual integral equations for the unknown spectral amplitudes. As obtained equation set is of the first kind, one has to provide their regularization in order to obtain a convergent numerical algorithm. Therefore, we use the method of the partial inversion of the problem operator. Eventually original equations are reduced to the matrix one of the second kind, which can be solved by using standard numerical methods. Developed approach does not contain principal limitation on geometrical parameters of the problem and provides an opportunity to compute the solution with any desired accuracy up to the machine precision.

Consider the diffraction of a dipole source field by the structure consisting of N+1 coaxial perfectly conducting disks with the same radii that are placed at the arbitrary distance h_n from the first one. The origin of the cylindrical coordinate system (r, ϕ, z) is in the center of the first disk so that all the other disks are placed in the domain $z>0$. A source field wave is incident on the structure from the domain $z<0$. Time dependence supposed to be $\exp(-i\omega t)$. Accounting the problem's symmetry one can describe the electromagnetic field using only one component of the Herz vector. The problem is to determine a scalar function $P(r, z; k)$, which characterizes the resulting field, here $k=2\pi/\lambda$ is the wave number. This function can be decomposed as a sum of the incident P_0 and the scattered P_S fields. It is convenient to expand the scattered field by using the Hankel integral transform in r

$$P_s(r,z;k) = \int_0^\infty a(\xi) J_0(\xi r) e^{-iz\gamma(\xi)} d\xi, \quad z<0, \tag{1}$$

$$P^{+}_{s,n}(r,z;k) = \int_0^\infty c_n(\xi) J_0(\xi r) e^{i(z-h_{n-1})\gamma(\xi)} d\xi,$$

$$P^{-}_{s,n}(r,z;k) = \int_0^\infty b_n(\xi) J_0(\xi r) e^{-i(z-h_n)\gamma(\xi)} d\xi,$$

$$h_{n-1} < z < h_n,$$

$$P_s(r,z;k) = \int_0^\infty d(\xi) J_0(\xi\rho) e^{i(z-h_N)\gamma(\xi)} d\xi, \quad z > h_N,$$

$$P_0(r,z;k) = -i \int_0^\infty \frac{\xi}{\gamma(\xi)} J_0(\xi\rho)\, e^{i|z+d|\gamma(\xi)} d\xi, \text{ - incident field.}$$

$\gamma(\xi) = \sqrt{\kappa^2 - \xi^2}$, $\mathrm{Im}\,\gamma \geq 0$, $n = 1,2,3...N$, the number of disks is $N+1$, unknown spectral amplitudes $a(\xi), d(\xi), b_n(\xi), c_n(\xi)$ are to be determined.

From the boundary conditions one can arrive to the dual integral equations for the unknown spectral amplitudes. Using the moment method, these equations can be reduced to the matrix ones. It is well known that efficiency of the moment method strongly depends on the proper choice of basic functions. We seek the solution as a series in terms of the functions $\phi_n^{(m)}(\xi)$

$$\phi_n^{(m)}(x) = \sqrt{4n+2m+3}\, J_{2n+m+3/2}(x) x^{-1/2} \tag{2}$$

The following properties take place:

$$\int_0^\infty \phi_n^{(m)}(\xi)\phi_s^{(m)}(\xi) d\xi = \delta_{ns}$$

$$\int_0^\infty \phi_n^{(m)}(\xi) J_m(\xi\rho) d\xi = \Phi_n^{(m)}(\rho) = \frac{n!}{\Gamma(n+3/2)} \sqrt{\frac{4n+2m+3}{2}}\, \rho^m (1-\rho^2)^{1/2} P_n^{(m,1/2)}(1-2\rho^2), \rho<1,$$

$$= 0, \rho > 1,$$

$$\int_0^1 \Phi_n^{(m)}(\rho) J_m(\xi\rho)\rho d\rho = \frac{1}{\xi}\phi_n^{(m)}(\xi),$$

where $P_n^{(\alpha,\beta)}(x)$ are the Jakobi polynomials.

Introduce the auxiliary functions $u_n^{\pm}(\xi)$

$$u_n^{\pm}=\xi\left((c_n \pm b_n)-(c_{n-1}e^{i(h_{n-1}-h_{n-2})\gamma(\xi)} \pm b_{n+1})e^{i(h_{n+1}-h_n)\gamma(\xi)}\right) \qquad (3)$$

On expanding the functions $u_n^{\pm(m)}(\xi)$ in terms of the functions (2):

$$u_n^{\pm}(\xi) = \sum_{s=0}^{\infty} C_{n,s}^{\pm}\phi_s^{(1)}(\xi)$$

one comes to the infinite matrix equation for the unknown coefficients $C_{n,s}^{\pm}$

$$B_{n,s}^{\pm} = \sum_{j=0}^{\infty} C_{n,j}^{\pm}A_{n,js}^{\pm} - C_{n,s}^{\pm} + \sum_{j=0}^{\infty}\sum_{r=0}^{n-1}(C_{n-r-1,j}^{+} + C_{n-r-1,j}^{-})D_{n,r;js}^{\pm} \pm \qquad (4)$$

$$\pm \sum_{j=0}^{\infty}\sum_{r=0}^{N-n-1}(C_{n+r+1,j}^{+} - C_{n+r+1,j}^{-})G_{n,r;js}^{\pm},\ n=1,2...N.$$

$$B_{n,s}^{\pm} = -i\int_0^{\infty} \phi_s^{(1)}(\xi)\, q(\xi)e^{ih_{n-1}\gamma(\xi)}(1 \mp e^{i(h_n-h_{n-1})\gamma(\xi)})\gamma(\xi)d\xi,$$

$$A_{n,js}^{\pm} = \int_0^{\infty}\phi_j^{(1)}(\xi)\,\phi_s^{(1)}(\xi)\,\varepsilon_n^{\pm}(\xi)\,d\xi,\ \varepsilon_n^{\pm}(\xi) = 1 + i\frac{\gamma(\xi)}{\xi}(1 \mp e^{i(h_n-h_{n-1})\gamma(\xi)}),$$

$$D_{n,q;js}^{\pm} = H_{n-1,n-q-2;\,js} \mp H_{n,n-q-2;\,js},\ G_{n,q;js}^{\pm} = H_{n+q+1,n;\,js} \mp H_{n+q+1,n-1;\,js}$$

$$H_{n,s;\,js} = \frac{i}{2}\int_0^{\infty}\phi_j^{(1)}(\xi)\phi_s^{(1)}(\xi)\, e^{i(h_n-h_s)\gamma(\xi)}\gamma(\xi)d\xi.$$

Integrand functions in the matrix elements have no singularities and decrease as ξ^{-4} or as $\exp(-h\xi)$ if $\xi \to \infty$, so that their calculation can be done using standard numerical methods.

MATHEMATICAL MODELING OF ELECTROMAGNETIC WAVE DIFFRACTION BY INHOMOGENEOUS DIELECTRIC CYLINDERS OF ARBITRARY CROSS-SECTION

A.Lerer and G. Kalinchenko
Rostov State University, Institute of Physics,194 Stachki Ave, 344090 Rostov on Don, Russia,
Email: lerer@iphys.rnd.runnet.ru
Email:hitech@aaanet.ru

ABSTRACT

The method of volume integral equations had been developed for simulation of 2-D electromagnetic waves diffraction problem. The efficient codes for simulation of the scattering by inhomogeneous dielectric cylinders of arbitrary cross-sections is carried out. The method proposed is based on the idea of analytical regularization of singular integral expression.

INTRODUCTION

For consideration of electromagnetic wave diffraction by dielectric body one can use both surface and volume integral equations (IE). In our opinion volume ones (VIE) have following advantages: VIE are more simple than surface IE (SIE), the nonuniformity and nonlinearity of dielectric do not turn out the solution to be rather complex, a spatial electric field distribution can be found out directly from a solution. Meanwhile the VIE have one essential deficiency – IE should be satisfied not only on the surface but also everywhere inside the dielectric body.

ANALYTICAL FORMULATION

The problem of E-polarization wave E^e diffraction by dielectric cylinder of nonuniform permittivity $\varepsilon_1(x,y)$ have been reduced to IE solution in the same as in [1]

$$E(x,y)=E^e(x,y)+k^2\int_S \tau(x',y')E(x',y')G(x,x',y,y')ds' \qquad (1)$$

where $\tau(x,y)=\varepsilon_1(x,y)-\varepsilon_2$, ε_2 – free space permittivity, S - cross-section of cylinder, G – Green function (GF). Putting into operation function $F(x,y)=\tau(x,y)E(x,y)$ we can rewrite (1) as

$$F(x,y)/\tau(x,y)=E^e(x,y)+k^2\int_S F(x',y')G(x,x',y,y')ds' \qquad (2)$$

In every case the GF has logarithmic singularity $G\approx G_0(r)=\frac{1}{2\pi}\log r$ when $r\to 0$. Therefore it is necessary to extract this singularity. Here we propose an effective method of singularity extraction. After an identical transformation (2) we get the following expression

$$F(x,y)/\tau(x,y)=E^e(x,y)+k^2F(x,y)I(x,y)+k^2\int_S[F(x',y')G(x,x',y,y')-F(x,y)G_0(r)]ds', \qquad (3)$$

where $I(x,y)=k^2\int_S G_0(r)ds'$, function $G_0(r)$ has the same singularity when $r \to 0$ as GF.

Using the first Green's formula with supposition $u = G_0$ and $v = r^2/4$ the integral $I(x,y)$ can be transformed to one taken along the line L bounding the area S .

$$\int_S G_0(r)ds' = -\frac{1}{4\pi}\int_L r(\log r - 1/2)\frac{\partial r}{\partial n'}dl'$$

where $r=\sqrt{(x-x')^2+(y-y')^2}$, n' - vector normal to L.

The expression under the integral in third term of (3) has no a singularity as well and therefore can be easy taken numerically. Stress that for same contours, for example, circle or rectangle this integral can be taken analytically.

Hence, we can calculate it by the one of well-known formulae of numerical integrating: $\int_S f(x',y')ds' \approx \sum_{n=1}^{N} A_n f(x_n,y_n)$, where coefficients A_n, x_n, y_n should be defined by choice of integrating formula. Then, IE (3) must be satisfied when $x=x_m, y=y_m$. As a result we derive a set of algebraic equations (SAE). For nonlinear dielectrics $\varepsilon_1=\varepsilon_1(x,y,|E|)$ we get nonlinear IE, which can be solved by method of disturbance. Initially we solve the IE with method described before for fundamental harmonics and as the result obtained (SAE). The permeability here depends on electric field and therefore it is a nonlinear system, which can be solved by approximation method. Then, for first harmonics we find IE analogous to (3) with substitution of the fundamental harmonics field instead of E^e. The fields of highest harmonics can be simulated in the same manner.

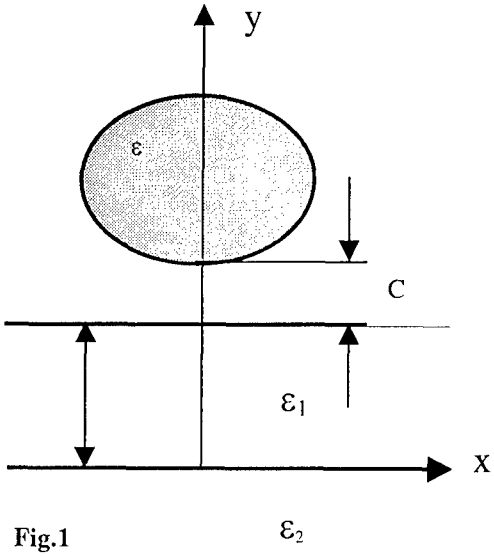

Fig.1

Due to good convergence of series and integrals it is enough to sum 20-30 terms in series and numerical quadrature to get a deviation up to 0.1%. The order of system of algebraic equations increases with increasing the dielectric body dimension via wavelength in dielectric as $N \approx \left[5\max(A,B)/\left(\lambda/\sqrt{\varepsilon}\right)\right]^2$.

RESULTS

In this paper we have calculated the power transmitting coefficients for diffraction by dielectric cylinder situated next dielectric planar waveguide layer shown in Fig.1, grating made of dielectric cylinders and dielectric cylinder setting inside of planar metallic waveguide.

As the illustration of our method we present in Fig.2 the results describing the diffraction of mode H_1 propagating in planar dielectric waveguide by dielectric cylinder when different distances of cylinder from waveguide. The curves here express the power transmission coefficient via normalized frequency $F=\frac{2\pi d}{\lambda}\sqrt{\varepsilon_1-\varepsilon_2}$ for linear regime. The waveguides of two geometrical dimensions are shown by different types of curves – solid and dotted ones. It is seen that resonance appears only if the inhomogeneity permeability is rather high. For

both waveguides under consideration the reflection coefficient is not high. Therefore the power, which is not passed through the inhomogeneity, radiates.

CONCLUSIONS

The problem of electromagnetic waves diffraction by nonuniform and nonlinear dielectric cylinders is solved with integral equation method in an efficient and accurate manner. In this paper, we have calculated the power transmitting coefficients for diffraction by grating made of dielectric cylinders, dielectric cylinder setting inside of planar metallic waveguide and dielectric cylinder situated next dielectric planar waveguide layer.

Hence, this investigation can become a basis for the studies of propagation of complex waves in nonlinear waveguide structures, generation of highest harmonics, capacity of light signal modulation, the demonstration of the possibility the vibration control devices creating, etc.

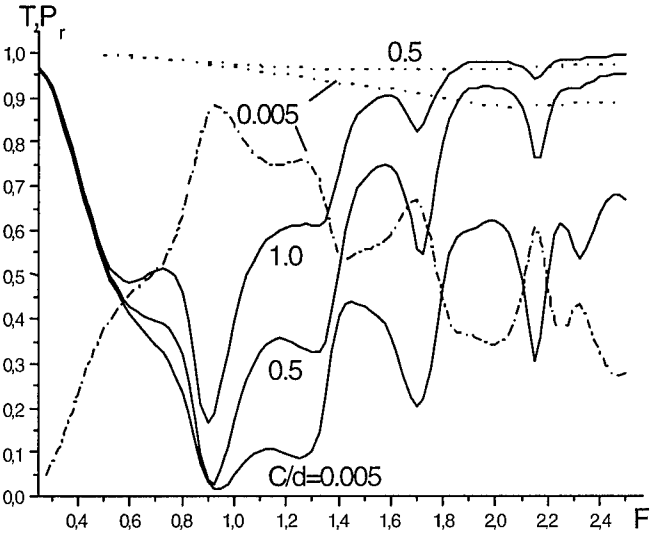

Fig. 2. Solid curves - $A/d=1, B/d=0.5, \varepsilon_1=2, \varepsilon_2=1, \varepsilon=10$, **dotted -** $A/d=1, B/d=0.5, \varepsilon_1=2.343, \varepsilon_2=2.372, \varepsilon=2.6$, **dash–dotted – emission loss** P_r.

REFERENCES

[1] Computer Techniques for Electromagnetics, Edited by R. Mittra. New York, Pergamon Press, 1973.

SIGNAL PROCESSING

DISCUSSION OF THE K-PULSE CONCEPTION

O.O.Drobakhin, D.Y.Saltykov, and V.G.Korotkaya

Radiophysics Dept., Dniepropetrovsk State University,
13 Nauchnaya Str., Dniepropetrovsk, 49050 Ukraine

ABSTRACT

A number of discrimination measures using K-pulse conception for the simplest object characterized by a single complex natural frequency has been investigated by a computer simulation. Besides the traditional weight function, the Hemming's function and function with the Fourier transform coinciding with the Batterworth function have been used. The Hemming's function has some advantages.

Ultrawide-band schemes of radar object discrimination have been under active investigation for last two decades [1,2]. According to K-pulse [3] conception special form of input signal is constructed, thus, output signal in time-domain does not contain late-time component. The last component represents reverberations at object natural frequencies and can be expressed with sum of exponentials. The zeros of K-pulse spectrum coincide with the poles of the frequency response of the object. The zeros completely annihilate the poles and thus late-time component is annihilated as well. Usually rather complex objects are investigated, that does not allow one to obtain fundamental properties. In this paper, object model in form $R(\omega) = A\,exp(j\varphi)/(\omega - \omega_p - \delta j)$ is explored.

If a K-pulse excitation with spectrum $K(\omega)$ is used, a response of an object with frequency function $R(\omega)$ can be calculated according to

$$P(\omega) = R(\omega) \cdot K(\omega) \tag{1}$$

After transformation into time-domain and obtaining signal $p(t)$ the decision about correspondence of the object and K-pulse is made by late-time component analysis. Under complete coincidence of the poles of object and zeros time-domain signal is equal to function $sin(x)/x$. To avoid oscillations in time domain, frequency weight function

$$W(\omega) = [1 - exp(-j\omega\tau)]/\, j\omega, \tag{2}$$

is used. Dirichlet weight function provides rectangular basic functions in time domain thus in time domain sharp boundary between early and late components occurs. But this problem is dual to low-pass filtering therefore the Batterworth weight functions can be applied alternatively. Both Dirichlet and Batterworth weight function have zeros in frequency domain, positions of which depend on value of natural frequencies of standard object.

In [1] discriminating measure

$$k_4 = \left[\sum_{i=M}^{M+W} p^2(t_i)\right] \Big/ \left[\sum_{i=0}^{M} k^2(t_i)\right] \tag{3}$$

has been suggested. In (3) $k(t)$ is the Fourier transformation of $K(\omega)$. Discriminating measure (3) has the evidential disadvantage if an object induces various values of a response amplitude due to a variation of an angle of an observation. Under the circumstances one can not separate a contribution of shifting of zeros and poles and changing of the amplitude in the value of k_4. Other measures for investigation used are identical to measures k_1, k_2, k_3 [4].

The requirement of providing optimal value implies the weight function with the maximal ratio of energy in the main lobe and the side lobes. The Hemming function has high properties and simplicity simultaneously. Besides, the Hemming function has not zeros in its spectrum. Traditionally the approach was applied for video-signals but in many cases measurements have to be carried out in frequency domain in band with nonzero initial value. In the capacity of time-domain signal can be used real, imaginary part of the Fourier transform of frequency domain data. The approach corresponds to processing of videopulse. Alternatively, modulus of the result of the transformation can be used. The last situation corresponds to processing of an envelope of the time-domain signal. Our numerical simulation has displayed higher sensitivity of the second approach in comparison with the first one to the difference of pole and zero. If at the frequency of the pole a value of weight function for the first case is greater than one for the second case, the opposite situation is observed. If values of weight functions are equal at the frequency of a pole, relation between accuracy of discrimination depends on the type of discrimination measure. Naturally, varying the initial phase value does not induce changing the value of a discrimination measure if the envelope of time-domain signal is used.

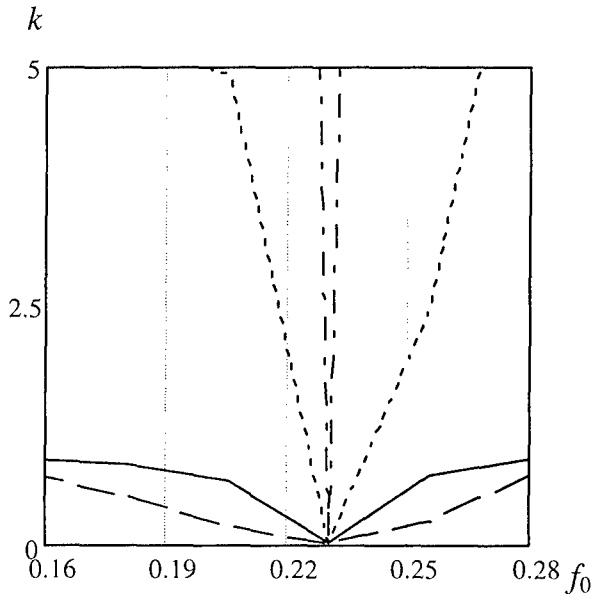

Figure 1

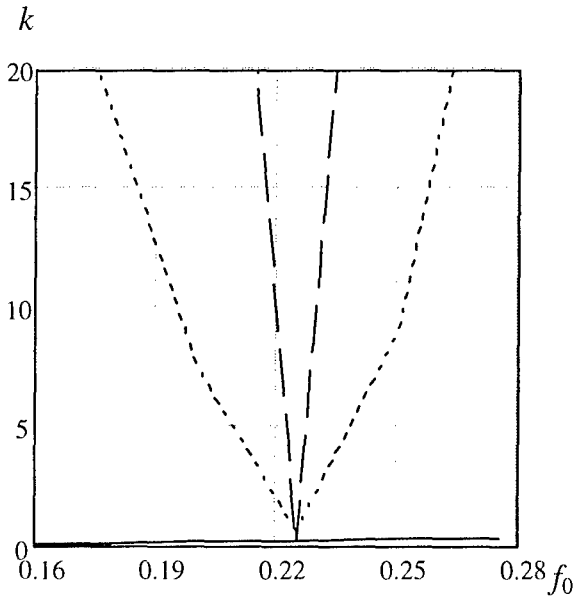

Figure 2

Some numerical measures of discrimination have been studied. The measures k_1, k_2, k_3, k_4 for normalized frequency 0.225 are presented in Fig.1, where solid line corresponds k_1 , dot line corresponds k_2 , dash line corresponds k_3 , dash-dot line corresponds k_4. It is evidently that k_4 provides more sharp characteristics and higher accuracy of estimation but choosing too small step can involve missing the fact of the pole and zero coincidence. The measure k_3 serves to

improvement of reliability. The numerical simulation has shown that simultaneous application of measures is appropriate.

The advantage of K-pulse is considered traditionally to be suppressing noise by weight function but the same function can hide the effect of zero and pole coincidence. Usually they suppose that more high level of noise is observed at the range of high frequencies of the spectrum but for measurements in frequency domain it is not valid. A comparison of the traditional and the Batterworth weight functions have been carried out. The view of measure k_4 for the Batterworth window (solid line), the Dirihlet window (dot line), and the Hemming window (dash line) is presented in Fig.2. The Hemming's window provides more sharp characteristic and therefore higher accuracy. According to the traditional K-pulse technique it is necessary to vary the weight function parameters in dependence from the value of frequency of standard object pole thus shifting the zero or even forming several zeros in the frequency band of the weight function occur. The approach can imply occasionally coincidence of weight function zero and the object pole and therefore the impossibility of recognition. This situation was confirmed by numerical simulation with Batterworth window and illustrated in Fig.2, where the corresponding measure k_4 has not minimum at the normalized frequency value equal to 0.225. Thus estimation of the pole value is impossible. The coincidence of a weight function zero and the object pole does not allow us to detect the fact of coincidence of the weight function zero and the object pole. Since the weight function serves to eliminate oscillations in time domain, discrimination can be realized with the same weight function but the reciprocal sequence of frequencies in the object response. For instance, according to the suggestions normalized frequency 0.225 is transformed to value 0.275. Probability of recoincidence of the weight function zero and the object pole is negligible small. The approach suggested has been applied successfully for the pole discrimination for the Batterworth window.

REFERENCES

[1] Ilavarasan P., Ross J.E., Rothwell E.J., Chen K., and Nyquist D.P. Performance of an automated radar target discrimination scheme using E pulses and S pulses // IEEE Trans. Antennas Propagat. 1993. vol. 41. № 5. P. 582-588.

[2] Primak S.L., Lo Vetri J., Damjanschitz Z. and Kashyap S. Auto-Regressive Filter-Based E-Pulse Discriminating Scheme // IEEE Trans. Antennas Propagat. 1999. vol. 47. № 1. P. 216-218.

[3] Fok F.Y.S., Moffat D.L. The K-Pulse and E-Pulse // IEEE Trans. Antennas Propagat. 1987. vol. 35. № 11. P. 1325-1326.

[4] Drobakhin O.O.,Saltykov D.Yu. 1-D Inverse Problem Solution for Multilayered Dielectric Structures using K-signal Conception // Conf. Proc. MMET-96. Lviv (Ukraine). 1996. P.432-435.

SCALAR QUANTIZATION IN THE PWL TRANSFORM SPECTRUM DOMAIN

Remigiusz Baran, Dorota Wiraszka, Wiera Dziech
Kielce University of Technology,
Al.1000-lecia PP 7, 25-314 Kielce, Poland
E-mail: ketrb@eden.tu.kielce.pl

ABSTRACT

The problem of image compression using the PWL (Periodic Walsh Piecewise-Linear) transform and optimal scalar quantization of PWL spectrum has been presented in the paper. Short description of the PWL transform has been included. Optimal Lloyd-Max Quantization has also been presented. The procedure of the presented compression method is based on quantization of class of scalar variables representing blocks of the image. Effectiveness of the compression method has been examined. Visual representation of the results of investigation has been included.

INTRODUCTION

Nostradamus wrote is his prophecies: "I see that world is getting smaller". Now, with respect to the new telecommunication applications, especially the Internet Network, we can say that he was probably right. The World Wide Web is favouring our generation, giving us incomparable with the past access to information. Nowadays we can hear that the XXI century will be called the information century. Requirement for transmitted and stored information will still be growing. Even without the gift of Nostradamus, it is possible to predict that this requirement will overtake the development of technology in the closest future. Thus, the problem of signal and image compression still has the fundamental priority in the field of digital signal processing. Various techniques aimed on this subject have been developed during the recent years. One of the most efficient methods is the transform coding method.

THE PWL TRANSFORM

The set of non-orthogonal PWL functions is obtained by integrating the Walsh functions repeated with T period [1]. The PWL functions are defined as follows [1,4,5,7,9]:

$$PWL(0,t)=1 \quad for \quad t\in(-\infty,+\infty), \qquad PWL(i,t)=\frac{2^{k+1}}{T}\cdot\int_{(mT)}^{(mT)+t} wal(i,\tau)\,d\tau \tag{1}$$

where:

i – number of the Walsh function, $i=1,2,\ldots,N-1$;

k – group index of the PWL function , $k=1,2,\ldots,\log_2 N$;

$m=0,\pm1,\pm2,\ldots,$ – the period number; $2^{k+1}/T$ – the normalization factor;

The PWL transform, for the continuous function $x(t)$ sampled at N points, is following:

$$x(t)=\sum_{i=0}^{N-1} c_i PWL(i,t), \text{ for } t\in(-\infty,+\infty) \quad c_0=\frac{1}{N}\sum_{n=0}^{N-1}x(n), \; c_i=-\frac{1}{2^{k+1}}\sum_{n=0}^{N-1}x(n)wal'(i,n) \tag{2}$$

where:

$i=1,2,\ldots,N-1$; $x(n)$ – samples of the $x(t)$

SCALAR QUANTIZATION

Quantization [2] is the step subsequent to sampling in image digitization. The quantization process maps a continuous variable x into a discrete variable x^*, which takes values from a finite set. The $x\rightarrow x^*$ mapping is usually a staircase function. The scalar quantization requires definitions of two sets of increasing values: set of decision levels - $p=\{t_k, k=1,\ldots,L+1\}$, with t_1 and t_{L+1} as the minimum and maximum values of x, respectively, and set of reconstruction levels -

$x^* = \{r_1, \ldots\ldots, r_L\}$, defined with accordance to the set p. If x lies in interval $[t_k, t_{k+1})$, then it is mapped to r_k. The quantizer introduces distortion $Q_E = x^* - x$, which any reasonable design method must attempt to minimize. The quantizers, useful especially in image coding techniques, are a zero memory quantizers. One of the zero memory quantizers, useful in image coding techniques, is the Lloyd-Max Quantizer [2,3], which minimizes introduced distortion for a given number of decision levels L and for given probability density function $p(x)$.

Two commonly used densities for quantization of image-related data are the Gaussian and Laplacian densities, which are described by following formula [2]:

$$\text{Gaussian: } p_G(x) = \frac{1}{\sqrt{2\pi\sigma^2}} \exp\left(\frac{-(x-\mu)^2}{2\sigma^2}\right) \quad \text{Laplacian: } p_L(x) = \frac{1}{\sqrt{2\sigma^2}} \exp\left(\frac{-\sqrt{2}|x|}{\sigma}\right) \tag{3}$$

where: σ^2 and μ - the variance and mean of x, respectively.

THE COMPRESSION SCHEME

The compression method considered in this chapter is a kind of zonal compression method [8]. The input image (N x N) is divided into blocks (M x M). Each of these blocks is then transformed using the PWL transform, what produces $(N / M)^2$ tables of spectrum coefficients (M x M). Next the spectrum coefficients are grouped with respect to their position, what gives M^2 new tables of grouped coefficients (M x M), only DC for instance. According to the grouped coefficients tables the matrix of variances is produced, constituting a base for the normalisation process. The normalisation process allows using the same quantizer to the data series of different variances. The variance matrix is used also in Integer Bit Allocation procedure [6] to produce the matrix of bit allocation, which is a basis to the quantization process of grouped coefficient tables. One of the input parameters to the compression scheme and the Integer Bit Allocation procedure is the average number of bits a allocated for one quantized table. As the expected probability density functions were Gaussian or Laplacian, the Lloyd-Max Quantizer has been applied. Quantization is the final step of the coder in the considered compression scheme. The coder sends to the transmission line: the variance matrix (M x M), M^2 matrices of indices (M x M) to the quantized values, M^2 vectors of quantized values (length of each vector depends on The Integer Bit Allocation procedure). The decoder of such a compression scheme consists of the denormalisation process, the coefficients inverse-grouping task and the inverse PWL transform step.

Distortions of the reconstructed image depend on a parameter. The number of information bits transferred by the transmission line depends on a parameter, as well. The distortion can be measured by a *MSE* error [10].

To count the number of information bits transferred to the decoder part, the compression factor has been introduced:

$$\eta = \frac{(8 \cdot N_x \cdot N_y - c) \cdot 100\%}{8 \cdot N_x \cdot N_y} \tag{4}$$

where: c - the number of information bits transferred by the transmission line.

THE RESULTS

Some results of application of the proposed compression method are presented in Fig. 1.

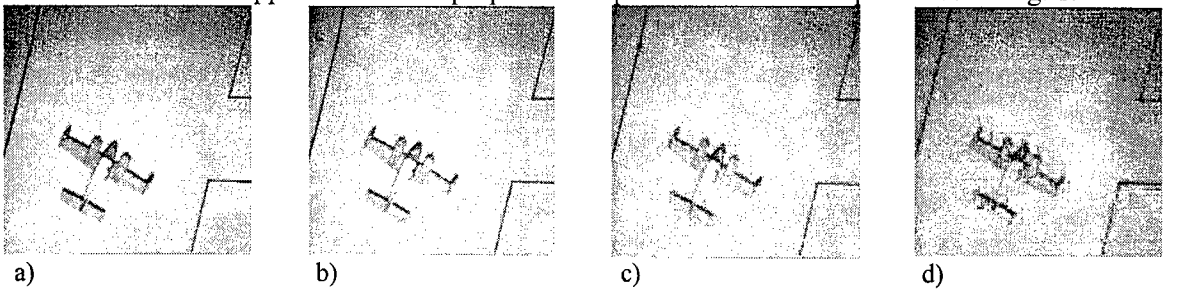

a) b) c) d)

Fig. 1. Compression results with various mean number of bits for quantized table a

a) original image
b) $a = 3.0$, $MSE = 10.0469$, $\eta[\%] = 32.0801$
c) $a = 1.0$, $MSE = 52.6115$, $\eta[\%] = 78.7598$
d) $a = 0.5$, $MSE = 102.9025$, $\eta[\%] = 88.9160$

MSE and the η factor versus the a parameter are depicted in Fig. 2.

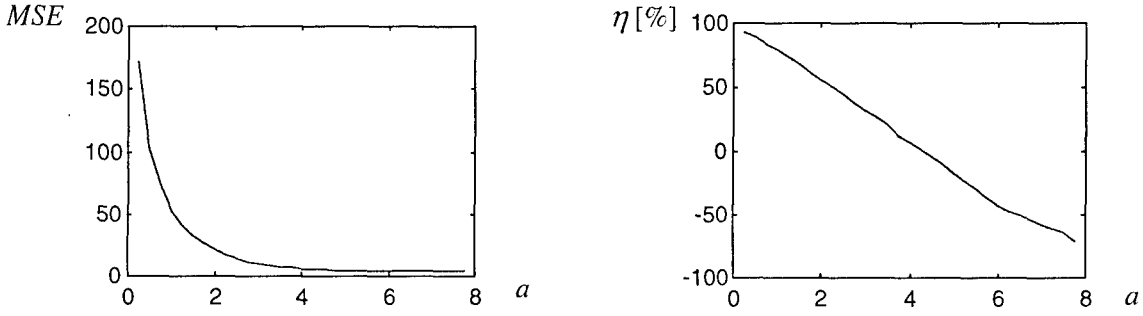

a) b)

Fig. 2. a) error *MSE* versus a parameter; b) the compression factor η versus a parameter

CONCLUSIONS

Average number of bits a decides on the number of bits allocated for particular tables of the PWL spectrum grouped coefficients. The smaller the a, the shorter the vectors of quantized output values and the more zero elements in the bit allocation table, thus smaller number of tables are being quantized. In the other words, the value of a is proportional to the transmitted information, and inversely proportional both to the mean-square error *MSE* and the compression factor η. Visual analysis of Fig.1 shows that the images obtained for $a < 1$ are strongly distorted (example d), what makes them unacceptable. The distortions obtained for $a = 1$ are hardly noticeable (example c). For $a > 1$ the distortions are unnoticeable for the human eye (example b). Above tendencies are confirmed by curves depicted in Fig.2. It is worth mentioning that for $a > 4$ the proposed method begins to show trends, which are inverse to the expectations: the information sent is greater than the input information. This can be noticed in Fig.2b.

ACKNOWLEDGMENTS

We gratefully acknowledge the assistance and support provided by Professor Andrzej Dziech from the University of Mining and Metallurgy in Cracow, Poland, who patiently supervised our work over this paper.

REFERENCES

1. Dziech A., *Przetwarzanie i przesyłanie sygnałów*, Skrypty Uczelniane Politechniki Świętokrzyskiej, Kielce 1985.
2. Jain A.K., *Fundamentals of digital image processing*, Prentice Hall International, Englewood Cliffs, NJ 1989.
3. Max J., *Quantizing for minimum distortion*, IRE Transaction on Information Theory, IT-6, 7-12, 1960.
4. Dziech A., Pardyka I., Biela-Wiraszka D., Chodorek R., *Zagadnienia kompresji i aproksymacji obrazów z zastosowaniem dwuwymiarowych przekształceń odcinkowo-stałych i odcinkowo-liniowych*, Materiały konf. Przetwarzanie Sygnałów'93, Poznań 1993.
5. Pardyka I., Smolewski I., *Piecewise-Linear Transforms*, Final Report of the Individual Fellowship within EEC, Wuppertal 1993.
6. Belgassem F., H., *Image and contour data compression using periodic piecewise-linear transforms*, Rozprawa doktorska, AGH Kraków 1997.
7. Pardyka I., Biela-Wiraszka D., Ślusarczyk P., Baran R., *Image compression using Piecewise-Linear Transforms*, XX Krajowa Konferencja Teorii Obwodów i Układów Elektronicznych, Kołobrzeg 1997.
8. Pavlidis T., *Grafika i przetwarzanie obrazów*, WNT, Warszawa 1987.
9. Pardyka I., Chodorek R., Biela D., *Problemy aproksymacji obrazów z zastosowaniem dwuwymiarowych przekształceń PWL*, Krajowe Sympozjum Telekomunikacji, Bydgoszcz 1992.
10. Skarbek W., *Metody reprezentacji obrazów cyfrowych*, Akademicka Oficyna Wydawnicza PLJ, Warszawa 1993.

MAXIMUM LIKELIHOOD TECHNIQUE FOR DIRECTION OF ARRIVAL ESTIMATION IN ADAPTIVE ARRAYS

Ildar R. Urazgildiyev

National S&R Center of Defense Technologies and Military Security of Ukraine
81, Melnokova str., Kiev, 04119, Ukraine
E-mail: u.ildar@ieee.org

ABSTRACT

A direction of arrival estimation technique based on unification of eigenstructure and maximum likelihood estimators is considered. The basic stages of proposed technique are estimation the number of signals, fast evaluation of the initial DOA estimates, and fast accurate definition of initial ones.

INTRODUCTION

The estimation of directions of narrow-band signals is the basic problem arising in radar, mobile and satellite communication, radio astronomy and many other applications. This problem is solved in a complex and dense environment as a rule. Therefore the adaptive (or "smart") antenna array with digital signal processing is considered to be the most efficient tool for direction of arrival (DOA) estimation.

Under the conditions of a priori uncertainty as well as small signal-to-noise ratio (SNR) the maximum likelihood (ML) estimator is known to approach asymptotic efficiency. A very serious shortcoming of the ML estimator is that it suffer from very computational cost.

In this context, the eigenstructure-based algorithms achieve a compromise between computational complexity and estimation performance at high SNR. However, the application of eigenstructure methods can be severely limited at low SNR and closely spaced sources.

In this paper the DOA estimation technique based on unification of eigenstructure and ML estimators is considered. The basic stages of proposed technique are estimation the number of signals, fast evaluation of the rough initial DOA estimates, and fast accurate definition of initial ones.

PROBLEM FORMULATION

We are concerned with DOA estimation for a class of signals that can be represented as [1]-[5]

$$\boldsymbol{x}(i) = \sum_{j=1}^{q} s_j(i)\boldsymbol{a}(\Theta_j) + \boldsymbol{n}(i), \qquad i = 1...L, \tag{1}$$

where q is the number signals, $\boldsymbol{x}(i)$ is a $N\times 1$ complex observation vector, $\boldsymbol{s}(i)$ is a $q\times 1$ complex signal vector, $\boldsymbol{n}(i)$ is a $N\times 1$ complex noise vector, $\boldsymbol{a}(\Theta)=(1, exp\{j\Theta\},..., exp\{j(N-1)\Theta\})^T$ is the $N\times 1$ vector corresponding to the DOA Θ, N is the number of sensors; and L is the number of snapshots.

The samples of noise vector $\boldsymbol{n}(i)$ are assumed to be independent Gaussian complex random vectors with mean $\boldsymbol{0}$ and covariance $\sigma^2\boldsymbol{I}$, where σ^2 is an unknown scalar constant and $\boldsymbol{I}$ is the identity matrix.

With the above given model, the problem to be solved is to determine the DOA's $\tilde{\boldsymbol{\Theta}} = \left(\tilde{\Theta}_1, \tilde{\Theta}_2, \ldots, \tilde{\Theta}_q\right)^T$ of signals from a finite set of observations $\boldsymbol{x}(1), \boldsymbol{x}(2), \ldots, \boldsymbol{x}(L)$.

DOA ESTIMATION TECHNIQUE

To solve mentioned problem the following approach is traditionally used. On the first stage, when a-priori information about the number of signals is absent, some algorithm of signal's detection and estimation of signal's number is applied. Among this type of algorithms Wax & Kailath [1] one can be chosen because it has good performances at low computational cost.
After calculation of the number of signals DOA estimates are found by means of the quasi-optimal eigenstructure-based algorithms like MUSIC [2] and Min-Norm [3]. Mentioned ones have acceptable computational cost and ensure high accuracy and resolution. However, in conditions of low SNR the root mean square error of the estimates obtained with the help of the quasi-optimal algorithms essentially exceed the Cramer-Rao bound. Therefore with the purpose of increasing of the DOA estimation accuracy we propose to include the third stage in the array signal processing. The object of this stage is to define more precisely the DOA estimates obtained by means of eigenstructure-based estimators.
To estimate DOA of received signals a recurrent ML algorithm can be used on the third stage. It is well known that ML estimate of $\boldsymbol{\Theta}$ can be written as follows [2]:

$$\tilde{\boldsymbol{\Theta}}_{ML} = \arg\max_{\Theta} \varphi(\boldsymbol{\Theta}), \qquad \varphi(\boldsymbol{\Theta}) = tr\boldsymbol{P}(\boldsymbol{\Theta})\boldsymbol{R}_L, \tag{2}$$

where tr is the trace of matrix; $\boldsymbol{P}(\boldsymbol{\Theta})$ is the projector onto the signal subspace; $\boldsymbol{R}_L$ is sampled correlation matrix of signals (1).
According to recurrent algorithm the $(k+1)$st iteration for locating the parameter vector $\boldsymbol{\Theta}$ which maximizes a criterion function $\varphi(\boldsymbol{\Theta})$ is given by [4]

$$\boldsymbol{\Theta}^{(k+1)} = \boldsymbol{\Theta}^{(k)} - \mu \boldsymbol{B}(\boldsymbol{\Theta})^{-1} \nabla(\boldsymbol{\Theta})\Big|_{\boldsymbol{\Theta}=\boldsymbol{\Theta}^{(k)}}, \tag{3}$$

where $\nabla(\boldsymbol{\Theta}) = \partial\varphi(\boldsymbol{\Theta})/\partial\boldsymbol{\Theta}$ is the gradient; $\boldsymbol{B}(\boldsymbol{\Theta}) = \partial^2\varphi(\boldsymbol{\Theta})/\partial\boldsymbol{\Theta}\partial\boldsymbol{\Theta}^T$ is the matrix of second derivatives and μ is the step constant.
Thus, the recurrent algorithm (3) makes it possible to define more precisely the DOA estimates obtained with the help of eigenstructure-based algorithms.

SIMULATION RESULTS

In order to demonstrate the performance of the proposed recurrent ML algorithm we compare it to the Cramer-Rao bound (CRB) and to the quasi-optimal MUSIC and Min-Norm algorithms in several simulated experiments. In all experiments to follow, a uniform linear array of N=10 omnidirectional sensors with half-wavelength spacing and two uncorrelated Gaussian sources (q=2) with equal power have been assumed. The number of statistically independent snapshots in each simulation runs was L=100. A total of 100 independent simulation runs were performed to obtain each simulated point. The signal scenario $\theta_1=10^0$, $\theta_2=15^0$ was considered in experiments. The comparison of performances is given in terms of DOA estimation root-mean square error (RMSE). The sample RMSE's of the obtained estimates are plotted on Fig.1.
The results confirm the theoretical prediction that is the recurrent ML technique achieves better performances than the MUSIC-like algorithms.

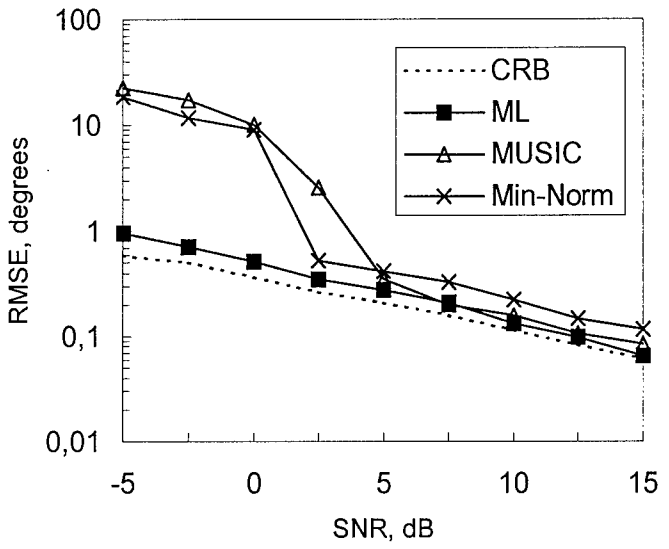

Fig.1. Experimental RMSE's of DOA estimation versus the SNR.

It is important to note that in the case of MUSIC-like algorithms it is not possible to resolve impinging signals due to false estimates having significant anomalous errors [5]. Substitution of false estimates to the initial vector Θ lead to that of recurrent process (3) will converge to the local maximum. To avoid this situation we propose to use the approach [5], which makes it possible to detect false estimates. Instead of mentioned ones the estimates close to the true ones must be chosen as initial value of vector Θ.

Computer simulations have been carried out to compare the computational cost of proposed recurrent ML estimator to that of eigenstructure-based algorithms. The simulation result shows that when the number of sensors N=10 and the number of observation point K=900 the calculation time of the recurrent ML estimator is in 7 times less than that of search ML algorithm (2) and in 2 times less than that of MUSIC one. At that calculation time does not grow when N and K increase.

CONCLUSION

The simulation verified dramatic improvements of threshold performance as compared with conventional eigenstructure-based algorithms. The computational cost of proposed ML technique is much lower than that of the traditional ML estimators.

REFERENCES

[1] Wax M. and Kailath T. "Detection of Signals by Information Theoretic Criteria". *IEEE Trans. on Acoustics, Speech and Signal Processing*, vol. 33, pp.387-392, Apr. 1985.

[2] Stoica P. and Nehorai A. "MUSIC, Maximum Likelihood and Cramer-Rao Bound". *IEEE Trans. on Acoustics, Speech and Signal Processing*, vol. 37, pp. 720-741, May, 1989.

[3] Nickel U. "Algebraic formulation of Kumaresan and Tuft superresolution method, showing relation to ME and MUSIC methods", Proc. Inst. Elec. Eng., Pt. F., vol.135. pp. 7-10, Feb.1988.

[4] Urazgildiyev I. and Vagapov A. "A Gradient Technique for Estimation of the Direction of Arrival and Carrier Frequency of Narrow-Band Signals". AP2000 Millenium Conference on Antennas & Propagation, Davos, vol.1, 9-14 April 2000.

[5] Urazgildiyev I. A Strategy of Joint Estimation of the Number and Directions of Narrow-Band Signals. Izvestija VUZOV – Radioelectronica, vol. 43, pp.67-73, Aug. 2000. (in Russian).

SIGNAL COMPRESSION BASED ON ZONAL SELECTION METHODS

Wiera Dziech, Remigiusz Baran, and Dorota Wiraszka
Kielce University of Technology,
Al.1000-lecia PP 7, 25-314 Kielce, Poland
E-mail: ketrb@tu.kielce.pl

ABSTRACT

Compression of signals in spectral domain consists in rejection of related transform coefficients and reconstruction of signals by inverse transform. There exist two basic methods used to select coefficients to be transmitted: *Threshold Selection* and *Zonal Selection*. In threshold selection the reconstruction is made with a subset of coefficients that are larger than a specified threshold. In zonal method the reconstruction is made with a subset of coefficients lying in predetermined zone. Only those coefficients are selected for further processing, the remaining coefficients are set to zero.

In this paper, zonal compression technique performed on chosen signals using different transforms are investigated. The mean square error (MSE) is used as a measure of signal reconstruction quality. Plots of the MSE versus compression percentage are included for comparison of methods.

INTRODUCTION

The fundamental goal of the digital signal compression is to reduce the bit rate for transmission and storage, while maintaining an acceptable signal reconstruction quality. One of the techniques for achieving signal compression is *Transform Coding*. In this method, the aim is to transform original signal to a new space where most of the energy would be concentrated in only few spectrum coefficients. Thus compression can be achieved by coding only those coefficients that have substantial energy.

Transform coding is considered as one of the most efficient methods for signal processing. A number of transforms have been investigated by many researchers for different types of signals, including Fourier, Hartley, cosine, sine, as well as Walsh, Haar and piecewise transforms. Computation complexity and compression ability are the two important factors in evaluating a transform. During the last few years, the application of wavelet transforms has emerged as an efficient compression tool.

Compression of signals in spectral domain consists in rejection of related transform coefficients and reconstruction of signals by inverse transform. In this paper, zonal compression technique performed on chosen signals using different transforms are investigated. The optimal spectral zone selection ensures achieving a minimum mean-square error of reconstruction.

TRANSFORM DESCRIPTION

A new class of transforms based on the integration of Walsh and Haar functions has been considered for zonal compression. This class is called *Piecewise - Linear Transforms* and includes WPL (Walsh Piecewise - Linear), PWL (Periodic Walsh Piecewise – Linear) and HPL (Haar Piecewise – Linear) transforms [1]. In this paper the HPL transform has been investigated. The set of periodic Haar piecewise-linear functions is determined by:

$$HPL(0,t)=\begin{cases}1, & \text{for } t\in[0,T]\\ 0, & \text{otherwise}\end{cases} \qquad HPL(i+1,t)=\frac{2^k}{T}\int_0^t har(i,\tau)d\tau \qquad (1)$$

where: $i = 0, 1, 2, \ldots, \log_2 N$, $k = 0, 1, 2, \ldots, \log_2 N$,
k - index of group of HPL functions.
$har(i, \tau)$ – Haar function.

The factor $(2^k/T)$ is applied to normalise the maximum amplitude of the HPL functions.
The next class of new transforms is wavelet transforms that become one of the most powerful tools in compression applications. The general idea of wavelet transform is to analyse signal according to its local frequency content. Detailed description can be found in chosen references [2,3,4]. As it is well known wavelet transform allows multi-rate digital signal processing because its coefficients are grouped in dyads of different length corresponding to different processing rates. Each dyad's coefficients are the signal expansion coefficients calculated in appropriate subspace to another.

COMPRESSION PROCEDURE

In zonal compression the coefficients outside a specified zone are set to zero. Then the inverse transformation has the same dimension as the forward transform. In another version of zonal compression all coefficients outside a selected zone are discarded completely (no zeros are replaced), and the inverse transform has a dimension equal to that of the selected zone. Thus the number of computations needed for the inverse transformation is reduced, and a zooming step is required to obtain the previous dimension of the reconstructed signal.
Selected zones usually depend on the structure of the energy distribution of the transform coefficients. In order to determine optimal spectral zone for chosen transform it is necessary to obtain the estimates of spectra on a given class of input signals. This problem has been considered in [6] and an upper bond on a wide class of signals has been determined.
Following transforms have been investigated in this paper: HPL, PWL, Walsh, Coiflet and Daubechies.

COMPRESSION RESULTS

To investigate compression ability the zonal compression method was applied to a random speech signal. The spectrum of the signal is compressed using one of selected transforms with zonal method.
Fig. 1. shows the original and reconstructed signals obtained by HPL transform for compression percentage equal to 50% corresponding to compression ratio 2:1.

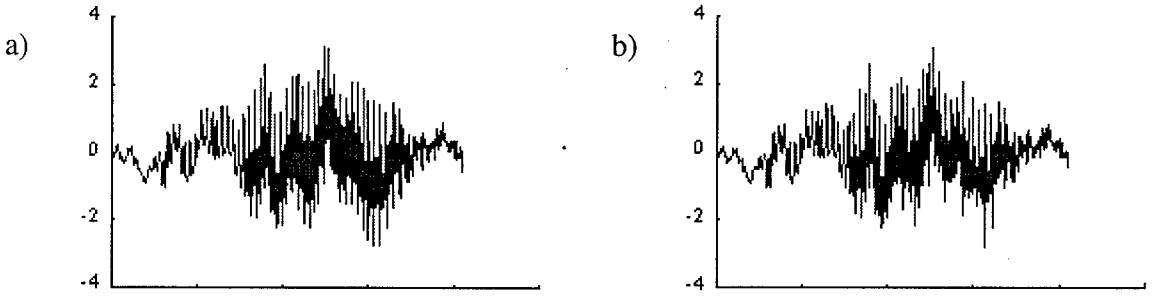

Fig. 1. a) original speech signal b) reconstructed signal

For the purpose of comparison the transform ability different transforms have been used for this investigation, and the results of compression have been compared using MSE criterion. The percentage of rejected coefficients was varied and the corresponding mean square error between the original and reconstructed signals has been calculated in each case. Plots of the MSE against the percentages of rejected coefficients are illustrated in Fig.2.

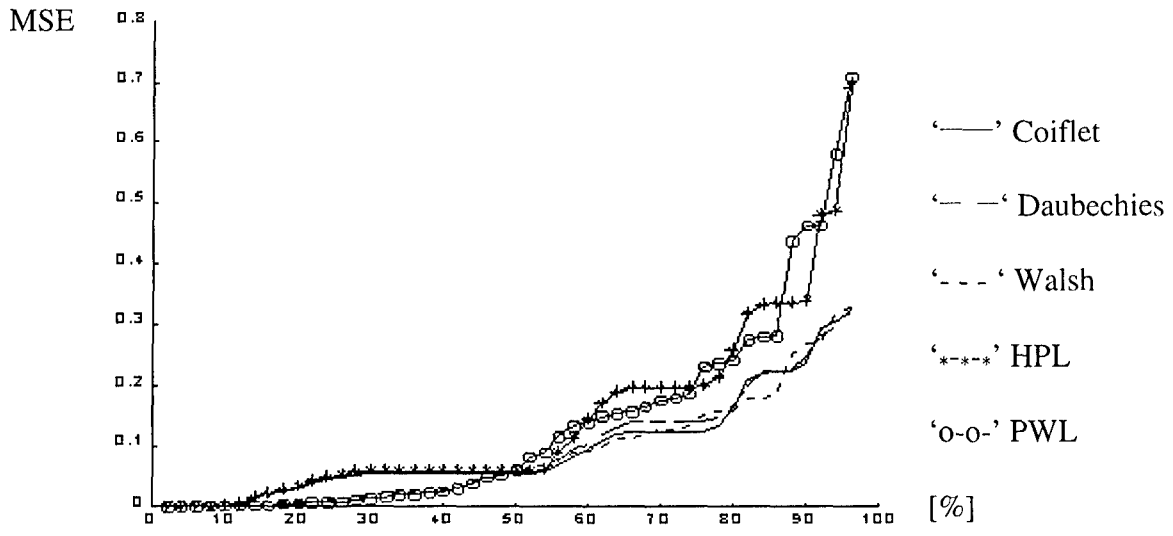

Fig. 2. MSE versus percentages of rejected coefficients.

CONCLUSION

Based on the simulation results obtained by using different transforms and zonal compression method, the following comparison remarks are worth mentioning. The zonal compression method allows reducing the number of spectrum coefficients up to compression ratio equal to 60%, without significant distortion, for all investigated transforms. It can be seen from plots of the MSE against the compression ratio that wavelet transforms give better results, in terms of the mean square error of the reconstructed signals, than the HPL and PWL transforms. It is the result of a multi-rate approximation, which takes place when we use bases functions from the spaces of different resolutions. Also the MSE plot obtained for the Walsh transform is close to that of wavelets. So these transforms are more suitable for representing considered shape signals in zonal compression method.

REFERENCES

[1] F.Belgassem, A.Dziech, *„Fast Algorithm for the Periodic Haar Piecewise Linear Transform"*, Proceedings of Int'l AMSE Conference, Brno, CZ, 1996.
[2] I.Daubechies, *„Ten Lectures to Wavelets"*, SIAM, 1992
[3] A Graps *„An Introduction to Wavelets"*, IEEE CS&E, 1995.
[4] N.J.Flige *„Multirate Digital Signal Processing"*, JW. & Sons, 1995.
[5] W.Dziech, D.Biela, *„Problemy kompresji sygnałów z zastosowaniem transformaty falkowej"*, KST'97, Bydgoszcz 1997.
[6] A. Pietrosian, *Optimal Zonal Compression of Images Based on Wavelet Transform,* Proc. Of IASTED Int. Conf. SIP'98, Las Vegas,USA,Oct.1998.

MATHEMATICAL METHOD OF THE TARGET HEIGHT DETERMINATION IN THE HF BAND ON THE BASE OF COMPUTATIONAL ELECTROMAGNETICS

A.V. Polyarus, S.A. Kovtun, and D.V. Karlov
Kharkov Military University, Svoboda sq.6, 61043, Ukraine

ABSTRACT

The possibility of radiating target height determination in the HF band is investigated in this paper. The distinguishing features for the height estimation are statistical characteristics of the useful signals that can be found by means of computational electromagnetics.

As known, communicating devices of the HF band are used now in aircraft. That is why every radiating aircraft can be detected at the great distances by means of the passive radar. But the latter usually determines only the azimuth of the incoming wave radiated by the airborne transmitter. The range of the target is estimated by several passive radars but the target height remains unknown. We confine attention here to determination of a target height and use for that the statistical features of the signals transmitted by an airborne communicating device.

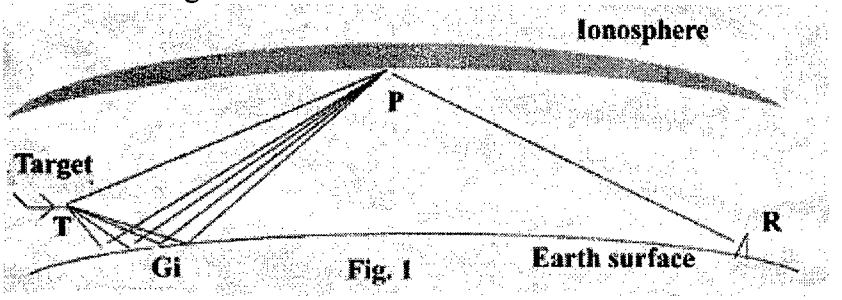

Fig. 1

The radiating target is an element of the radar channel that consists of this target, ionosphere and the passive radar (Fig.1). As a rule, the airborne antenna has a wide pattern in the HF band and the waves propagate to the terminal point (point R in Fig.1) by the paths TPR and TG_iR, where G_i is the i-th mirror point on the rough earth surface. As it has been shown in [1], the number of mirror points n is approximately equal to number of the correlation distance ρ of the heights earth roughnesses placing along the length of irradiated region. In the presence of great surface irregularities the mirror points number can be reduced owing to shading of any part of the reflecting surface by another one. Figs. 2,a,b show the number of total n (dashed lines) and unshading n_s (solid lines) mirror points as functions of the target height for earth rough surfaces with various statistical characteristics. The curves 1 were calculated for $\rho = 200\,\text{m}$, $\sigma = 3\,\text{m}$ and the curves 2 - for $\rho = 2500\,\text{m}$, $\sigma = 3\,\text{m}$, where σ^2 is variance of earth roughness heights scintillations. As it follows from these plots the signals forming conditions depend on the target height. The direct wave field of vertical or horizontal polarization is determined as

$$E_{1vh} = j\frac{\sqrt{60PG}_{vh}}{r_1}F_{1vh}(\theta)e^{j(\varphi - k\cdot r_1)}, \qquad (1)$$

where P, G_{vh} are the radiating power and maximum antenna gain on the vertical (v) or horizontal (h) polarization; φ is the initial wave phase; k is wave number; F_{1vh} is the value of

normalized airborne antenna pattern in the vertical plane into the direction of the pathwave that comes to the observation point R; r_1 is the path length between the points T and R.

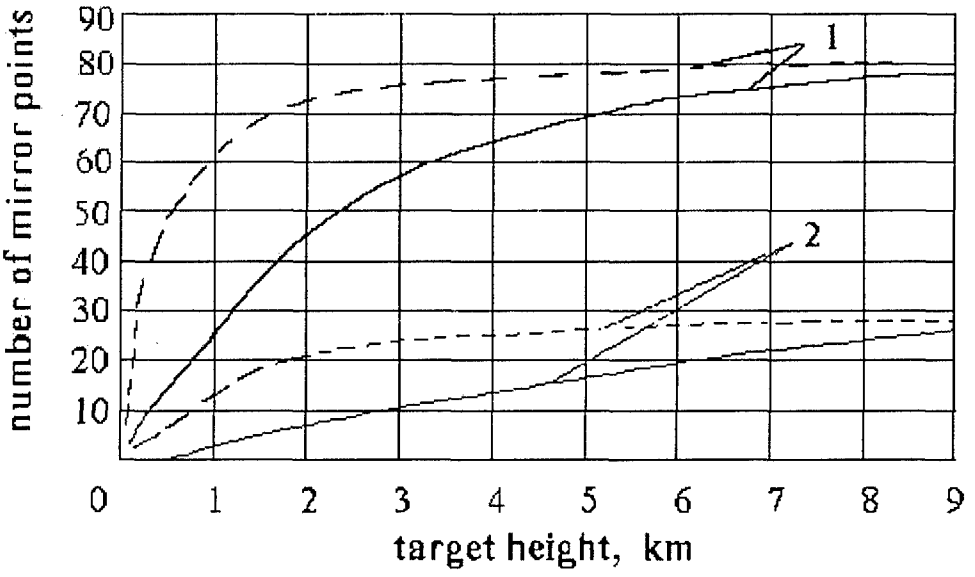

Fig. 2

The ground reflected field at the observation point

$$E_{2vh} = j\sqrt{60PG_{vh}}\sum_{i=1}^{n_s}\frac{\dot{R}_{vh}(\vartheta_i)}{r_{2i}}K_{si}F_{2vh}(_i\vartheta_i)e^{j(\varphi_i+\varphi-kr_{2i})}, \qquad (2)$$

where $F_{2vh}(\vartheta_i)$ is the value of normalized airborne transmitting antenna pattern into direction of the i-th mirror point in the vertical plane, $\dot{R}_{vh}(\vartheta_i)$ is complex coefficient of radiowave reflection from the earth surface, φ_i is a random phase shift caused by small-scale earth irregularities height of that is h and therefore $\varphi_i = 2kh_i\sin\vartheta_i$. The roughness coefficient in formula (2) $K_{si} = \exp(-2(kh_i\sin\vartheta_i)^2)$, r_{2i} is path length between the $i-$th mirror point and the observation point R. The formulas (1),(2) do not take into account the ionosphere influence and multiple reradiation between earth irregularities. We determine the result field at the point R as a sum of direct and scattering fields if $\frac{1}{r_1} \approx \frac{1}{r_{2i}} \approx \frac{1}{r}$, i. e.

$$\dot{E}(t) = j\frac{\sqrt{60PG_{vh}}}{r}e^{j(\varphi-kr_1)}\dot{B}(t), \qquad (3)$$

where $\dot{B}(t)$ is modulating factor that can be easily found from the formulas (1)..(3)

$$\dot{B}(t) = F_{1vh}(\theta) + \sum_{i=1}^{n_s}\dot{R}_{vh}(\vartheta_i)K_{si}F_{2vh}(\vartheta_i)e^{jk\Delta r_i}, \qquad (4)$$

where $\Delta r_i = r_1 - r_{2i}$. It depends on time accidentally as the parameters characterizing conditions of waves reflection from the earth surface are changed owing to aircraft

moving. Therefore the statistic simulation of modulating factor is realized for the $\dot{B}(t)$ analysis.

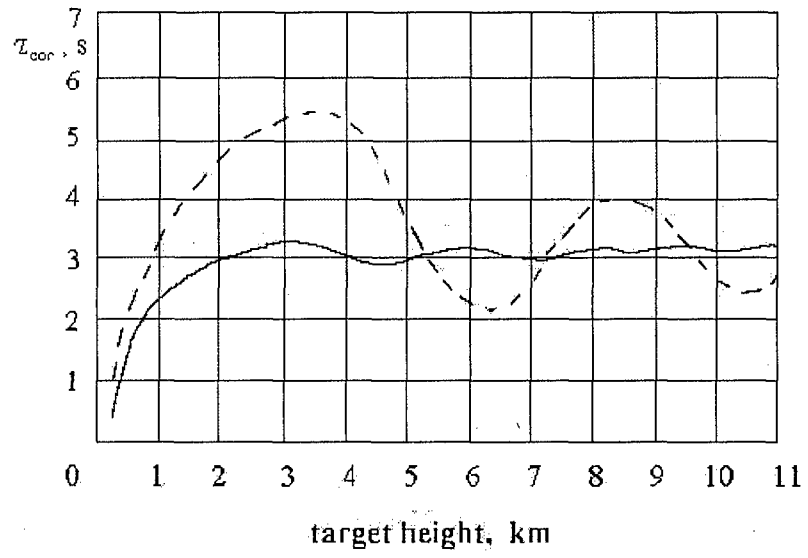

Fig. 3

Fig. 3 shows the graphs of dependence of the modulating factor correlation interval τ_{cor} from the target height flight h for vertical polarization of waves. The results have been received for hilly areas when $\rho = 2000\,\text{m}$ and $\sigma = 10\,\text{m}$. The dash line illustrates the dependence $\tau_{cor}(h)$ for one accidental realization of earth rough surface and solid line is dependence averaged by 10 accidental realizations. In general one can mark out some height ranges within that the correlation intervals of modulating factor differ considerably. For our example there are two ranges: range of small and great heights. The ionosphere influences can be taken into account when the earth passive radar receives simultaneously the signal of airborne transmitter and signal of oblique-incidence ionosphere sounding. The frequencies of these signals and their paths propagation must differ slightly. Similar experiments have been carried out at the beginning of 1990s [2]. The statistical characteristics of the above mentioned signals at the great heights were alike in these experiments. It confirms the main conclusions of the mathematical simulation.

REFERENCES

[1] Mikhailovsky A.I., Fuks I. M. Statistical characteristics of the number of mirror points on accidental surface at the small-angle incidence.- Radiotekhnika and electronika, 1993, №1, pp. 112..122 (in Russian).

[2] Bogdanov G. F., Borsoev V. A., Zastenchik L. L., Zubarev V. P., Kolyada A. P., Lazarenko V. M., Mazurov V. F., Naumov A. F., Ovsyannikov P. V., Polyarus A. V., Shvaiko P. P. Statistical characteristics of the oblique-incidence ionosphere sounding signals radiated from the board of aircraft.- Theses of reports of the XYII conference on radiowaves propagation, Ulianovsk, 1993.-p.28 (in Russian).

ATOMIC QUASI-INTERPOLATION IN THE PROBLEM OF DIGITAL SIGNAL PROCESSING

Victor F. Kravchenko*, and Michael A. Basarab**

*Institute of Radio Engineering and Electronics of the Russian Academy of Sciences.
103907, Center, GSP - 3, ul. Mokhovaya, 11, Moscow, Russia.
Tel: (095) 9024737, 9214837; Fax: (095) 9259241; E-mail: kvf@mx.rphys.mipt.ru.

** A.N. Podgornyi Institute of Problems of Engineering Industry,
National Academy of Sciences of Ukraine.
61046, ul. Dm. Pozharskogo, 2/10, Kharkov-46, Ukraine.
Tel: (0572) 959577, 942774; E-mail: rvachev@ipmach.kharkov.ua.

ABSTRACT

Iterative algorithm to obtain undetermined coefficients of local quasi-interpolants is proposed. The question of the iterative scheme convergence is investigated, and optimal value of the iterative parameter is obtained.

INTRODUCTION

In the practice of digital signal processing we usually deal with a discrete set of function's values defined on finite intervals. To restore the whole function it is necessary to approximate it in arbitrary way. One of the most traditional approaches is to interpolate this function by means of algebraic polynomial P(x). But this way has some drawbacks connected with non-compactness of polynomial support. At present, compactly supported functions (B-splines, atomic functions, etc.) are widely used as convenient mathematical tool for the approximation of local functions. This work is devoted to the numerical method of local quasi-interpolation of periodic differentiable functions defined at a discrete set of equally spaced knots. Our technique does not require analytical solving of the system of linear equations and is based on Jacobi iterative procedure and finite-difference theory.

SETTING OF A PROBLEM

Let $f(t) \in \tilde{W}_p^r[-\pi;\pi]$ be periodic function with continuous derivations. Define the regular mesh Δ_N : $t_i = ih$, $h = \pi / N$, $i = \overline{-N, N}$ and suppose that $f(t)$ is determined at the points

$$\tau_k = \tau_{k,r} = \left(4k - 1 + (-1)^r\right)\pi /(4N).$$

Due to periodicity of $f(t)$, the sets $\{t_i\}$, $\{\tau_k\}$ can be expanded to real line beyond the limits of interval $[-\pi;\pi]$ with the mesh width h. In this work we shall approximate $f(t)$ with the help of elements of $UP_{N,r}$ where the latter is a space of translations and dilatations of atomic function up(x) [1-3]:

$$\sum_k d_k \operatorname{up}\left(\frac{x+\pi}{2^r h} - k2^{-r}\right).$$

The space $UP_{N,r}$ has a basis consisted of translations and dilatations of compactly supported function $\operatorname{fup}_r(x)$; $\operatorname{supp} \operatorname{fup}_r(x) = \left[-\frac{r+2}{2}, \frac{r+2}{2}\right]$. Therefore atomic interpolation for $f(t)$ of order r is realized by means of the following expression:

$$\Phi_{N,r}(f;t)=\sum_{k=-N-M}^{N+M}c_k\varphi_{r,k}(t),\quad \Phi_{N,r}(f;\tau_j)=f(\tau_j),\quad M=[(r+1)/2],$$

where $\varphi_{r,k}(t)\equiv \mathrm{fup}_r\left(\frac{t+\pi}{h}-k+\frac{h}{4}(1-(-1)^r)\right)$ for $|t-\tau_k|\le\frac{r+2}{2}h$. Functions $\varphi_{r,k}(t)$ always can be normalized in a natural way:

$$\sum_k\varphi_{r,k}(t)\equiv 1.$$

Using the interpolation conditions

$$\Phi_{N,r}(f;\tau_j)=\sum_{k=-N-M}^{N+M}c_k(f)\varphi_{r,k}(\tau_j)=f(\tau_j),$$

and taking into account properties of $\varphi_{r,k}(t)$ and periodicity of $f(t)$ we obtain the following linear system of equations with respect to unknown coefficients $\{c_j\}$:

$$c_{-N-j}=c_{N-j},\quad j=0,...,[r/2],$$

$$\sum_{k=-M}^{M}b_{|k|}c_{j+k}=f_j,\quad j=-N,-N+1...,N, \tag{1}$$

$$c_{-N+j}=c_{N+j},\quad j=1,...,[r/2].$$

where $c_j\equiv c_j(f)$, $f_j\equiv f(\tau_j)$, $b_k\equiv\varphi_{r,0}(kh)$.

QUASI-INTERPOLATION ALGORITHM

By analogy with the case of B-splines [4-5] construct the local atomic quasi-interpolant:

$$\Phi_{N,r}^{(p)}(f;t)=\sum_{k=-N-M}^{N+M}c_k^{(p)}(f)\varphi_{r,k}(t).$$

The coefficients $c_k^{(p)}(f)$ are defined by values of $f(\tau_i)$ not on the whole mesh but only at the points close to τ_k. Present (1) in matrix form:

$$BC=F.$$

The Jacobi scheme [6] to obtain unknown components of vector C has the form:

$$\frac{C^{(k+1)}-C^{(k)}}{\theta}+BC^{(k)}=F,\quad k=0,1,... \tag{2}$$

Here $C^{(k)}$ are sequential approximations; $\theta\le 2$ is iterative parameter; initial approximation $C^{(0)}=F$. The more k is, the more high order of approximation we have. The problem is to find the value θ providing the best convergence of sequential approximations to exact solution of the system (1). By analogy with (2) let us write expressions for error $Z^{(k)}=C^{(k)}-C$ and residual $R^{(k)}=BC^{(k)}-F$:

$$\frac{Z^{(k+1)}-Z^{(k)}}{\theta}+BZ^{(k)}=0,\quad k=0,1,...;\qquad \frac{R^{(k+1)}-R^{(k)}}{\theta}+BR^{(k)}=0,\quad k=0,1,...$$

Theorem 1. *The scheme (2) provides the following rate of convergence in Euclidean metrics:* $\left\|Z^{(k+1)}\right\|_2\le\rho(\theta)\left\|Z^{(k)}\right\|_2$; $\left\|R^{(k+1)}\right\|_2\le\rho(\theta)\left\|R^{(k)}\right\|_2$. *Here* $\rho(\theta)=\sqrt{1-2\theta\alpha_B\alpha}$ *where* α_B *and* α *are the minimal eigenvalues of matrices B and E–θB/2 respectively;* $\min\rho(\theta)=\rho(1)=\sqrt{2(1-b_0)}$.

It can be shown that

$$c_j = \sum_{s=0}^{\infty}(-1)^s\left(\sum_{i=1}^{M} a_i \Delta^{2i}\right)^s f_j, \quad j=-N,-N+1,...,N,$$

where Δ^n is a central finite difference of order n, and coefficients $\{a_j\}$ are defined by recurrent expressions

$$a_M = b_M, \quad a_{M-s} = b_{M-s} + \sum_{i=1}^{s}(-1)^{i+1} C^i_{2(M-s+i)} a_{M-s+i}, \quad s=1,2,...,M.$$

According to the scheme (2) with θ=1 and $c_j^{(0)} = f_j$, sequential approximations to the components of exact solution $c_j^{(k)}$ will take the form:

$$c_j^{(k)} = \sum_{s=0}^{k}(-1)^s\left(\sum_{i=1}^{M} a_i \Delta^{2i}\right)^s f_j, \quad j=-N,-N+1,...,N. \tag{3}$$

Denote the quasi-interpolant corresponding to coefficients (3) by $\Phi_{N,r}^{(k)}(f;t)$.

Theorem 2. *Suppose* $b_0 - 2\sum_{i=1}^{M} b_i = q > 0$ *and* $f(x) \in C^{M(2k+2)}$. *Then we have the following estimation:* $\left\|\Phi_{N,r}^{(k)}(f;t) - \Phi_{N,r}(f;t)\right\|_{C[-\pi;\pi]} = O(h^{2k+2})$.

Finally, optimize (3) so that $\Phi_{N,r}^{(k)}(f;t)$ will be exact for polynomial of order r:

$$c_j^{(k)} = \sum_{s=0}^{M}(-1)^s \sum_{\{p_i\}}\left(\prod_{i=1}^{M} a_i^{p_i}\right)\Delta^{2\sum_{i=1}^{M} ip_i} f_j. \tag{4}$$

Here the set of indexes $\{p_i\}$ must satisfy the following conditions:

$$\sum_{i=1}^{M} p_i = s, \quad \sum_{i=1}^{M} ip_i \le M.$$

CONCLUSION

The main advantage of the novel quasi-interpolation algorithm is that it does not depend on regularity of the mesh, and is applicable for the case of nonregular one in the space R^n.

REFERENCES

[1] Rvachev V.L., Rvachev V.A. Nonclassical methods of approximation theory in boundary value problems. Kiev. Naukova Dumka, 1979. (In Russian)

[2] Kravchenko V.Ph., Rvachev V.A.// Zarubezhnaya radioelectronika, №8 (1996), 6-22.

[3] Kravchenko V.F., Zamyatin A.A.// Proc. III Intern. Symp. MSMW'98, Kharkov, Sept. 15-17, 1998, 413-415.

[4] de Boor C., Fix G. Spline approximation by quasi-interpolants.// J. Approx. Th., **8**, №1 (1973), 19-45.

[5] Lych T., Schumaker L.L. Local spline approximation methods// J. Approx. Th., **15**, №4 (1975), 294-325.

[6] Hageman L.A., Young D.M. Applied Iterative Methods, Academic Press, 1981.

APPLICATION OF THE WAVELET ANALYSIS FOR DETECTING ULTRA-WIDEBAND SIGNALS IN NOISE

Leonid F. Chernogor and Oleg V. Lazorenko

V. Karazin Kharkiv National University, Kharkiv, Ukraine
E-mail: Leonid.F.Chernogor@univer.kharkov.ua

ABSTRACT

To improve detection of anthropogenic and natural UWB signals against the background of noise, the wavelet analysis has been applied.

INTRODUCTION

Recently ultra-wideband (UWB) signals (an example is given in Fig. 1a) have found a wide variety of applications in solving different engineering and science problems. Such signals convey more information than ordinary narrow- and wide-band signals by a factor of $\mu / \mu_n >> 1$ (here μ is the UWB signal index, and μ_n the narrow-band signal index). The engineering tradeoffs in the design of any UWB system involve the development of new techniques for signal generation, reception, and processing. Therefore it is important to apply new methods for the detection of anthropogenic and natural UWB signals against background noise.

WAVELET ANALYSIS APPLICATION

Each wavelet is a UWB signal by definition. Therefore the wavelet spectrum of any UWB signal turns out to be more narrow than its Fourier spectrum because of the similarity between the signals and the basic wavelet transform functions. Such a wavelet spectrum of the UWB signal in Fig. 1a was obtained using the Dobecci basic wavelet, and it is shown in Fig. 2b. In that figure W is a wavelet amplitude spectrum, a is the scale factor and b is the translation factor. In Fig. 2, it can be seen that UWB signal and noise wavelet spectra are widely separated when the additive interference is weakly correlated (i.e. its correlation interval is much less than the characteristic scale of UWB signal changes). In the time space, the signal, noise and their mixture are represented in Fig. 1a-1c, and the results of the wavelet filtering with different scale factors a are shown in Fig. 1d-1n. The amplitude signal-to-noise ratio is equal to 1/5. It has been shown that there is an optimum number of terms in the inverse discrete wavelet transform. This number depends, on one hand, on a sufficiently good reconstruction of the signal form, and, on the other hand, on noise minimization. The optimum number of terms for signal reconstruction and detection has been determined as a function of the signal-to-noise ratio.

REFERENCES

[1] The transforms and applications handbook / Editor-in-chief, Alexander Poularikas. -CRC Press, USA, 1996, 1103 pp.

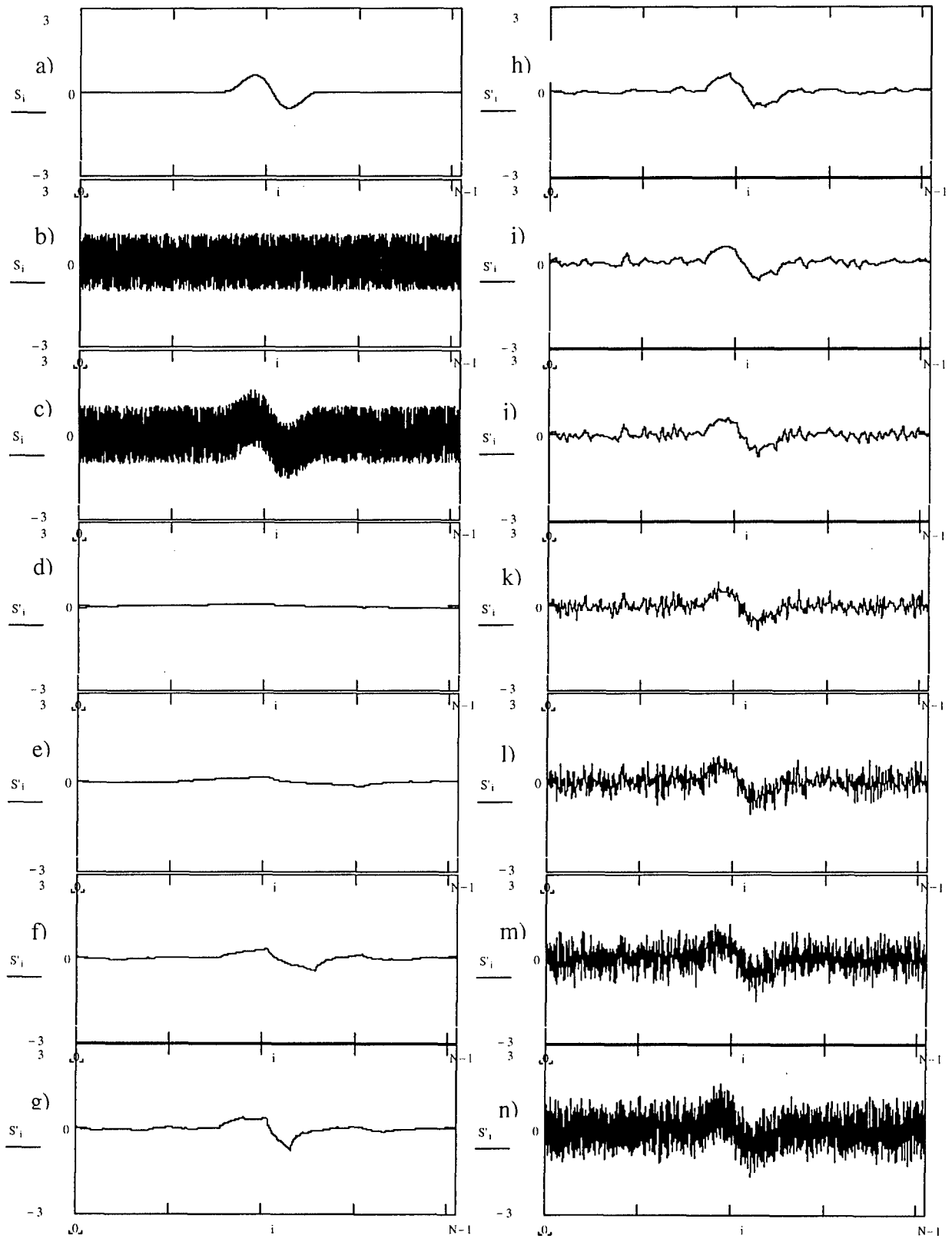

Fig. 1. The UWB signal model (a), the noise model (b), the additive mixture of that signal and noise with the amplitude signal-to-noise relation, which is equal to 1/5 (c), and they after wavelet filtration with different values of wavelet spectrum parameter a (d-n).

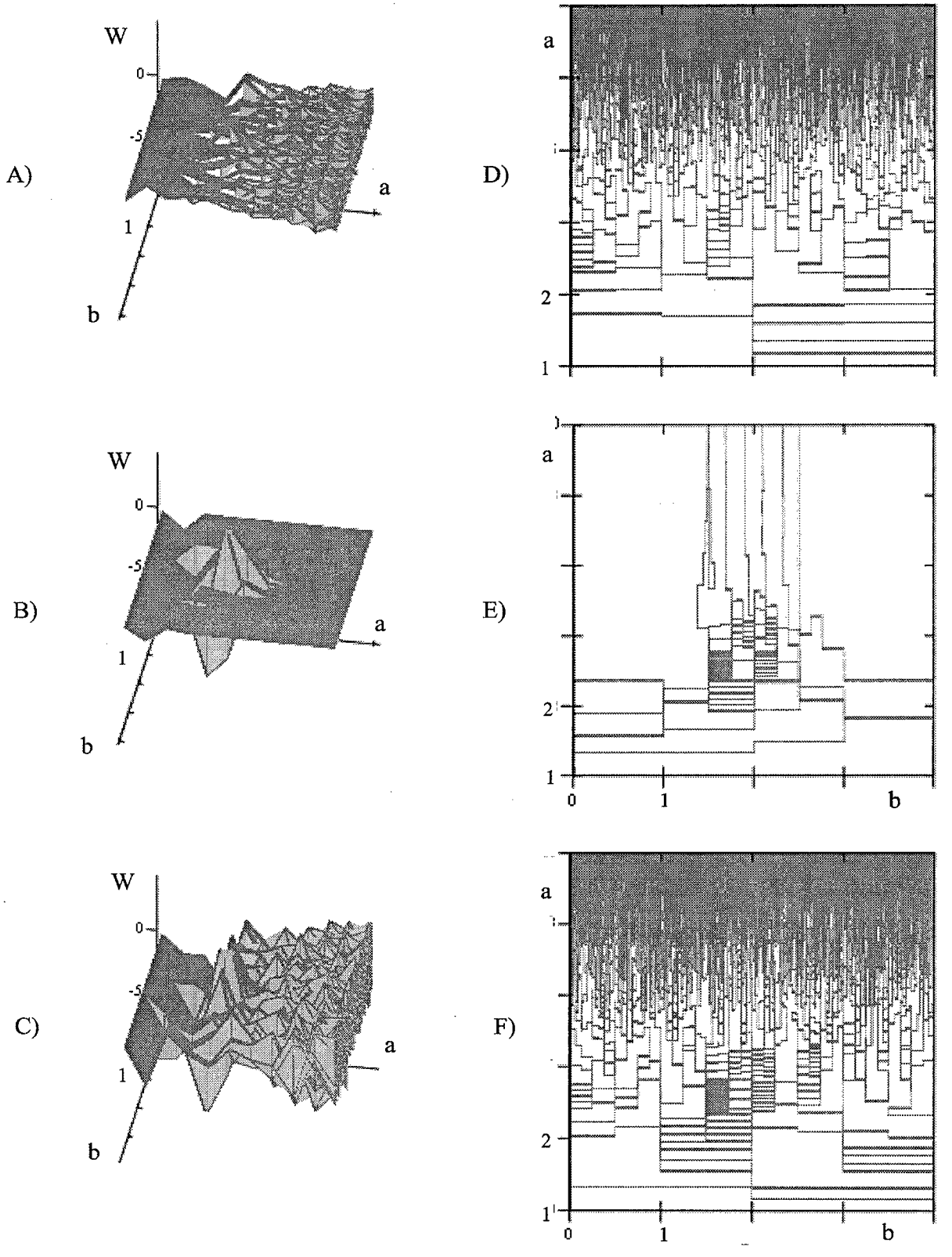

Fig. 2. A and D are the noise wavelet spectra, Ь and E are UWB signal wavelet spectra, C and F are the wavelet spectra for additive mixture of that signal and noise. W is the spectrum amplitude, a and b are the wavelet spectrum parameters.

2D MATRIX FILTERING OF GROUND PENETRATING RADAR DATA

V. Kovalenko, and S.A. Masalov
Usikov Institute of Radio Physics and Electronics of NAS of Ukraine

12, Ak. Proskury str., Kharkov, 61085, Ukraine
E-mail: smith@ire.kharkov.ua

Specially designed 2D matrix filters can provide a flexible tutorial for the processing of ground penetrating radar data. Brief overview of such filters application and design of the two filters is presented. The first adaptive filter is well suited for separation of large non-contrast objects, layered subsurface structures, etc. The second one provides migration of GPR data sets and increases the horizontal resolution of images.
Key words: ground penetrating radar, 2D matrix filtering.

Ground penetrating radars (GPR) constitute a saturated with various problems but quickly developing direction in the applied radio physics [1]. A successful use of the GPR demands involving of various computer aided mathematical algorithms for the obtained data treatment.
The common methods of GPR data processing can be divided in three heterogeneous groups:

- Electro magnetic based approaches, which are aimed on obtaining the approximate solution of the video pulse inverse diffraction problem. The typical algorithms of this class are synthetic aperture method [2,3], complex natural resonance expansion method [4], etc.
- Adaptations of the geo acoustic techniques, such as predictive deconvolution, migration and similar methods [5].
- Image processing algorithms, which are disengaged from the data genesis.

The 2-D matrix filtration algorithms are in wide use in various images processing application and their construction may not be based on the specific data origin. Here we demonstrate results of the common filtering [1] of the GPR data and introduce the adaptive algorithm for the two-dimensional edge-detective matrix filter.
On the other hand, it is possible to construct the matrix filters for the optimal data processing taking into account the specific character of the data formation. We discuss the design of the filter, which can be used for spatial data convolution in order to increase the horizontal resolution of the GPR image. The filter design is based on the specific geometry relation between the parts of the GPR and the subsurface object under the investigation in the bistatic sounding formation.

FORMATION OF A GPR IMAGE

The subsurface scanning routing consists of serial illuminations of the probing pulses and recording of the electromagnetic signals reflected by the media (echo-returns) in several points on the surface. Usually the GPR data are stored as a set of the electromagnetic echoes recorded in N points along the route of the scanning. The resulting matrix of $M \times N$ is called the echo-profile or the scan and represents the diffraction image of the subsurface section $[x_0, x_1] \times [z_0 = 0, z_1]$, where M represents the quantity of the time points in each return, $[x_0, x_1]$ is the length of the scan and z_1 is defined by the recording time of echo-returns, the GPR sensitivity, medium properties, etc. Then the scan can be represented as a brightness picture (see Fig. 1a).

COMMON MATRIX FILTERING OF THE GPR DATA

The basic matrix filtration methods involve the convolution of the matrix S, which represents the scan, with a specially formed matrix F_m[1] of $m \times m$ (m is odd). It means that the elements $\tilde{S}_{ij}$ of the filtered image are derived from the scan S and the sliding matrix F_m as follows:

$$\tilde{S}_{ij} = \sum_{k=1}^{m}\sum_{l=1}^{m} F_{kl}\bar{S}_{i+\frac{m+1}{2}-k,\,j+\frac{m+1}{2}-l}, \tag{1}$$

$$\bar{S}_{\alpha\beta} = \begin{cases} S_{\alpha\beta}, \text{ if } 0<\alpha\le M \text{ and } 0<\beta\le M \\ 0, \text{ otherwise} \end{cases} \tag{2}$$

An example of the common matrix filter is the horizontal edge detector. This filter is constricted with the following sliding matrix F_m:

$$F_m^{hor} = \frac{1}{2m^2-m}\begin{pmatrix} -1 & -1 & .. & .. & -1 \\ . & . & . & . & . \\ m & m & ... & m & m \\ . & . & . & . & . \\ -1 & . & . & . & -1 \end{pmatrix} \tag{3}$$

Increasing of m leads to amplifying of the filtering effect. Now let us construct the filter to detect slope edges. It can be easily seen that the sliding matrix

$$F_m^{s_1} = \frac{1}{N_F}\begin{pmatrix} m & -1 & .. & .. & -1 \\ -1 & m & . & . & . \\ . & . & ... & . & . \\ . & . & . & . & . \\ -1 & . & . & . & m \end{pmatrix}, \tag{4}$$

where $N_F = \sum_{k,l}\left|F_{m,kl}\right|$, will produce the filter, which detects the slopes in the directions from the left-upper to the right-lower angle of the scan (Fig.1b). Changing the angle of the matrix diagonal filled with m's, one can construct the edge detectors $F_m^{s_i}$ that amplify images of various inclined brinks. Let us define the set $P = \left\{F_m^p\right\}_1^{R_m}$ of the matrixes with all-possible angles of m-diagonals. Now we can construct an adaptive filter for the slopes detecting taking the elements of the filtered scan in the form:

$$\tilde{S}_{ij} = \max_{p\in P}\left\{\left|\sum_{k=1}^{m}\sum_{l=1}^{m} F_{kl}^{p}\bar{S}_{i+\frac{m+1}{2}-k,\,j+\frac{m+1}{2}-l}\right|\right\} \tag{5}$$

The filter designed by (5) defines the maximum slope in each point of S and amplifies the direction chosen. This results in the optimum detecting of large non-contrast objects, such as seam inclinations, etc. (Fig. 1c).

DESIGN OF A DECONVOLVING MATRIX FILTER

It is possible to construct matrix filters taking into account the origin of the data. Let us construct the filter, which deconvolves traces from subsurface objects, in the case of the bistatic sounding scheme use [3] (Fig. 2 a). It is easy to see that the variation of the path length s_{top} between the receiving and transmitting antennas via the point (x^*, z^*) on the subsurface

object leads to forming of the hyperbola-like trace in the scan (Fig.2 b). Denoting the triangulation scheme from the Fig. 2a one obtains:

$$s_{top} = \sqrt{(x - x^*)^2 + z^{*2}} + \sqrt{(x + A - x^*)^2 + z^{*2}} \tag{6}$$

$$s_{\min} = \sqrt{A^2 + 4z^{*2}} \tag{7}$$

Then, we form the F_{mn} sliding $m \times n$ matrix in the following form :

$$F_{mn} = \frac{1}{N_F} \begin{pmatrix} 0 & \dots & 0 & 0 & 1 & 1 & 1 & 0 & 0 & \dots & 0 \\ 0 & \dots & 0 & 1 & -1 & -1 & -1 & 1 & 0 & .. & 0 \\ . & . & . & . & . & . & . & . & . & . & . \\ 0 & 0 & 1 & -1 & 0 & \dots & 0 & -1 & 1 & 0 & 0 \\ 0 & 1 & -1 & 0 & 0 & \dots & 0 & 0 & -1 & 1 & 0 \\ 1 & -1 & 0 & 0 & 0 & \dots & 0 & 0 & 0 & -1 & 1 \end{pmatrix}, \tag{8}$$

where entries of 1 and -1 are placed in the hyperbola-like form. If this hyperbola is congruent to the one defined by (2) and (3), the use of the filter based on this sliding matrix focuses the data image, transforming the object traces into spots (see Fig. 2c). As seen from the figures, such a filter significantly increases the horizontal resolution in the data set.

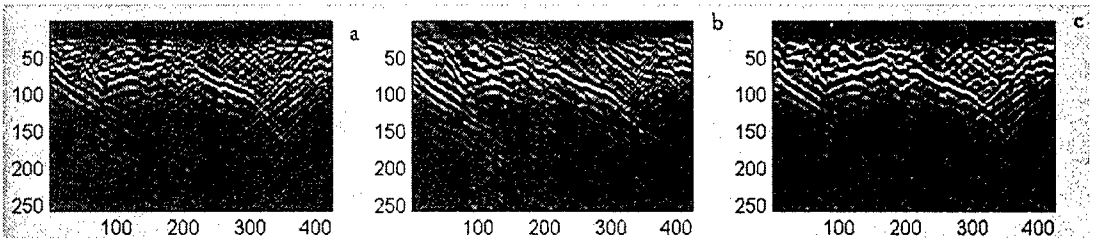

Fig.1 a - The scan of a lake in Kharkiv; **b** - the diagonal vertex outlined scan; **c** - adaptively filtered scan.

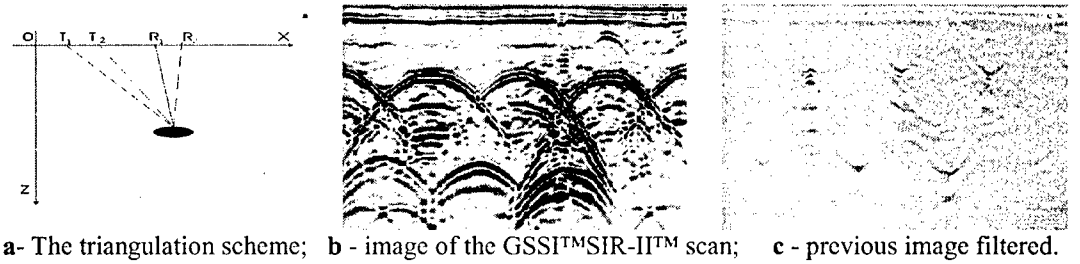

Fig.2 a- The triangulation scheme; **b** - image of the GSSI™SIR-II™ scan; **c** - previous image filtered.

REFERENCES

[1] Daniels D.J. Ground Penetrating Radar. — Inspec/IEE, 1996. – 300p.

[2] Osumi N., Ueno K. Microwave Holographic Imaging of Underground Objects. //IEEE Transaction on Antennas and Propagation. 1985. - №2. - P.152-159.

[3] Kovalenko V., Masalov S.A. Probe Pulse Shape Estimation In Synthetic Aperture Method. // Proc of IEEE AP-S International Symposium, Orlando, Florida, (11-16, July). - 1999 -P.1792-1796

[4] Baum C.E. et al. Singularity Expansion Method. // Proc. IEEE — 1991— 79 — №10. – P. 1481-1492

[5] Hagedoorn J.G. A Process of Seismic Reflection Interpretation // Geophys.Prospect. — 1954. — 2.— P. 85-127.

PROPAGATION AND REMOTE SENSING

ANTENNAS FOR NEAR-FIELD RADIOTHERMOMETRY[1]

Yurasova N.V., Gaikovich K.P., Reznik A.N., and Vaks V.L.

Institute for Physics of Microstructures RAS, GSP-105, Nizhny Novgorod, Russia, 603600,
Phone: 8312 327920, Fax: 8312 675553, E-mail: gai@ipm.sci-nnov.ru

ABSTRACT

The application of electrically-small antennas in the area of subsurface radiometry make possible measurements of the quasi-stationary field of a thermal emission (evanescent modes at interface) [1]. New one-wavelength methods of non-invasive temperature sounding of absorbing media, such as water and living tissue, can be developed using such measurements. The quasi-stationary field component is formed in media in another way in comparison with the ordinary used wave (propagating) component. Our theoretical analysis shows that the effective depth of the formation of quasi-stationary component depends on the height of antenna above the surface of a medium and on the antenna size. At the surface this skin-depth could be very small (for small antennas); it increases with the antenna height, and at the height comparable to wavelength in the medium it converges to skin-depth for the wave component of thermal emission.

THEORETICAL ANALYSIS

The main technical problem of these measurements is to achieve a good matching and high efficiency of electrically-small antenna in the near-field region above absorbing media taking into account the strong influence of the media on antenna parameters. The measured antenna temperature T_a can be expressed for contact measurements as

$$T_a = (1-R)[\eta T_{eff} + (1-\eta)T(0)] + RT_{ns} \qquad (1)$$

where R is the reflectivity from antenna, h is the efficiency, T_{ns} is the temperature of radiometer noise at the antenna, $T(0)$ is the temperature of antenna at the medium surface. The good matching minimizes the reflectivity R. At $R \to 0$ and $\eta \to 1$ one has $T_a=T_{eff}$. The efficiency of electrically-small dipole antennas falls proportionally to the factor $(l/\lambda)^4$. Our analysis shows that the antenna efficiency is much higher in vicinity of a lossy medium in comparison with the antenna in free-space. The efficiency depends also on antenna material. In Fig.1-2 the results of theoretical analysis are shown for achievable efficiency of the simple dipole antennas with the matching resonant circuit (made using the ordinary copper (Cu) at two different temperatures and using high-T_c superconductor film (YBaCuO)) as a function of the size and the height above the medium surface. It is possible to see that the minimum achievable size of antenna at wavelength λ = 30 cm could be about 1 mm. It is also difficult to obtain a high enough efficiency without the superconductor technology at the antenna heights above 1 cm. But it is clear that just now it is possible to have a good efficiency at contact measurements using the ordinary copper antennas in the wide region of antenna sizes. The efficiency can also be enhanced by means of the more sophisticated antenna design. The results of our first attempts to build such antennas form the main contents of this paper.

[1] This work is supported by Russian Science Ministry State contract *No.*107-3(00-P).

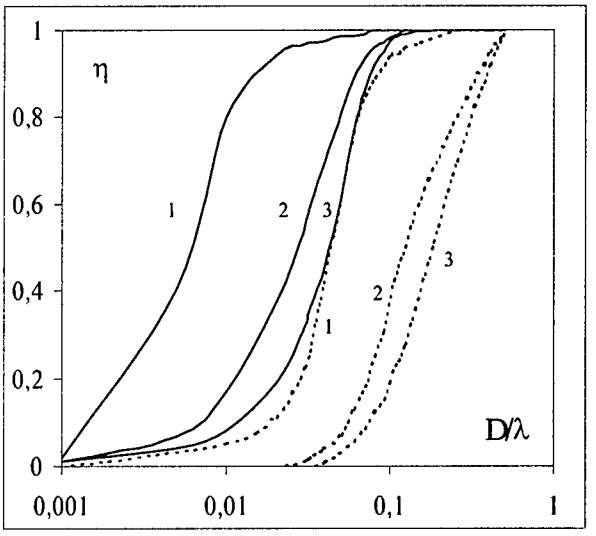

Fig.1. Calculated antenna efficiency as a function of the size-wavelength relation: 1 –superconductor, 2 – copper at 77 K, 3 – copper at 290 K. Solid lines – contact measurements (h=0), dashed – free-space.

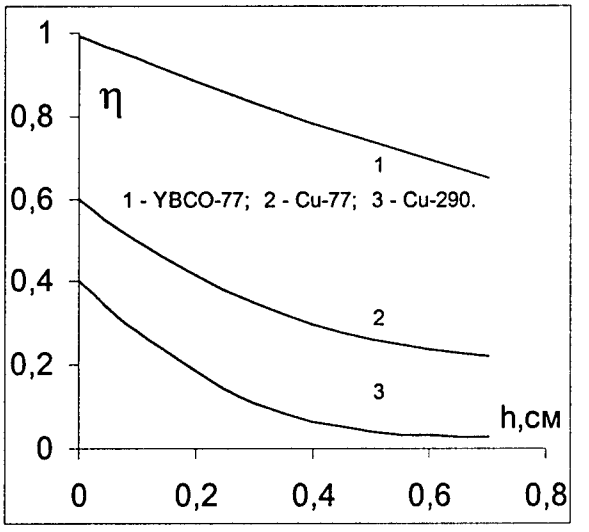

Fig.2. Calculated efficiensy of 1-cm dipole antenna as a function of the antenna size at λ = 30 cm.

ANTENNA DESIGN AND TESTING

We have developed antennas with high enough efficiency. These copper antennas include two stripline planar dipoles and the resonant circuit to achieve the antenna-medium matching. The antenna schema is shown in Fig.3. Effective sizes of antennas are about 1 cm, the operating frequency is 950±100 MHz (frequency band of the radiometer). The reflection coefficient, efficiency, and sensitivity of antennas have been studied in dependence on the frequency and the dielectric parameters of the measured medium (see in Fig.4,5). The water was chosen as a medium the dielectric parameters of which have the strong dependence on the temperature and the salinity. Thus, the temperature and salinity dependence of antenna parameters was investigated. Antenna in the contact with the living tissue also has been investigated. In Fig.6,7 one can see the reflection coefficient R, efficiency η and sensitivity dT_b of radiometer (all the parameters averaged over the radiometer band). These parameters are practically independent on the temperature and the salinity of water.

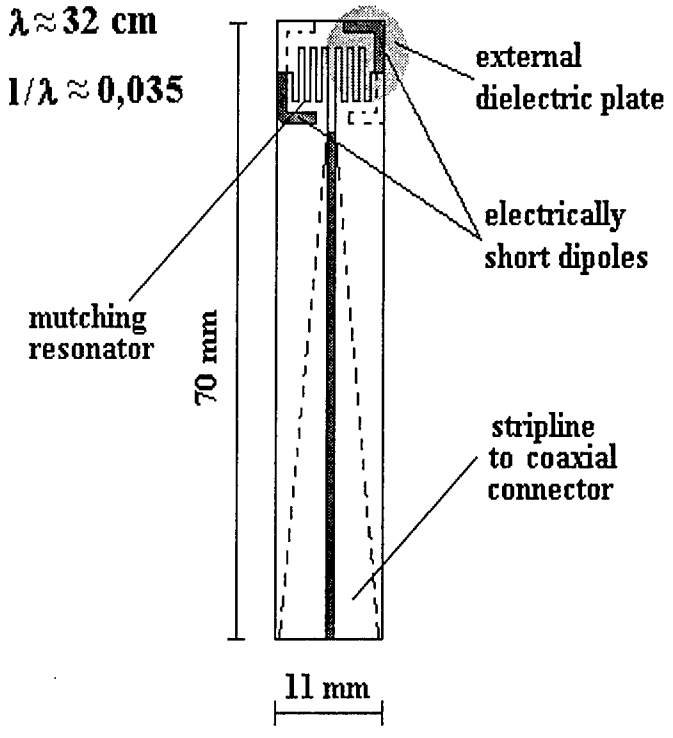

Fig.3. Near-field antenna design.

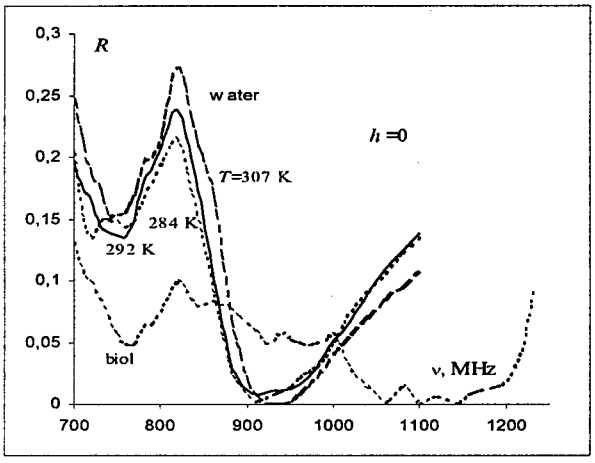

Fig.4. Frequency dependence of the antenna reflectivity at three different temperatures for water medium and for living tissue at 37 C.

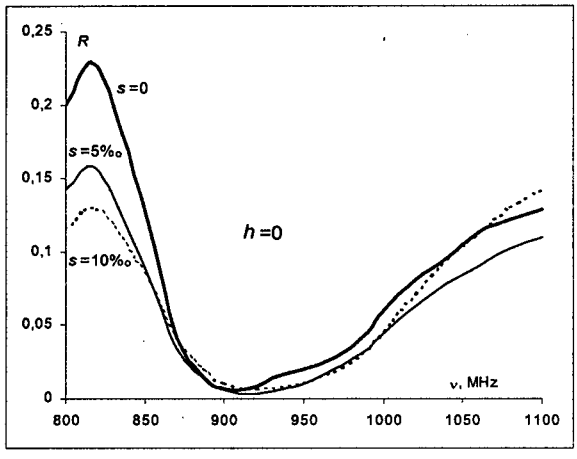

Fig.5. Salinity dependence of the antenna reflectivity at three different values of water salinity.

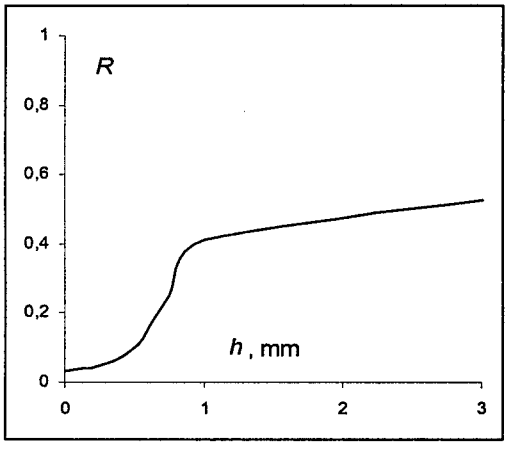

Fig.6. The height dependence of antenna reflectivity in the radiometer frequency band.

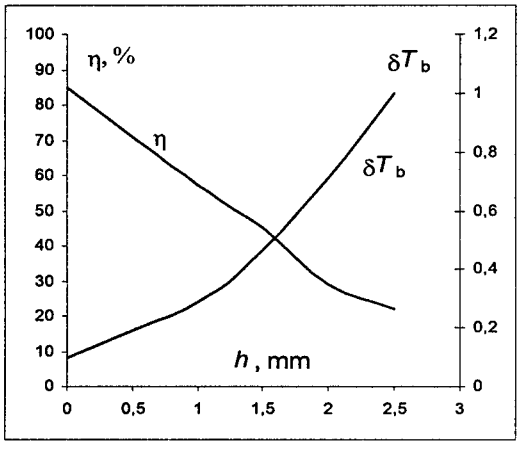

Fig.7. The height dependence of antenna efficiency and radiometer sensitivity in the radiometer band.

All the parameters are very suitable for contact measurements at $h = 0$ (on the water surface) but they fall drastically with the increasing of the antenna height up to 1 mm. Of course, it is possible to improve these parameters on the base of antennas with a tunable resonant circuit to match them at each height independently. For the further matching improvement, the possibilities of antennas based on high-temperature superconductor technology [2] should be used. But the achieved antenna parameters permit to solve the main problem – to detect near-field effects at large temperature gradients in the temperature-stratified water.

It is worth noting that the reflectivity has strong enough dependence on the dielectric parameters outside the radiometer frequency band (see Fig.4, 5), so it is possible to use this dependence for media parameters diagnostics.

REFERENCES

[1] Gaikovich K.P., Reznik A.N., Vaks V.L. Near-Field Effects in Thermal Radio Emission (present issue).

[2] Abramov V.I., Klimov A.Y., Reznik A.N., Tagunov B.B. Electrically small strip antenna of a high-temperature superconductor. Tech. Phys. Lett., 1994, 20(10), 792-794.

POLARIZATION OF THE THERMAL RADIATION OF THE CLOUDY ATMOSPHERE IN MILLIMETER WAVELENGTH BAND

Alexander M. Osharin, and Arkady V. Troitsky

Radiophysical Research Institute, N.Novgorod, Russia
E-mail: osh@nirfi.sci-nnov.ru, Telephone : 8312 366751, Fax : 8312 369902.

ABSTRACT

Results of the ground based radiometric observations, indicating the presence of significant polarization differences in thermal microwave radiation of the cloudy winter-spring atmosphere are reported. Interpretation of the observational data is carried out on the basis of polarized radiative transfer modeling in mix-phase clouds, containing ice crystals and supercooled water drops.

APPARATUS AND MEASUREMENT PROCEDURE

The study of the thermal microwave radiation of the cloudy atmosphere was carried out by a 94 GHz modulation radiometer, receiving atmospheric radiation simultaneously on the two orthogonal linear polarizations - vertical and horizontal. Radiometer has cone-shaped horn antenna with half-power beam width 4^0. Fluctuational sensitivity for both channels was 0.2 K for integration time 1 sec. Decoupling between the two polarization channels was not worse then 15 dB. Total transmission coefficients for both channels from antenna to PC were equalized with accuracy not worse then 0.5% and controlled by the two unpolarized sources - clear atmosphere and black body, placed to the far zone of antenna pattern perpendicular to the electric axis of the horn. Black body was kept at an ambient air temperature. The same sources were used as standards to calibrate radiometer channels in both radio brightness and polarization difference scales. Atmosphere brightness temperature measurements were carried out on fixed zenith angles equal to 40^0, 60^0, and 70^0. Absolute precision of the measured brightness temperature on both polarizations was~2 K. Polarization difference measurement precision was estimated as 0.4 K.

RESULTS AND INTERPRETATION OF EXPERIMENT

Ground based polarimetric observations of the cloudy atmosphere microwave radiation were carried out during January-July period of 1999 in Nizhny Novgorod, Russia, at 94 GHz. The observations showed significant polarization of the winter-spring clouds thermal radiation. An example of the registered brightness temperature on both polarizations (curves v and h) and corresponding polarization differences(curve v-h) at zenith angle 70^0 is illustrated in fig.1. The beginning and the end of each time realization curve corresponds to the unpolarized clear sky radiation, i.e. to the zero level of the polarization difference. For winter-spring atmosphere the polarization difference of ~1 K at 70^0 was detected in more then 80% of realizations for ambient air temperature <+7 ^{0}C. The ambient air temperature through all the period of observations varied from -16 ^{0}C up to +29 ^{0}C. The polarization difference value had irregular

character, chaotically changing its sign. Its absolute value was decreased as zenith angle decreased. The maximum absolute value of the polarization difference observed was as much as 9 K. Polarization differences were not correlated with cloud liquid water content, which was determined simultaneously from the brightness temperature estimations at 94 GHz, depending mainly upon integrated water content.

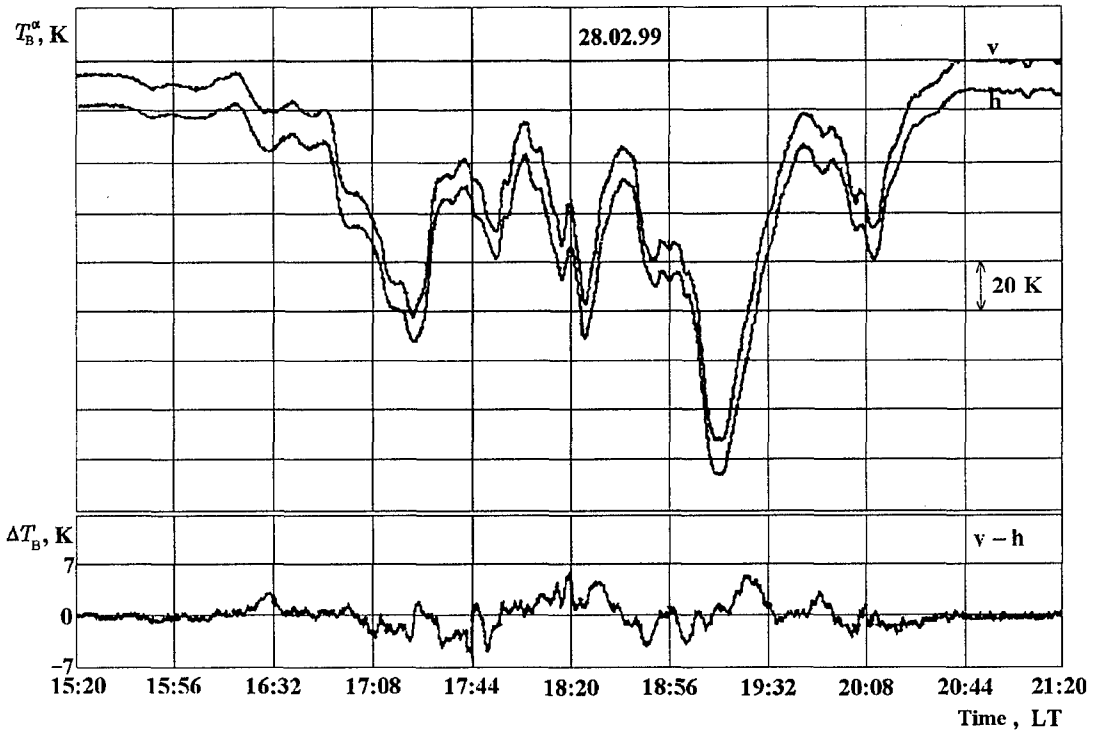

Fig.1

THEORY AND COMPUTER SIMULATION

The interpretation of the observational data was carried out on the basis of the vector radiative transfer equation (VRTE) in a plane-parallel layer, containing sparsely distributed spheroids, having statistically azimuthally symmetric space orientation [1,2]. The elements of the extinction and phase matrices, entirely expressed in terms of the scattering function amplitudes, averaged over size and azimuth ϕ orientation of the particles, were calculated by DDSCAT code [3], slightly modified to fit VRTE computations. Solution of the system of radiative transfer equations was found numerically by using discrete ordinate eigenanalysis method [2].

Fig.2 shows polarization differences $\Delta T_B = T_{B,v} - T_{B,h}$ at 94GHz versus azimuth angle for mix-phase cloud, containing ice spheres and supercooled water drops. Fig.3 illustrates ΔT_B angular dependency for mix-phase clouds, containing horizontally oriented ice plates. Thickness of the cloud layer was set equal to 2 km in both cases, cloud bottom height - 1 km. The surface boundary throughout all calculations was treated as black body emitter to attribute all polarization characteristics entirely to cloud particles. Maximum size of ice particles in distribution was taken to be 2 mm, corresponding maximum size for water drops-100 μm. The total amount of specific water content inside cloud was kept constant at $Q = 0.2$ gm/m^3, while the proportion between water and ice phases was varied. Thick solid curves in Figs.2

and 3 exhibits ΔT_B for purely crystalline cloud, dashed curves correspond to specific water content $Q_w = 0.05$ gm/m^3, dotted curves – to $Q_w = 1$ gm/m^3, thin solid – $Q_w = 0.15$ gm/m^3.

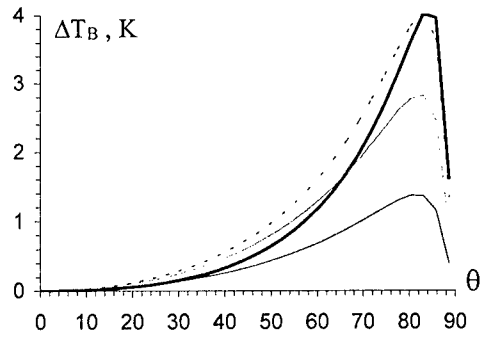

Fig.2

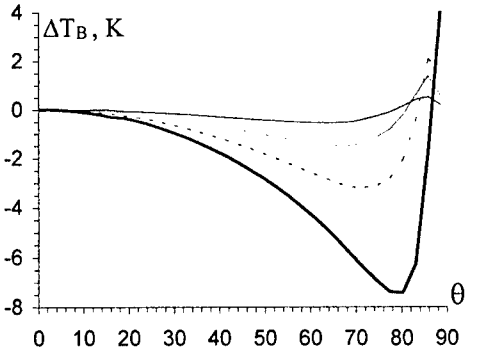

Fig.3

Mode diameter for spheres and plates in modified gamma-type particle size distribution was set to be $D_M = 500\,\mu$m. The studies show the sign of the polarization difference depends on the shape of the crystals and specific water drops content and may change with viewing zenith angle. It is interesting to note, that in the case of spherical ice particles polarization difference ΔT_B for clouds, containing moderate water fraction amount (see dashed curves in Fig.2) prevails over that for purely crystalline cloud in a wide range of zenith angles. Nevertheless, as the water drops content in the cloud is becoming more and more pronounced, the polarization difference ΔT_B reduces its value as it should be. The picture for plates (Fig.3) is somewhat different. In this case the polarization difference is gradually depressed as water drops content in the cloud are becoming predominant practically at all viewing angles except for those, where ΔT_B changes its sign. The largest absolute values of ΔT_B in this case are characteristic for purely crystalline clouds. Fig.3 also demonstrates how cloud water drops content influences the sign of the polarization differences: the more water portion inside cloud the less zenith angle at which ΔT_B changes its sign.

The work was supported by the Russian Foundation for Basic Research Fund, grant No. 00-02-16037.

REFERENCES

[1] «Light Scattering by Nonspherical Particles. Theory, Measurements, and Applications», Edited by M.I. Mishchenko, J.W. Hovenier, L.D. Travis, Academic Press, 2000.

[2] L.Tsang, J.A. Kong, R.T.Shin, «Theory of microwave remote sensing», Wiley, N.Y., 1985.

[3] B.T. Draine, «The discrete-dipole approximation and its application to interstellar graphite grains», Astrophys J., **333**, 1988.

SOME PECULIARITIES OF THE HF SIGNAL WHEN LOCATING THE SEA SURFACE

M. V. Ignatenko *, S.N. Kolesnik** and M.V. Tinin*
*Irkutsk State University, 664003, Irkutsk, 20 Gagarin Blvd.
**Irkutsk Military Aviation Engineering Institute
E-mail vmt@api.isu.runnet.ru

ABSTRACT

Obtaining information about the state of the sea surface using HF radars has been the subject of intensive studies over the last several decades. In most of the theoretical investigations a plane wave with a definite wave vector is taken as an incident wave. In real conditions, however, a wave beam of a finite width is incident on the scattering sea surface, which should be taken into account when investigating the form of the spectrum and processing it to derive information about the sea surface.

This paper investigates the scattering of electromagnetic waves from the sea surface with due regard for the finiteness of the beam of the receive and transmit antennas; a numerical simulation is used to investigate the of these beams on the spectrum structure of the received signal. In addition, a study is made of the influence of the finiteness of the coherent integration time and the spectral width of the sounding signal on the form of the received spectrum.

In HF location, information about the sea surface is derived from the spectrum of the received signal envelope. In the case of the scattering of a plane harmonic wave, of the entire continuous spectrum of sea waves, only one component scatters, which has a frequency approximately equal to the double frequency of the sounding signal, and the received spectrum consists of two lines spaced from the carrier frequency by a certain frequency [1]. The amount of shift depends on the sounding signal frequency, and the line width is determined by the resolving power of the spectrum analyzer at the receiving end, associated with the coherent integration time. The presence of just two lines is explained by the fact that all waves on the sea surface are customarily divided into two waves: those traveling from the receiver, and those arriving at the receiver.

In real conditions, with a finite width of the beam of the transmit antenna, the wave beam of a finite width is incident on the scattering sea surface. In addition it is necessary to take into account the finiteness of the spectral width of the sounding signal. Let us consider the influence of these factors on the structure of the received spectrum.

For the vertical polarization of a separate scattered spectral component with a frequency f, using perturbation theory it is possible to obtain the following expression

$$\tilde{E}_z^{(1)}(f) = -\iint_{\Sigma} \left(\frac{\partial \varphi_z}{\partial x'} \frac{\partial \varsigma}{\partial x'} + \frac{\partial \varphi_z}{\partial y'} \frac{\partial \varsigma}{\partial y'} \right) E_{0z}(f, x', y') \Big|_{\varsigma=0} dx'dy', \qquad (1)$$

where φ_z is Green's function, $\varsigma(x',y',t)$ is the inhomogeneous sea surface, $E_{0z}(f, x', y')$ is the vertically polarized incident wave, and is the area of the scattering surface.

An inverse Fourier transform of the expression (1), taking into account the signal's and receiver's frequency characteristic and the antenna beams, gives the form of the received signal.

The envelope of the received signal, by virtue of the variability of the sea surface $\varsigma(x',y',t)$, will also change with the time, which is described by the time correlation function. A Fourier-transform of this correlation function, in view of the finiteness of the integration time, gives the desired spectrum.

For the sake of simplicity in calculations, we assume that the time window of coherent integration and the envelope of the sounding signal have the Gaussian forms, and the beams of the receive and transmit antennas decompose into two Gaussian components, one of which depends on the azimuth angle, and the other depends on the elevation, with the receiver including a matched filter. With these assumptions, some of the integrals can be integrated analytically, with the result that only the integral over elevation remains.

As a result, we obtain the following expression for the received spectral density

$$S(F)=\int_0^{\pi/2} d\theta \sin\theta\cos^4\theta |A(\theta)|^2 \tilde{W}(2k\cos\theta)\times$$

$$\times\exp\left[-2(2\pi\Delta f)^2\left(\frac{z_0-D\sin\theta}{c\sin\theta}\right)^2-\frac{\sigma_\tau^2}{2}\left(2\pi F-\sqrt{2kg\cos\theta}\right)^2\right] \qquad (2)$$

where $A(\theta)$ is the product of the receive and transmit beams in the vertical plane, $\tilde{W}(\chi)$ is the spatial spectrum of irregularities of the sea surface, Δf is the spectral width of the sounding pulse that is inversely proportional to the pulse duration for the AM signal and equal to the deviation of the frequency for the chirp-signal with a large bandwidth-duration product, z_0 is the altitude of the antenna above sea level, D is the distance of the antenna to the scattering area, c is the velocity of light, σ_τ is the width of the coherent integration time window, g is the gravitational constant, and $k=2\pi f_0/c$ is the wave number for the carrying frequency f_0.

The resulting expression (2) was used in a numerical simulation. Simulation results were plotted in decibels relative to a maximum value of the received signal spectrum. The plots represented only one-half of the received signal. Some of the results are exemplified in Fig. 1. The spectrum consists of peaks whose maxims are shifted on both sides of the carrier frequency by an amount approximately coinciding with the shift of the "Bragg lines" in the scattering spectrum of the plane wave. Widths of the peaks depend on the vertical beam width, the width of the coherent integration window, and on the emitted signal spectrum.

To elucidate the effect of each of the above-mentioned three factors on the form of the spectrum requires that any two factors do not suppress the action of the third one. To accomplish this, we selected a broad (in elevation) beam, a narrow window or a narrow spectrum of the emitted spectrum, and the remaining factor was varied.

In addition to the obvious narrowing of the spectrum with an increase in the width of the coherent integration time window, there is an influence of the beam, the emission spectral width, and of the radar altitude on the width of the received spectrum. This is explained by the fact that, with a decrease in the beam width, we send a narrower wave beam (in the limit of one plane wave), the scattering occurs in a smaller area, and there is a decrease in the widths of peaks (in the limit of the delta function). On the other hand, the narrowing of the received signal spectrum with an increase in the width of the emitted signal spectrum is explainable by

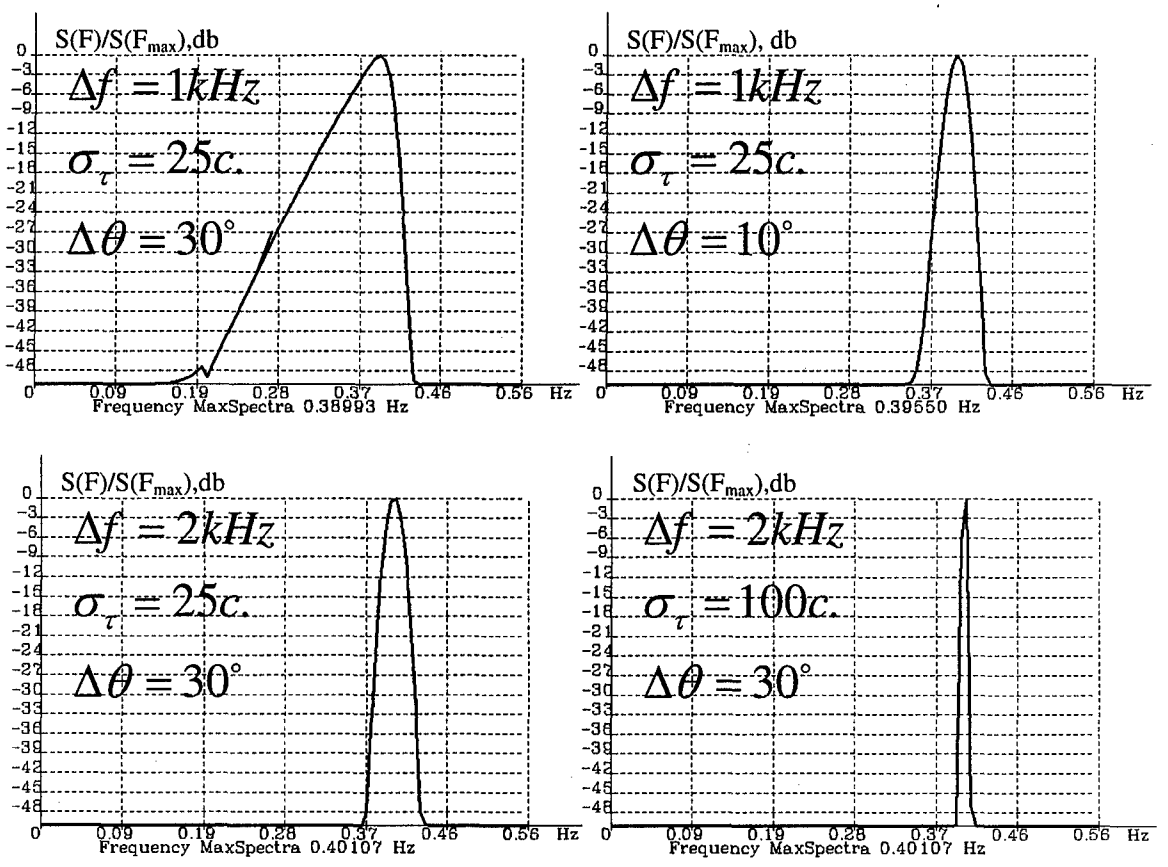

the fact that a decrease in the pulse duration is accompanied by a decrease in the area of the illuminated region. Effectively, this means that we narrow the beam, thus narrowing the width of peaks. Starting from the width of the emitted signal spectrum of several kilohertz with a further increase of the emitted spectral width, under other equal conditions, modifies received spectrum $S(F)$ only slightly. It was also ascertained that with an increase in elevation above sea level of the antenna, the spectrum broadens, which is associated with an increase of the dependence of the "Bragg line" on the angle of incidence of an individual component of the wave beam.

Thus the form of the spectrum at the sounding of the sea surface depends not only on the coherent integration time but also on the spatial-time spectrum of the sounding signal.

This work was done with support from the Russian Foundation for Basic Research under grants Nos. 00-02-17780 and 00-15-98509.

REFERENCES

[1] Barrick D.E. Remote Sensing of Sea State by Radar, "Remote Sensing of the Troposphere", Chap.12 – Washington: U.S. Government Printing Office, – 1972.

[2] Bass F.G. and Fuks I.M. The Scattering of Waves From a Statistically Rough Surface. Moscow: Nauka, 1972.

THE ESTIMATION OF THE AIR HUMIDITY IN THE LOWER TROPOSPHERE WITH THE USE OF THE DOUBLE-FREQUENCY RADIOACOUSTIC SOUNDING SYSTEM

Yury N. Ulyanov, and Nina G. Maksimova
Kharkov State Technical University of Radio Electronics
Lenin Av. 14, Kharkov 61166 Ukraine
Tel: +380 572 409 430

INTRODUCTION

Atmosphere double frequency radio acoustic sounding (DF RAS) is considered as the method of indirect non-contact remote determination of radio physical properties of the low troposphere. As compared with the other non-contact methods, such as, for example, the laser and radiometric ones, this one stands out because of the high vertical resolution of tens of meters.

THEORETICAL BACKGROUND

In our work on air humidity measurement in the atmosphere with the RAS system (RASS), we started from the known dependence of the sound molecular attenuation on its frequency, the air humidity and temperature. When carrying out RAS at two frequencies and measuring a ratio of RF echoes powers P_1 and P_2 appropriate to these frequencies, the value of sound absorption factors difference as a function of height R can be obtained as follows:

$$\Delta\alpha_{1,2}(R)=\frac{P_2(R)}{P_1(R)}\frac{d}{dR}\left[\frac{P_1(R)}{P_2(R)}\right] \qquad (1)$$

The finding of humidity is reduced to solving the inverse task, which consists in subsequent comparison of obtained values of $\Delta\alpha_{1,2}$ (for temperature T measured with RAS at a time) with the ones computed from the known theoretical dependence of $\Delta\alpha_{1,2}$ on humidity, given in [1]. The root-mean-square error of air relative humidity (F) definition σ_F (with no regard of error σ_T of radioacoustic temperature definition due to its smallness), according to the equation (1), is:

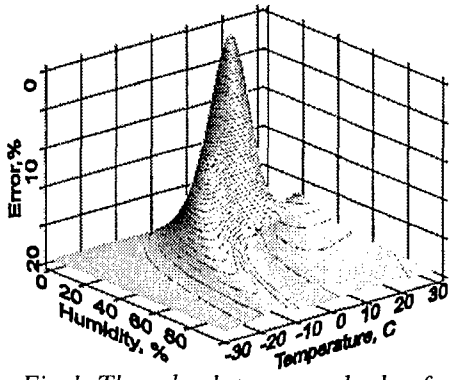

Fig.1. The absolute errors body of humidity measurement with DF RASS

$$\sigma_F=\frac{\partial F}{\partial\Delta\alpha_{1,2}}\sigma_{P_1/P_2}(R_2-R_1)^{-1}\left[\left(\frac{P_{22}}{P_{21}}\right)^2+\left(\frac{P_{11}}{P_{12}}\right)^2\right]^{\frac{1}{2}}, \qquad (2)$$

where:

σ_{P_1/P_2} is the measurement error of echoes power ratio; R_1 and R_2 are heights of measurement layer borders; P_{11}, P_{12} and P_{21}, P_{22} are values of echo power received from borders of the layer under investigation for the first and second frequencies.

Fig. 1 shows the absolute errors body for R=100 m and sound frequencies 3,4 and 6,8 kHz. It can be seen that the humidity measurement accuracy increases with the temperature increase and the humidity decrease.

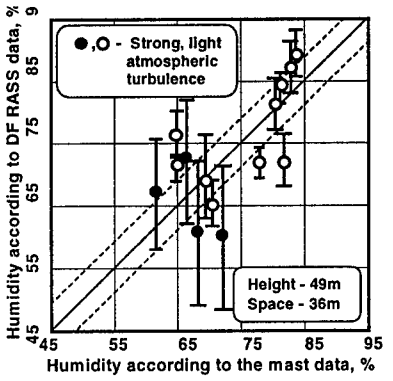

Fig 3. *Results of comparison measurements*

MAIN FEATURES OF DF RASS

DF RASS is a coherent double-frequency Doppler radar of continuous radiation [2] with the built-in pulse sodar channel, used both as a source of sound radiation with central frequencies of 3,4 and 6,8kHz for DF RAS [3] and as a sodar radiator, which jointly with an acoustic receiving antenna is applied for the atmosphere turbulent structure monitoring (see Fig. 2). The double-frequency radio-transmitter contains a nonlinear element and a band-pass filter at the output, in order to eliminate the influence of the mutual instability of output power levels in frequency channels of 1,5 and 3,0 GHz. The filter selects the first and the second harmonics of the RF power amplifier output signal.

TECHNIQUE OF AIR HUMIDITY DETERMINATION

Double-frequency acoustic sounding pulses are radiated to the atmosphere in the alternate radiation mode and irradiated with appropriate double-frequency microwaves. Measurements of parameters of radio echoes reflected by acoustical atmospheric inhomogeneities are carried out for given height levels during 20 to 30 minutes. The results are averaged. A number of levels and a distance between them are chosen in view of a full picture of the atmosphere meteorological parameters vertical distribution to be mapped. For every height level, echo-signals parameters measurement is preceded by operations on the compensation of the influence of the sound wind refraction on their characteristics (by displace-ment of the acoustic source along the transversal truss with respect to its initial position, and rotation of the entire antenna system windward). Besides, the system is tuned for the Bragg condition to be met.

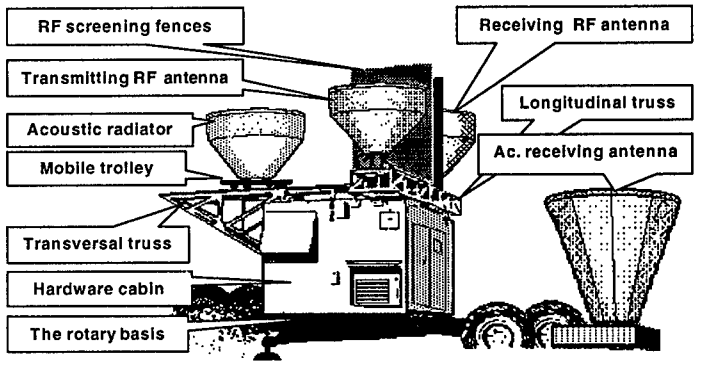

Fig. 2. *General view of the instrument complex*

RESULTS

The measurements of the air humidity with DF RASS were carried out at the Odessa hydrometeorological institute (OHMI) testing ground arranged nearby the coastal line. The obtained results were compared with the ones received through the 50-meter mast-mounted humidity sensors. The results of comparison measurements under different atmospheric conditions are shown in Fig.3. One can see the well noticeable negative influence of the turbulence on the measurement accuracy of air humidity with DF RASS: the correlation coefficients for the major part of data are at a level of 0.75, whereas the data obtained under light turbulence conditions are close to 0.86.

Fig. 4 shows an example of complex (with DF RASS and sodar) atmosphere sounding under day and night typical conditions. There are given profiles of temperature T, humidity F, wind V obtained with RASS, rawinsond and mast-mounted sensors, and turbulence factor K

obtained with sodar. To the right of K, the behavior of the first and second frequency echo-signals amplitudes under light turbulence is shown.

It is clearly seen from Fig.4, that under daytime conditions, when the values of turbulence factor (K) consi-derably exceed the night ones, the confidence interval of RAS data in the average three times exceeds the night-time one, being well correlated with that of wind data. It can be concluded from this that under strong turbulence, when operating in the alternate radiation mode, radioacoustic soundings of the first and the second frequency take place in different turbulent situations, what deteriorates DF RASS results.

In order to weaken the influence of turbulence on the DF RASS results, the authors propose for the DF RAS hardware to be reconstructed for operation in the double-frequency synchronous radiation mode. Accordingly, the technique of the air humidity determination should be improved. In this case, the humidity and with it the air refractivity at radio frequencies can be defined with the accuracy as high as the radiosonde one.

CONCLUSIONS

The atmospheric turbulence is a main error source of air humidity measurement with DF RASS. The improvement of DF RAS equipment and technique of air humidity determination can give one the power instrument of defining the air refractivity at radio frequencies.

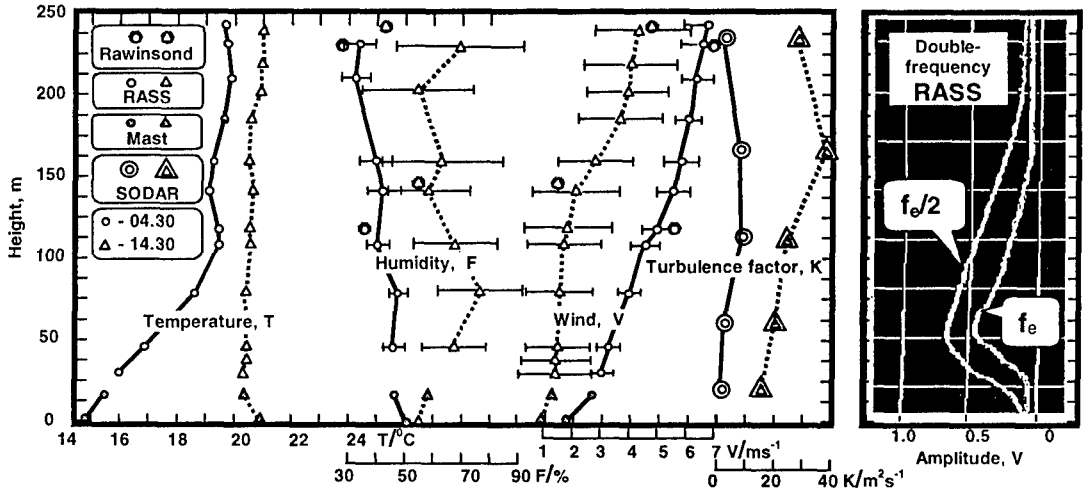

Fig. 4. *Example of complex sounding under night and daytime conditions*

ACKNOWLEDGEMENTS

We thank all the staff of OHMI scientific laboratory and especially its leader Javorsky A.Y. for the help in carrying out our investigations.

REFERENCES

[1] ANSI S1. 26-1978 (ASA 23-1978).American national standard.

[2] Ulyanov Y. N. Dual frequency radioacoustic system / Proc. VII all union symp. On laser and acoust. atm. sounding. Tomsk, 1984, v. II, p. 196-199. (in Russian).

[3] Proshkin E. G. Radioacoustic sounding in atmospheric boundary layer investigations/ Proc. ISARS" 96, Moscow, p 6.105-6.108.

LIDAR SIGNAL MODEL FROM REMOTE AEROSOL FORMATIONS IN DOUBLE SCATTERING APPROACH

Bryukhanova V.V. and Samokhvalov I.V.

Tomsk State University

Radio Physics Department, 36, Lenin Avenue, Tomsk, 634050, Russia; leo@elefot.tsu.ru

ABSTRACT

Lidars are applied in many geophysics, meteorology and atmospheric optics research. However, the problem of the lidar data interpretation is not solve yet. It is necessary to take into consideration the multiply scattering (MS) when laser radiation propagates in optical dense aerosol formations.

The paper discusses the problem of numerical simulations of the lidar returns that account for contributions from single and double scattering from dense aerosol formations. We have analyzed the lidar equation that was obtained earlier [1] for an inhomogeneous atmosphere with the account for single and double scattering. It is shown in the paper that double scattering "forward-backward" and "backward-backward" photon trajectories equally contribute to the backscattering intensity. This significantly simplifies the lidar equation, if the sounding pulse penetrates the cloud to the depth that is small as compared with the diameter scattering volume at the cloud top.

INTRODUCTION

While studying the propagation of laser radiation through the optically dense aerosol formations, one should take into account the effects of multiple light scattering (MS). A thorough description of MS is possible by the radiation transfer equation. Unfortunately, no analytical solution of this equation has been so far derived in a general form. The approximate methods of solving this equation developed up to now such as the Monte-Carlo method and small-angle approximation, that are most widely used, enable obtaining quite good results in solving the so-called direct problem, i.e. in calculating the backscattering signals. However, these approaches are unable to analyze the effects of lidar performance parameters and optical properties of the medium sounded on the return signal structure and on the intensity of different orders of multiple scattering as well.

In the general form, the lidar return can be presented as a sum of return signals due to different orders of multiple scattering

$$P(r) = P^{(1)}(r) + P^{(2)}(r) + \ldots + P^{(i)}(r). \qquad (1)$$

The single scattering return power is described by the lidar equation that is applicable at small optical thickness of the media sounded

$$P^{(1)}(r) = \frac{P_0 A c \tau_p}{8\pi r^2} X(\pi, r)\sigma(r)e^{-2\tau(r)}, \qquad (2)$$

where, $P^{(1)}(r)$ is the single scattering return power that comes back to the receiving optics of a lidar from a scattering volume at the range r; P_0 is the power of sounding radiation; A is the

area if the lidar receiving optics; c is the speed of light in air; τ_p is the sounding pulse duration; X(π,r) is the backscattering phase function; $\sigma(r)$ is the volume backscattering coefficient at the distance r;

$\tau(r)=\int_0^r \alpha(z)dz$ is the optical thickness of the sounding path interval from 0 to r; $\alpha(z)$ is the volume extinction coefficient that is determined by the scattering coefficient $\sigma(z)$ and the absorption coefficient $\kappa(z)$, $\alpha(z)=\sigma(z)+\kappa(z)$.

In sounding clouds, one ought to take into account higher orders of multiple scattering. However, calculating the higher orders of multiple scattering (i>2) faces some problems in physical statement of the problem and in calculating the contributions coming into the total signal from different orders of multiple scattering. Besides, as the experience shows, it is sufficient to consider only double scattering under condition that $\tau \le 3$.

DOUBLE SCATTERING SIGNAL FROM AEROSOL FORMATION

The general expression for $P^{(2)}(r)$ has been derived earlier [1] in the following form

$$P^{(2)}(r)=\frac{P_0 A c \tau_p}{16\pi} e^{-2\tau(r)}\left[I_1+I_2\right] \tag{3}$$

where $I_1=\int_{\theta_0}^{\pi/2}\int_H^r \frac{\sigma(z)\sigma(z_1)}{R(z,\gamma,r)} X(z,\gamma)X(z_1,\pi-\gamma)\sin\gamma d\gamma dz$,

$I_2=\int_{\pi/2}^{\pi}\int_{z_{II}(\gamma)}^{r} \frac{\sigma(z)\sigma(z_1)}{R(z,\gamma,r)} X(z,\gamma)X(z_1,\pi-\gamma)\sin\gamma d\gamma dz$,

$R(z,\gamma,r)=r^2\cos^2\frac{\gamma}{2}\left(1+\frac{(r-z)^2}{r^2}\tan^2\frac{\gamma}{2}\right)$,

$z_1=z+\frac{r(r-z)\cos\gamma}{r-z\sin^2\gamma/2}$, $\qquad z_{H(\gamma)}\cong r\left(1-\frac{r-H}{r}\cot^2\frac{\gamma}{2}\right)$

SPECIFIC FEATURES IN THE FORMATION OF THE DOUBLE SCATTERING FLUX FROM REMOTE AEROSOL FORMATION

In sounding dense aerosol media, the depth of a laser pulse penetration into a medium is small as compared with the distance H to the nearest boundary of the medium:

$$\frac{r-H}{r}\approx\frac{r-H}{H}<<1 \tag{4}$$

In this case the scattering volume is bounded by the plane z=H, from the lidar side. If we deal with an airborne or a space-based lidar, this plane in determined by the cloud top, for example. If the condition (6) holds and

$$r-H\le H\cdot\tan\theta_0/2 \tag{5}$$

then the expression for $P^{(2)}(r)$ can be essentially simplified.

Thus at [(r-z)/r]<< 1 we can take z_1, in Eq.(5) to be approximately equal to $r\left(1-\frac{r-z}{r}\tan^2\frac{\gamma}{2}\right)$. Now we can make the following substitution in Eq.(3)

$$\xi = \frac{r-z}{H\cdot\tan\theta_0/2}.$$

and then changing new variables once more

$$U = \xi\cdot tg^2\,\gamma/2, \qquad \beta = \pi-\gamma.$$

After these substitutions the integrals entering the expressions (5) for $I_1(\xi,\gamma)$ and $I_2(U,\beta)$ become identical. Therefore, expressions (5) can be written in the following form.

$$P^{(2)}(r) = \frac{P_0 A c\tau_p H\tan\left(\theta_0/2\right)}{4\pi r^2} e^{-2\tau(r)} \times \int_0^{\pi/2}\int_0^{\xi_0} \sigma(\xi)\sigma(\xi_1)X(\xi,\gamma)X(\xi_1,\pi-\gamma)\tan\frac{\gamma}{2}\,d\xi d\gamma, \qquad (6)$$

It was taken into account, while writing this formula, that $0\le\xi\le 1$ and

$$\xi_1 = \xi\cdot\tan^2\frac{\gamma}{2}, \qquad \xi_0 = \frac{r-H}{H\cdot\tan\left(\theta_0/2\right)}.$$

If (r-H)>H·tan(θ_0/2), the cross size of the scattering volume for the second order of scattering will be determined both by the medium boundary and by the receiver field-of-view angle.
The general expression for the lidar return in the double scattering approximation has the following form

$$P^{(2)}(r) = \frac{P_0 A c\tau_p H\tan\left(\theta_0/2\right)}{4\pi r^2} e^{-2\tau(r)} \times \left\{ \begin{array}{l} \int_0^{\gamma_1}\int_0^{\xi_0} \dfrac{\sigma(\xi)\sigma(\xi_1)X(\xi,\gamma)X(\xi_1,\pi-\gamma)\tan\left(\frac{\gamma}{2}\right)}{1+\xi^2\dfrac{H^2\tan^2\left(\theta_0/2\right)}{r^2}\tan^2(\frac{\gamma}{2})}\,d\xi d\gamma + \\ \int_{\gamma_1}^{\pi/2}\int_0^{\xi'(\gamma)} \dfrac{\sigma(\xi)\sigma(\xi_1)X(\xi,\gamma)X(\xi_1,\pi-\gamma)\tan\left(\frac{\gamma}{2}\right)}{1+\xi^2\dfrac{H^2\tan^2\left(\theta_0/2\right)}{r^2}\tan^2\left(\frac{\gamma}{2}\right)}\,d\xi d\gamma \end{array} \right\}, \qquad (7)$$

where

$$\gamma_1 = 2\arctan\frac{r\cdot\tan\theta_0/2}{r-H}, \qquad \gamma_2 \approx \pi-\gamma_1.$$

As is seen from the expression obtained, the return signal due to double scattering, at (r-H) > H·tan(θ_0/2), depends on both the depth at which sounding pulse penetrates into the cloud and on the cross size of the scattering volume at the range r from a lidar.
We also have simplified Eq. (6) and Eq. (7) in special cases of atmospheric stratification.

REFERENCES

[1] Samokhvalov I.V. // Rep. SA USSR. Ser. PAO. 1979. V. 15. № 12. C. 1271-1279.

ANALYSIS OF ELECTROMAGNETIC CHARACTERISTICS OF MULTI-LAYERED PERIODIC STRUCTURES WITH TURNING LAYERS

Dmitry Kokody and Sergey Prosvirnin

Institute of Radio Astronomy of National Academy of Sciences of Ukraine
4, Krasnoznamennaya st, Kharkov, 61002, Ukraine,
Fax: 38 0572 476506. E-mail: prosvirnin@rian.kharkov.ua

ABSTRACT

The characteristics of reflection and transmission of multi-layered double-periodic structures with C - shaped inclusions in cells are considered. The case with turning of each second layer of the system on 90 degrees is researched. It loosens the dependence of reflection and transmission operators on the polarization of an incident wave.

INTRODUCTION

In recent years, much attention has been given to so-called photonic band-gap materials in microwaves. The one type of this structure is double-periodic array with the metal patches of different shapes contained in cells. Locating such arrays on dielectric substrates one for the another and agglomerate their in three-dimensional structures is possible to obtain broad of transmission and reflection in the microwave range.

The dependence of the operators of reflection and transmission on the polarization of incident wave was observed under identical orientation of metallic elements on all layers of system. This dependence can be attenuated by turning each second lay on 90 degrees. Absolute values of the reflection and transmission coefficients in one propagated wave regime at the polarization of incident wave along axis of array periodic do not differ at this case. The values of coefficients are approximately equal to such in any other polarization.

MATRIX OF REFLECTION AND TRANSMISSION OF ONE LAYER

The array periodic in two directions with complex inclusions in cells is considered. Period of array is equal in two direction and designate d_x. Plane electromagnetic wave is incident on layer: $\vec{E}^i = \vec{P}\exp\left(-i\vec{k}^i\vec{r}\right)$, where $\vec{P}$ is the vector of polarization, $P=1$; $\vec{k}^i$ is the wave vector of an incident wave, $k^i = k$, $k = \omega\sqrt{\varepsilon_0\mu_0}$. The time dependence $e^{i\omega t}$ is supposed. If the periods of an array are less than a wavelength $\kappa=d_x/\lambda< 1$, both in reflected and in transmitted fields, only the main one is propagated on a normal to array space harmonic: $\vec{E}^r = \vec{R}\exp(-ikz)$, $\vec{E}^t = \vec{T}\exp(ikz)$.

The vectors $\vec{R}$ and $\vec{T}$ are interlinked to a vector of polarization of incident wave: $\vec{R} = \hat{r}\,\vec{P}$, $\vec{T} = \hat{t}\,\vec{P}$, where $\hat{r}, \hat{t}$ are operators of reflection and transmission [1]. If non propagating space harmonics are not taken into account, the matrices of operators are the following: $\hat{r} = \begin{pmatrix} r_{xx} & r_{xy} \\ r_{yx} & r_{yy} \end{pmatrix}$, $\hat{t} = \begin{pmatrix} t_{xx} & t_{xy} \\ t_{yx} & t_{yy} \end{pmatrix}$, where r_{xx}, t_{xx} and r_{yy}, t_{yy} are coefficients of reflection and transmission of an incident electromagnetic wave, polarized along an axis Ox and Oy, respectively. The elements r_{xy}, r_{yx}, t_{xy}, t_{yx} determine the transformation of polarization (appearance

crosspolarization) after reflection and transmission of an array. They can be calculated through a method described in [2].

OPERATORS OF REFLECTION AND TRANSMISSION FOR THE SYSTEM OF DOUBLE-PERIODIC ARRAY WITH TURNING LAYERS

We consider the arrays of C-shaped strips with following geometrical sizes: radius of a inclusion is a=1.25 mm, angular size of a rupture is 2φ=20 degrees, width of strip is $2w$=0.1 mm. It allows to arrange a long strip in cell which is smaller than λ and to get resonance on low frequencies. This strip has a form with symmetric layout (see Fig. 1a), the non-diagonal elements of matrices of reflection and transmission are equal to zero. There is no turn of polarization plane at transmitting wave through an array.

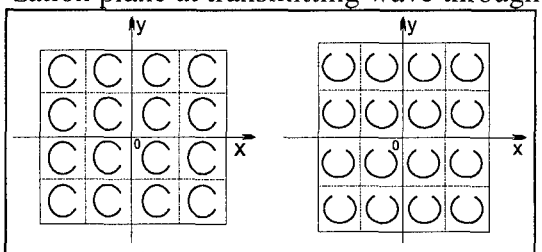

Fig. 1a Fig. 1b

The arrays are located on a dielectric substrate in practice. It complicates the calculations, as it is necessary to consider two cases of incidence of an electromagnetic wave: on the side of array and on the substrate. A method of solution of a diffraction problem in this case is the same as in [2].

The system of two arrays one of which is turned on 90 degrees is considered. In Fig. 1a layer without turn of inclusions, in Fig. 1b - with turn is shown. For the first array the matrix of reflection and transmission are following: $r_1^{\pm} = \begin{pmatrix} r_{xx}^{\pm} & 0 \\ 0 & r_{yy}^{\pm} \end{pmatrix}$, $t_1^{\pm} = \begin{pmatrix} t_{xx}^{\pm} & 0 \\ 0 & t_{yy}^{\pm} \end{pmatrix}$. For observance of the one-wave mode only it is not allowed to bring together arrays on very close distances (in our case distance between arrays L=2.5 mm Fig. 2). The plus-sign means incidence of wave on the side of array, minus - on a substrate. For the second array the operators $r_2^{\pm}, t_2^{\pm}$

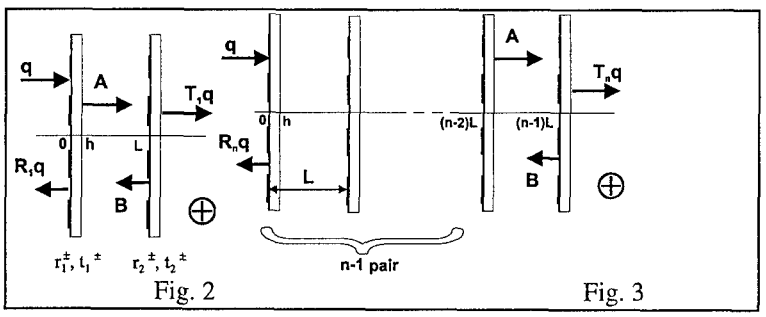

Fig. 2 Fig. 3

differ from first one by the changing of diagonal elements. We can find solution for operators of reflection and transmission for the system of two arrays using a operator method

$$R_1^{\pm} = r_1^{\pm} + t_1 \mp e r_2^{\pm} e \left(I - r_1^{\mp} e r_2^{\pm} e\right)^{-1} t_1^{\pm}$$
$$T_1^{\pm} = t_2^{\pm} e \left(I - r_1^{\mp} e r_2^{\pm} e\right)^{-1} t_1^{\pm} \quad (1)$$

where e is propagator operator $e = \begin{pmatrix} e^{ik\Delta} & 0 \\ 0 & e^{ik\Delta} \end{pmatrix}$, Δ=L-h. If we construct from such pairs of arrays the complex structure, see Fig.3 we can get recursion relations, similar (1)

$$R_n^{\pm} = R_{n-1}^{\pm} + T_{n-1}^{\mp} e R_1^{\pm} e \left(I - R_{n-1}^{\mp} e R_1^{\pm} e\right)^{-1} T_{n-1}^{\pm}$$
$$T_n^{\pm} = T_1^{\pm} e \left(I - R_{n-1}^{\mp} e R_1^{\pm} e\right)^{-1} T_{n-1}^{\pm} \quad (2)$$

Absolute values of elements of matrices of reflection and transmission for two-layer structures are shown in Fig. 4a. The same characteristics for four-layer structures are shown in Fig. 4b.

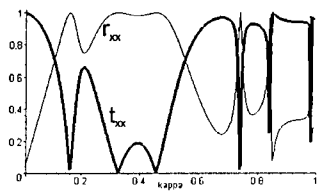

Fig. 4a

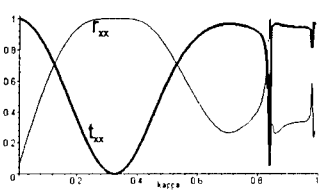

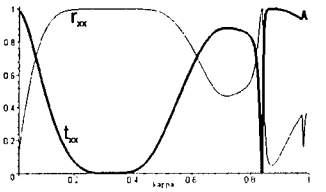

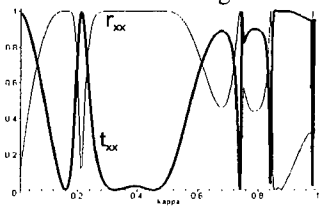

Fig. 4b

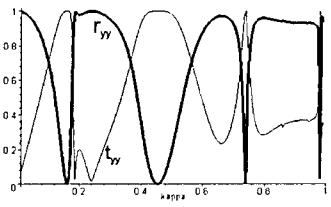

Fig. 5

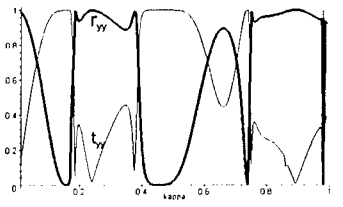

Fig. 6

Graphics of reflection and transmission for the system consists of two and four layers without turning (Fig. 5 and 6). These results coincide with those of [3].

CONCLUSION

Rather wide zones of reflection and the transmission of incident electromagnetic wave have been obtained both for the case with and without turn layers. These zones appear at first due to the frequency-selection property of each single array and secondly due to a wave interference between layers in the system of arrays. The coefficients of reflection and transmission in a case of incidence of an electromagnetic wave on the side of array and on the substrate differ only by phases.

Comparing results obtained at research of structures without turning layers with results obtained at usage of turning layers, we can see that in the second case there is no difference in values of elements of matrix of reflection and transmission with polarization of an incident wave along one axis of periodicity from values of the same units of operators with polarization of an incident wave along other axis. Similar results are expected to be obtained also by an arbitrary polarization of incident radiation.

REFERENCES

[1] T.D.Vasilyeva and S.L.Prosvirnin. Electromagnetic wave diffraction by the plane array of chiral strip elements of complex shape. Physics of wave processes and radio systems, vol.1, no.4, pp.5-9, 1998 (in Russian).

[2] S.L.Prosvirnin Transformation of polarization when wave reflection by microstrip array of complex shape elements. Radiotechnika i electronika, 1999, v. 44, 6, pp. 681-686 (in Russian).

[3] S.L.Prosvirnin, S.A.Tretyakov, T.D.Vasilyeva, A.Fourrier-Lamer, S.Zouhdi. Analysis of reflection and transmission of electromagnetic waves in complex layered arrays. Helsinki University of Technology, Electromagnetics Laboratory Report Series, Espoo, October 1999, Report 314, 15p.

DIPOLE MODEL OF ELECTROMAGNETIC WAVE PROPAGATION IN REGULAR 3D LATTICES OF SCATTERERS

Pavel A. Belov

St. Petersburg Institute of Fine Mechanics and Optics,
St. Petersburg, Russia
E-mail: belov@green.ifmo.ru.

ABSTRACT

In this presentation we consider artificial (photonic) crystals formed by dielectric or metallic inclusions arranged in the nodes of a regular three-dimensional lattice with parallelepipedal elementary cell of the general kind. The background medium is an isotropic dielectric. Oblique propagation of plane electromagnetic waves in such a structure is under consideration. A simple analytical theory of plane-wave propagation which takes into account full-wave electromagnetic interactions of all inclusions is developed.

INTRODUCTION

In the literature, this problem has been treated using numerical techniques. Available analytical models are restricted to either low-frequency or resonant regimes. Our goal is to develop an analytical approach valid in a wide frequency range. A simple analytical theory of plane-wave propagation [1] which takes into account full-wave electromagnetic interactions of all inclusions is developed. The dipole model of interactions and the local-field approach are used. The main restriction of our theory is the requirement of rather small size of the inclusion compared to the wavelength, which is self-consistent with the dipole assumption of the electromagnetic interaction of the lattice. However, our interaction model takes into account the phase shift of the wave not only over a cell but also over the scatterer volume (using high-frequency polarizability). Hence, our theory must describe properly the dispersion at the low-frequency band.

BASIC DISPERSION THEORY

The dispersion equation is obtained from Oseen's cancellation theorem and the condition of polarization periodicity. The spatial dependence of polarization in the region placed rather far from the crystal boundary is described by wave vector $\vec{k} = (k_x, k_y, k_z)^T$ in the form $\vec{p} = \vec{p}_0 e^{i\vec{k}\vec{r}}$ (the eigenwaves without the incident wave contribution) and the following equation holds:

$$\vec{p}_0 = \overline{\overline{\alpha}}(\omega) \cdot \sum_{(m,n,l)\neq(0,0,0)} \overline{\overline{G}}(\omega, \vec{R}_{m,n,l}) \cdot e^{i\vec{k}\vec{R}_{m,n,l}} \cdot \vec{p}_0 \qquad (1)$$

Here $\vec{p}_0$ is the dipole moment of reference inclusion, $\overline{\overline{\alpha}}$ is polarizability dyadic, $\overline{\overline{G}}$ is known dyadic describing electric field produced by a dipole, $\vec{R}_{m,n,l} = (am, bn, cl)^T$ and ω is frequency.

For calculation of 3D lattice sums specific method based on Poisson summation formula [4] is used. The layer-layer interactions are considered using the Floquet representation of the field produced by periodically polarized layers, as in [2], including evanescent modes in the model

of interactions of adjacent layers. Electromagnetic interactions of inclusions inside one reference layer considered as in [3,5]. The result of such calculation is:

$$\sum_{(m,n,l)\neq(0,0,0)} \overline{\overline{G}}(\omega,\vec{R}_{m,n,l})\cdot e^{i\vec{k}\vec{R}_{m,n,l}} = \begin{pmatrix} C(k_x,k_y,k_z;a,b,c) & D(k_x,k_y,k_z;a,b,c) & D(k_x,k_z,k_y;a,c,b) \\ D(k_x,k_y,k_z;a,b,c) & C(k_y,k_z,k_x;b,c,a) & D(k_y,k_z,k_x;b,c,a) \\ D(k_x,k_z,k_y;a,c,b) & D(k_y,k_z,k_x;b,c,a) & C(k_z,k_x,k_y;c,a,b) \end{pmatrix} \tag{2}$$

$$C(k_x,k_y,k_z;a,b,c) =$$

$$= \frac{i}{2ab\varepsilon\varepsilon_0}\sum_{m=-\infty}^{+\infty}\sum_{n=-\infty}^{+\infty}\frac{K^2-p_m^2}{\sqrt{K^2-p_m^2-q_n^2}}\left[\frac{e^{ic\left(\sqrt{K^2-p_m^2-q_n^2}+k_z\right)}}{1-e^{ic\left(\sqrt{K^2-p_m^2-q_n^2}+k_z\right)}}+\frac{e^{ic\left(\sqrt{K^2-p_m^2-q_n^2}-k_z\right)}}{1-e^{ic\left(\sqrt{K^2-p_m^2-q_n^2}-k_z\right)}}\right]+$$

$$+\frac{1}{2\pi a\varepsilon\varepsilon_0}\sum_{(K^2-p_m^2)<0}\sum_{n\neq 0}\left(K^2-p_m^2\right)\cdot K_0\left(\sqrt{p_m^2-K^2}\,|bn|\right)+ \tag{3}$$

$$+\frac{1}{2\pi ab\varepsilon\varepsilon_0}\sum_{(K^2-p_m^2)\geq 0}\left(K^2-p_m^2\right)\cdot\left(\sum_{n\neq 0}\left[\frac{\pi i}{\sqrt{K^2-p_m^2-q_n^2}}-\frac{b}{2n}\right]+\frac{\pi i}{\sqrt{K^2-p_m^2-q_0^2}}\right.$$

$$\left.+b\left(\ln\frac{b\sqrt{K^2-p_m^2}}{4\pi}+\gamma+i\frac{\pi}{2}\right)\right)+\frac{1}{2\pi a^3\varepsilon\varepsilon_0}\sum_{m\neq 0}\left(\frac{1}{|m|^3}-\frac{ika}{m^2}\right)\cdot e^{ia(k|m|+k_x m)}$$

$$D(k_x,k_y,k_z;a,b,c) =$$

$$= -\frac{i}{2ab\varepsilon\varepsilon_0}\sum_{m=-\infty}^{+\infty}\sum_{n=-\infty}^{+\infty}\frac{p_m q_n}{\sqrt{K^2-p_m^2-q_n^2}}\left[\frac{e^{ic\left(\sqrt{K^2-p_m^2-q_n^2}+k_z\right)}}{1-e^{ic\left(\sqrt{K^2-p_m^2-q_n^2}+k_z\right)}}+\frac{e^{ic\left(\sqrt{K^2-p_m^2-q_n^2}-k_z\right)}}{1-e^{ic\left(\sqrt{K^2-p_m^2-q_n^2}-k_z\right)}}\right]+$$

$$+\frac{1}{\pi a\varepsilon\varepsilon_0}\sum_{(K^2-p_m^2)<0}\sum_{n\neq 0}p_m\sqrt{p_m^2-K^2}\,K_1\left(\sqrt{p_m^2-K^2}\,|bn|\right)\cdot\sin(k_y bn)- \tag{4}$$

$$-\frac{i}{2ab\varepsilon\varepsilon_0}\sum_{(K^2-p_m^2)\geq 0}p_m\left(\frac{q_0}{\sqrt{K^2-p_m^2-q_0^2}}+\sum_{n=1}^{+\infty}\left[\frac{q_n}{\sqrt{K^2-p_m^2-q_n^2}}+\frac{q_{-n}}{\sqrt{K^2-p_m^2-q_{-n}^2}}\right]\right)$$

Here $K=\sqrt{\varepsilon}\omega/c_l$, $p_m=k_x+\frac{2\pi m}{a}$, $q_n=k_y+\frac{2\pi n}{b}$.

This theory gives an analytical model for the effective propagation constant, which can be universally applied in a very wide frequency range from the quasi-static regime to the Bragg reflection region.

NUMERICAL CALCULATIONS

Numerical calculations was made and dispersion curves for structure under consideration are obtained. Dispersion curves for crystal formed by spherical inclusions with $\alpha/a^3=0.2$ are

shown in Fig.1. (dependance of normalized frequency on wave vector - points Γ, M, K of first Brillouin zone have coordinates (0,0,0); (0,1,0); (0,1,1), respectively). For comparison with the above result we illustrate the band-gap structure of the extremely dense lattice by Fig. 2. ($\alpha / a^3 = 1$). This case has no practical meaning since even for touching dielectric spheres so big polarizability is not reachable. However, if we would have got the lattice from resonant inclusions (our theory is available for arbitrary dipole scatterers) this value of polarizability would be possible. In this case one could obtain the complete bandgap even for a simple cubic lattice (which does not possess the bandgaps being prepared from simple inclusions such as ellipsoids, cubes, etc.). This observation looks like rather important since the photonic crystals with the same frequency properties as complex lattices provide (such as the diamond or yablonovite lattices) could be obtained, probably, from the simplest lattices of complex-shape inclusions.

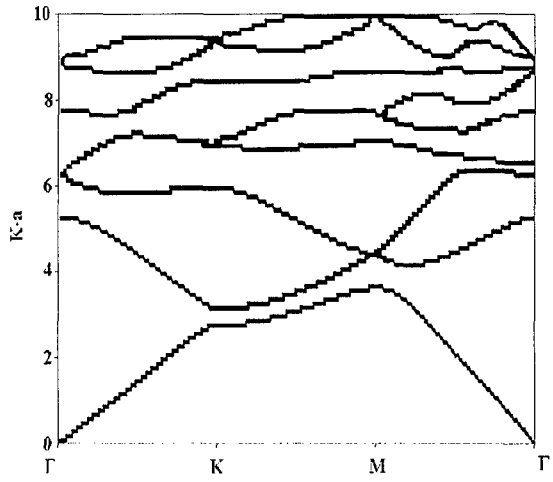

Fig. 1. Dispersion curves for $\alpha / a^3 = 0.2$

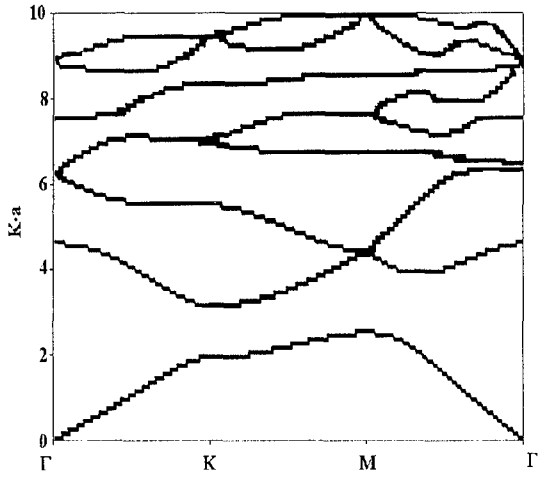

Fig. 2. Dispersion curves for $\alpha / a^3 = 1$

CONCLUSION

The new approach for simple and prompt numerical calculating the dispersion curves of the photonic crystals prepared from the smooth dielectric or metallic inclusions with sufficiently simple shape and small wave size is presented. It is also shown that the primitive cubic lattice of the dipole scatterers with high polarizability can possess a complete photonic bandgap.

REFERENCES

[1]. P.A. Belov, C.R. Simovski, Oblique propagation of electromagnetic waves in regular 3D lattices of scatterers (dipole approximation), Proc. of SPIE, Vol. 4073, 2000.
[2]. C.R. Simovski, P.A. Belov, M.S. Kondratjev, Electromagnetic interaction of chiral particles in three dimensional arrays, J. Electrom. Waves Applic., Vol. 13, pp. 189-203, 1999.
[3]. C.R. Simovski, M.S. Kondratjev, P.A. Belov, S.A. Tretyakov, Interaction effects in two-dimensional bianisotropic arrays, IEEE Trans. Ant. Prop.,Vol. 47, No. 9, pp.1429-1439, 1999.
[4]. Collin R.E., Field Theory of Guided Waves, IEEE Press, NY, Philad., USA, 1991.
[5]. P.A. Belov, C.R. Simovski, M.S. Kondratjev, Problem of the local field for plane grids with bianisotropic particles, Proc. SPIE, Vol. 3039, pp.680-691, 1997.

TRANSIENT RADIO WAVE SCATTERING BY AERATION ZONES

Sergey A. Masalov and Olexander O. Puzanov

Usykov Institute for Radiophysics and Electronics of NASU
12 Proscura St., Kharkiv, 61085 Ukraine,
e-mail: masalov@ire.kharkov.ua, puzanov@ire.kharkov.ua

It was shown that the availability of water can be detected only by a reflection from capillary fringe situated in the region contiguous with water. One has to take into account this result to more exact determination of the water depth in a ground. It has been established the observed pulse acquires a duration above a source pulse. The calculation results have shown that measurement errors of frequency dependencies of permittivities and specific conductivities that are used as initial data manifests during calculation of diffraction fields for structures of large depth (that are more than 2-3 meters). This is the result of small amplitudes of pulses reflected from discontinuities lied deep. In fact these errors bring into occurring of a "false reflection" preceding before reflections from capillary fringe and water. This effect betokens a violation of the causativity law and is a consequence of the disturbed in some measure connection of real and imaginary parts of complex permittivity. As it is known, this connection is determined after the Kramers-Kronig' relations. On this basis the conclusion is made about the necessity of refinement of source experimental data whereby this relations in parallel instances.

This paper is devoted to the problem of simulation of nonsinusoidal radiowaves interaction with a ground. We take into account that humidity is distributed in the ground depth according to the continuous law. This law, dependent on the influence of atmospheric precipitates and ground water is ordinary complex and influences essentially on outcomes of radar sounding of the earth surface. Frequency dependencies of the ground electrical parameters obtained as a result of full-scale measurements are used as input data. Below we show the influence of humidity in the active moisture exchange subhorizon and in the capillary fringe area on the reflected field character. We ascertain also how measurement errors of the input data influence on calculation results.

The ground areas from the surface down to the groundwater level are referred to as aeration zones (AZ). Their depth can be different depending on local conditions, however the depth determines typical laws of humidity distribution [1,2]. Clearing up of features of videopulses scattering in AZ in the context of interpretation of data of earth surface sounding is our main purpose.

The method used by us [3,4] consists of finding the solution in the frequency domain using normal impedances of partial areas (the source structure is divided into slabs with sufficiently small thickness) and it consists also of subsequent transition to the time domain by numerical taking of the inverse Fourier transformation. We analyze the considered below transients on the base of the results obtained earlier for more simple cases [4].

1. At first we consider differences in the reflected field character at two different humidity states of AZ, formed by slabs of sand (1 m in thickness), clay (0.5 m) and water. Suppose that the single polar Gaussian pulse of the10 ns duration is incident on this ground structure. Let us analyze two cases. In the first case we neglect humidity variation, typical for the area of capillary fringe situated in the near-level subhorizon. At that, suspect that the humidity W of sand and clay is constant down to the boundary of water and is equal to 2.5 %. In the second case assume that the area of capillary fringe is bounded completely by the slab of clay, humidity of which increases gradually from the value W=2.5 % up to the limiting one W=17 % [5] as approaching the boundary of water (Fig.1).

Time dependences of the reflected field are showed in Fig.2. The dashed line corresponds to the case of the constant value of humidity, and the continuous line — to the case of continuous humidity variation. The first observable pulse (Fig. 2a)) is reflected from the upper boundary of

sand. It is quite obvious that its form and amplitude is identical in both cases. The differences start to appear under reflection from the boundary of sand and clay (Point 1 indicated in Fig. 2a) with arrow). One can clearly see the beginning of reflection from water, (Point 2), if humidity of clay is constant. If the humidity increases gradually, then the precise boundary, designated by the break on the time dependence in the previous case, flattens. It is concerned with the fact the increase of clay conductivity reduces to a noticeable increase of its contribution into the reflected field. But this contribution is still smaller than the contribution of water in the first case. Besides radiation reaches water now and returns being attenuated notably. As a consequence of both called reasons, the amplitude of the reflected pulse diminishes, and owing to reflection the pulse obtains a superior duration in the all extended area of capillary fringe.

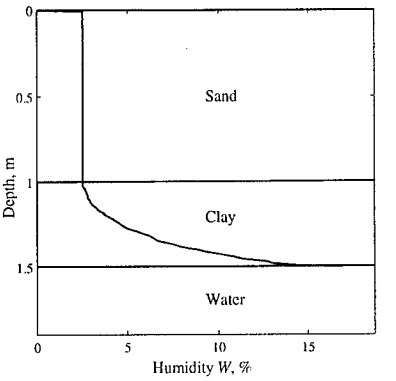

Fig. 1. *The law of humidity variation in depth for the two-layer aeration zone*

It is possible to draw a conclusion that the availability of water can be detected only by an outgoing pulse reflection from the capillary fringe area. The moment of the reflection beginning coincides obviously with the reflection from the capillary fringe. It is important to consider the indicated circumstance for more precise determination of water depth in soil.

In both cases at the moment of leaving the ground, the pulse reflected from water is reflected back partially without change of its negative polarity. But, as it is possible to see from Fig. 2, having got to water, the pulse is reflected from it in twice and changes the polarity for positive. With a constant value of clay humidity one can see breaks on the trailing edge of the main (first) reflection from water, which testify the presence of multiple reflections-over between sand-clay and clay-water boundaries (points 3 and 4 in Fig. 2a), see also Fig. 2b)). At the same time the trailing edge asperities smooth away granting the continuous increase of clay humidity ()). This is the consequence of larger losses in the environment.

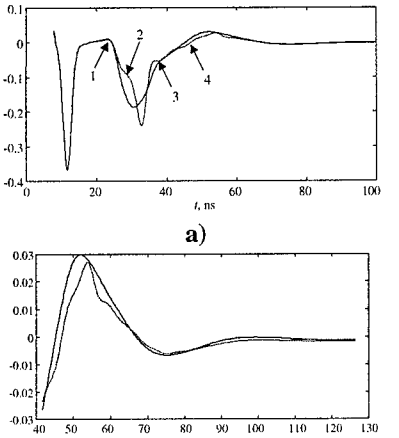

Fig. 2. *Time dependences of the diffraction fields for the single-polar Gaussian videopulse of the 10 ns duration for the aeration zone with a depth of 1.5 m, formed by the slab of sand (1 m) and clay (0.5 m): the solid line - at humidity distribution in depth according to Fig.1, the dashed line - at the fixed humidity W=2.5 % of both slabs*

2. The representative depth of AZ can be 5-6 meters. Let us analyze features of videopulse interaction with a such zone, assuming that the subhorizon of active moisture exchange has the power of 0.5 meters, the subhorizon of variable humidifying — 4 meters and the near-level subhorizon — 1 meter (such depth of the latter is characteristic of clays and loams). Assume that the absolute humidity of the first subhorizon varies within the limits of 5-2.5 %, humidity of the second one — within the limits of 2.5-3.5 % and of the third one — within the limits of 2.5-17 %. Consider two cases. Let all AZ be formed by chestnut loam in the first case, and let the near-level horizon be represented by clay in the second case. The law of humidity variation showed in Fig.3 remains identical in the both cases.

The results of calculations are adduced in Fig.4. It is possible to see that the increase of humidity at a depth of 0.5 m under transition from the active moisture exchange subhorizon to the variable humidifying subhorizon results in the emergence of a negative pulse, following immediately the one reflected from the upper AZ boundary. In both cases these initial parts of the curves,

coincide. Differences are possible to observe for the reflections from the capillary levitation area and from water, which are also merged with each other, as well as in previous cases. The solid line corresponds to the case of loam in the near-level subhorizon, and the dotted line — to the case of clay. The value of permittivity of chestnut loam is more than the one of clay, and the absorption is less than the clay one in the outgoing pulse spectrum. Therefore the pulse reflected from water has a major time delay, minor duration and a major amplitude in case of loam.

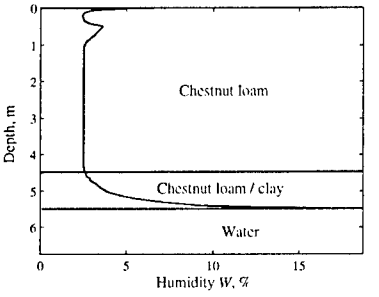

Fig. 3. *Laws of humidity distribution in depth for a two-layer/single-layer AZ of the 5.5 m depth considering the presence of three representative subhorizons: the active moisture exchange one, the variable humidifying one and the capillary levitation one*

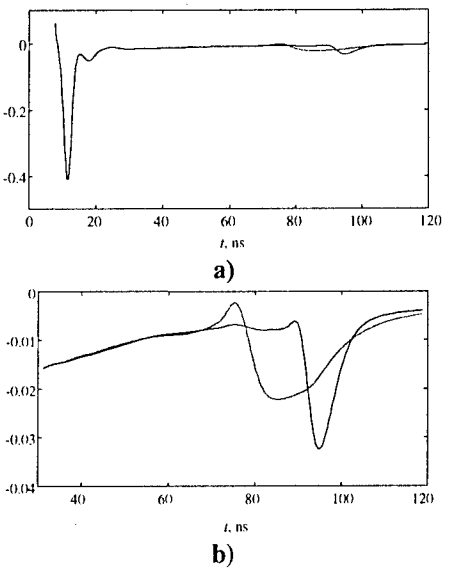

Fig. 4. *Time dependences of the diffraction fields for the single-polar incident videopulse of the 10 ns duration for the AZ with a depth of5.5 m. The law of humidity distribution in depth corresponds to Fig. 3: the solid line – the all AZ, including the area of capillary fringe, is formed by loam, the dashed line — if there is clay in the capillary fringe area*

In the latter case, which differs from the previous one in considerably large depth of the ground structure, the errors of full-scale measurements of frequency dependences of permittivity and specific conductivity, used by us, were showed. Actually in Fig. 4. it is possible to see the physically unstipulated pulse of approximately three times smaller amplitude, which precedes r eflections from the capillary fringe boundary or water. Thus, the errors of full-scale measurements have resulted in violation of causality law what was the consequence of connection disturbance in real and imaginary parts of complex permittivity. This connection, as it is known, is given by Kramers-Kronig' relations and is based upon the causality principle. The same thing appears when calculation of a field, reflected from a homogeneous structure with a constant value of humidity and frequency-dependent data. But calculations for dielectric parameters independent on frequency (at the local connection in time between vectors of electric displacement and of the electric field strength) do not bring into such effect. So it is necessary to refine source data on the basis of Kramers-Kronig' relations for more correct simulation of non-stationary processes for structures with large slabs depths. This correction should be actualized by the part of the permittivity complex function, which is measured with the least error.

REFERENCES:

[1]. *Babinets A.E. and other.* Bazovaya gidrogeologicheskaya stantsiya Feofaniya // Vyyavlenie zakonomernostey vodno-solevogo rezhima v zone aeratsii i vodonosnykh gorizontakh. — K.: 1981. — 38 s. (Prepr. / AN Ukrayiny. In-t geol. nauk). — P. 25-28.

[2]. *Sitnikov A.B.* Dinamika vody v nenasyschennykh i nasyschennykh gruntakh zony aeratsii. — K.: Naukova dumka, — 1978. — 210 p.

[3]. *Brekhavskikh L.M.* Volny v sloistykh sredakh. — M.: Izdatel'stvo Akad. nauk SSSR, 1957. — 504 p.

[4]. *Masalov S.A.,PuzanovA.O.* Rasseyanie videoimpul'sov na sloistykh strukturakh grunta // Radiophizika i radioastronomiya. — 1998. — V. 3, №4. — P. 393-404.

[5]. *Leschansky Yu.I.,Ul'yanychev N.V.* Raschiot electricheskikh parametrov peschanno-glinistykh gruntov na metrovykh-santimetrovykh volnakh. // Izv. vuzov — Radiofizika. — 1980. — V. 23, № 5. — P. 530-532.

ANTENNA THEORY

TWO REFLECTOR NON SYMMETRIC SHAPED ANTENNA SYSTEMS

Elman Hasanov
Department of Mathematics, Faculty of Arts and Science, Isik University,TR-80670, Maslak, Istanbul,Turkey
E-mail: elman@isikun.edu.tr

ABSTRACT

Two reflector antenna systems with non symmetric reflecting surfaces under GO approximation are investigated. It is shown, that the problem of forming desired far field pattern leades to solving the system of partial differential equations with respect to mapping functions between wave fronts. One of these equations is non linear and expresses energy conversation law. It is shown that this equation can be solved separetly in the class of non smooth functions which has a discontinuty of first kind along a given curve.

INTRODUCTION

Consider two reflector shaped antenna system. Assume that the ray with coordinates (θ,φ)eminated from the point source, placed in the origin after two reflections from mirrors transforms to the ray with coordinates (x, y). Such a way given system generates a mapping functions $x = x(\theta,\varphi)$, $y = y(\theta,\varphi)$ between initial spherical and outgoing plane wave fronts (Fig.1). It can be shown that [1] these functions satisfy a single quasi linear partial differential equation of the form

$$\frac{\partial^2 T}{\partial\varphi\partial x}\frac{\partial x}{\partial\theta}-\frac{\partial^2 T}{\partial\theta\partial x}\frac{\partial x}{\partial\varphi}+\frac{\partial^2 T}{\partial\varphi\partial y}\frac{\partial y}{\partial\theta}-\frac{\partial^2 T}{\partial\theta\partial y}\frac{\partial y}{\partial\varphi}=0 \tag{1}$$

where $T=\ln M$,

$$M=(1+\cos\theta)\left[\left(m\cos\varphi-x\tan\frac{\theta}{2}\right)^2+\left(m\sin\theta-y\tan\frac{\theta}{2}\right)\right]$$

and m is the total optical length from source to aperture. Relationship between amplitude distrubations, whish governors the shape of the far field pattern, by means of mapping functions $x = x(\theta,\varphi)$, $y = y(\theta,\varphi)$ can be written as

$$\frac{\partial x}{\partial\theta}\frac{\partial y}{\partial\varphi}-\frac{\partial y}{\partial\theta}\frac{\partial x}{\partial\varphi}=\pm\frac{A_1^2(\theta,\varphi)}{A_2^2(x,y)} \tag{2}$$

where $A_1(\theta,\varphi)/\sin\theta$ and $A_2(x,y)$ are the corresponding amplitude distrubations over initial and outgoing wave fronts, respectively. Sign "+" corresponds to classical Cassegren system and sign "-" to Gregory system ([2]). Equation (2) is a relationship of geometrical nature and can be investigated separetly.

FINDING MAPPING FUNCTIONS

Let F and G be bounded and covex regions in (θ,φ) and (x,y) planes with boundary curves $(\theta(t),\varphi(t))$ and $(x(t_1),y(t_1))$, respectively. $t_1 = t_1(t)$ is transformation of parameter. $\theta(t)$, $\varphi(t)$, $x(t_1)$, $y(t_1)$ are differentiable functions, $0 \le t \le T$, $0 \le t_1 \le T_1$, $\theta(0)=\theta(T)$, $\varphi(0)=\varphi(T)$, $x(0)=x(T_1)$, $y(0)=y(T_1)$. Let $x^0(\theta,\varphi)$ be a smooth function defined on the region F and satisfying conditions

a) $x^0(\theta(t),\varphi(t)) = x(t_1(t))$

b) $\left|\frac{\partial x^0}{\partial\theta}\right| + \left|\frac{\partial x^0}{\partial\varphi}\right| \neq 0$ for $(\theta,\varphi)\in F$

c) from each point of F passes one and only one curve of the family $x^0(\theta,\varphi) = const$

$$\frac{\partial x^0}{\partial\theta}\frac{\partial y}{\partial\varphi} - \frac{\partial y}{\partial\theta}\frac{\partial x^0}{\partial\varphi} = \pm\frac{A_1^2(\theta,\varphi)}{A_2^2(x^0(\theta,\varphi),y)} \tag{3}$$

Substituting $x^0(\theta,\varphi)$ into equation (2) we have

For simplicity we shall assume that function $A_2(x,y)$ do not contain y implicitly. (3) is a linear partial differential equation of first order with respect to $y(\theta,\varphi)$ and can be solved by well known characteristic method. In this case characteristics are the solutions of the system of ordinary differential equations

$$\frac{d\theta}{d\tau} = \frac{\partial x^0}{\partial\varphi} \tag{4}$$

$$\frac{d\varphi}{d\tau} = -\frac{\partial x^0}{\partial\theta} \tag{5}$$

$$\frac{dy}{d\tau} = \pm\, A_1^2(\theta,\varphi)/A_2^2(x^0(\theta,\varphi)) \tag{6}$$

(4) and (5) form a Hamilton system with hamiltonian $x^0 = x^0(\theta,\varphi)$. For this reason projections of solution of (4) - (6) $(\theta(\tau),\varphi(\tau),y(\tau))$ onto (θ,φ) plane (i.e. the curves $(\theta(t),\varphi(t))$) coincide with the family $x^0(\theta,\varphi) = const$ in this plane. Now let

$$\vec{\xi}(t,\tau) = (\theta(t,\tau),\varphi(t,\tau),y(t,\tau)) \tag{7}$$

be a solution of (4)-(6) corresponding to initial curve $(\theta(t),\varphi(t),y(t))$. In general case it can not be guaranteed that $\vec{\xi}(t,\tau)$ can be projected one to one onto the plane (θ,φ) i.e. be represented in the form $y_0 = y_0(\theta,\varphi)$, but it can be shown that each point in F has at least two image on the (7). Thus (7) is 2 - fold surface over the F. If both folders coincide then we get a solution of the form $y_0 = y_0(\theta,\varphi)$, which together with $x_0 = x_0(\theta,\varphi)$ gives the solution of the problem, i.e. transforms F to G and boundary of F to boundary of G. If these folders do not coincide then using them we may construct one valued function over F which satisfies the boundary condition and has a discontinuity of first kind along certain curve laynig in F. Indeed, let C be any curve transversally (i.e. without tangency) intersecting all curves of the family $x^0(\theta,\varphi) = const$. Curve C divides region F into two subregions F_1 and F_2 such that $F_1 \cap F_2 = \varnothing$, $F_1 \cup F_2 = F$ Over each these subregions (7) has two folders. One of these folders is formed from the characteristics outgoing from those part of the curve $(\theta(t),\varphi(t),y(t))$, which lies in this subregion. Combining parts with such

properties for each subregions of F we obtain an one valued function $y_0 = y_0(\theta,\varphi)$ over F having discontinuity along the curve C and satisfying $y_0(\theta(t),\varphi(t)) = y(t_1(t))$. Illustrate described procedure on example. Let $F = \{(\theta,\varphi), \theta^2 + \varphi^2 \le 1\}$ and $G = \{(x,y), x^2 + y^2 \le 1/2\}$. Assume that $A_2(x,y) = 1$ and $A_1(\theta,\varphi) = (1+\theta^2+\varphi^2)^{-2}$. Let $x^0(\theta,\varphi)$ be a family of hyperbolas, once covering region F :

$$x^0(\theta,\varphi) = \frac{\theta}{\sqrt{1+\theta^2+\varphi^2}} = const \tag{8}$$

Substituting into equation (3) yields

$$\frac{\partial y}{\partial \theta}(\theta\varphi) + \frac{\partial y}{\partial \varphi}(1+\varphi^2) = -\frac{1}{\sqrt{1+\theta^2+\varphi^2}} \tag{9}$$

Characteristic system is

$$\frac{d\theta}{d\tau} = \theta\varphi, \qquad \frac{d\varphi}{d\tau} = 1+\varphi^2 \tag{10}$$

$$\frac{dy}{d\tau} = -\frac{1}{\sqrt{1+\theta^2+\varphi^2}} \tag{11}$$

After integrating this system , we obtain a conjugate to (8) family of hyperbolas, again once covering F :

$$y^0(\theta,\varphi) = \frac{\varphi}{\sqrt{1+\theta^2+\varphi^2}} = const$$

which together (8) yields solution of the given problem.

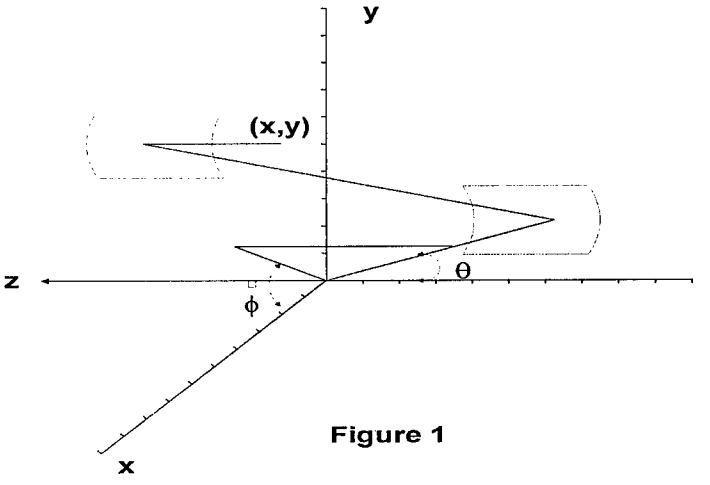

Figure 1

REFERENCES

[1] Gasanov E.E. (Hasanov E.E.), Kinber B.Ye. "On the Transformation of the non - Homocentrical Waves After Two Reflection ,"Soviet Journal of Communication Tech. And Electronics , **34** (1989) No.1, 67 - 72..

[2] Hasanov E.E. Polat B. On the realization of Optical Mappings and Transformation of Amplitudes by means of an Aspherical "Thick" Lens. Inter. Journal of Electron. And Communications (AEÜ) **54** (2000) No.2, 109-113.

FOCUSING SYSTEMS BASED ON MICROSTRIP REFLECTARRAYS

A.O. Kasyanov

Taganrog State University of Radio Engineering
44 Nekrasovsky street, GSP-17A, Taganrog, Russia, 347928,
Phone (86344) 61733, E-mail: airpu@ tsure.ru

ABSTRACT

Focusing systems constructions and mathematical model are considered. These systems allow realizing a focussing of antenna feed field by a microstrip reflectarray. The mathematical model is obtained by integral equation method. Besides microstrip reflectarray properties are investigated by waveguide simulation experimental method. Seven variants of focusing reflector are investigated in the given paper. The reflector antenna with a flat focussing system experimental model is designed. The measured and calculated patterns of this antenna are given. These researches can be used to develop antennas with optimum parameters.

INTRODUCTION

The optical feed circuit application for radiators excitation is a way of reducing the antenna array cost. Usually these antenna arrays are supplied with such circuits for a radiator feed, which are applied for reflector and lens antennas excitation. Such antenna arrays have little bit lower values of efficiency in comparison to the prototypes, namely, reflector antennas. But these antennas allow realizing electronic scanning and they can be made in the form of conformal-type antennas.

THEORY

In this paper, the application of periodic microstrip antenna array for designing a flat reflector is considered. Such reflectors can be used as a component of onboard radio engineering systems. Besides they can be used for stationary telecommunication systems, satellite television, etc. Similar principal function of flat reflector is to ensure feed spherical or cylindrical wave transformation to a plane wave. To achieve this effect it is necessary to realize a feed electromagnetic wave phase correction. The phase correction is achieved by creation of an additional phase delay in radiators of antenna array. The phase delay magnitude should be increased from the marginal elements to central radiators. The usually required phase delay magnitude is determined by account, that is based on the geometric optics method [1].

If the microstrip elements are used as antenna array radiators, it will allow solving the problem of designing a cheap flat reflector in the most convenient way. This way is based on a choice of radiator geometry and its constructive sizes. The mathematical model of a flat infinite microstrip reflectarray is developed in the paper [2]. This model allows selecting the reflectarray radiator parameters on the basis of computing experiment results. The numerical analysis bases on the following initial parameters: radiator topology, substrate permittivity and permeability, as well as sizes of an array unit cell. The method based on an integral equation system solution was selected as the analysis method. The magnetic field integral equations were formulated concerning magnetic currents surface density distributions on the antenna array aperture. This antenna array is excited by the incident plane wave. The numerical analysis results are scattering fields and reflection factor of the reflectarray.

NUMERICAL RESULTS

First of all we investigate a possibility of a necessary phase delay realization with a reflection from a reflectarray of the non-loaded radiators. To solve the formulated problem, we shall change topology and sizes of the strip elements and to define a copolarization reflection factor phase. The principal problem of these numerical experiments is selecting such variants, that ensure the needed phase delay. Therefore calculations were carried out in a case, when the array-exciting plane wave is incident along the normal direction. However, the flat reflector design requires that the incident wave angle variation is taken into account. An each reflectarray radiator and its feed mutual location determine this angle. We analyze the application possibility of several reflectarray types as a flat focusing reflector. These arrays differ by the type of the used radiator. First we shall analyze the reflectarray, whose radiators have the simple shape microstrip elements.

The microstrip vibrators have the simplest shape. We have calculated and measured such arrays reflection factors. The relation between the phase delays and vibrators relative length was defined in these researches. The calculation [1] and experimental results allowed making a conclusion, that printed strip dipole arrays are suitable for a flat focusing reflector design. The reflection factor phase variation velocity is greatest by a resonant length of the vibrator. Besides, in this case phase varies in significant limits. However, high phase characteristic steepness can reduce to the unstable numerical solution. This circumstance complicates the designing of such reflector because of the high requirements to its performance accuracy. Eventually, in this case reflector bandwidth will be the narrowest.

The similar calculations in a case, when the microstrip radiators have the square shape, are given in [2]. The phase delay variation range in this case is also rather great. In this case, the relation between phase delay and square element relative size was close to linear. Such relation can be obtained only if the reflectarray dielectric substrate is rather thick. This case corresponds to the reduced Q-factor value of reflectarray microstrip resonator. The reflector design problem requires a compromise between a steepness value and possible reflection factor phase variation range. This compromise is achieved by a choice of a substrate thickness, because in this case we can control the phase characteristic steepness.

We investigated a shape phase characteristic control possibility by additional reflectarray microstrip element complication. This complication is directed on introducing auxiliary frequency-dependent elements. The auxiliary elements change the reflectarray resonance and frequency properties. Let such auxiliary element be a tail. First of all we shall connect a tail to a microstrip vibrator. However, the numerical experiments have shown that the vibrator supplied by one or several tails does not allow receiving required parameters.

The phase performance shape comes nearer to a desirable form if the tail is connected to the microstrip element, which has the rectangular or square shape [3]. The reflectarray phase characteristics are given in Fig.1. The reflectarray parameters are: $d_x = 11{,}7$ mm; $d_y = 16$ are steps of array; $a = 9{,}9$ mm; $b = 7{,}2$ mm - microstrip patch sizes. The ε of the substrate used is $2{,}2$, and its thickness is 16mm. The microstrip line segment is a tail. This segment width is $0{,}9$ mm. The tail connection place is the middle of that microstrip patch edge, which has a greater size. The free tail edge is left breaked. The relationship between the phase shift of the field re-radiated from an infinite reflectarray and the length of the connected tail is investigated. This is shown by a solid line in Fig.1. It is shown that in this case we manage to ensure reflection factor phase regulation over a wide range and to save a phase characteristic linearity. The phase growth rate appears quite acceptable. Eventually such radiators practically

do not change a crosspolarization level. Thus, they can be recommended for such focusing reflector construction, which will work on linear polarization.

It is known [4] that the flat reflector can be made as a printed ring reflectarray. We have done a numerical analysis of such arrays phase characteristics. The relationship between the phase shift of the field re-radiated from an array and the excited plane wave incident angle was investigated. The numerical analysis has shown that the reflection factor phase varies rather slowly and smoothly. Actually, we shall consider a reflectarray, which is described in [4]. Let the excited field have a frequency of 8,5 GHz. If the incident angle varies from 0 up to 45 degrees, then the phase shift variation will be less than 20 degrees.

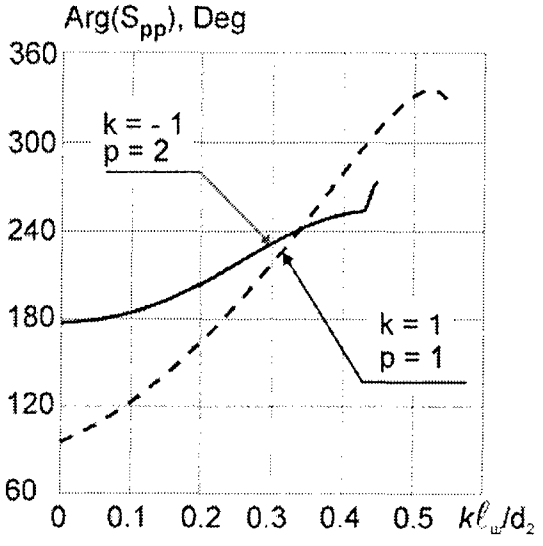

Fig. 1

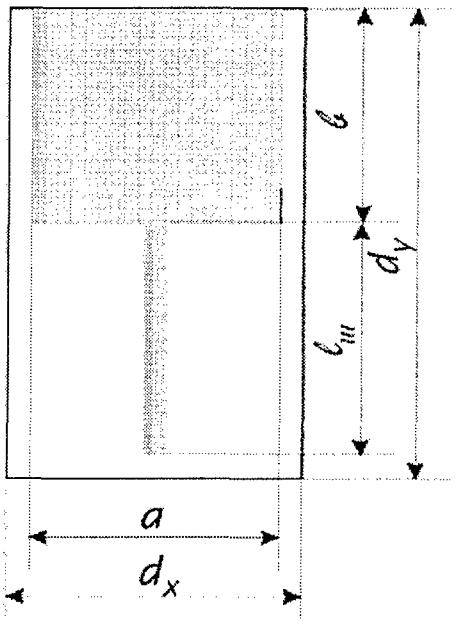

The calculation results for a square shape microstrip loops reflectarray are given in [5]. The relationship between the phase shift of the field re-radiated from an infinite reflectarray and the microstrip loop radius was investigated. It is shown that in this case we can control reflection factor phase over a wide phase shifts range. The compromise between a phase characteristic steepness value and possible variation range of reflection factor phase is achieved by a choice of the reflectarray steps values. Besides the microstrip re-radiators shape allows to expand such reflectarrays application region. In fact, the microstrip loop is a circular polarization re-radiator. Therefore, in this case a field phase correction is achieved as good as at linear or circular polarization.

MEASUREMENTS

First of all we have selected the design of reflectarray which has the best relationship between a phase shift and parameters of a reflectarray radiator. This variant was applied for a flat reflector design. The parabolic antenna is the prototype of such flat reflectarray. The way of feed wavefront correction is the key feature of such antenna. This feature distinguishes our antenna from a parabolic antenna. The correction of wavefront in a parabolic antenna is carried out, due to the special profile of a reflector. The correction of wavefront in our reflectarray is carried out, due to a special choice of a radiator construction. The radiator of an array provides the required phase shift value of a scattering wave. A flat reflector operating at 9.4 GHz has been designed and fabricated using the screen printing technique. It has a diameter of 25 cm and 0.46 F/D ratio. The substrate is 6 mm thick and permittivity of 2.05. A backfire antenna was used as the feed. This antenna contains active vibrator and wire reflector. These two vibrators are excited by rectangular waveguide. The whole system is shown in Fig. 2.

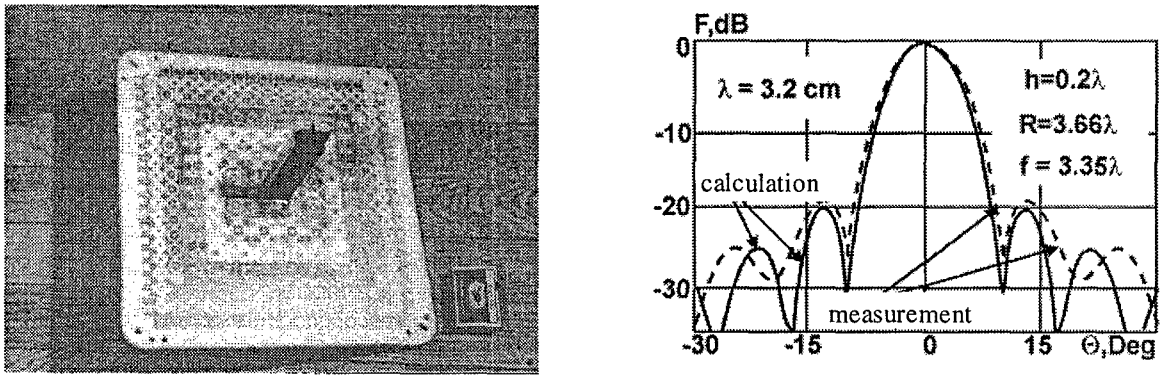

Fig. 2

The antenna was measured at the 3.2 cm wavelength. Fig. 2 shows the E-plane radiation pattern of the antenna. The pattern has been shown by solid line. It is obtained by scattering field superposition of single radiators. We have used the "element by element" technique. The relation between the current distribution into radiator and incident angle of its exciting plane wave was also taken into account.

REFERENCES

[1] Obukhovets V.A., Kasyanov A.O. Phase correcting zonal reflector from flat diffraction microstrip array//Antennas, Radiocommunication Systems and Means (ICARSM'97), Proc. of III Int. Conf. - Voronezh: VSU, 1997, Vol. 1. P. 174-178.

[2] Kasyanov A.O., Obukhovets V.A. Current control in a microstrip array with loaded elements (in Russian) /Radioengineering — 1995. — No.12. — P.32-36.

[3] Zhnang Y., Litva J., Wu C., Wu K.-L. Modeling studies of microstrip reflectarrays//IEE Proc. Microwaves, Antennas and Propag. — 1995. — 142. No.1 — P. 78—80.

[4] Guo Y.J., Barton S.K. Phase Correcting Zonal Reflector Incorporating Rings. IEEE Transactions on Antennas and Propagation, vol. AP-43, 1995, No. 4, p.350-355.

[5] Obukhovets V.A. The constructive synthesis problems of reflective type antenna arrays//Antennas. — 1997, vol. 2(39). — Moscow IPRZHR. — P. 17-24.

ANALYSIS METHOD OF THE INPUT IMPEDANCE OF A SPIRAL ANTENNA WITH GIVEN CONFIGURATION

Mikhail B. Protsenko, Ivan V. Tankov and Valentin V. Gromozdin

Sevastopol State Technical University, Sebastopol, Ukraine
Tel: 0692 235-127, e-mail: rt.sevgtu@stel.sebastopol.ua, tankov075@stel.sebastopol.ua

ABSTRACT

A method of analysis of spiral antenna input impedance is presented. It is based on the generalized transmission line theory (TLT) that accounts for the wave nature of electromagnetic field. Application of the iterative analysis method of equivalent transmission line is discussed for the adopted model. Numerical modeling and experimental results for the flat Archimedean spiral antenna input impedance are presented.

INTRODUCTION

The input impedance computation of spiral antennas is a difficult electromagnetic problem because of lack of a suitable coordinate system, in which the curved wire surface coincides with one of the coordinate surfaces. In this case, it is impossible to separate the variables in the electromagnetic field equations [1]. Therefore, empirical data [2] or simplification and approximation in the formulation of analyzed problem are used in the estimation and analysis of spiral antenna input impedance.

Empirical data application is essentially limited because of various antenna design peculiarities, namely spiral antennas. Therefore, we use the generalized TLT for the analysis of the spiral antenna input impedance in this paper. Here, Kirchgchoff's equations [3] are explained instead of the Maxwell's equations of the rigorous electromagnetic field theory [1].

INPUT IMPEDANCE MODEL OF SPIRAL ANTENNAS

On the basis of TLT, Kirchgchoff's equations subject to radiation losses are:

$$dU/ds = I \cdot Z; \quad dI/ds = U \cdot Y, \tag{1}$$

where Z, Y are distributed impedance and conductance, respectively.

Taking into account, that solution of (1) can be represented in the form of travelling-wave series in terms of $exp(\pm \gamma s)$ [3] and boundary conditions the input impedance for a spiral antenna with a given configuration can be determine with account to the wire length as:

$$Z_{input} = W \cdot \left[\left(Z + W \cdot th\gamma s \right) / \left(W + Z \cdot th\gamma s \right) \right]. \tag{2}$$

where s is the running coordinate on the equivalent line wire axis having the origin at the output, W and γ are the wave impedance and the electromagnetic-wave propagation constant along the equivalent line:

$$W = \sqrt{Z \cdot Y^{-1}}, \quad \gamma = \sqrt{Z \cdot Y}. \tag{3}$$

Taking into account the vector potential method [1], $\vec{E} = -gradV - \left(jk/\sqrt{\varepsilon\mu} \right) \cdot \vec{A}$.

To find the equivalent line parameters, it is necessary to satisfy the current continuity low and the electromagnetic boundary conditions, namely the tangential component of the electric field vector is zero at the wire surface, provided that the skin-effect is neglected. Then, we have (4) and if it suppose that the current flows in the direction of the wire axis if the wire

cross-section is small in comparison with the wavelength and is constant along the axis. Therefore, the deferential operators in (4) can be written as (5)

$$grad V = -j\left(k/\sqrt{\varepsilon\mu}\right)\cdot \vec{A}; \quad div\vec{J} = -j\left(k/\sqrt{\varepsilon\mu}\right)\cdot \rho. \tag{4}$$

$$grad V = \vec{s}_0 \cdot \left(dU/ds\right); \quad div\vec{J} = dI/ds. \tag{5}$$

where $\vec{s}_0$ is the unit vector directed along the wire axis and related to the observation point.

Transforming (4) to the Kirchgchoff's equation form (1) we can obtain the equivalent line parameters on the basis of expressions (5):

$$W_0 = \left(\sqrt{\mu/\varepsilon}/4\pi\right)\sqrt{\int_s G(R)\cdot\left(\vec{s}_0,\vec{s}_1\right)\cdot exp\left(-j\gamma s_1\right)\cdot ds_1 \cdot \int_s G(R)\cdot exp\left(-j\gamma s_1\right)\cdot ds_1}; \tag{6}$$

$$\gamma_0 = j\gamma\sqrt{\left(\int_s G(R)\cdot\left(\vec{s}_0,\vec{s}_1\right)\cdot exp\left(-j\gamma s_1\right)\cdot ds_1 \Big/ \int_s G(R)\cdot exp\left(-j\gamma s_1\right)\cdot ds_1\right)}, \tag{7}$$

where $G(R) = exp\left(-jkR\right)/R$ is the scalar Green's function of the free space, R is the distance between the observation and integration points, the indices of "0" and "1" denote the observation and integration points, respectively.

In general, the equations (6) and (7) are not fully defined because of the presence of γ characterizing the propagation of the current travelling wave. By using the iterative analysis method, we can eliminate this uncertainty. In particular, we can use the free-space electromagnetic-wave propagation constant as the first approximation. On the basis of the obtained equation (7), the propagation constant can be recalculated. Such an iterative process can be continued until the computed values stop changing within a needed accuracy.

The dependences of wave impedance and propagation constant are nonlinear because of the radiator inhomogeneity and a usage of infinitely narrow exciting gap model leading to fringe peaks. Let us average the calculated parameters along the wire in order to eliminate the nonlinearity. That is to say:

$$W^* = s^{-1}\int_s W_0^*\left(s_0\right)\cdot ds_0; \quad \gamma^* = s^{-1}\int_s \gamma_0^*\left(s_0\right)\cdot ds_0,$$

where the symbol "*" denotes the first approximation.

ANALYSIS OF THE INPUT IMPEDANCE OF A SPIRAL ANTENNA

A flat two-arm Archimedean spiral is chosen for the analysis. This antenna can form required directional and polarization characteristics in a wide band [4].

The antenna arm is parametrized by the following equations in the Cartesian coordinate system: $x = a\cdot\alpha\, cos(\alpha)$, $y = a\cdot\alpha\, sin(\alpha)$, where a is the spiral constant, α is the winding angle, $0 < \alpha \le 2\pi n$, n is the antenna turn number.

The Green's function $G(R)$ in (6), (7) and scalar product of the tangential unit vector with the current element $d\vec{s}$ can be determined for a two-arm spiral antenna as follows:

$$G(R) = \left[exp\left(-jkR_{01}\right)/R_{01}\right] - \left[exp\left(-jkR_{02}\right)/R_{02}\right]; \quad \left(\vec{s}_0,\vec{s}_1\right) = -\left(\vec{s}_0,\vec{s}_2\right) = cos\left(\beta\right) \tag{8}$$

where $R_{01} = a\sqrt{C-B}$, $R_{02} = a\sqrt{C+B}$, $C = \alpha_0^2 + \alpha_1^2 + \left(r/a\right)^2$, $B = 2\alpha_0\alpha_1\, cos\left(\alpha_0 - \alpha_1\right)$, $\beta = arctg\left(\dfrac{sin\,\alpha_0 + \alpha_0\, cos\,\alpha_0}{cos\,\alpha_0 - \alpha_0\, sin\,\alpha_0}\right) - arctg\left(\dfrac{sin\,\alpha_1 + \alpha_1\, cos\,\alpha_1}{cos\,\alpha_1 - \alpha_1\, sin\,\alpha_1}\right)$, r is the wire radius.

The parameters R_{01}, R_{02} and β are shown in Fig. 1.

The results of numerical modeling are shown in Fig. 2, namely, the frequency dependences of R_{input} and X_{input} are presented for the following antenna parameters: $a = 0{,}0222\,\lambda_0/rad$; $0{,}06\,rad \le \alpha \le 12{,}56\,rad$; $r/a = 0{,}01$. For a comparison, there are the experimental ($x\,x\,x$) and theoretical results ($o\,o\,o$) computed by the moment method [5] are also presented for the antenna input impedance.

Experimental and theoretical results are in agreement. This is a good evidence that we have achieved the needed calculation accuracy of the spiral antenna input impedance even in the first approximation (6), (7).

The input impedance in the studied frequency range is nearly constant. This confirms that the suggested current model is justified in the flat-spiral antenna research [4].

It is necessary to note that the presented analysis method has some advantages before the other similar methods: first of all, the antenna excitation problem solved by means of differentiation and integration is simpler; besides, one can determine the antenna input impedance by iterations with any accuracy.

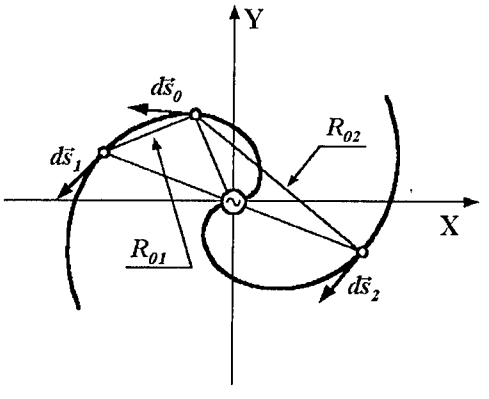

Figure 1 Geometry of spiral antenna

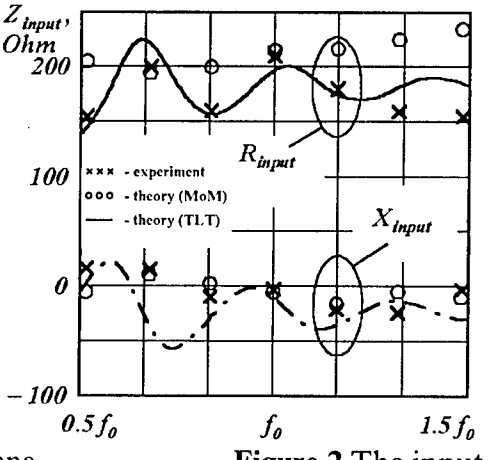

Figure 2 The input impedance of spiral antenna

REFERENCES

[1] V.V. Nikolskii, *Electromagnetics and Propagation*, Moscow, Nauka, 1973, *(in Russian).*

[2] M.S. Juk, Yu.B. Molochkov, *Design of Lens, Scanning and Wide-Band Antennas and Microwave devices*, Moscow, Energiya, 1973, *(in Russian).*

[3] G.Z. Aizenberg, *Microwave Antennas*, Moscow, Svyaz', 1962, *(in Russian).*

[4] L.M. Lobkova, M.V. Ivashina, L.N. Stepanov, I.V. Tankov "Mathematical Model and Geometrical Parameters Optimization of the Flat Spiral Antennas of Diverse Configurations", *Proc. of Int. Conf.*, Sevastopol, Crimea, Ukraine, 1998, pp. 458-461.

[5] H. Nakano, K. Hirose, I. Ohshima, and J. Yamauchi "An Integral Equation and Its Application to Spiral Antennas on Semi-Infinite Dielectric Materials", *IEEE Trans. Antennas Propagat.*, vol. AP-46, pp. 267-274, Feb. 1998.

RESEARCH ON NEW ANTENNAS FOR MOBILE RADIO COMMUNICATIONS

V. V. Ovsyanikov

Dnepropetrovsk State University,49050, Dnepropetrovsk, Naukovy lane 9, korp.12
phone (0562) 43-36-30; e-mail: root@net-rff.dsu.dp.ua

ABSTRACT

Results of consideration of new two-frequency wire antennas for the base stations of mobile systems of radio communication are presented. It is shown that not for all ratios of the two operating frequency values the acceptable pattern at the upper one of the combining frequencies is provided. The results of study obtained by the methods of integral equation and equivalent transmission line are given.

For widening the base station bandwidth in mobile radio communications, in a number of cases two-stub and multi-stub wire antennas are applied [1]. However, their characteristics are not well studied that is the reason of research on similar antennas by rigorous methods.

A system of two closely located parallel wire antennas (the distance is $d \ll \lambda$), which have finite thickness ($2r_a$) and different lengths ($2L_1$ and $2L_2$), is considered. Here, a set of two integral equations (IEs) is written:

$$\begin{cases} \int\limits_{-L_1}^{L_1} \dot{I}_1(z')\cdot\dot{G}_{11}(z,z')\,dz' + \int\limits_{-L_2}^{L_2} \dot{I}_2(z')\cdot\dot{G}_{12}(z,z')\,dz' = F_1(z), \quad (-L_1 \le z \le L_1), \\ \int\limits_{-L_1}^{L_1} \dot{I}_1(z')\cdot\dot{G}_{21}(z,z')\,dz' + \int\limits_{-L_2}^{L_2} \dot{I}_2(z')\cdot\dot{G}_{22}(z,z')\,dz' = F_2(z), \quad (-L_2 \le z \le L_2), \end{cases} \qquad (1)$$

where $\dot{G}(z,z')$ is the Green's function and $F(z)$ is the excitation function.

For the solution of this system, complex currents in each of wires are presented as polynomials of the N-th power [2] :

$$\dot{I}_1(z) = \sum_{n=1}^{N_1} \dot{I}_{1n}\left(1-|z|/L_1\right)^n; \qquad \dot{I}_2(z) = \sum_{n=1}^{N_2} \dot{I}_{2n}\left(1-|z|/L_2\right)^n \qquad (2)$$

Then, by the method of collocations, the system of IEs (1) is reduced to a set of algebraic equations. After the solution of the latter by computer we determine resulting complex input impedance ($\dot{Z}_{in}$) of the system of two symmetric wires $2L_1$ and $2L_2$, connected in parallel in the center ($z=0$) and excited by the generator with a voltage V :

$$\dot{Z}_{in} = V \Big/ \left(\sum_{n=1}^{N_1} \dot{I}_{1n} + \sum_{n=1}^{N_2} \dot{I}_{2n} \right). \qquad (3)$$

The graphic dependences of the voltage standing wave coefficient, VSWR (K_s), obtained from (3) for electrical length L_1 two-stub of asymmetrical wire antenna (curve 1), loaded on a feeder having the wave resistance of 50 Ohms is given in Fig.1. It shows that unlike a usual one-stub asymmetrical wire antenna (curve 2), two-stub one (curve 1) provides at the ratio of the frequencies 1:2 good input parameters ($K_s < 2$). The first consecutive

resonance in this antenna arises at $L_1 \approx 0.24\lambda$, and the additional second resonance at $L_1 = 2L_2 \approx 0.5\lambda$, where λ is the wavelength. It arises extremely due to presence of the vibrator L_2 close L_1.

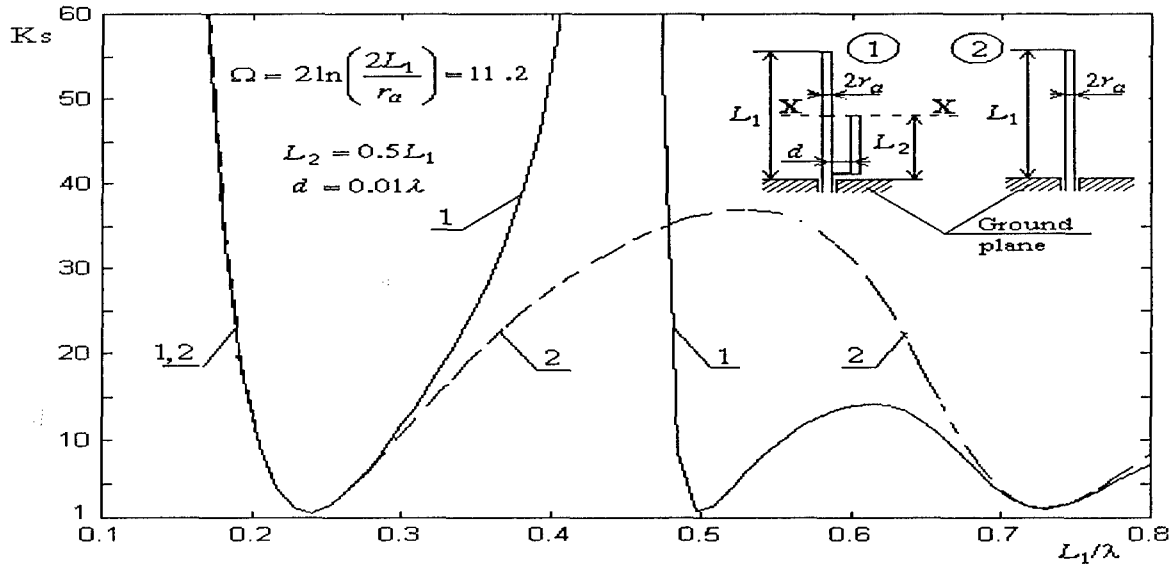

Fig 1. VSWR versus electrical length $L_1(L_2)$ for a two-stub antenna (curve 1) and a one-stub antenna (curve 2).

Consider the current distributions on the both stubs of the two-stub antenna that were obtained by solving with computer the set of IEs (1) for the antennas with various the ratios of frequencies and the stub lengths (Fig.2).

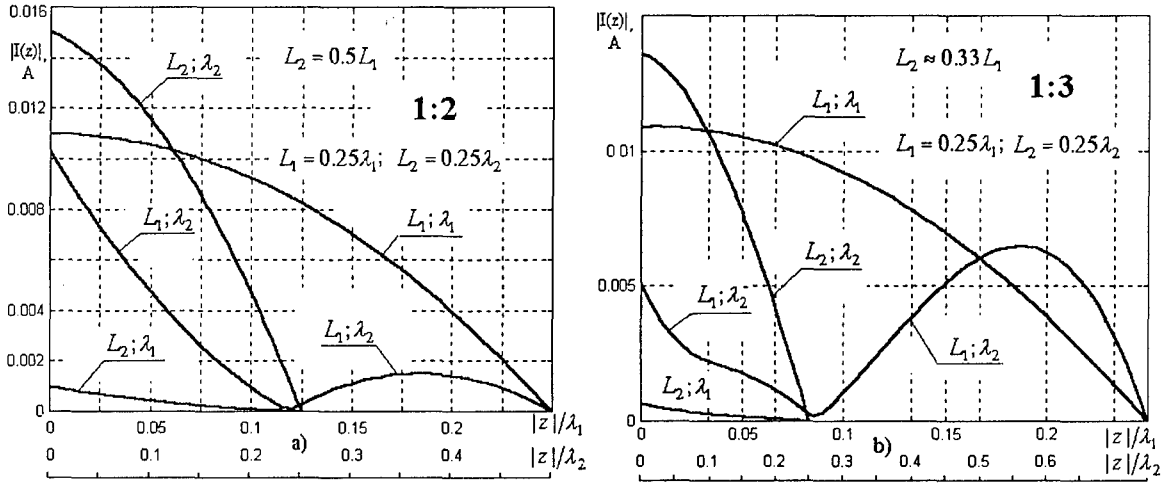

Fig 2. The current distributions along a two-stub antenna: a) $f_2 = 2f_1$; b) $f_2 = 3f_1$.

According to Fig.2, the current amplitudes at the frequency f_2 on the standing out parts $(L_1 - L_2)$ of antenna L_1 are equal, respectively, to ~10% and ~50% against the current amplitudes at the frequency f_2 of antenna L_2. From this it follows that in the first case (Fig.2a) a standing out part $(L_1 - L_2)$ is almost not excited by the current with the frequency f_2, and this current is cut-off in the plane X-X (Fig.1). Here, at both frequencies f_1 and f_2,

antenna has the patterns similar to the ones of a quarter-wave wire. Thus the requirements of the mobile radio communication antennas are satisfied. In the second case (Fig.2b), the standing out part ($L_1 - L_2$) is excited intensively by the current with the frequency f_2, and the antenna pattern at the frequency f_2 has zeroes in the directions of probable correspondents of mobile radio communication that is extremely undesirable. This negative phenomenon in similar antennas for the frequencies with ratios 1:3, 1:5 and the like has not been mentioned in any literature sources.

This effect can be explained by the absence of potential difference between the stubs L_1 and L_2 in the plane X-X (fig.1). The potential difference is proposed to be provided by including into standing out part ($L_1 - L_2$) a reactive load, for example, of inductance type [3]. Here, it is necessary to provide two conditions: 1) close to zero or minimum of potential on the stub L_1 at the frequency f_2 in the plane X-X, and 2) creating a regime of consecutive current resonance at frequency f_1 in the antenna.

These conditions are formulated in following transcendental equation:

$$L = \frac{W_1}{4\pi f_1}\left\{ctg\left[\xi\frac{2\pi}{\lambda_1}(L_1 - h_L)\right] - tg(\xi\frac{2\pi}{\lambda_1}h_L)\right\} =$$

$$= \frac{W_2}{4\pi f_2}\left\{ctg\left[\xi\frac{2\pi}{\lambda_2}(L_1 - h_L)\right] - tg\left[\xi\frac{2\pi}{\lambda_2}(h_L - L_2)\right]\right\}, \qquad (4)$$

where L is the inductance value, W_1, W_2 are the wave resistances of the stubs L_1 and ($L_1 - L_2$), h_L is the coordinate of the inclusion of inductance L, ξ is the coefficient of wave shortening.

The equation (4) can be easily solved for L and h_L by the method of iterations or by the graphical method.

For determination of the place of including the load L and its value, and form and value of the current distribution in antenna, a set of IEs is proposed:

$$\begin{cases} \int_{-L_1}^{L_1} \dot{I}_1(z')\dot{K}_{11}(z,z')\,dz' + \int_{-L_2}^{L_2} \dot{I}_2(z')\dot{K}_{12}(z,z')\,dz' + i\omega\varepsilon_a \dot{I}_1(h_L)Z_L, \; for\; (|z| \ge h_L) = \\ \qquad = i\omega\varepsilon_a V_1, \quad (-L_1 \le z \le L_1), \\ \int_{-L_1}^{L_1} \dot{I}_1(z')\dot{K}_{21}(z,z')\,dz' + \int_{-L_2}^{L_2} \dot{I}_2(z')\dot{K}_{22}(z,z')\,dz' + i\omega\varepsilon_a \dot{I}_1(h_L)Z_L, \; for\; (|z| \ge h_L) = \\ \qquad = i\omega\varepsilon_a V_2, \quad (-L_2 \le z \le L_2), \end{cases} \qquad (5)$$

where $K_{ij} = \frac{\partial}{\partial z'}G_{ij}(z,z') - k^2\int_{-z}^{z} G_{ij}(\xi,z')d\xi$,

$Z_L = iwL$ is the reactance of the load L, V is the voltage of exciting generator.

REFERENCES

1. A. Y. Grif, Satellite Antennas, Moscow, Simvol-R, 1998 (in Russian).
2. Popovic B.D. Polinomial approximation of current along thin symmetrical cylindrical dipoles. Proc. IEE, 1970, v.117, № 5, p.873-878.
3. V.V. Ovsyannikov, Wire Antennas with Reactive Loads, Moscow: Radio I Svyaz, 1985 (in Russian).

BLINDNESS ANGLES IN MICROSTRIP PHASED ARRAYS PATTERNS

A.O.Kasyanov, and V.A.Obukhovets

Taganrog State University of Radio Engineering, Russia.
Russia, 347928, Taganrog, GSP-17 A, Nekrasovsky str., 44,
Phone (86344)6-18-83, Fax (86344) 6-50-19, E-mail: vao@tsure.ru

ABSTRACT

This report describes the analysis of infinite arrays of printed dipoles. A rigorous and efficient moment method procedure is used to calculate the array impedance versus scan angle. The scan blindness phenomenon is observed and discussed. The analysis uses an equivalent circuit representation at the feed point location in the unit cell, which is derived from the moment method solution of the periodic problem. It is therefore applicable to all scan angles, arbitrary shaped structures, arbitrarily placed feed points, lossy conductors, and dielectric substrates. This rigorous theory capable of predicting the occurrence of blind spots. Measurements from a waveguide simulator of a scan blindness condition confirm the theory.

INTRODUCTION

This report presents a rigorous but efficient solution to the problem of an infinite planar array of printed dipole antennas on a grounded dielectric substrate. The model of an infinite planar array is used because microstrip phased arrays can contain hundreds to thousands of elements. Such arrays can operate at microwave or millimeter wave frequencies on dielectric substrates, where surface wave coupling can lead to scan blindness, where no effective power is transmitted or received by the array. Another point of interest to the array designer is the variation of antenna impedance with scan angle, which is important for impedance matching.

Usually a microstrip antenna is excited either by a microstrip feed or a coaxial feed. The dipoles are assumed to be centerfed, so feed lines are not explicitly considered, although for thin substrates the effect of a balanced feed line through the substrate should be small. It can be assumed that the patch is excited by a linearly polarized plane wave [1]. This model gives result which are valid for most of practical microstrip antennas. It is shown that we can define the input impedance of microstrip dipole by using this model.

THEORY

The solution process begins by creating Thevenin's equivalent circuit at the feed point location [2]. To solve for the open-circuit voltage of the equivalent circuit, the problem is first solved with the feed removed. This is done by solving the moment method integral equation for the unknown surface density of aperture magnetic current. This current is approximated by «rooftop» function expansion. For an x-directed printed dipole, the open-circuit voltage V_{oc} is then found by integrating the total electric field over the length of the feed gap Δx. Replacing the feed gap by a perfectly conducting patch gives the short-circuit current I_{sc}. This involves solving integral equation with the feed gap replaced by a perfectly conducting patch. From the open-circuit voltage and the short-circuit current, the Thevenin circuit impedance of the microstrip phased array can be calculated

$$Z_{th} = \frac{V_{oc}}{I_{sc}}.$$

It should be noted that for both open-circuit voltage and short-circuit current calculations, the microstrip phased arrays consist only of conducting patches supported by dielectric substrate. Then it is assumed, that Z_{th} is input impedance of phased array microstrip dipole Z_{in}. By using Z_{in}, we can determine [3]

$$R(\theta,\varphi) = \frac{Z_{\text{in}}(\theta,\varphi) - Z_{\text{in}}(0,0)}{Z_{\text{in}}(\theta,\varphi) + Z_{\text{in}}^{*}(0,0)},$$

where R is reflection coefficient in feed line connected with microstrip dipole, θ and φ is the phased array scan angles. If $R(\theta_{bl},\varphi_{bl}) = 1$, then θ_{bl} and φ_{bl} are the microstrip phased array blindness angles. This rigorous theory is capable of predicting the occurrence of blind spots.

NUMERICAL RESULTS

This section presents some typical results, in the form of reflection coefficient versus scan angle and similar relationships of an array element polarizing scattering matrix. An infinite planar array contains of identical dipoles printed on a grounded dielectric slab. The printed dipoles parameters are depicted as L and w, where L is the dipole length, w is the dipole width. The dielectric substrate has the following parameters: ε_r is related permittivity, h is

thickness. The dipole array periodicity is d_1 in E-plane and d_2 in H-plane. Fig. 1 shows the reflection coefficient magnitude $|R|$ (curve 1) and phase $\arg(R)$ (curve 2) in E-plane of scan for ε_r=2,55, $L = 0{,}39\lambda$, $w = 0{,}02\lambda$, $h = 0{,}19\lambda$, $d_1 \times d_2 = 0{,}5155\lambda \times 0{,}5000\lambda$. Note the presence of a unity reflection coefficient magnitude at $\Theta = 48^0$, where Θ is the scan angle. Therefore, in this case the scan blindness angle Θ_{bl} is equal 48^0. Other feature of relationship $|R|(\Theta)$ is Wood's anomaly at $\Theta = 69^0$. The presence of the last feature is confirmed by Fig.2 that shows the array elements polarizing scattering matrix S_{pp} variation in scan angle sector. If an incident wave polarization is vertical then index p is equal 1 (curves 1 is magnitude and 2 is phase). The case of a horizontal polarization is shown by curves: 3 is magnitude and 4 is phase.

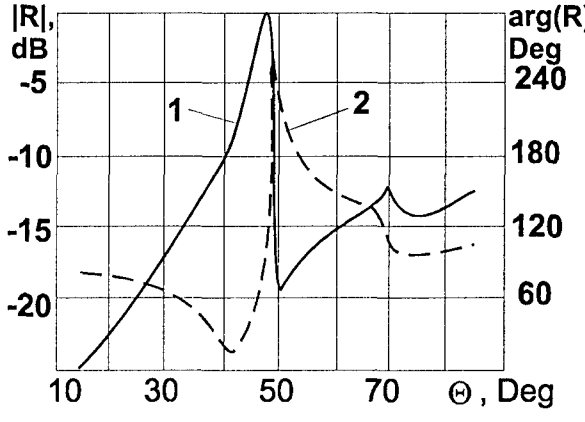

Fig. 1

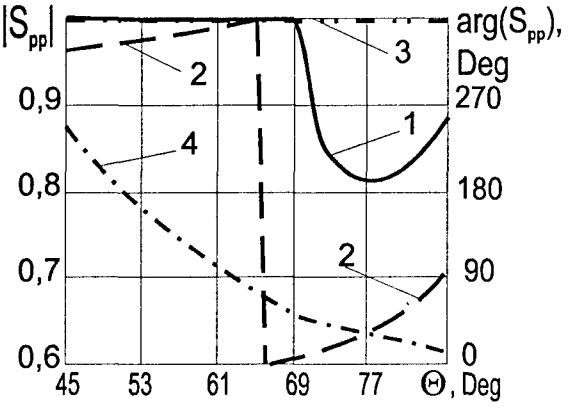

Fig. 2

It is shown that presented theory is capable of predicting the occurrence of blind spots

REFERENCES

[1] *Bailey M.C., Deshpande M.D.*, Gardiol F. Integral Equation Formulation of Microstrip Antennas //IEEE Trans. on Antennas and Propag. — 1982. — v.30. N4.— P.651—656.

[2] *Epp L., Chan C.H., Mittra R.* Periodic Structures with Time-Varying Loads //IEEE Trans. on Antennas and Propag. — 1992. — v.40. N3.— P.251—256.

[3] *Pozar D.M.* Analysis of an Finite Phased Arrays of Printed Dipoles //IEEE Trans. on Antennas and Propag. — 1985. — v.33. N10.— P.1045—1053.

EXCITATION OF THE INFINITE PERFECT CONDUCTING BICONE WITH IMPEDANCE AZIMUTAL SLOTS

A.A.Beletsky
Taganrog State University of Radioengineering
AiRPU dept., TSURE, Nekrasovsky, 44, GSP-17A, Taganrog, Rostov region, Russia, 347928
e-mail: beletsky@tgn.ru

ABSTRACT

The problem of the excitation of the infinite perfect conducting bicone with azimuth impedance slots on the surface by the arbitrary external sources is considered. The special case of the excitation by the homogeneous on azimuth magnetic current loop is investigated comprehensively. The eigen and complementary conductivities of impedance slots versus slots location are shown. Transition to the finite bicone radiator problem is considered. The calculated antenna patterns for several cases are depicted.

INTRODUCTION

The investigation of the bicone surface electromagnetic properties is of a great interest [1], because it can serve as a basis for designing wideband antennas. To obtain necessary characteristics, surface slots with dielectric filling are often used. Although the problem for the cone antenna with azimuth impedance slots is solved in [2], there are still no results for the bicone surface. Here the excitation problem of the infinite perfect conducting cone of arbitrary cone angles with azimuth impedance slots on the surface by arbitrary external sources distribution at one frequency is solved in general form.

THE PROBLEM STATEMENT

In the infinite homogeneous isotropic linear space of known parameters $\tilde{\varepsilon}_a$, μ_a there is the infinite perfect conducting bicone of known arbitrary cone angles γ_1, γ_2 (Fig. 1). On the bicone surface there are several azimuth slots at distance $R_{s_f}^{(f)}$ from the bicone apex, where $f = 1,2$ is the surface number, $s_1 = 1,\ldots,M_1$, $s_2 = 1,\ldots,M_2$, $M_{1,2}$ are slots count on the each surface. The width of the slots ΔR is small relative to the wave length. On the surface of the slots impedance boundary conditions are fulfilled. The surface impedances of the slots are denoted as $Z_{S_f}^{(f)}$. The boundary condition for the perfect conducting surface are met on the other bicone surface. Arbitrary external electric $\mathbf{j}^{e,p}(p)$ and magnetic $\mathbf{j}^{m,p}(p)$ currents distribution of one frequency ω is given in the volume V_j. The radiation condition are met at infinity. The problem is to find the electric field intensity and the magnetic field strength in the surrounding space.

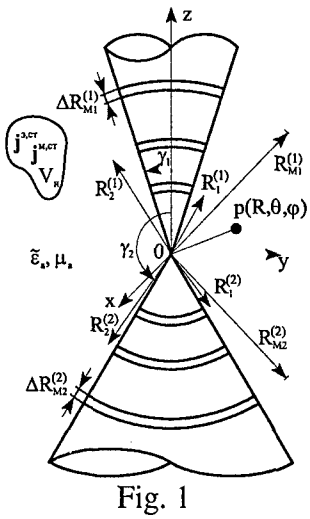

Fig. 1

ANALYSIS

The solution of the problem is based on the integral relation for the magnetic field strength $\mathbf{H}(p)$ [3]. For the auxiliary field $\mathbf{E}^m(q;p)$, $\mathbf{H}^m(q;p)$ we take the field of the magnetic dipole of direction $\mathbf{b}$ with the moment $I^m L = 1$ located in the point p in presence of the

infinite perfect conducting bicone without slots. Using the boundary conditions for the auxiliary field we have $\mathbf{E}^m = \mathbf{i}_\theta E_\theta^m$ ($\theta = \gamma_1$ or γ_2) on the bicone surface. Out of the slots the surface magnetic current is absent. On the slots surface due to their small width we can write $\mathbf{J}^m = \mathbf{i}_\varphi J_\varphi^m$. Dividing the slots surface into C sectors of the same angular size $\Delta\varphi = 2\pi / C$ and assuming the surface magnetic current density on the each sector to be constant we have:

$$\mathbf{bH}(p) = f(p) + \sum_{s_1=1}^{M_1}\sum_{c=1}^{C} J_\varphi^m(q_{s_1,c}^{(1)})\, s(q_{s_1,c}^{(1)}; p) + \sum_{s_2=1}^{M_2}\sum_{c=1}^{C} J_\varphi^m(q_{s_2,c}^{(2)})\, s(q_{s_2,c}^{(2)}; p), \qquad (1)$$

where

$$f(p) = -\int_{V_j}\left[\mathbf{j}^{e,p}(q)\mathbf{E}^m(q;p) - \mathbf{j}^{m,p}(q)\mathbf{H}^m(q;p)\right] dV_q, \qquad (2)$$

$$s(q_{s_f,c}^{(f)}; p) = \sin\gamma_f \int_{R_{sf}^{(f)}-\Delta R/2}^{R_{sf}^{(f)}+\Delta R/2} \int_{c\Delta\varphi}^{(c+1)\Delta\varphi} H_\varphi^m(R', \gamma_f, \varphi'; p)\, R'\, dR'\, d\varphi', \qquad (3)$$

$q_{s_f,c}^{(f)}$ is the point on one of the sectors. To obtain the required magnetic field strength $\mathbf{H}(p)$ we must find unknown surface magnetic current densities on all the sectors. Choosing $\mathbf{b} = \mathbf{i}_\varphi$ and using the impedance boundary conditions we have $H_\varphi = J_\varphi^m / Z$. Putting the observation point p on the surface of the arbitrary sector we obtain from (1):

$$\sum_{s_1=1}^{M_1}\sum_{c=1}^{C} J_\varphi^m(q_{s_1,c}^{(1)})\, s(q_{s_1,c}^{(1)}; p) + \sum_{s_2=1}^{M_2}\sum_{c=1}^{C} J_\varphi^m(q_{s_2,c}^{(2)})\, s(q_{s_2,c}^{(2)}; p) - \frac{1}{Z} J_\varphi^m(p) = -f(p), \qquad (4)$$

where function $\rho(q_{s_f,c}^{(f)}; p) = s(q_{s_f,c}^{(f)}; p)$ when points $q_{s_f,c}^{(f)}$ and p are the same, it is the eigen conductivity of the sector, and in the case the points are different it is the complementary conductivity of the sectors. Sequentially putting observation point on each of the sectors we get a linear set of algebraic equations on unknown surface magnetic current densities. The solution of the system and the statement (3) gives us the required magnetic field strength. The electric field intensity can be then found from the Maxwell's equations directly.

MAGNETIC CURRENT LOOP EXCITATION

Consider the antenna excitation by the magnetic current loop with the homogeneous on azimuth linear magnetic current density. In this case the required magnetic field density has only azimuth component and does not depend on φ coordinate. The auxiliary field can be found by the vector eigen functions method [4] as it was done in [5]. Numerical calculations of the own and complementary conductivity versus slots locations were carried out for two slots (one per surface) on equal distance from the bicone apex ($R_1^{(1)} = R_1^{(2)}$) and following parameters values: $\gamma_1 = 60^\circ$, $\gamma_2 = 120^\circ$, $\Delta R = 0.01\lambda$. Obtained results are shown in Fig. 2. Case (a) corresponds to the own conductivity, case (b) — to the complementary one. In both figures solid line is used for resistance (real part), and dashed line for susceptance (image part) of the conductivity.

TRANSITION TO THE CASE OF A FINITE BICONE

To consider the finite bicone radiator problem we used the following condition for the required magnetic field strength $\mathbf{H}(R,\gamma_{1,2},\varphi)=0$ when $R\to\infty$ (in the far zone). In such case the bicone can be shortened and we can obtain the model of the finite bicone radiator. To satisfy this condition one can, for example, choose complex surface impedance of two slots while fixing their locations on the bicone. Other slots parameters help us to obtain necessary antenna pattern. Using this techniques sample antenna patterns (solid line in Fig. 3), as well as partial patterns of the external source (dashed line) and the slots (dotted line) was calculated. The excitation was made by the magnetic current loop of radius $R_0=0.01\lambda$ and $\theta_0=90^\circ$. Slots location was $R_1^{(1)}=R_1^{(2)}=1.75\lambda$ for the case (a) and $R_1^{(1)}=R_1^{(2)}=2.60\lambda$ for the case (b).

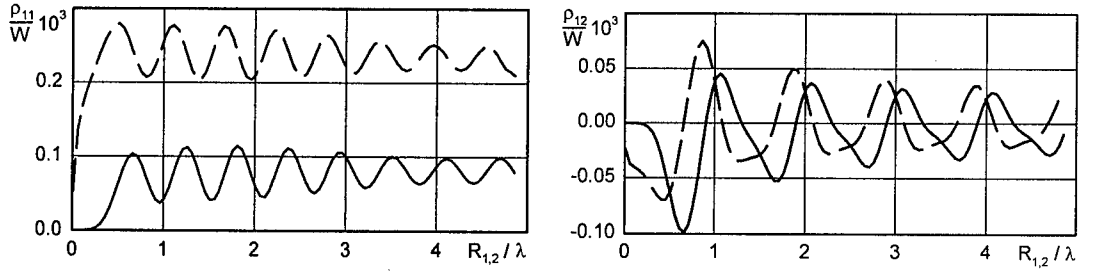

a b

Fig. 2. Eigen and complementary slot conductivities

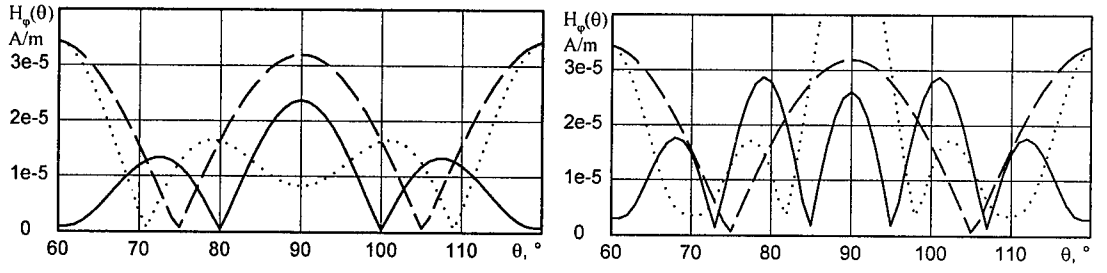

a b

Fig. 3. Antenna patterns

CONCLUSION

The solution of the excitation of the infinite perfect conducting bicone presented here is new and has certain scientific importance. The obtained results can be used for designing and analysing new radiators based on the bicone surface.

REFERENCES

[1] Voskresensky D.I., Ponomarev L.I, Filippov V.S. Convex scanning antennas. — M.: Sov. radio, 1978. [In Russian]

[2] Chaplin A.F., Tensin V.S. The field of the loaded circular slots array on the cone. // Radioelectonica, 1982, V.25, ¹ 2, pp.71–74. [In Russian]

[3] Markov G.T., Chaplin A.F. Excitation of the electromagnetic waves. — M.: Radio and Svyaz', 1983. — 296 p. [In Russian]

[4] Stratton J.A. Theory of the electromagnetic. — M., 1948. — 540 p. [In Russian]

[5] Petrov B.M., Balabuha N.P. Cone excitation by the arbitrary external currents distribution. // Radioelectonica, 1977, V.20, ¹ 11, pp.10–15. [In Russian]

3-D ANALYSIS OF THE COMPACT CELLULAR PHONE ANTENNAS

A. Bijamov. K. Tavzarashvili, R. Zaridze, and G. Bit-Babik
LAE, Tbilisi State University, Georgia; e-mail: lae@resonan.ge

ABSTRACT
Compact adaptive volume-resonant antennas with beam-steering capability can be employed in wireless applications. The described antennas can radiate the energy in desired direction within certain range of angles by changing the amplitudes and phases of feeding currents of the dipoles printed on the dielectric substrate with a conductive back surface. The improved efficiency entails a lower RF exposure of the user for equal power emitted compared to conventional cellular phone antennas. The 3-D Method of Integrated Auxiliary Sources (MAS) is employed to study the performance of the presented antenna.

INTRODUCTION
The majority of the existing antennas for portable mobile communication devices do not satisfy the requirements of high efficiency. The main reason is that their pattern is omni-directional whereas the radiation of RF energy just in the direction of a base station is enough for the reliable communication. The variability of the radiation characteristics of the antenna located in close proximity to the user body is also a significant drawback and worsens the efficiency of antenna because substantial portion of the total emitted energy is absorbed by the user in this case. Improvement of the efficiency of antenna increases the lifetime of rechargeable batteries [1].

MODEL
A 3-D structure is taken as the model of the antenna (Fig. 1). The dielectric medium with permittivity ε and permeability μ inside the antenna is used to increase the electrical sizes of the antenna for the beam steering. A thin perfectly conducting layer covers the backside to reduce back radiation. The printed dipoles of variable length, width and a gap in their center will be used as radiating elements and are fed with different amplitudes and phase shift. This gives a beam-steering capability to redirect the RF radiation in desirable direction and reduce the total radiated energy. The number of such dipoles, distances between them, phase shifts of feeding currents, permittivity and permeability of the substrate material as well as the sizes of the antenna and the area shielded by the conducting layer are the optimization parameters of the antenna.

METHOD
The problem is solved using the MAS [2]. According to the general algorithm of the MAS the fields inside and outside the body are represented by auxiliary sources located on the auxiliary surfaces outside and inside the body, respectively. The currents on auxiliary surfaces (auxiliary sources) are expanded in terms of sub-domain base functions which on the each sub-area of the auxiliary surface are piece-wise linear along the direction of the current and piecewise constant in the perpendicular direction. The fields radiated by these auxiliary currents inside and outside the antenna must satisfy the appropriate boundary conditions on the surface. Particularly the tangential components of the total electric and magnetic fields must be continuos on the dielectric surface of the body and the tangential component of the total electric field must vanish on the metal parts of the body.

It is known that the MAS gives fast convergence in comparison with singular Integral Equations and this effect becomes apparent if the all Scattered Field Singularities (SFS) [1-3] are taken into account. That is the case when the auxiliary surface encloses all SFS. In the present antenna structure the main SFS are the edge singularities of the printed dipoles and backside reflector, that due to geometry of the antenna are located directly on the real surface, so that they appear outside the auxiliary surfaces. To overcome the problem with the edge singularities and fulfil the condition on the edge by the Method of Auxiliary Sources it is sufficient to place some of the auxiliary sources of appropriate type close to the mentioned SFS [1-3].

The antenna surface is split into rectangular patches. As an auxiliary source a pair of neighbor patches is taken. On such pairs an elementary current is defined, flowing perpendicularly to the common boundary of the patches. Its magnitude decreases linearly from the common edge to the ends, where it turns to zero.

RESULTS

Using the described Method the following results in case of rectangular antenna excited in the middle of the spattered metal vibrator were obtained.

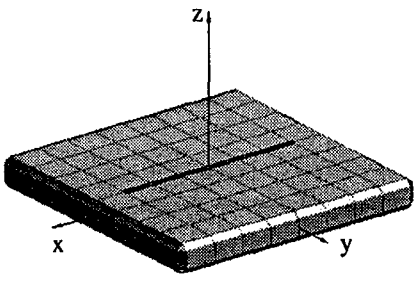

Fig 1. Antenna geometry

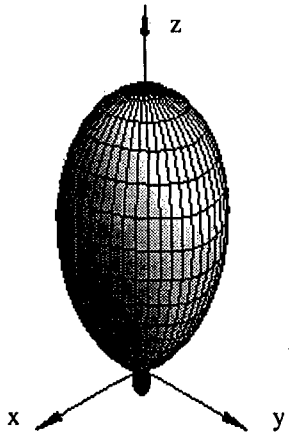

Fig 2. Radiation pattern

Geometrical sizes of the antenna are as follows: length 5cm, width 5cm, height 0.6cm, rounding radius for the edges of substrate 0.2 cm. Vibrator length 3.6cm, width 0.1cm, excitation applied at the center of gap 0.9 mm. Permittivity of antenna loading is 8, the excitation frequency 2GHz.

In Fig 2-4 patterns of the antenna are shown. The next figures 5a and 6a present the near field distribution of an

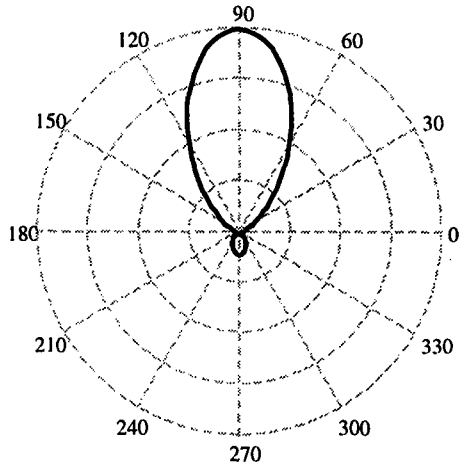

Fig. 3 Radiation pattern in YOZ plane
Maximum of radiation: 20.83 mV/m at 90 deg
Half-power beamwidth: 60.00 deg. at 100 m;

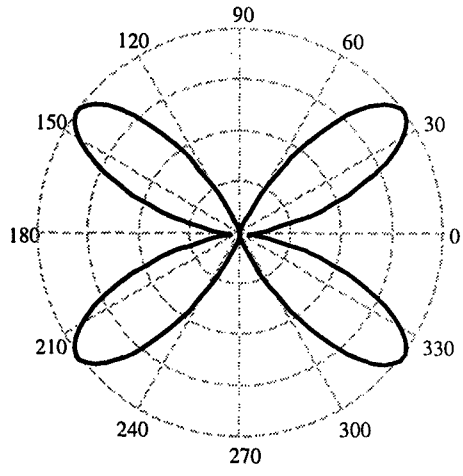

Fig. 4 Radiation pattern in XOY plane
Maximum of radiation: 0.75 mV/m at 216 deg
Half-power beamwidth: 38.00 deg. at 100 m;

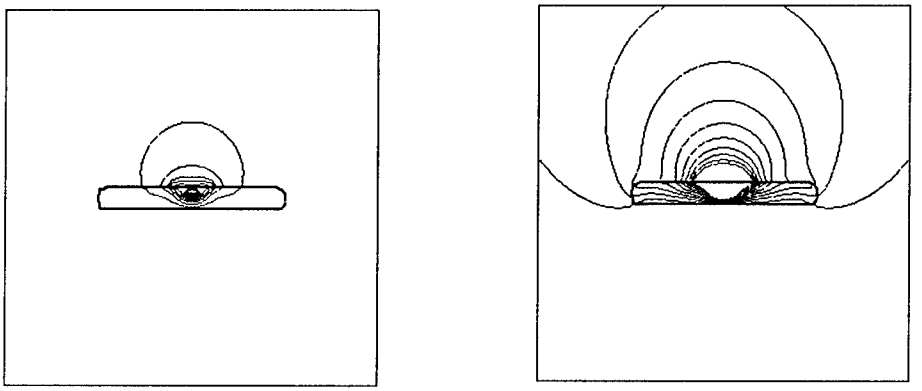

a) b)

Fig. 5
Ex field distribution in YOZ plane

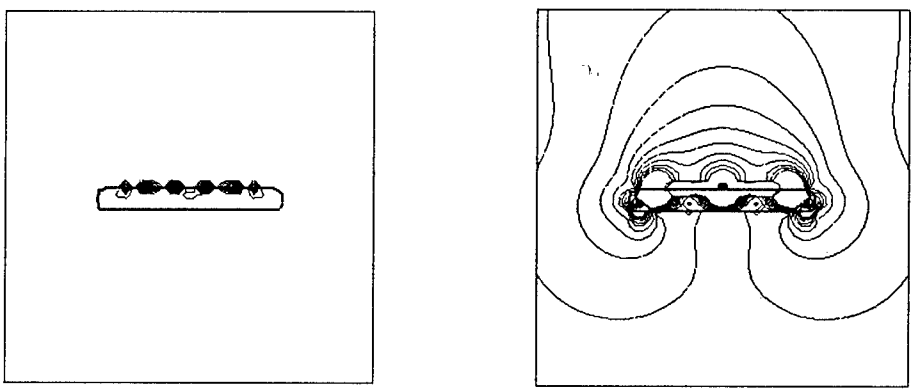

a) b)

Fig. 6
Ex field distribution in XOZ plane

antenna. Figs. 5b and 6b represent the fields with cut high magnitude levels.

REFERENCES

[1] R. Zaridze, G. Bit-Babik, K. Tavzarashvili, A. Bijamov. "The Method of Auxiliary Sources Applied to the Analysis of Adaptive Transverse Resonant Antennas." Proc. of the IEEE AP-S Intern. Symp. July 11-16, 1999, Orlando Florida, pp.2524-2527

[2] R. Zaridze, G. Bit-Babik, D. Karkashadze, R. Jobava, D. Economou and N. Uzunoglu. "The Method of Auxiliary Sources (MAS), Solution of propagation, Diffraction and Inverse Problems using MAS. Institute of Communication and Computers Systems," Athens, Greece, 1998, pp. 52.

[3] R. Zaridze, G. Bit-Babik, Ph. Shubitidze, R Jobava, K. Tavzarashvili, D. Karkashadze. "Generalized Method of Auxiliary Sources (MAS) and Applications." Proceedings of the 4-th Conference on Electromagnetic and Light Scattering by Nonspherical Particles: Theory and Applications, September 20-21, 1999, Vigo, Spain, pp. 289-296.

MODELING OF A SLOT-EXCITED FLAT DISK MICROSTRIP ANTENNA

N.Y. Bliznyuk, A.I. Nosich

Institute of Radiophysics and Electronics NASU
Ulitsa Proskury 12, Kharkov 61085, Ukraine
Tel.: 380 572 326129, Fax: 380 572 441105, e-mail: natali@info.kharkov.ua

ABSTRACT

Galerkin's method combined with the method of analytical regularization in the Hankel-transform domain is used to analyze a circular-disk metallic microstrip antenna excited by a horizontal magnetic dipole. This method has a controlled accuracy in the resonant range, and a much smaller matrix size in comparison to solutions obtained by direct applications of the Method of Moments.

INTRODUCTION

When microstrip structures are considered, many numerical techniques such as FDTD yield very large systems of linear equations. The known numerical solutions and commercial CAD packages based on the integral equations and the conventional method-of-moments (MOM) also require significant CPU time and memory resources [1]. Besides, near the sharp resonances both MOM and FDTD have a well known loss of accuracy [2]. Our method enables one to reduce noticeably the memory size and the computational time due to a much smaller truncated matrix size needed for a practical accuracy, and few numerical integrations for filling the matrix.

PROBLEM FORMULATION

Consider the geometrical configuration shown in Figure 1: a metallic circular disk of zero thickness, separated from the ground plane by a dielectric substrate of thickness h and permittivity ε. We shall assume that this structure is excited by a horizontal magnetic dipole (HMD) located on the ground plane in the origin of the cylindrical coordinates $\{\rho, \varphi, z\}$ of the axis z. Such a source simulates a slot feed. The disk and the ground plane are assumed to be perfectly electric conducting (PEC), the lossless substrate and the ground plane being infinite. All geometrical and wavelength parameters are dimensionless and normalized by the disk radius a.

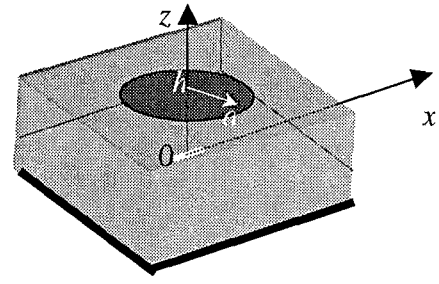

Figure 1: Geometry of the problem

The total electromagnetic field $\{\mathbf{E}, \mathbf{H}\}$ must satisfy the Maxwell equations in the layered medium, the tangential-components continuity at the dielectric surface, the PEC boundary conditions on the disk and the ground plane, a modified radiation condition, which takes into account the presence of the surface waves, and the edge condition on the disk rim. We shall assume the time dependence in the form $e^{i\omega t}$.

METHOD OF REGULARIZATION

The total electromagnetic field components in the free half-space and in the substrate satisfy the Helmholtz-type equations whose general solution in cylindrical coordinates is the following Hankel transform:

$$\int_0^\infty J_n(\kappa r)\left[F_{0,\varepsilon}^- e^{-\gamma_{o,\varepsilon} z} + F_{0,\varepsilon}^+ e^{-\gamma_{o,\varepsilon} z}\right]\frac{\kappa}{\gamma_{o,\varepsilon}} d\kappa \tag{1}$$

where κ, γ_0 and γ_ε are the radial and vertical components in the free half-space and in the substrate, respectively, of the wavenumber: $k_{0,\varepsilon}^2 = \omega^2 \varepsilon_{0,\varepsilon}\mu = \kappa^2 + \gamma_{0,\varepsilon}^2$; $F_{0,\varepsilon}^{-,+}$ are the unknown functions. Further, after satisfying the PEC and continuity boundary conditions and combining some of the terms we obtain a set of coupled dual integral equations (DIE), as it has been done in [3]:

$$\begin{cases} \int_0^\infty J_0(\kappa r)\alpha_0(\kappa) d\kappa = 0, & r > 1 \\ \int_0^\infty J_0(\kappa r)\left\{\beta_0^+(\kappa)\left[\alpha_0(\kappa) + \alpha_2(\kappa)\right] + \beta_0^-(\kappa)\left[\alpha_0(\kappa) - \alpha_2(\kappa)\right]\right\} d\kappa = \Pi_0 & r \le 1 \end{cases} \tag{2}$$

$$\begin{cases} \int_0^\infty J_2(\kappa r)\alpha_2(\kappa) d\kappa = 0, & r > 1 \\ \int_0^\infty J_2(\kappa r)\left\{\beta_2^+(\kappa)\left[\alpha_0(\kappa) + \alpha_2(\kappa)\right] + \beta_2^-(\kappa)\left[\alpha_0(\kappa) - \alpha_2(\kappa)\right]\right\} d\kappa = \Pi_2 & r \le 1 \end{cases} \tag{3}$$

where $\beta_0^+ = -\beta_2^+ = -\dfrac{\gamma_o \gamma_\varepsilon \sinh(\gamma_\varepsilon h)}{k a_0^2 D_m(\kappa)}$, $\beta_0^- = \beta_2^- = \dfrac{\sinh(\gamma_\varepsilon h)}{D_e(\kappa)}$,

$D_m(\kappa) = \gamma_\varepsilon \sinh(\gamma_\varepsilon h) + \varepsilon\gamma_0 \cosh(\gamma_\varepsilon h)$, $D_e(\kappa) = \gamma_\varepsilon \cosh(\gamma_\varepsilon h) + \gamma_0 \sinh(\gamma_\varepsilon h)$.

Real zeros of the denominators D_m and D_e determine propagation constants of the TM and TE surface wave modes of the lossless substrate that can propagate in the structure considered due to the excitation. Functions $\Pi_0(\kappa)$ and $\Pi_2(\kappa)$ are determined by excitation and depend on material and electrical parameters of antenna.

In (2)-(3) we introduced the unknown Hankel-transfom of the current densities on the disk $\alpha_0(\kappa)$ and $\alpha_2(\kappa)$. The next step is to transform DIE (2)-(3) into a block infinite matrix equation of the Fredholm second kind that guarantees convergence of numerical solution. Therefore we discretize DIE by using a Galerkin's projection scheme (GPS) with two sets of judiciously chosen basis functions that satisfy the edge condition on the disk rim in the image domain and provide the analytical Hankel transform:

$$\xi_n^m(\kappa) = \sqrt{4n + 2m + 3}\, J_{2n+m+3/2}(\kappa)\kappa^{-1/2}, \tag{4}$$

where m is the order of the Bessel function in DIE. The functions (4) are proportional to the spherical Bessel functions and are orthogonal on the interval $\kappa \in (0, \infty)$. We expand the unknown functions $\alpha_{0,2}(\kappa)$ in terms of these bases:

$$\alpha_0(\kappa) = \sum_{n=0}^{\infty} a_n^0 \xi_n^0(\kappa), \quad \alpha_2(\kappa) = \sum_{m=0}^{\infty} a_m^2 \xi_m^2(\kappa), \tag{5}$$

where a_n^0 and a_m^2 are unknown expansion coefficients. Further, we extract the free-space disk static (singular) parts of each of DIE by introducing the function $\Omega(\kappa)$, such that

$$\beta_0^+(\kappa) = \frac{-\kappa}{(1+\varepsilon)k_0^2}\left\{1 - \Omega(\kappa)\right\}, \quad \Omega(\kappa) = 1 - (1+\varepsilon)\frac{\gamma_o \gamma_\varepsilon \sinh(\gamma_\varepsilon h)}{\kappa D_m(\kappa)} \tag{6}$$

Here, if $k \to 0$, and $h/a \to \infty$, $\Omega(\kappa) = 1 + 0(\kappa^{-2})$ as $\kappa \to \infty$. Due to both this extraction and the expansion in terms of functions (4), we can invert analytically and diagonalize the second equations of each DIE (2)-(3). Here we use the analytical transform, the property of orthogonality of the Bessel functions and obtain a block-type infinite matrix equation in the transform domain:

$$\begin{cases} a_k^0 + \sum_n a_n^0 A_{kn}^{00} + a_{k-1}^2 - \sum_m a_m^2 A_{km}^{02} = \varsigma B_k^0 \\ a_m^2 + \sum_m a_m^2 A_{km}^{22} + a_{k+1}^2 - \sum_n a_n^2 A_{kn}^{02} = -\varsigma B_k^2 \end{cases} \tag{7}$$

where $A_{kn}^{00} = \int_0^\infty \xi_k^0(\kappa)\xi_n^0(\kappa)\left(\frac{\varsigma}{\kappa}\beta^-(\kappa) - \Omega(\kappa)\right)d\kappa$, $A_{km}^{22} = \int_0^\infty \xi_k^2(\kappa)\xi_m^2(\kappa)\left(\frac{\varsigma}{\kappa}\beta^-(\kappa) - \Omega(\kappa)\right)d\kappa$,

$A_{km}^{02} = \int_0^\infty \xi_k^0(\kappa)\xi_m^2(\kappa)\left(\frac{\varsigma}{\kappa}\beta^-(\kappa) + \Omega(\kappa)\right)d\kappa$, $A_{kn}^{20} = \int_0^\infty \xi_k^2(\kappa)\xi_n^0(\kappa)\left(\frac{\varsigma}{\kappa}\beta^-(\kappa) + \Omega(\kappa)\right)d\kappa$,

$B_k^0 = \int_0^\infty \xi_k^0(\kappa)b_0(k)d\kappa$, $B_k^2 = \int_0^\infty \xi_k^2(\kappa)b_2(k)d\kappa$, $\varsigma = -k_0^2(1+\varepsilon)$,

$$b_0 = \frac{1}{\pi}\left[\frac{\varepsilon\gamma_0}{D_m(\kappa)} + \frac{(1-\varepsilon)\kappa^2 \sinh(\gamma_\varepsilon h)}{2D_m(\kappa)D_e(\kappa)}\right], \quad b_2 = -\frac{1}{2\pi}\frac{(1-\varepsilon)\kappa^3 \sinh(\gamma_\varepsilon h)}{D_m(\kappa)D_e(\kappa)}.$$

It can be shown that $\sum_{k,n=0}^{\infty} |A_{kn}|^2 < \infty$ [3]. Hence, (7) is the second–kind Fredholm equation in a space of square-summable number sequences l_2. The solution of (7) is similar to the cases of the vertical electrical dipole excitation and dielectric disk printed antenna considered in [3,4]. Both computer time and memory recourses have been decreased approximately in hundred times without a loss of calculation accuracy.

CONCLUSIONS

The method of analytical regularization combined with the Galerkin method has been developed to determine the fundamental antenna effects of a circular metallic patch antenna on a dielectric substrate backed by a PEC ground plane and excited by a centered horizontal magnetic dipole. Due to analytical inversion of the free-space static-part operator, the dual integral equations in transform domain proved possible to be converted into the infinite matrix equation of the Fredholm second kind. This matrix equation has been solved by means of the efficient numerical procedure. It is stable in the resonant region and enables one to reduce significantly the machine-time and memory resources.

REFERENCE

[1] J.R. Mosig, R.C. Hall, and F.E. Gardiol, 'Numerical Analysis of Microstrip Patch Antennas", in J.R. James and P.S. Hall (Eds.), Handbook of Microstrip Antennas, Peter Peregrinus, London, 1989, pp. 391-453.

[2] G.L. Hower, R.G. Olsen, J.D. Earls, J.B. Schnieder, 'Inaccuracies in numerical calculation of scattering near natural frequencies of penetrable objects,' *IEEE Transactions on Antennas and Propagation*, AP-41, 7, 1993, pp. 982-986.

[3] N.Yu. Bliznyuk, A. I. Nosich, A. N. Khizhnyak, 'Accurate Computation of a Circular-Disk Antenna Axisymmetrically Excited by an Electric Dipole', *Microwave and Opt. Technol. Lett.*, May 5, 2000, p.211-216.

[4] N.Yu. Bliznyuk, A.I. Nosich, Numerical Modeling of Axially Symmetric Dielectric Disk Antenna exited by Vertical Electric Dipole, *AP2000 Proceedings*, Davos, Switzerland, April 2000

REFLECTIVE TYPE ANTENNA ARRAYS AS THE SMART COVER ELEMENTS

V.A.Obukhovets, A.O.Kasyanov, and S.V.Piven

Taganrog State University of Radio Engineering, Russia.
GSP-17 A, Nekrasovsky str., 44, Taganrog, 347928, Russia
Tel.: (86344)6-18-83, Fax (86344) 6-5019, E-mail: vao@ tsure.ru

ABSTRACT

In this paper, the microstrip reflective antenna arrays (RAA) are considered. The possible RAA application area is discussed and it is shown that RAA are the very attractive type for smart cover designing at microwaves. Computer simulation is made using mathematical model based on periodical structures theory and integral equation system solution. Some numerical results presented prove the possibility of RAA application as smart cover microwave modules.

INTRODUCTION

Reflective type antenna arrays have a series of remarkable properties in comparison with other types of antennas. Having practically all possibilities, which are peculiar to antenna arrays of so called transfer type, RAA differ by a greater simplicity and reduced cost. To their number first of all it is possible to refer the antenna arrays (including scanning ones) constructed with the use of optical type beamforming systems and various types of diffraction gratings. RAA can be fed by a field of an incident plane wave or concentrated source connected with the array port through Y-circulator. The radiators of a reflective array can be loaded by uncoupled loads possessing generally a complex character of an impedance, or by multiport network of a complicated structure - so-called beamforming networks.

An angular, polarizing and frequency filters, slowing down systems, etc. can be constructed on the base of RAA. The microstrip technology is the most perspective one of their manufacturing. In this case RAA not only have minimum possible mass and dimensions, but also can be designed as conformal arrays. It is also possible to make the multiport network as a microstrip printed circuit and place it on the second layer in immediate proximity from the elements of the array. Array elements control system can be made as another printed circuit board arranged at the next layer. There may be other layer(s) with some auxiliary elements and circuits. Such RAA packaging are irreplaceable as onboard antenna systems.

The potential microstrip reflective array application area is extremely wide: radar, telemetry, communication systems, systems of targets identification, ecological monitoring systems, etc. However, in last years the completely new direction, which is capable to join and even to integrate the above listed variants of RAA applications, is a very timely topic among the specilaists. That is so-called smart covers ("clever covers", "intellectual covers", "smart materials", "smart structures") [1,2]. Such covers are supposed to integrate different functions of many devices and to solve a lot number of problems. They are: creation of flexible rebuilt beamforming antenna systems; systems of sensors operating at various frequency bands, signal (pre)processing systems; scattering fields control systems, adaptive antenna arrays and adaptive antiradar covers, etc. In USA the problem of developing smart covers was announced as a priority scientific and engineering problem. Under the judgment of the foreign experts its successful solution will allow in XXI century to ensure the military superiority in the world.

The reflective microstrip RAA are the most convenient variants of smart covers designing at microwaves. Several possible application of microstrip RAA are considered as the elements of smart covers for antenna arrays creation, electronically tuned frequency (or angular) selective surfaces, polarization filters, radants, decoupling structures for EM compatibility systems, etc. The numerical simulation was made using simple physical model of RAA re-radiating element (Fig.1). It is

shown that the model is Floquet channel, where 1 is the microstrip re-radiating element, 2 is the ground plane, 3 and 4 are controllable loads. The dielectric substrate has thickness of h and the volume V_2. Other RAA parameters d_1 and d_2 are steps of array.

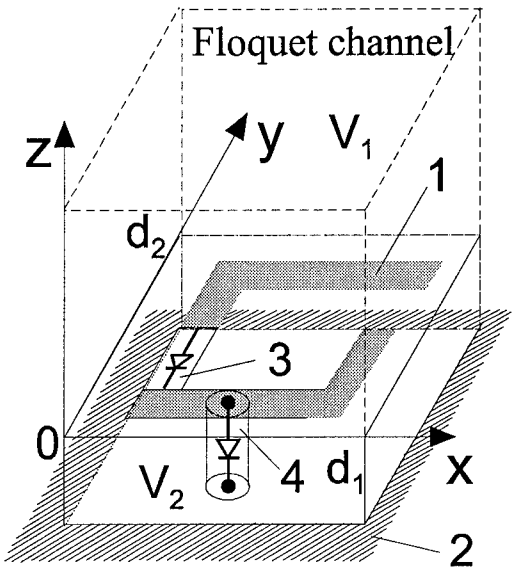

It is shown that RAA re-radiating element consists of conducting plate of arbitrary shape with several shunts which connect the patches both element by element (Fig.3) and with the screen (Fig.4). Those shunts may be short circuits. But some of them may represent diode switches for fields control. In that case their impedance distribution functions $Z_l(z)$ are none zero ones.

The diodes (Fig.3) are 2D-type controllable elements. The diodes in Fig.4 are 3D-type controllable elements.

The purpose of the present work is to construct a controllable RAA mathematical model, and then to analyze possibilities of scattering fields control by such smart cover.

Assume that plane electromagnetic wave excites this structure. Now it is possible to construct a model of a lattice.

MATHEMATICAL MODEL

Microstrip RAA being used as a smart microwave cover has a large number of re-radiating elements. Thus, RAA mathematical model is founded on the concept of periodical structures. The basis of a model is the system of integral equations concerning distribution of surface magnetic currents $J^{M}_{x,y}(x,y)$ in one period aperture of array and electric currents $I^{\vartheta}_{z}(z)$ on the shunts. The integral equations system is:

$$\int_{S_A}\left\{J^{M}_{x}(q)\left[\Gamma^{1x}_{22x}(q,p)+\Gamma^{2x}_{22x}(q,p)\right]+J^{M}_{y}(q)\left[\Gamma^{1y}_{22x}(q,p)+\Gamma^{2y}_{22x}(q,p)\right]\right\}ds_q + \sum_{l=1}^{N}\int_{-d}^{0} I^{\vartheta}_{z_l}(z')\Gamma^{2z}_{21x}(x_l,y_l,z'/x,y,0)dz' = -H^{inc}_{x}(p), \tag{1}$$

$$\int_{S_A}\left\{J^{M}_{x}(q)\left[\Gamma^{1x}_{22y}(q,p)+\Gamma^{2x}_{22y}(q,p)\right]+J^{M}_{y}(q)\left[\Gamma^{1y}_{22y}(q,p)+\Gamma^{2y}_{22y}(q,p)\right]\right\}ds_q + \sum_{l=1}^{N}\int_{-d}^{0} I^{\vartheta}_{z_l}(z')\Gamma^{Mz}_{21y}(x_l,y_l,z'/x,y,0)dz' = -H^{inc}_{y}(p), \tag{2}$$

$$\int_{S_A}\left\{J^{M}_{x}(q)\Gamma^{2x}_{12z}(q/x_l,y_l,z)+J^{M}_{y}(q)\Gamma^{2y}_{12z}(q/x_l,y_l,z)\right\}ds_q + \sum_{l=1}^{N}\int_{-d}^{0} I^{\vartheta}_{z_{ij}}(z')\Gamma^{2z}_{11z}(x_l,y_l,z')/x_l,y_l,z)dz' = 2\pi a\cdot Z_l(z)I^{\vartheta}_{z_l}(z). \tag{3}$$

Where S_A is the unit cell aperture, N is the number of shunts, a is the shunt radius, $H^{inc}_{x,y}(p)$ is incident plane wave field, $\Gamma^{(1,2)\nu}_{i,j\,\mu}(q/p)$ are the tensor Green function components. For exterior

(superscript 1) and interior (index 2) areas of the array they are determined from a solution of the appropriate auxiliary problems. Above mentioned currents obtained from system (1) - (3) solution allows to determine all main performances of RAA.

NUMERICAL RESULTS

The mathematical model allows to analyze numerically the microstrip RAA as functional modules for several types of device designing. Integral equation set was solved by the moment method using the "rooftop" function currents expansion [3].

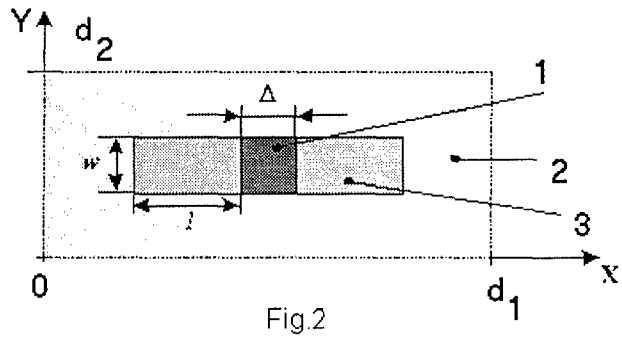

Fig.2

Some numerical results of investigating the microstrip RAA properties have been shown in [3]. The above mentioned outcomes concern arrays, in whose structure there are controllable loads of a 3D-type. Now we shall consider scattering performances of RAA with 2D-type controllable loads. The model of these loads is shown in Fig. 2, where 1 is the microstrip vibrator, 2 is the dielectric substrate, and 3 is the resistive inclusion. The resistive inclusion is 2D-type controllable load model. The resistive inclusion has a surface resistance R (Ohm/m). The X-component of an electrical current distribution in a microstrip vibrator with a 2D-type controllable load is shown in Fig. 3. The light strip in Fig.3 is a 2D-type controllable load. Such RAA element of a polarizing scattering matrix frequency relationships are shown in Fig. 4. The value of a surface resistance R is a parameter in these relationships.

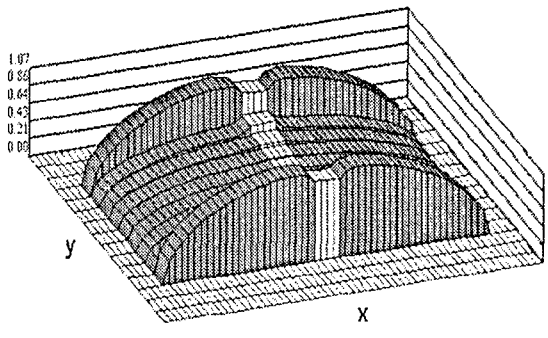

Fig. 3

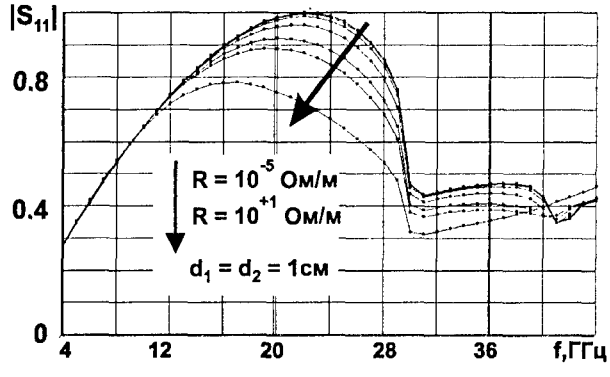

Fig. 4

REFERENCES

[1] USAP Join Navy for "Smart" Towed Decoy. Aviation Week and Space Technology, 1995, p.40.

[2] FitMimona Bernard. Smarter Weapons. Aerospace. 1995, vol.22, No.7, p.26-29.

[3] Kasyanov A.O., Obukhovets V.A. Current Control in Microstrip Antenna Array with Loaded Elements//"Radiotehnika", 1995, No. 12, p.32-36 (in Russian).

EM ANALYSIS OF PBG SUBSTRATE MICROSTRIP CIRCUITS FOR INTEGRATED TRANSMITTER FRONT END

Andrey S. Andrenko, Yukio Ikeda, Kazutomi Mori, and Osami Ishida

Information Technology R&D Center
Mitsubishi Electric Corporation
5-1-1 Ofuna, Kamakura, Kanagawa 247-8501, Japan
Fax: 81-467-41-2519
E-mail: andrey@isl.melco.co.jp

ABSTRACT

In this work, electromagnetic analysis of a novel photonic bandgap (PBG) substrate microstrip line circuit is presented and its applications in integrated antenna amplifier transmitter front end are discussed. Method-of-Moments based Sonnet Suite has been used for full-wave 3D electromagnetic simulation of the microstrip on high-density substrate having rectangular air blocks. It is shown that a single row of air blocks consisting of only 3-5 elements of an optimized dimensions produce very steep and wide (up to 10 GHz) bandgap for microstrip mode. The results obtained demonstrate that such a structure has high potential for designing novel low-pass and bandpass filters and integrated amplifier tuning elements. Transmission-line-circuit method has been applied in obtaining analytical conditions of stopband and passband for the circuit considered. The proposed structure can be mass-produced by micro drilling in a conventional high-density substrate.

INTRODUCTION

During the last decade, increasing attention has been focused on the development and applications of photonic bandgap configurations in RF/microwave integrated devices. Their applications include increasing the gain and bandwidth improvement in patch antenna design [1], broad band power amplifier [2], and microwave bandpass filter design [3]. Currently, compact layout and efficient performance are important factors for the development of the next-generation communications wireless handsets. In integrated transmitter front ends, the design of an amplifier output circuit becomes a major issue, as it has to provide both matching and tuning functions into the active element-antenna configuration. Accurate simulation of the periodic circuit used is required as it provides deep insight into the propagation and scattering properties as well as geometry optimization for the better practical performance. In this paper, we present the EM simulation of PBG-like high-density substrate microstrip circuit and discuss its potential for harmonic tuning in a MMIC integrated power amplifier and transmitter front end design.

ANALYSIS AND DESIGN

The geometry of the structure considered is depicted in Fig. 1. Microstrip PBG circuit is formed by periodic array of material blocks in the substrate. Generally, it is possible to assign any value of dielectric constant to the blocks, both higher and lower of that of the substrate. In the present study, we consider rectangular air blocks introduced in alumina substrate ($\varepsilon_r = 10.5$) for enabling the effects of high/low characteristic impedance distribution along the circuit as well as local scattering and diffraction within the host dielectric layer.

Method-of Moments based Sonnet simulation suite has been used for the detailed numerical analysis of scattering and propagation properties of microstrip line on the PBG-like periodic substrate because it explicitly incorporates 3-D material blocks in planar dielectric layers of the circuit. Simulation data show that, because of microstrip mode field confinement, S-parameters of one-row PBG substrate microstrip are practically identical to those of three-row structure of the same geometry. Hence, the size of air blocks used would define the transverse dimension of the proposed circuit making it of the order of 2-3 mm.

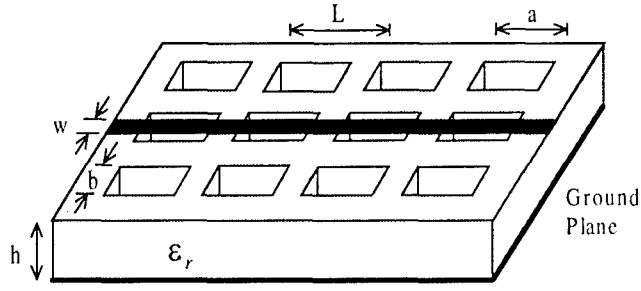

Fig. 1. Geometry of a periodic PBG substrate microstrip line.

The example of a 5-element PBG circuit S-parameters is presented in Fig. 2. Deep and wide stopband from 7.9 to 17.9 GHz is produced. In this case, if an active device fundamental frequency is set at 4 GHz, both second and third harmonics are placed within the circuit stopband and don't reach the antenna integrated with amplifier. Moreover, the phase characteristics of the reflected signals have to be taken into account for achieving high efficiency of amplifier considered. Simulation results show that the circuit with S-parameters presented in Fig. 2 is perfectly short for the second harmonic and very close to open circuit for the third harmonic. This example demonstrates that an ideal case of amplifier class-F operation characterized by high efficiency can be provided by an output PBG circuit. It should be noted that the passband and stopband frequencies as well as phase characteristics depend on the period and the size of substrate's air holes and are therefore scalable in a wide frequency range.

The initial circuit design can be based on the Bragg condition, which together with evaluation of phase constant of microstrip mode for two-layer substrate by spectral-domain approach yields the following approximate formula for the central stopband frequency

$$f_c = \frac{c}{4L} \tag{1}$$

It should be noted that (2) can be used only to evaluate the single stopband frequency for the given period L, however the other important design parameters of a PBG substrate microstrip structure, such as stopband width and passband frequencies, would be obtained from EM simulation of an actual periodic configuration. According to transmission matrix approach, the total voltage-current transmission matrix of a periodic circuit is defined as

$$[F_T] = [F]^N, \tag{2}$$

where $[F]$ is the matrix of one period and N is the number of elements. Defining $[F]$ as a matrix product of microstrip over air block and that on the conventional substrate with length l=L-a and expressing F -matrix of a two-port circuit in terms of line impedance and phase length yields

$$[F]=\begin{bmatrix} (\cos\theta_1\cos\theta_0 - C\sin\theta_1\sin\theta_0) & jZ_0(\cos\theta_1\sin\theta_0 + C\sin\theta_1\cos\theta_0) \\ jZ_0^{-1}(\cos\theta_1\sin\theta_0 + C^{-1}\sin\theta_1\cos\theta_0) & (\cos\theta_1\cos\theta_0 - C^{-1}\sin\theta_1\sin\theta_0) \end{bmatrix}, \quad (3)$$

where $\theta_1 = 2\pi a\lambda^{-1}$, $\theta_0 = 2\pi l\lambda_\varepsilon^{-1}$, $C = Z_1 Z_0^{-1}$ and Z_1, Z_0 are the characteristic impedance of the line over air block and substrate, respectively. Substituting (3) into (2) and using relations between S-parameters and A,B,C,D parameters of matrix (2), one can obtain the conditions of passband $|S_{11}| = 0$ and stopband $|S_{11}| = 1$.

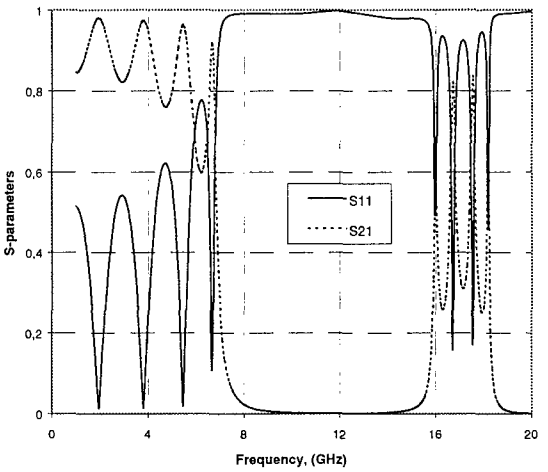

Fig. 2. S-parameters of 5-element PBG substrate microstrip circuit with a=6.0mm, b=2.5mm, L=9.5mm. Parameters h and w correspond to 50 Ohm microstrip line.

The formulas and simulation results reveal the fact that the number of passbands on the frequency axis between origin and the stopband equals the number of elements forming the periodic structure while the PBG circuit consisting of the very few blocks of the optimized geometry produces deep and wide stopband. Calculated distribution of current density along the microstrip line shows that within the stopband the current from an input port penetrates only one period of PBG circuit, which makes it possible to substantially reduce the length of the filter considered.

CONCLUSIONS

EM simulation of microstrip PBG high-density substrate circuit has been presented. The results obtained demonstrate high potential of the proposed structure for the design of integrated antenna power amplifier tuning circuits and compact microwave filters.

REFERENCES

[1] Y. Qian, R. Coccioli, D. Sievenpiper, V. Radisic, E. Yablonovitch, and T. Itoh, " A microstrip patch antenna using novel photonic band-gap structures," *Microwave Journal*, vol. 42, no. 1, pp. 66-76, Jan. 1999.

[2] V. Radisic, Y. Qian, and T. Itoh, "Broad-band power amplifier using dielectric photonic bandgap structure," *IEEE Microwave Guided Wave Lett.*, vol. 8, no. 1, pp. 13-14, Jan. 1998.

[3] M.J. Erro, T. Lopetegi, M.A.G. Laso, D. Benito, M.J. Garde, F. Falcone, and M. Sorolla, "Novel wideband photonic bandgap microstrip structures," 29th European Microwave Conf. Proc., Munich, 1999, pp. 345-348.

ANALYZING THE HF FIELD IN THE WAVE ZONE OF THE ANTENNA USING THE NORMAL-MODE APPROACH

Vitaly V. Khakhinov

Institute of Solar-Terrestrial Physics SD RAS
P.O.Box 4026 Irkutsk, 664033, Russia
E-mail: khakhin@iszf.irk.ru

ABSTRACT

An analysis is made of the overall representation of the HF field as a series of normal modes at wave zone ranges of an arbitrary emitter, based on using Poisson's approximation summation formula, as a result of which the series of normal modes is transformed to the integral. Inside the Earth-ionosphere waveguide, the integral is evaluated by the stationary phase method, and the field is determined by characteristics of two normal modes. At the ground, the integral is brought to Fock's diffraction formula, which calculates the field in the regions of geometrical shadow and semi-shadow. The computational formulas make it possible to use algorithms and programs of the normal mode approach that were developed for long-range radio paths.

INTRODUCTION

Historically, the normal mode approach was developed in regard to the long-distance communication problem [1,2]. It is along long-range radio paths where the signal field is formed by a small number of normal modes. The method affords high versatility and speed in numerical calculations of HF field characteristics within large regions of the Earth-ionosphere waveguide at ranges from one hop to radio echo with many-second-long delays. The main problem when using the method at shorter ranges implied the need for summation of a series of ~10^5 normal modes. In [3], authors proposed method of calculation based on transforming a series of normal modes using Poisson's formula. This offers a way of investigating the effectiveness of the method in calculations at wave zone ranges of the antenna field.

ANALYZING THE HF RADIATION FIELD

Consider the spherical Earth-ionosphere waveguide in the geocentric frame of reference with the polar axis passing through the emitter center. In the selected waveguide model, an arbitrary j-th component of the electric field represents a series in terms of normal modes:

$$E_j(\boldsymbol{r}) = \sum_n p_j R_n(y) D_n(\boldsymbol{I}, R_n(y_0), F_n) e^{i(\nu_n \theta - \pi/4)} \qquad (1)$$

Here $\boldsymbol{r} = (r, \theta, \varphi)$ is the radius-vector of the observation point, $y = r/a$, a is the Earth radius, $y_0 = 1 + h/a$, h is the antenna altitude, p_j is the polarization factor, D_n corresponds to coefficients characterizing the degree of excitation of normal modes by the antenna with a given distribution of current $\boldsymbol{I}$, and R_n and ν_n are eigenfunctions and values of the radial boundary-value problem:

$$R_n(y) = C_n\left[u(x_n)\cos\left(\frac{1}{2i}\ln\tilde{V}_n\right) - v(x_n)\sin\left(\frac{1}{2i}\ln\tilde{V}_n\right)\right], \tag{2}$$

$$\nu_n = ka\gamma_n + i\nu_{2n},$$

where $x_n = -\left(\frac{3}{2}ka\int_{\gamma_n}^{y}\sqrt{1-\gamma_n^2/y^2}\,dy\right)^{\frac{2}{3}}$, $x_{1n} = x_n(y=1)$, $\tilde{V}_n = \frac{\omega_2(x_{1n})}{\omega_1(x_{1n})}V_n$, V_n is the reflectance of the normal mode from the Earth spherical surface, C_n is a normalization factor, and $\omega_{1,2}(x_n) = u(x_n) \pm iv(x_n)$ is the first and second Airy functions. The number of the waves combined is ~10^5.

First we consider the situation where the observation point lies high above the ground. In this case it is appropriate to use asymptotic representations of the Airy functions at large negative values of the argument. Radial functions and their derivatives take the form of a WKB solution, which are representable as the sum of two exponentials. In (1), four terms appear under the summation sign. We transform (1) using Poisson's formula into a series in terms of integrals. The field in the wave zone of the antenna describes the zeros term of the series:

$$E_j(\boldsymbol{r}) = \frac{J_0}{c}\int_n \sum_{n=1}^{4} W_q e^{i(ka\psi_q - \pi/4)}dn \tag{3}$$

Explicit expressions for the amplitudes W_q and phases ψ_q are readily obtained, and are not given here. Because of the factor ka~10^5 involved in the phases, it is possible to evaluate the integrals by the stationary phase method. Equations defining stationary points have the next form:

$$d\psi_q/dn = 0 \tag{4}$$

Only two equations of four have strict solutions. Let n_1 and n_2 be the solutions to equations (4). Upon integration in (3), we get:

$$E_j(\boldsymbol{r}) = \frac{J_0}{c}\sum_{q=1}^{2}\frac{F_q}{G_q}p_j e^{i(ka\psi_q - \pi/2)} \tag{5}$$

We do not reproduce here the explicit expressions of the quantities involved in (5), but note the following. By comparing equations (6) with trajectory equations of rays in the wave zone of the antenna in geometrical optics, we obtain the well-known relations between the spectral parameter of the central normal mode of the wave train that forms the geometrical ray and the angular characteristic of this ray:

$$\gamma_q = y_b\cos\Delta_{bq} = y\cos\Delta_q = \cos\Delta_t. \tag{6}$$

These relations can be used to obtain a geometrical-optics interpretation of the quantities involved in (5). An analogue of F is the antenna beam, G is the factor of spherical divergence, and V is Fresnel's reflectance.

ANALYZING THE FIELD AT THE GROUND

We are coming now to the question of the field near the ground. In this case the domain of values of spectral parameters of the normal wave group, describing the field, is defined by the inequality:

$$|1-\gamma_n| \le 4m/ka\,, \quad m=(ka/2)^{1/3} \tag{7}$$

In this case it is possible to expand: $x_n \approx x_{1n} - kh/m$.

Upon the transformation of the series (1) by Poisson's formula in (3), we integrate with respect to x_{1n}. We consider the two terms in which in the case of an excess of the altitude of the observation point y an asymptotic expansion of the Airy functions leads to the above-mentioned WKB solutions describing the field inside the waveguide. Upon factoring the slowly-varying amplitude terms outside the integral sign, and after straightforward manipulations, we get:

$$E_j = \frac{F_n p_j}{2ac}\sqrt{\frac{m}{\pi \sin\theta}}\int \omega_1(x_n)\left(\omega_2(x_n) - \tilde{V}_n\omega_1(x_n)\right)e^{im\theta x_{1n}}dx_{1n}. \tag{8}$$

The resulting integral representation for calculating the field at the ground is within the factors associated with the selection of the system of units, and the directional patterns are consistent with the diffraction formulas obtained by V.A.Fock [4]. These formulas are obtained by investigating the field of dipole, which elevated over the Earth's spherical surface. The integral represents the attenuation factor.

CONCLUSIONS

In the overall representation of the HF field as a series of several tens of thousands of normal modes, we have included such factors as the Earth sphericity, the antenna characteristics, the displacement of the waves as they are reflected from the ground, and the characteristics in the regions of shadow and semi-shadow. At the range of direct visibility, the field is determined by characteristics of two normal modes. Computational formulas are straightforward, and each quantity has its interpretation known in the geometrical optics method or in the diffraction theory.

This work was done with support from the RFBR, a grant for leading schools of the Russian federation No. 00-15-98509.

REFERENCES

[1] Krasnushkin P.E. Normal Mode Approach,, A Applied to the Problem of Long-Range Radio Communications. Moscow: Izd-vo MGU, 1947, 52 p.

[2] Kurkin V.I. Orlov I.I. and Popov V.N. Normal Mode Approach in the HF Radio Communication peoblem. Moscow: Nauka, 1981, 122 p.

[3] Popov V.N. and Potekhin A.P. The structure of the HF impulse field in the Earth-wavegide. In: Issledovaniya po geomagnetizmu, aeronomii i fizike Solntsa. Moscow: Nauka, 1982, v.59, pp. 68-76.

[4] Fock V.A. Problems of Diffraction and Propagation of Electromagnetic Waves. Moscow: Sov. Radio, 1970, 520 p.

ACCOUNT OF MUTUAL RESISTANCE OF ARBITRARY SEPARATED TWO WIRE ANTENNAS

Sergey N. Sorokin, and Vladimir V. Savelyev
Taganrog State University of Radioengineering, E-mail airpu@tsure.ru
22 Chekhov str., Taganrog, 347915, Russia

ABSTRACT
In this work, the task of calculation of a field of the linear antenna arbitrary separated from feed points is solved. The received results are used for calculation of mutual resistance between vibrators depending on distance between them.

Let us consider a task of calculating the mutual resistance of vibrators of arbitrary length in the following statement. Assume a symmetric vibrator of length $L_1=2l_1$ is located in free space. Here l_1 is the length of the vibrator shoulder as shown in Fig.1. We assume, that the thickness of the vibrator it is much more less than working wavelength, and the current in the vibrator is distributed by the sine wave law

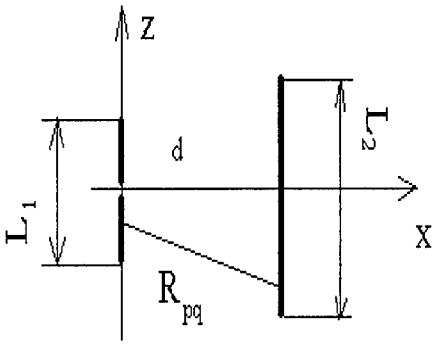

fig. 1

$$I(z)= I_p \sin(\beta z), \qquad (1)$$

where I_p is the peak value of a current on the vibrator.; $\beta=2\pi/\lambda$; λ is the working wavelength.
For short vibrators it can not be achieved in any points of the vibrator.
An expression for calculating the component of a complete field formed by vibrator 1 on the surface of vibrator 2 must be found. Vibrators 1 and 2 are parallel. The centre of the second vibrator will defend from points of a feed of the first vibrator on distance d. On the basis of the received expressions, the mutual resistance of system of two parallel vibrators must be calculated.

To solve this taks, we shall choose the local system of coordinates. Its beginning is compatible with points of a feed of the first vibrator, and the axis z is directed along a shoulder of the vibrator. Then, the longitudinal component of a vector of intensity of an electrical field will be defined by the following equation

$$E_z = -\frac{ikWI_{01}^{э}}{4\pi}\int_{-l_1}^{l_1} sink(l_1-|z_1|)\frac{e^{-ikR_{pq}}}{R_{pq}}[1+U/k^2]dz_1, \qquad (2)$$

Where $R_{pq}=\sqrt{d^2+z_1^2-2z_1z_2+z_2^2}$, d is the distance between the centers of vibrators;

$\dot{I}_{01}^{э,cm}$ is the complex amplitude of a current in the vibrator 1;

z_1 is the coordinate of an integration point on the surface of the first vibrator;

z_2 is the coordinate of a supervision point of a field on the surface of the second vibrator,

$$U=\{\frac{3ik(x_n-x_m)^2}{R_{pq}^2}-ik-k^2(x_n-x_m)^2/R_{pq}+\frac{3(x_n-x_m)^2}{R_{pq}^3}-\frac{1}{R_{pq}}\}/R_{pq},$$

The expressions for a component of a intensity vector of the magnetic field can be derived similarly.

Using the given expression, the following formula for calculation of mutual resistance of vibrators with numbers n and m was obtained:

$$Z_{nm}=\frac{ikW}{4\pi\ sin(kl_m)sin(kl_n)}\int_{-l_n}^{l_n} sink(l_n-|x_n|)\int_{-l_m}^{l_m} sink(l_m-|x_m|)\times \frac{e^{-ikR_{pq}}}{R_{pq}}[1+U/k^2]dx_m dx_n, \tag{3}$$

Note, that this expression can be used for calculating the pattern of vertical vibrators arrays [1].

The chosen current approximation allows with sufficient accuracy to predict mutual resistance of thin vibrators. But for vibrators of final thickness this approximation can result in significant errors even in a case, when length of the vibrator is equal to half of length of a wave of a raised field. It occurs because, for vibrators of final thickness, the current distribution along the vibrator can differ considerably from the specified one. To increase the accuracy of calculations, the current on the vibrator can be represented as decomposition to a series of system of orthogonal functions. Then, the expression for a current has the form [2]

$$I(x)=\alpha_m\sum_{n=1}^{N} I_n\ cos[(2n-1)\pi x/L] \quad , \tag{4}$$

where α_m is the proportionality factor, dependent on the distance between vibrators,

I_n is the amplitudes of basic functions, determined from the integrated equation,

N is the maximal number of basic functions.

In this case, factors of proportionality should be found from the equation set, into which the mutual resistance between vibrators will be entered. In this case, the iterative methods must be used. First, we find the current distribution on the single vibrator of final thickness. Second, by formula (3) we find mutual resistance of vibrators. The third step consist in calculating the correction factors by using the obtained value of mutual resistance. Then we repeate the second and third steps and obtain the desirable accuracy. The practice shows that 3 - 5 recurrences are enough to obtain a stable value of the correction factors and mutual resistance. The offered method is much easier than a direct solution of a set of integrated equations for several vibrators.

REFERENCE

[1] Sorokin S. N., Saveljev V. V. Use of computer algebra with account of the electromagnetic fields, created by systems of connecting vibrators. // Electromechanics, 1999, № 4, p.109-111/

[2] Computer techniques for electromagnetics. Edited by R. Mittra, University of Illinois, Pergamon Press, 1973. -486p.

MATHEMATICAL MODEL OF RADIATION FROM OPEN-ENDED CIRCULAR WAVEGUIDE EXCITED BY SYMMETRICAL TM_{01} AND TE_{01} MODES

A.V. Shishkova, N.N. Gorobets, and L.V. Orlova
Kharkov National University, 4 Svobody sq., Kharkov, 61077, Ukraine
E-mail: artel@online.kharkiv.com

A mathematical model of the radiation from an open-ended circular waveguide excited by the symmetrical modes TM_{01} and TE_{01} has been developed. Easy to use and reliable approximation expressions, which allow calculating power radiation pattern both for TM_{01} and TE_{01} waveguide excitation on the whole observation space, have been obtained. The mathematical model is based on the accurate solution developed by Weinstein. It has been shown that the approximation absolute error does not exceed 0.6 dB and 1.5 dB till the level – 30 dB for TM_{01} and TE_{01} modes respectively.

FORMULATION OF THE PROBLEM

At present, the problem concerned with increasing the accuracy of antenna system calculations is an important and urgent one for modern microwave engineering. Unfortunately, not so many antenna systems have accurate solution of the radiation problem. One of these is a problem of the radiation from an open-ended circular waveguide. For the first time, it was solved by L.A.Weinstein [1]. The radiation characteristics from an open-ended circular waveguide calculated by Weinstein method are well correlated with experimental data. It should be noted that this technique seems to be the only possibility to extend the range of the radiation theoretical investigation for such an antenna. The well-known aperture methods [2] do not allow to calculate the radiation characteristics for a multimode waveguide, but also give the results different from the experimental ones. In practice, the aperture Kirchhoff technique is often used for obtaining the radiation characteristics. However, this method produces accurate results only for the main lobe of the power pattern. It causes essential errors in the description of the side-lobe and backward radiation. In addition, this method does not allow to obtain phase pattern and to analyze the radiation from a multimode waveguide.

It is important to note that characteristics obtained by means of the accurate solution clearly interpret the physical processes of diffraction on the open-ended waveguide, namely:

1. This method takes into account the reflection of the mode excited in waveguide and the appearance of the higher-order modes transformed from the forward-propagating mode in some frequency bands. In particular, the TM_{01} mode can be transformed into TM_{0n} modes. This fact allows investigating the effect of higher-order modes on the radiation characteristics.
2. The accurate theory allows calculating the higher-order mode reflection, caused by diffraction on the open-ended waveguide.

However, in spite of all obvious advantages of the accurate theory, its practical utilization faces some difficulties. The final analytical expression given in [1] can not be used for obtaining the algorithm and the computation program. The difficulties are connected with the complex variable function theory and the factorization method used for the boundary problem solution. The analytical expressions both for power pattern and for phase one have many singularities, which should be carefully investigated. At last, the expressions for the phase pattern include infinite sums, which can be evaluated by means of hypergeometric digamma

and tetragamma functions. These difficulties concerned with the cumbersome and complicated final calculation expressions can be overcome if the computations once carried out would be approximated by simple functions with some beforehand assumed accuracy.
The purpose of the present paper is to obtain a simple mathematical model of the radiation from open-ended circular waveguide exited by symmetrical TM_{01} and TE_{01} modes.

APPROXIMATE MODEL

Based on the Weinstein accurate solution, an algorithm and a program for calculation of the amplitude and phase pattern have been developed. Using the computed results of the radiation characteristics from the open-ended circular waveguide, the mathematical model has been obtained. This model allows the exact calculation of the power pattern for symmetrical TM_{01} and TE_{01} waveguide excitation both for one-mode and multimode waveguide on the whole observation-space. The approximation functions of two variables, where the first one is connected with the directivity of a radiator (θ angle) and the second one is connected with the waveguide diameter ($x=2\pi a/\lambda$ is the undimensional wave number, a is the waveguide radius, λ is the wavelength), have been derived.
The approximation expressions for the power pattern, normalized to the power at the major radiation maximum, have been derived for TE_{01} and TM_{01} modes as follows:

$$P_{apr}^{TE} = \frac{1-|\cos\theta|}{1-\cos\theta_m}\left(\cos\frac{\theta-\theta_m^h}{2}\prod_{n=2}^{N_h}\frac{x\cos\theta-\gamma_n^h}{x-\gamma_n^h}\right)^2\left(\sum_{j=1}^{8}H_j\cos(j-1)\theta\right)^{MH}; \qquad (1)$$

$$P_{apr}^{TM} = \left(\frac{tg(\theta/2)}{tg(\theta_m/2)}\cos\frac{\theta-\theta_m^e}{2}\prod_{n=1}^{N_e}\frac{x\cos\theta-\gamma_n^e}{x-\gamma_n^e}\right)^2\left(\sum_{j=1}^{8}E_j\cos(j-1)\theta\right)^{ME}, \qquad (2)$$

where $\gamma_n^e=\sqrt{x^2-\nu_n^2}$, $\gamma_n^h=\sqrt{x^2-\mu_n^2}$; N_e, N_h is the number of higher-order modes, which can propagate in the waveguide for fixed parameter x for TM_{01} and TE_{01} excitation respectively ; ν_n is the n-th root of zero order Bessel's function, μ_n is the n-th root of first order Bessel's function. θ_m^e, θ_m^h are the angles of major maximum power direction for TE_{01} and TM_{01} modes respectively. The approximate expressions for θ_m^e, θ_m^h have been obtained as follows:

θ_m^e =99.55/x+10.99-0.568x, $x<\nu_2$; θ_m^h = 78.78/x+17.84-0.904x, $x<\mu_2$;
θ_m^e =142.08/x-0.48+0.018x, $\nu_2<x<\nu_6$; θ_m^h = 147.98/x+1.64-0.0485x, $\mu_2<x<\mu_5$. (3)

The approximate expressions for coefficients E_j and H_j for one mode range have been determined.

For TM_{01} mode:

$\nu_1<x<\nu_2$; ME=3
E_1= 1.0454/x+0.392-0.0455x;
E_2= -0.2436/x+0.8436-0.0519x;
E_3= -0.2571/x+0.2119+0.0317x;

For TE_{01} mode:

$\mu_1<x<\mu_2$; MH=4
H_1= 1.4933/x+0.3792-0.0367x;
H_2= -1.742/x+1.0065-0.0451x;
H_3= 0.1153/x+0.1296+0.0248x;

E_4= 0.2286/x-0.1438+0.0488x; H_4= 0.0217/x-0.1192+0.0347x;
E_5= 0.2046/x-0.1842+0.0522x-0.0028x^2; H_5= 0.12995/x-0.0409+0.0103x;
E_6= 0.1343/x-0.0782+0.0185x-0.001x^2; H_6= 0.006/x-0.0371+0.0063x;
E_7= -0.0793/x+0.0697-0.0208x+0.0023x^2; H_7= 0.13476/x-0.0361+0.0038x;
E_8= -0.048/x+0.0583-0.0182x+0.0018x^2. H_8= 0.01633/x-0.0136+0.00179x.

Since the expressions (1), (2) approximate the normalized pattern, the approximation relations between the power in the main maximum and the excited mode power have been found. These expressions allow computing the non-normalize power pattern.

$$P_E^0 = (-5.0849/x^2+5.5051/x-2.1425+0.3057x)x/(x-2), \quad x<\nu_2,$$
$$P_H^0 = (-11.6569/x^2+8.2601/x-2/2897+0.2426x)x/(x-3.75), \quad x<\mu_2, \qquad (4)$$

The power radiation characteristics for TE_{01} and TM_{01} modes have been computed using Weinstein's method and the developed mathematical model. The non-normalized power patterns calculated by means of the approximate expressions (1), (2) and (4) for TM_{01} mode for three values of x parameter (x=2.5, 5.5, 8.5) are presented in Fig. 1. The solid line is the characteristics computed by Weinstein theory; the lines with marker are the patterns obtained by the developed mathematical model. One can see that the calculations made in terms of the approximate model exactly describe the radiation sidelobes as well as the main lobe of the pattern. The absolute error of the approximation does not exceed 0.6 dB and 1.5 dB till the level –30 dB for TE_{01} and TM_{01} modes, respectively.

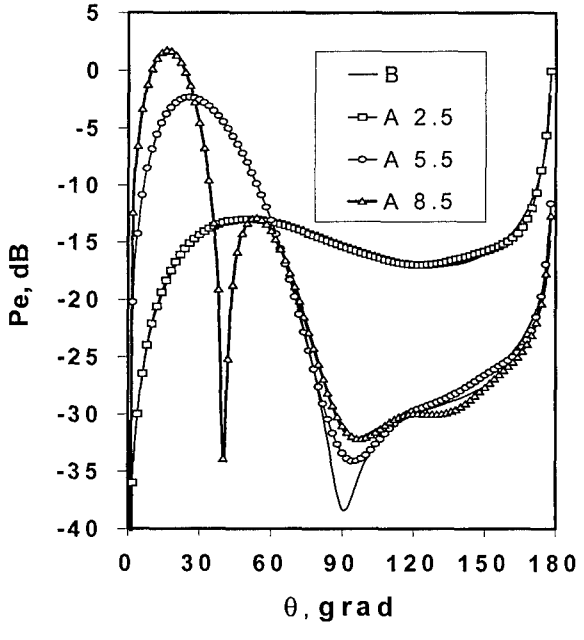

Fig. 1.

CONCLUSION

A mathematical model of the radiation from an open-ended circular waveguide excited by symmetrical TE_{01} and TM_{01} modes has been developed in a wide frequency bandwidth. The model takes into account five modes, which arise due to the diffraction on an open-ended waveguide. Recently the mathematical model for the radiation from an open-ended circular waveguide excited by the dominant mode TE_{11} has been derived [3]. The model for TE_{11} mode and the proposed in this paper mathematical model can be used to derive and calculate the radiation characteristics for a waveguide, operating on TM_{01}+TE_{01}, TE_{11}+TM_{01} or TE_{11}+TE_{01} modes.

REFERENCES

[1] Weinstein L.A. Theory of diffraction and factorization method. Moscow, Soviet Radio Publish, 1966 [in Russian].
[2] Fradin A.Z. Ultrahigh frequency antennas, Moscow, Soviet Radio Publish, 1957 [in Russian].
[3] Gorobets N.N., Orlova L.B., Shishkova A.V. Mathematical model of radiation from open-ended circular waveguide. Preceeding of III International Conference on Antenna Theory and Techniques, pp. 324-325, Sep., 1999.

RADIATION OF DIELECTRIC-COATED LONGITUDIONAL AND TRANVERSAL SLOT ANTENNAS IN A PLANE WAVEGUIDE

E.A. Shorokhova, O.S. Rusakova, and V.A. Yashnov

Nizhny Novgorod State University, Radiophysics Faculty
Gagarina Avn. 23, Nizhny Novgorod, 603600, Russia.
Phone: (8312) 65-61-27; e-mail: vay@rf.unn.runnet.ru

ABSTRACT

In this paper, a problem of radiation of longitudinal and transversal slot antennas placed on the circular perfectly conducting cylinder with magnetodielectric coating in a plane waveguide is considered. The calculation reduces to solution of the Helmgolz equations for the electric and magnetic vector potentials. The solution of the problem is obtained in an approximation of a thin antenna (in relation to the wavelength) and given distribution of electric field intensity along the slot. Expressions for the electromagnetic field intensity, radiation power, and conductivity of the longitudinal and transversal slot antennas are obtained. They are presented in a form of double series over the eigenfunctions of the perfect plane waveguide and the azimuth eigenfunctions of the cylinder. Such a representation is very convenient for numerical calculations. Using the expressions obtained the numerical calculations of real and imaginary parts of the radiation conductivity and impedance are performed. An influence of the magnetodielectric coating and geometrical parameters of the problem on antenna characteristics is analysed.

Slot antennas hold a special position in the antenna theory and engineering. They are widely used as airborne transmitting antenna. Although the study of their characteristics is carried out beginning with 40^{th} years [1], the development of exact and approximate calculation methods is subject of much current interest [2, 3]. Considerable recent attention has been focussed on radiation peculiarities for the slot dielectric-coated antennas [3]. In the paper we study an influence of magnetodielectric coating on characteristics of longitudinal and transversal slot antennas placed on the surface of a circular perfectly conducting cylinder in a plane waveguide with perfectly conducting walls.

The problem geometry is shown in Fig.1 for a case of longitudinal slot antenna. Here a is the radius of the cylinder, b is the radius of magnetodielectric cylindrical coating, L is the distance between the perfectly conducting walls of the plane waveguide, d and l are the sizes of the slot with a coordinate of its center z_0. It is assumed that coating of the antenna has the ralative dielectric permittivity ε_1 and the ralative magnetic permeability μ_1, and the waveguide is filled with a medium determing by the constants ε_2 and μ_2. It is suggested that the electric field intensities along the slot for the longitudinal and transversal slot antennas are respectively

$$E_{\varphi s}(z) = E_0 \cos\left(\frac{\pi(z - z_0)}{l}\right), \tag{1}$$

$$E_{zs}(\varphi) = E_0 \cos\left(\frac{\pi a}{l}\varphi\right). \tag{2}$$

Here E_0 is the amplitude of the electric field.

The problem is decided using the Helmgolz equations for the electric and magnetic vector potentials with the Lorenz calibration:

$$\Delta A_j + k_j^2 A_j = 0, \tag{3}$$

$$\Delta F_j + k_j^2 F_j = 0, \tag{4}$$

where $k_j = \omega\sqrt{\varepsilon_0 \varepsilon_j \mu_0 \mu_j}$ is the wavenumber in coating ($j=1$) and in the waveguide ($j=2$), ω is the circular frequency, ε_0 and μ_0 is electric and magnetic constant of the vacuum.

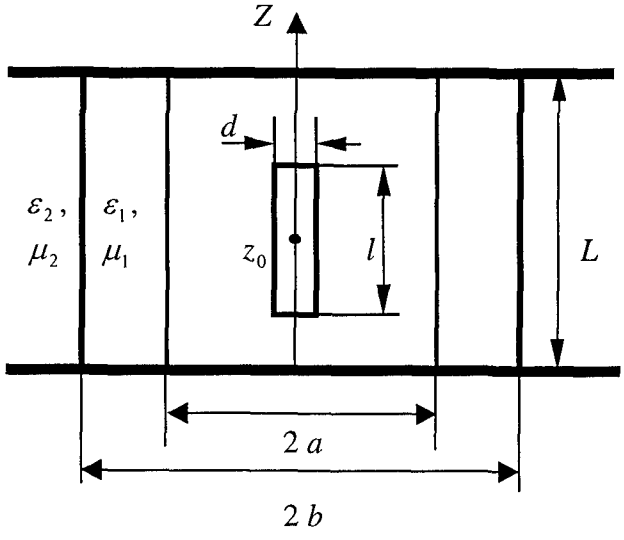

Fig. 1

The following boundary conditions are used:

(i) at $r = a$

$$E_z^{(1)} = 0,\ E_\varphi^{(1)} = -E_\varphi^s$$

(for the longitudinal slot antenna)

$$E_\varphi^{(1)} = 0,\ E_z^{(1)} = -E_z^s$$

(for the transversal slot antenna);

(ii) at $r = b$

$$E_\varphi^{(1)} = E_\varphi^{(2)},\ E_z^{(1)} = E_z^{(2)},$$

$$H_\varphi^{(1)} = H_\varphi^{(2)},\ H_z^{(1)} = H_z^{(2)}.$$

Here E_φ^s and E_z^s is given by the expressions (1) and (2). Solutions of the equation (3) and (4) are sought in the form of double series over the eigenfunctions of the plane waveguide with perfectly conducting walls and the azimuth eigenfunctions of the cylinder. Using the expressions obtained for the potentials it can be found electromagnetic fields, radiation power and conductivity of the longitudinal and transversal slot antenna.

To cite the final formula for the radiation conductivity of the longitudinal slot antenna:

$$G^{(l)} = -\frac{16i}{\pi^3 \varsigma_1} \frac{(k_0 l)^2}{k_0 L\, k_0 a} \sum_{n=1}^{\infty} \sum_{m=0}^{\infty} \varepsilon_m \frac{g^2}{\beta^2} Q_{nm}^{(l)}, \tag{5}$$

where we use the denotations:

$$Q_{nm}^{(l)} = \tilde{\kappa}_{1n} \frac{H_m^{(2)}(\tilde{\kappa}_{1n} k_1 a)}{\dot{H}_m^{(2)}(\tilde{\kappa}_{1n} k_1 a)} \left\{1 - d_{nm}^{(l)}\right\},\ \varsigma_j = \varsigma_0 \sqrt{\frac{\mu_j}{\varepsilon_j}},\ \varsigma_0 = \sqrt{\frac{\mu_0}{\varepsilon_0}},$$

$$d_{nm}^{(l)} = \left[1 - \frac{\tilde{\kappa}_{2n}}{\tilde{\kappa}_{1n}} \frac{\varsigma_1}{\varsigma_2} \frac{\Delta_e \Delta_s^{(l)}}{\Delta} \frac{\dot{H}_m^{(2)}(\tilde{\kappa}_{1n} k_1 a) \dot{H}_m^{(2)}(\tilde{\kappa}_{2n} k_2 b) H_m^{(2)}(\tilde{\kappa}_{2n} k_2 b)}{H_m^{(2)}(\tilde{\kappa}_{12n} k_1 b)}\right] \frac{\Delta_5}{\Delta_3} \frac{H_m^{(2)}(\tilde{\kappa}_{12n} k_1 b)}{H_m^{(2)}(\tilde{\kappa}_{1n} k_1 a)},$$

$$\Delta_e = 1 - \frac{\Delta_4}{\Delta_1} \frac{\tilde{\kappa}_{2n}}{\tilde{\kappa}_{1n}} \frac{\varepsilon_1}{\varepsilon_2} \frac{H_m^{(2)}(\tilde{\kappa}_{2n} k_2 b)}{\dot{H}_m^{(2)}(\tilde{\kappa}_{2n} k_2 b)},\ \Delta_m = 1 - \frac{\Delta_2}{\Delta_3} \frac{\tilde{\kappa}_{2n}}{\tilde{\kappa}_{1n}} \frac{\mu_1}{\mu_2} \frac{H_m^{(2)}(\tilde{\kappa}_{2n} k_2 b)}{\dot{H}_m^{(2)}(\tilde{\kappa}_{2n} k_2 b)},$$

$$\Delta_s^{(l)} = \frac{H_m^{(2)}(\tilde{\kappa}_{1n} k_1 b)}{\dot{H}_m^{(2)}(\tilde{\kappa}_{1n} k_1 a)} \left\{\frac{\dot{H}_m^{(2)}(\tilde{\kappa}_{1n} k_1 b)}{H_m^{(2)}(\tilde{\kappa}_{1n} k_1 b)} - \frac{\Delta_2}{\Delta_3}\right\},\ \Delta = -\frac{\Delta_0}{(k_0 L)^2 \tilde{\kappa}_{2n}^2} + \Delta_e \Delta_m \left[\dot{H}_m^{(2)}(\tilde{\kappa}_{2n} k_2 b)\right]^2,$$

$$\Delta_0 = \frac{nm\pi}{k_2 b} H_m^{(2)}(\tilde{\kappa}_{2n} k_2 b) \left\{1 - \frac{\tilde{\kappa}_{2n}^2}{\tilde{\kappa}_{1n}^2} \frac{\varepsilon_2 \mu_2}{\varepsilon_1 \mu_1}\right\},\ \tilde{\kappa}_{jn} = \sqrt{1 - \frac{1}{\varepsilon_j \mu_j} \left(\frac{n\pi}{k_0 L}\right)^2}.$$

$$\Delta_1 = H_m^{(1)}(\tilde{\kappa}_{1n} k_1 b) H_m^{(2)}(\tilde{\kappa}_{1n} k_1 a) - H_m^{(1)}(\tilde{\kappa}_{1n} k_1 a) H_m^{(2)}(\tilde{\kappa}_{1n} k_1 b),$$

$$\Delta_2 = \dot{H}_m^{(1)}(\tilde{\kappa}_{1n}k_1 b)\dot{H}_m^{(2)}(\tilde{\kappa}_{1n}k_1 a) - \dot{H}_m^{(1)}(\tilde{\kappa}_{1n}k_1 a)\dot{H}_m^{(2)}(\tilde{\kappa}_{1n}k_1 b),$$

$$\Delta_3 = H_m^{(1)}(\tilde{\kappa}_{1n}k_1 b)\dot{H}_m^{(2)}(\tilde{\kappa}_{1n}k_1 a) - \dot{H}_m^{(1)}(\tilde{\kappa}_{1n}k_1 a)H_m^{(2)}(\tilde{\kappa}_{1n}k_1 b),$$

$$\Delta_4 = \dot{H}_m^{(1)}(\tilde{\kappa}_{1n}k_1 b)H_m^{(2)}(\tilde{\kappa}_{1n}k_1 a) - H_m^{(1)}(\tilde{\kappa}_{1n}k_1 a)\dot{H}_m^{(2)}(\tilde{\kappa}_{1n}k_1 b),$$

$$\Delta_5 = H_m^{(1)}(\tilde{\kappa}_{1n}k_1 a)\dot{H}_m^{(2)}(\tilde{\kappa}_{1n}k_1 a) - \dot{H}_m^{(1)}(\tilde{\kappa}_{1n}k_1 a)H_m^{(2)}(\tilde{\kappa}_{1n}k_1 a),$$

Numerical calculations of the real part of radiation conductivity $\left(G^{(l)} = \varsigma_0 G\right)$ for the longitudinal slot antenna as a function of the parameter $k_0 L$ (see Fig.2) have been performed using formula (5) for the following values of the electrical and geometrical parameters: $\varepsilon_1 = 5$ (solid line), $\varepsilon_1 = 3$ (dotted line), $\varepsilon_1 = 1$ (dash-dot line), $\varepsilon_2 = 1$, $a/L = 0.5$, $b/L = 0.51$, $l/L = 0.5$, $d/a = 0.01$, $z_0/L = 0.5$.

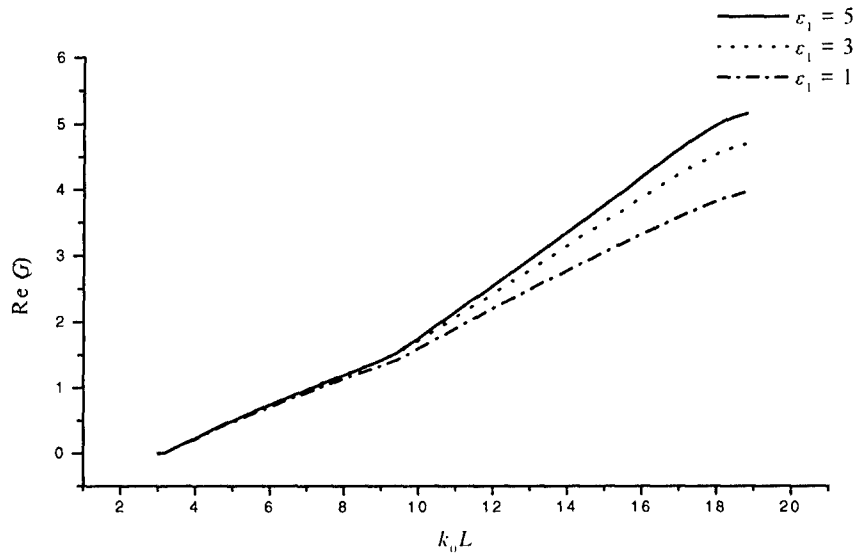

Fig. 2.

Basing on these data the following conclusions can be formulated. Firstly, at frequencies lower than the first critical frequency of the waveguide $(k_0 L < \pi)$ the radiation of the longitudinal slot antenna is unavailable. Secondly, even thin magnetodielectrical coating of the slot antenna has a noticeable influence on its characteristics. In particular, an increase in the antenna radiation power is observed with growing ε_1.

REFERENCES

[1] J. R. Wait, "Electromagnetic radiation from cylindrical structures", Pergamon Press, New York, 1959.

[2] Park J.K., Eom H.J. Radiation from multiple circumferential slots on a conducting circular cylinder. - IEEE Trans. on Antennas Propagat., 1999, vol.47, no.2, pp. 287-292.

[3] Ragheb H.A., Johar U.M. Radiation characteristics of an infinite dielectric-coated axially slotted cylindrical antenna partly embedded in a ground plane. - IEEE Trans. on Antennas Propagat., 1998, vol.46, no.10, pp. 1542-1547.

ANALYSIS OF DISTURBED PATTERN STATISTICAL CHARACTERISTICS FOR APODIZED MULTIELEMENT WAVEGUIDE SLOT ANTENNAS

A.V.Kabanov, and V.V.Lukin
Dept. 504, State Aerospace University, 17 Chkalova St, 61070, Kharkov, Ukraine
Tel. +38 0572 442352, +38 0572 448789, Fax +38 0572 441186
e-mail: lukin@mmds.kharkov.ua

The statistical analysis of disturbed patterns for waveguide slot apodized multielement antennas is performed. Both spatially independent and correlated phase errors with variances typical for practice are considered. The numerical simulation results are obtained for classical amplitude distributions and apodization functions earlier proposed by authors. It is shown that the mean maximal side lobe level of disturbed patterns gradually increase in comparison to potential level due to error influence. However, in the sense of statistical characteristics of the main lobe width and maximal side lobe level for disturbed patterns the proposed apodization functions provide appropriate results.

INTRODUCTION

For waveguide slot multielement antennas the required pattern characteristics are usually provided by means of proper selection of an apodization function (AF), i.e. amplitude distribution of irradiated field on antenna aperture. In practice, not all known AFs can be realized in waveguide slot antennas because of constructive and technological restrictions [1] imposed by the fact that the slots placed in the waveguide wide wall should have some minimal distance between them. That is why only few known AFs can be implemented, besides, in our paper [1] we have proposed several new AFs that are potentially able to ensure the maximal side lobe level (MSLL) of antenna pattern within the limits from –30 to –40 dB.
In practice, the desired amplitude-phase distribution can be realized with some errors, they occur due to slot intercoupling, random shifts of their phase centers with respect to ideal positions and other reasons [2]. This inevitably leads to difference between theoretical and practically obtained characteristics of antenna pattern. And the latter ones (for disturbed patterns) are usually worse than potentially reachable. That is why often a question arises how stable are the proposed solutions with respect to degrading factor (noise, errors) influence. Statistical analysis of disturbed patterns [2] can give an answer and provide data necessary for analysis and practical recommendations.

APPROACH TO DISTURBED PATTERN STATISTICAL ANALYSIS

The influence of errors results in degradation of the majority of the basic characteristics of antenna pattern. In particular, the pattern main lobe width (MLW) can increase [2], [3]. But usually this increase is not too large and it does not exceed 1...2% (this dependence is confirmed by numerical simulation results presented below). The pattern side lobes are commonly more severely affected by errors and the pattern MSLL can increase by few or even tens dB in comparison to the case of pattern for ideal amplitude phase distribution.
Below we consider only the phase errors as a factor supposed to be the dominant for waveguide slot antennas. Two different cases are exploited: the spatially independent errors (correspond to the value $\gamma = 2$ in Table) and the spatially correlated phase errors ($\gamma = 0.1$). An

exponential model [2], [3] of spatial correlation function is used. As it is shown in [2], [3] the influence of these types of errors on disturbed pattern statistical characteristics can be rather different. Besides, in opposite to [2] it was decided to evaluate not the parameters of the mean disturbed pattern but the mean parameters of disturbed patterns. Two values of the phase error variance σ_φ^2, 0.005 and 0.01 (expressed in rad^2) have been analyzed. They are rather typical for practical applications. It should be noted that this level of phase errors can be considered as relatively large distortions [3] since the disturbed pattern has practically random behavior of the side lobes and the mean MSLL is mainly determined by the error variance and the used AF.

The statistical characteristics of disturbed patterns have been analyzed for five AFs: the Dolph-Chebyshev AF that potentially provides the MSLL=-40dB (it can not be implemented in waveguide slot antennas but serves for comparison purposes), the Gauss AF (α_G=2.2) which is one among the best known AFs that can be implemented, the Kaiser-Bessel AF on pedestal, the AF Cos^2 on pedestal 0.1 with optimal parameters, the AF Riss on pedestal [1]. The latter three AFs have been proposed by us and their parameters were optimized. The potential MSLL and MLW values for the corresponding patterns are given in Table (See rows with notation "potential"). In simulations we considered the case of equidistant antennas with element spacing equal to half wavelength and the number of elements N=80. The mean values and variances have been estimated for MSLL and MLW of disturbed patterns. They are presented in Table.

ANALYSIS OF NUMERICAL SIMULATION DATA

Numerical simulation data prove that the phase errors (at least, for the analysed variances of errors) do not lead to considerable expanding of the pattern main lobe width. It is smaller than 0.1% and the root mean square of this parameter is also much smaller than its mean. That is why it is possible to state that the pattern MLW is very stable with respect to error influence. Of course, the larger the error variance the larger the variance of the MLW. Spatially correlated errors usually result in larger variations of the disturbed pattern MLW than the spatially independent errors.

On the contrary, the disturbed pattern MSLL is much more affected by the phase errors. It is well seen that the mean MSLL can differ from potential one by about 3...12 dB. The mean MSLL depends upon phase error variance and it increases by 1.5...2.5 dB when σ_φ^2, changes from 0.005 to 0.01. The MSLL mean value also considerably depends upon are the phase error spatially correlated or independent. The spatially correlated errors result in larger MSLL mean and variance than spatially independent ones.

The most interesting aspect is that all the considered AFs provide the mean MSLLs (for equal σ_φ^2 and γ) that do not differ too much from each other. Only for the AF "Riss on pedestal" the results are noticeably worse. However, all the other apodization functions produce practically the same results as the Dolph-Chebyshev AF. At the same time the functions "Cos^2 on pedestal" and "Gauss, α_G=2.2" lose to the Dolph-Chebyshev pattern only by 2% in the mean MLW. Taking into account the fact that they both can be realized in waveguide slot multielement antennas, it is possible to state that the proposed apodization functions provide very good characteristics of disturbed patterns which are stable enough with respect to phase error influence and it is worth using them in practice.

Table. Numerical simulation results

γ, and σ_φ^2	MSLL		MLW	
	Mean ($\times 10^{-3}$)	Variance ($\times 10^{-7}$)	Mean ($\times 10^{-2}$)	Variance ($\times 10^{-7}$)
Dolph-Chebyshev				
Potential	0.1000 (-40.00 dB)	0	3.15612 (1.81°)	0
2.0, 0.01	1.1865 (-29.26 dB)	0.99475	3.15809	1.18529
2.0, 0.005	0.7856 (-31.50 dB)	0.25965	3.15862	1.17243
0.1, 0.01	1.6913 (-27.72 dB)	10.7710	3.15778	1.04698
0.1, 0.005	1.0110 (-29.95 dB)	3.61643	3.15674	1.08382
Kaiser-Bessel (with initial. MSLL = -40dB) on pedestal 0.1				
Potential	0.2387 (-36.21dB)	0	3.64904 (2.09°)	0
2.0, 0.01	0.9459 (-30.24 dB)	1.24052	3.65023	0.75185
2.0, 0.005	0.5429 (-32.65 dB)	0.50699	3.64992	0.38234
0.1, 0.01	1.4163 (-28.48 dB)	14.8791	3.65391	5.16944
0.1, 0.005	0.8691(-30.60 dB)	4.10893	3.65053	2.86942
Cos^2 on pedestal 0.1.				
Potential	0.1038 (-39.84 dB)	0	3.28959 (1.89°)	0
2.0, 0.01	1.0026 (-29.99 dB)	1.17269	3.29190)	1.21100
2.0, 0.005	0.5693 (-32.45 dB)	0.32444	3.29065	1.06600
0.1, 0.01	1.4327 (-28.44 dB)	8.97947	3.29104	1.10510
0.1, 0.005	0.8150 (-30.89 dB)	2.71024	3.29156	1.19549
Riss on pedestal 0.17.				
Potential	0.3135 (-35.04 dB)	0	3.22166 (1.85°)	0
2.0, 0.01	1.8132 (-27.42 dB)	2.89361	3.22161	0.53533
2.0, 0.005	1.4485 (-28.39 dB)	1.30831	3.22171	0.28151
0.1, 0.01	2.3560 (-26.29 dB)	15.2454	3.22595	4.18791
0.1, 0.005	1.7493 (-27.57 dB)	4.81943	3.22237	2.01905
Gauss, α_G=2.2				
Potential	0.3488 (-34.57dB)	0	3.22864 (1.85°)	0
2.0, 0.01	1.1363 (-29.45 dB)	1.45071	3.22700	1.77002
2.0, 0.005	0.7667 (-31.15 dB)	0.61537	3.22826	1.15377
0.1, 0.01	1.7354 (-27.61 dB)	9.77945	3.23172	2.49530
0.1, 0.005	1.1224 (-29.50 dB)	3.02311	3.23196	2.63400

REFERENCES

[1] Lukin V.V., Kabanov A.V., Ponomarenko N.N. Apodization functions for antenna arrays with constructive-technological restrictions: Proceedings of ICATT'99. - Sevastopil, Ukraine, September 1999, pp. 219-224

[2] Y.S. Shifrin Statistical antenna theory (State-of-the-art, key development directions). – Kharkov, 1985, 181p.

[3] Zelensky A.A., Lukin V.V., Anukhin I.P. Apodized Array Pattern Analysis and Synthesis for Spatially Independent and Correlated Errors Influence under Constructive and Technological Restrictions// Proceedings of Intern. Conference PIERS'94, Noordwijk, Netherlands, July 1994, pp.440-443.

SHAPED FEED SYSTEMS FOR THE DUAL-REFLECTOR ANTENNAS

Dmitry Y. Razdorkin, and Marina V. Romanenko

Rostov Research Institute of Radiocommunication
130 Nansena, Rostov-na-Donu, Russia
Tel.: 34-07-44, E-mail: **mvrom@icomm.ru**

The multivariable optimization technique for the shaped feed system of the dual-reflector antennas with the given circularly symmetric main reflector is described. The optimization criterion is the gaining of the maximum overall aperture efficiency η_a. Parameters for the optimum search are the mutual layout of the antenna elements, features of output energy distribution at the aperture and the subreflector profile. On the basis of the carried out analysis of the dual-shaped reflector antennas the technique of the optimum feed system search was developed for different shapes of the given main reflector. The program application of the algorithms for the dual-shaped antenna synthesis and algorithms of the optimization is realized on the C ++.

The problem of the shaped feed system design with the high aperture efficiency η_a in all working frequencies band is very important for the multiband dual-reflector antennas with the large electrical aperture sizes ratio ($f_H / f_L = 2 \div 3$) and the given circularly symmetric main reflector. In the present work the minimization of amplitude and phase deviations in the main reflector aperture is analyzed.

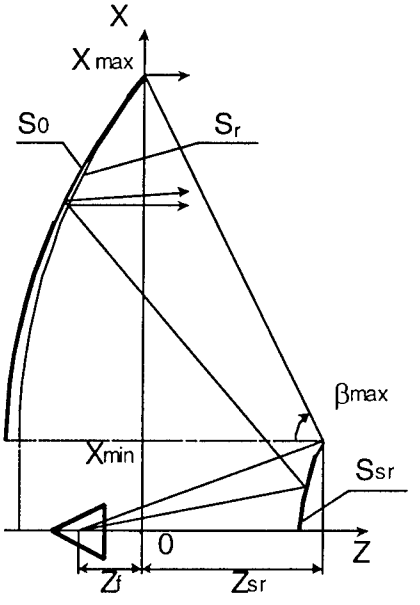

Fig. 1. Shaped feed system for the reflector antenna

The examined technique of the Cassegrain antennas optimization is based on the replacement of its feed system with the feed system from the dual shaped antenna under the condition of the insignificant deviation of main and shaped reflector profiles (Fig. 1) [1]. In this case the aperture power density does not change. The only phase error distribution in the antenna

aperture is reason of the aperture efficiency reduction. For the circularly symmetric reflector antenna the aperture efficiency varies as

$$\eta_a = \frac{\left| \int_{X_{\min}}^{X_{\max}} \sqrt{I(x)} \exp\left(-j 2\pi/\lambda \, \Delta\Phi(x,\mathbf{p})\right) x dx \right|^2}{2 \int_{X_{\min}}^{X_{\max}} I(x) x dx}, \quad (1)$$

where $I(x)$ is the aperture power density, $\Delta\Phi(x,\mathbf{p})$ is the aperture phase distribution, λ is the wavelength. The vector $\mathbf{p}$ defines the feed system optimized parameters. The technique described in [1] assumed the feed system optimization only on the irradiation corner of the main reflector $\beta_{\max}$ when the uniform amplitude distribution $I(x) = const$ in the aperture is given. The efficiency of such antenna optimization ceases to be essential to the reflector diameters $D > (200 \div 300)\lambda$ and the relation $d/D = (0{,}05 \div 0{,}1)$.

In the present work, the influence of the amplitude distribution function and the mutual layout of the synthesized elements of the shaped system on the aperture phase errors and the resulting aperture efficiency is analyzed. In general, the vector of optimized parameters is a function of the amplitude distribution function $I(x)$, the irradiation angle of the main reflector edge $\beta_{\max}$ and the relative displacement of elements

$$\mathbf{p} = \mathbf{p}\left(I(x), \beta_{\max}, \Delta z_f, \Delta z_{sr}\right)$$
$$\Delta z_f = z_f - z_f', \Delta z_{sr} = z_{sr} - z_{sr}', \quad (2)$$

where z_f, z_{sr} are the element positions for the shaped feed system, z_f', z_{sr}' are their positions after optimization.

For the analysis of influence of the decaying amplitude distribution on the resulting aperture efficiency with the shaped feed system the distribution is used

$$I(x) = \left(1 - \alpha\left(x/X_{\max}\right)^2\right)^{2p}, \quad (3)$$

where $\alpha = 1 - \exp\left(\ln(\Delta)/p\right)$, $0 \le \alpha \le 1$, $p \in N = \{0,1,2,...\}$, Δ is the power level at the aperture edge.

The numerical results show that for the antenna with diameters $D/\lambda > 300$ the shaped amplitude distribution becomes more effective than the uniform distribution. The use of the shaped feed system with such type of distribution is most efficient at designing of multiband systems with the large ratio of the high and lower frequencies. If the amplitude distribution is uniform, the aperture efficiency quickly decreases with the frequency increase. Shaping for the aperture distribution decreases the phase errors in the aperture and makes the antenna design less critical to the growth of the working frequency (Fig. 2).

It is shown that the insignificant change of the feed and subreflector mutual layout from originally calculated by the dual-shaped antenna synthesis algorithm allows the minimization of the phase aperture distribution errors of the designed antenna as well. This type of the optimum feed system can be used for the designing antennas with the main reflector diameter up to 200÷300 wavelengths and the uniform aperture distribution.

Aperture efficiency dependencies for shaped feed systems of different types are shown in Fig. 3.

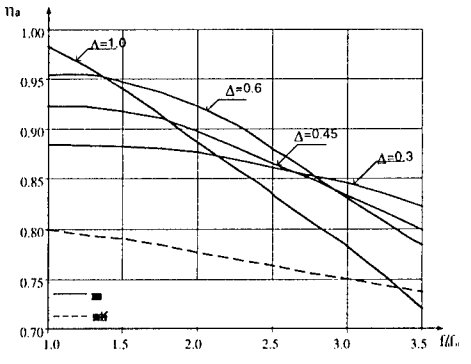

Fig. 2. Frequency dependences of the aperture efficiency

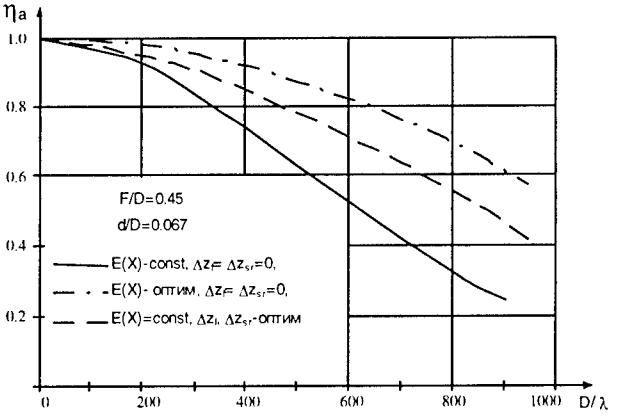

Fig. 3. Dependence of aperture efficiency on parameters of the optimization

On the basis of the carried out analysis of the dual-shaped reflector antennas, the technique of the optimum feed system search was developed for different shapes of the given main reflector.

In the program application of shaped feed systems, the algorithms of one- and multiparameter search are realized for the optimization of the different feed systems by the criterion of a maximum overall aperture efficiency. As the derivative of the function η_a determining the optimization criterion can not be defined analytically, the optimization algorithms can not be implemented on the gradient method basis. For the one-dimensional optimization (for example, the optimization of the feed system by the angle of the energy transform) the square-law approximate algorithm for the function η_a with the subsequent linear optimization is implemented. For feed systems with the optimum output energy distribution and angle of the energy transform the program implementations of algorithms coordinated of descent is designed on the basis of one-parameter algorithm of linear search. The algorithm of random search with adaptation is used for feed systems optimizing the mutual layout of the units of the antenna [3].

In case of feed systems inverting the field of the primary feed, the additional optimum search algorithm is implemented at the dual-shaped antenna synthesis with inverse boundary conditions.

The program application of the algorithms for the dual-shaped antenna synthesis and algorithms of the optimization is realized on the C ++.

REFERENCES

[1] Bandukov V.P., Pokras A.M. Shaped feed system for dual-reflector antenna (In Russian). - Telecommunication. - 1973. - Num. 10. - Pp. 59-63.

[2] M.V. Romanenko. The uniform approach to dual-shaped symmetrical reflector system (in Russian). " Antennas, radiocommunication and means " (ICARSM-97), Proceeding of the 3 International Conference, Voronezh-May-97. - Pp. 204-214.

[3] Rastrigin L.A., Ripa K.K. The adaptation of the random search (in Russian). – Riga: Knowledge – 1978.

COMPLEX MEDIA, BEAMS AND PLASMAS

DENSITY OF THE SPATIAL WEIGHT DISTRIBUTION IN THE MULTI-LAYERED HIGHLY SCATTERING RANDOMLY INHOMOGENEOUS MEDIA

I.V.Meglinsky[a, b], S.J.Matcher[a]
[a] - School of Physics, University of Exeter, Exeter, EX4 4QL, Devon, UK
[b] - Department of Physics, Saratov State University, Saratov, 410026, Russia
E-mail: I.V.Meglinsky@exeter.ac.uk

The density of photon spatial weight distribution for the optically turbid highly scattering homogeneous medium is considered. It turned out that boundary of the half-infinite non-absorbing multiple scattering medium divided the escaped photons into two roughly mirror symmetrical groups. This allows to include the partial photon reflection and refraction on the boundaries of medium or medium layers in the calculation of spatial photon density distribution for the complex optically turbid highly scattering multi-layered media.

INTRODUCTION

The propagation of light in complex inhomogeneous multi-layered highly scattering optically turbid media is of interest to a wide range of disciplines. In the last decade, it was widely simulated as photon migration by Monte Carlo technique for many diagnostic purposes in biomedicine [1-3]. However, in case when a medium contains hidden boundaries between the internal layers with different refractive indices the direct simulation of a photon tracing by all possible trajectories is prohibitive, as they exponentially increase in their number. A more reasonable method of solving this problem [1-3] is based on the comparison of a uniformly distributed random number ξ, generated each time a photon packet crosses a boundary, to the Fresnel's reflection coefficient $R(\alpha_i)$ [4]. But, this approach of simulation disrespects the numerous parts of the photon packets, produced on the layers boundaries. In this work we consider the density of the photon spatial weight distribution on the surface of the optically turbid highly scattering non-absorbing homogeneous semi-infinite medium. Describing the influence of the medium boundary on the photon spatial weight distribution at the medium boundary, we calculate the spatial photon density distribution in a medium, taking into account the processes of photon reflection and refraction on the layer boundaries in a complex multi-layered medium.

MODEL OF LIGHT PENETRATION IN THE MEDIUM

Let us consider a highly scattering multi-layered (5 layers) homogeneous medium filling the half-space (z>0), where the scattering coefficients μ_s of the layers are 100, 60, 40, 50, 30 mm^{-1}, absorption coefficients μ_a - 0.1, 0.015, 0.05, 0.075, 0.015 mm^{-1}, anisotropy factors g - 0.85, 0.8, 0.9, 0.95, 0.75, the refractive indices n 1.5, 1.34, 1.4, 1.37, 1.4, and thickness of the layers are 20, 100, 150, 80, 7500 μm. The photon packet propagation is simulated in respect to standard Monte Carlo technique [1-3], but in framework of our simulation the changes of statistical weight W of photon packets according to the formulas occurs on the medium boundary only, i.e.:

$$W = W_0(1 - R_{1,0}(\alpha_i))\prod_{q=1}^{M-2} R_{m_q,k_q}(\alpha_i)\,. \qquad (1)$$

Here, $W_0=W_{in}(1-R_{0,1}(\alpha_i))$ is the initial weight of a photon packet in a medium, W is the detected weight of a photon packet, α_i is the angle of incidence, M is the total number of photon packet–boundary interaction events, m_q and k_q indicate the number of layers and direction of the q-th photon packet boundary crossing. It is easy to define the total weight of a photon packet on the detector area as a sum:

$$W = \sum_{j=1}^{N_{Ph}} \left(W_1 + W_2 + W_3\right)_j\,, \qquad (2)$$

where $W_1 = W_0(1-R_{1,0}(\alpha_i))$, $W_2 = W_0(1-R_{1,0}(\alpha_i))R_{1,0}(\alpha_i)$, and $W_3 = W_0(1-R_{1,0}(\alpha_i))\prod_{q=1}^{M_j} R_{k_q,m_q}(\alpha_i)$, N_{ph} is the total number of detected photon packets. As the angle distributions of the photon packets on the medium boundary are the same for the photon packets which are once partially reflected on the boundary only $P_1(\alpha_t)$ and for the photons once refracted and reflected while escaping the medium $P_2(\alpha_t)$ (FIG.1), we can express sum of W_1 and W_2 as:

$$\langle W_2 \rangle \approx \langle W_1 \rangle \langle R_{1,0}(\alpha_i) \rangle . \tag{3}$$

where $\langle ... \rangle$ denotes an average over all photon packets paths.

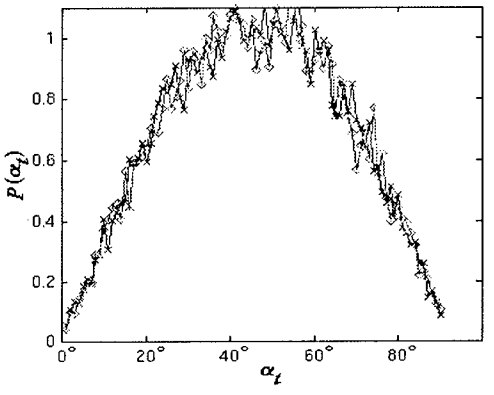

FIGURE 1.

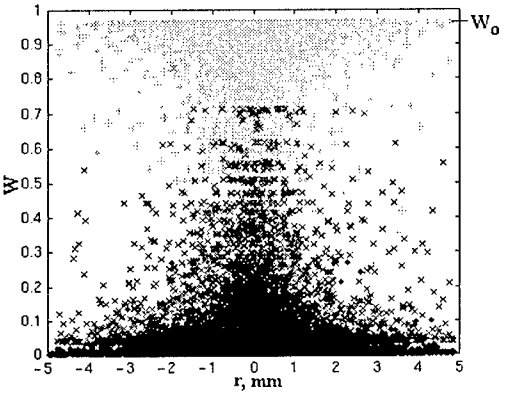

FIGURE 2.

Fig. 1. *The surface photon escaping angle distribution function $P(\alpha_t)$: (-×-) - for the photon packets once partially refracted on the boundary while escaping the medium; (-◊-) - for the photon packets once partially reflected and then refracted on the boundary while escaping the medium.*

Fig. 2. *The density of spatial photon weight distribution W(**r**) on the boundary of the medium. (+) indicates the density of spatial photon weight distribution for photon packets which experienced only two acts of the interaction on the medium boundary (entering and escaping the medium); (×) shows the density of spatial photon weight distribution for photon packets, experienced three acts of the interaction with the boundary (partially internal reflection on the surface of the medium, initial and final refraction); (·) presents the distribution W(**r**) for all other photon packets, experienced more than three acts of the interaction with the boundary.*

Moreover, the density of photon spatial weights distribution on the medium boundary (i.e. $<W_1>$ and $<W_2>$, respectively) are roughly mirror symmetrical about $\frac{1}{2}W_0\left(1-\langle R_{1,0}(\alpha_i)\rangle\right)$ or approximately 0.46 in current simulation (FIG.2).

In other words, the boundary of the medium works as a semi-transparent mirror, and multiplier $R_{1,0}(\alpha_i)$ in the second summand W_2 of (3) can be considered as the operator responsible for the symmetry of the parts 1 and 2 (see FIG.2). But, as the weight of high order boundary interacted photon packets W_3 in (3) is negligible small (see FIG.2), partially reflected on the medium boundary photon packets might be taken into account with ease:

$$W_{Total}(\mathbf{r}) = < W_1(\mathbf{r}) > (1 + < R_{1,0}(\alpha_i) >) . \tag{4}$$

Thus, the total spatial photon weight distribution for a complex multi layered medium is:

$$W(\mathbf{r}) = \sum_{k=1}^{L} W_k(\mathbf{r})\left(1 + \chi_k R_{k,k+1} + \chi_k R_{k-1,k}\right), \tag{5}$$

where $\chi_k = \frac{W_k(\mathbf{r}_2)}{W_k(\mathbf{r}_1)}$, $W_k(\mathbf{r}_1)$ is the amount of the photon weight in the top point $\mathbf{r}_1$ of the k-th layer on the OZ, $W_k(\mathbf{r}_2)$ is the amount of the photon weight in the last point in the k-th layer on the OZ.

The absorption of the medium layers is included regarding the modified Beer-Lambert law as:

$$W = \left[W_0 (1 - R_{1,0}(\alpha_i)) \prod_{j=1}^{M-2} R_{m,k}(\alpha_i) \right] \exp\left(-\sum_{q=1}^{N_v} \mu_{aq} l_q \right) . \quad (6)$$

Here, N_v is the number of scattering events for a v-th photon packet, l_q is a random pathlength that photon packets move in step q, μ_{aq} is the absorption coefficient on the q-th layer of the medium. The spatial photon density distribution in a complex multi-layered highly scattering inhomogeneous medium is simulated as [5]:

$$Q(\mathbf{r}) = -\frac{\partial}{\partial \mu_a} \ln\left(\frac{I}{I_0}\right) = - - \frac{\partial}{\partial \mu_a(\mathbf{r})} \ln\left(\frac{1}{N_{ph}} \sum_{i=1}^{N_{ph}} U_i W_i(\mathbf{r}) \right), \quad (7)$$

W is the weight of the i-th detected photon packet, U is a function: U=1 if the i-th photon packet has scattered in a point $\mathbf{r}$ of the medium, and U=0 for all other cases.

RESULTS AND CONCLUSIONS

Fig.3-a presents the results of the simulation of the spatial photon density distribution in a complex multi-layered highly scattering inhomogeneous medium including the refraction and reflection processes as it defined above. Fig.3-b shows same results calculated by the typical Monte Carlo algorithm [1-3].

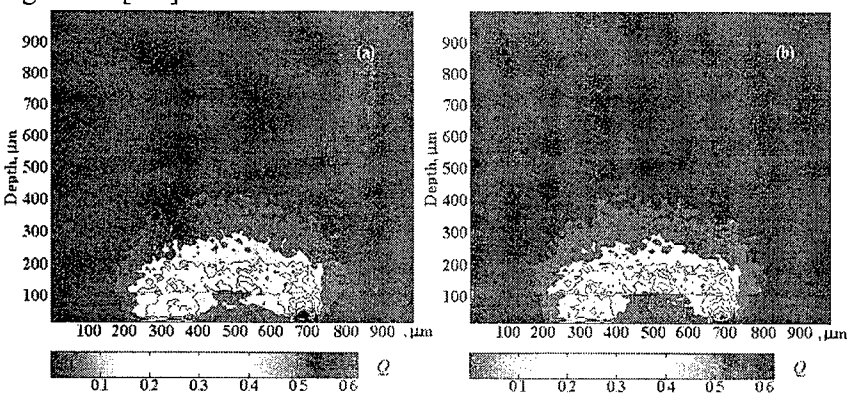

FIG.3. *The contour of the spatial detector depth sensitivity [5]: (a) - calculated by the typical algorithm [1-3]; (b) - calculated as it described above. The source-detector spacing - 300 μm; diameter of the source and detector 100 and 50 μm, numerical aperture - 0.2.*

In conclusion, we studied the spatial photon density distribution in a complex multi-layered highly scattering inhomogeneous medium. We found that boundary of the medium divides the spatial photon weight distribution in two roughly symmetrical parts. This allows to propose a new simple technique of calculation of the spatial photon density distribution in complex optically turbid multi-layered highly scattering media, taking into account all possible photon trajectories, including the partial photon reflection and refraction on the internal boundaries of the layers of the medium. These approach could be used for the approximate solutions in wave theory propagation and in imaging reconstruction fields.

We acknowledge EPSRC support under grant GR/L89433.

REFERENCES

[1]. M. Keijzer, S.L. Jacues, S.A. Prahl, and A.J. Welch, Laser Surg. Med., **9**, 148, (1989).
[2]. I.V. Yaroslavsky, V.V. Tuchin, Optica & Spectrosc., **72**, 505, (1992).
[3]. L. Wang, S.L. Jacques, L. Zheng, Computer Methods and Programs in Biomedicine, **47**, 131, (1995).
[4]. M. Born, E. Wolf, Principles of Optics: Electromagnetic Theory of Propagation, Interference and Diffraction of Light, 6th edn., Pergamon Press, (1986).
[5]. I.V. Meglinsky, S.J. Matcher, in Coherence Domain Optical Methods in Biomedical Science and Clinical Applications IV, V.V. Tuchin; J.A. Izatt; J.G. Fujimoto Eds., *Proc. SPIE*, **3915**, pp.18-24, 2000.

MULTIPLE LIGHT SCATTERING BY RANDOM AND DETERMINISTIC STRUCTURES.

Irina L. Maksimova

Saratov Department of the Institute of Radioengineering and Electronics
Russian Academy of Science
38 Zelenaya st., Saratov, 410019, Russia
E-mail: MaksimovaIL@info.sgu.ru

ABSTRACT

A numerical study of two-dimensional photonic structures of finite set of parallel cylinders is presented. A rigorous theory in which each cylinder is characterized by its scattering matrix, which links the diffracted field to the incoming one, is used.

The effects of multiple scattering play a substantial role in light propagation in dense disperse systems. The mutual interactions of the scatterers complicate the light scattering. A rigorous theory of multiple scattering has certain disadvantages if compared to the method of describing the radiation propagation in media containing correlated discrete densely packed scatterers. This theory has been intensively developed in late decades because the problems that are expected to be solved are of interest for a wide range of scientific disciplines.
This paper deals with the problem of calculating the spatial characteristics of laser radiation scattered by layers formed by circular cylinders. To reveal the aspects only due to the spatial order degree we advantageously restrict ourselves by considering particle systems of high-symmetrical types. We consider light scattering induced by array of L parallel infinite cylinders with precisely specified coordinates immersed in a homogeneous background. The plane incident wave is normal to the axes of cylinders. The problem is two-dimensional: The cylinders are infinite in the Z direction and the incident field is also Z invariant.

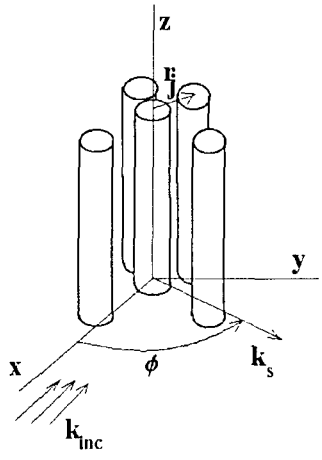

The theory is based on a self-consistent approach that identifies incident and scattered fields around each cylinder. The electromagnetic field that is incident upon the surface of the j-th cylinder consists of two parts: the original incident waves $E_{inc}(j)$ and the scattered fields of all the other cylinreds $E_s(l,j)$, which can be written as:

$$E_i(j) = E_{inc}(j) + \sum_{l \neq j}^{L} E_s(l, j) \tag{1}$$

The total incident field $E_i(j)$, scattered field $E_s(j)$ and internal field $E_1(j)$ can be expanded as

$$E_i(j) = \sum_{n=-\infty}^{\infty} E_n p_n^j N_n^{(1)}(j), E_s(j) = -\sum_{n=-\infty}^{\infty} E_n b_n^j N_n^{(30}(j), E_1(j) = \sum_{n=-\infty}^{\infty} E_n f_n N_n^{(1)}(j), \tag{2}$$

where N_n is the vector cylindrical functions, $E_n = \frac{(-i)^n}{k} E_0$. The interactive scattering coefficients are given by $b_n^j = b_n p_n^j$, where b_n are exactly the Mie coefficients for isolated j-th cylinder.

From the Graf's addition theorem for Bessel Functions, the scattering problem is reduced to the solution of a linear system.

$$p_n^j = e^{i\vec{k}_{inc}\vec{r}_j} - \sum_{l \neq j}^{L} \sum_{v=-\infty}^{\infty} b_v^l A_v^n(l, j) \tag{3}$$

Using the asymptotic iteration method we solved this system.

The total scattered field in the far field asymptotic can be written as

$$E_{stotal}(\theta) = \sum_{j=1}^{L} E_s(j) = -E_0 \sqrt{2/\pi kr}\, e^{ikr - i\pi/4} \sum_{j=1}^{L} e^{-i\vec{k}_s \vec{r}_j} \sum_{n=-\infty}^{\infty} b_n^j e^{-in\theta} \tag{4}$$

where θ is the angle between $\vec{k}_{inc}$ and $\vec{k}_s$.

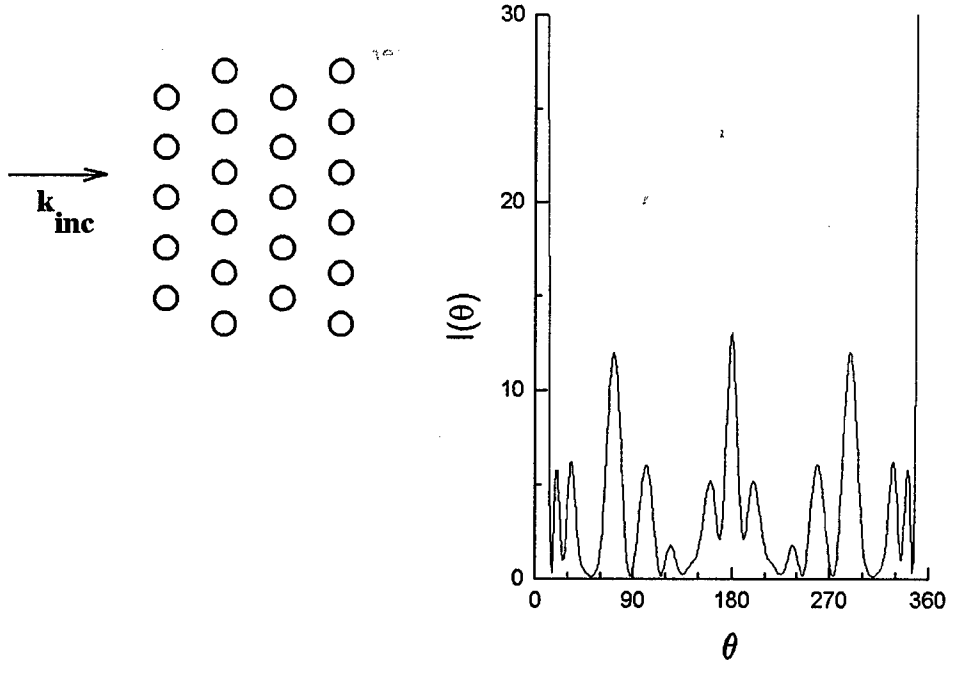

Intensity in θ-direction is

$$I(\theta) = |E_{stotal}(\theta)|^2 \tag{5}$$

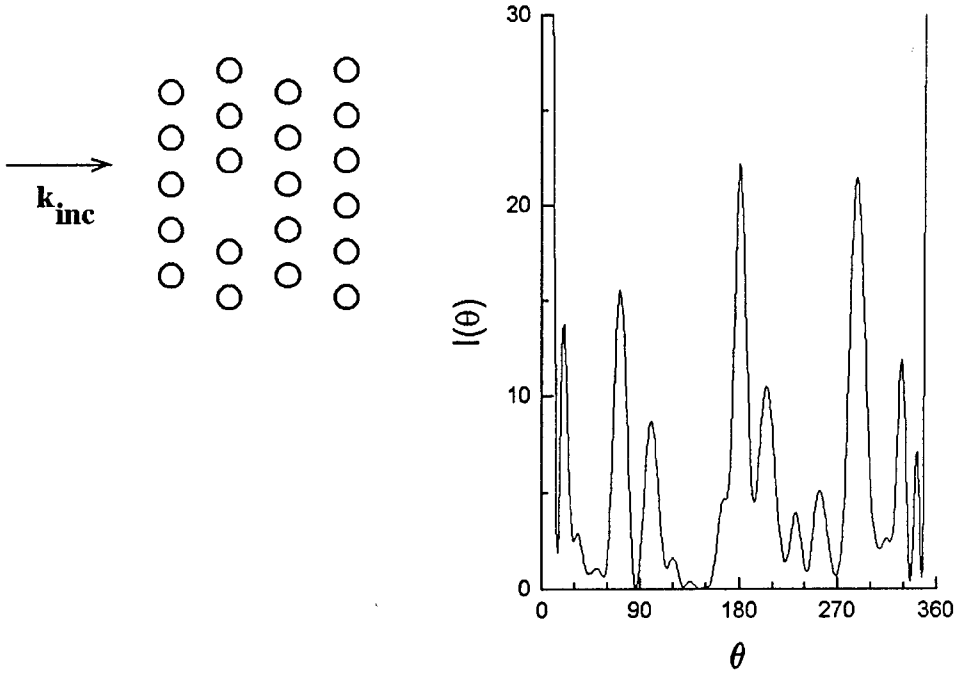

The method enables us to give an accurate description of all the characteristics of the electromagnetic field scattered by a finite set of parallel cylinders and to study the influence of defects on optical properties of photonic crystals (1). Spectral dependences of the transmittance of crystal consisting of finite number of cylinders with different spatial structure are investigated. Special attention is paid to the crystal with defect when some cylinders have been removed from ideal lattice.

Spatial characteristics of the scattering intensity from the set of cylinders with fractal dimension are computed. For random structures the dispersion relations are analyzed in quasi-crystalline approximation. The phenomenon of non-linear dependence of effective propagation constant on the number density of scatterers is investgated numerically. The model of layers formed by closely-packed systems of long cylinders is used to calculate the degree of circular dichroism of the eye cornea (2).

REFERENCES

[1] G. Tayeb, D. Maystre Rigorous theoretical study of finite-size two-dimensional photonic crystals doped by microcavities. J. Opt. Soc. Am. A, 1997, v.14, No.12, p.3323-3332

[2] V.F. Izotova, I.L. Maksimova, I.S. Nefedov, S.V.Romanov Investigation of Mueller matrices of anisotropic nonhomogenous layers in application to optical model of cornea. Appl. Opt., 1997, v.36, N0.1, p.164-169

QUASILINEAR THEORY OF INTERACTION BETWEEN SURFACE PLASMONS AND AN ELECTRON BEAM MOVING PARALLEL TO A PLASMA SURFACE IN VACUUM

Y.O. Averkov, and V.M. Yakovenko

Institute of Radiophysics and Electronics, National Academy of Sciences of Ukraine
12 Acad. Proskura Street, 61085 Kharkov, Ukraine. E-mail: ***averkov@online.kharkiv.net***

QUASI-LINEAR EQUATIONS

Let us consider the homogeneous semiconductor plasma, which is placed into the half-space $(y<0)$ in the absence of external magnetic field. The nonmonoenergetic electron beam moves along the axis (ox) in the half-space $(y>0)$ (vacuum) at the velocity of v_0. The beam density n_b is assumed to be much less than the semiconductor plasma density n_p. Besides we will assume that there are a lot of surface plasma waves which have various wave-vectors $\vec{q}$ and various phases and propagate simultaneously on the boundary (y=0) along the axis (ox). From statement of the problem it follows that the excitation of surface plasmons occurs only due to movements of the beam electrons along the axis (ox). That is why we will consider the one-dimensional problem and will describe statistics of the beam electrons by the "background" distribution function $F(k_x)$ that satisfies to the following normalization condition:

$$\int_{-\infty}^{\infty} F(k_x)\frac{dk_x}{2\pi} = \overline{n}_b, \tag{1}$$

where $\overline{n}_b = n_b S$ is the linear density of the beam electrons, S is the cross-sectional area of the electron beam. Henceforward at numerical evaluations we will suppose that $S \propto q_x^{-2}$. Taking into account one-dimensionality of our problem we will hide the index "x" at k_x, q_x. The initial system of kinetic equations for the averaged distribution function of resonant electrons of the beam F_k and for the distribution function of plasmons N_q (in the case of $N_q >> 1$) is:

$$\begin{cases} \dfrac{\partial F_k}{\partial t} = \sum\limits_q N_q\left[W_{k+q,q}\left(F_{k+q}-F_k\right)\delta\left(E_{k+q}-E_k-\hbar\omega_q\right) - W_{k,k-q}\left(F_k-F_{k-q}\right)\delta\left(E_k-E_{k-q}-\hbar\omega_q\right)\right], \\ \dfrac{\partial N_q}{\partial t} = N_q\sum\limits_k W_{k+q,q}\left(F_{k+q}-F_k\right)\delta\left(E_{k+q}-E_k-\hbar\omega_q\right), \end{cases} \tag{2}$$

where $\omega_q = \omega_0/\sqrt{\varepsilon_0+1}$ is the frequency of the slow surface plasmon $(c\to\infty$, here c is the light velocity in vacuum), $\omega_0 = \left(4\pi e^2 n_p/m^*\right)^{1/2}$ is the frequency of Langmuir oscillations of plasma, m^* is the effective mass of plasma electrons, ε_0 is the dielectric constant of the semiconductor lattice, $W_{k,q}$ is defined by the following expression [4]:

$$W_{k,q} = \frac{2\pi}{\hbar}\left|w_{k,q}\right|^2, \quad w_{k,q} = \frac{e\hbar(k_1^2-k_2^2)}{m_0 q^2 L_y}\left[\frac{\hbar\pi\omega^{-1}{}_q}{2S(\varepsilon_0+1)}\right],$$

where k_1, k_2 are the wave vectors of electrons "before" and "after" scattering, $w_{k,q}$ is the matrix element of Hamiltonian of interactions between an electron beam and an electromagnetic

wave, L_y is the dimension of the system along the axis (oy). Note that ε_0 is equal to its bulk value for homogeneous isotropic plasma. We assume that the electrons are reflected specularly from the boundary.

The transition from Eq.(2) to quasi-linear equations [1-3] for F_k and for the spectrum density of surface plasmons energy ε_q is carried out on the following assumptions:

$$|q/k| << 1, N_q = |\varepsilon_q / \hbar\omega_q| \tag{3}$$

Actually, this means the transition to the case of diluted plasma in which the relative change of the momentum of the beam electron at excitation (or absorption) of the plasmon is negligible.

Expanding the right-hand side of Eq.(2) with respect to q/k and turning from summations over q and k to appropriate integrals, we obtain the following system of quasi-linear equations:

$$\begin{cases} \dfrac{\partial \varepsilon}{\partial t} = 2\gamma\varepsilon, \\ \dfrac{\partial F}{\partial t} = \dfrac{\partial}{\partial v}\left(D \dfrac{\partial F}{\partial v} \right), \end{cases} \tag{4}$$

where the wave numbers q and the velocities of the electrons v satisfy the following expression $\omega_q = qv$, which allows to consider the values F_k and ε_q as the functions of the velocity v. Thanks to this fact we can hide the indexes "q" and "k" at these values in Eq. (4),

$$\gamma = \frac{\pi e^2 v^3}{\hbar\omega^2{}_q(\varepsilon_0 + 1)L_y S}\frac{\partial F}{\partial v}, \; D = \frac{2\pi e^2 \varepsilon}{\omega_q m^2{}_0(\varepsilon_0 + 1)L_y S},$$

Let at initial moment of time the functions $\varepsilon_0(v)$ and $F_0(v)$ are:

$$\varepsilon_0(v) = T_p, \; F_0 = \frac{\sqrt{2\pi}\hbar\bar{n}_b}{m_0 v_{T_b}} \exp\left(-\frac{(v - v_0)^2}{2v^2_{T_b}} \right), \tag{5}$$

where T_p is the temperature of semiconductor plasma in energy units, $v_{T_b} = \sqrt{T_b / m_0}$ is the thermal velocity of the beam electrons, T_b is the temperature of the beam electrons in energy units. The boundaries of the plateau v_1, v_2 of the distribution function $F_\infty(v)$ in quasi-equilibrium state are defined by the following continuity conditions:

$$F_0(v_1) = F_\infty(v_1), \; F_0(v_2) = F_\infty(v_2), \tag{6}$$

where $F_\infty(v)$ is found from the condition of conservation of resonant electrons.

It is clearly that in the case of neglecting of distribution function of plasma electrons the left boundary of the plateau is $v_1 = 0$. The right boundary v_2 and $F_\infty(v)$ are:

$$v_2 = v_0 + \sqrt{2} v_{T_b} \ln^{1/2}\left(\frac{v_0}{\sqrt{2\pi} v_{T_b}} \right), \; F_\infty = \frac{\pi\hbar\bar{n}_b}{v_2 m_0}\left\{ \Phi\left[\ln^{1/2}\left(\frac{v_0}{\sqrt{2\pi} v_{T_b}} \right) \right] + \Phi\left[\frac{v_0}{\sqrt{2} v_{T_b}} \right] \right\}. \tag{9}$$

The energy of oscillations in quasi-equilibrium state $\varepsilon_\infty(v)$ is:

$$\varepsilon_\infty(v) = \varepsilon_0(v) + \frac{\pi m_0 \bar{n}_b}{\omega_q} v^3 \left\{ \frac{v}{v_2}\left[\Phi\left(\ln^{1/2}\left(\frac{v_0}{\sqrt{2\pi} v_{T_b}} \right) \right) + \Phi\left(\frac{v_0}{\sqrt{2} v_{T_b}} \right) \right] - \Phi\left(\frac{v - v_0}{\sqrt{2} v_{T_b}} \right) - \Phi\left(\frac{v_0}{\sqrt{2} v_{T_b}} \right) \right\} \tag{10}$$

The dependencies of the spectral density of surface plasmons on their phase velocity (in terms of c) $\varepsilon_\infty(v)-\varepsilon_0(v)$ are shown in Fig.1 at the scale of $1/S$ for $v_0 = 0.05c$ (solid line) and $v_0 = 0.1c$ (dash line), $T_b = 5000$ K. The density of the beam electrons and the plasmon frequency are: $\bar{n}_b \approx 10^{14}$ м$^{-3}$, $\omega_q \approx 5\cdot 10^{12}$ с$^{-1}$. Fig.1. shows that at the boundaries of the plateaus the conditions $\varepsilon_\infty(0)=\varepsilon_0$, $\varepsilon_\infty(v_2)=\varepsilon_0$ take place and maximums of the spectral density of plasmons are shifted to initial velocity of the beam v_0. It should be noted that with decreasing the beam temperature the maximum of the plasmon spectrum shifts to the initial velocity of the beam v_0. Besides let us note that the spectrum of the surface plasmons qualitatively corresponds to the spectrum in the case of homogeneous bulk plasma [5]. The energy loses of the electron beam for the whole relaxation time is ($\bar{v}_0 >> \bar{v}_2 \geq 1$):

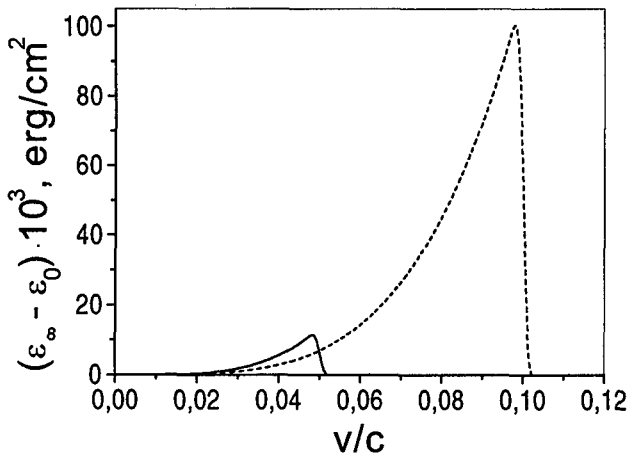

Fig.1.

$$\Delta\varepsilon = \frac{\pi \bar{n}_b m_0}{5\omega_q}\Phi(\bar{v}_0)\bar{v}_0^3\left[\frac{\Phi(\bar{v}_2)}{\Phi(\bar{v}_0)} - \frac{1}{4}\right] + O\left(v_0^3\frac{v_{T_b}}{v_0}\right). \qquad (11)$$

CONCLUSION

Thus, in the present work the quasi-linear theory of interaction between surface plasmons and nonmonoenergetic electron beam moving parallel to the semiconductor boundary is developed. For the quasi-equilibrium state the distribution function of the beam electrons, the spectrum of the surface plasmons and the value of the power losses of the electron beam for the whole relaxation time are derived.

REFERENCES

[1] V.D.Shapiro. On the influence of the electrostatic instabilities on plasma conductivity and temperature // Izvestia *Vuzov. Radiofizika.* 1961, V.4, No.5, pp.867-874. (In Russian)

[2] A.A.Vedenov, E.P.Velihov, R.Z.Sagde-ev. Quasi-linear theory of plasma oscillations // *Nuclear Fusion. Supplement.* 1962, Part 2, p.465-475. (In Russian)

[3] W.E.Drummond, D.Pines. Non-linear stability of plasma oscillations // *Nuclear Fusion. Supplement.* 1962, Part 3, p.1049-1057.

[4] N.N.Beletskii, V.M.Svetlichnyi, D.D. Khalameida, V.M.Yakovenko. Super-high frequency phenomena in non-homogeneous semiconductors. Kiev, Naukova Dumka, 1991, 216 p. (In Russian)

[5] A.A.Vedenov, D.D.Rutov. Quasi-linear effects in beam instabilities // *Vopr. Teor. Plasmy.* 1972, No.6, pp.3-21. (In Russian)

INVESTIGATION OF THE PLANE WAVE BEHAVIOR WITHIN BIANISOTROPIC MEDIA

K. A. Vytovtov
Radiophysics Department, Dnipropetrovsk State University
13 Naukova str., Dnipropetrovsk, Ukraine, E-mail: vytovtov@ap1.net-rff.dsu.dp.ua

INTRODUCTION

Various chiral media both isotropic and anisotropic present an increased interest for theoretical and experimental investigation. Isotropic media have been described in detail in [1,2]. Theory of chiral-ferrite media have been presented in [3]. Plane wave propagation within bianisotropic media has been considered in [4,5]. However, theory of bianisotropic media when nondiagonal terms in chirality tensor and permittivity tensor are not equal to zero has not been presented early.

STATEMENT OF THE PROBLEM

The homogeneous lossless bianisotropic media described by the constitutive relations

$$\begin{aligned} \vec{D} &= \overline{\overline{\varepsilon}}\,\vec{E} + j\overline{\overline{\xi}}\,\vec{B}; \\ \vec{H} &= j\overline{\overline{\xi}}^{T}\,\vec{E} + \mu_0^{-1}\vec{B}, \end{aligned} \tag{1}$$

where

$$\overline{\overline{\varepsilon}} = \begin{vmatrix} \varepsilon_{xx} & \varepsilon_{xy} & 0 \\ -\varepsilon_{xy} & \varepsilon_{xx} & 0 \\ 0 & 0 & \varepsilon_{zz} \end{vmatrix}, \quad \overline{\overline{\xi}} = \begin{vmatrix} \xi_{xx} & \xi_{xy} & 0 \\ -\xi_{xy} & \xi_{xx} & 0 \\ 0 & 0 & \xi_{zz} \end{vmatrix}, \tag{2}$$

are considered in this paper. It is assumed that the plane harmonic wave with frequency ω propagates along arbitrary direction within considered media.

Our purpose is investigation of the wave behavior within these media. At first it is necessary to obtain and study the analytical expressions of the wavenumbers for arbitrary direction of wave propagation. Then it is interesting to consider two particular cases: 1) the wave propagation along the bianisotropy axis, 2) the wave propagation normally to the bianisotropy axis.

Wavenumbers of the eigenwaves. The wavenumbers are obtained starting from the compartibility condition of Maxwell's equations, which can be written in following form

$$a_4 k^4 + a_3 k^3 + a_2 k^2 + a_1 k + a_0 = 0, \tag{3}$$

where

$$a_4 = \mu_0\left(2\xi_{xx}\xi_{zz} - \xi_{xx}^2 - \xi_{zz}^2\right)\cos^4\alpha + \left[-\varepsilon_{xx} + \varepsilon_{zz} + \mu_0\left(\xi_{xx}^2 + \xi_{zz}^2 - \xi_{xy}^2 - 2\xi_{xx}\xi_{zz}\right)\right]\cos^2\alpha + \varepsilon_{xx} + \mu_0\xi_{xy}^2;$$

$$a_3 = j2\omega\mu_0\varepsilon_{xy}\left(\xi_{zz} - \xi_{xx}\right)\cos\alpha\sin^2\alpha;$$

$$a_2 = \omega^2\mu_0\left[\left(\varepsilon_{xx}^2 + \varepsilon_{xy}^2 + \mu_0\xi_{xx}^2\varepsilon_{xx} + \mu_0\xi_{xy}^2\varepsilon_{xx} + 2\mu_0\xi_{xx}\xi_{zz}\varepsilon_{xx} + \mu_0\xi_{zz}^2\varepsilon_{xx} - \right.\right.$$

$$\left.\left. - 4\mu_0\xi_{xx}^2\varepsilon_{zz} - \varepsilon_{xx}\varepsilon_{zz}\right)\cos^2\alpha - \mu_0\xi_{xy}^2\varepsilon_{xx} + 2\mu_0\xi_{xx}\xi_{zz}\varepsilon_{xx} + \varepsilon_{xx}^2 + \varepsilon_{xy}^2 + \mu_0\xi_{xx}^2\varepsilon_{xx} + \mu_0\xi_{zz}^2\varepsilon_{xx} + \varepsilon_{xx}\varepsilon_{zz}\right];$$

$$a_1 = j4\omega^2\mu_0^2\xi_{xx}\varepsilon_{xy}\varepsilon_{zz}\cos\alpha; \quad a_0 = \omega^4\mu_0^2\varepsilon_{zz}\left(\varepsilon_{xx}^2 + \varepsilon_{xy}^2\right).$$

This four order algebraic equation can be solved analytically, although it cannot be reduced to square equations. Here we write wavenumbers in analytical form

$$k_{1,2} = \sqrt{\frac{\beta_0}{2}} + \sqrt{-\beta_0 - \frac{a_2}{2a_4} + \frac{3a_3^2}{16a_4^2} - \frac{\left(-4a_2a_3a_4^2 + a_3^3a_4 + 8a_1a_4^3\right)\sqrt{2}}{32a_4^4\sqrt{\beta_0}}} - \frac{a_3}{4a_4}; \tag{4}$$

$$k_{3,4} = \sqrt{\frac{\beta_0}{2}} + \sqrt{-\beta_0 - \frac{a_2}{2a_4} + \frac{3a_3^2}{16a_4^2} + \frac{\left(-4a_2a_3a_4^2 + a_3^3a_4 + 8a_1a_4^3\right)\sqrt{2}}{32a_4^4\sqrt{\beta_0}}} - \frac{a_3}{4a_4}, \tag{5}$$

were β_0 is an arbitrary root of the third order equation

$$\beta^3 + \frac{8a_2a_4 - 3a_3^2}{8a_4^2}\beta^2 + \left(\frac{\left(8a_2a_4 - 3a_3^2\right)^2}{256a_4^4} - \right.$$

$$\left. - \frac{-64a_1a_3a_4^2 + 256a_0a_4^3 + 16a_2a_3^2a_4 - 3a_3^4}{256a_4^4} \right)\beta - \frac{\left(-4a_2a_3a_4 + a_3^3 + 8a_1a_4^2\right)^2}{64a_4^6} = 0 \ ,$$

which can be solved analytically by Kardano–Ferrary's method.

Note that there are four different wavenumbers and consequently there are four different eigenwaves.

The expressions of the electromagnetic field components can be obtained directly from Maxwell's equations in analytically form, but they are unwieldy and that is why they are not written here. However it should be noted that in general case the eigenwaves are plane, non-transversal waves, and the ones include all six components of the electromagnetic field.

Wave propagation along bianisotropy axis. If a harmonic wave propagates along the bianisotropy axis then all four wavenumbers are different and four different eigenwaves are within the media: two of these are right-circular-polarization waves and other two of these are left-circular-polarization waves. Resulting right-polarization wave is a pulsation as $\left||k_1|-|k_4|\right| \ll 1$. Analogously, resulting left-polarization wave is a pulsation as $\left||k_2|-|k_3|\right| \ll 1$. Resulting electric field is periodic function of space coordinate z.

Wave propagation normal two bianisotropy axis. In this case two plane non-transversal wave propagate within bianithotropic media as the equation (3) is bi-square. The expressions of the field component are obtained directly from Maxwell's equations, but they are not represented here as the ones are very unwieldy. Each of these wave is elliptic polarizated and includes all six field components.

NUMERICAL EXAMPLE

For example, infinite homogeneous medium with uniaxial bianisotropy is considered. The terms in (2) are $\varepsilon_{xx} = 1.14\varepsilon_0$, $\varepsilon_{xy} = j0.5\varepsilon_0$, $\varepsilon_{zz} = 1.20\varepsilon_0$, $\xi_{xx} = 2.54\omega 10^{-16}$, $\xi_{xy} = j\omega 10^{-17}$, $\xi_{zz} = 2.55\omega 10^{-16}$. Fig.1 shows the dependence of the wavenumbers on the angle between bianisotropy axis and propagation direction on frequancy 2GHz. It is interesting that two of four wavenumbers are smaller then the wavenumber of a wave in vacuum on given frequency. Now consider the plane harmonic wave propagating along the bianisotropy axis within considered media. Fig.2 demonstrates the dependence of x- and y-component of the resulting wave electric field on space coordinate z. The wave frequency is 2GHz. Analyzing these results we can see that the x- and y-components are non-harmonic periodic functions of coordinate z. The amplitude of the resulting electric field is the periodic function of the space coordinate z and the resulting electric field is elliptic polarized. Analogously, it is possible to show that resulting magnetic field is elliptic polarized and its amplitude is periodic function of z. Let us consider wave propagation normally to the bianisotropy axis. In this case each elliptic polarized eigenwave includes all six field components. Moreover, one of these waves has a right-elliptic-polarization, the other have left-elliptic-polarization. The ellipses described by the vectors of the electric field strength are shown in Fig.4. It is important that the wavenumber of the right-elliptic-polarized wave is greater than the wavenumber in vacuum and the wavenumber of the left-elliptic-polarized wave is smaller than the wavenumber in vacuum.

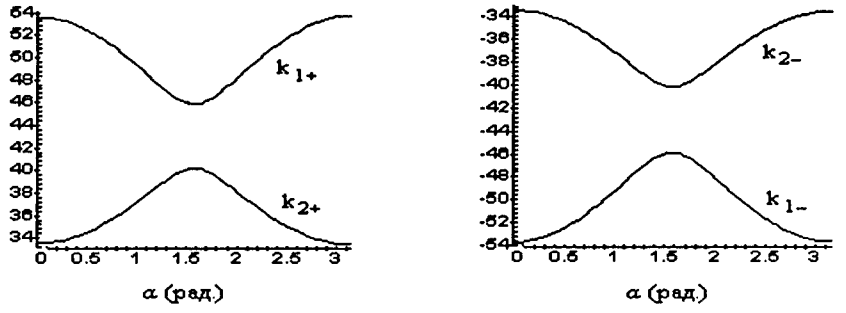

а) б)

Fig.1. Dependence of the wavenambers on the angle

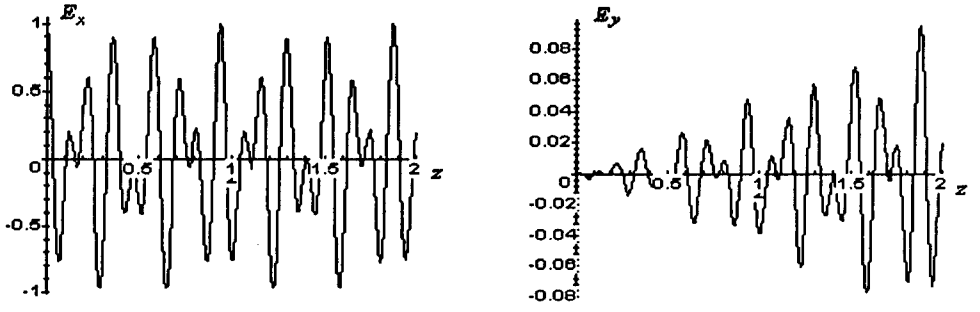

Fig.2. Dependence of x- and y-components of the resulting electric field on coordinate z

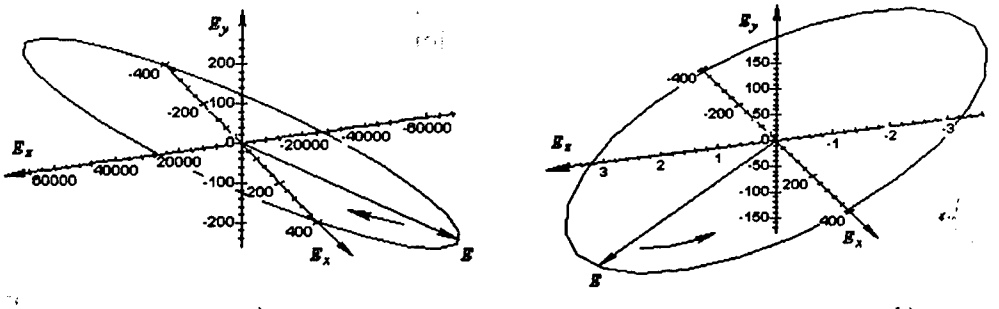

a) b)

Рис.3.The ellipses described by the electric field strength vectors for the wave propagation normally to the bianisotropy axis a) a right-elliptic-polarization wave b) a left-elliptic-polarization wave

REFERENCES

[1] D. L. Jaggard, A. R. Mickelson, and C. H. Papas, On electromagnetic waves in chiral media, Appl. Physics, vol.18, pp.211–216, 1979.

[2] I.V.Lindell, A.H.Sihvola, S.A. Tretyakov, A.J.Viitanen, Electromagnetic waves in chiral and bi-isotropic media, Boston and London, Artech House,1994.

[3] C.M.Krowne, Nonreciprocal electromagnetic properties of composite chiral-ferrite media.–IEE Proceedings-H.–Microwaves, antenas and propagation.–vol.140,N.3,1993.–pp.242–248.

[4] A.J.Viitanen, I.V. Lindell, Plane-wave propagation in a uniaxial bianisotropic medium with an aplication to a polarization transformer.–International Journal of Infrared and Millimeter Waves, vol.14.–N.10, 1993.–pp.1993–2010.

[5] S.A.Tretyakov, A.A.Sochava, Reflection and transmission of plane electromagnetic waves in uniaxial bianisotropic materials.– International Journal of Infrared and Millimeter Waves, vol.15.–N.5, 1994.–pp.829–855.

GAS DISCHARGE SUSTAINED BY THE NONPOTENTIAL SYMMETRIC SURFACE WAVE IN MAGNETIZED HETEROGENEOUS PLASMA COLUMN

V.P. Olefir[1], N.A. Azarenkov[1], and A.E. Sporov[2]

[1]Department of Physics and Technology, Kharkiv National University, 61077 Kharkiv, Ukraine

[2]Electro–Physical Scientific & Technical Centre of National Academy of Sciences of Ukraine, 61002 Kharkiv, Shernyshevskogo st. 28, P.O. Box 8812, Ukraine

ABSTRACT

This report is devoted to the research of the dispersion properties, damping rates and radial wave field structure for electromagnetic azimuth–symmetric high–frequency surface wave (SW) in radial inhomogeneous cylindrical waveguide structure with given plasma density radial profile. The dependence of plasma density axial profile in the discharges sustained by the considered SW in diffusion controlled regime from the plasma heterogeneity was also studied. External steady magnetic field is directed along the axis of the waveguide system. Plasma is considered in hydrodynamic approximation as cold and weakly collisional medium with constant value of effective electron–neutral collision frequency for momentum transfer. Axial structure of SW sustained gas discharge was studied for the case when SW characteristics and axial electron density vary slightly along the discharge length.

THEORETICAL FORMULATION

The intensive theoretical and experimental research of gas discharges sustained by high–frequency travelling SW are stipulated by their wide practical using in numerous technological applications. SW, that sustains the discharge, is the eigen wave of discharge structure. This is the characteristic feature of such discharges and leads to the strong influence of the SW properties on the axial distribution of discharge parameters. Up to now, the SW properties and gas discharge axial structure were mainly studied for the waveguide structures with uniform plasma filling. However, in real discharge systems plasma density is always inhomogeneous in radial direction and the conditions of upper hybrid resonance may take place at the periphery of plasma column [1]. The efficiency of energy transfer from SW into gas discharge plasma can be increased substantially in such regions, where electromagnetic waves transform into plasma waves [2]. This process can affect greatly the plasma density axial structure in SW sustained gas discharges. The main aim of this report is to determine the influence of plasma density radial profile on the SW properties and on the plasma density axial structure in the discharges sustained by the symmetric SW in diffusion controlled regime.

SW considered propagates in magnetized waveguide structure that consists of radial inhomogeneous plasma column with radius R_p and the metal waveguide wall with radius R_m ($R_p < R_m$). External steady magnetic field $\vec{B}_0$ is directed along the axis of the waveguide structure. Plasma is considered in hydrodynamic approximation as cold and slightly absorbing medium with constant effective electron – neutral collision frequency ν in the discharge volume. This frequency is much less than SW generator frequency ω. Plasma density radial profile $n(r)$ was chosen in Bessel–like form given by $n(r) = n(0)\, J_0\left(\mu\, r\, R_p^{-1}\right)$. Heterogeneity parameter μ varies from $\mu = 0$ (radial homogeneous case) to $\mu = 2.4$ (perfect ambipolar diffusion profile). The SW propagation is governed by the system of Maxwell equations. This

wave possesses all six components of electromagnetic field. In the case of inhomogeneous plasma density radial distribution this system, for arbitrary discharge parameters (plasma density radial profile, external magnetic field value, geometrical parameters of discharge structure), can be solved only with the help of numerical methods. In the case considered, when plasma density, SW wavelength and its amplitude vary slightly along the discharge column at the distances of wave length order, the solution of the system of Maxwell equations in cylindrical coordinate system (r,φ,z) for SW field components $\vec{E},\vec{H}$ can be found in WKB form:

$$\vec{E},\ \vec{H}(r,\varphi,z,t)=\vec{E},\ \vec{H}(r)\exp\left(i\left[\int_{z_0}^{z}k_3(z')dz'+m\varphi-\omega t\right]\right), \tag{1}$$

where k_3 and m are axial and azimuth wavenumbers, respectively.

Applying expression (1) to the system considered one can reduce it into the system of four ordinary differential equations for the tangential SW components [2]. General solution of the system reduced can be written as the linear combination of two linearly independent vectors of solutions ($E_z^{1,2}$, $E_\varphi^{1,2}$, $H_z^{1,2}$, $H_\varphi^{1,2}$), that satisfy the boundary conditions at the axis of waveguide system [2]. If $r=0$, the tangential components of SW electric and magnetic fields turn to zero. The fulfillment of boundary conditions at the waveguide metal wall (vanishing of SW electric field tangential components) leads to a set of two linear equations. The existence conditions of this set yield a local dispersion equation in the form:

$$E_z^1(R_m)E_\varphi^2(R_m)-E_z^2(R_m)E_\varphi^1(R_m)=0. \tag{2}$$

Due to the SW symmetry properties, one can choose such vectors $(1,0,0,0)$ and $(0,0,1,0)$, as linear independent vectors of solutions [2]. In spite of the low value of collision frequency $(\nu<<\omega)$ it is necessary to keep imaginary addends in the expressions of the permittivity tensor of magnetized plasma. These imaginary addends enable one to do numerical integration of the set of ordinary differential equations in the region when upper hybrid resonance occurs. Therefore, the complex local dispersion equation (2) is obtained, the real part of its complex solution for wavenumber gives wavelength, and imaginary part gives SW damping rate.

To solve the dispersion equation (2) one must first solve the system of ordinary differential equations with the help of Gear method under the fixed values of k_3 and ω. Then, with the help of Muller method, one can find the eigen value of k_3 or ω. To improve the ortogonal properties of the solution vectors one must use the Godunov ortogonalize procedure on the whole integration path [3].

In the case considered it is possible to obtain axial electron density variation as an intricate function of attenuation coefficient. The axial profile of dimensionless density $N=\omega_{pe}^2\omega^{-2}$ can be theoretically determined from the energy balance equation of gas discharge stationary state in diffusion controlled regime [4]. If assume power that maintains an electron in the discharge θ and electron effective collision frequency for momentum transfer ν are constant in discharge volume, one can obtain equation that governs plasma density axial distribution in the form:

$$\frac{dN}{d\xi}=-\frac{2N\alpha}{\nu\omega^{-1}\left(1-(d\alpha/dN)N\alpha^{-1}\right)}, \tag{3}$$

where $\alpha=\mathrm{Im}(k_3R_p)$ is the dimensionless damping rate and $\xi=\nu z(\omega R_p)^{-1}$ is the

dimensionless axial coordinate [4].

DISCUSSION

Unlike the usual dispersion equation connecting wave frequency and wave length under the fixed value of plasma density, the local dispersion equation in this considered case connects local value of plasma density and wavelength under the fixed value of generator frequency ω. The dispersion properties of SW considered are represented in Figs.1,2. Numbers 1–7 in the figures correspond to the μ value 0.0, 1.0, 1.5, 2.0, 2.2, 2.3 and 2.405,

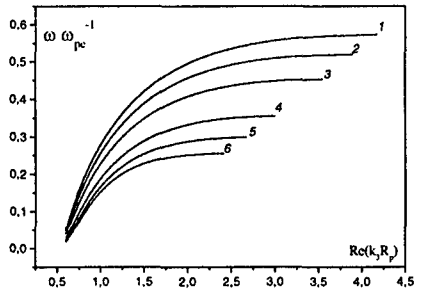

Figure 1

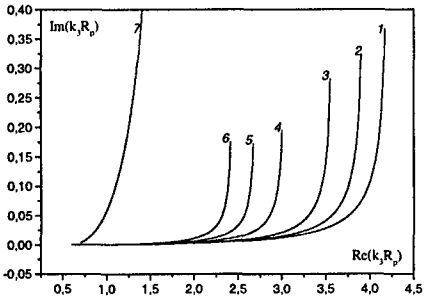

Figure 2

respectively. It was shown that SW dispersion characteristics essentially depend on the heterogeneity parameter μ. The increasing of the μ value leads to the decreasing of SW phase velocity (Fig.1). Damping rate the SW essentially increases with the increasing of parameter μ value (Fig.2). SW damping rate grows sharply in the case when the condition of upper hybrid resonance is fulfilled at the periphery of plasma column (curve 7 in Fig.2).

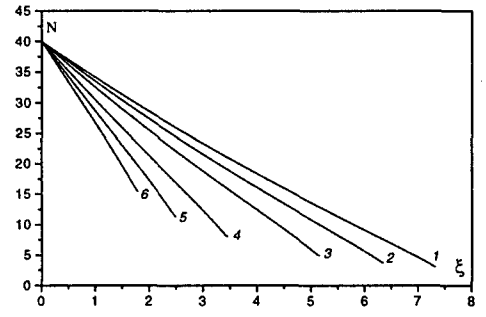

Figure 3

The results of numerical investigation of plasma column axial structure sustained by symmetric SW are presented in Fig.3. Gradual increasing of heterogeneity parameter μ leads to growth of maximum possible plasma density and to the decreasing of discharge length. When upper hybrid resonance takes place, the maximum possible plasma density sharply grows and discharge length greatly decreases due to effective energy transfer from SW to plasma electrons.

This work was supported by the Science and Technology Center in Ukraine (STCU, Project #1112).

REFERENCES

[1] Peres, M. Fortin, J. Margot, *Phys. Plasmas* 3, 1754 (1996).
[2] Karbushev N.I., Kolosov U.A., Polovkov A.I. *Phisica Plasmy*, **18**, №1, 54 (1992).
[3] Godunov S.K. *Uspehi Mat. Nauk.*, **16**, p. 171 (1961).
[4] M. Moisan, Z. Zakrzewski, *Journal of Physics D: Applied Physics*, **24** 1025 (1991).

HIGH HARMONIC GENERATION IN A CLASSICAL ANHARMONIC OSCILLATOR

D. Yu. Churmakov
Belarussian State University
Lubimova 13 -1- 46, Minsk 220117, Belarus
e-mail: churmakov@mail.ru

ABSTRACT

The purpose of this article is to present a calculation of high harmonic generation by a classical anharmonic oscillator using counter-propagating light. We use the model of quartic anharmonic Duffing oscillator as one of the simplest centrosymmetric system for analysis.

ANHARMONIC OSCILLATOR MODEL DESCRIPTION

The potential of our anharmonic oscillator can be written as

$$V(x)=\frac{\omega_0^2}{2}x^2+\frac{\beta x^4}{4} \tag{1}$$

and correspond to the sum of harmonic oscillator potential, of frequency ω_0 and anharmonic quartic term. Consequently the equation of motion is

$$\ddot{x}+\omega_0^2 x=\frac{e}{m_e}E(t)-\beta x^3, \tag{2}$$

where β parametrizes the anharmonicity; e, m_e are the electron charge and mass, respectively. We have considered here $E(t)$ to be the resulting field applied to an atom. The resulting polarization is assumed to be $P=en_e x$, where n_e is the electron density.
The characteristic frequency ω_0 is considered to be 10ω corresponding to the typical ratio between the ionization potential of a noble gas and photon energy of a low-frequency laser. According to [2] the anharmonicity parameter β is resonable to choose around $2\times10^{35}(As)^{-2}$ to correspond to the measurements of the third harmonic emission, i.e. the third harmonic amplitude of the Fourier spectrum.

NUMERICAL CALCULATION

Following the scheme suggested in [3], we use two counter-propagating pulses of different duration τ. They were chosen to be of the Gaussian shape

$$E_{1,2}(t) = E_{0_{1,2}} \cos(\omega, t) \exp\left(-2 \ln\left(\frac{t}{\tau_{1,2}} - cut \right)^2 \right), \tag{3}$$

where superscript (1) corresponds to the first (shorter) pulse, and (2) correspons to the longer one, ω being the carrier frequency. The parameters of the pulses are:

$$T = \frac{2\pi}{\omega} = 2.5 fs,\ \tau_1 = 20 fs,\ \tau_2 = 160 fs,\ I_1 = 1.6 \times 10^{14} \frac{W}{sm^2},\ I_2 = 4.5 I_1,\ cut = 3.2,$$

where $I_{1,2}$ is the peak intensity of the pulses. We study the influence of gas slab length on the harmonic efficiency. For this matter we have performed calculation for a fine grid of lengths. It was found that the efficiency versus gas slab length (the efficiency means the ration of harmonic amplitude in the presence of counter pulse to that in the absence) can be raised by two orders of magnitude.

REFERENCE

[1] Ph. Balcou, A L'Huillier, and D. Eskande, Phys. Rev A v. 53, p. 3456 (1996).
[2] J. Peatross, D. D. Meyerhofer, Phys. rev. A, 52, p. 3975 (1995).
[3] J.Peatross, S.Voronov, and I. Porkopovich, Optics Express, v.1, p. 108, (1997).
[4] J. Peatross, H.V. Fedorov, K.C. Kulander, J. Opt. Soc. Am. B. 12, 863 (1995).
[5] A. L'Huillier, L.A. Lompr\'{e}, G. Mainfray et al., in International Conference on Multiphoton

SIMULATION MODELING OF STATISTICAL CHARACTERISTICS OF THE RADIO WAVE IN A LAYER WITH RANDOM INHOMOGENEITIES OF DIELECTRIC PERMITTIVITY

N.T. Afanasiev*, S.N. Kolesnik** and M.V. Tinin*
*Irkutsk State University, 20 Gagarin Blvd., Irkutsk, 664003, Russia
**Irkutsk Military Aviation Engineering Institute
E-mail vmt@api.isu.runnet.ru

ABSTRACT

This paper presents the methods of generation a random field of dielectric permittivity with a given correlation function. Results are derived from performing a simulation modeling of the mean intensity and a spatial correlation function of the wave field, the dispersion of angles of arrival, and spatial correlation functions of the amplitude and phase of the wave that has propagated through the layer with random inhomogeneities of dielectric permittivity. A comparison is made of the results of calculations of fluctuation characteristics of the radio wave by approximate formulas obtained with the perturbation method with results of a simulation modeling.

Theoretical investigations into fluctuations of parameters of the radio wave that has propagated through the layer of a randomly-inhomogeneous medium have important applications in a number of practical problems, such as space radio communications, radio navigation, remote sensing of terrestrial covers from space, etc. Considerable advances made in geometrical optics calculations of fluctuations of radio wave characteristics have been achieved mainly owing to perturbation theory. As is known, however, the perturbation method has a limited field of application [1]. Therefore, recent trends are toward increased use of the simulation modeling techniques where the model of a randomly-inhomogeneous medium is specified in the form of a random set of localized inhomogeneities of dielectric permittivity of different scales, and a calculation of fluctuations of radio wave characteristics is performed by rigorous geometrical optics formulas .

This paper presents the results of a numerical simulation of statistical characteristics of the radio wave that has propagated through a randomly-inhomogeneous layer. Calculations were carried out to the geometrical optics approximation. To generate a random field of dielectric permittivity we used a model in the form of the sum of Gaussian irregularities that is characterized by a Gaussian correlation function [2].

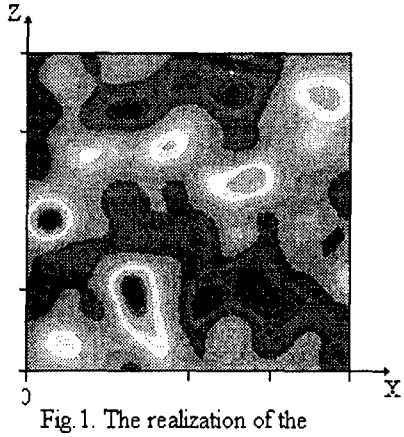

Fig. 1. The realization of the random field of irregularities.

Fig.1 exemplifies one of the realizations of the random field of irregularities. In such a model, we calculated numerically (NC) and using the method of small disturbances (MSD) the standard ray deviation σ_x, the standard angle deviation σ_β, the dispersions of the eikonal, and of the amplitude, and the correlation function of the field, eikonal, amplitude of the radio wave at the reception point.

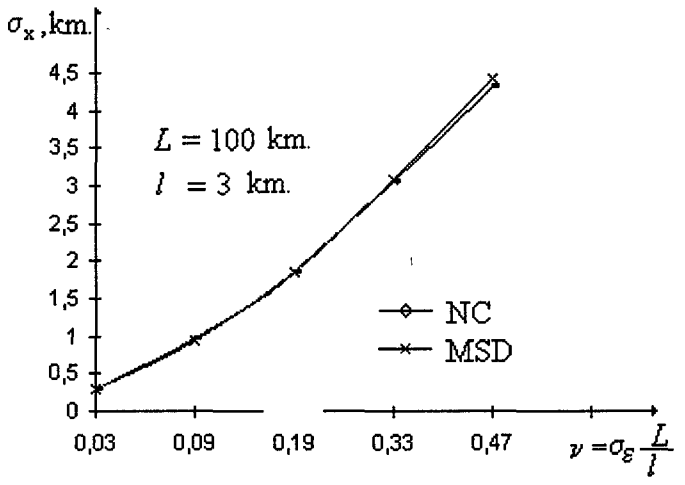

Fig.2. The dependece of standard ray deviation on the parameter ν.

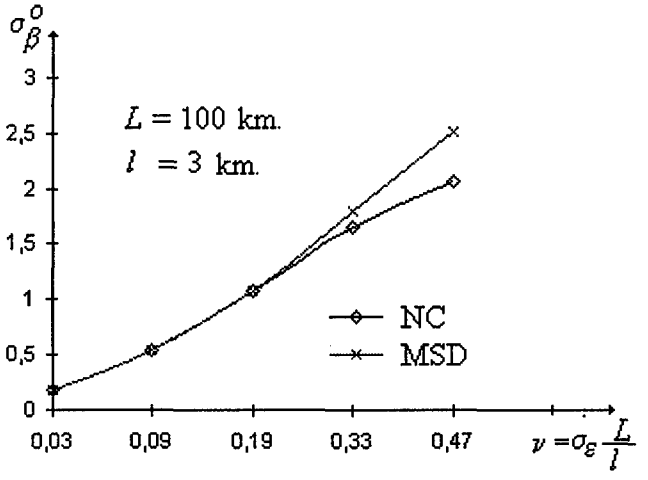

Fig.3. The dependece of standard angle deviation on the parameter ν.

As an example, Fig. 2 presents the dependence of σ_x on the parameter $\nu = \sigma_\varepsilon \frac{L}{l}$, where $\sigma_\varepsilon{}^2$ is the dispersion of dielectric permittivity, *L=100 km.* is the thickness of the layer with irregularities, and *l=3 km.* is the irregularity scale. Fig. 3 is a plot of σ_β in degrees versus parameter ν. It is evident from the figures that the MSD describes reasonably accurately the behavior of σ_x up to the values of $\nu \approx 0.33$ and σ_β up to the values of $\nu \approx 0.19$, respectively. Furthermore, the σ_β dependencies calculated using the MSD and numerically when $\nu > 0.19$ behave differently. According to the MSD, σ_β continues to increase, while the numerically inferred σ_β reaches the saturation level. This seems to be due to the fact that the trajectory of rays, while passing through the layer with random irregularities, depart rather strongly from the undisturbed trajectory. Therefore, the probability that such rays arrive at the reception points, is very low. Besides, it is apparent from Figs. 2 and 3 that a saturation of σ_β sets in when σ_x becomes of order *l*.

Fig. 4 illustrates the results of a numerical and asymptotic calculation of the spatial correlation function of the eikonal on the parameter $\nu = 0.09$. Fig. 5 illustrates the results of a numerical and asymptotic calculation of the standard eikonal deviation of on the parameter ν.

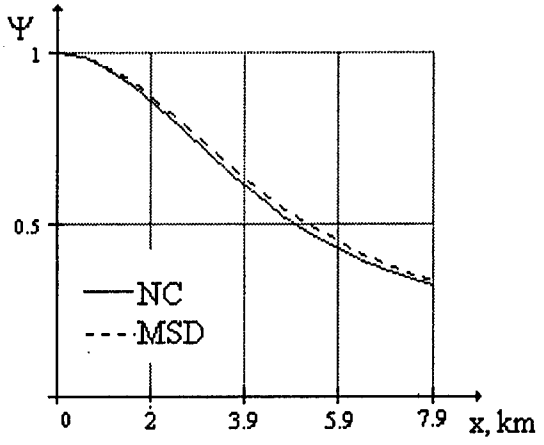

Fig.4. The spatial correlation function of the eikonal for $\nu = 0.09$

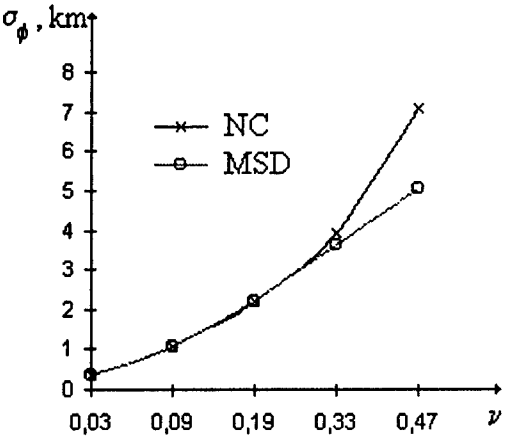

Fig.5. The dependence of standard eikonal deviation on the parameter ν.

This work was done with support from the Russian Foundation for Basic Research under grants Nos. 00-02-17780 and 00-15-98509.

REFERENCES

[1] S.M. Rytov, Yu.A. Kravtsov and V.I. Tatarsky. Introduction to Statistical Radio Physics. Part 2. Moscow: Nauka, 1978.

[2] N.T.Afanasiev, S.N.Kolesnik and M.V.Tinin. Using the Method of Perturbations in Ray Problems of Radio Wave Propagation in a Randomly-Inhomogeneous Ionosphere. Abstracts of Papers to the 9th All-Russia Scientific Conference "Propagation of Radio Waves", Kazan, 1999.

INTERACTION OF NATURAL OSCILLATIONS OF AN OPEN RESONATOR WITH AZIMUTHAL SURFACE WAVES OF PLASMA COLUMN

P.N. Melezhik

Usikov Institute of Radio Physics and Electronics, National Academy of Sciences of Ukraine
12 Akad. Proskury Str., Kharkov, 61085, Ukraine

ABSTRACT

A mathematically rigorous solution was found for a 2D problem about the natural oscillations of an open resonator in the form of a metal column with a longitudinal slot containing a circular plasma column inside. The dependences of the decrement of azimuth surface wave (ASW) attenuation on the effective wave number were obtained on the basis of the numerical implementation, and the interaction between the natural oscillations of the slot cylinder and the azimuth surface oscillations of the plasma column was analyzed.

SOLUTION OF THE SPECTRAL PROBLEM

Consider an open resonator (OR) in the form of a column with the radius a having a longitudinal slot of 2ϑ. In the middle of OR, a plasma column with the radius a_{pl} is located that has the following parameters: $k_p = \frac{\omega_p}{c}$, $k_c = \frac{\omega_c}{c}$, and $\tilde{\nu} = \frac{\nu}{c}$, where ω_p and ω_c are the plasmatic and electron cyclotron frequencies, respectively, and ν is the frequency of plasma electron collisions. The statements and the solution of the spectral problem are similar to those described in [1]. As a result, we derive an uniform set of linear algebraic equations of the second order in the unknowns $\left(x_m^p\right)_{m=-\infty}^{\infty}$, $p = 1,2$.

$$x_n^p = \sum_{j=1}^{2} \sum_{m=-\infty}^{\infty} A_{nm}^{pj}(k) x_m^j, \qquad p, j = 1,2 \tag{1}$$

where the matrix elements $\left\{A_{mn}^{pj}(k)\right\}_{n,m=-\infty}^{\infty}$, $p, j = 1,2$ were determined in [1]. It was proven that the elements of the diagonal matrix $\left\|A_{mm}^{ii}(k)\right\|$, $i = 1,2$ at $|m|,|n| \to \infty$ tend to zero, the same as $O\left(m^{-2}, n^{-2}\right)$, and the matrices $\left\|A_{mn}^{12}(k)\right\|$ and $\left\|A_{mn}^{21}(k)\right\|$ determine in the domain l_2 the nuclear, finitely meromorphic in R_k operator-functions. Then, $A(k) = \left\|A^{pl}\right\|_{p,j=1}^{2}$ is the nuclear operator-function that depends finitely-meromorphically on $k \in R_k$. Hence, the spectrum of the complex natural frequencies of the structure under consideration is discrete and finitely multiple, and k_0 is a characteristic number of the operator-function $I - A(k)$ if and only if k_0 satisfies the equation

$$\det\left(I - A(k_0)\right) = 0, \tag{2}$$

where $\det\left(I - A(k_0)\right)$ is the infinitely characteristic determinant of the operator-function $I - A(k)$.

THE NUMERICAL RESULTS

Fig.1 demonstrates the dependences of the frequency (Fig.1,a) and the decrement of ASW attenuation (Fig.1,b) on the effective wave vector $k_0 = \frac{m}{k_p a}$, where m is the number of the azimuth harmonics, k_p is the plasma frequency, and a is the radius of the metal column. These data were obtained in the numerical solution of Eq. (2).

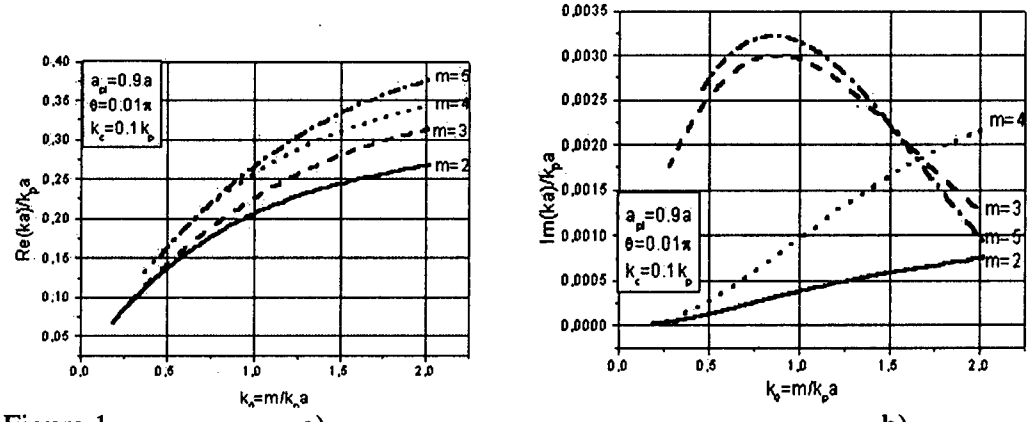

Figure 1. a) b)

The comparison with the results obtained in [2] shows that the behavior of the natural frequency, described by using an approximate model, qualitatively coincides with the results obtained by a rigorous method for all values of $m = 2, 3, 4, 5$. The quantitative values of the frequencies and the decrement of the ASW attenuation, as well as the behavior of the decrement of the ASW attenuation with even and odd numbers, were substantially different.

Consider the long wave part $ka_1 < 1$. Here, it is characteristic that the plasma column itself has a surface natural oscillation, whose real part of the natural frequency is approximately equal to the so-called ultimate frequency of surface wave [3], $k = \frac{k_p}{\sqrt{2}}$. On the other hand, in the case of H-polarized electromagnetic oscillations, a single cylinder with a longitudinal slot also has an natural oscillation in the long wave part, whose natural frequency is determined by the formula $k = \frac{1}{a_1}\left(-2\ln\left(\sin\vartheta_1/2\right)\right)^{-1/2}$. In this view, it may be interesting to analyze the behavior of these natural frequencies in the OR with a plasma insert by varying the parameters of the latter.

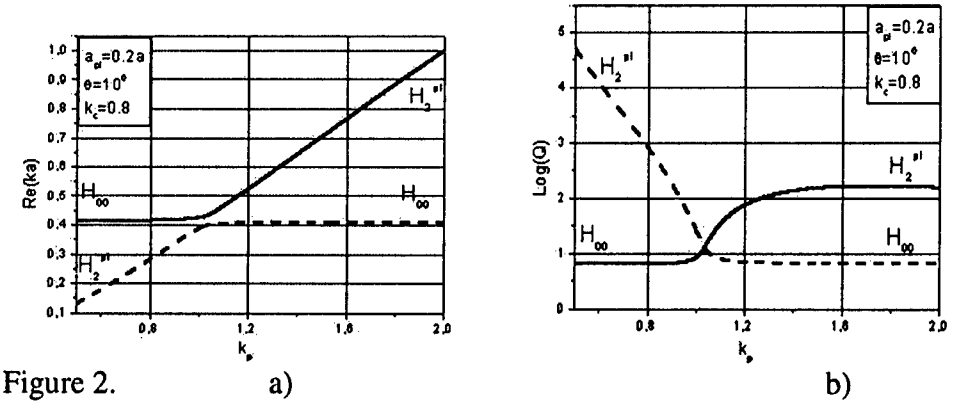

Figure 2. a) b)

Fig.2 illustrates the dependences of the real parts Re(ka) of these natural frequencies and the decimal logarithms of Q-factors $Log(Q)$, and the corresponding natural oscillations on the plasma frequency. Proceeding from the behavior both of Re(ka) and $Log(Q)$, it is obvious that, according to [4], the natural oscillations of the open resonator have an inter-mode coupling with the natural oscillations of the plasma column.

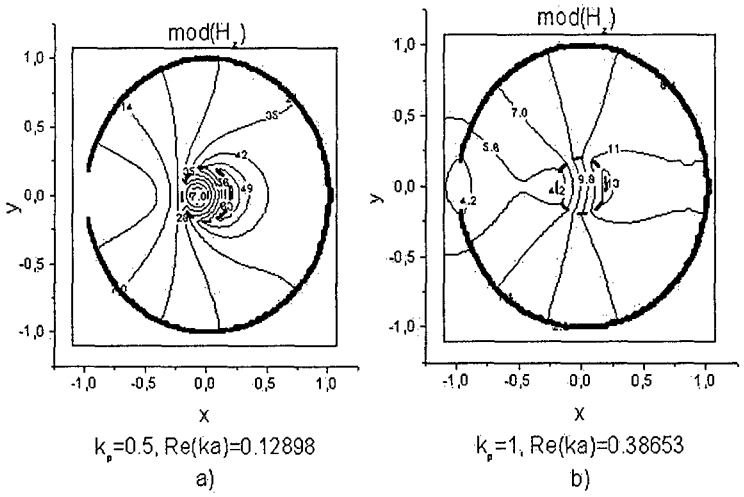

Figure 3.

It can be clearly seen in Fig.3 showing the curves of the equal values of the module ($|H_z|$)of the full magnetic field H_z that is excited in the resonator by an H-polarized plane electromagnetic wave at the real parts of natural frequencies for a plasma column. Here, the values of the plane wave frequency used for forming fields are shown by a dashed line in Fig.2,a).

As seen, by $k_p = 0.5$, up to the coincidence point [4], the field excited in OR is an natural field of ASW H_2^{pl}. By $k_p = 1$, near the coincidence point, the field is hybrid and has components of the ASW field H_2^{pl} and the natural field of OR H_{00}. By $k_p = 2$, after the coincidence, the field in OR corresponds to the H_{00} oscillation mode of an OR without cylinder. Such behavior of natural frequencies and fields, as it was shown in [4], is characteristic of the inter-mode oscillation coupling.

REFERENCES

[1] A.V. Brovenko, P.N. Melezhik, A.Y. Poyedinchuk, and V.P. Shestopalov. Spectral and diffraction characteristics of open resonators with hyrotropic (plasmatic) inserts. Izvestiya VUZov. Radiophysika, V.36, No.9, p. 1161-1175,1996.

[2] V.A. Girka, and N.A. Girka. Radiation of azimuth surface waves from a narrow waveguide slot. Radiotekhnika i Elektronika, V.37, No.3, p.419-422, 1992.

[3] A.N. Kondratenko. Surface and volume waves in a limited plasma. Moscow, Energoatomizdat, 1985.

[4] P.N. Melezhik, A.Y. Poyedinchuk, Y.A. Tuchkin, and V.P. Shestopalov. About analytical originis of eigemmode coupling. Dokl. Akad.Nauk SSSR, V.300, No.6, pp.1356-1359, 1988

PECULIARITIES IN THE NONLINEAR ELECTROMAGNETIC RESPONSE OF A THIN METAL FILM CARRYING A STRONG DC CURRENT

S.A. Derev'anko, G.B. Tkachev, and V.A. Yampol'skii

Usikov Institute of Radiophysics and Electronics, NASU
12 Acad. Proskura St., 61085 Kharkov, Ukraine
E-mail: stanislv@ire.kharkov.ua

ABSTRACT

The nonlinear interaction of a DC current flowing in a thin metal film with an external AC electromagnetic field is studied theoretically. The nonlinearity is due to the influence of the DC magnetic field and the magnetic field of the wave on the form of the electron trajectories. This magnetodynamic mechanism of nonlinearity is typical for pure metals at low temperatures. We find that such an interaction causes sharp kinks in the temporal dependence of the AC electric field at the surface of a sample. The phenomenon of amplification of the electromagnetic signal at the metal surface is also predicted.

INTRODUCTION

It is already known that metals possess quite peculiar nonlinear electrodynamical properties. In metals because of the high concentration of electrons it is rather hard to deviate the system significantly from the equilibrium position. Thus in metals all the mechanisms of nonlinearity typical for plasma or semiconductors are inefficient. The only effective mechanism in metals is associated with the influence of the self magnetic field of a current or an electromagnetic wave on the trajectories of the charge carriers. This mechanism (which is called the magnetodynamic mechanism) does not imply a significant departure of the electron subsystem from the equilibrium.

In the present work we investigate a novel manifestation of the magnetodynamical nonlinearity – the interaction of an external electromagnetic wave with a strong transport DC current, flowing in a thin metal film. We assume that the thickness d of the sample is much less than the electron mean free path l. It is known (see [1]) that in the static case (when the external AC field is absent) the peculiarities in the nonlinear response of the film are due to the presence of the plane at which the magnetic field changes sign within the sample. The spatially sign-alternating antisymmetrical field of current entraps a portion of electrons into a potential well. The trajectories of such particles are almost flat curves wound around the plane of the sign alternation. At the same time there exist electrons that do collide with the boundaries of the metal (fly-trough electrons) with the ratio of the conductivities of fly-through and trapped electrons being $\varepsilon = (dR)^{1/2}/l$, where $R \propto I^{-1}$ is the characteristic radius of curvature of the electron trajectories in the magnetic field of the current[1].

[1] Yet there exists another group of electrons – the surface electrons –that collide only with one of the boundaries of the film (see Fig.1). In the diffuse-reflection case considered here, their influence on the nonlinear conductivity of metal is negligible and therefore they are disregarded henceforth.

In our problem the external AC magnetic field parallel to the self-field of the current shifts the plane at which the magnetic field changes sign towards one of the faces of the film. That in turn leads to the significant diminution in the conductivity of the trapped carriers. In this situation the conductivity of metal depends substantially on time and, consequently, strong nonlinear effects in the response of the sample should arise.

FORMULATION AND GEOMETRY OF THE PROBLEM

We consider a metallic film of thickness d along which a DC current I is flowing. The sample is symmetrically illuminated from both sides by a monochromatic electromagnetic wave whose vector is collinear with the vector of the self-magnetic field of the current. We introduce a coordinate system with the x axis directed along the normal to the faces of the film. The plane $x=0$ corresponds to the center of the sample. The y axis is chosen along the current, and z axis is parallel to the vector of the magnetic field $\boldsymbol{H}_{tot}(x,t)$ which is the sum of the magnetic field of the current $\boldsymbol{H}(x,t)$ and the magnetic field of the wave $\boldsymbol{h}(x,t)$:

$$\bar{H}_{tot}(x,t) = \{0,0,H(x,t)+h(x,t)\}. \tag{1}$$

We assume that the electron scattering at the boundaries of the sample is diffuse.
In this geometry Maxwell's equations have the form

$$-\frac{\partial H_{tot}(x,t)}{\partial x} = \frac{4\pi}{c} j(x,t), \quad \frac{\partial E(x,t)}{\partial x} = -\frac{\partial H_{tot}(x,t)}{\partial t}, \tag{2}$$

where $j(x,t)$ and $E(x,t)$ are the y components of the current density and the electric field. The boundary conditions on Eqs. (2) are

$$H_{tot}(\pm d/2,t) = h_m \cos\omega t \mp H. \tag{3}$$

The symbol H denotes the absolute value of the magnetic field of the current at the surface of the metal, and h_m is the amplitude of the wave. The field H is determined by the total current I via the relation: $H = 2\pi I/cD$. The relation between H and h_m is arbitrary.

We consider the quasistatic situation, when the wave frequency ω is much lower then the relaxation frequency ν of the charge carriers. Here we assume that the magnetic field of the wave inside the sample is quasiuniform and practically the same as its value at the surface: $h(x,t) \cong h_m \cos\omega t$. In other words, the characteristic scale $\delta(\omega)$ for variations of the alternating magnetic field of the wave in metal is much larger than the film thickness d.

NONANALYTIC TIME DEPENDENCE OF THE ELECTRIC FIELD OF THE WAVE AT THE SURFACE OF THE FILM.

The current density $j(x,t)$ is determined by solving Boltzman's transport equation. The transport equation is linearized with respect to the electric field $E(x,t)$, which is a sum of the uniform potential field $E_0(x,t)$ and the solenoidal wave field $E_{sol}(x,t)$:

$$E(x,t) = E_0 + E_{sol}(x,t). \tag{4}$$

In our problem the nonlinearity is due entirely to the total magnetic field $H_{tot}(x,t)$ in the Lorentz force. While calculating the current density we restrict our consideration to the leading approximation in the small parameter $d/\delta(\omega)$. In such a case as we have said, the magnetic field of the wave, $h(x,t)$, is spatially uniform and is equal to the value at the boundaries of the film, $h(x,t) = h_m \cos\omega t$. The electric field $E(x,t)$ in this approximation is also independent of

the coordinates and is equal to the potential field $E_0(t)$. For uniform electric and external magnetic fields the current density of the particles was obtained in Ref.[1].

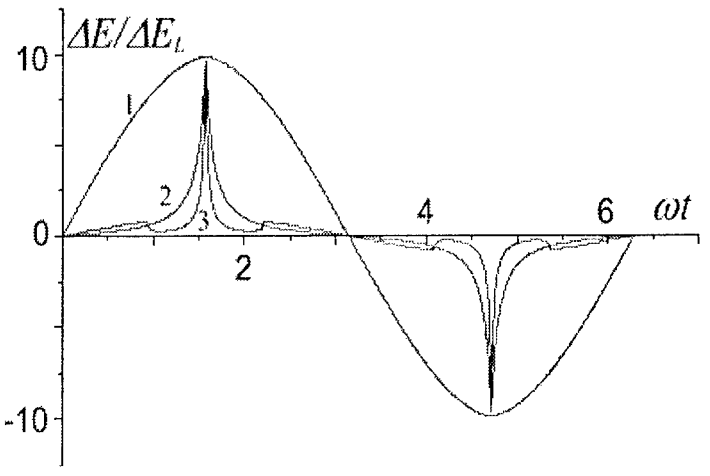

Fig 1 The difference ΔE in the values of the electric field of the wave at the boundaries of the film as a function of time at a fixed value of the current ($H=300H^*$) and the different amplitudes h_m/H^*. The ratio of the mean free path l to the film thickness d equals 30.

Inserting this current density (in a slightly modified form) into Maxwell's equations Eq.(2) and appending boundary conditions Eq.(3) we arrive at a certain boundary problem. One is not able to obtain solution in an explicit form and numerical calculations should be involved. In the present paper we were interested in the difference $\Delta E(x,t)=E_{sol}(d/2,t)-E_{sol}(-d/2,t)$, the quantity being proportional to the rate of change of the magnetic flux through a cross section of the sample perpendicular to the vector of the total field $H_{tot}(x,t)$. Figure 1 shows the function $\Delta E(t)$ over a wide range of values of the wave amplitude h_m at a large value of the magnetic field H of the current, when the condition $H>>H^*$ holds, with H^* being the value of the magnetic field at which the characteristic arc of the electron trajectory $(Rd)^{1/2}$ is equal in order of magnitude to the mean free path l, i.e. when the inequality $\varepsilon<<1$ is fulfilled. The value ΔE is normalized to the amplitude of the corresponding quantity in the absence of the transport current ΔE_L. We see that the ratio of the oscillation amplitude ΔE_m to the linear value ΔE_L does not depend on h_m. One has the following expression for ΔE_m:

$$\frac{\Delta E_m}{\Delta E_L}=0.83\left(\frac{H}{H^*}\right)^{1/2}\frac{l}{\ln(R/d)}, \qquad \left(\frac{H}{H^*}\right)^{1/2}\sim\varepsilon>>1. \tag{7}$$

The ratio $\Delta E_m/\Delta E_L$ is determined by the value of the magnetic field H of the current and can be much greater then unity. In other words, there is an amplification of the electric signal at the surface of the film. At small wave amplitudes (curve 1, $h_m = H/300$) the signal is quasi-harmonic. As h_m increases, however, kinks appear on the function $\Delta E(t)$. Curve 2 ($h_m = 2H/3$) has kinks at the extrema, i.e., at the time when the magnetic field of the wave $h_m\cos\omega t$ goes to zero. These features are due to the considerable contribution of the trapped electrons into the nonlinear conductivity. Curve *3* corresponds to the case $h_m = 5H/3$, where there are no trapped electrons during a part of the wave period. In that case the function $\Delta E(t)$ contains additional kinks arising at the times of the appearance and disappearance of the plane $x=x_0(t)$ at which the total magnetic field changes sign.

REFERENCES

[1] E.A. Kaner, N.M. Makarov, I.B. Snapiro, and V.A. Yampol'skii, Zh.Eksp.Teor.Fiz. **87**. 2166 (1984) [Sov.Phys.Jetp **60**, 1275 (1984)].

PROPAGATION OF SURFACE POLARITONS IN FINITE SUPERLATTICES WITH DISSIPATION

N.N. Beletskii, and Y.V. Bludov
Institute of Radiophysics and Electronics, National Academy of Sciences of Ukraine
12 Acad. Proscura St., Kharkov 61085, Ukraine
E-mail: bludov@ire.kharkov.ua

ABSTRACT

The paper deals with the theoretical investigation of surface polaritons (SP) in finite superlattice (SL). The SL are considered to be formed of the finite number of parallel two-dimensional electron systems (2DES) which are placed into the external quantizing magnetic field. The external magnetic field is supposed to be directed perpendicularly to 2DES. It is found that when the dissipation in 2DES is taken into account the new mode of SP - an additional surface polariton (ASP) appears in the spectrum of SP. The properties of ASP depend strongly upon the value of momentum relaxation frequency ν of electrons in 2DES. It is shown that at small values of ν with the increasing of 2DES number in the SL the character of ASP dispersion curve changes. In the case of high values of ν the effect of separating of ASP's dispersion curve from the usual SP with the increasing of 2DES amount is predicted.

INTRODUCTION

SP in semiconductors with SL are the object of great interest of physicists. The theoretical investigation of SP in SL, consisting of finite number of layers, are of great interest from the experimental and practical points of view [1-4]. For the finite SL, formed of a finite number of 2DES, SP were theoretically investigated both in the absence [1] and in the presence of external classical [2] and quantizing [3,4] magnetic field. It was shown that in nondissipative case the amount of modes of SP spectrum is equal to the number of 2DES in finite SL. But when the dissipation is taken into account [4] the SP spectrum contains an ASP, which properties depends strongly upon the value of momentum relaxation frequency ν of electrons in 2DES. However in paper [4] the dependence of the ASP properties upon the number of 2DES in finite SL has not been investigated.

In this paper we consider SL consisting of a finite number M of infinitely extended 2DES, arranged at the equal distance d from each other in planes $z = 0, d, \ldots, (M-1)d$. The constant quantizing magnetic field $\vec{B}$ is directed perpendicularly to the 2DES along the axis z (the axis of SL). We suppose that 2DES are imbedded into the uniform dielectric medium with dielectric constant ε. We admit that the Landau-level filling factor $\aleph$ is equal in all 2DES ($\aleph = \pi\ell^2 n$, $\ell = \left(c\hbar/eB\right)^{1/2}$ is the magnetic length and n is the electron density in 2DES).

DISPERSION RELATION

To obtain a dispersion relation, we used solutions of Maxwell's equations for TE- and TM-waves in media $md < z < (m+1)d \left(m = 0, 1, \ldots, M-2\right)$, $z < 0$ and $z > (M-1)d$ with standard boundary conditions. The tangential components of the electric field E_x, E_y were considered to be continuous across the interface and the tangential components of the magnetic field H_x, H_y were considered to be discontinuous across the interface. The values of discontinuity are equal to $H_{x2} - H_{x1} = \frac{4\pi}{c} j_{ys} = \frac{4\pi}{c}\left(\sigma_{yx}E_x + \sigma_{yy}E_y\right)$ and

$H_{y2} - H_{y1} = -\frac{4\pi}{c} j_{xs} = -\frac{4\pi}{c}\left(\sigma_{xx}E_x + \sigma_{xy}E_y\right)$. We obtained the dispersion relation in the form like in papers [3,4]. Since all effects, we are interested in, take place under condition $k\ell << 1$, the spatial dispersion of 2DES conductivity tensor, obtained in [5], can be neglected and nonzero components of 2DES conductivity tensor take the form:

$$\sigma_{xx}(\omega) = \sigma_{yy}(\omega) = \frac{2e^2}{h}\frac{\aleph\gamma}{1+\gamma^2}, \sigma_{xy}(\omega) = -\sigma_{yx}(\omega) = \frac{2e^2}{h}\frac{\aleph}{1+\gamma^2},$$

$\gamma = (\nu - i\omega)/\Omega, \Omega = eB/m^*c$ is the cyclotron frequency, m^* is the effective mass of electrons.

NUMERICAL RESULTS

As a model of 2DES we used a heterostructure $GaAs/Al_xGa_{1-x}As$ with parameters: $m^*=0.068m_0$, $\varepsilon=12$. When the dissipation is taken into account, we consider that the SP wavenumber k is a real value, but the SP frequency $\omega = \omega' + i\omega''$ is a complex value. Fig. 1a,b presents spectrum $\omega'(k)$ (solid curves) and damping $\omega''(k)$ (dashed curves) when $\aleph$=5, M=5, $\delta = \Omega d/c = 0.1$ in the cases: (a) $\Gamma = \nu/\Omega = 0.02$; (b) Γ=0.1. As it can be seen from Fig.1, at small values of ν the SP spectrum contains ASP (dispersion curve 6). Properties of usual SP (dispersion curves 1-5), which exist in SL also in nondissipative case, have been described in paper [3]. It should be noticed that at small ν the dispersion curve of ASP exists on the left from the light line $\omega' = kv_d$ (here $v_d = c/\sqrt{\varepsilon}$ is the velocity of light in the dielectric surrounding 2DES) and has the end-point of the spectrum, defined by the condition $\mathrm{Re}\, p = 0$. In this case the ASP dispersion curve does not cross usual SP dispersion curves. Besides that, with the increasing of k the damping of ASP gradually decreases and vanishes at the end-point of the spectrum. At high values of ν the properties of ASP changes entirely. So, in that case the fastest mode of usual SP (dispersion curve 1 on Fig.1a) is split into two branches. One of them (curve 1 on Fig.1b) almost coincides with the light line and has the end-point of the spectrum $\mathrm{Re}\, p = 0$. The second branch in the vicinity of light line is blended with the ASP and the resulting dispersion curve 6 has minimum near the light line. With further increasing of ν the end-point of dispersion curve 1 shifts into the lower-frequency region and the minimum on dispersion curve 6 becomes smoother.

Fig.2a,b presents dispersion curves of ASP for different values of M. The parameters of the SL are the same as in previous case: (a) Γ=0.02; (b) Γ=0.1. As one can see from Fig.2a, at small values of ν and at small values of M the dispersion curve of ASP possesses such properties. When the value of k increases, the ASP frequency decreases (except small region near end-point of spectrum). With the increasing of M the ASP dispersion curve becomes more slanting. After exceeding some critical value of M the ASP character changes: with increasing of k ASP frequency also increases. At higher values of M the ASP dispersion curve becomes steeper. Notice, that there exists another critical value of M, at which ASP is characterized by minimum damping. At high values of ν, as one can see from Fig.2b, with the increasing of M the ASP dispersion curve separates from the fastest mode of usual SP.

CONCLUSIONS

We have calculated spectrum and damping of SP in finite SL with dissipation. We predicted an effect of changing of ASP properties and a phenomenon of the separating of ASP dispersion curve from the usual SP mode with an increasing amount of 2DES in SL.

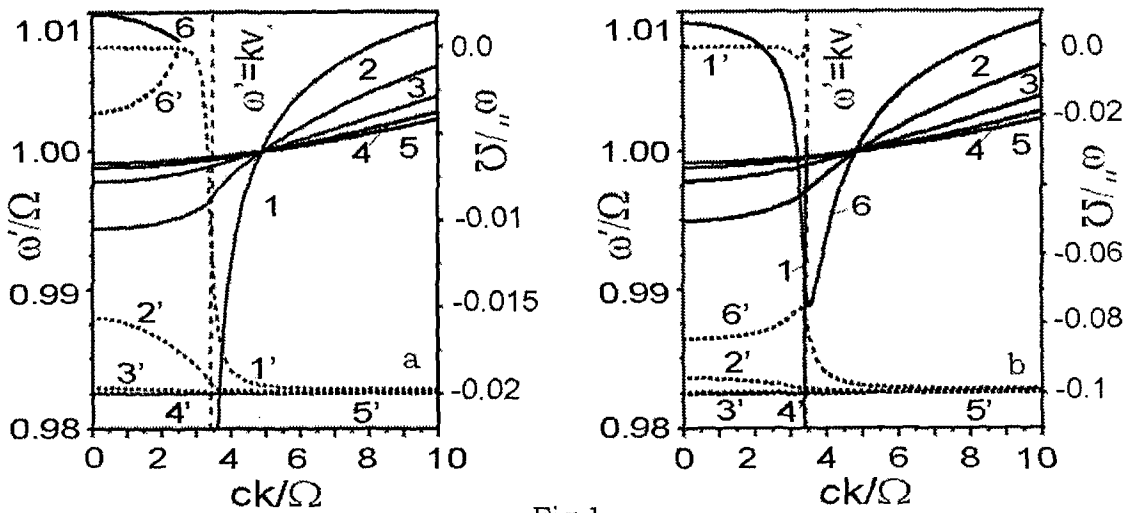

Fig. 1

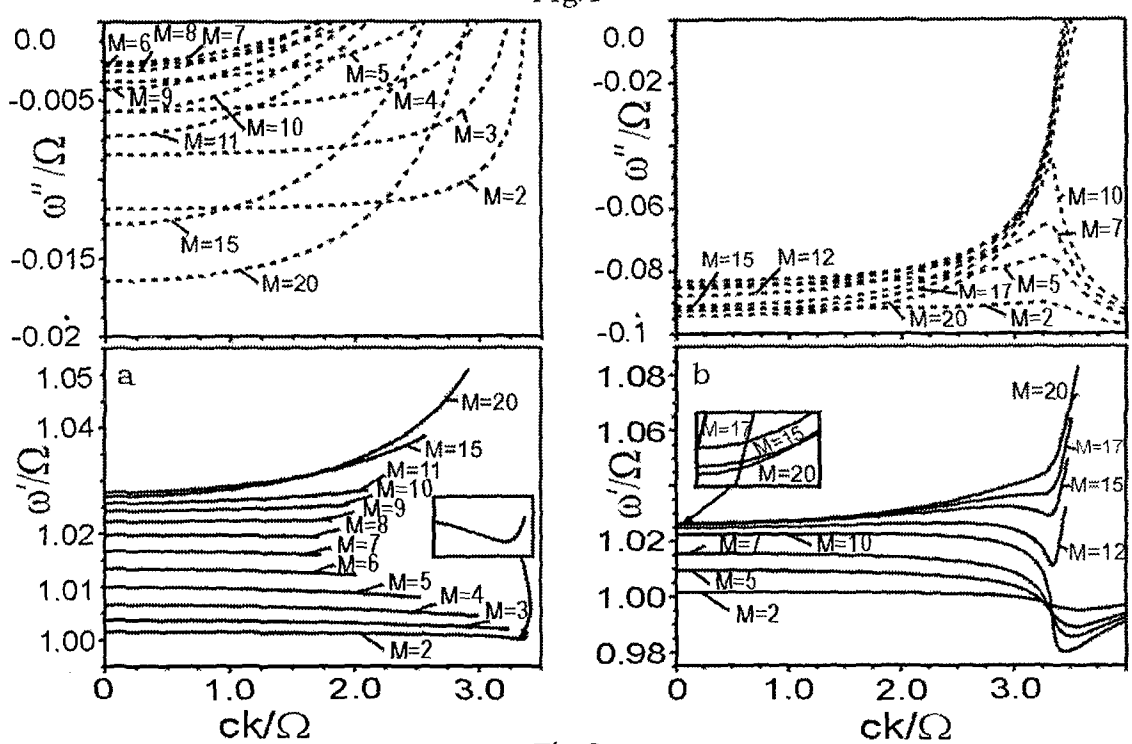

Fig. 2

REFERENCES

[1] Jain J.K., Allen P.B. // Phys. Rev. Lett. **54**, 2437 (1985)
[2] Albuquerque E.L. Fulco P., Farias G.A. et al. // Phys. Rev. B **43**, 2032 (1991)
[3] Bludov Y.V. // Ukrainian Journal of Physics **44**, 1266 (1999)
[4] Bludov Y.V. // Radiophysics and Electronics **3**, 106 (1998)
[5] Aronov I.E., Beletskii N.N. // J.Phys.: Condens. Matter **8**, 4919 (1996)

NONLINEAR INTERACTION OF THE WAVES IN PERIODIC SEMICONDUCTING SUPERLATTICE PLACED IN A MAGNETIC FIELD

A. A. Bulgakov, and O. V. Shramkova
Institute of Radiophysics and Electronics, National Academy of Sciences of Ukraine
12 Ac. Proskura St, Kharkov, 61085, Ukraine
Tel:+380 (572) 448-323, Fax:+380 (572) 441105, E-mail: bulgakov@ire.kharkov.ua

The nonlinear interaction of the waves in layered-periodic semiconductor-dielectric superlattice located in a magnetic field is examined in the paper. For the theoretical investigations of nonlinear processes we use the procedure of "three-wave interaction".

Let us consider the structure, that was derived by a periodic recurring of a semiconductor layer of a thickness d_1 and of a dielectric layer with a thickness d_2. Let us direct an axis Z perpendicularly to boundaries of stratums. The external magnetic field is supposed to have applied in a direction of an axis OY. Let us examine the distribution of magnetoplasma waves in a plane XOZ, that is perpendicularly to the magnetic field. Then, in consequence of homogeneity of a medium in a direction OY, it is supposed, that $\partial/\partial y = 0$. The result is that the Maxwell's equations disintegrate on the equations for two polarizations. Let us consider the polarization with the components of the fields E_x, E_z, H_y distinct from zero. From the Maxwell's equations with allowance of continuity of a tangential components of electromagnetic field on the boundaries of a structure with the help of Floquet's theorem we shall receive a dispersion relation :

$$\cos\bar{k}d = \cos k_{z1}d_1 \cos k_{z2}d_2 - \frac{\varepsilon_{f1}\varepsilon_2}{2k_{z1}k_{z2}}\left[\left(\frac{k_{z1}}{\varepsilon_{f1}}\right)^2 + \left(\frac{k_{z2}}{\varepsilon_2}\right)^2 - k_x^2\left(\frac{\varepsilon_{\perp 1}}{\varepsilon_{\text{II}_1}\varepsilon_{f1}}\right)^2\right] \sin k_{z1}d_1 \sin k_{z2}d_2, \qquad (1)$$

$$k_{z1} = \left[\frac{\omega^2\varepsilon_{f1}}{c^2} - k_x^2\right]^{1/2}, \quad k_{z2} = \left[\frac{\omega^2\varepsilon_2}{c^2} - k_x^2\right]^{1/2}, \quad \varepsilon_{f1} = \varepsilon_{\text{II}1} + \varepsilon_{\perp 1}^2/\varepsilon_{\text{II}1},$$

$$\varepsilon_\perp = -i\varepsilon_0\frac{\omega_p^2\omega_H}{\omega\left[\omega^2 - \omega_H^2\right]}, \quad \varepsilon_{\text{II}} = \varepsilon_0\left(1 - \frac{\omega_p^2}{\left[\omega^2 - \omega_H^2\right]}\right),$$

$\bar{k}$ is the wave number describing the periodicity (so-called Bloch's wave number); k_{z1}, k_{z2} is the wave numbers in a direction Z ; ε_f is the Voigt's permeability; ω_H, ω_p are the cyclotron and plasma frequencies. The influence of the magnetic field in the superlattice is exhibited in the area between the frequencies ω_{01} and ω_{02}, where

$$\omega_{01,02} = \pm\frac{\omega_H}{2} + \left(\frac{\omega_H^2}{4} + \omega_{ps}^2\right)^{1/2},$$

ω_{ps} is the frequency of surface plasmon on the semiconductor-dielectric boundary.

We carried out a numerical solution of the equation (1) for a structure with the parameters: the first layer is the semiconductor of a type InSb (ε_{01}= 17.8), second layer is the dielectric (ε_2= 2), d_1=1e-2cm, d_2=1.5e-2cm, H_0 = 1000 oersted.

We obtain the coupling equation [1] with the help of the procedure explained in detail in the work [2], in which the common method of the analysis of three-waves processes in periodic mediums was offered. The procedure is founded on the Green's formula:

$$\int_a^b \left[\tilde{f}^*(\hat{L},f) - (\tilde{\hat{L}},\tilde{f})^* f\right] dv = f\tilde{f}\Big|_a^b,$$

$\hat{L}$ is the linear differential operator, $\tilde{\hat{L}}$ is the transposed operator, f and $\tilde{f}$ are the eigenfunctions of the operators.

If the resonant conditions (conditions of synchronism)

$$\begin{cases} \omega' + \omega'' - \omega = 0 \\ k_x' + k_x'' - k_x = 0 \\ \bar{k}' + \bar{k}'' - \bar{k} + 2\dfrac{\pi L}{d} = 0, \end{cases} \qquad (2)$$

$L=0,\pm 1,...$ is realize, the equation for the amplitude of the wave k $C_k(z)$ is:

$$\frac{dC_k}{dz} = W_{k,k',k''} C_{k'} C_{k''}. \qquad (3)$$

The equations for two others waves are found by the permutation of the indexes. In the relation (3) $W_{k,k',k''}$ is the matrix coefficient. The expression for the coefficient is unwieldy and can't be shown here. The matrix element is the sum of the four addendum of a shape:

$$f_s \frac{\cos k_s d_1 - 1 + i \cdot \sin k_s d_1}{k_s},$$

where k_s is the one of the combinations $k_{z1} + k_{z1}' + k_{z1}''$, $k_{z1} - k_{z1}' - k_{z1}''$, $k_{z1} + k_{z1}' - k_{z1}''$, $k_{z1} - k_{z1}' + k_{z1}''$, f_s is a coefficient defined with the help of the amplitudes of fields of interacting waves.

The conditions of interaction of the first and second harmonics with the frequencies $\omega = \omega'$ and $2\omega'$ are analyzed in the paper. In this case the conditions of synchronism are:

$$\begin{cases} \omega = 2\omega' \\ k_x = 2k_x' \\ \bar{k} = 2\bar{k}' + 2\dfrac{\pi L}{d} \end{cases} . \qquad (5)$$

The conditions (2) and (5) in the superlattice differ from the homogeneous nonlinear medium by the presence of the specific law for the Bloch's numbers. The result is the new type of an interaction:

$$\bar{k} = \bar{k}' - \bar{k}' = 0. \qquad (5a)$$

It is possible to observe two types of interaction: 1) the first and second harmonics are located in the different allowed bands in an interval of frequencies $\omega_{01} - \omega_{02}$; 2) the first harmonic lays in an interval $\omega_{01} - \omega_{02}$ and the second one lays higher then the ω_{02}.

In the periodic medium $W_{k,k',k''}$ is a complex magnitude (in homogeneous one $W_{k,k',k''}$ is an imaginary number [3]). The result is the peculiarities in the dynamics of a process of interaction. Let us mark that $W_{k,k',k''}$ can be much more (modulo) in periodic medium than in homogeneous one. In the work is shown that it is connected with the resonance on the period of a structure. Such value of a resonance is in the forbidden band, where the laws of the synchronism don't take place. That is why the maximum of $W_{k,k',k''}$ is on the boundary of a zone. The second factor influencing on the magnitude of $W_{k,k',k''}$ is the equality to zero of one of k_s magnitudes (see (4)). This condition can be considered as a nonlinear resonance. The dependence $W_{2k',k'}$ on frequency is shown in a Fig.1. The numerical solution of equation (3) is presented in a Fig.2.

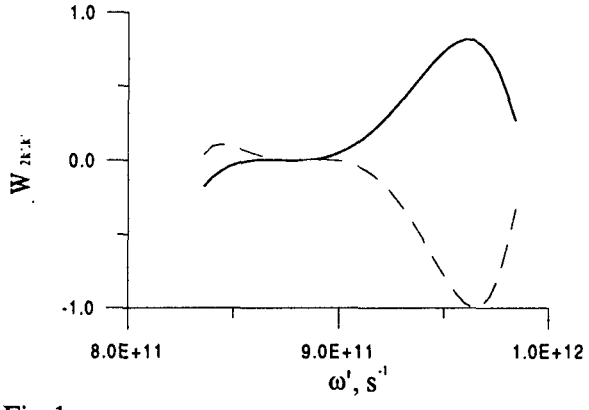

Fig.1

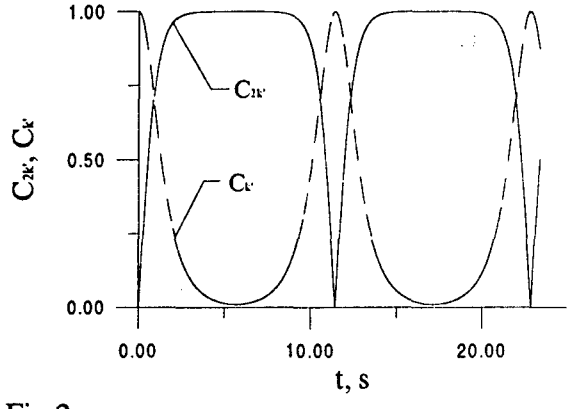

Fig.2

REFERENCES

[1] A.A. Bulgakov, S.A.Bulgakov, L.Vazquez, "Second harmonic resonant excitation in optical pe riodic structures with nonlinear anisotropic layers", Phys. Rev. E , v.58, p. 7887-7898, 1998;

[2] F.G.Bass, A.A.Bulgakov, "Kinetic and electrodynamic phenomena in classical and quantum semiconductor superlattices", New-York, Nova Science Publisher Inc., pp. 498, 1997;

[3] J.Weiland, H.Wilhelmsson, "Coherent non-linear interaction of waves in plasmas", Oxford, Pergamon press, pp.224, 1977

THE BOUNDARY PROBLEMS OF ELECTROMAGNETIC THEORY OF PLANAR CHIRAL STRUCTURES

Gennady G. Goshin and Natalia E. Lugina*

Tomsk State University of Control System and Radioelectronics
40 Lenina Ave., Tomsk 634050 Russia (3822) 413643

*Siberian Physical &Technical Institute
1 Novosobornaya sq., Tomsk 634050 Russia (3822) 413983
E-mail: nata@public.tsu.ru

ABSTRACT

In this report we present a theoretical investigation of two types of plane structures. One of them represents a chiral slab restricted by perfectly conducting screen on its bottom (grounded chiral substrate). Another one is a plane system of isolated line wires located on the grounded chiral substrate. The influence of wire system on waveguide properties of a grounded chiral substrate and radiation field of source is investigated.

INTRODUCTION

Chiral structures with different properties continue to attract attention of researchers. Since 90-s, the International Conferences on chiral problems take place every year [1, 2]. The interest of the researchers concerns the investigation of wire system on a chiral substrate [3, 4]. In the present report, the influence of line wire system on waveguide properties of a grounded chiral substrate and radiation field of source is investigated.

STATEMENT OF THE PROBLEM

If edge effects are neglected then for the solution of described above problems we can use the model that is a flat unbounded chiral slab placed on a screen. One of the possible formulation of the model problems can be follows: chiral slab $|x,y| \le \infty$, $-d \le z \le 0$ with parameters ε_2, μ_2, ξ (region 2) is located in Cartesian coordinate system x,y,z. Half-space above slab $z > 0$ presents homogenous media with parameters ε_1, μ_1, where sources are located (fig.1). We take line source as the traveling wave current distribution along the y axis

$$j_y^e = I_y^e e^{i\eta y} \delta(x - x_0)\delta(z - z_0), \qquad (1)$$

$\eta = k_1\beta$, $k_1 = \omega\sqrt{\varepsilon_1\mu_1}$, $\beta = c/V$, V - phase velocity of current wave, c - light velocity. The wave processes are assumed to be stationary with time dependence $e^{-i\omega t}$.

The boundary conditions for given structures are four conditions of continuity for the components of full field on the boundary of media and two homogeneous condition on the screen.

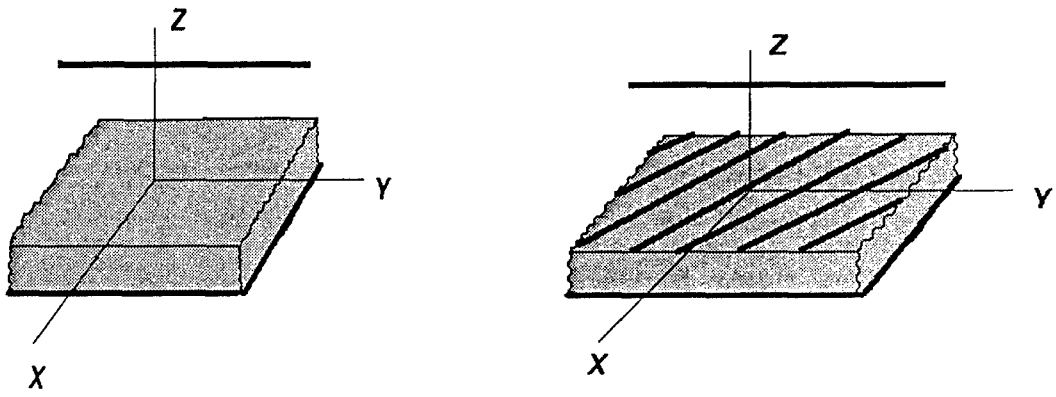

Figure 1. Geometry of the model problems

Both problems were solved by means of presentation of fields through potentials of circularly polarized waves $U^{\pm}(x,y,z)$ and using the integral Fourier transformation in complex plane. Potentials of secondary field in regions 1 and 2 have the form

$$U_1^{\pm}(x,y,z) = e^{i\eta y}\int_{-\infty}^{+\infty} A_1^{\pm}(\chi,\eta)e^{i\chi(x-x_0)+iq_1 z}d\chi, \quad z>0;$$
$$U_2^{\pm}(x,y,z) = e^{i\eta y}\int_{-\infty}^{+\infty}\left\{A_2^{\pm}(\chi,\eta)e^{-iq_{\pm}z} + A_3^{\pm}(\chi,\eta)e^{iq_{\pm}z}\right\}e^{i\chi(x-x_0)}d\chi, \quad -d<z<0, \tag{2}$$

where $q_1 = \sqrt{k_1^2-\eta^2-\chi^2}$, $q_{\pm} = \sqrt{k_{\pm}^2-\chi^2-\eta^2}$, $k_{\pm} = k_c(1\pm\xi\, w_c)$, $k_c = \omega\sqrt{\varepsilon_c\mu_2}$, $w_c = \sqrt{\mu_2/\varepsilon_c}$, $\varepsilon_c = \varepsilon_2 + \xi^2\mu_2$. Unknown functions $A_{1,2,3}^{\pm}(\chi,\eta)$ are determined from boundary conditions and have complex form.

RESULTS

Analysis of solution has shown that there are excited both continuous and eigenvalue wave spectra in the considered structures. The propagation constants of continuous wave spectrum connect with the branch points of integrand $q_1 = 0$, $q_{\pm} = 0$. Asymptotically evaluated in the far field integrals at $z>0$ define characteristics of radiation the under investigation structures, which were calculated for different parameters of problems. Discrete spectrum of waves is defined by residues in poles of integrand. Dispersion curves of discrete spectrum waves are presented in the manner of Brilliouin diagrams (fig.2). In particular cases obtained results coincide with known ones.

Fulfiled calculations allow to do following physical conclusions:

- unlike homogeneous dielectric slab on a screen in chiral slab occurs the transformation of waves of discrete spectrum in hybrid, but beside wave of main type disappears cut-off on frequency;
- chirality increases deceleration of waves of discrete spectrum;

- in the radiation field appears crosspolarized component, at nonphased excitation asymmetry of diagrams are observed.

Located over chiral slab the line wire system in discrete spectrum

- is reason of presence of slow wave, which without the line wire system does not exist;
- serves by the reason of excitation quick waves in slab;
- the wave with the most deceleration can result in unidirectional transform of energy at nonphase excitement;
- intensifies an asymmetry of radiation diagrams;
- results in absence of radiation in the plane of structure;
- results in narrowing the radiation diagrams and reducing a number of lobes.

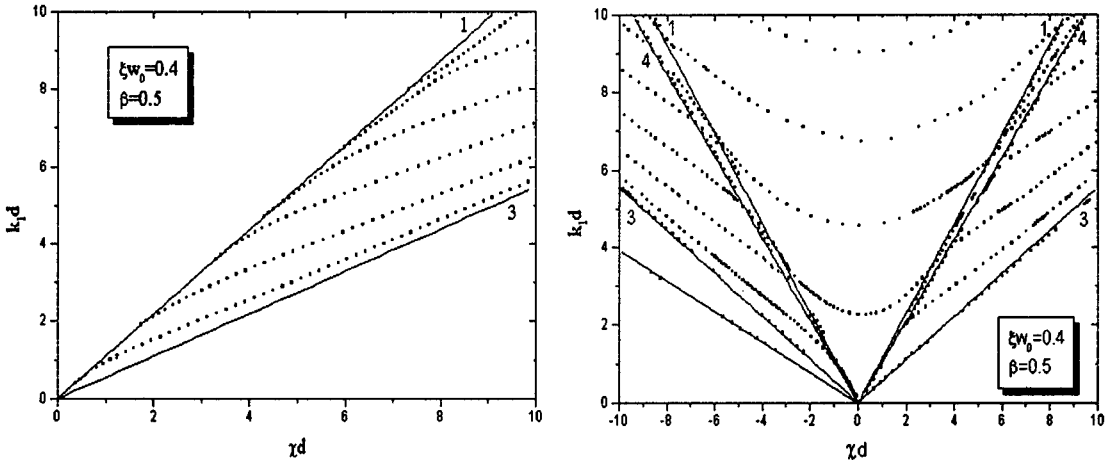

Figure 2. Brilliouin diagrams for guided modes in a grounded chiral slubstrate on a screen (left)
and one with wire system (right)
($\alpha = 1.0, \varepsilon_2 = 2.0, \mu_1 = \mu_2 = 1.0, w_0 = 120\pi$ Ohm; $1 - q_1 = 0$, $3 - q_+ = 0$, $4 - q_- = 0$)

Considered problems are referred to the quasithree dimensional class. However their deciding by means of simple integration on η can be dedicated on three-dimensional case. Line wire system in combination with chiral slab can be perspective at the development at microwave, for instance, broadband antennas, modulators, valve devices in strip performance.

REFERENCES

[1] Proceedings of BIANISOTROPICS'97 International Conference and Workshop on Electromagnetics of Complex Media // Ed. Werner S. Weiglhofer. Department of Mathematical University of Glasgow, Great Britain, 5-7 June 1997, 318 p.

[2] Proceedings of BIANISOTROPICS'98. The 7th International Conference on Complex Media // Eds. Arne F. Jacob and Jens Reinert. Technische Universitat Braunschweig, 3-6 June 1998, 328 p.

[3] Goshin G., Lugina N. The quasithree-dimensional problem on excitation of line wire system on a chiral substrate // Proc. 6th Int. Conf. on Math. Methods in EM Theory, Lviv, 1996. - P.316-319.

[4] Goshin G., Lugina N. Boundary problem on excitation of spiral wire system on a plane chiral substrate // Proc. 7th Int. Conf. on Math. Methods in EM Theory, Kharkov, 1998. - V.2, P.664 -666.

MATHEMATICAL MODEL OF A SPHERICAL FRACTAL EMITTER

Volodymir M. Onufriyenko[2], and Eldar I. Veliev [1]
[1] Institute of Radiophysics and Electronics, National Academy of Sciences
Ulitsa Proskury, 12, Kharkov, 61085, Ukraine
e-mail: veliev @ dut.kharkov.ua
[2] State Technical University,
Zhukovsky Str., 64, Zaporizhzhya, 69063, Ukraine
e-mail: onufr @ zstu.zaporizhzhe.ua

Abstract. Results of mathematical simulation of a spherical fractal emitter for the first time represented. The application of fractional calculation for mathematical model generation is justified. The α-characteristic of the magnetic field component of a symmetric spherical emitter and current distribution on a surface is retrieved. The properties of a spherical fractal emitter are defined. The outputs are confirmed by matching of the obtained formulas and graphs with known data.

Introduction

Rise of interest to designing different devices of UHF of a range with fractal structure (see, e.g., [1],) boosted application of fractional calculation (see, e.g., [2]) in the electromagnetic theory [3,4]. Results on learning physical and geometrical properties of fractal fields now are obtained [5,6], in particular, in the radiation theory [7,8].

In [6] is shown, that the α-characteristics of a field, which are generated α-dimensional by a Hausdorff's measure of the fractal object, can be constructed with the application of fractional integration $\alpha - 1$ measure (or fractional derivation of $\alpha + 1$ measure). The enumeration of outcomes of simulation of a spherical emitter further represented.

Formulation

The attempts of measurement of a usual current with density $j(P)$ on a fractal surface unit dS^{α} inevitably reduce in necessity of input of the fractal α-characteristic $d^{\alpha}J(P)$ on a unit dS. Thus,

$$d^{\alpha}J(r)d^{\alpha}S = j(r)l^{-\alpha}\frac{\mu(\alpha)}{r^{1-\alpha}}dS = j^{\alpha}(r)dS \quad , \tag{1}$$

where $\mu(\alpha) = \Gamma(\alpha)\frac{2\pi^{\alpha/2}}{\Gamma(\alpha/2)}$ is defined by sort of a coating unit; $\Gamma(.)$ - Euler's gamma-function.

Let us consider an emitter as a sphere. Let its surface has fractal properties. A fractal current we set as a thin spherical stratum with radius a. The surface current density $j^{\alpha}(r,\theta)$ does not depend on a lateral angle. Dependence of a current density on a meridional corner θ we set by the α_{θ}-characteristic $D^{\alpha_0}\Theta(\theta)$, and dependence on radius by the α_r-characteristic $D^{\alpha_r}R(r)$:

$$\vec{j}^{\alpha}(r,\theta) = D^{\alpha_r}R(r)D^{\alpha_\theta}\Theta(\theta).$$

At such symmetry the electromagnetic field will have three components, equal to zero, E_φ, H_θ and H_r. On an emitter surface a current density is $j^\alpha(a,\theta) = H_\varphi^\alpha(a,\theta)$, and complete current is $J^\alpha(a,\theta) = 2\pi a \sin\theta\, j^\alpha(a,\theta)$.

For determination of a current density $j^\alpha(r,\theta)$ from Maxwell equations, in view of the indicated symmetry, we obtain the α-characteristic of the magnetic component

$$D^\alpha H_\varphi^\alpha = {}_aD_r^{\alpha r} R^\alpha(kr)\, {}_0D_\theta^{\alpha\theta}\Theta^\alpha(\theta),\ {}_aD_r^{\alpha r} R^\alpha(kr) = \frac{C_n}{\sqrt{r}} H^{(2)}_{n+\frac{1}{2}}(kr),\ {}_0D_\theta^{\alpha\theta}\Theta^\alpha(\theta) = \frac{d}{d\theta} P_n(\cos\theta)$$

(here: C_n - harmonics amplitude; $H^{(2)}_{n+\frac{1}{2}}(kr)$ - half-integer order Hankel's function; $P_n(\cos\theta)$ – Legendre polynomials.

According to designed model, the electromagnetic field (2) spherical fractal emitters, as well as in case of a classical emitter, represents a space *n*-order harmonic of an electrical wave. At *n*=0 the field is identically equal to zero. It means, that for the indicated model the emitter is impossible to create which isotropicly radiates on all directions.

The field of an emitter with a space first order harmonic comes nearer to the field diagram of a linear dipole fractal emitter with length equal to radius of an orb [7, 8].

In the total, density of a fractal current looks like

$$j^\alpha(r,\theta) = \sum_{n=1}^{\infty} C_n\, {}_0I_{kr}^{\alpha r}\left(\frac{C_n}{\sqrt{r}} H^{(2)}_{n+\frac{1}{2}}(kr)\right) {}_0I_\theta^{\alpha\theta}\left(\frac{d}{d\theta} P_n(\cos\theta)\right).$$

RESULTS AND DISCUSSION

In Fig. 1 the radial part $R^\alpha(kr)$ is shown, and in Fig. 2 - meridional part $\Theta^\alpha(\theta)$, which determine a current density on a surface of an ideal spherical emitter (dashed line) and on a surface of an emitter with fractal properties (solid line).

We score the following: 1) offset of maximas of $\Theta^\alpha(\theta)$ curves in the side of major corners θ, that reduces in rotational displacement of a polar pattern (it depends on the value of a scaling metric α); 2) considerable increase of wattless currents, and it reduces in decrease of an efficiency and emitter passband; 3) power reallocation of 2^α-poles in emitters petals with

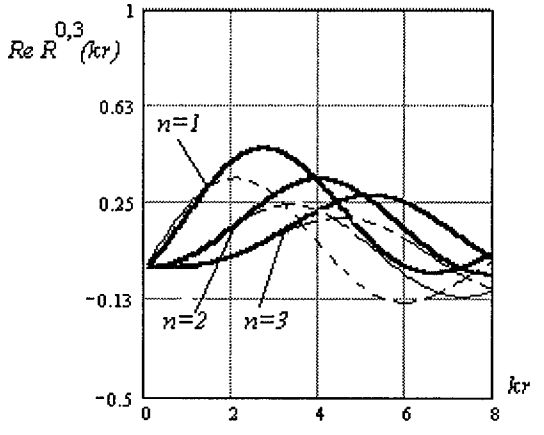

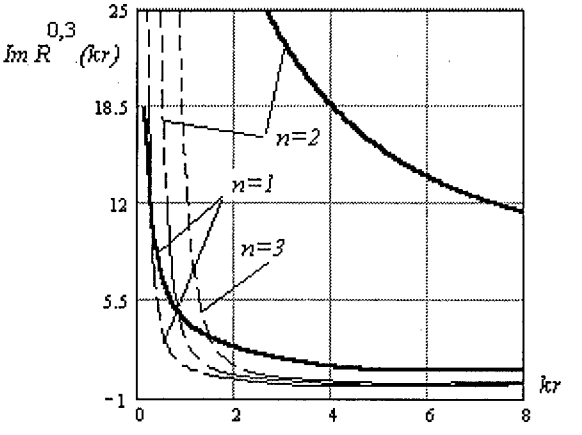

Fig. 1

a higher order space harmonic in comparison with classical multipoles; 4) confirmation of known experimental datas about offset of the characteristics of an actual emitter, that is stipulated by existence 2^{α} –poles in actual physical systems.

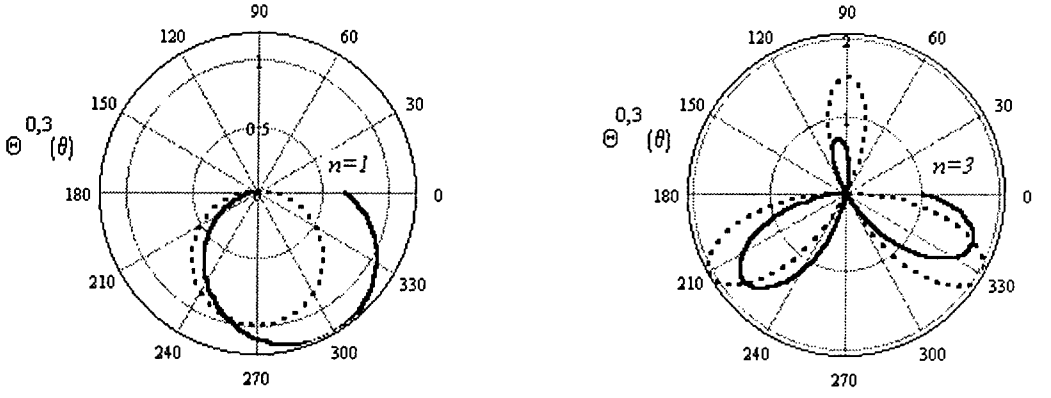

Fig. 2

CONCLUSION

The discussion of calculations results on designed radiation model of a sphere with fractal structure of surface currents allocation points presence of known properties of a classical emitter (alternation of phase-alternating currents; values fissile and wattles currents). There are also new effects (rotational displacement of a polar pattern, power reallocation a 2^{α} –poles etc.). The obtained results allow explaining influence of 2^{α} –poles to the form of a polar pattern, on the value of an antenna factor, and also possibility of designing pencil-beam and isotropic emitter.

REFERENCES

[1]. Fractals in physics. Ed. By L. Pietronero and E. Tosatti.- M.:Mir.- 1988 (originally published in English by ICTP Trieste, Italy, 1985).

[2].K.B.Oldham and J.Spanier. The Fractional Calculus.-New York:Academic Press, 1974.

[3]. N. Engheta. Fractional Calculus and Fractional Paradigm in Electromagnetic Theory. Conference Proceedings 1998 International Conference on Mathematical Methods in Electromagnetic Theory (MMET-98), Kharkov, Ukraine, June 2-5,1998, V.1, pp. 43-49.

[4]. V. Onufrienko. New Description of Spatial Harmonics of Surface Waves. Conference Proceedings 1998 International Conference on Mathematical Methods in Electromagnetic Theory (MMET-98), Kharkov, Ukraine, June 2-5,1998, V.1, pp.219-221.

[5]. V. Onufrienko. Physical-geometrical interpretation of α-characteristics of electro-magnetic field. Radiofisika i elektronika. Institute of Radiophysics and Electronics of the National Academy of Sciences of Ukraine, Vol.4, No.1, pp.7-10,1999 (in Ukrainian).

[6]. V.M.Onufrienko. Interaction of a Plane Electromagnetic Wave with by Fractal Metallized Surface. Radiofisika i elektronika. Institute of Radiophysics and Electronics of the National Academy of Sciences of Ukraine, Vol.4, No.2, 1999 (in Ukrainian).

[7]. E.I.Veliev and V.M.Onufrienko. Fractal Electrical and Magnetical Radiators. Proceedings Third International Kharkov Symposium " Physics and Engineering of Millimeter and submillimeter waves " (MSMW ' 98). V.1.-Kharkov (Ukraine) .-1998.-P. 357-359.

[8]. E.I.Veliev and V.M.Onufrienko. Radiation of waves by the fractal surface element. Proceedings of 3rd International Conference Antenna Theory and Techniques (ICATT-99), Sevastopol, Ukraine, 8-11 Sept., 1999, pp.160-161,131-132.

ONE-DIMENSIONAL OPTIMIZATION OF SILICON SOLAR CELLS

M.A. Ustyantsev, V.A. Antonova, and G.I. Churyumov

Kharkov Technical University of Radio Electronics
14 Lenin Ave., Kharkov 61166, Ukraine
Tel.: +38 0572 409362 Fax: +38 0572 409113
E-mail: m.ustyantsev@ieee.org

ABSTRACT

One of the most important problems in the design of modern photo-voltaic cells is increasing their efficiency. The solution of this problem is connected with an investigation of new types of solar cells as well as optimization of the output characteristics of present devices. In this paper, formulation of the problem and one-dimensional (1D) simulation technique developed for computer modelling and optimization of the high-efficiency silicon solar cells is discussed.

INTRODUCTION

The development of the high-efficiency silicon solar cells has currently been in the center of attention [1,2]. It is necessary to note that computer modeling of physical effects in semiconductor structures used to design solar cells is one promising approach in order to carry out a complete theoretical analysis [3,4]. Among the questions which have to be solved in order to raise the efficiency of the silicon solar cells, it is necessary to mention the ones connected with optimization of n^+–p junction depth, decrease of leakage currents, etc. In this paper, the problem of optimization of an n^+ – p junction depth in the silicon solar cells is considered.

SILICON SOLAR CELLS MODEL

Schematic drawing of basic structure of a mono-crystal silicon solar cell is shown in Fig. 1. It is known that the efficiency of the silicon solar cells depends on n^+–p junction depth. There is an optimal value of this parameter where solar cell operates most efficiently. This is caused, on the one hand, by a specificity of photon processes taking place in the materials which are contained in the solar cells, and on the other hand, by the features of their designs.

For optimization of a solar cell we used its mathematical model possessing an abrupt n^+–p junction as well as the constant levels of doping on each side of the n^+–p junction. As a result, we can suppose that electric field outside of depletion layer of the n^+–p junction is equal to zero (Fig. 1).

A parameter that we selected in order to optimize of n^+–p junction depth is the total photo-current which is generated by all spectrum of solar radiation. In this case, the n^+–p junction depth will be optimal at a point on the axis x where the total photo-current has maximum.

For the incident light of the wavelength λ and intensity or flux $F(\lambda)$, electron-hole pairs are generated at the distance x from the surface at a rate

$$G(x) = \int_{\lambda} \alpha(\lambda) F(\chi) [1 - R(\lambda)] \exp[-\alpha(\lambda) x] \, d\lambda \qquad (1)$$

where $\alpha(\lambda)$ is the local absorption coefficient; $R(\lambda)$ is the surface reflectivity; $F(\lambda)$ is the density of photons.

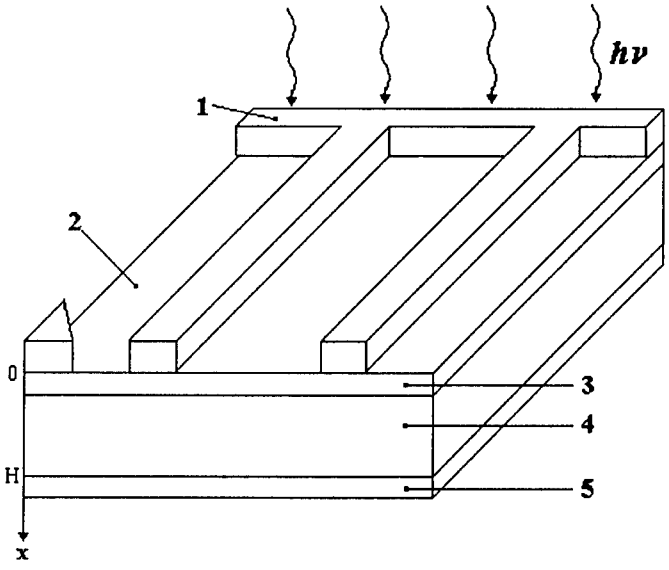

1 – collector contact; 2 – antireflection coating; 3 – n^+- layer; 4 – p - silicon; 5 – back continuous collector contact

Fig. 1 Basic structure of solar cell

Under low injection conditions 1D stationary equations are written as [1]:

$$G_n - \frac{n_p - n_{p0}}{\tau_n} + \frac{1}{e}\frac{dJ_n}{dx} = 0 \tag{2}$$

$$G_p - \frac{p_n - p_{n0}}{\tau_n} + \frac{1}{e}\frac{dI_p}{dx} = 0 \tag{3}$$

Here, expressions for the photo-current contributions in the p- and n-region, J_n and J_p, are therefore given by the diffusive currents

$$J_n(\lambda) = qD_n\frac{dn(x)}{dx} \tag{4}$$

$$J_p(\lambda) = D_p\frac{dp(x)}{dx} \tag{5}$$

where q is the electron charge; $D_{n,p}$ is diffusion factor.
For n^+–p region we can obtain integro–differentual equation which describes distribution of holes in n-layer

$$D_p\frac{d^2p_n}{dx^2} - \frac{p_n - p_{n0}}{\tau_p} + \int_\lambda \alpha(\lambda)F(\lambda)[1 - R(\lambda)]\times\exp[-\alpha(\lambda)x]d\lambda = 0 \tag{6}$$

where τ_p the hole lifetime.

A similar integro-differentual equation for the electron distribution in the p–layer can be written as

$$D_p \frac{d^2 n_p}{dx^2} - \frac{n_p - n_{p0}}{\tau_n} + \int_{\lambda} \alpha(\lambda) F(\lambda)[1 - R(\lambda)] \times \exp[-\alpha(\lambda) x] d\lambda = 0 \qquad (7)$$

Taking into account that equations (6) and (7) have no analytical solution we used the numerical methods with the following initial conditions:

$$D_p \frac{d(p_n - p_{n_0})}{dx} = S_p (p_n - p_{n_0}) \text{ at } x=0. \qquad (8)$$

$$D_n \frac{d(n_p - n_{p_0})}{dx} = S_n (n_p - n_{p_0}) \text{ at } x = H \qquad (9)$$

$$p_n - p_{n0} = 0 \text{ and } n_p - n_{p0} = 0 \text{ at } x=x_i . \qquad (10)$$

The total photo-current as a function of wavelength is then given by the sum of diffusion currents in the *p*-, *n*- regions and depletion region [1]:

$$J_L = J_p + J_n + J_{dl} \qquad (11)$$

where $$I_{dl} = q\Gamma_0 \left[1 - \exp\left(-\alpha \left| x_p - x_n \right|\right)\right] \exp\left(-\alpha \left| x_p - x_n \right|\right) \qquad (12)$$

By using the results of numerical solution of equations (6) and (7) in view of (8)-(10), and (12) and substituting their values in (11), we determine the total photo-current of a silicon solar cell.

REFERENCES

[1] S.M. Sze. *Physics of Semiconductor Devices*, 2nd edition. John Wiley, 1981.

[2] A.L. Fahrenbruch and R.H. Bube, *Fundamentals of Solar Cells*, Academic Press, 1983.

[3] G. Heiser, Armin G. Aberle, Stuart R. Wenham and Martin A. Green. Two-dimensional numerical simulations of high-efficiency silicon solar cells, *Microelectronics Journal*, 26 (1995) 273-286.

[4] Pietro P. Altermatt, Gernot Heiser, Martin A. Green Numerical quantification and minimization of perimeter losses in high-efficiency silicon solar cells, *Progress in Photovoltaics: Research and Applications*,vol.4, 355-367 (1996).

SIMULATION OF A NON-LINEAR INTERACTION IN THE COMBINED MAGNETRON

T. I. Frolova, G. I. Churyumov
Kharkov State University of Radio Electronics
14 Lenin Ave., Kharkov, 61166, Ukraine
Tel.: +380 572 409362, Fax: +380 572 409113
Email: frolova@kture.kharkov.ua

ABSTRACT

In the last few years the development of efficient crossed-field tubes is connected with a creation of new non-traditional designs. In this paper a mathematical model of new combined magnetron and the features of modes of its operation are discussed.

INTRODUCTION

An application of new technologies is a promising approach to the problem of development of advanced crossed-field tubes. The development of non-traditional crossed-field tubes is a good example of usage of this approach [1]. Among the possible advantages of non-traditional designs in comparison with the classical designs of tubes (for instant, magnetron), we can mention a suppression of interpulsing spurious oscillations in re-entrant beam, self-modulated CFAs, providing their stable operation in frequency band and the creation of cold cathode, self-modulated, re-entrant beam amplifier [2]. Besides, a considerable advance has been made in studying of new designs of the magnetron oscillators and, in particularly, combined magnetron [3]. However, there is a number of unclear questions concerning non-linear interaction of two electronic beams with electromagnetic wave of the resonant delay line. Their solution cannot be made a priory without theoretical investigations of given interaction mechanism by using self-consistent mathematical models of the tube. The choice of such a mathematical model is determined by a compromise between the list of problems, which have to be solved, and possibilities of a hardware. The application of full-scale simulation allows not only to calculate basic parameters of tubes, and to evaluate their limiting values as well as to explain the possible anomalous physical effects and to point out the ways of their elimination.

In this paper, the features of a mathematical model of combined magnetron are discussed. Mathematical modelling of the electron-wave processes is considered in three-dimensional approximation on one wavelength with usage of the conditions of a quasi-periodicity (quasi-periodical model [4]).The emphasis is on the study of physical regularities governing the electron-wave interaction in the tube and on determination of the optimum performance of its operation.

THEORY

Fig. 1 shows schematically the full classification of crossed field tubes with the azimuthal symmetry. The classical crossed-field tubes with azimuthal symmetry can be considered as electron-wave systems, in which a re-entrant electron beam interacts with a (synchronous) slow electromagnetic wave («the re-entrant electron beam + RF wave» systems). As it has been shown in [1], non-traditional crossed-field tubes are the examples of future advanced technologies, which are connected with the creation of a new design of the tubes. These tubes are defined as electron-wave systems, in which a re-entrant electron beam interacts with two synchronous electromagnetic waves («re-entrant electron beam + two RF waves» systems), or two re-entrant electron beams interact with a synchronous electromagnetic wave («two re-entrant electron beams + RF wave» systems).

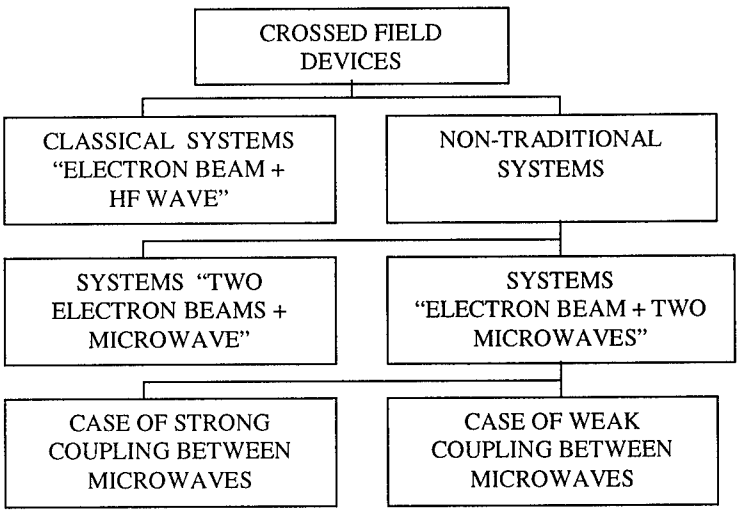

Fig. 1

The angular domain of the interaction space corresponding one wavelength in the combined magnetron, schematically, is shown in Fig. 2. There is an interaction of the inner and outer electronic beams with electromagnetic field of the resonant delay line. A special feature of this interaction is that electron beams have an opposite sense of rotation, i.e. inner beam rotates around internal cathode clockwise and outer one rotates around external cathode anti-clockwise. The average drift velocities of inner (i) and outer (o) beams are $v_e^{i,o} = E_0^{i,o} / B_0^{i,o} \approx U_a^{i,o} / d^{i,o} B_0^{i,o}$, where $U_a^{i,o}$ is the anode voltage; $B_o^{i,o}$ is magnetic field: $d^{i,o}$ is the distance between cathode and anode. Indices (i) and (o) in the expressions above correspond to the inner and outer interaction spaces of the tube, respectively. It is known that the condition of its efficient operation will be the following: $v_e^i \approx v_e^o \approx v_f^{+,-}$ (synchronism condition), where $v_f^{+,-}$ is the phase velocity of synchronous spatial harmonic, and indices (+) and (-) are associated with its rotation clockwise and anti-clockwise. There are two operating modes in the combined magnetron to satisfy the synchronism condition. In the first case, we have $U_a^i \neq U_a^o$ (two power supplies) and $B_o^i = B_o^o = const$. The second case (when $U_a^i = U_a^o$ and $B_o^i \neq B_o^o$) is preferable as it enables one to use a single (in common) power supply. The possible distribution of the magnetic field in this case can be easily realized using a standard magnet. An example of such distribution is described in [3].

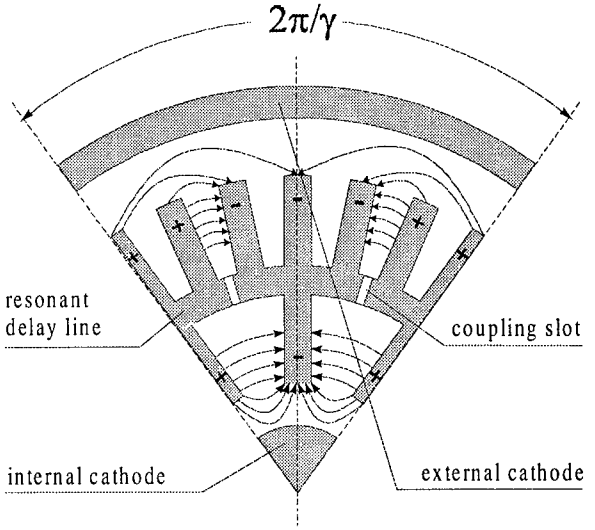

Fig. 2.

The particle-in-cell (PIC) method was chosen as a basis for computer modelling of the non-linear interaction in combined magnetron. The simulation was carried out in one-wave approximation by using three-dimensional mathematical model. It was suggested that the distribution of electromagnetic field both in the internal and external interaction spaces of the tube corresponded to the π –mode oscillation of the resonant delay line. In this case the resonant electromagnetic field can be presented as a superposition of two traveling waves having equal amplitudes. Total electromagnetic field (both its rotational and potential components) in the inner and outer interaction spaces can be written in the form [5]:

$$\vec{E}_{i,o}(\vec{r}.t) = \sum_r (C_{+r}\vec{E}_{+r} + C_{-r}\vec{E}_{-r}) - grad\ \Phi_{i,o}\ , \qquad (1)$$

where $$C_{+r} = -\frac{i}{2(\omega - \omega_r)}\frac{1}{N_r}\int_V \vec{J}_e^{\,i}\vec{E}_{+r}dV \quad ; \qquad (2)$$

$$C_{-r} = -\frac{i}{2(\omega + \omega_r)}\frac{1}{N_r}\int_V \vec{J}_e^{\,o}\vec{E}_{-r}dV \quad ; \qquad (3)$$

The expressions (2) and (3) are the equations of excitation. Their solution allows to find the rotational component of electromagnetic field and to determine the change in time of the amplitudes and phases of electromagnetic waves propagating in the opposite directions. For the calculation of the space-charge field (potential component of electromagnetic field), it is necessary to solve a Poisson equation in the inner and outer regions of the interaction space.

$$\frac{1}{r}\frac{\partial}{\partial r}\left(\frac{\partial \Phi_{i,o}}{\partial r}\right) + \frac{1}{r}\frac{\partial^2 \Phi_{i,o}}{\partial \varphi^2} + \frac{\partial^2 \Phi_{i,o}}{\partial z^2} = \frac{\rho_{i,o}}{\varepsilon_0} \quad . \qquad (4)$$

Solution of equations (2), (3) and (4) enable us to calculate a total electromagnetic field in the interaction spaces of the tube. The final stage of computer modelling of the physical processes in combined magnetron is a solution of equations of motion for two (inner and outer) electron beams

$$\frac{d\vec{u}^{\,i,o}}{dt} = \eta(\vec{\tilde{E}}_{i,o}(\vec{r},t) + \vec{E}_0^{\,i,o} + \left[\vec{u}^{\,i,o} \times \vec{B}_0^{\,i,o}\right]) \qquad (5)$$

Thus, in this work we have considered a self-consistent system of integro-differential equations, which can be used in a non-linear analysis of the physical processes in combined magnetron. Besides, we have analyzed the features of magnetron operation.

REFERENCES

[1] Churyumov G.I., Sergeev G.I. New concepts of development of crossed-field microwave devices with azimuthal symmetry. *Proc. 8-th Int. Symp.Non-Linear Electromagnetic Systems (ISEM-97).* 12-14 May, Braunschweig, 1997, p. 295-296.

[2] Churyumov G.I., Sergeev G.I. Simulation and modelling of self-modulated re-entrant beam crossed-field amplifier. *IEEE Trans. Electron Devices*, vol. 46, May 1999, pp. 1063-1069.

[3] Frolova T.I., Churyumov G.I., Sergeev G.I Computer modelling of the electron-wave interaction in combined magnetron. *Proc. 1-st Int. Vacuum Electronics Conference (IVEC'2000).* 2-4 May, Monterey, 2000. pp. 551-554.

[4] Yu S.P., Kooyers G.P., Buneman O. Time-depend computer analysis of electron-wave interection in crossed field, *J. Appl. Physics*, 1965, vol.36, ¹ 8, p.2550-2559.

[5] Vaynshteyn L.A., Solnthev V.A. *Lectures on Microwave Electronics,* Moscow: Sov. Radio, 1973 (in Russian).

EFFECTIVE ELECTROMAGNETIC PARAMETERS OF STRONGLY FLUCTUATING STATISTICALLY LAYERED BIANISOTROPIC MEDIUM

A.V. Malyuskin , M. P. Perepechai, S. N. Shulga

Kharkov National University, Department of Theoretical Radiophysics
4 Svobody Sq., 61077 Kharkiv, Ukraine
e-mail: Alexander.V.Malyuskin@univer.kharkov.ua

ABSTRACT

The macroscopic electromagnetic (EM) response of a strongly fluctuating statistically layered bianisotropic medium is obtained by using renormalization approach of the strong fluctuation theory. Extending the existing works for anisotropic media, this paper treats the effective constitutive parameters for a statistically layered bianisotropic medium with random permittivity and permeability dyads and random tensors of magneto-electric coupling.

INTRODUCTION

The principal element of multiple-scattering theory for an EM field in random media is a calculation of effective constitutive parameters (ECP) of a random medium. The ECP describe the properties of a fluctuating medium with respect to a statistically mean field, i.e. the field averaged over fluctuations. Once the ECP are known, one can investigate the propagation of the mean field within a random medium using the methods developed for deterministic media. In this paper we determine ECP of a strongly fluctuating statistically layered bianisotropic medium in terms of deterministic background medium and the correlation functions of random perturbations using renormalized version [1] of the random-medium theory. This work can be thought as an extension of the strong-fluctuation theory of disordered anisotropic media [2] to a more general class of bianisotropic random media.

THEORY

Bianisotropic media represent a wide class of complex linear media with internal magneto-electric coupling between electric and magnetic fields. In a random bianisotropic medium, constitutive relations that connect random time-harmonic: $\exp(-i\omega t)$, electric and magnetic inductions $\vec{D}_r(\vec{R})$, $\vec{B}_r(\vec{R})$ and EM field intensities $\vec{E}_r(\vec{R}), \vec{H}_r(\vec{R})$ have the form

$$\vec{D}_r = \hat{\varepsilon}_r \cdot \vec{E}_r + \hat{\xi}_r \cdot \vec{H}_r , \qquad \vec{B}_r = -\hat{\zeta}_r \cdot \vec{E}_r + \hat{\mu}_r \cdot \vec{H}_r \tag{1}$$

where the $\hat{\varepsilon}_r(\vec{R})$and $\hat{\mu}_r(\vec{R})$ are the random permittivity and permeability tensors, respectively, while $\hat{\xi}_r(\vec{R})$ and $\hat{\zeta}_r(\vec{R})$ are the random tensors of magneto-electric coupling, $\vec{R} = (x, y, z)$. Statistical geometry of the random medium filling the whole space $-\infty < x, y, z < \infty$ is described by statistical moments of all orders for the tensorial complex-valued random fields $\left[\eta_{ik}^{(r)}(\vec{R})\right]$, $\eta = \varepsilon, \mu, \xi, \zeta$. We will consider the fundamental case, where the mean profile $\left|\left\langle \eta_{ik}^{(r)}(\vec{R}) \right\rangle\right|$ is independent of $\vec{r}$, and may depend on z, while for any $n = 2,3,4,...$ and arbitrary admissible choice of indices $j_1, k_1, j_2, k_2, ...$ the n-th

statistical moment $\left\langle \eta_{j_1 k_1}(\vec{R}_1)\eta_{j_2 k_2}(\vec{R}_2)\ldots\eta_{j_n k_n}(\vec{R}_n)\right\rangle$ should depend on $z_1, z_2, z_3, \ldots, z_n$ and the differences $r_1 - r_2, r_2 - r_3$ only, $\vec{r} = (x, y, 0)$.

The following investigation will be performed using convenient six-vector formalism [3], which have been extensively applied in studying EM phenomena in bianisotropic media. In the six-vector notation (1) can be rewritten in compact form

$$\mathbf{d}_r = \mathbf{M}_r \cdot \mathbf{e}_r \tag{2}$$

Here, the 6-vectors $\mathbf{d}_r, \mathbf{e}_r$ and the 6-dyad $\mathbf{M}_r$ are determined as

$$\mathbf{d}_r = \begin{bmatrix} \vec{D}_r(\vec{R}) \\ \vec{B}_r(\vec{R}) \end{bmatrix}, \qquad \mathbf{e}_r = \begin{bmatrix} \vec{E}_r(\vec{R}) \\ \vec{H}_r(\vec{R}) \end{bmatrix}, \qquad \mathbf{M}_r = \begin{bmatrix} \hat{\varepsilon}_r & \hat{\xi}_r \\ -\hat{\zeta}_r & \hat{\mu}_r \end{bmatrix}$$

The 6-dyad $\mathbf{M}_e$ of the ECP is defined by the conventional identity [1,2]

$$\left\langle \mathbf{M}_r(\vec{R}) \cdot \mathbf{e}_r(\vec{R}) \right\rangle \equiv \mathbf{M}_e \cdot \left\langle \mathbf{e}_r(\vec{R}) \right\rangle \tag{3}$$

In line with the renormalization approach of the strong-fluctuation theory, introduce a deterministic background bianisotropic medium with constitutive parameters $\hat{\varepsilon}(z), \hat{\zeta}(z), \hat{\xi}(z), \hat{\mu}(z)$ which form the 6-dyad $\mathbf{M}$. The 6-vector EM field $\mathbf{e}_b(\vec{R})$ created in such medium by impressed 6-vector sources $\mathbf{j}(\vec{R})$ can be represented in terms of the 6-dyadic Green's function of the background medium $\mathbf{G}(\vec{R}, \vec{R}')$

$$\mathbf{e}_b = \frac{4\pi}{c} \int \mathbf{G}(\vec{R}, \vec{R}') \cdot \mathbf{j}(\vec{R}') d\vec{R}' \tag{4}$$

The key detail of the theory is a regularized representation of the Green's 6-dyadic

$$\mathbf{G}(\vec{R}, \vec{R}') = (1/ik_0)\mathbf{G}^{(s)} \delta(\vec{R} - \vec{R}') + \mathbf{G}^{(rg)}(\vec{R}, \vec{R}') \tag{5}$$

that was established in [4]. In (5), the first term corresponds to the singular part of the Green dyadic, $\mathbf{G}^{(s)}$ is a constant 6-dyadic, and the second term is the regular part of the Green dyadic. The thorough discussion of regularization procedure a reader can found in [4]. Treating the random medium as a perturbation of the background medium one can establish an equivalence between the original excitation problem for stochastic EM field and the integral equation [1, 2]

$$\mathbf{f}(\vec{R}) = \mathbf{e}_b(\vec{R}) - ik_0 \int d\vec{R}' \mathbf{G}^{(rg)}(\vec{R}, \vec{R}') \cdot \mathbf{K}(\vec{R}') \cdot \mathbf{f}(\vec{R}') \tag{6}$$

with respect to a new 6-vector field variable $\mathbf{f}$

$$\mathbf{f}(\vec{R}) = \left[\mathbf{I} + \mathbf{G}^{(s)} \cdot (\mathbf{M}_r - \mathbf{M})\right] \cdot \mathbf{e}_r(\vec{R}) \tag{7}$$

and random 6-dyad perturbation

$$\mathbf{K} = (\mathbf{M}_r - \mathbf{M}) \cdot \left[\mathbf{I} + \mathbf{G}^{(s)} \cdot (\mathbf{M}_r - \mathbf{M})\right]^{-1} \tag{8}$$

where $\mathbf{I}$ is the identity 6-dyad. Introduce an auxiliary 6-dyad $\mathbf{K}_e$ by the identity

$$\left\langle \mathbf{K} \cdot \mathbf{f} \right\rangle \equiv \mathbf{K}_e \cdot \left\langle \mathbf{f} \right\rangle \tag{9}$$

From (7), (8) and (9) one can obtain the relation between $\mathbf{K}_e$ and the ECP 6-dyad $\mathbf{M}_e$

$$\mathbf{M}_e - \mathbf{M} = \mathbf{K}_e + \mathbf{K}_e \cdot \mathbf{G}^{(s)} \cdot (\mathbf{M}_e - \mathbf{M}) \tag{10}$$

Using the solution of (6) $\mathbf{f} = \left[\mathbf{I} + ik_0 \mathbf{G}^{(rg)} \cdot \mathbf{K}\right]^{-1} \cdot \mathbf{e}_b$ in (9), $\mathbf{G}^{(rg)} \equiv \int d\vec{R}' \mathbf{G}^{(rg)}(\vec{R}, \vec{R}') \cdot \ldots$ is the integral operator with the 6-dyad kernel $\mathbf{G}^{(rg)}(\vec{R}, \vec{R}')$, we obtain the solution for $\mathbf{K}_e$

$$\mathbf{K}_e = \mathbf{T}\cdot\left\langle \left(\mathbf{I}+ik_0\,\mathbf{G}^{(rg)}\cdot\mathbf{K}\right)^{-1}\right\rangle^{-1} \tag{11}$$

in terms of the so-called transition operator [5]

$$\mathbf{T} = \left\langle \mathbf{K}\cdot\left(\mathbf{I}+ik_0\,\mathbf{G}^{(rg)}\cdot\mathbf{K}\right)^{-1}\right\rangle \tag{12}$$

Unfortunately, the exact expression (11) does not bring the final result because of practical impossibility to invert the relevant operators in (11) and (12) both rigorously and in closed form. A feasible representation for $\mathbf{K}_e$ can be obtained via expanding the right-hand side of (11) in powers of $\mathbf{K}$

$$\mathbf{K}_e = \langle\mathbf{K}\rangle + (ik_0)^2\left[\langle\mathbf{K}\rangle\cdot\mathbf{G}^{(rg)}\cdot\langle\mathbf{K}\rangle - \langle\mathbf{K}\cdot\mathbf{G}^{(rg)}\cdot\mathbf{K}\rangle\right] + \ldots \tag{13}$$

To assure the fastest rate of convergence of this series, a requirement $\langle\mathbf{K}\rangle \equiv 0$ must be imposed. This provides also elimination of secular terms, i.e. terms, including at least one mean value $\langle\mathbf{K}\rangle$ as a multiplier. Condition $\langle\mathbf{K}\rangle \equiv 0$ specifies the constitutive parameters of the background medium that remain unspecified yet. Indeed, due to (8)

$$\left\langle(\mathbf{M}_r-\mathbf{M})\cdot\left[\mathbf{I}+\mathbf{G}^{(s)}\cdot(\mathbf{M}_r-\mathbf{M})\right]^{-1}\right\rangle \equiv 0 \tag{14}$$

holds. Equation (14) can be easily solved via straightforward manipulations. Reconsidering expansion (13) we may write it in compact form

$$\mathbf{K}_e = \sum_{n=2}^{\infty}\mathbf{K}_e^{(n)} \tag{15}$$

$$\mathbf{K}_e^{(2)} = \langle\mathbf{V}\cdot\mathbf{K}\rangle = -ik_0\langle\mathbf{K}\cdot\mathbf{G}^{(rg)}\cdot\mathbf{K}\rangle, \qquad \mathbf{K}_e^{(3)} = \langle\mathbf{V}^2\cdot\mathbf{K}\rangle = -k_0^2\langle\mathbf{K}\cdot\mathbf{G}^{(rg)}\cdot\mathbf{K}\cdot\mathbf{G}^{(rg)}\cdot\mathbf{K}\rangle$$

$$\mathbf{K}_e^{(n)} = \langle\mathbf{V}^{n-1}\cdot\mathbf{K}\rangle - \sum_{m=2}^{n-2}\langle\mathbf{V}^m\rangle\cdot\mathbf{K}_e^{(n-m)}, \quad n = 4,5,6,\ldots, \qquad \mathbf{V} = -ik_0\,\mathbf{K}\cdot\mathbf{G}^{(rg)}$$

Due to relation (10) analogous expressions arise for the ECP

$$\mathbf{M}_e = \mathbf{M}+\tilde{\mathbf{M}} \qquad \tilde{\mathbf{M}} = \sum_{n=2}^{\infty}\tilde{\mathbf{M}}^{(n)} \tag{16}$$

$$\tilde{\mathbf{M}}^{(2,3)} = \mathbf{K}_e^{(2,3)} \qquad \tilde{\mathbf{M}}^{(n)} = \mathbf{K}_e^{(n)} + \sum_{m=2}^{n-2}\mathbf{K}_e^{(m)}\cdot\mathbf{G}^{(s)}\cdot\tilde{\mathbf{M}}^{(n-m)}, \qquad n = 4,5,6,\ldots$$

Representation (16) constitutes the product of our study. It is clear from the analysis that local component of the ECP coincides with the constitutive parameters of the background medium while arising due to perturbations non-local components of the ECP are given by the 6-dyad $\tilde{\mathbf{M}}$.

REFERENCES

[1] N. P. Zhuck, *Phys. Rev. B*, vol. 51, N. 21, p. 15636, 1994.

[2] N. P. Zhuck , *Journ. Electromagn. Waves Appl.* N. 7, p. 1653, 1993.

[3] I. V. Lindell, A. H. Sihvola, K. Suchy, *Journ. Electromagn. Waves Appl.* N. 7, p. 1653, 1993.

[4] N. P. Zhuck, A. S. Omar, *Progress in Electromagnetic Research*, vol. 12, Ch. 10, p. 219, 1997

[5] M. Lax, *Rev. Mod. Phys.*, vol. 23, N. 4, p. 287, 1951.

REFLECTION OF A LASER BEAM FROM A GYROMAGNETIC LAYER WITH A MAGNETO-DIELECTRIC SUBSTRATE

Dimrity N. Goryushko*, and Alexander A. Shmat'ko**
Kharkov National University, Faculty of Radio Physics

* Ukraine, 61184, Kharkov, Kork st., 44, apt. 115
tel. +38 (0572) 20-57-07, E-mail: gor.nipi@ugp.viaduk.net

** Ukraine, 61077, Kharkov, Svobody sq., 4
tel. +38 (0572) 45-71-33, E-mail: Alexandr.A.Shmatko@univer.kharkov.ua

ABSTRACT

For the control of laser beam characteristics by means of electrical method, the gyromagnetic films fixed on a dielectric substrate can be used. The beam scattering on such a structure is considered. The spatial distribution of the reflected field in the cross-section is obtained by means of the Fourier analysis.

BASIC PART

Wave beams are the eigenwaves of laser sources and other optoelectronic devices. In such systems, a gyromagnetic film fixed on a dielectric layer can be used as a control e0lement. With the aid of magnetic field applied to the gyromagnetic sample it is possible to modify the parameters of reflected and transmitted beams: the shape of the beam, its curvature and amplitude, direction of the axis of propagation, the magnitude of lateral displacement, etc.

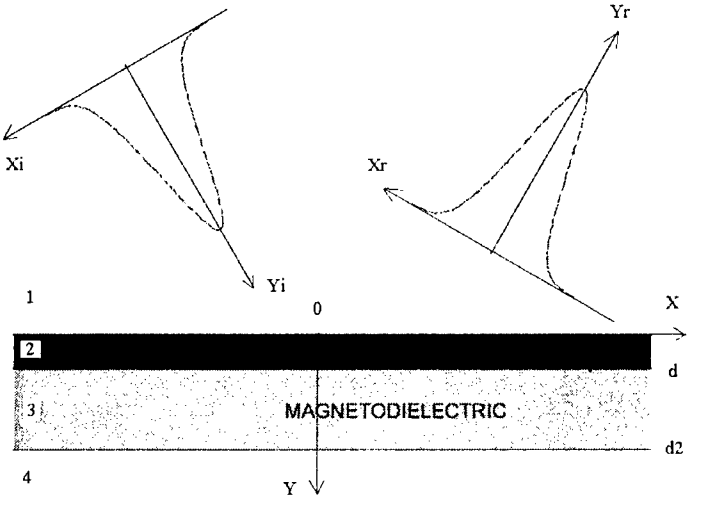

Fig. 1. The wave beam scattering on the two-layer structure

A two-dimensional problem of the scattering of electromagnetic field of the realistic apertures in the form of a wave beam on a gyromagnetic ferrite film fixed on a magneto-dielectric layer (fig. 1) is solved. It is formulated for the equation

$$(\Delta + \kappa^2 \varepsilon \mu_\perp) E_Z = 0, \qquad (1)$$

where $\mu_{\perp} = \mu_T - \frac{\alpha^2}{\mu_T}$, for ferrite $\hat{\mu} = \begin{vmatrix} \mu_T & -i\alpha & 0 \\ i\alpha & \mu_T & 0 \\ 0 & 0 & \mu_L \end{vmatrix}$.

As the incident fields, the wave beams with Gaussian (2) and cosine (3) field distributions in the cross-section are chosen:

$$E^i_Z(x_i,0) = \frac{e^{-(x_i/w)^2}}{\sqrt{\pi}w} \qquad (2)$$

$$E^i_Z(x_i,0) = \begin{cases} \cos(\pi x_i / w), & |x_i| \le w/2 \\ 0 \quad , & |x_i| > w/2 \end{cases} \qquad (3)$$

The EZ- polarization of the initial field is considered, as the case of the HZ- polarization does not lead to new phenomena. The solution of the problem is carried out by means of the spectral method with the application of the Fourier analysis. The spectral method enables one to simplify the problem. The field of the incident wave beam is represented as a superposition of partial plane monochromatic waves with varying amplitudes that are incident on the studied structure under different angles, and thus the original problem is reduced to the problem of scattering of a partial plane electromagnetic wave with specific amplitude on the considered structure. Expression for the reflection coefficient of a plane electromagnetic wave from a multilayer magneto-dielectric structure is known [3]. The presence of gyrotropy in one of the layers (gyromagnetic film) results in significant modification of the expression for the plane wave reflection coefficient and, as a result, in changing the transmitted and scattered fields characteristics. An analytical expression for the reflection coefficient of a plane wave from the studied structure is found and, with the aid of the Fourier analysis, the spatial distribution of the scattered field for two types of the incident field is obtained. In the scattering of the fields of realistic apertures, a number of phenomena is observed, namely: deformation of the field with the distance, lateral and angular displacement of the beam axis, etc. These phenomena, as the analysis shows, are mainly connected to the angular dependence of the phase and amplitude of the reflection (transmission) coefficient.

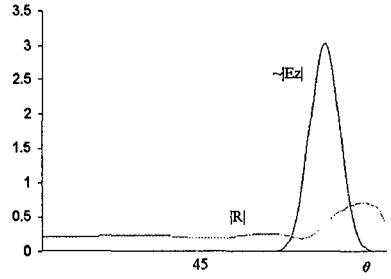

Fig.2. The form of the initial gaussian field spatial distribution and the absolute value of the reflection coefficient

The presence of gyrotropy essentially changes the spatial structure of the fields. As an example, two kinds of initial field distribution are considered and the main features of their form change during the reflection from a gyromagnetic film with a magneto-dielectric substrate are established. In Figs. 4a and 4b, the spatial distributions of the field in the cross-section of the reflected wave beam for different parameters of magnetization α are shown (parameter α depends on the value of the magnetization field). As the figures demonstrate, at the increasing of the magnetizing field value the magnitude of the angular displacement of the beam axis is increased, that is connected to the much stronger angular phase change of the

Fig.3. Spatial field distribution in the cross-section for the cosine field distribution for $\theta=55°,\alpha=0.3,\mu_T=1.9,\varepsilon_F=5,\varepsilon 1=\varepsilon 4=\mu 1=\mu 4=1,\varepsilon 3=3.6,\mu 3=5,d/\lambda=3/20,d2=10\lambda$, a) $w=5\lambda$, b) $w=3\lambda$.

scattered on the ferrite film field as compared to the magneto-dielectric substrate. Sometimes (Fig. 4a), the splitting of the beam on several beams can be observed. Depending on the ratio between the wavelength and the width of the laser beam, the oscillations of the field envelope can be observed (Figs. 3a, 3b), their amplitude and form varying with the propagation of the field from the structure. Thus, by changing parameters of a gyrotropic film, namely, adjusting the magnitude of the magnetization field, it is possible to change the amplitude and the phase of reflection (transmission) coefficient of the plane wave. This can be used for efficient beam control in the laser and optoelectronic devices.

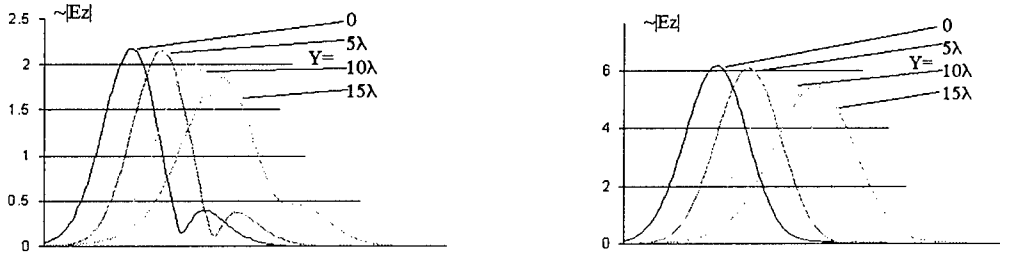

Fig.4. Spatial field distribution in the cross-section of the gaussian beam for ($\theta=49°,\mu_T=1.9,\varepsilon_F=5,\varepsilon 1=\varepsilon 4=\mu 1=\mu 4=1,\varepsilon 3=3.6,\mu 3=5,d/\lambda=3/20,d2=10\lambda,w=3\lambda$) a) $\alpha=0.1$, b) $\alpha=1.1$

REFERENCES

[1] R.P. Riesz and R. Simon, "Reflection of a gaussian beam from a dielectric slab", *J. Opt. Soc. Am.* Vol.2, No.11, (1985)

[2] T. Tamir and H.L. Bertoni, "Lateral displacement of optical beams at multilayered and periodic structures", *J. Opt. Soc. Am.* 61, 1397-1413, (1971)

[3] L.M. Brekhovskikh, *Waves in Layered Media,* Moscow: AN SSSR Publ., 1957 (in Russian).

AUTHORS LIST

G

H

I

J

K

L

M

N

O

P

R

S

T

U

V

W

Y

Z

Signed for print 11.08.2000.
Format 60x84/8. Edition 100 copies. Volume 1.
Order no. M-2-250700.

Prepared and printed by the KONTRAST Publishing Center
Prospekt Lenina 38, room 5, Kharkov, 61166, Ukraine
t./f. +380-572-194913, t. +380-572-304391

AD NUMBER	DATE	DTIC ACCESSION NOTICE

1. REPORT IDENTIFYING INFORMATION

A. ORIGINATING AGENCY

National Academy of Sciences

B. REPORT TITLE AND/OR NUMBER

MINET 2000 Drill Conference

C. MONITOR REPORT NUMBER

8915 EE 02

D. PREPARED UNDER CONTRACT NUMBER

N62101-00-M-E175

2. DISTRIBUTION STATEMENT

APPROVED FOR PUBLIC RELEASE

DISTRIBUTION UNLIMITED

PROCEEDINGS

RE

1. I

2. C

3. A

4. L

5. D

DT

1. A

2. I

DTIC

OCT 95

TIONS ARE OBSOLETE